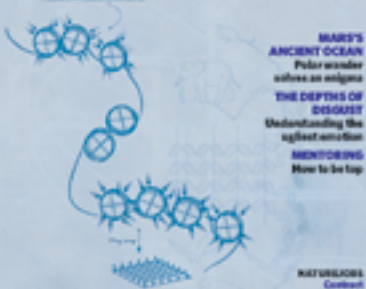


# nature

Volume 447 Number 7147



MAESTRO'S  
ANCIENT OCEAN

Polar wanderer  
wakes an ancient

THE DEPTHS OF  
DISJOINT

Understanding the  
biggest omission

MENTORING  
How to be top

NATUREJOBS

Contract  
research

## DECODING THE BLUEPRINT

The ENCODE pilot maps  
human genome function

## Evolution and the brain

With all deference to the sensibilities of religious people, the idea that man was created in the image of God can surely be put aside.

The vast majority of scientists, and the majority of religious people, see little potential for pleasure or progress in the conflicts between religion and science that are regularly fanned into flame by a relatively small number on both sides of the debate. Many scientists are religious, and perceive no conflict between the values of their science — values that insist on disinterested, objective inquiry into the nature of the Universe — and those of their faith.

But there are lines that should not be crossed, and in a recent defence of his beliefs and disbeliefs in the matter of evolution, US Senator Sam Brownback (Republican, Kansas) crosses at least one. Senator Brownback was one of three Republican presidential candidates who, in a recent debate, described himself as not believing in evolution. He sought to explain his position with greater nuance in a 31 May article in *The New York Times*, in which he wrote: "Man was not an accident and reflects an image and likeness unique in the created order. Those aspects of evolutionary theory compatible with this truth are a welcome addition to human knowledge. Aspects of these theories that undermine this truth, however, should be firmly rejected as atheistic theology posing as science."

Humans evolved, body and mind, from earlier primates. The ways in which humans think reflect this heritage as surely as the ways in which their limbs are articulated, their immune systems attack viruses and the cones in their eyes process coloured light. This applies not just to the way in which our neurons fire, but also to various aspects of our moral thought, as we report this week in a News Feature on the moral connotations of disgust (see page 768). The way that disgust functions in our lives and shapes our moral decisions reflects not just cultural training, but also biological evolution. Current theorizing on this topic, although fascinating, may be wide of the mark. But its basis in the idea that human minds are the product of evolution is not atheistic theology. It is unassailable fact.

This does not utterly invalidate the idea that the human mind is, as Senator Brownback would have it, a reflection of the mind of God. But the suggestion that any entity capable of creating the Universe has a mind encumbered with the same emotional structures and perceptual framework as that of an upright ape adapted to living in small, intensely social peer-groups on the African savannah seems a priori unlikely.

In Brownback's defence, it should be acknowledged that these are deep waters. It is fairly easy to accept the truth of evolution when it applies to the external world — the adaptation of the orchid to wasps, for example, or the speed of the cheetah.

It is much harder to accept it internally — to accept that our feelings, intuitions, the ways in which we love and loathe, are the product of experience, evolution and culture alone. And such acceptance has challenges for the unbeliever, too. Moral philosophers often put great store by their rejection of the 'naturalistic fallacy', the belief that because something is a particular way, it ought to be that way. Now we learn that untutored beliefs about 'what ought to be' do, in fact, reflect an 'is': the state of the human mind as an evolved entity. Accepting this represents a challenge that few as yet have really grappled with.

It remains uncertain how the new sciences of human behaviour emerging at the intersections of anthropology, evolutionary biology and neuropsychology can best be navigated. But that does not justify their denunciation on the basis of religious faith alone. Scientific theories of human nature may be discomforting or unsatisfying, but they are not illegitimate. And serious attempts to frame them will reflect the origins of the human mind in biological and cultural evolution, without reference to a divine creation. ■

**"Scientific theories of human nature may be discomforting or unsatisfying, but they are not illegitimate."**

## Academic diversity

US universities must act to recruit and retain minority faculty members.

The diversity of the typical American research university is widely admired, but is fashioned mainly on the basis of students and staff recruited from abroad. The universities have done less well at harnessing the talents of the racial minorities within the US population.

So-called under-represented minorities — African Americans, Latinos and Native Americans — formed more than a quarter of the American population in 2000, and are projected to account for more than 40% of it by 2050. Yet according to a 2005 study of 50 élite universities, undertaken by Donna Nelson, a chemist at the University of

Oklahoma, they account for only 3% of tenured or untenured faculty in mathematics, physics, chemistry, biology and astronomy. Numbers are only slightly higher in engineering (4.6%).

Sharp economic divisions between whites and minorities in the United States makes it unlikely that any solutions confined to academia itself will ever achieve parity. It remains the case, however, that universities and their science departments could be doing more to enrich the diversity of their faculty.

Departments often pin the blame for the lack of minority recruitment on the small 'pipeline' of minority PhD holders, saying that universities compete for the few qualified minority candidates available. That line of thinking has contributed to the emphasis on boosting the flow of minorities through PhD programmes, and several laudable mentoring and fellowship initiatives, such as the Ford fellowships, exist to do that. But studies show clearly that faculty diversity has

not kept pace with increasing diversity in the PhD pool.

One aspect of the problem concerns the tendency of departments to go out of their way to recruit minority candidates only to replace previous minority representation. In one study of science and engineering departments in 27 universities, of 1,500 faculty hired during 2000–04, only 157 were African American, Latino or Native American. But nearly three out of five of the new hirings merely replaced minority faculty members who had left the institution.

This is the proverbial 'revolving door' in action. Under-represented minorities are brought in as assistant professors, sometimes through special programmes that aim to improve diversity, only to leave shortly thereafter. Universities that focus on recruitment without placing equal emphasis on retention are not going to achieve the diversity that they seek.

Any successful assault on the persistent problems that universities have faced in nurturing diversity is likely to require the active involvement of under-represented minority faculty themselves. But this group is hard to unify, comprising as it does people who hail from disparate backgrounds and who are shaped by different experiences and social pressures. It can be hard to unite such a diverse group behind a single

cause, yet their ranks are so small that full participation is crucial.

Discrimination, where it exists, may be hard to prove in individual cases, but can be identified by collecting appropriate, campus-wide data. Universities need to keep careful track not just of how many under-represented minority researchers they hire, but of how long they stay. The 27-university study found that institutions were rarely tracking data about departures alongside data about hiring.

Tenured faculty members must also learn to recognize the modern face of racial discrimination. This can take many subtle forms: neglecting to recommend a minority colleague to speak at a conference, subconsciously assuming that a minority researcher has a lesser role in a collaboration, or failing to recognize the added time a minority assistant professor may spend advising minority students.

The controversy at the Massachusetts Institute of Technology (MIT) over biological engineer James Sherley's tenure (see page 762) has pushed the institute to embark on a new study that will evaluate racial disparities among its faculty. It is a project that MIT has discussed but left undone for years, and a step that could sensibly be followed by other leading universities. It shouldn't take a hunger strike to prod them into action. ■

## Mentors of tomorrow

**Everyone knows bad peer review when they come across it — but too few are nurturing good referees.**

There is nothing more infuriating: you are an experienced scientist who has sent one of your best-ever papers to a journal, and what do you get back? A set of referees' comments that appals you. One reviewer asserts that the work is simply uninteresting and insufficiently original. Another displays wilful bias in relating their criticisms to results by a competitor whose outlook differs radically from yours. And a third has unreasonable expectations of what should be achieved. Not only are you upset, but your student co-author is devastated.

Such a trio of inadequate referees' reports would rightly make an author doubt the credibility of the editor, who has a duty to ensure fair play. But they might also give the offended author reason to reflect a little. What right has he or she to expect a high quality of peer review? What training is being given in his or her own lab to ensure that the next generation understands how to do a good job of critically appraising others' work? And as the pressures on researchers grow — bureaucracy from institutions and funding agencies, incentives to apply the outcomes of research — the very motivation to do a conscientious job of peer review is itself under pressure.

The fact is that the skills required to be a conscientious peer reviewer cannot and should not be taken for granted in young scientists. The culture of peer review is hugely variable — some heads of research groups take such training seriously, others do nothing. A more robust culture of good refereeing needs to be sustained — and that needs strong mentors.

*Nature* has for some years campaigned for good mentoring in the

laboratory, particularly through a set of awards introduced in 2005 (see [www.nature.com/npg/\\_community/nature\\_awards.html](http://www.nature.com/npg/_community/nature_awards.html); the entry period for this year's awards, which are for researchers in South Africa, closes this week). On page 791, we publish a guide to all aspects of mentoring, derived from the diverse and very specific endorsements of good practice received through the nominations process.

Many of the goals of mentoring are self-evident. But the explicit fostering of ethics in the lab is rare. And ethical practice includes doing justice to other researchers in critically assessing their work.

So what are the elements of good peer review? The most important aspect is attitude, which should be one of constructive objectivity. This includes not only avoiding scientific bias, but also leaving behind any preconceptions about the labs in which the work was done.

The content should be constructive, too. To summarize the paper and highlight its strengths and essential significance not only shows a proper sense of engagement, but also helps both author and editor to benefit from a fresh perspective. But it is in making critical comment that a referee genuinely adds value, provided that such comments are constructively and collegially expressed. If there are experimental weaknesses or alternative interpretations, it helps to suggest experiments to strengthen the case or resolve ambiguities. If inadequate credit is given to previous work or if the paper fundamentally lacks originality, it is a good idea to provide appropriate references.

This may all seem obvious to the experienced reviewer. (Readers can find more on good peer review, and can comment on it and on this Editorial, at <http://blogs.nature.com/peer-to-peer>.) But it is only by careful oversight of a young scientist's attempts at reviewing real papers that the benefits of this experience can be passed on. *Nature* and *Nature* journals encourage the involvement of younger scientists by a referee, provided the authors' need for confidentiality is respected and the additional reviewer identified. Such mentoring should be routine in research team leadership, if standards are to be kept high. ■

# RESEARCH HIGHLIGHTS

## What makes a queen?

PLoS One 2, e509 (2007)

What makes a queen a queen, and a worker a worker? For honey bees (*Apis mellifera*) the answer is now clear: an enzyme called target of rapamycin (TOR) helps to create the sharp division between castes. TOR is involved in nutrient-sensing and growth control.

Gro Amdam of Arizona State University in Tempe and her colleagues found that expression of the gene that encodes for TOR was higher in honey-bee larvae destined to become queens than in those destined to be workers. Moreover, when TOR was blocked chemically or genetically, larvae developed traits of worker bees.



K. WOTH/PHOTOLIBRARY.COM

## PHYSIOLOGY

### Itching for relief

Science 316, 1494–1497 (2007)

For some it's a chance encounter with poison ivy; for others it's an ongoing struggle with latex sensitivity. Whatever the source, the itchy agony of contact dermatitis is a familiar ailment. Now, researchers suggest that relief could come from the compounds, called cannabinoids, that give marijuana its mind-altering properties.

Thomas Tüting and Andreas Zimmer of the University of Bonn in Germany and their team showed that inhibiting cannabinoid receptors — either genetically or chemically — enhances skin hypersensitivity to allergens in mice. Applying topical cannabinoids or inhibiting an enzyme that degrades endogenous cannabinoids relieves the inflammation associated with allergic dermatitis.

## METABOLISM

### Hunger linked to fidgeting

Cell Metab. 5, 450–463 (2007)

Scientists have identified a molecular link between feeling hungry and fidgetiness: a transcription factor known as *Bsx*. This could be a target for combating obesity, they say.

Mathias Treier from the European Molecular Biology Laboratory in Heidelberg, Germany, and his colleagues showed that *Bsx* regulates in mice both the level of spontaneous physical activity and two brain peptides that regulate how much the mice eat. Mice lacking *Bsx* moved less and showed different eating behaviours.

The *Bsx* gene is conserved across species, so may also be involved in energy balance in humans. The scientists speculate that mutations in *Bsx* may explain why some

over-eaters become obese whereas others do not: people with normal copies of the gene may be better at matching their activity levels to their food intake.

## VIROLOGY

### Stowaway

PLoS Pathog. 3, e75 (2007)

A genetic study suggests that the yellow fever virus reached South America from western Africa some 300 to 400 years ago, probably in ships carrying slaves.

Juliet Bryant and Alan Barrett of the University of Texas in Galveston and their colleague analysed 133 samples of yellow fever virus, taken from 22 countries over 76 years.

By comparing the viruses' RNA sequences, the team showed that South American strains are more closely related to those in western



Africa than either group is to those in eastern Africa. The viruses can be traced back to an ancestral strain that existed in Africa within the past 1,500 years.

## CLIMATE SCIENCE

### Precarious on reflection

Proc. Natl Acad. Sci. USA 104, 9949–9954 (2007)

A world in which greenhouse warming was offset by human interventions could end up a drier, more precarious place, models predict.

H. Damon Matthews and Ken Caldeira at the Carnegie Institution in Stanford, California, modelled changes in climate due to increased greenhouse gases with and without 'geoengineering' interventions, such as the addition of dust to the stratosphere to reflect sunlight back into space. The models show that geoengineering could prevent the world's average temperature from rising, but it would produce drier continents than seen today or in models with no such intervention.

If geoengineering efforts were started but then failed or were abandoned, and carbon dioxide emissions had continued throughout, climate shifts could be abrupt and severe, with warming taking place at up to 4 °C per decade.

## CANCER BIOLOGY

### Deactivate to defend

Cell 129, 969–982 (2007)

Researchers have found that PP2A proteins defend against cancer by turning down the activity of a cancer-promoting enzyme.

Many tumours have mutated forms of proteins from the PP2A family, which regulate other proteins by removing phosphate groups. Some of the cancer-linked mutations are in a particular part of PP2A (the A $\beta$  subunit), the role of which in cancer wasn't understood.

BETTMANN/CORBIS

William Hahn's group at the Dana-Farber Cancer Institute in Boston, Massachusetts, used RNA silencing to prove that cells with the mutated subunit became cancerous. They next used mass spectrometry to identify which cellular proteins bind only to this subunit. One protein did: the enzyme GTPase RalA, which has already been linked to cancer. The team then found evidence that the A<sub>β</sub> subunit deactivates the enzyme, implying that the subunit is a bona fide tumour suppressor.

#### MATERIALS SCIENCE

### Let's twist again

Angew. Chem. Int. Edn doi:10.1002/anie.200700708 (2007)

Researchers in Japan have introduced a new twist, quite literally, to the control of light.

Masaki Horie of the RIKEN Institute of Physical and Chemical Research in Saitama, Kohtaro Osakada of the Tokyo Institute of Technology and their colleagues made a molecular crystal from rotaxanes, which consist of molecular chains threaded through hoops.

The crystal's colour switched from green to orange when its temperature was pushed above 128 °C, accompanied by a change in the way the crystal rotates polarized light. The team attributes this to a phenyl group on the end of each rotaxane's chain that twists out of alignment with phenyls on its hoop.

#### NEUROBIOLOGY

### Brain tangle

Neuron 54, 713–720 (2007)

By combing through the genomes of 1,411 people, researchers have identified a gene that influences an individual's risk of developing late-onset Alzheimer's disease.

One version of the gene — which encodes the protein Gab2 — is protective; another boosts risk of the disease. The gene plays a role only in people who already have an elevated risk of Alzheimer's because they carry a particular form of another gene, known as *APOE*.

Eric Reiman of the Banner Alzheimer's Institute and Dietrich Stephan of the Translational Genomics Research Institute, both in Phoenix, Arizona, and their colleagues also show that Gab2 is expressed in brain regions that are susceptible to the neuronal tangles characteristic of Alzheimer's. They propose that Gab2 normally protects against tangles, and that the risky version of the gene produces a dysfunctional form of the protein.

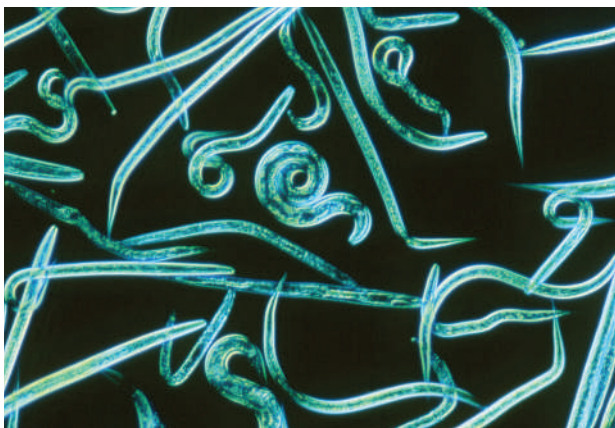
#### DEVELOPMENTAL BIOLOGY

### Worms' talk

Nature Chem. Biol. doi:10.1038/nchembio.2007.3 (2007)

When food runs low or life gets too crowded, the nematode worm *Caenorhabditis elegans* (pictured below) signals to its neighbours that it's time to slow down. The chemical signal — known as the 'dauer' pheromone — causes the worms to stop moving and subsist on stored fat until conditions improve.

Researchers had previously identified one component of the pheromone cocktail, but it did not seem strong enough to trigger the dauer response on its own. Now, Jon Clardy and his colleagues at Harvard Medical School in Boston, Massachusetts, report the isolation of two related compounds. All three are members of a class of sugars called ascarosides, but the most recent pair are about 100 times more effective at triggering the dauer response than the first one found.



S. STAMMERS/SPL

#### NANOTECHNOLOGY

### Miniature painting

Nano Lett. doi:10.1021/nl070462b (2007)

How does one apply a layer of paint one molecule thick to the inside of a tiny hole?

Amit Meller and Meni Wanunu of Boston University, Massachusetts, wanted to do this to turn their nanopores — tiny holes drilled through a sheet of silicon — into smart sensors for detecting single molecules or pH. The coated pores work as sensors because the pore's conductance changes when molecules or ions enter inside and interact with the paint.

For pores with a diameter greater than 10 nanometres, simply dipping the device into a solution of organosilane molecules did the trick, creating a neat and durable layer of organosilanes. The researchers managed to paint smaller pores too, by driving the solution through the hole to prevent clogging.

## JOURNAL CLUB

Robert Langer

Massachusetts Institute of Technology, USA

**A bioengineer sees a future for safe gene-silencing therapies.**

The possibility of treating genetic disorders by modifying gene expression has been an attractive yet elusive goal for decades. Problems with the safety and efficacy of various types of gene therapy have held back progress. In particular, there have been some high-profile failures, including a number of deaths during clinical trials.

But seminal studies reported by Andrew Fire and Craig Mello in 1998 led to a potentially new class of therapeutic agent. These researchers, who went on to share a Nobel prize for their work, found that small pieces of RNA, dubbed siRNAs, can silence genes.

Although switching off genes may have fewer complications than adding new ones, the safe and effective delivery of genetic agents remains a critical challenge. I was therefore pleased to see a recent paper reporting tests of an siRNA-delivery system in monkeys (J. Heidel *et al.* Proc. Natl. Acad. Sci. USA 104, 5715–5721; 2007), suggesting that safe, repeated systemic administration of siRNAs is possible.

Mark Davis of the California Institute of Technology in Pasadena and his colleagues created nanoparticles composed of siRNAs and a novel polymer based on the sugar cyclodextrin. These particles were injected into the monkeys and their health was monitored. The monkeys tolerated multiple doses of siRNA of increasing amounts.

This paper was of interest to me not only because my group works on lipid formations that might serve as delivery systems for siRNA or other genetic agents, but also because I was pleased to see a former student doing well. Jeremy, the first author, once worked in my lab as an undergraduate.

Studies such as this one are bringing back to the field the excitement that surrounded gene therapies in the 1980s.

Discuss this paper at <http://blogs.nature.com/nature/journalclub>

## NEWS

# Can a Saudi university think freely?

Saudi Arabia might seem an unlikely spot for a vibrant new multicultural research university. The kingdom is at or near the bottom of rankings for science and technology research and has one of the world's worst track records on academic freedom, not to mention women's and other human rights.

Despite all this, the country's plans for the multibillion-dollar King Abdullah University of Science and Technology (KAUST) have not only secured the help of a blue-ribbon advisory panel of international academics, but have them gushing with superlatives. They say it could be an entrée into academic freedom in the region when it opens in 2009.

"I'm a tremendous enthusiast," says Frank Rhodes, president emeritus of Cornell University in Ithaca, New York, and a panel member. "It's going to be of enormous significance for the whole Middle East and beyond." Frank Press, president emeritus of the US National Academy of Sciences and another member of the panel, adds: "They might achieve what no one has ever done — build a world-class university in less than a generation. This could be nation-changing."

One reason for such optimism is the scale of the venture. Saudi Arabia currently invests a pittance on research — 0.25% of its GDP. The king's donation is expected to be several billion dollars, making it one of the world's top ten university endowments.

The country will spend another US\$2 billion building a vast campus town on the Red Sea coast 90 kilometres north of Jeddah and \$100 million a year for ten years creating joint labs with top research groups worldwide. The



King Abdullah's money will make KAUST's endowment among the ten biggest worldwide.

graduate university will have interdisciplinary centres instead of departments and will focus on regional interests such as water and energy.

Unlike Saudi Arabia's other state-run universities, KAUST will be managed by independent trustees. Their autonomy will be guaranteed by the endowment, which will be managed abroad by a foundation claimed to be independent of Saudi control. Only a third of the 600 faculty

**"The university is wonderful on paper, but I'm sceptical it will bear fruit."**

members and 2,000 students are expected to be Saudis. "KAUST is not only a signal of interest in international partnerships, but to bring international researchers to the kingdom," says panel member Calestous Juma, an expert in international development at Harvard University. He adds that this signifies an opening up of both science and society in the kingdom.

KAUST has outsourced recruitment to top university departments worldwide, which will get cooperative deals worth millions of dollars annually in return. One appointment will be of particular interest: KAUST's founding president, to be selected by an international committee. What if the committee chooses a woman? "The search is merit-based; if a woman is the best candidate we will have no problem with that," says Mohammed Mulla, a university spokesman.

Members of the search committee say that it may be difficult to find a woman willing to take the post, given the severe restrictions placed on women in the kingdom, but insist that if there is any interference in their choice they will resign.

Reassurance on human rights was a precondition before panel members agreed to take part, says Press. "The Saudis agreed that at this university, this town, there would be no discrimination on sex, religion or ethnicity — that there would be complete freedom."

Some seasoned Middle East watchers are more wary. "The bureaucratic police state will no doubt buy the best scientific equipment and personnel that money can buy,"

## Hawaiian solar telescope meets resistance

Will the world's biggest solar telescope displace the goddess of mist?



Park managers and native Hawaiians are objecting to a plan to build a solar telescope, raised nearly 44 metres above the ground, next to Haleakala National Park on the Hawaiian island of Maui. They say the project could harm endangered species and would erode the value of the region as a natural resource and cultural site.

"The whole purpose of a national park system is to ensure that such places aren't compromised," says Marilyn Parris, the park's superintendent.

T. KERKONAY/K. C. ENVIRONMENTAL/F. RIZZO



## MEETING FOR A PARTY

Famed chemist celebrates 65th birthday by showcasing next generation of scientists.

[www.nature.com/news](http://www.nature.com/news)

AI-LAN LEE

says Ziauddin Sardar, a UK-based writer on the cultures of Islam and science. "But it cannot provide the atmosphere of criticism and openness that scientific research needs to flourish."

"The university sounds wonderful on paper, but I'm sceptical it will bear fruit," adds Nader Fergany, director of the Almishkat Centre for Research in Giza, Egypt. "Saudi Arabia has produced expensive white-elephant universities before." The King Abdulaziz City for Science and Technology, for instance, established in 1977, has not had any significant international impact. And Fergany doubts that the regime can deliver on its promise of autonomy. A first test, he says, will be whether a non-Saudi is allowed to be founding president.

Fergany, who was lead author of the landmark series of Arab Human Development Reports published by the United Nations Development Programme between 2002 and 2005, also doubts that the university represents a move towards greater freedom. "I would be less pessimistic if the kingdom had an overall atmosphere of opening up and reform," he says. "But the restrictions of the regime are so pervasive that an isolated campus on the Red Sea is not going to make an impact on the country."

Another sticking point is relations with Israel, a research powerhouse in the region that shares many interests, such as water, with KAUST. Mulla says that Saudi Arabia cannot cooperate "at the present time" with countries with which it does not have diplomatic relations — which would mean no formal collaboration between KAUST and Israeli institutions.

"It's a delicate issue," says Mulla, and it is being left to the side for the moment. The board has agreed to accept this situation, after receiving assurances that KAUST will be free to recruit Israeli faculty and students. ■

Declan Butler

The proposed Advanced Technology Solar Telescope (ATST) would tower above a cluster of smaller facilities already in use a few hundred metres from the Haleakala summit, traditionally revered by Hawaiians as the home of the mist goddess Lilinoe.

With its four-metre aperture, ATST would be the largest solar telescope ever built, and it is intended to allow solar physicists to better understand the dynamics of the Sun's magnetic field. The project is spearheaded by the National Solar Observatory, and collaborators include the University of Hawaii's Institute for Astronomy

and the US Air Force Research Laboratory. If the \$230-million project wins approval, construction may begin as early as 2009.

Installing the ATST high up, where there is less air turbulence, and in Maui's relatively dust-free, stable atmosphere, would give physicists the best chance of resolving magnetic features on the Sun's surface spanning some 30 kilometres across, explains Craig Foltz, programme manager at the US National Science Foundation. "Believe me, if we could build it smaller and lower, we would," he adds.

But in a letter last month to the

National Science Board, which will need to approve the project, the National Park Service's regional director Jonathan Jarvis argued that replacing Haleakala's summit with a man-made structure as the tallest feature on Maui would completely alter the visitor experience. And with the only access to the observatory site being through the national park, he is worried that construction vehicles will damage the narrow 1930s road and harm endangered nene and 'ua'u bird populations.

Because the Haleakala summit carries cultural and spiritual significance for Hawaiian people,

an added concern is that further development will erode the spiritual value of the mountain top for native Hawaiians.

"We're not against science and the acquisition of knowledge, but science has ethics," says Ed Lindsey, a native Hawaiian and president of Maui Cultural Lands, a Maui-based organization set up to protect and restore Hawaiian cultural resources. "If you destroy things that have meaning to native people, you ultimately destroy the people." Lindsey says Maui Cultural Lands is prepared to file a lawsuit if all else fails. ■

Lucy Odling-Smeet



Tourists still flock to the desert complex that once housed an experiment in self-sustainability.

## Biosphere 2 finds a buyer

The terrarium Biosphere 2 is to become a research conversation piece for a new housing development in Arizona.

Last week, the 1.4-hectare glass enclosure and about 700 hectares of land around it in the desert foothills outside Tucson were sold for US\$50 million. Its new owner, CDO Ranching & Development, is securing permits to build 1,500 houses around the edifice.

The University of Arizona in Tucson is negotiating with the new owners to lease the facility for climate experiments.

Texas oil billionaire Ed Bass spent about \$200 million on the project. In 1991, the glass bubble became the centre of worldwide attention when eight people were sealed inside for a two-year 'experiment' in self-sustainability. But the

project failed — oxygen had to be pumped in from outside, and the experiment ended early amid much squabbling both inside and outside the bubble.

By 1996, Columbia University in New York City had taken over managing the facility. It planned extensive research projects on climate, soil and plant dynamics. But Columbia withdrew from the arrangement at the end of 2003 as part of a litigation settlement with the facility's corporate owner, Decisions Investments.

The University of Arizona had been negotiating for several years to attempt to buy the Biosphere 2 complex, now largely used for tours by the curious. Local politicians also want it preserved as it is a landmark that attracts tourists. ■

Rex Dalton

# Genome project turns up evolutionary surprises

The latest studies of the instructions embedded in the human genome are revealing how evolution has shaped our species.

On page 799 of this issue<sup>1,2</sup>, and in a themed issue of *Genome Research*<sup>3</sup>, scientists report the first findings from a project called ENCODE. This 'encyclopedia of DNA elements' attempts to discover how our cells make sense of the DNA sequence in the human genome. Already, ENCODE is up-ending one piece of conventional scientific wisdom: the idea that biologically relevant DNA resists change over evolutionary time.

ENCODE aims to catalogue all the "functional elements" in the genome — the DNA sequences that control how and when our cells use our genes. Most of these controls seem to be written into so-called non-coding DNA, which does not make a detectable protein product. Because organisms depend on functional elements working correctly, scientists have long thought that such elements should not change much over evolutionary time. So researchers have mostly looked for key functional elements in non-coding DNA that is the same across species, known as conserved or constrained DNA.

But ENCODE is the first project to compare long stretches of non-coding DNA across many mammals, from mice to monkeys to humans. This comparison suggests that evolutionary processes don't always freeze functional DNA in place.

"The fact that we found so much functional

sequence that did not seem to be evolutionarily constrained across all mammals is really surprising," says Elliott Margulies of the National Human Genome Research Institute in Bethesda, Maryland, who co-chaired one of the ENCODE analysis groups.

The finding comes from the ENCODE pilot project, which used multiple methods to collect and analyse data on just 1% of the human genome — not an easy task (see 'Scaling up to a monumental task'). In one part of the project, groups of experimental biologists used a suite of laboratory techniques to find out what portions of the genome might be functional. Meanwhile, groups of computational biologists compared the ENCODE sequences across humans and 28 other animals to find constrained regions of DNA that had changed little throughout evolution.

But when the different groups compared their results, they found that their predictions about key portions of the genome didn't always agree: the biologists' list of functional sequences didn't match the computational group's list of constrained sequences.

At first, many were sceptical of this result, says John Stamatoyannopoulos of the University of Washington in Seattle, a co-chair of one of the ENCODE analysis groups. "It raised some eyebrows," he says. "But eventually all the ENCODE groups started coming out with the same thing." Overall, biologists found no evidence of function for about 40% of the



constrained ENCODE regions. On the flipside, about half of the functional elements found in non-coding DNA were totally unconstrained.

The finding that many constrained regions weren't considered to be functional is not too surprising, because it is unlikely that ENCODE included enough tests on enough different types of cells to capture every major aspect of biology. But the idea that important DNA might also be unstable is newer, and intriguing, because it undermines the assumption that biological function requires evolutionary constraint.

"We're generalizing this principle over mammals, and over many functional elements," says Ewan Birney, head of genome annotation at the European Bioinformatics Institute in Cambridge, UK, and a leader of ENCODE. "We're coming out quite strongly that this is not merely a curiosity of our genome — it's a really important part of the way our genome works."

But how can major components of the mammalian genome change essentially randomly over time? That is not entirely clear. The authors of the ENCODE paper speculate that the unconstrained genomic regions are evolving "neutrally" — that is, they are

## Scaling up to a monumental task

ENCODE, largely funded by the US National Human Genome Research Institute (NHGRI) in Bethesda, Maryland, began in 2003, the year the complete sequence of the human genome was first announced. But if scientists thought that that 13-year quest was difficult, ENCODE could prove even harder, says the NHGRI's Eric Green. "I think sequencing the genome is going to look so easy compared with what ENCODE is trying to accomplish," he says.

ENCODE is now scaling up from its pilot phase to cover

the entire human genome. The pilot showed how challenging this task will be. It involved 308 scientists from 10 countries. But even more dauntingly, it unites scientists from two different scientific cultures — experimental and computational biology. And comparing the results of all the different experiments included in the project proved difficult, because not every lab performs them in exactly the same way.

ENCODE also revealed that the genome is far more

complex than scientists expected. Last month, the NHGRI announced a US\$62.4-million project — modENCODE — to perform ENCODE analyses on the model organisms fruitflies and roundworms<sup>4</sup>. It is hoped that this will help scientists make sense of the data when ENCODE is complete. The NHGRI has already spent \$42.5 million on ENCODE and plans to extend the analysis to the rest of the human genome at a cost of about \$20 million a year.

E.C.



ARCTIC-IMAGES/CORBIS

constantly changing in ways that are neither good nor bad for the individual. This means that, on the whole, many genetic changes simply don't affect overall biology.

This has major consequences for understanding the relationship between genetics and biology, Birney says. "It means, for example, that if you look at some conserved piece of biology — say, how the kidneys work in mice and humans — not all of those bits of biology will be conserved or constrained at the level of the DNA bases, and that's quite a strong shift."

But not everyone agrees with that take. For example, John Mattick at the University of Queensland in Brisbane, Australia, argues that the widely accepted calculation of the baseline, or neutral, rate of mammalian evolution is flawed. Because measurements of constraint rely on a comparison with the neutral rate, it is possible that many of ENCODE's so-called unconstrained regions really aren't unconstrained, Mattick argues.

"I would have said that this finding suggests that many regions of our genome are evolving under weak selection pressure, or that our measurements of the neutral rate of evolution

The ENCODE project aims to catalogue all the 'functional elements' in the human genome.

are incorrect," says Mattick, who is an author on the ENCODE paper.

In fact, Mattick thinks scientists are vastly underestimating how much of the genome is functional. He and Birney have placed a bet on the question. Mattick thinks at least 20% of possible functional elements in our genome will eventually be proven useful. Birney thinks fewer are functional. The loser will buy the winner a case of the beverage of his choice.

Meanwhile, other scientists are gathering data to answer new questions raised by ENCODE. Many hope that other ongoing studies, such as comparable genome sequences from additional primate species, will help decide which parts of the ENCODE data to study first.

**Erika Check**

1. The ENCODE Project Consortium *Nature* **447**, 799–816 (2007).
2. Greatly, J. M. *Nature* **447**, 782–783 (2007).
3. *Genome Res.* **17**, Issue 6 (2007).
4. *Nature* **447**, 361 (2007).

## WORDWATCH

**Cyber warming:** The greenhouse effect caused by carbon dioxide emitted specifically by the manufacture, operation and disposal of computers. A UK government task force has been set up to tackle the issue.



STOCKBYTE SILVER/GETTY

## ON THE RECORD

**"We could not talk about a football World Cup, but about a World Cup at limited altitude."**

Bolivian President Evo Morales slams a decision by FIFA, soccer's governing body, to ban international matches at elevations above 2,500 metres.

## SCORECARD

### Postage stamps



Dutch mail company TNT Post has launched a range of seed-impregnated stamps that can be planted after use, and will sprout a range of flowers.

### US vacations



A survey shows that 20% of US holidaymakers take their laptops so they can stay in touch with the office — and some 40% check their work e-mail while they're supposed to be relaxing.

## NUMBER CRUNCH

**7 minutes 54 seconds**

is the average duration of coitus, according to a US survey.

**14,191 kilometres**

is the distance travelled by Earth around the Sun during that time, British astronomers calculate.

**143 million kilometres**

is the total amount the Earth moves during sex if you factor in the expansion of the Universe. For a precise, personalized distance based on your specific latitude (and performance), visit [www.earthmove.info](http://www.earthmove.info).

Sources: BBC News, FourFourTwo, [inhabitat.com](http://inhabitat.com), ABC News, Cheltenham Science Festival

# Researcher refuses to back down over race case

Up on the seventh floor of Building 16 at the Massachusetts Institute of Technology (MIT) in Cambridge, biological engineer James Sherley already has his schedule for 1 July mapped out. "I plan on coming into my office, just like I normally do," he says. "They'll have to come in here and drag me out."

Time is running out for the stem-cell researcher — a year and a half, one hunger strike and countless e-mails after being denied tenure. MIT has told him that 30 June is his last day. But Sherley has no intention of going quietly.

Sherley, who is African-American, has argued that racial discrimination and colleagues' conflicts of interest marred his tenure process. Under-represented minorities (African-American, Hispanic and Native American) make up only 3.6% of the senior faculty at MIT; the US national average is 3.5% in natural science and engineering at élite research universities.

"I am just tired of racism," says Sherley. "Here I am again at a point where I am being denied something that I deserve because of my race."

Frank Douglas, who is African-American, also resigned in protest as executive director of MIT's Center for Biomedical Innovation this month: "I leave because I would [not] be able to advise young Blacks about their prospects of flourishing in the current environment."

Sherley says signs of discrimination were evident from the moment he arrived at MIT, eight years ago. Requests to expand his lab space were denied, he says, and his lab was rarely invited to speak at departmental seminars.

**"I am being denied something that I deserve because of my race."**

In March, faculty members at the biological engineering department expanded on their decision not to grant Sherley tenure, saying the process was "as free as humanly possible from bias and racism". "External letters from experts in the field of stem-cell biology were not strong enough," they wrote. They point out that two-thirds of the \$1.5 million in external funds used to fund Sherley's pre-tenure research came from grants on which Sherley was not the primary investigator. On average, only a third of MIT assistant professors receive tenure.

During the years before the decision, Sherley published six peer-reviewed research papers. Of the two other candidates in his department who were awarded tenure around the time when Sherley's case was being considered, one had published 12 papers during the same period, the other 18. Both bodies of work

were cited on average twice as often as Sherley's. However, the value of Sherley's research cannot be appreciated merely by counting citations, says George Church, a Harvard

University biologist. "It takes a little digging to see it," he says. "They don't give him any credit for the creativity."

Sherley has tackled several open questions in stem-cell biology. He re-evaluated the 'immortal strand' hypothesis proposed more than 30 years ago as a mechanism by which adult stem cells prevent the accumulation of mutations in their DNA. In 2006, after his tenure application was denied, Sherley was awarded the National Institutes of Health Director's Pioneer Award for challenging research directions.



Not everyone feels Sherley's work warrants tenure. "I thought the decision not to grant tenure was correct," says Nancy Hopkins, an MIT biologist who led the institute's evaluation of gender equality in the late 1990s. "I did not detect bias that affected this outcome. However, unintentional racial bias, like gender bias, is unavoidable in our society."

Some speculate that Sherley's controversial opposition to embryonic stem-cell research was a factor. Sherley, who studies adult stem cells, has been critical of embryonic stem-cell research on ethical and practical grounds.

Sherley ended his March hunger strike after 12 days, when, according to him, MIT agreed to re-evaluate his case. MIT says no such agreement was ever made and no further investigation is needed. Sherley says that MIT has failed to hold up its end of the bargain; the university says that the inquiry held before the strike by

# Plans falter over EU research infrastructure

## MUNICH

Europe has a plan for building large research facilities for scientists to share. Now all it needs to do is figure out which ones may actually become reality — not an easy task. Last week, a high-level meeting in Hamburg ended without concrete suggestions for which projects to take forward.

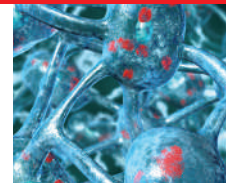
The list of facilities that European scientists would like funded is long and diverse, from biobank projects to particle accelerators. Some, such as the €360-million (US\$480-million) research icebreaker *Aurora Borealis* and the €1-billion European X-ray Free Electron Laser (XFEL), have already won full or partial approval.

But many others, including a planned €150-million Extreme Light Infrastructure laser initiative and the €1-billion European Spallation Source (ESS) for neutron research, are still but dreams.

Thirty-five projects have been identified as key by the European Strategy Forum on Research Infrastructures

(ESFRI). But paying for them all would cost more than €14 billion. "We all know that it won't be possible to have them all," says Beatrix Vierkorn-Rudolph, who is on the ESFRI executive board and an official at the German research ministry.

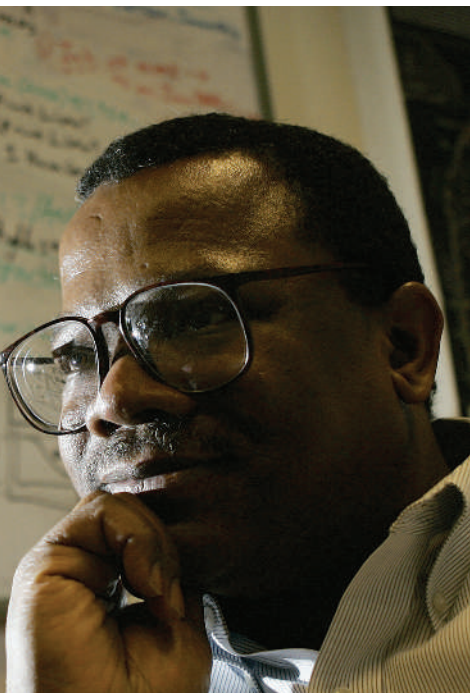
Governments of the 27 member states, together with the ESFRI and national



### STEM CELLS HELP PRIMATES WITH PARKINSON'S

Monkey studies highlight multiple stem-cell abilities.  
[www.nature.com/news](http://www.nature.com/news)

D. MACK/SPL



Biological engineer James Sherley claims racial discrimination cost him tenure at MIT.

a committee of senior faculty members, who were approved by Sherley, is sufficient.

His complaints have triggered one change, though: after the hunger strike, MIT announced a new initiative on race. It includes a study modelled on the 1999 investigation led by Hopkins on female scientists, and aims to quantify differences such as salary, lab space and the time between tenure and promotion to full professor. The study is due to be completed in September 2008.

For Sherley, the results will come too late. "His term as a member of the faculty ends on 30 June," says MIT chancellor Phillip Clay. "The review process is complete." ■

Heidi Ledford

See Editorial, page 753.

funding agencies, now must winnow out those projects to be built from those to be abandoned. This October, they will announce which projects on the list will receive initial funding for technical design studies; an updated roadmap is to be produced by autumn 2008. Projects that are chosen for funding will require one country to take the lead, as Germany has done for the XFEL and the icebreaker.

But even that can be tricky, as negotiating the details of multinational EU projects is a notoriously cumbersome process. Building the XFEL, for example, required separate bilateral agreements between Germany and all the 12 other participating countries. And although Germany had said early on that it would cover 60% of the building costs and 75% of the operational costs, it took almost four years to finalize

agreements with all partners.

The money must come from some extra pot, as the EU's seventh Framework programme for research, which runs from 2007 to 2013, has only an embryonic budget for infrastructures — just enough to fund design studies and facilitate access to existing machines. Peter Tindemans, who chairs the ESS initiative, suggests that a fraction of the EU's overall budget surplus, some

€3 billion to €4 billion each year, should be put aside for funding research facilities. That's twice the current EU spending on infrastructures, and roughly equal to US spending.

"The ministers say research infrastructures are an area where Europe needs to act as a union," says Tindemans. "Let's remind them of their promise to put their money where their mouth is." ■

Quirin Schiermeier

## Stem-cell paper corrected

The authors of a controversial paper on stem cells publish a correction of their work in this week's issue of *Nature* (see page 880), but say their overall conclusions still stand.

The paper in question, published in 2002, claimed to find evidence for so-called 'multipotent adult progenitor cells', or MAPCs, in mouse bone marrow (Y. Jiang *et al.* *Nature* 418, 41–49; 2002). The work was led by Catherine Verfaillie, now director of the Stem Cell Institute at the Catholic University of Leuven, in Belgium.

The correction states that figures showing proteins on the surface of the MAPCs contained many errors, including duplications. Verfaillie's group provides replacement data and says that the correction does not undermine the paper's conclusion that MAPCs can give rise to a wide range of different cell types.

The paper challenged the prevailing idea that only stem cells derived from embryos were highly flexible. Some of its results have been reproduced by other labs, but no one has been able to replicate the work independently in its entirety.

"I believe that despite the hype over the mistake, we and *Nature* made the conclusion that the final findings of the paper still stand," says Verfaillie.

This February, an investigation convened by the University of Minnesota — Verfaillie's former institution — found that her group had used incorrect procedures in the *Nature* paper, and that some of the data contained in it might be flawed. The investigation was a response to questions from a reporter from the magazine *New Scientist*, who pointed out that the figure corrected today was partly reproduced with different labels in another paper in the journal *Experimental Hematology* (Y. Jiang *et al.* *Exp. Hematol.* 30, 896–904; 2002).

In response to the investigation, *Nature*

convened a peer-review panel to analyse the data from the 2002 paper. According to *Nature*, the experts concluded that although the figure data were flawed, the paper's conclusions are still valid.

No allegations of fraud or misconduct have been levelled at Verfaillie or anyone from her group. There are still two investigations ongoing — one at the University of Minnesota and one at the Catholic University of Leuven — into a second set of allegations raised by *New Scientist*. These concern data from a paper in the journal *Blood* (M. Reyes *et al.* *Blood* 98, 2615–2625; 2001) and data in a US patent filing.

Verfaillie says her group cannot explain how the errors in the *Nature* paper occurred: "Why this happened, we have not been able to determine," she says. ■

Erika Check



A. KING/AP

Catherine Verfaillie defends her team's work.

# Indian scientists battle journal retraction

## BANGALORE

A high-profile case in India continues to escalate. A government committee has cleared a top cancer researcher and his group of wrongdoing after a US journal retracted their paper over charges of data manipulation. But India's ethics watchdog, the New Delhi-based Society for Scientific Values (SSV), charges the committee with "possible complicity" in attempting to save the reputation of an award-winning scientist and the image of a prominent government research institute.

The arguments centre on a 2005 paper in the *Journal of Biological Chemistry* (JBC), which examined signalling pathways in the development of skin cancer (Rangaswami, H., Bulbule, A. & Kundu, G. C. *J. Biol. Chem.* **280**, 19381–19392; 2005). It was authored by Gopal Kundu — 2004 winner of the India's highest honour in science, the Bhatnagar prize — and two colleagues at the National Centre for Cell Science (NCCS) in Pune.

The journal retracted the paper in February 2007 after an investigation prompted by an anonymous email. The authors were told that the paper contained "data that was reproduced without citation and with different labelling" from a paper the same group had published in 2004 (Rangaswami, H., Bulbule, A. & Kundu, G. C. *J. Biol. Chem.* **279**, 38921–38935; 2004). Journal editors claimed the errors amounted to "deliberate misrepresentation".

Kundu and his team deny this, saying that both papers described similar experiments run on very similar cell types. "The apparent similarity between two loading control blots — out

**"Our detailed investigation shows there was no manipulation."**

of the 100 or so blots in the papers — did not affect the conclusions in any way," adds first author Hema Rangaswami, now a postdoc at the University of California in San Diego. "We feel *JBC*'s decision to withdraw our paper was totally unfair." But Shelagh Ferguson-Miller, chair of the publications committee for the journal's publisher, says that it does not plan to reconsider the paper's withdrawal.

A seven-member committee, set up by the Department of Biotechnology, which oversees the NCCS, appears to back up Rangaswami's claims. In its 30 May report, the committee said the allegations were baseless. "Our detailed investigation shows there was no manipulation," says Govindarajan Padmanabhan, chairman of the committee. He adds that the journal did not analyse the researchers' raw data, but instead relied on image analysis of published figures. Padmanabhan says the committee plans to appeal to the journal to rescind the withdrawal.

But the SSV claims its own findings, released on 28 April, suggested that the group fabricated images in the second paper from blots in the first paper. Sohan Modak, a former member of the centre's governing council and whose complaint launched the SSV investigation, says he remains convinced the images are the same.

The jury may still be still out, but Kundu has already paid a price. His nomination to the fellowship of the Indian National Science Academy has been held up. And Rangaswami's PhD hangs in the balance: she has not yet been called to defend her thesis at Pune University.

**K. S. Jayaraman**

DINODIA PHOTO LIBRARY



Reputation on the line?: the National Centre for Cell Science in Pune, India.

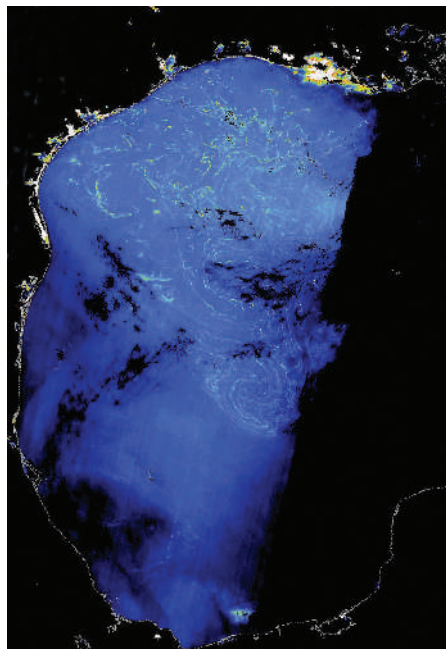
## G8 leaders make progress towards Kyoto successor

A climate agreement reached by world leaders at last week's G8 summit in Germany has "re-energized" the process to find a successor to the Kyoto treaty, says Yvo de Boer, executive secretary of the United Nations body that oversees the Kyoto protocol. De Boer, who will lead the negotiations in Bali in December, says that the deal sends "an important signal to developing countries" ahead of the climate-change summit.

G8 leaders, including US President George W. Bush, have agreed to "consider seriously" the decision made by the European Union, Canada and Japan to at least halve global emissions by 2050. Although some environmental groups have criticized the agreement's lack of hard targets, the G8 communiqué notes it is "vital" that major emitters agree to a detailed global framework by 2009 (see <http://tinyurl.com/28xyta>). This, says de Boer, raises the likelihood that a follow-on agreement for Kyoto will be in place before the current treaty expires in 2012.

## Satellite detects invasive seaweed's fluorescence

Sargassum, a dense floating brown seaweed famous for entangling ships in the Sargasso Sea, has been detected from space for the first time, thanks to the European Space Agency's Envisat. The satellite's Medium Resolution Imaging Spectrometer (MERIS) detects fluorescence emission from chlorophyll, and is unique among



Sargassum in the Gulf of Mexico, seen from space.

## Kamchatkan mudslide wipes out study sites

A massive mudslide on 3 June in the Valley of Geysers, on the Kamchatka Peninsula in the far east of Russia, has loosed an estimated 4.5 million cubic metres of rock, gravel, snow and ice onto the World Heritage site.

Scientists have been sent to investigate the extent of the damage. Juergen Wiegel, a microbiologist at the US University of Georgia in Athens, who has previously worked in the region, says the slide will "definitely" affect future research into unique extremophiles living in the vents. The loss "is very sad", he says.



I. SHPILENOV

Botanists worry for rare plants in the valley, and wildlife officials are concerned about salmon — an important food source for other animals in the region. Geologists add that mud caps over the geysers could cause explosions.

ocean-observing satellites in being able to pick up emissions at 709 nanometres. This allowed scientists at the Institute of Ocean Sciences in British Columbia, Canada, and the University of South Florida in Tampa to detect lines of the seaweed in the Gulf of Mexico. Being able to measure sargassum from space should improve estimates of ocean primary productivity; the alga has spread as an invasive species to many spots around the world.

## Transit of Earth-like planet eludes astronomers

Astronomers who had been anxiously keeping an eye on the dwarf star Gliese 581, in hopes of observing an Earth-like planet pass in front of it, have been met with disappointment so far. The star's light, as viewed by the Canadian Space Agency's MOST space satellite, has been remarkably constant — meaning the recently spotted planet 581c has not passed between the star and Earth. Data collected from such a pass would have allowed a precise determination of the planet's size and composition.

Astronomers have not yet had time to check whether another planet, 581d, passes between the star and Earth, but say the odds for this are very slim. Some say that 581d, which is cooler than 581c, may have more promising conditions for the possible formation of complex life in that system.

## US House votes to free up federal stem-cell funding

The US House of Representatives voted on 7 June to loosen restrictions on federal stem-cell funding. The bill, passed by the Senate in April (see *Nature* 446, 842; 2007), allows US funding for research on stem cells derived from left-over embryos at fertility clinics.

But President Bush quickly made clear he would again veto the measure, which he first quashed last July (see *Nature* 442, 335; 2006).

Speaking at the G8 summit in Germany, Bush highlighted research published last week showing that adult mouse cells can be reprogrammed to an early embryonic state without the need for eggs or embryos (see *Nature* 447, 618–19; 2007). "These reports give us added hope that we may one day enjoy the potential benefits of embryonic stem cells without destroying human life," he said. The Senate may succeed in mustering the two-thirds majority needed to override a veto; its vote in April was 63–34, with three absentees. At 247–176, the House remains dozens of votes short of a veto-proof majority.

## EU ministers fail to agree on Galileo rescue plan

Galileo, the EU's proposed satellite navigation rival to the US's global positioning system, has an uncertain future. The partnership set up between the public sector and European aerospace companies to develop the project was pronounced dead at a meeting of EU transport ministers in Luxembourg last Friday.

Progress had stalled mainly because the companies couldn't agree on the sharing of costs. The ministers said they would come up with a new funding plan by this autumn, in which the EU or governments may end up picking up the €2.4-billion (US\$3.6-billion) bill for completing the 30-satellite system.

### Correction

The News Feature 'Seeking absolute security' (*Nature* 447, 372–373; 2007) incorrectly stated that Hoi-Kwong Lo and his colleagues hacked into a quantum-cryptographic system that did not use the standard BB84 protocol for quantum security. In fact, the system did use BB84.

# BUSINESS

## Shades of success

Light-emitting diodes are seen by many as the light source of the future. But as **Kurt Kleiner** reports, their adaptation will take time.

When a newly expanded Wal-Mart store opened in Burton, Michigan, last month, it seemed like just another case of American gigantism — the 19,000-square-metre 'supercentre' sells everything from power tools to potatoes, employs 430 people, and boasts 30 checkout aisles.

But over in the frozen-food section, something more interesting than mere wretched excess was happening. The display cases are lit not with fluorescent bulbs, but with light-emitting diodes (LEDs). The LEDs last longer than the fluorescent bulbs they replace — and are so energy efficient that Wal-Mart expects to save \$2.6 million a year by installing them in 500 stores nationwide.

It's a niche application for a new kind of lighting that, advocates say, could one day replace conventional bulbs in factories, offices and homes. LEDs make sense for Wal-Mart's freezers because fluorescent bulbs are less efficient at cold temperatures, whereas LEDs are unaffected. But even at room temperature LEDs are more energy efficient than standard incandescent bulbs, and they are poised to overtake compact fluorescent bulbs too.

### Rival technology

Global sales for LED lighting are currently worth just US\$200 million a year in a \$15-billion global market for general lighting, says Robert Steele, an analyst at the market-research firm Strategies Unlimited in Mountain View, California. But supporters of the technology claim that it could supersede its rivals as its efficiency rises further and as costs fall. "Maybe the best analogy is semiconductors compared to vacuum tubes," Steele says. "I think it's a very compelling technological argument."

LEDs are semiconductors that emit light when an electric current passes through them. The first ones were dim, and came only in red. Then green and blue LEDs added some variety, and opened the possibility of mixing colours to create white light. However, the relatively low efficiency of green LEDs made the solution less than ideal. Their main use to date has been for indicator lights on electrical

equipment, and for flat-panel televisions.

But in 1996, Shuji Nakamura, an engineer then working for Nichia in Tokyo and now at the University of California, Santa Barbara, developed the first 'white' LED by coating a blue LED with a yellowish phosphor. The blue and yellow light that results mixes to create white light.

Initially, the quality of the light was considered too 'cold' for most tastes, with too much blue in it. But by adding red phosphors, companies such as Cree of Durham, North Carolina, and Philips Lumileds in San Jose, California, created 'warmer' lights that have a spectrum closer to that of the Sun.

### A bright future

Manufacturers have also managed to increase the brightness of LEDs. An incandescent bulb produces about 20 lumens per watt of power consumed, and a compact fluorescent produces about 60 lumens per watt. Commercially available LEDs now average about 30 lumens per watt, but over 100 lumens per watt has been reached in the laboratory. Most people expect LEDs to outperform fluorescent bulbs within a few years, according to Jagdish Rebello, an analyst at iSuppli, an electronics market-analysis firm based in El Segundo, California.

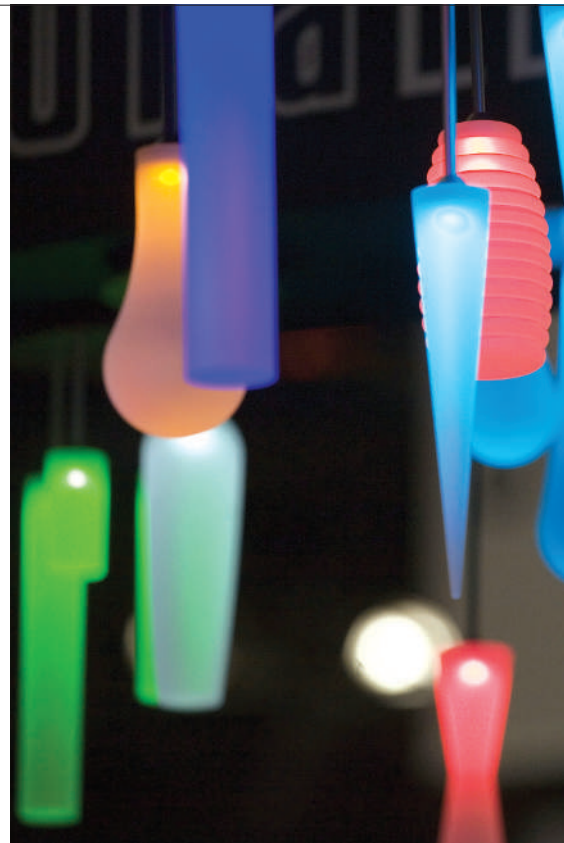
LEDs remain pricey, however. The LED equivalent of a conventional light bulb would currently cost about \$60 — although the price is falling sharply as the efficiency of LEDs goes up. And they last for 50,000 hours or more, compared with around 15,000 hours for fluorescent bulbs, and only about 1,000 hours for an incandescent bulb.

A standard incandescent bulb converts only about 5% of its power into light (the rest is lost as heat), and a fluorescent bulb converts about 20%. At the moment, LEDs can manage about 17%. In theory, they could be 100% efficient, but realistically they are only likely to reach about 50% efficiency, says Nadarajah Narendran, research director at the Lighting Research Center at Rensselaer Polytechnic Institute in Troy, New York.

Right now, their long life and physical

**"Less energy use and longer life haven't historically been strong motivators for consumers."**

— Steve Landau



resilience make LEDs attractive for niche applications, such as Wal-Mart's freezers. White LEDs are starting to dominate the top-end market for torches in some countries, and they are gradually being adopted in landscape and street lighting, for which the labour costs of regular bulb replacement are high. But within a few years, increases in efficiency should bring the costs of LEDs low enough for them to become common in offices and homes, says George Crawford, chief technology officer of Philips Lumileds.

### Power struggle

Even then, they are unlikely to displace the light bulb outright, at least in the home. "Less energy use and longer life haven't historically been strong motivators for consumers," explains Steve Landau, a spokesman for Philips Lumileds. He points out that fluorescent bulbs have been slow to replace incandescents for home use, despite their edge in efficiency. And when they do appear in homes, it is unlikely to be simply as a straight replacement for existing bulbs.

LEDs use direct current, so to use the alternating current of mains electricity, an LED has to contain current conversion circuitry. Heat management is a further problem: LEDs radiate waste heat out of the back of the chip. If you make a 'bulb' that radiates light outward in all



M. LENNIHAN/AP PHOTOS

**Spot on:** light-emitting diodes could offer an energy-efficient alternative to conventional bulbs.

directions, you end up concentrating all of the heat inward, which will eventually degrade the semiconductor.

So although replacement bulbs are available, and will probably get cheaper and better, LEDs may well conquer the home market only when consumers don't actually have to buy them. Crawford predicts that the technology will end up being incorporated into custom-made fixtures, and pre-installed fittings in newly built homes of the future. Not trying to mimic a conventional bulb plays to the LED's strengths. The a.c. to d.c. conversion can be built into the fixture, or into the wiring of the new home. Because LEDs last so long, consumers will rarely need to buy replacements. And because they are small (about 5 millimetres square) and flat, they can be pointed in any direction, with fittings designed to send light exactly where it is needed.

But manufacturers of compact fluorescents won't give up their market share without a fight. There are billions of existing conventional outlets that are unlikely ever to house an LED. "Old technologies always die hard," says Steele. The adaptation of LEDs "will take years, probably a couple of decades", he says. "But it's going to happen."

## IN BRIEF

**BACK IN BUSINESS** Shares in British nanotechnology company Oxonica fell by more than half, from 118p to 53p, when trading resumed on 6 June. It had been suspended on 27 April after problems emerged with the company's largest contract, to supply diesel-fuel additives to Petrol Ofisi, a Turkish oil company (see *Nature* 446, 963; 2007). The contract has now been terminated. Oxonica, which originally spun off from the University of Oxford in 1999, makes nanoparticle-based additives that are widely used by bus companies in Britain.

**STAFF TURNOVER** British drugmaker AstraZeneca has become the fifth major drug firm to part company with its chief financial officer this spring. Jon Symonds, who has held the position at AstraZeneca for the past ten years, is leaving to become a managing director at Goldman Sachs. Since February, Merck, Pfizer, Wyeth and Amgen have also announced the departures — some voluntary, others not — of their top accountants. The change at AstraZeneca comes 18 months after David Brennan took over as chief executive, as the company struggles with product-pipeline failures and competition from generics.

**REGULATION JAM** China has published a comprehensive five-year plan to rebuild its system for regulating food and drug safety, *The Wall Street Journal* reported. The plan includes national monitoring of adverse reactions to drugs and extensive inspections of food-processing plant. "Monitoring and administering food and pharmaceutical safety must be at the very heart of grassroots and base work," the paper quoted the plan as saying. The plan appeared a week after a row broke out in the United States over the safety of toothpaste made in China.

## MARKET WATCH

### NANOTECHNOLOGY STOCKS



Nanotechnology stocks have enjoyed a good run lately. But although mainstream stock indices have risen over the past two months, nanotech has stalled as investors have started to lose patience with some of the more fancied companies in the sector.

The Lux Research nanotechnology index, which tracks companies that make or use nanotech products and technologies, stagnated over that period — and a few of its component companies have taken a serious hit.

One of the worst performers was Nucrust Pharmaceuticals in Wakefield, Massachusetts, whose stock has halved from a peak of US\$4 in late March. The company has established a successful business selling nanocrystalline silver used in wound dressings, but it is struggling to win approval for what investors had hoped would be a yet-more lucrative line in dermatology drugs.

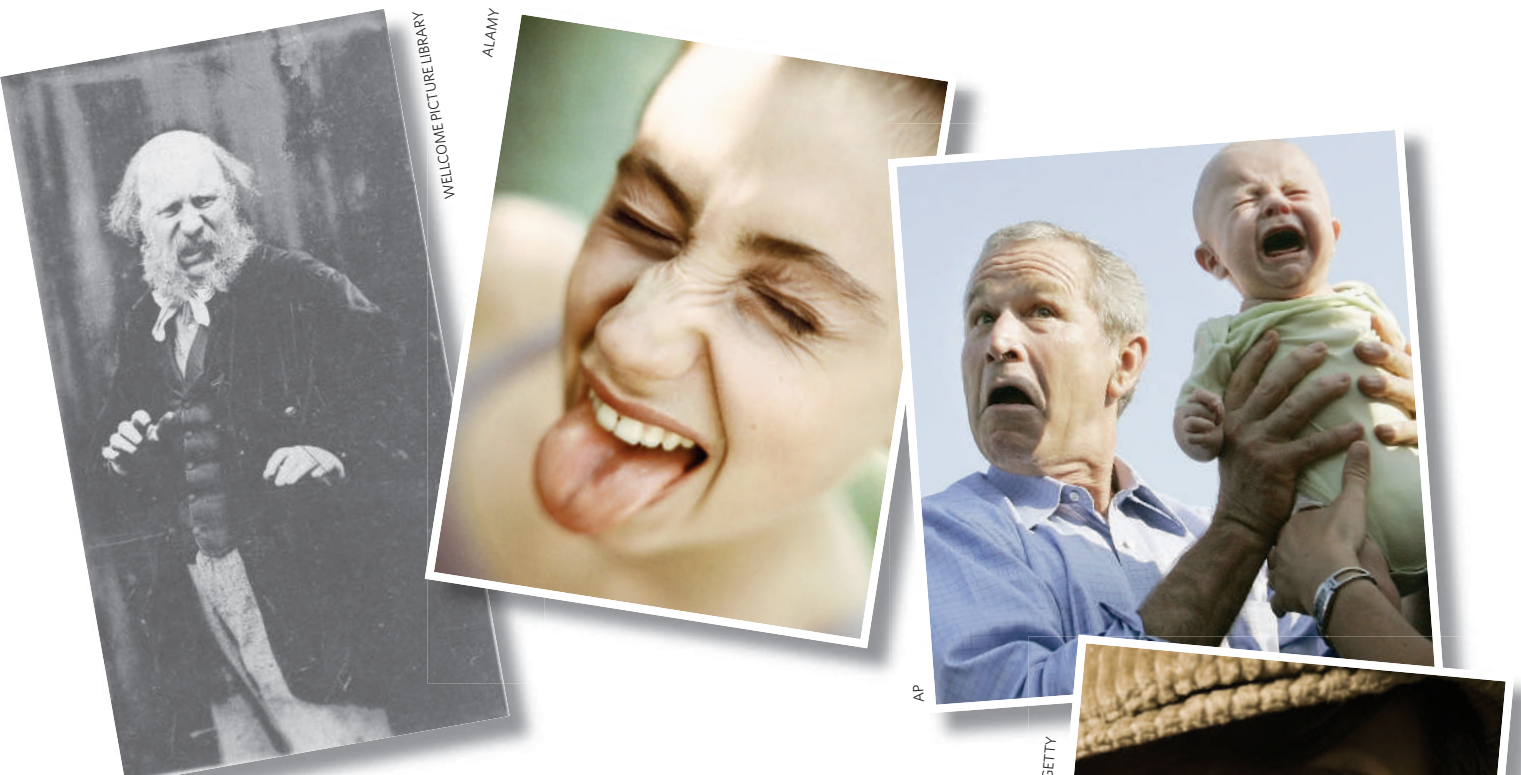
Things have been just as bad at Symyx

Technologies in Santa Clara, California. Stock in this nanotech materials company plunged from \$18 to \$11 on 26 April, after it announced a small quarterly loss. The company has made extensive changes to its management, but the stock hasn't recovered any of its losses.

Arrowhead Research, a diversified nanotech company based in Pasadena, California, has fared better: its price has moved steadily upwards from \$4 at the end of March, when it took over Carbon Nanotechnologies, a nanotubes company in Houston, Texas, to more than \$7 today.

But overall, the market has been sluggish. "It had been running level with the Nasdaq," says Peter Hebert, chief executive of Lux Research, the New York consultancy that compiles the index. "But over the past couple of months, it has underperformed."

**Colin Macilwain**



# The depths of disgust

Is there wisdom to be found in repugnance? Or is disgust 'the nastiest of all emotions', offering nothing but support to prejudice? **Dan Jones** looks at the repellent side of human nature.

In 1997, Dolly the sheep unleashed bioethical responses of every conceivable flavour, from the ruminatively utilitarian to the emotionally outraged. Leon Kass, a bioethicist at the University of Chicago, Illinois, who chaired President Bush's Council on Bioethics from 2002 to 2005, combined scholarly and visceral responses in a much cited essay entitled 'The Wisdom of Repugnance'. He did not go quite so far as to say that the revulsion reportedly evoked by the prospect of human cloning was in itself an argument against such endeavours. But he got fairly close:

*"We are repelled by the prospect of cloning human beings not because of the strangeness or novelty of the undertaking, but because we intuit and feel, immediately and without argument, the violation of things that we rightfully hold dear... Shallow are the souls that have forgotten how to shudder."*

Kass had aired the same worries at the advent of *in vitro* fertilization treatment in the 1970s, and similar reactions continue to bedevil biomedical developments today, such as in the debate over the creation of human-animal hybrids for stem-cell research. But in recent years, a loose band of interdisciplinary psychologists and neuroscientists has been putting together a new picture of the emotion that underlies such responses to biology: disgust.

Drawing on both evolutionary theory and moral philosophy, their work casts doubt on the idea that disgust embodies a deep-seated wisdom. Instead it provides an emerging portrait of an evolutionarily constrained emotion that is a poor guide to ethical action.

These scholars see disgust as a basic emotion that, like fear, anger, sadness and joy, is found across all cultures. All around the world pus, maggots, rotting food and scavenging animals such as rats produce the distinctive facial expression of disgust: nose wrinkled, mouth agape, lips raised. When severe, the feeling of revulsion can be accompanied by throat clenching, nausea and vomiting. In evolutionary terms, the adaptive value of such reactions seems to be to prevent people from eating contaminated foodstuffs and to get rid of any they have ingested. Disgust is related to bodily purity and integrity, with things that should be on the outside — such as faeces — kept out, and things that should be on the inside — such as blood — kept in.

Although the experience of disgust feels primal, the emotion does not seem to be widespread in other animals. Many species exhibit distaste in response to the sensory properties of food — such as sourness and bitterness — and a monkey, cat or human infant might spit out something disagreeable. But only humans beyond infancy will reject food on the basis of

where it might have been and what it might have touched (see 'Gut reactions'). "Disgust is a much more cognitive and emotional feeling than distaste," says Paul Rozin, a psychologist at the University of Pennsylvania, Philadelphia, who has pioneered research on the subject. "It involves understanding what a food is and where it comes from."

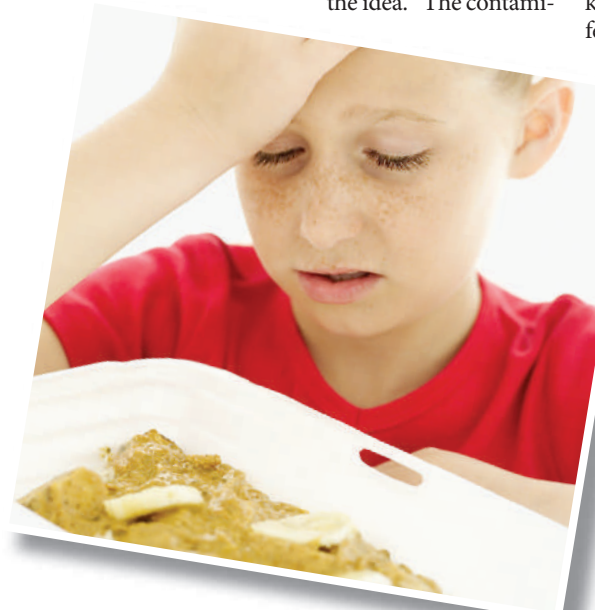
Part of its complexity is that disgust carries with it the notion of contamination; otherwise-edible food that has been touched even fleetingly or innocuously by something viewed as disgusting will be avoided. Most people, Rozin has found, won't drink juice that has been whisked with a sterilized cockroach or drink out of a meticulously cleaned bedpan. Rozin suggests that it is the cognitive sophistication of this idea that explains why the emotion is absent in other animals and infants.

### Basic instinct

But what is the link between visceral or 'core' disgust — the feeling you get when you encounter an unflushed toilet — and a disgusted reaction to something much more abstract, such as the idea of animal chromosomes in a part-human embryo?

A clue is the language of moral indignation itself. "All cultures and languages that we have studied have at least one word that applies both to core disgust (cockroaches and faeces) and also to some kind of social offence, such as sleazy politicians or hypocrites," says Jonathan Haidt, a psychologist at the University of Virginia in Charlottesville and a former student of Rozin's. People labelled as disgusting in this way evoke fears of contamination just as rotting food does. When Rozin asked people about the prospect of wearing Hitler's carefully laundered sweater, most didn't feel at all comfortable with the idea. "The contami-

GETTY



## Gut reactions

Jonathan Haidt from the University of Virginia in Charlottesville and Paul Rozin from the University of Pennsylvania in Philadelphia, with various colleagues, have developed a questionnaire to discover how prone a person is to disgust by recording how strongly they agree or disagree with a series of statements. For example:

- I might be willing to try eating monkey meat, under some circumstances.
- It would bother me to be in a science class and to see a human hand preserved in a jar.
- I never let any part of my body touch the toilet seat in public restrooms.
- It would not upset me at all to watch a person with a glass eye take the eye out of the socket.
- Even if I was hungry, I would not drink a bowl of my favorite soup if it had been stirred by a used but thoroughly washed fly swatter.
- It would bother me to sleep in a nice hotel room if I knew that a man had died of a heart attack in that room the night before.

For an interactive version of the full test, and explanation of the results, see <http://yourmorals.org/>

D.J.

nation of disgust is generalized to moral issues, and that's a very deep feature of disgust," he says. "If it was just metaphorical then Hitler's sweater wouldn't be so offensive."

Paul Bloom, a psychologist at Yale University is sceptical. He agrees that disgust drives some moral judgements, but points out that they are mainly those relating to behaviour that involves bodily fluids or contact — gay sex, for instance — rather than more abstract issues. Just as people don't really lust for a car or genuinely thirst after knowledge, suggests Bloom, they don't really feel disgust at more abstract issues. "When we

say something like 'This tax proposal is disgusting, we're using a metaphor,' he says. "It's a very powerful metaphor, but it doesn't elicit the same disgust or nausea as primary disgust elicitors such as faeces and body fluids."

But Haidt thinks he has found clues pointing to a physiological reality for moral disgust. Whereas anger pushes the heart rate up, being viscerally disgusted makes it drop. With his student Gary Sherman, Haidt showed people hooked up to a heart monitor video footage of morally negative but not viscerally disgusting behaviour, such as an American neo-Nazi meeting. The participants said that the video triggered disgust and anger, and on average their heart rates fell, not rose. What's more, those who reported increased clenching in

their throat had a greater drop in heart rate, making the link with core disgust look stronger. "We think that this is the first physiological evidence that socio-moral disgust really is disgust and not just metaphor or anger," says Haidt of the as yet unpublished work.

Brain imaging studies might also point to an overlap between core and moral disgust. Jorge Moll, a cognitive neuroscientist at Rede Labs D'Or, Rio de Janeiro, Brazil, used magnetic resonance imaging (MRI) to monitor the flow of blood in the brains of 13 healthy adult volunteers as they mulled over situations evocative of core disgust and those that elicit self-reported moral disgust or indignation<sup>2</sup>. He found that core and moral disgust recruit overlapping brain areas, particularly the lateral and medial orbitofrontal cortex, suggesting that the emotions are related. These regions of the brain are activated by unpleasant sensory stimuli, and they connect with other emotion-related areas, such as the amygdala.

As well as showing overlap, Moll's work suggests that core and moral disgust also activate some distinct areas. They produced similar activity in the posterior orbitofrontal cortex, but moral disgust produced greater activity than core disgust in the more evolutionarily recent anterior region, which some think is involved in more abstract emotional associations.

### Moral foundations

Moll's original work can be criticized because some of the 'moral disgust' scenarios also featured elicitors of core disgust, such as rats. But in a paper to be published in *Social Neuroscience*<sup>3</sup>, Moll and his colleagues created 'cleaner' scenarios that describe pure moral violations without a visceral element, and arrived at much the same results. And last October, the team presented evidence suggesting that the lateral orbitofrontal cortex was also activated when volunteers made decisions on whether to oppose charitable organizations that had moral agendas different from their own — on abortion, gun control or the death penalty, for example<sup>4</sup>. It seems that just thinking about some sorts of moral conflict is enough to get parts of the brain implicated in disgust ticking over.

Even if moral and visceral disgust are not the same emotion, visceral disgust will sometimes affect ethical judgements. Susan Fiske and Lasana Harris, psychologists at Princeton University in New Jersey, have used MRI to probe the disgust evoked by images of people such as drug addicts or the unkempt poor and homeless<sup>5</sup>. Their findings seem to support an unsurprising but depressing conclusion. Not only did the amygdala and insula fire up (taken to indicate fear and disgust, respectively), the medial prefrontal cortex, which is usually active when

thinking about people and social situations, as opposed to thinking about objects, was less active. This can be interpreted as evidence that disgust goes some way to trumping empathy and compassion. "When we respond to a homeless person with disgust, we avoid considering the person's mind," says Fiske. "We treat the person as equivalent to a pile of garbage."

Also disturbing is the way in which disgust can play a similar role in interactions with people who offer none of the objective correlates of visceral disgust. Its role may be tied to the evolutionary process, though, in that disgust is broadened out from the original purely hygienic concerns to the more general moral role that Rozin, Haidt and their colleagues see it playing today. Visceral disgust is in essence an emotion of distancing — of avoiding or expelling the contaminant. Marc Hauser, a psychologist at Harvard University who has worked with primates, suggests that this aspect of disgust made it a suitable raw material for evolution to work with in building up instinctive distinctions between the in-group and the out-group. The force with which such distinctions are felt may promote survival, and thus have adaptive value in the face of natural selection.

Drawing distinctions between in-group and out-group — us and them — "is not something the human line invented", says Hauser. It is seen in various social animals. But humans are peculiarly preoccupied with these distinctions. Some, such as the football team someone supports, are not widely accepted by outsiders as carrying moral weight. Others, including our political and religious affiliations, are value-laden to the core. "The moral faculty, which deals with moral problems, is going to have a deep connection

## The basis of belief

Although disgust may be built into the human moral faculty, that faculty does not work the same way in everyone, and the moral weight given to repugnance may thus differ from person to person. Paul Bloom from Yale University, working with David Pizarro and Yoel Inbar at Cornell University, Ithaca, New York, has recently explored how reactions to disgust relate to political and ideological views of the world. Their results bring into focus the fault lines of the notorious 'culture wars' that divide liberals and conservatives on myriad social issues.

In an unpublished study,

Bloom and his colleagues asked self-identified political liberals and conservatives to take a well-established written test for measurement of sensitivity to disgust, and then recorded their attitudes on a range of moral and social issues. They found that, even when controlling for factors such as age, class and gender, the more prone to disgust a person was, the more he or she was likely to hold conservative views on social debates. The link was especially strong in attitudes to abortion and gay rights, both of which are potentially rich in the type of imagery that can prompt

visceral disgust. On the more abstract concepts, the link between sensitivity to disgust and conservatism was not statistically significant for any given issue, but when the issues were aggregated it became so, according to Inbar. Pizarro says he has preliminary data suggesting sensitivity to disgust is also related to attitudes to cloning and stem-cell research.

This finding fits with work by psychologist Jonathan Haidt and graduate student Jesse Graham from the University of Virginia in Charlottesville, on the foundations of the moral faculty. A psychological

with issues of 'in' versus 'out,'" claims Hauser.

Evolution suggests that the human moral faculty — the psychological systems that make judgements about right and wrong, what's permissible and what isn't — was cobbled together from pre-existing brain systems over millions of years of biological and cultural evolution. Along the way, it latched onto disgust as a useful tool. "The experimental data point to the possibility that our disgust system might have been adapted by evolution to allow us to reject or disapprove of abstract concepts such as ideologies and political views that are deeply influenced by culture, as well as social groups associated with

'disgusting' concepts," says Moll.

Some theories of the evolution of human cooperation and altruism suggest that inter-group conflict was a potent force driving cooperation within groups, the most cooperative being the most successful at surviving. In making symbolic distinctions between us and them visceral, disgust could potentially foster greater cohesion within groups by bringing people together in defence against a common out-group. "Disgust works for the group as it does for the individual — what is in the group is 'me' and what is not is 'not me,'" says Haidt. "Where core disgust is the guardian of the body, moral disgust acts as the guardian of social body — that's when disgust shows its ugliest side."

### Repulsive alliances

Propagandists throughout history have been quick to pick up on the possibilities raised by the blurring of visceral disgust into a weapon for the in-group/out-group border patrol. Nazi propaganda depicted Jews as cockroaches and rats; Hutu instigators denigrated Tutsis as cockroaches during the Rwandan genocide. As with the sight and smell of a dispossessed street person, identifying the enemy with an object of disgust throws up strong emotional barriers to empathy. "That's why I say that disgust is the nastiest of all emotions," says Hauser.

"Our moral disgust/indignation brain network is the source of prejudice, stereotyping and sometimes outward aggression," says Moll. Fiske agrees, saying the picture of disgust painted by data from psychology and neuroscience should make us think twice about drawing on revulsion as a basis for our personal moral judgements. History seems to



**Out with the old:**  
vomiting could  
have an adaptive  
role in evolution.



tradition that draws on the work of Lawrence Kohlberg — known for his work in moral development — portrays morality as consisting of two central issues: whether someone was treated unfairly

and whether someone was harmed. Then, in the late 1980s, anthropologist Richard Shweder developed the idea that ethical concepts around the world cluster into three overlapping but distinct

bear this out. Women (especially menstruating ones), the mentally and physically disabled, and inter-racial sex have all been viewed with disgust, and are still viewed as such by some. But few people in liberal societies today would defend such attitudes and many have genuinely ceased to feel them. If disgust wasn't a good moral indicator then, why should it be now?

Some defenders of disgust accept at least some of the implications of the current research. Kass emphasizes that he does not claim that repugnance is a sufficient guide in moral matters. "It is at most a pointer, and of course the objects of disgust are to a considerable extent and in many cases culturally malleable," he says. At the same time, Kass is sceptical of throwing out the baby with the disgusting bathwater. Although he acknowledges that disgust has historically been used and abused to persecute ethnic and religious minorities and to promote the mistreatment of women, he doesn't rule out a role for disgust in morality: "It does not follow from these examples that repugnance about, say, the eating of human flesh (or excrement) or father-daughter incest is unlinked to the moral/aesthetic truth about these practices."

One way forward is to at least recognize the part played by disgust and to be vigilant in its surveillance. And in the special case of bioethics, it also means thinking carefully about what is actually being proposed, rather than concentrating on outrageous scenarios that elicit emotion even while straining credulity. "It is almost impossible to consult our moral intuitions on bioethical questions when we have so little experience of their outcomes," says Haidt. "We can make up all sorts of sci-fi futures but



**Beauty or beast: things that once disgusted can in new contexts be tolerated.**

it's not even worth thinking about them because our intuitions are just too unreliable."

No one is arguing that emotion has no role in moral judgements. Indeed, the whole basis of this new approach is to argue that emotion is inseparable from morality, and that feelings matter deeply. But that does not mean all emotions are created equal. The distinctions that

domains — the ethics of autonomy (individual rights and freedom from harm), community (respect for tradition, hierarchy and authority) and divinity (spiritual purity and sanctity). Haidt and Graham, drawing on both lines of work, have suggested five foundations to explain the ethical intuitions observed across cultures: a concern for harm to people; fairness; in-group loyalty; respect for authority; and spiritual purity and sanctity. Disgust, they think, is most closely tied to the last of these.

Haidt and Graham used a questionnaire to probe 1,613 self-identified liberals and conservatives about the weight they gave to these different concerns in their moral judgements<sup>6</sup>. Respondents were asked to rate the relevance

of 15 such concerns (three for each foundation) in making moral judgements, such as "Was anyone harmed?", "Did someone act unfairly?" or "Did someone betray the in-group?". Whereas liberals typically draw on just the first two foundations — harm and fairness — conservatives tend to be concerned with all five. "Liberals see only a subset of the moral domain — there's a lot more going on that they're not aware of," says Haidt. "We liberals often find it difficult to understand what the big deal is about homosexuality and even first-trimester abortion. But there's more to morality than we used to think — the areas of sacredness and divinity, and group-loyalty have barely been touched."

D.J.

disgust has evolved to police those between the in-group and out-group, and to some extent the sacred and profane (see 'The basis of belief'), are much more subjective than the aspects of life dealt with by the other emotions that Haidt and his colleagues see contributing to morality. "Disgust didn't evolve to track things that we would normally consider morally important, unlike empathy, which is triggered by the real pain or suffering of others," says David Pizarro of Cornell University in Ithaca, New York.

Still, disgust is an emotion we are stuck with. The challenge, suggests Hauser, is to make people more reflective about what they say and think. He cites the success that advocates of political correctness have had in lowering the prevalence of casually sexist and racist language. Moll suggests optimistically that cultivating cultural and personal values of tolerance and empathy could function as an antidote to the toxic effects of disgust. This may all sound a little wishy-washy; the implications of this research, as well as the research itself, deserve critical examination from well beyond the confines of the small group of scientists currently involved. But it is hard not to conclude that, by thinking less with our guts, and more with our heads and hearts, we might be able to push back the boundaries of our moral world.

**Dan Jones is a freelance writer in Brighton, UK.**

1. Kass, L. R. *New Republic* **216**, 17–26 (1997).
2. Moll, J. *et al.* *Cogn. Behav. Neurosci.* **18**, 68–78 (2005).
3. Moll, J. *et al.* *Social Neurosci.* (in the press).
4. Moll, J. *et al.* *Proc. Natl Acad. Sci. USA* **103**, 15623–15628 (2006).
5. Harris, L. T. & Fiske, S. T. *Psychol. Sci.* **17**, 847–853 (2006).
6. Haidt, J. & Graham, J. *Social Justice Res.* (in the press).

**See Editorial, page 753.**



# FEEL THE FORCE

When two objects separated by a vacuum are barely a whisker apart, a strange attraction comes into play. **Philip Ball** meets the physicists who are trying to make something out of nothing.

**N**othing can come of nothing," wrote Shakespeare, but Harvard physicist Federico Capasso aims to prove him wrong. Because of the fluctuating nature of the sub-microscopic quantum world, 'nothing' — a vacuum — can generate an attractive force between two objects that are very close to each other. This Casimir force, named after its discoverer, Dutch physicist Hendrik Casimir, has long been regarded as a scientific curiosity. But Capasso believes that it can be tamed and modified in ways that could benefit technology at the microscopic scale. Thanks largely to his vision, the field of Casimir engineering is beginning to take shape.

The Casimir force is so weak it is almost undetectable. As a result, much of the work on this ghostly interaction has been concerned with simply detecting and characterizing it. Hardly anyone has thought about whether it could be put to good use.

But Capasso believes that there is "a whole zoo of interesting stuff" that can be done with the force. He wants to use it to make new microscopic devices, such as motion and position sensors<sup>1</sup>. "I love to think of myself as a designer," says Capasso, "and here the question is, can we design quantum fluctuations?"

These fluctuations lie at the heart of the attractive force. All materials — and vacuums too — are pervaded by fluctuating electromagnetic fields. These fluctuations in two closely separated surfaces can get in step, leading to an electrical attraction between them. That gives rise to the familiar van der Waals

force, famous for helping geckos to climb glass walls: an illustration that this fundamentally quantum-mechanical effect has observable everyday consequences.

But experiments in the 1940s showed that this attractive force falls off more rapidly than expected at separations of more than 10 nanometres or so (see 'Into the gap'). In 1948, Casimir explained why. The fluctuations of one surface are 'communicated' to the other by fluctuations of the electromagnetic field in the vacuum in between. But as the gap gets bigger, it takes longer for this 'signal' to cross, and so there is a time delay: the surface fluctuations get out of step, and the force therefore gets weaker. This weaker attraction is now generally called the Casimir force, although in a sense it is simply a modification of the van der Waals force.

It took several more decades for this elusive effect to be measured directly. The Casimir force falls off rapidly with increasing separation and is tiny beyond a few tens of nanometres. But its strength increases with the area of the interacting surfaces, so it becomes detectable if the surfaces are big enough. This does, however, mean holding two parallel surfaces only a microscopic distance apart, which is technically demanding, especially given that such surfaces are generally rather rough and so may not have a well-defined separation.

That's why the Casimir force wasn't detected unambiguously with high precision until 1997,

when Steve Lamoreaux, then at the University of Washington in Seattle, measured the interaction between a gold-plated hemisphere and a gold plate attached to a torsion pendulum: a horizontal bar suspended by a wire. As the objects were brought to within a few micrometres of each other, the force caused the pendulum to twist<sup>2</sup>.

## Weak and feeble?

It is difficult to imagine that a force so weak that it is hard to measure at all is likely to be significant in applied science, either as a problem or an opportunity. But the small scales

on which engineering is now being conducted have revitalized interest in the Casimir force. Mechanical devices such as vibration sensors and switches are now routinely made with parts that are just a few micrometres big.

These microelectromechanical systems (MEMS) are just the right size for the Casimir force to exert itself: they have surface areas big enough, yet gaps small enough, for the force to draw components together and perhaps lock them tight — an effect called stiction. Such permanent adhesion is a common cause of malfunction in MEMS devices, and in 1998 Jordan Maclay and his co-workers at the University of Illinois in Chicago suggested that the Casimir force might be responsible for it<sup>3</sup>.

This makes sense to MEMS researchers such as Ho Bun Chan at the University of Florida in

**"This is a phenomenon that most researchers try to avoid rather than study."**

— Ho Bun Chan

Gainesville. "The components in MEMS are designed to be very close to each other," says Chan, who has worked on Casimir forces in these systems. "Under the right circumstances, the Casimir force can become significant and affect the operation of the device. It can initiate the pull-in of components that eventually leads to stiction."

He admits that so far there have been no reports of this, but adds that most researchers in this field have probably seen it unknowingly. One attempt to look for it explicitly was made in 2001, when physicists Eyal Buks and Michael Roukes at the California Institute of Technology in Pasadena investigated stiction between a nanoscale gold beam, fixed at both ends, and an adjacent gold electrode<sup>4</sup>.

### Sticking point

They brought the two metal surfaces into contact using the capillary forces of a droplet of water placed between them, and found that the beam stayed stuck after the water had evaporated. The interaction was a combination of the van der Waals force where the surfaces were in contact, and the Casimir force where there was a gap.

Chan notes that in experiments he has done, the smallest possible separation between two MEMS surfaces is about 60 nanometres or more. "If we go beyond this distance, we find that the plates jump into contact, presumably due to the Casimir force," he says. "However, this is a phenomenon that most researchers try to avoid rather than study."

Although more work is needed to find out

whether the Casimir force triggers stiction in MEMS, Capasso and his co-workers have verified that it can be detected in such devices. They think that the force could in fact be used to start mechanical motion. "As you load more and more MEMS devices on to a chip, at some point you have to contend with this effect," Capasso says. "Either you must avoid it or you must use it."

Capasso's fascination with the Casimir force began during the 1990s, while he was working at Bell Labs in Murray Hill, New Jersey. In 2001, he and his Bell colleagues devised a MEMS device that enabled them to probe the Casimir force in an accurate and controlled way<sup>5</sup>. The device measured the attraction between a gold-coated sphere and the surface of a see-saw made from two square silicon plates that were coated in gold (see picture, overleaf).

The Casimir force between the plates and sphere drew one side of the see-saw upwards. The tilt increased sharply at separations of less than about 150 nm, but the researchers could detect it for separations of at least 300 nm. The amount the plate tilted matched very closely that predicted from Casimir's theory. In principle, the researchers can exert precise control over the Casimir interaction because electrodes beneath the see-saw (used to measure its movement) offer the option of tilting the plate using electrostatic interactions. Because this would entail

balancing electrostatic forces, elastic forces in the see-saw and the Casimir interaction, the researchers can control the interaction in ways that might be exploited in future MEMS devices.

Further opportunities for engineering the Casimir force arise because the interaction depends on the composition of the interacting materials. There have even been predictions of a repulsive Casimir force. "Between two flat plates with vacuum in between, the Casimir force is always attractive," says physicist Astrid Lambrecht of the Kastler Brossel Laboratory in Paris. But with another medium in between the plates, such as certain types of liquid, she says, you can have repulsion.

No one has yet seen a repulsive Casimir force experimentally. It requires picking materials that have the appropriate electromagnetic responses at different wavelengths. But earlier this year, Capasso reported experiments on two gold surfaces immersed in ethanol<sup>6</sup>. The force between them remained attractive, but it was only half as strong as that when the surfaces were separated by air. "This is a stepping-stone experiment," he says. "By replacing one of the surfaces with silica or Teflon, we might expect to see a repulsive force. But it is very difficult stuff — you have to be paranoid about possible sources of error." Capasso believes that engineering a repulsive force could be used

**"As you load more and more devices on to a chip, at some point you have to contend with the Casimir effect."**

— Federico Capasso

E. GRINNELL/HARVARD UNIV.



Federico Capasso (right) and Jeremy Munday set up an experiment to investigate the ghostly interactions caused by the Casimir force.

## Into the gap

In the 1940s, Theo Overbeek and Evert Verwey at the Philips Research Laboratories in Eindhoven, the Netherlands, made accurate measurements of the attractive van der Waals force predicted to exist between all atoms, molecules and small particles owing to random fluctuations in their clouds of electrons. This force was thought to be fully explained by the 1930 quantum-mechanical theory of Fritz London. But Overbeek and Verwey found that at separations beyond a few nanometres the strength of the attraction declined more quickly than London's

theory predicted.

Overbeek correctly suspected that the difference was caused by the finite speed of light. A fluctuation in the electromagnetic field of one of the bodies cannot be felt by the other faster than the time taken for an electromagnetic wave to propagate between them. This means that it becomes necessary to take into account the electromagnetic fluctuations of the vacuum too. But Overbeek lacked the theoretical knowledge needed to tackle that problem, and so he approached Hendrik Casimir for help.

In collaboration with Dik Polder,

also at Philips, Casimir calculated how this delay alters the character of the attractive force. In 1948, Casimir worked out the theory for two 'ideal' metal plates (which reflect light perfectly) separated by a gap. But no real material behaves this way, and in the 1950s Evgeny Lifshitz and his co-workers in the Soviet Union worked out how the theory is modified when some light gets absorbed by the materials. This allowed the Casimir force to be generalized to a broad class of materials, including insulators.

The theory correctly describes the attractive interaction that

results from quantum fluctuations at all separations, covering both the Casimir (long-range) and van der Waals (short-range) regimes. Arguably a lot of subsequent confusion could have been avoided if these two 'forces' hadn't acquired separate names, as they are ultimately derived from the same cause.

Overbeek didn't succeed in measuring the Casimir force until 1978, when he detected it between a small metal sphere and a metal plate. But accurate measurements that could be compared closely with theory had to wait for another two decades.

P.B.

to induce 'Casimir levitation', which might be used to make friction-free micro-bearings. It could also provide routes for avoiding Casimir-induced stiction in microengineering.

Because the Casimir force stems from electromagnetic fluctuations, it is sensitive to the way materials interact with light. So optical properties such as birefringence, in which the refractive index is different in different directions, can also affect the force. This means that the interaction between two birefringent plates should depend on their orientation: the plates will tend to align with each other. If they are moved out of alignment, a torque will act to restore it.

Capasso hopes to observe this effect by suspending a birefringent disk over a plate, perhaps levitating it using a repulsive Casimir force<sup>1,7</sup>. "We can give the disk a kick with laser light, then shut off the light and watch it rotate back," he says. It should be possible to detect

this rotation by looking at how light bounces off the disk. Capasso and his colleagues are planning an experiment like this, using disks of barium titanate tens of micrometres across suspended in ethanol above a calcite crystal.

### Attractive proposition

Capasso thinks that such studies could bring together hitherto separate communities — those who work on quantum optics and electrodynamics, and those who work in materials physics. He suspects, for example, that interesting things might happen to the Casimir force close to phase transitions in materials that alter their electronic or optical properties — such as the transition between an insulating and a metallic material, or between a normal metal and a superconductor. His group is currently looking for these effects in the interaction between a gold sphere and a thin slab of a high-temperature superconductor. Any such effect is likely to be small, but he thinks it is worth a try.

A former co-worker of Capasso, Davide Iannuzzi, now at the Free University of Amsterdam, proposed one such experiment

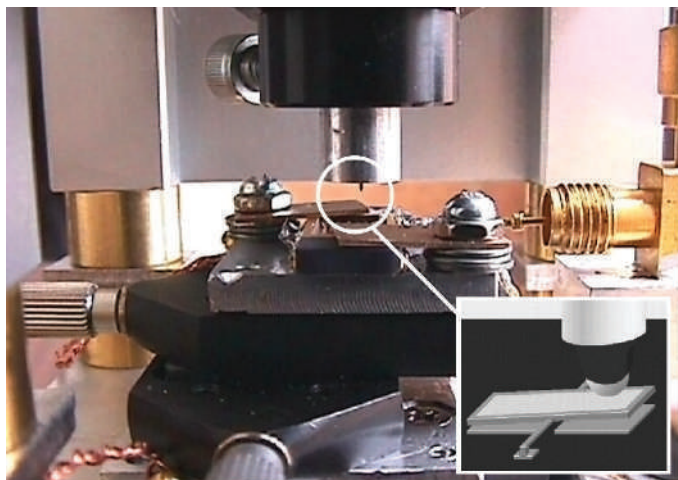
that involved measuring the force between a gold plate and a sphere coated with stacked thin films of magnesium and nickel, which switches from being reflective to transparent when exposed to hydrogen. To their surprise, the researchers saw no change in the strength of the force on adding hydrogen<sup>8</sup> — they had expected the change in the material's reflectivity to affect the Casimir force. "It was a negative result that probably told us more than a positive result would have," says Capasso. One explanation may be that for this material, wavelengths much longer than the visible range contribute significantly to the Casimir force, and that adding hydrogen doesn't alter the reflectivity much at these wavelengths.

So, as they continue to investigate this quirk of nature, researchers are finding that the Casimir force is more slippery than they first imagined. But this exploration of how, and how much, empty space can be engineered has only just begun. It looks sure to demonstrate that there's a lot you can make out of nothing. ■

Philip Ball is a consultant editor for *Nature*.

**"It is very difficult stuff — you have to be paranoid about possible sources of error."**

— Federico Capasso



Balancing act: this device allowed the Casimir force between a metallic see-saw and a spherical electrode (inset) to be measured.

1. Capasso, F., Munday, J. N., Iannuzzi, D. & Chan, H. B. *IEEE J. Select. Top. Quantum Electr.* **13**, 400–414 (2007).
2. Lamoreaux, S. K. *Phys. Rev. Lett.* **78**, 5–8 (1997).
3. Serry, F. M., Walliser, D. & Maclay, G. J. *J. Appl. Phys.* **84**, 2501–2506 (1998).
4. Buks, E. & Roukes, M. L. *Phys. Rev. B* **63**, 033402 (2001).
5. Chan, H. B., Aksyuk, V. A., Kleiman, R. N., Bishop, D. J. & Capasso, F. *Science* **291**, 1941–1944 (2001).
6. Munday, J. N. & Capasso, F. *Phys. Rev. A Rapid Comm.* (in press); preprint at <http://arxiv.org/0705.3793> (2007).
7. Munday, J. N., Iannuzzi, D., Barash, Y. & Capasso, F. *Phys. Rev. A* **71**, 042102 (2005).
8. Iannuzzi, D., Lisanti, M. & Capasso, F. *Proc. Natl. Acad. Sci. USA* **101**, 4019–4023 (2004).

## Students unite to create State of the Planet course

SIR — Ours is a world in crisis. We are despoiling our habitat, outstripping our resources and failing to provide an acceptable living standard for much of the world's population. Although academic institutions are equipped to help remedy these problems by informing the leaders of tomorrow, they often fail to do so. Increasing pressure for specialization has led universities to trade breadth for depth in curricula, thereby depriving students of an understanding of complex, interconnected global issues. For example, solutions to our energy crisis span economics, engineering and politics, yet the typical student is exposed to only a portion of this spectrum.

Here, we propose a first step in addressing such shortcomings. We, the undersigned graduate students, have created a campus-wide 'State of the Planet' course at Cornell University under the mentorship of faculty members Tom Eisner and Mary Lou Zeeman (see [www.nbb.cornell.edu/neurobio/BioNB321](http://www.nbb.cornell.edu/neurobio/BioNB321)).

Our goal is threefold: to improve understanding of complex issues; to add global context to disciplinary education; and to motivate action and involvement. To this end, we recruited experts, mostly resident faculty members and community leaders, to address the challenges we agreed were paramount.

Administrative support was quick to materialize, as was a pool of enthusiastic participants. We launched the course in January 2007, after campus-wide publicity highlighting its multidisciplinary nature. Our 250 current students come from 45 different majors ranging broadly across the humanities and basic and applied sciences. In lectures, experts familiar with our most pressing global problems emphasize how solutions span disciplines. Students participate in discussion groups led by graduate assistants, where they not only build on ideas presented in lectures, but also set up projects aimed at solving problems.

Mid-semester student evaluations have been overwhelmingly positive, with 93% saying that the course has changed their views on education, career plans and lifestyle, and 95% believing that their peers should also take this course.

Comments include: "This course has influenced my perspectives on almost everything, from the food I eat to how long I leave my computer on" and "The course demonstrates how many different skills and backgrounds can help shape policy that is instrumental for the planet".

We are continuing to expand our course in the hope that it will become a campus-wide requirement. Our vision is that other

universities will adopt similar courses as a curriculum component for all students. We extend an open invitation to like-minded people at other institutions to join us, and others launching parallel efforts, in what we believe will be a modest but fundamental change to university education.

We maintain the optimistic belief that, given the right information, people will change their habits and their world. But the burden is on us, as educators, to motivate this change.

**Krystal L. Rypien, Jill Anderson, Jason Andras, Rulon W. Clark, Gretchen A. Gerrish, James T. Mandel, Marie L. Nydam, Daniel K. Riskin**

Department of Ecology and Evolutionary Biology, Cornell University, Ithaca, New York 14853, USA

interbreed in captivity.

This case study illustrates the significance of the work of traditional systematists, as highlighted in your Editorial 'The legacy of Linnaeus' (Nature 446, 231–232; 2007). Linnaean taxonomy is the science of classification of organisms based on diverse character sets. DNA barcoding can supplement this, but cannot replace it.

**U. Kutschera**

Institute of Biology, University of Kassel, Heinrich-Plett-Strasse 40, D-34109 Kassel, Germany

## Slang's not so slick when you remember its origins

SIR — As African-Americans and as scientists, we are appalled and disappointed in your News Feature 'Pimp my antibody' (Nature 446, 964–966; 2007), which summarizes recent developments in antibody therapy. Despite your misguided attempt to be humorous and socially 'hip', we are dismayed at the cavalier use of the word 'pimp' in a scientific journal, especially one as reputable as *Nature*.

A pimp is defined as a person who controls and exploits a prostitute. Unfortunately, urban/hip-hop culture (and increasingly, mainstream American culture) has embraced the flamboyant, vulgar and misogynistic pimp lifestyle. This has led to a new, related meaning of the term 'to pimp'. However, no amount of manipulation can remove this term from its immoral origins. That such a headline appeared in *Nature* indicates the extent to which our society has become desensitized to such imagery. Use of this term in a scientific context is highly inappropriate, because it could be seen as endorsing such a lifestyle.

Although most scientists desire their work to be understood and appreciated by the average non-scientist, inclusion of such offensive slang only degrades the article and the science it describes.

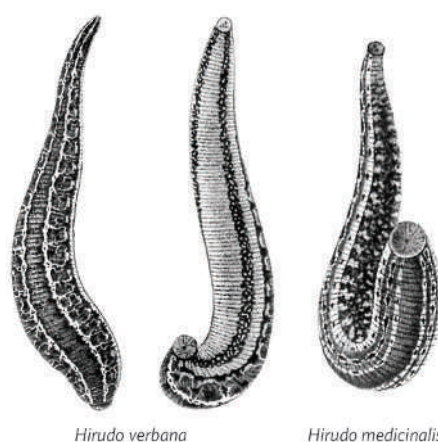
We are especially concerned about the use of such language in an international journal. The United States' multifaceted culture has global influence, but this is one aspect that should not be spread and legitimized. *Nature* should continue to inspire scientific discovery and inform the international scientific community of noteworthy progress, without promoting disrespectful and demeaning imagery.

**Renée M. Ned\***, **Lisa N. Steele†**

\*Tucker, Georgia 30084, USA

†Atlanta, Georgia 30324, USA

Science publishing issues of interest to authors are regularly featured at **Nautilus** (<http://blogs.nature.com/nautilus>), where we welcome comments and debate.



the eighteenth century. On Plate 10 of Georges Cuvier's book *Iconographie Du Règne Animal* (Baillière, Paris, 1829), shown here, the medicinal leech *H. verbana* Caren, 1820 is depicted in dorsal and ventral views, and is juxtaposed to its sister taxon, *H. medicinalis* Linnaeus, 1758.

These drawings show the characteristic, species-specific pigment patterns of both 'leech varieties' in remarkable detail. Cuvier's original figures are of the same quality as recently published photographs of these blood-sucking annelids, which do not

## BOOKS &amp; ARTS

# Dirt cheap soil

Precious few societies have taken care of their most fundamental resource.

## Dirt: The Erosion of Civilizations

By David R. Montgomery  
University of California Press: 2007.  
295 pp. \$24.95, £15.95

### Eric A. Davidson

If everyday expressions offer clues to what we value, then the common use of 'dirt-cheap' to describe anything inexpensive speaks poorly of our appreciation for soil. Like water and air, soil is not efficiently traded and priced in the marketplace, and yet we could not live without it. It doesn't take a rocket scientist to figure out that food security and human well-being depend on fertile soil. That expression implies admiration for the intelligence of rocket scientists, and similar praise is due to Earth scientist David Montgomery, whose new book insightfully chronicles the rise of agricultural technology and the concomitant fall of soil depth just about everywhere in the world, from prehistoric to modern times. The topic could not be more timely, as recent large-scale expansion of maize (corn) in the United States and sugar cane in Brazil for biofuel production signals a new era of competition between the energy and food sectors for the globally finite resource of arable land and the remaining good soil.

Montgomery catalogues a tragically recurrent pattern. Starting with the first farmers in the Tigris and Euphrates River basins, across the Mediterranean of the ancient Greeks and Romans, through bronze, iron and industrial ages, repeated in the Americas and in Asia, and up to contemporary practices on industrial mega-farms and smallholder slash-and-burn fields. In each case, agriculture expanded on good land, which fuelled population growth, followed by further agricultural expansion onto marginal land, ultimately leading to soil erosion, declines in agricultural productivity, and often societal collapse and emigration.

Perhaps owing to the repetitive nature of this story, the writing is not as captivating as Jared Diamond's in *Collapse* (Viking, 2004), which similarly charts the interplay between the prosperity and longevity of civilizations and their husbandry of several kinds of inherited natural capital. Equally provocative, however, Montgomery asserts that the rise and fall of many civilizations, generally lasting from 800 to 2,000 years, roughly corresponds to how long it takes for their soils to erode away.



B. FORSTER/GETTY IMAGES

Dust in the wind: civilizations collapse when their soil runs out.

Not all is gloomy. A precious few examples of good soil management are described. Montgomery also cites philosophers, agronomists, and soil scientists from ancient Greece onwards, showing that we have known for a long time how to obtain good crop yields and simultaneously conserve soil. Reasons that such sage advice has seldom been followed include perverse economic incentives and land tenure laws, imposed by governments that reward mining the soil for short-term profits. Montgomery offers a wealth of interesting examples.

The Lincoln Memorial in Washington DC now stands where colonial ships once sailed in the Potomac River and is built on the sediments washed downstream from former colonial tobacco farms. High prices paid for tobacco in Europe, a plentiful supply of cheap land in the American colonies, and tax revenue for the British government generated from tobacco sales motivated both private and government sectors to seek maximum crop yields rather than promote sound agricultural management. These shocking changes become obvious over many decades and centuries, but soil often slips away at a rate that a farmer may not perceive during a single lifetime.

Further advances in technology will probably increase crop productivity, and some expansion of agricultural land is still possible,

but Montgomery argues that soil has become a scarce resource. More than a history lesson of the legacies of past civilizations, the book raises a critical concern for modern times. We are currently losing soil at least 20 times faster, on average, than it is being replaced through natural processes. To meet the demands for food and, more recently, energy, we need Montgomery's scholarly, historical perspective, as well as the ability to project current trends of land management to future scenarios.

In the final chapter, the author offers a vision of organic farming for both large and small farms. Soil conservation can also be promoted without going totally organic, and I doubt that we can feed 7–10 billion people entirely without fertilizers and pesticides. We probably need the proverbial cleverness of rocket scientists to figure out what sustainable agriculture fully entails, but it is clear that soil conservation must be its central tenet.

When I talk to elementary school classes about soil, I start by distinguishing it from dirt. Kids quickly catch on that soil nourishes plants in forests, grassland, farms, and gardens, whereas dirt is soil transported to places where it is unwanted, such as under fingernails, on the living room carpet and in sediments of reservoirs and estuaries. The greatest strength of this book is its persistent and forceful

demonstration of a lesson that adult societies have yet to embrace — societies prosper and persist best when they figure out ways to keep their soil where it belongs and not treat it as if it were dirt cheap. ■

Eric A. Davidson is a senior scientist at the Woods Hole Research Center, 149 Woods Hole Road, Falmouth, Massachusetts, USA. He is the author of *You Can't Eat GNP* (Perseus Press, 2000).

## Secret life of plants

### The Emerald Planet: How Plants Changed Earth's History

by David Beerling

Oxford University Press: 2007. 304 pp.  
£14.99

#### Paul Falkowski

Plants are an inextricable part of the human experience. They provide us with food and fibre, drugs and building materials, fuel and fodder, fragrances and shelter. Although we are literally beholden to plants for our very existence, the geological history of plants and their role in transforming Earth's biology and chemistry is a largely unsung tale.

This book tries to capture the stories for a scientifically literate reader. It is not written, nor intended to be, a popular science blockbuster, but rather an accessible monograph, in the modern sense, that examines basic questions that palaeobiologists and geochemists have addressed for decades. When did oxygen-producing organisms evolve? How did they come from the oceans to invade land? Once on land, how did they transform the rocky world in which they found themselves to create soils and environments conducive to terrestrial animals, such as ourselves?

The author, David Beerling, trained in palaeobiology and geochemistry, tells two stories in parallel. One is the history of Earth and how photosynthetic organisms transformed it. The other is the history of humans who sought to understand Earth's history. Both are eloquently and engagingly merged in a scholarly, yet generally accessible book that bespeaks of the author's love for plants, the geological history of Earth and the history of science.

Traditionally, Earth's biological history has been inferred from fossils. The fossil record of plants extends back to about 420 million years, yet the fossil record of animals is at least 200 million years older, and fossils of marine microorganisms extend back several billion years (although the validity of some of the earliest microfossils has been questioned). So when did oxygen-producing organisms first appear on Earth?

We are not certain; molecular fossils (organic remnants of organisms that are physically lost in the fossil record) suggest that the earliest oxygen-producing microbes — cyanobacteria — evolved about 3 billion years ago. Over the past 50 years, geochemists, armed with mass spectrometers and other sophisticated instruments, have been able to piece together isotopic

records of carbon and sulphur, from which the oxidation state of Earth can be inferred. These records suggest that the atmosphere of our planet 'flipped' from a mildly reducing, anaerobic condition to a mildly oxidizing, low-oxygen state about 2.3 billion years ago. Subsequently, cyanobacteria responsible for the generation of oxygen were appropriated via a series of symbiotic associations, and spread throughout the oceans as eukaryotic algae.

One clade among these algae successfully garnered a foothold on land and became the progenitor of all higher plants. This book describes how terrestrial plants transformed the surface of the planet, not only by accelerating the oxidation of the atmosphere (a process pioneered by algae), but by accelerating the weathering of rocks to form soils and release nutrients, thereby transforming the terrestrial landscape.

Beerling provides for the reader a fascinating history of the discovery of fossils and the inferences drawn from them. For example, he describes how the French palaeontologist, Charles Brongniart, described in 1894 the discovery of a fossil dragonfly with a wingspan of 63 cm. Such an enormous insect cannot fly without extraordinarily high levels of oxygen; indeed, such gigantic insects are taken as support for geochemical models that suggest

oxygen concentrations during the Carboniferous period were upwards of 30% or more — about 50% higher than current oxygen level of 21%. The discovery of fossil forests and dinosaur remains in polar regions, such as Greenland and Antarctica, clearly suggest that 200 million years ago these environments were much warmer than today, presumably as a consequence of significantly higher concentrations of CO<sub>2</sub> in Earth's atmosphere.

Beerling argues that the long-term changes in atmospheric oxygen and carbon dioxide are driven not only by tectonics and slow chemical reactions, but by plants. Indeed, he develops a set of examples that explore how the evolution of plants and animals altered the history of Earth as much as geological processes did.

The emerald portion of our blue planet — the largely terrestrial photosynthetic world — owes its existence to the oceanic realm. Perhaps ironically, Beerling virtually ignores the lowly cyanobacteria, without which there would be no higher plants.

Be that as it may, this book is a wonderful example of the nascent field of Earth systems science, in which geologists and geochemists try to document changes in Earth's environment throughout the planet's history, and biologists try to understand how the core metabolic processes of life altered the distribution of elements on the planet's surface. Beerling describes how we came to understand the importance of oxygen in the nineteenth century, yet to this day we still do not fully understand the mechanism by which the energy of the Sun is used to split water to form the gas on which all animal life is dependent. ■

Paul Falkowski is in the Department of Geological Sciences and the Institute of Marine and Coastal Sciences, Rutgers University, New Brunswick, New Jersey 08901-8521, USA.



Deep roots: plants such as this fossil tree have shaped Earth's chemistry and geology.

# The obscure clarity of starlight

Anselm Kiefer builds monumental souvenirs of the night sky.

## Pete Jeffs

"Your age and my age and the age of the world cannot be measured in years," wrote Austrian author Ingeborg Bachmann in her poem *Das Spiel ist aus* (The game is up). It is the sheer size of Anselm Kiefer's *Sternenfall* (Falling stars) installation in the restored Grand Palais in Paris that projects the visitor into the immeasurable.

The German artist is the first exhibitor in a new annual event called *Monumenta*. Each year, the Grand Palais will host a different artist to show work of monumental proportions. Kiefer's mega-installation, on view until 8 July 2007, reflects his interest in the astronomical sky.

Kiefer is among the most important contemporary artists. He gained notoriety in 1969, with his series of photographs entitled *Besetzungen* (Occupations), which depict the artist amongst European landscapes making the Hitlerian salute.

In 1993, he moved to the south of France. It was perhaps the vast, starry

skies of his new home in Barjac that led him to contemplate the heavens, and the cosmic reality that we ourselves are born of stardust. He frequently uses sunflower seeds; the "heliotropic spiralling seed-head is a condensed 'negative print' of the starry night sky, a cosmos full of black stars".



He has also been influenced by the ideas of Robert Fludd, the sixteenth century thinker, that each plant on Earth has a celestial equivalent, and the human body is a condensed version of the cosmos. But alongside this mysticism, Kiefer makes full use of modern astronomy.

His *Monumenta* exhibition comprises

seven cavernous 'houses' each containing one or many canvases, such as the 2001 painting *Andromeda*, illustrated here. On entry, the visitor is confronted with a pile of rubble, littered with books made of lead and the glass shards of fallen stars, each numbered from a recent star map. The

rubble is that of a collapsed tower entitled *Dashed Hope*, one of three built from hollow concrete blocks. Of the other towers, one, the title piece of the exhibition, stands 17 metres high. The third tower, rising eight metres above the spectator, is called *Sun Ship*, evoking a giant vessel. An array of sunflowers, a solar motif, protrudes from the top.

Shortly before his death in 1986, Joseph Beuys, Kiefer's compatriot and fellow artist, told Kiefer that through immense personal effort we can enter a domain "where cathedrals may be built". In *Monumenta*, Kiefer not only enters that domain, but brings back souvenirs from the starry voyage.

**Pete Jeffs is an artist who lives and works in Paris.**

A. KIEFER/EDITIONS DU REGARD

## Bloggers unite

### The Open Laboratory: The Best Writing on Science Blogs 2006

Edited by Bora Zivkovic

Lulu: 2007. 336 pp. \$19.85, £10.99

#### Paul Stevenson

*The Open Laboratory* is a collection of writing from science blogs, selected and published by the energetic US biologist-blogger Bora Zivkovic with the help of the blogging community. In the run-up to the first conference of science bloggers earlier this year in North Carolina, Zivkovic took it upon himself to collate the fifty best posts put up by the end of 2006. Topics include micro black holes, bird migration, human sleep patterns, evolution, quantum mechanics and psychology. The writing ranges from PhD students enthusing about concepts from their research areas, to opinion pieces on themes such as the rights and wrongs of particle-physics funding, intelligent design and political interference in science policy.

This wide-ranging book provides something — hopefully many things — for everyone. Par-

ticularly enjoyable is browsing entries about areas of science away from one's own research interests. As a physicist, I learned a lot about the origin of mitochondria from the representative entry of Carl Zimmer's award-winning blog *The Loom*. I was pleased, too, to see entries from some of the highly trafficked blogs that I habitually read and enjoy, such as *The Panda's Thumb* and *Cocktail Party Physics*.

By their nature, blogs are dynamic. A post typically bristles with links out to elsewhere on the web and accretes an ever-changing exchange of comments between readers and the author. To capture this energy and texture in a static book is a challenge that the editor fully acknowledges in his introduction. The solution Zivkovic fixes on for *The Open Laboratory* is to pick posts that he feels work in isolation, to list links as footnotes and to omit the comment strings.

The results of this snapshot editing process are mixed, and sometimes sloppy. For example, the freewheeling satire of the post, "Hurray for being eaten by a bear!", from the blog *Thoughts From Kansas* is hard to appreciate out of con-

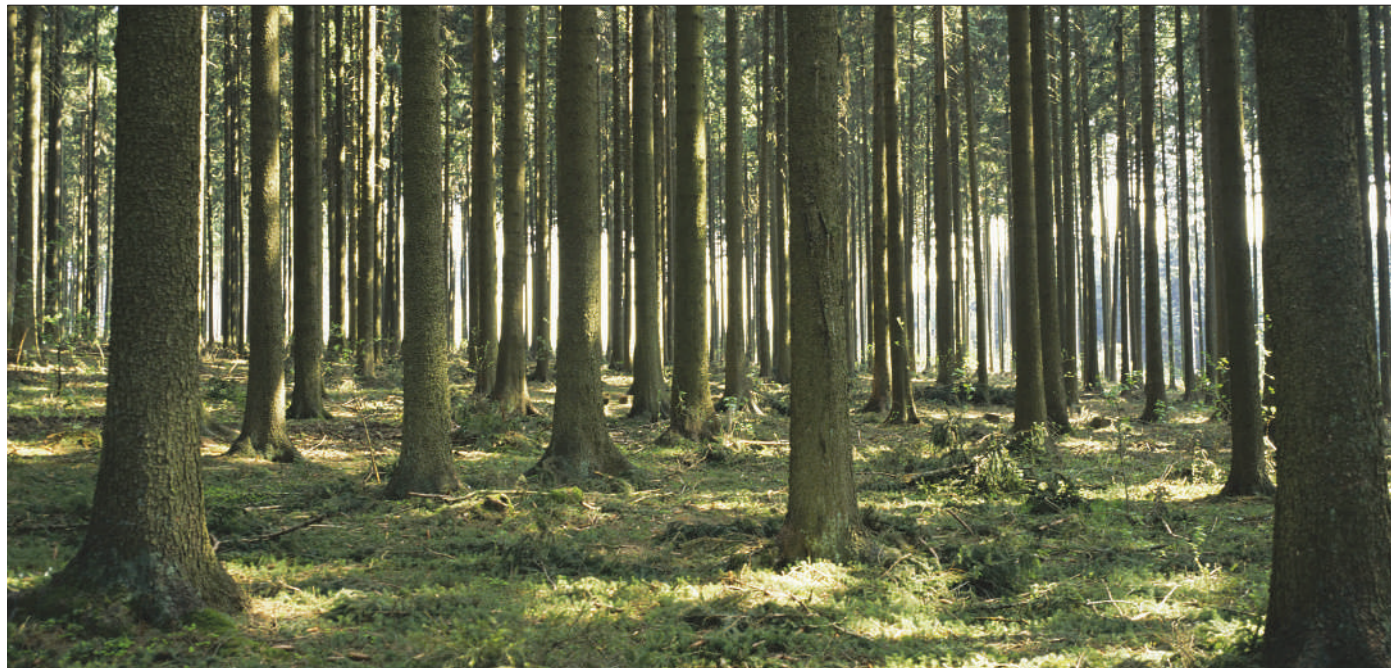
text. Plus, the URLs supplied reveal curious differences between the printed posts and those online. Why, for instance, does a graph that links rising bear attacks to rising temperature in the book, plot bear attacks against human population on the web?

The entries highlight the great variety of styles that can thrive in the blogosphere. Most of the pieces are a little chattier than the usual book or magazine article, but those chosen are formal enough not to grate on the printed page. Occasionally, the prose is loftier than a typical popular science book. Some even veer too much towards the tone of a research article — leaving terms like suprachiasmatic nucleus or a zygomaticomaxillary suture unexplained.

The book works well enough as a standalone anthology of science writing, but I share the editor's hope that it will prompt eager print readers hitherto unfamiliar with the vibrant young medium that is science blogging to have a look, and maybe even have a go. Nominations for next year's anthology are already being sought (<http://openlab.wufoo.com/forms/submit-form/>). It will be interesting to see how this project develops over coming years as the blogosphere itself evolves.

**Paul Stevenson is a nuclear physicist at the University of Surrey, Guildford, GU2 7XH, UK.**

## NEWS &amp; VIEWS



BOTANICA/PHOTOLIBRARY.COM

## ENVIRONMENTAL SCIENCE

## Nitrogen impacts on forest carbon

Peter Högberg

**Does the extra nitrogen input from anthropogenic sources mean that more carbon from the atmosphere is being locked up in boreal and temperate forests? 'Yes' is the answer to emerge from the latest analysis.**

Since the Industrial Revolution kicked into gear, at around the beginning of the nineteenth century, the atmospheric concentration of carbon dioxide has increased from 280 to 380 parts per million<sup>1</sup>. Starting a century later, there has been an even more dramatic increase in the industrial fixation of atmospheric nitrogen into agricultural fertilizers, and in the production of nitrogen oxides from combustion processes in vehicles and industry. Together, these anthropogenic nitrogen sources now exceed natural biological nitrogen fixation<sup>2</sup>.

The fraction of this nitrogen that ultimately becomes deposited on temperate and boreal forests might increase tree growth, and the sequestration of atmospheric CO<sub>2</sub> into wood<sup>3</sup>. Or perhaps the capacity of these forests to use extra nitrogen for growth is marginal or non-existent<sup>4</sup>. On page 848 of this issue, Magnani and colleagues<sup>5</sup> report that nitrogen deposition can, indeed, drive carbon sequestration in most temperate and boreal forests.

The carbon and nitrogen cycles in forests interact in many and complex ways<sup>6,7</sup>. But increased input of nitrogen to forests with a poor natural supply evidently increases foliar

biomass and the concentration of the photosynthesizing enzyme RUBISCO (Fig. 1a, overleaf). These changes lead to greater capture of energy in sunlight and greater photosynthesis per unit area of forest. They also cause a shift in the allocation of plant carbon from roots and their symbiotic mycorrhizal fungi towards above-ground structures such as woody tree trunks (Fig. 1b). As carbon in wood has a much longer residence time than the carbon allocated to short-lived roots and the associated mycorrhizal fungi, nitrogen deposition will increase carbon sequestration by forest ecosystems. The retarding effect of nitrogen on the decomposition of plant litter and soil organic matter has the same effect<sup>8</sup>.

Hundreds of nitrogen-fertilizer trials have documented growth increases in northern temperate and boreal forests<sup>6</sup>, especially in areas away from major sources of pollution. Some researchers have thus surmised that nitrogen deposition will also increase carbon sequestration in forest ecosystems (see ref. 3, for example). But others infer that the unnaturally high levels of nitrogen that leach to groundwater and stream water in areas of high nitrogen

deposition indicate that extra nitrogen does not stimulate carbon sequestration by trees<sup>9</sup>, and that relatively little of the nitrogen added to forests becomes immobilized in wood<sup>4</sup>.

To address this controversy, Magnani *et al.*<sup>5</sup> analysed the carbon balance across a network of forest sites encompassing the levels of nitrogen deposition experienced by most of western Europe and the conterminous United States. The carbon balance, or net ecosystem production (NEP), is the balance between ecosystem carbon fixation through photosynthesis and its release back to the atmosphere through plant and soil respiration. This balance was chiefly determined by the so-called eddy-covariance method — the simultaneous measurement of the upwards or downwards movements of bubbles of air (created by turbulence over rough surfaces such as forest canopies), and of the concentration of CO<sub>2</sub> in the bubbles moving up or down. Very high temporal resolution can be obtained with this technique, although diurnal, seasonal and interannual variations in NEP are typically of most interest. Another advantage of this approach is that the equipment, which is placed several metres above the forest canopy,

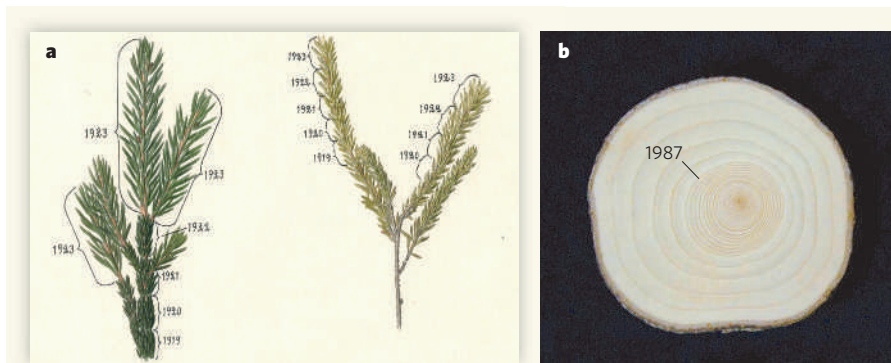


**Figure 1 | Growing influence.** **a**, The effect of nitrogen addition on foliar biomass and colour — a painting of branches from one of the first forest fertilization experiments, carried out in the 1920s. Note the longer and darker-green needles from the fertilized tree on the left. **b**, The effect of nitrogen on stem growth (this trunk is about 13 cm in diameter). Note the conspicuously thicker tree rings after fertilization began in 1987. (Illustrations courtesy of Sune Linder.)

sees and integrates the 'footprint' of a relatively large area (often 1 km<sup>2</sup> or more). Problems are that the carbon balances of both natural and managed forests vary considerably during the lifetime of a forest, and that the method is so new that it has not yet been used through the life cycle of individual forests.

To distinguish the true effect of nitrogen deposition, Magnani *et al.*<sup>5</sup> first had to remove the major sources of variability in NEP, which are related to natural disturbances (such as fire) or anthropogenic disturbances (such as forest harvesting). They did this by modelling the mean lifetime NEP using eddy-covariance data from temporal sequences accounting for different stages in forest lifetime. Both ecosystem production and respiration correlated positively with mean annual temperature, but NEP did not because its two components responded similarly to temperature.

Magnani *et al.*<sup>5</sup> could then demonstrate a strong positive relation between mean lifetime NEP — that is, carbon balance — and the deposition of nitrogen. Their analysis captures annual deposition levels of up to 15 kg nitrogen per hectare (10,000 m<sup>2</sup>), and is thus representative of about 90% of western Europe and the conterminous United States. It does not refute the view that some forests are nitrogen-saturated<sup>4,9</sup>. But it does show that, in most forests of the Northern Hemisphere at higher latitude, forest capacity to respond to extra nitrogen with increased carbon sequestration is not near saturation.

However, a note of caution is that whereas the carbon balance clearly responds positively to additions of nitrogen, this response is expected to be an order of magnitude smaller<sup>10</sup> than the regression presented by Magnani *et al.*<sup>5</sup> suggests (see Fig. 3d on page 850). A hectare of nitrogen-limited forest is supposed to sequester roughly 30 kg carbon in the trees and an additional 10 kg carbon in the soil per kilogram of nitrogen added to the ecosystem<sup>10</sup>; this response becomes drastically reduced at rates of nitrogen addition above 50 kg nitrogen per hectare per year<sup>10,11</sup>. The exact relation between nitrogen addition and the response of the

carbon balance thus needs clarification.

Such clarification is essential because of the serious practical questions that arise in this area of research. Should forests be fertilized with nitrogen to sequester more atmospheric CO<sub>2</sub>? And should strategies to reduce levels of CO<sub>2</sub> emissions include forest fertilization to produce more wood and wood products to replace fossil fuels, or to replace concrete as a building material (large amounts of CO<sub>2</sub> are generated during concrete production)? Positive answers require the demonstration that such artificially

fertilized forests can return reasonably quickly to their natural nitrogen-limited condition, and that the environmental impact, including effects on biodiversity, is minimal within and downstream of the treated area.

On the other hand, some forests in densely populated areas in particular are certainly nitrogen-saturated, and they suffer from the adverse impact of excess nitrogen deposition from the atmosphere<sup>9</sup>. These effects include excessive leaching of nitrate and changes in the species composition of the flora<sup>9</sup>. Safeguarding the health of these forests in the long run will require reductions of uncontrolled nitrogen emissions. ■

Peter Högberg is in the Department of Forest Ecology and Management, SLU — Swedish University of Agricultural Sciences, SE-901 83 Umeå, Sweden.

e-mail: peter.hogberg@sek.slu.se

1. Falkowski, P. *et al.* *Science* **290**, 291–296 (2000).
2. Vitousek, P. M. *et al.* *Ecol. Appl.* **7**, 737–750 (1997).
3. Townsend, A. R. *et al.* *Ecol. Appl.* **6**, 806–814 (1996).
4. Nadelhoffer, K. J. *et al.* *Nature* **398**, 145–148 (1999).
5. Magnani, F. *et al.* *Nature* **447**, 848–850 (2007).
6. Tamm, C. O. *Nitrogen in Terrestrial Ecosystems* (Springer, Berlin, 1991).
7. Hyvönen, R. *et al.* *New Phytol.* **173**, 463–480 (2007).
8. Berg, B. & Matzner, E. *Environ. Rev.* **5**, 1–25 (1997).
9. Aber, J. D. *et al.* *BioScience* **48**, 921–934 (1998).
10. Hyvönen, R. *et al.* *Biogeochemistry* doi:10.1007/s10533-007-9121-3 (2007).
11. Högberg, P. *et al.* *Glob. Change Biol.* **12**, 489–499 (2006).

## GENOMICS

# Encyclopaedia of humble DNA

John M. Greally

**Researchers of the ENCODE consortium have analysed 1% of the human genome. Their findings bring us a step closer to understanding the role of the vast amount of obscure DNA that does not function as genes.**

We usually think of the functional sequences in the genome solely in terms of genes, the sequences transcribed to messenger RNA to generate proteins. This perception is really the result of effective publicity by the genes, who take all of the credit even though their function is basically limited to communicating genomic information to the outside world. They have even managed to have the entire DNA sequence referred to as the 'genome', as if the collective importance of genes is all you need to know about the DNA in a cell.

We should have guessed that this was merely prima-donna behaviour on the part of narcissist genes when the sequencing of the human genome revealed that they comprise only a small percentage of the DNA. And our confidence should have been shaken when some sequences located far from any genes were found to be strikingly conserved<sup>1</sup>, indicating that they have some important function. Now, on page 799 of this issue<sup>2</sup>, the ENCODE

Project Consortium shows through the analysis of 1% of the human genome that the humble, unpretentious non-gene sequences have essential regulatory roles (Fig. 1).

We are increasingly being forced to pay attention to our non-gene DNA sequences. For example, in attempts to find the cause of an inherited disease, investigators study hundreds of thousands of sequence variations in the genome, known as single nucleotide polymorphisms (SNPs), to see which ones are non-randomly associated with the disease. Recently, such studies<sup>3–6</sup> revealed several sequence variations associated with type 2 diabetes and its related manifestations, but only a minority of the identified SNPs were located within genes. So, if we are to understand this insight into the causes of human diseases, we need to know what the functions of the non-gene majority are.

The aim of the ENCODE (encyclopaedia of DNA elements) project is exactly that — to

identify every sequence with functional properties in the human genome<sup>7</sup>. The results of the pilot phase of this project<sup>2</sup>, which involved an analysis of 1% (30 megabases) of the human genome, are not good news for genes, which will no longer be able to hog the limelight. Even this preliminary study reveals that the genome is much more than a mere vehicle for genes, and sheds light on the extensive molecular decision-making that takes place before a gene is expressed.

A valuable aspect of the project is that, when possible, ENCODE researchers addressed the same question using several different techniques. For example, combining microarray and sequencing approaches with computational analyses, they found that many more sections of the genome are transcribed into RNA than had previously been recognized. The concordance of these approaches lends strength to the conclusions, which are challenging to those accustomed to the idea that only protein-coding sequences are expressed. If you look hard enough, you can find evidence that most of the human genome is transcribed as RNA at some time or another.

This pervasive transcription could be due to either many unrecognized sites in the genome that initiate transcription, or a previously unsuspected tendency for the RNA polymerase enzyme to stay on the DNA and keep going when it has already finished its job of expressing a gene. This question is addressed by the second component of the ENCODE report<sup>2</sup>, which looks at the regulation of transcription. These results are much more satisfying, probably because they are less challenging to our preconceptions on the subject.

First, the authors identified the locations of the transcription start sites, and correlated these with how the DNA is packaged around histone proteins to form chromatin. They then identified where within the chromatin certain histones are marked by chemical modifications, and identified positions at which transcription-regulatory proteins were binding to the DNA. They found evidence of regulatory functions for sequences at transcription start sites, as expected, but also at other sites in the DNA. The combinations of regulatory marks differed between those at promoters (sequences upstream of genes that regulate their expression) and those elsewhere, indicating that the non-promoter sequences have distinct functions that are yet to be defined.

The transcriptional regulators identified by the ENCODE investigators clearly occur in patterns within very short genomic regions. When one zooms out to look at more DNA at a time, it becomes apparent that there is also a larger-scale organization to the genome. Although the significance of this organization remains unclear, it parallels the scale of organization of another genomic phenomenon — the regulation of DNA replication. Sequences associated with this process have long been known to be organized into domains of

hundreds of thousands of base pairs<sup>8</sup>. A strength of the coordinated ENCODE approach is the ability to correlate DNA replication with large-scale patterns of the organization of transcriptional regulators in the same cell types. Accordingly, the authors show that early-replicating regions are enriched in histone modifications associated with gene activation, and late-replicating regions are marked with repressive modifications.

The final question the ENCODE researchers addressed related to sequences that are known to be highly conserved<sup>1</sup>, but that are not part of recognized genes. Having defined regulatory sequences within the 1% of the genome,

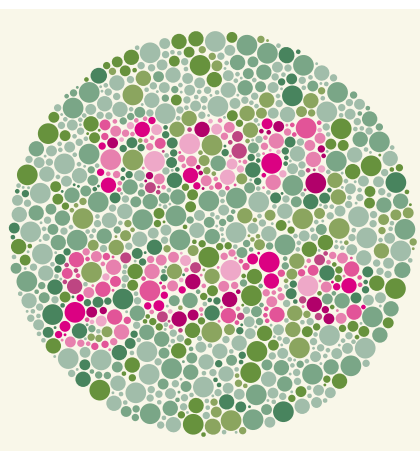


**Figure 1 | Hidden message.** Ishihara's test for red-green colour deficiencies uses several coloured plates, similar to this one, in which a number is disguised in a different colour within the dot pattern. Similarly, we are so fascinated by genes (green dots) that we have become blinded to non-gene components (magenta dots) of the genome. However, in studying 1% of the genome, the researchers of the ENCODE consortium<sup>2</sup> found that non-gene sequences have essential regulatory functions, and thus cannot be ignored.

the authors could ask whether these sequences are unusually well conserved and, conversely, whether highly conserved sequences are functional. The answer to both questions was a qualified 'yes'. Some very conserved sequences are not obviously functional, but this isn't of much concern, as it is possible that looking at more tissues would have revealed cell-type-specific functions. In addition, a minority of obviously functional sequences is not very well conserved, but the authors acknowledge that sequence conservation studies may not be sensitive enough to detect retention of a transcription-factor binding site in the context of extensive local sequence divergence. This offers a glimpse of a potentially fascinating area of research — studying sites of conserved function but with mostly diverged sequences, and looking for the preservation of very small sequence motifs that would elsewhere be considered noise and disregarded.

So how much have we learnt about the functional regions of this 1% of the genome

through the ENCODE study<sup>2</sup>? The significance of the different parts of the study varied. For example, the ascribed function of long transcripts that are not translated into proteins is very speculative. It is interesting that these non-coding transcripts are found at sites of genomic imprinting<sup>9</sup> (in which the allele expressed is predetermined by the parent from which it originated), but this could be due to the intensive study of imprinted loci, at which non-coding RNA has yet to be shown to have consistent functional significance. Furthermore, the large-scale organization of the genome doesn't have much immediate effect on elucidating the function of individual sequences within them. Instead, the discrete, local, regulatory processes will be most relevant in the short term — for instance, in the interpretation of association studies when the informative SNPs are not within, and are thus not altering, gene sequences<sup>3–6</sup>.

The big question is how the ENCODE consortium will scale-up its efforts to study the remaining 99% of the human genome. One problem to address is the choice of cell types for such studies. In the pilot phase, the consortium decided, for pragmatic reasons, to include certain cell lines — such as the HeLa and HL60 cells — that are easily grown in culture so that they could be distributed to geographically dispersed researchers. However, a disadvantage of using such cell types is that they often have broken chromosomes that have unusual additions and losses of DNA from different regions of the genome. So whether the regulatory processes in these cell lines are representative of those in primary cells from the human body is, to say the least, questionable.

The other concern is the possibility that certain regulatory processes are cell-type specific. If the ENCODE project is to succeed in defining every regulatory element in the genome, the investigators will have to study the entire genome of every possible cell type, which is a daunting task. So although the glimpse we are provided by the ENCODE consortium into the ordered complexity of 1% of the human genome is tantalizing, the insights only confirm the challenges that lie ahead. However, as long as we continue to implicate the function of regions containing non-gene sequences in human disease, we will have to embrace this challenge.

John M. Greally is at the Albert Einstein College of Medicine, Bronx, New York 10461, USA.  
e-mail: jgreally@aecon.yu.edu

1. Dermitsakis, E. T., Reymond, A. & Antonarakis, S. E. *Nature Rev. Genet.* **6**, 151–157 (2005).
2. The ENCODE Project Consortium *Nature* **447**, 799–816 (2007).
3. Saxena, R. *et al.* *Science* **316**, 1331–1336 (2007).
4. Scott, L. J. *et al.* *Science* **316**, 1341–1345 (2007).
5. Steinthorsdóttir, V. *et al.* *Nature Genet.* **39**, 770–775 (2007).
6. Sladek, R. *et al.* *Nature* **445**, 881–885 (2007).
7. The ENCODE Project Consortium *Science* **306**, 636–640 (2004).
8. White, E. J. *et al.* *Proc. Natl Acad. Sci. USA* **101**, 17771–17776 (2004).
9. O'Neill, M. J. *Hum. Mol. Genet.* **14**, R113–R120 (2005).

## PLANETARY SCIENCE

# Mars at the tipping point

Maria T. Zuber

**There's a big problem with the idea of ancient oceans on Mars: if they were contained within the 'shoreline' visible today, sea level would not have been level. Could it be that Mars has since tipped over?**

Despite spectacular *in situ* chemical and geological evidence for water on the surface of ancient Mars, courtesy of NASA's Opportunity and Spirit rovers<sup>1,2</sup>, the temporal persistence and the spatial extent of surface water during the planet's early years remain unclear. Early studies raised the possibility that there was once an ocean in the lowlands of Mars's northern hemisphere<sup>3,4</sup> (Fig. 1), an idea based on the identification of 'palaeo-shorelines' in orbital images. Given the absence of preserved shorelines of a similar age — at least 2 billion years old — on Earth, their identification on Mars is necessarily a subjective endeavour<sup>5</sup>. Nevertheless, credible additional analyses do support the hypothesis<sup>6,7</sup>. On page 840 of this issue, Perron *et al.*<sup>8</sup> present a quantitative analysis that removes arguably the main objection to the shoreline interpretation.

This objection is that a shoreline must follow a line of constant gravitational potential: the 'geoid' on Earth, the 'areoid' on Mars. Mapped onto a topographic profile that indicates the level of fill, such an equipotential surface represents 'sea level'. Once Mars's topography and gravitational field had been accurately mapped<sup>9–11</sup> in the late 1990s, it became apparent that the traces of the previously hypothesized shoreline deviated from an equipotential surface. Unless these deviations could be explained, the observed features could not plausibly have originated as the edge of an ocean. Given the extent of the mapped shorelines, which extend over thousands of kilometres, any explanation for this deviation would have to reflect a process that was global in scale.

Perron *et al.*<sup>8</sup> demonstrate that the deviations

of a couple of prominent palaeo-shorelines might be explained by a phenomenon known as 'true polar wander'. This is the reorientation of a planet with respect to its spin axis, and requires a significant mass redistribution on or within a planet<sup>12</sup>. In essence, the authors calculated how the topography of a planet deforms in response to a change in rotational potential as the planet reorients in response to a large load, and tested whether this could have been responsible for the modification of the mapped shorelines.

But why would a planet reorient itself at all? In general, a planet rotates stably around its axis of minimum inertia. The plane normal to that axis, approximately the equatorial plane, is often flattened owing to the centrifugal effect of rotation. The equatorial region of Mars has a huge excess mass associated with the vast Tharsis volcanic province (Fig. 1). Earth's largest volcano, Mauna Loa, which rises almost 10 kilometres above the Pacific Ocean floor to form a large part of the island of Hawaii, has an estimated volume of some 40,000 km<sup>3</sup>. The volume of Tharsis is about 10,000 times greater. Such a bulging waistline would be impressive enough on Earth, but is even more so on Mars, which has only an eighth of Earth's volume.

Tharsis probably formed early in martian history<sup>13</sup>, during the planet's Noachian era<sup>14</sup>, some 3.8 billion years or more ago. Wherever on Mars Tharsis originally formed, its massive load would have reoriented to situate itself near the equator, and so form a stable rotational configuration. Structural superposition relationships indicate that the shorelines post-date the emplacement of Tharsis, and so its formation

**50 YEARS AGO**

When reindeer were introduced into Scotland some ten years ago, a significant factor was that the various ground, rock and tree lichens eaten by reindeer play little part in the diet of red deer, roe deer, sheep, or other indigenous animals... In northern Scandinavia there are more than 600,000 domesticated reindeer and in the northern USSR approximately two million, valued for their meat, skins, milk and hair, and for transport. These benefits have led to imports of reindeer in Alaska, Canada and South Georgia... There were many reindeer in Scotland in prehistoric times, and these were probably hunted with red deer. Why the wild reindeer died out while the red deer remained is unknown... reindeer meat was probably more popular, and the pre-firearm techniques of the chase were not adequate to eliminate the fleet red deer.

From *Nature* 15 June 1957.

**100 YEARS AGO**

The closing months of 1906 and the opening months of 1907 are likely to be long remembered by electrical engineers as a period of a remarkable rerudescence of interest in the subject of incandescent electric lamps. For many years the familiar carbon filament lamp has been the only commercial incandescent electric lamp, in spite of its threatened extinction by the invention of the Nernst lamp in 1897–1898. The feeling of uncertainty caused by this discovery was short-lived... the electrical world settled down with the conviction that the threatened revolution was not destined to be achieved. But in the meantime inventors were busy... The tungsten lamp appears to have a brilliant future before it. A lamp working at a little more than 1 watt per candle brings electric lighting almost to the level of gas for cheapness... a radical improvement has long been wanting, and there seems every reason to believe that it has at last been made.

From *Nature* 13 June 1907.

50 & 100 YEARS AGO

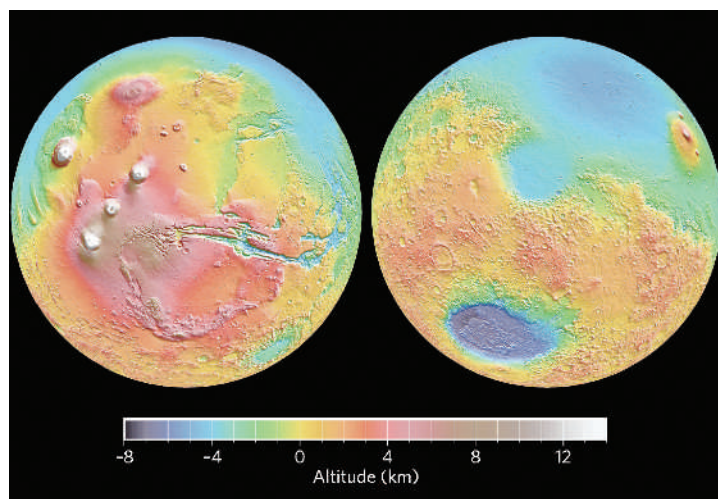


**Figure 1 | Topographic maps of Mars.** These maps show the Tharsis province (in red and yellow in the left-hand image), and the lowlands of the northern hemisphere (in blue in the upper parts of both images) that are the proposed site of an ancient ocean.

is ruled out as the source of shoreline deformation. Any subsequent mass redistributions would have been considerably less than that associated with the formation of Tharsis, and would almost certainly have left Tharsis close to Mars's equatorial plane. But might Mars have reordered itself less comprehensively in more recent times, in the Hesperian epoch — middle martian history — roughly 2.8–3.7 billion years ago?

Perron *et al.*<sup>8</sup> believe so. The first question they address successfully is whether there is a path of true polar wander that can explain the deviation of the putative shorelines from equipotential surfaces. The supplementary question is whether plausible candidates exist that could have driven such a reorientation during middle martian history. The Elysium volcanic province, which is in the opposite hemisphere to Tharsis, is a possibility, as is the massive Utopia basin that is buried beneath the northern plains, or a redistribution of mass associated with large-scale convection in the interior of Mars. Other, arguably less likely, possibilities include the addition of even more volcanic material during the late-stage accretion of the Tharsis volcanic pile, or the mass associated with the putative ocean itself.

Evidence for recently discovered sedimentary depositional features on Mars<sup>15</sup> and models that support the possibility of sustained groundwater upwelling at Meridiani Planum, the landing site of the Opportunity rover<sup>16</sup>, have, for the time being, focused attention away from the idea of an ancient ocean or oceans to explain Mars's watery past. Perron and colleagues now resuscitate that possibility. Their result<sup>8</sup> hints that, despite dramatic recent advances made possible by various rovers and orbiters, the understanding of the 'blue' history of the red planet is far from complete. ■

Maria T. Zuber is in the Department of Earth, Atmospheric and Planetary Sciences, Massachusetts Institute of Technology, Cambridge, Massachusetts 02139, USA.  
e-mail: zuber@mit.edu

1. Squyres, S. W. *et al.* *Science* **305**, 794–799 (2004).
2. Squyres, S. W. *et al.* *Science* **306**, 1709–1714 (2004).
3. Baker, V. R. *et al.* *Nature* **352**, 589–594 (1991).
4. Parker, T. J. *et al.* *J. Geophys. Res.* **98**, 11016–11078 (1993).
5. Malin, M. C. & Edgett, K. S. *Geophys. Res. Lett.* **26**, 3049–3052 (1999).
6. Head, J. W. *et al.* *Science* **286**, 2134–2137 (1999).
7. Carr, M. H. & Head, J. W. *J. Geophys. Res.* **108**, doi:10.1029/2002JE001963 (2003).
8. Perron, J. T. *et al.* *Nature* **447**, 840–843 (2007).
9. Lemoine, F. G. *et al.* *J. Geophys. Res.* **106**, 23359–23376 (2001).
10. Yuan, D.-N. *et al.* *J. Geophys. Res.* **106**, 23377–23401 (2001).
11. Smith, D. E. *et al.* *J. Geophys. Res.* **106**, 23689–23722 (2001).
12. Goldreich, P. & Toomre, A. *J. Geophys. Res.* **74**, 2555–2567 (1969).
13. Phillips, R. J. *et al.* *Science* **291**, 2587–2591 (2001).
14. Tanaka, K. L., Scott, D. H. & Greeley, R. in *Mars* (eds Kieffer, H. H. *et al.*) 345 (Univ. Ariz. Press, Tucson, 1992).
15. Malin, M. C. & Edgett, K. S. *Science* **302**, 1931–1934 (2003).
16. Andrews-Hanna, J. C., Phillips, R. J. & Zuber, M. T. *Nature* **446**, 163–166 (2007).

## PALAEOBOTANY

## Forests frozen in time

Kirk R. Johnson

**Just over 300 million years ago, a forest was dropped below sea level by an earthquake and swiftly buried. Such rapid events provide snapshots of lost ecosystems, sometimes on a huge spatial scale.**

Fossil plants preserve a vast amount of information about ancient ecosystems and climates. But much of this information is difficult to retrieve because plants fall apart both during life and after death, and many extinct groups are still poorly described because not all of their organs are known. However, the rooted nature of plants means that vegetation can be buried in place, preserving spatial and ecological information that could never be retrieved for mobile organisms.

Writing in *Geology*, DiMichele *et al.*<sup>1</sup> report an extraordinary occurrence of a catastrophically buried forest, now exposed on the roofs of tunnels and chambers of a coal mine in Vermillion County, Illinois. By surveying the mine, they have documented the vegetation of an Upper Carboniferous forest covering an area greater than 1,000 hectares. Such extensive data allow them to map both the small-scale

and large-scale spatial patterns of the 307-million-year-old forest, and statistically to resolve ecological gradients.

Dispersed plant parts are rapidly recycled by soil organisms and reduced to their organic constituents within months. Well-preserved palaeobotanical remains are therefore direct evidence of rapid burial below the level of destructive processes occurring in soils. For this reason, fossil plants represent the least time-averaged of any terrestrial fossils, and present opportunities to capture precise data about ancient ecosystems and climates. Rapid burial can result from various mechanisms. In the case of the Illinois forest, which grew in a coastal mire, local tectonic subsidence dropped the forest floor to sea level quickly enough for the plants to be preserved in place. The rate of this type of subsidence is difficult to measure, but DiMichele *et al.*<sup>1</sup> argue that it must have

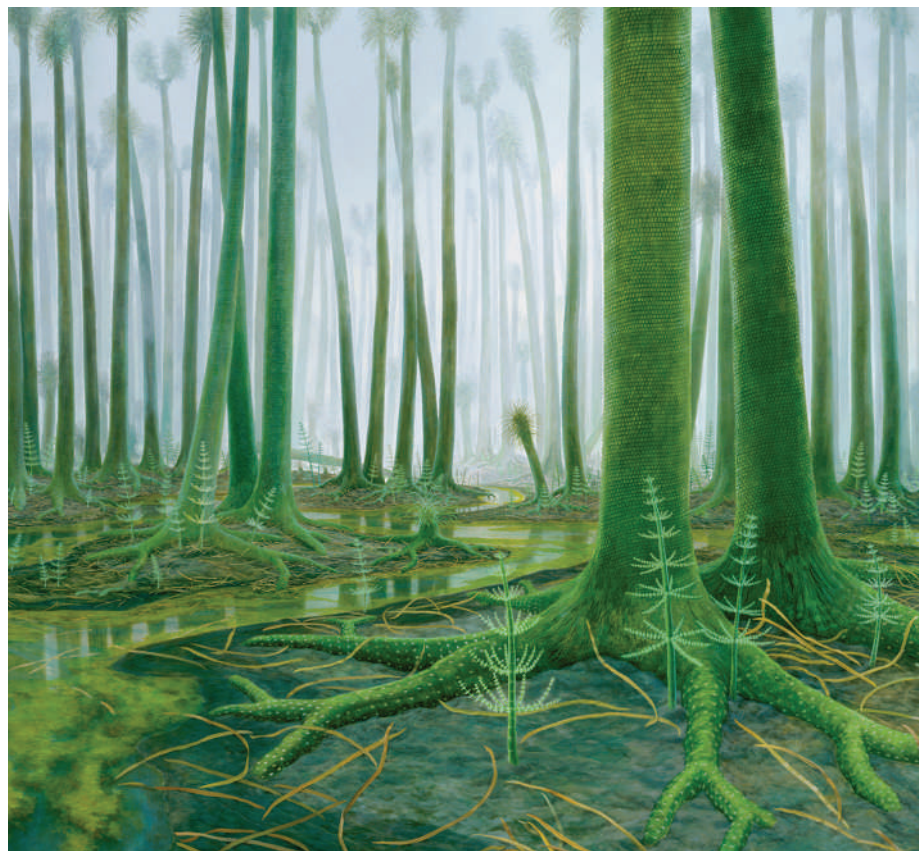


**Figure 1 | In the mire.** A reconstruction of a lycopod forest similar to that preserved intact in a coal mine in Vermillion County, Illinois, and described by DiMichele *et al.*<sup>1</sup>. These forest giants (which sometimes exceeded 40 metres in height) were characterized by sparse canopies and photosynthetic bark, properties that suggest that sunlight penetrated to the forest floor. (Painting by J. Vriesen and K. Johnson. Reprinted with permission from the Denver Office of Cultural Affairs.)

## OPTICAL MEMORY

## The secret of the stone

While casually sipping his Martini, a secret agent scans the glamorous guests filling the room. His eyes rest on an innocent-looking woman in a simple dress adorned with a single pale stone. Has he recognized that the stone is the key to all the information that is holding his adversary's evil organization together?

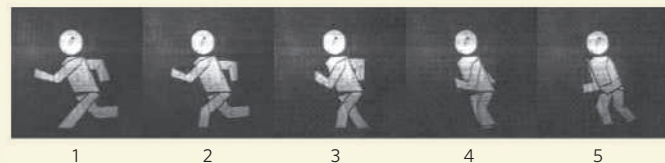
Yuko Ishii *et al.* would have recognized this hidden device. They have developed a holographic information storage system in which a piece of the mineral ulexite is a key component (Y. Ishii *et al.* *Opt. Express* **15**, 7218–7223; 2007). As each stone is unique and irreproducible, only the stone that is used to store the information can retrieve it again.

In holographic memory, information is stored optically in a light-sensitive crystal. An 'object'

laser beam (containing information) produces an interference pattern with a reference beam, and the pattern is inscribed on the crystal. Information is retrieved again by using a third beam, in combination with the reference laser.

The beauty of the technique is that multiple images can be stored in the same volume, by slightly changing the settings of the reference beam at each recording step.

Although it cannot yet beat magnetic disks in terms of price and performance, holographic data storage has its own advantages, and could become more competitive if its storage capacity could be improved. One way to achieve this is to use random reference beams, which can be generated by randomly rotating a diffuser in front of the reference laser. But this requires



a computer-controlled rotator and an algorithm to impose the randomness.

Ishii and colleagues' approach is much simpler and more compact. They use a piece of ulexite as the diffuser and rotate it in regular steps. Because each piece of mineral has a unique composition, the random pattern of reference beams produced cannot be replicated by any other stone. Furthermore, only that stone can be used to retrieve the data. Ishii

*et al.* demonstrate the effectiveness of the scheme by holographically storing images of a running figure and retrieving them as an animation with six frames per second (see figure).

The authors note that the stone could be worn as part of an accessory and so be carried without attracting suspicion — except, that is, from a secret agent who has kept up with the scientific literature.

Liesbeth Venema

occurred within two months to provide the quality of preservation seen in the mine.

Volcanic ash falls and mud flows are another, and demonstrably instant, method by which vegetation can be buried and preserved. Indeed, many fossil plant sites characterized by superb preservation seem to have a component of volcanic ash deposition in their genesis. For example, Wing *et al.*<sup>2</sup> described a 4-kilometre-long transect through a Late Cretaceous meadow, dating to about 71.7 million years ago, that had been preserved in a 2–4-metre-thick slurry of volcanic ash. In this case, not only arboreal but also herbaceous vegetation was found rooted where it grew. Wing *et al.* were able to map the vegetation according to soil type, and to show that angiosperm herbs were more prevalent in better drained sites, whereas ferns and cycads trended towards the mires.

These 'plant Pompeii's' have an additional advantage in that they are preserved in a medium that is itself amenable to radiometric dating. Volcanic ash beds often contain sardine or zircon crystals that formed in magma chambers shortly before eruption, trapping radioactive potassium and uranium, respectively. Ash-bed floras are literally buried in a matrix of fossil 'clocks'. As the precision of dating techniques increases, the ability to resolve the age of *in situ* deposits also increases. Because of better mass spectrometers and laboratory practices, error bars have been getting smaller during the past few years, and errors at the two-sigma statistical level have crept down from 0.5% to 0.1%, and in some labs are heading for 0.05% or even less<sup>3,4</sup>.

EARTHTIME<sup>5,6</sup> is an international project intended to consolidate these gains by reducing

interlaboratory variability, and to understand the differences in precision and accuracy of different dating methods (especially between uranium–lead and argon–argon geochronology). This precision is being combined with the ability of the astronomical timescale to define individual 22,000-year Milankovitch cycles<sup>7</sup>, which are due to variation in Earth's orbit. All in all, we can look forward to a time when events that occurred as long ago as the beginning of the Cretaceous, some 145 million years ago, can be directly and precisely measured in thousands of years rather than hundreds of thousands or millions of years. Sedimentological evidence for instantaneous deposition could then pin-point an event to a period of a few months or less within the window of a few thousand years.

DiMichele *et al.*<sup>1</sup> have taken advantage of the near-instantaneous deposition, superb preservation and great extent of their fossil forest to statistically analyse the distribution of different tree species across an ancient landscape. Carboniferous rainforests were composed of completely different major tree groups from those that exist today. For example, lycopods (Fig. 1), the largest trees in these forests, stood above understoreys of tree ferns, pteridosperms (extinct seed ferns), cordaitaleans (extinct seed plants related to conifers) and sphenopsids (trees related to living horsetail rushes). The authors' analysis shows that the ecology of these long-extinct forests can be retrieved, and that forest heterogeneity on the local scale can be resolved from ecological gradients on a landscape scale.

There is good evidence that vegetation is in dynamic equilibrium with climate<sup>8</sup>, and it is

becoming clear that some climate change can occur on a subdecadal timescale<sup>9</sup>. In circumstances in which a fossil site has been buried over a period of between hours and months, with climate change occurring in decades and geochronological resolution improving by the day, we are entering a world in which the term 'geological time' is becoming less relevant and we are forging the tools to resolve rapid events in real time. A new partnership between palaeontologists and geochronologists will revolutionize the way we think about rates of change — even for events that occurred hundreds of millions of years ago. Just because something happened a long time ago does not mean it took a long time to happen. ■

Kirk R. Johnson is at the Denver Museum of Nature and Science, 2001 Colorado Boulevard, Denver, Colorado 80205, USA.  
e-mail: kirk.johnson@dmns.org

1. DiMichele, W. A., Falcon-Lang, H. J., Nelson, W. J., Elrick, S. D. & Ames, P. R. *Geology* **35**, 415–418 (2007).
2. Wing, S. L., Hickey, L. J. & Swisher, C. C. *Nature* **363**, 342–344 (1993).
3. Storey, M., Duncan, R. A. & Swisher, C. C. *Science* **316**, 587–589 (2007).
4. Furin, S. *et al.* *Geology* **34**, 1009–1012 (2006).
5. Kerr, R. A. *Science* **302**, 375 (2003).
6. www.earthtime.org
7. Kuiper, K. F., Wijbrans, J. R. & Hilgen, F. J. *Terra Nova* **17**, 385–398 (2005).
8. Webb, T. *Vegetatio* **67**, 75–91 (1986).
9. Alley, R. B. *Quat. Sci. Rev.* **19**, 213–226 (2000).

## Correction

In the caption to Figure 1 of the News & Views article "Planetary science: Cracks under stress" by Andrew J. Dombard (Nature **447**, 276–277; 2007), the number for the conversion of 91 kelvin to centigrade should, of course, be –182 °C.

## OBITUARY

# Chauncey Starr (1912–2007)

Physicist, engineer and leader in the development of nuclear power.

Chauncey Starr — veteran of the Manhattan District Project, pioneer of the peaceful uses of atomic energy and founder of EPRI, the Electric Power Research Institute — died on 17 April. The previous day, we had held a celebration of his recent 95th birthday at EPRI, with Chauncey holding forth on his life experiences and lessons learned. He was in fine fettle. The following morning, before leaving for his office at EPRI, as he had been doing ever since his official retirement 30 years previously, he took his usual short nap after breakfast. But this time, he didn't wake up. It is hard to conceive of a more graceful way to end a long and fulfilling career.

Starr was born in Newark, New Jersey, the second son of Jewish–Russian immigrants. Educated in the local public-school system, he went on to earn degrees in engineering and physics at Rensselaer Polytechnic Institute, New York. His 1935 PhD thesis examined the thermal and electrical properties of rectifying copper-oxide junctions. I used to kid him that if he had accidentally introduced some calcium impurities into his samples, he might have discovered today's family of high-temperature cuprate superconductors.

He then joined Percy Bridgman's group at Harvard University to work on the thermal transport properties of metals at high pressure. This is one of the most difficult of condensed-matter experiments to carry out, given the confounding background of containment vessel and thermometry. Starr, however, devised a differential method that could much more accurately determine the thermal diffusivity (thermal conductivity and specific heat) of metals in such a situation. This was an especially notable advance at the time: Bridgman had published work suggesting that the Wiedemann–Franz law, which links the thermal and electrical conductivities of metals, and was one of the lynchpins of the then emerging quantum theory of solids, may not apply to metals under pressure.

With his new technique, Starr was able to show that this conclusion resulted from systematic errors in Bridgman's previous experiments. To claim that he saved Bridgman from not receiving his future Nobel prize may be a stretch, but he certainly rescued his boss from major embarrassment. Twenty-five years later, in 1962, I undertook my doctoral work in that same group at Harvard. At that time, several of my fellow students were still using the methods Starr had pioneered.

From Harvard, Starr went on to a



postgraduate position in the Magnet Lab at the Massachusetts Institute of Technology, where he added cryogenics and magnetic measurements to his portfolio of experimental skills. In 1940, he took a post with the US Navy's Bureau of Mines, leading a group of engineers analysing pressure-wave propagation from mine explosions and exploring the effects of these waves on various hull geometries. Immediately after Pearl Harbor, he and a colleague tried to enlist in the army, but were told that what they were doing would be a greater contribution to the war effort than fighting in foxholes.

Word of Starr's technical and leadership skills spread throughout the then small community of American physicists, and in 1942 he was invited to join the staff of E. O. Lawrence at the University of California Radiation Laboratory at Berkeley. Lawrence's intention (largely unknown to Starr at the time) was to train him in the principles of cyclotron resonance for eventual reassignment to the 'calutron' or 'racetrack' uranium-235 separation project at Oak Ridge, Tennessee, which at the time was not reaching its production goals.

Lawrence asked Starr to form and lead a team of several hundred engineers, to troubleshoot the early-production calutrons through experiments performed on a small-scale model he was to construct. The ensuing improvements were incorporated into new production machines, and by the spring of

1945 sufficient  $^{235}\text{U}$  had been separated to provide the critical mass for a weapon.

Many years later, Starr and Floyd Culler, wartime chief of chemical physics at Oak Ridge, were in my office reminiscing about the days when they watched their technicians use tweezers to pick apart flakes of  $^{235}\text{U}$ , embedded in halide impurities, for shipment to Los Alamos and assembly into the Little Boy bomb. The hair on the back of my neck quite literally stood up. On the morning of 6 August 1945, when the uranium atoms in those flakes split in the sky over Hiroshima, my father was stationed with the US Navy in Manila Bay in the Philippines. Starr was convinced that the decision by President Truman to use atomic weapons against Japan was correct, making invasion unnecessary and thus saving the lives of countless Japanese and Allied servicemen that would otherwise have been sacrificed. Maybe my Dad would have been among them.

After the war, Starr transferred to the Clinton Lab at Oak Ridge to participate in the design work on reactors for nuclear power led by Eugene Wigner and Alvin Weinberg. In 1946, he was hired by North American Aviation to initiate their nuclear programme, later forming and becoming president of a new division of the company, Atomics International. There, in collaboration with Wally Zinn at Argonne National Lab in Illinois, he pioneered the application of atomic energy to the generation of electricity. It was this that he considered his most important contribution to the world.

In 1966, he left the power-reactor industry to become dean of engineering at the University of California, Los Angeles, before moving on, six years later, to found EPRI under contract from the US electric utility industry. In the first of these jobs, he made pioneering contributions to the academic discipline of risk analysis. In the second, among other achievements, he stood firm to establish an environmental division at EPRI despite the vigorous opposition of a number of utility executives, who simply wanted to ignore issues such as the acid rain caused by emissions from power plants using fossil fuels.

For his accomplishments, Chauncey Starr received numerous awards — including honorary degrees, membership of national and international academies, and medals from heads of state. But I know that the recognition he found most personally satisfying came near the end of his life: he was able to witness the rebirth of interest in nuclear power in the United States, the fruit of his younger days, which had lain dormant for so many years.

## Paul M. Grant

Paul M. Grant is at W2AGZ Technologies, 1147 Mockingbird Hill Lane, San Jose, California 95120, USA.  
e-mail: w2agz@pacbell.net

## FEATURE

# Nature's guide for mentors

Having a good mentor early in your career can mean the difference between success and failure in any field. **Adrian Lee, Carina Dennis and Philip Campbell** look at what makes a good mentor.

The *Nature* awards for creative mentoring in science were created on the premise that the mentorship of young researchers — although fully deserving of recognition — is perhaps the least remarked on of all the activities that take place in the lab. Indeed, there is no established definition of what constitutes good scientific mentoring. This article attempts to remedy that situation, drawing on the evidence from competitions for *Nature's* awards. These are held on a national or regional basis, with the most recent taking place last year, when the focus was on Australasia. Previous competitions have been held in the United Kingdom, and the next competition will be in South Africa (see [www.nature.com/nature/mentoringawards/southafrica/index.html](http://www.nature.com/nature/mentoringawards/southafrica/index.html)).

The response to the competition in Australasia was remarkable, with more than 70 groups of 'mentees' submitting their achievements and the reasons why they believed their mentor excelled, with each of the nominated mentors giving a personal view of how they approach mentoring. The quality of applications was outstanding and the panel, all experienced in refereeing papers and grant applications, commented that this was one of the hardest evaluative tasks they had ever undertaken. However, there could be only two winners and they have been lauded elsewhere (see *Nature* 444, 966–968; 2006).

Having been involved in judging the awards — whether in Australia or in the United Kingdom — we realized that within the pages of the applications was an immense resource that could provide a basis for reflection on what comprises good mentoring. These reflections are presented here, with examples of just a few of the hundreds of quotable quotes included in the nominations supporting the mentors. The attributes that we highlight represent a distillation of the opinion of more than 350 scientists writing as nominated mentor or their nominating mentees (and it was the latter whose comments were all-important for the judges).

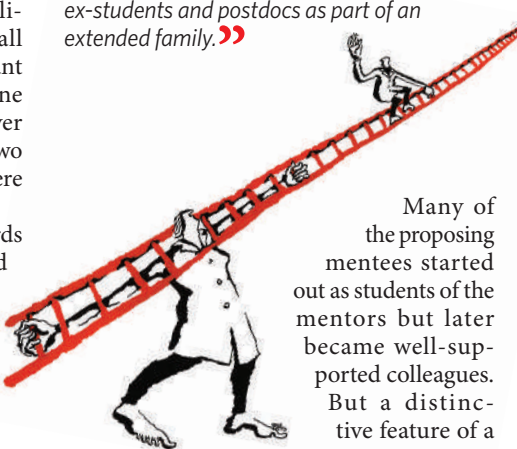
We hope that this material will be especially useful to younger scientists as they start out on their careers as mentors — be it PhD supervisor or scientific team leader. But others stand to benefit from it too. Indeed, we challenge readers who are established leaders of groups and supervisors of young scientists to look at the evidence of what comprises good mentoring,

reflect on your practices and determine whether there are lessons here that could see you alter your approach. Such changes could be to the ultimate benefit of those under your charge and, given the lasting and broad influence of good mentors highlighted by the competition, to science as a whole.

All the quotes included here were taken word-for-word from the applications, either from proposing mentees or the mentors themselves. For obvious reasons they have been depersonalized and are unattributed.

## A mentor for life

**“**M, without any doubt, sees all his interactions with people as lifelong. He always keeps in touch with ex-students, postdocs and so on after they have moved on. Even if he is not directly helping them, he keeps himself aware of their activities and at times informs them of things he believes would be of interest or useful, to them. He genuinely treats his ex-students and postdocs as part of an extended family.**”**



Many of the proposing mentees started out as students of the mentors but later became well-supported colleagues.

But a distinctive feature of a great mentor as opposed to a great

supervisor seemed to be a special focus on helping to build the mentee's career. A natural consequence of the care and effort the mentors put into supporting the careers of their students/staff was that the majority of them became mentors for life: their advice continued to be valued, friendships grew and the links were maintained.

**“**For me there is a difference between a supervisor and a mentor. With the latter you find that you are not simply a student with a research project, but a student

with a career in front that the mentor helps you start.**”**

## Personal characteristics

### Enthusiasm

**“**First and foremost, M is incredibly passionate about science. She eats, sleeps and breathes science. Her enthusiasm is absolutely infectious, and it creates a wonderful atmosphere in her laboratory.**”**

**“**It is the nature of supervision that you have to explain/teach some key concept time after time as each new student arrives. Each time I had to make it feel to the student postdoc that it was the first time I had ever explained the concept; each time I had to tell it with sparkle to help inspire them to seek to know more. At times it was hard to stay 'inspirational'; but to fail would have meant to me that I should quit as a supervisor. You need to understand, as an old and wise friend once said to me, 'Remember, they stay the same age, you get older!'**”**

Passion, enthusiasm and positivity were words dominating the majority of the mentee reports. Whether these are traits we can cultivate or create is debatable. The lesson seems to be that it is very important to be as enthusiastic about your students' research as you are about your own. If you are not, then the question becomes: is the student working on the correct project? If you are not passionate about their project, how can you properly support them? This should also be a lesson to administrators, who may sometimes allocate students to projects and supervisors for expediency rather than a genuine concern for the student or indeed the staff member.

### Sensitivity

**“**When things go wrong, it is important to find out why things happened the way they did. There could be personal factors (sickness, relationship break-ups) that contribute to unhappy decisions or results. Although I may not be able to provide the solution to personal problems, I can provide a sympathetic ear as well as advice or direction to support services.**”**

This quote speaks for itself but there were a number of examples in which mentors were

BELE MELLOR

very sensitive to their charge's circumstances and showed compassion and understanding. When a student or colleague exhibits unusual behaviour or lack of progress there will be a reason. Mentors need to listen, hear and support. Also, many mentors were sensitive to mentees' needs that were not strictly professional, such as finding the right balance between work and family responsibilities; coping with cultural transitions after a move from a different part of the world; developing confidence in a culture that may not be welcoming; or opposing ethnic or gender bias if it arises.

**“***M also knows that it is important to have a work-life balance. He's made it easy for a postdoc with young children to return to the lab part time. It's encouraging as a young scientist to see that there are lab heads who are supportive of people being able to spend time with their family but still have a chance to develop their careers.* **”**

#### Appreciating individual differences

**“***Again it is important to cater for personal traits. Some of my student colleagues need to dot every i and cross every t as they design a set of critical experiments that we have all agreed are important. Others, with, I suspect, an equal success rate, need to jump in, risk making a mess of a few highly critical experiments but gain an instant understanding of either what not or what to try. Allowing both approaches is sometimes difficult, but necessary.* **”**

We are all different in how we work and in what motivates us. The mentees were clearly very appreciative of an ability to carefully craft development activities to enhance and extend personal strengths. Special effort is needed to try to understand all those in a team and deal with them differently. And however much you want that student/colleague to work on that project, sometimes you have to help them make decisions about their career directions.

**“***Not everybody wants to be a leading researcher and some have skills that make them better suited to other occupations. There is little point in encouraging young people to take on a career to which they may be unsuited or that they will find stressful or uninteresting. So I believe it is* **”**

*necessary sometimes to encourage them into other directions.* **”**

#### Respect

**“***She treats her colleagues, regardless of whether they are doing a PhD or if they are a fellow professor, with the same high regard. In doing so, M inspires confidence in her collaborators.* **”**

It is sadly true that laboratories exist where the PhD students are seen as extra pairs of hands rather than genuine collaborators. Although the supervisors may well be successful and grants be funded courtesy of those extra hands, they will never have the satisfaction of working in the stimulating environments described in all of the applications for the mentor awards and will never truly be respected themselves.

#### Unselfishness

**“***His magnanimity in sharing his own ideas and delight in seeing others succeed has also been an inspiration, not just for myself but for a whole generation of younger scientists.* **”**

**“***Most importantly, M has no intellectual jealousy. She was always happy to see others succeed, pushing them forward into the limelight while standing back in the shadows herself.* **”**

There are leaders of some big and important groups who are more concerned with using group members to promote their own scientific standing. Letting your students/colleagues take your ideas and run with them, and being free and willing for them to take credit is not always easy but is always appreciated. What do you lose by allowing them to be lead authors even if the idea was yours?

**“***His lack of defensiveness was very important to me. On several occasions I've published papers that were critical of some aspect of his work — and he helped me to articulate the issues and supported me in getting them published.* **”**

**“***I believe that it is too easy for mentors to create grand (manipulative) plans for their younger colleagues.* **”**

*I believe it is important for mentors to suppress the desire to paint the grand picture, instead it is imperative that they learn to understand their colleagues and how to assist them to fulfil their dreams.* **”**

**“***It was not uncommon to hear that she had lobbied for an opportunity for a postdoc to speak at a conference rather than doing so herself because she recognized the value of becoming known, especially given our distance from North America and Europe.* **”**

#### Support for other than one's own

**“***M is just as diligent in fostering careers of people who he thinks can advance science as he is at fostering his own students. This action is consistent with a motive that goes beyond mere ego and represents service to the advancement of science.* **”**

The impact of a good mentor goes far beyond his or her own boundaries. Within the applications were many examples of support outside the mentor's group. Indeed a number of the mentee support documents were from those who had never actually been in the mentor's laboratory but whose lives had nevertheless been touched.

#### Teaching and communication

**“***M's enthusiasm was infectious for many undergraduate students, and I have no doubt in saying that her delivery of the subject matter was instrumental in fuelling my interest in X as a subject.* **”**

The tension between research and teaching remains at all universities. Success in both is not mutually exclusive and it was striking, but not surprising, that many of the exemplary mentors were exemplary teachers. Many of the mentees who themselves have gone on to very successful careers and have international reputations in science would not have gone down that pathway if they had not been exposed to their future mentor as a teacher.

Those who work in university administration need to remember the benefit of exposing undergraduate students to top scientists to increase the number of graduate students. Up-and-coming young scientists should put effort into their teaching in order to inspire and interest their future mentees. Good mentors encourage their students to teach as soon as they start their PhD, not only to supplement their income but, more importantly, to develop skills that will benefit them in the long term.

Also, many of the great mentors were great communicators, not only of science itself but also of enthusiasm for it to diverse audiences such as schools or local societies. This is not a universal talent and can even be damaging to all concerned if done badly. The good mentors appreciated that such activities can be very valuable training for the communicator

and encouraged their students and younger colleagues to develop these skills.

**“**I first encountered M as a year-11 high-school student in a small country town. The Royal Australian Chemical Institute had commissioned M to travel to regional Victoria and put on a ‘chemistry show’. I remember the explosions, the foam tower spilling its contents over the stage, and M pretending that he hadn’t noticed the chemical mayhem around him. And I remember that it was about this time that I became interested in chemistry. **”**

**“**Students need experience talking about their research in many different forums. Conference attendance is crucial so that they have the opportunity to discuss with other researchers and to develop new ideas. But it is equally important that students have the opportunity to discuss their work in lay terms, whether it is being presented to parents, teachers, or to doctors and nurses as S has done. **”**

### Tips for mentors

Throughout the mentees’ reports and the mentors’ reflections on their mentoring styles were descriptions of activities used by the mentors that contributed to their success. A number of these tips are reproduced here for those readers embarking on a scientific career — or those in full flight — in order to stimulate thinking about mentoring. There is no magic formula; these are simply examples of what the mentees thought worked for them.

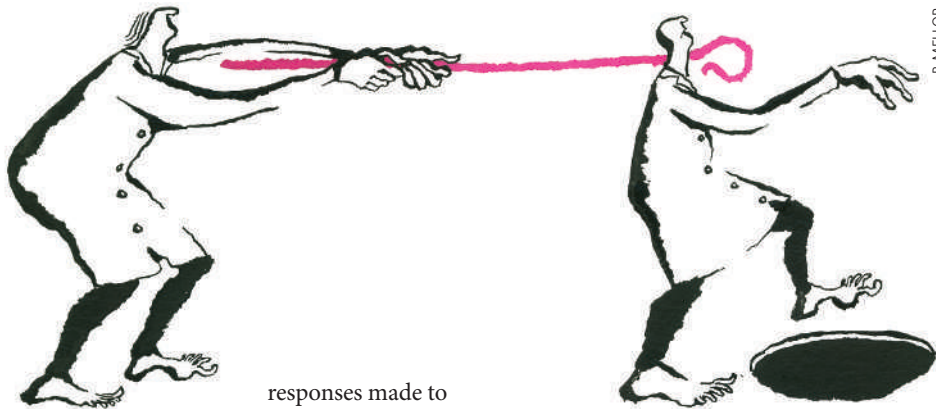
### Availability: the open door

**“**First, her door is always open, even now in her retirement she can never say ‘come back later’. I now greatly admire this skill for I find myself struggling with administration and feeling guilty in making appointments to see students. M always put scientific discussion first. **”**

**“**I cannot remember him ever cancelling an appointment with me despite the tremendous demands on his time (he was head of department for some of the time that I was his student). **”**

**“**M was always accessible, and she always made it abundantly clear to her students that she would rather talk about science with them than do just about anything else. **”**

If there was one theme that came through all the reports it was this one. Availability is the standout quality appreciated by the mentees. Despite enormous workloads and responsibilities, the mentor was always there and the door was always open. They never failed to respond to an urgent request immediately. Mentees marvelled at e-mails answered in 20 minutes,



responses made to drafts in two days and the willingness to listen to their problems.

The regular meeting is clearly an important strategy that some mentors use as well as having an open door. The most impressive was the mentor who set aside a whole day to meet each group member individually for half an hour. The day included a journal-club meeting for all, followed by a research discussion over drinks at the end of the day. An advantage of having a routine that all knew was that it made it easier for students to plan their work and for the mentor to avoid committee meetings on that day. Morning or afternoon coffee breaks are also great daily opportunities for discussion. In these meetings, good mentors encouraged troubleshooting unsuccessful experiments rather than discarding them as a result of incompetence. Indeed there was a common theme that analysis of failure was as important as success.

### Inspiration, optimism

**“**Going to M’s office with your head down, armed with a plot or calculation showing that the project seemed to be going nowhere, you will leave believing that you’ve solved the mysteries of the Universe. **”**

**“**On many occasions I remember walking into her office convinced that I had been wasting my time, and then ten minutes later walking out with a smile and the sure knowledge that what was a bad result was indeed just what I needed! **”**

The ‘walk into the office dispirited/a failure/miserable and yet walk out inspired and optimistic’ phenomenon is a special feature of interaction with the great mentors. There were many comments similar to those above. Attributes that allowed the mentor to cause these almost spiritual experiences included: a broad vision of how science works, a big-picture view and a conviction that unexpected results are often the most interesting and point towards novel insight.

### Balancing direction and self-direction

**“**M displays the right balance of direction in a project and letting someone discover and develop insights for themselves. **”**

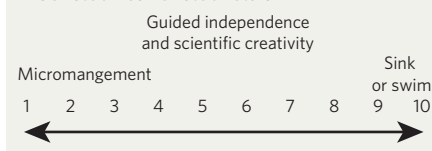
Supervisors who micromanage their students or have very specific ideas of how the science in a lab should be done can stifle the student. **”**

**“**The scientific acumen to, on the one hand, encourage promising ideas and, on the other, recognize a ‘dead end’ is one of M’s great mentoring skills. **”**

Given the large number of comments on getting the balance right, this is a major component of good mentoring. Just how much guidance to give can be a challenge. There were many negative comments about those who have been seen to micromanage. Yet there was also criticism of those who let students run free and learn by their mistakes.

The skill lies in giving young researchers the freedom to expand on their ideas but gently reining them in when they are off track. There were no clear clues as to how to develop this skill. Possibly awareness of how you do it could encourage you to change. Where do you place yourself on the direction–self-direction scale?

#### The direction–self-direction scale



**“**His advice was almost always given in the form of suggestions, so that we were able to digest them and form our own judgment about their worth. With hindsight I recognize this as a deliberate strategy designed to encourage independence of thought and critical thinking. As a PhD student, M made me feel like his collaborator. This is probably the greatest single lesson I have tried to take from M and apply to my own research group, to encourage and prompt students to follow their own ideas and judgement, and to provide an environment where this is possible. **”**

A special challenge is, even if you are prepared to encourage independence, what can you do that nurtures research creativity?

“When I conducted an experiment using two different sources of the one tissue that was never in the research programme, M, instead of saying ‘No, stick to the programme’, asked me why I thought that was a good experiment to do and then complimented me for thinking laterally about the programme.”

“If and when your ideas did not come to fruition there was no criticism, only encouragement to learn from the mistakes made, if any, and encouragement to develop other avenues of scientific attack. This ‘judgement’-free environment allowed one to attempt to implement challenging techniques, knowing that there was no ‘skin off one’s nose’ for trying.”

#### The art of questioning and listening

“There is always another question to ask. The questions seem innocuous but nothing is as it seems to be; there are more insights to be gained by probing away. M also never imposes her will, but she persistently keeps the questions flowing to help the answer come along.”

One of the strategies used in developmental workshops to help young academics become better small-group teachers is to practise answering students’ questions with a question, in order to lead them towards both an answer and a better understanding of what they are learning. It is always easier to give the answer. The same is true when you start to mentor your PhD students and younger colleagues.

“Rather than directly providing me with interesting ideas, he is able to ask the right questions to allow me to come up with my own theories and ideas.”

This is a skill and it can be practised even though it is time-consuming. It is a skill highly valued by the mentees, as was the equally important skill of active listening.

“The major aspects of practice and personality are her ability to listen patiently, even when she knows better, and to point the mentored person to a more complete understanding of the issues implicit in a particular problem. This she does with deceptively simple questions that frequently do not elicit an immediate response, but ultimately allow a more rational interpretation of all the facts.”

#### Being widely read and widely receptive

“As a new assistant professor with my own young graduate students, I can appreciate the subtle ways in which M fostered good habits of constantly surveying the literature and exploring research outside the immediate bounds of my own interests. I hope that I can guide my students in a

similar, low-key way that M encouraged in me.”

“Often, M would leave the latest, hottest paper on my desk, with an enthusiastic note attached that not only conveyed his own excitement about the field, but also piqued my interest.”

An enabler of good science is keeping abreast of the literature. A defining characteristic of many of the great mentors was wide reading outside their field. Mentees appreciated sharing in this reading, and also the deliberate strategy of using key papers as a base for discussion either at group or individual meetings or by the casual dropping of reprints as described above. Again, time-consuming but valued.

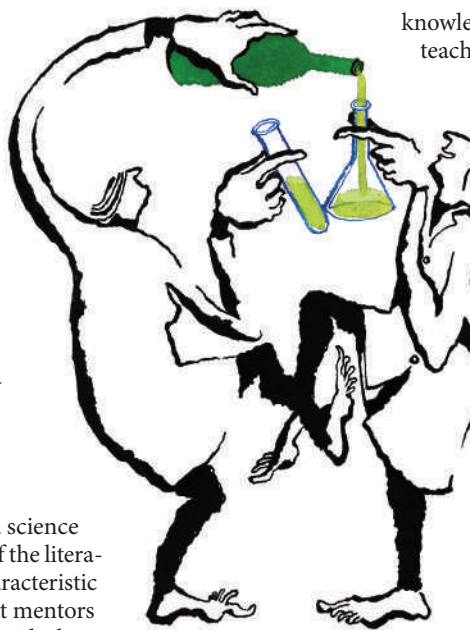
“For a rigorous scientist of international acclaim, I found her to be very open-minded, and she encouraged my exploration of different avenues of research, even when these fell outside her direct expertise (if need be, M was very willing to study new areas of enquiry in order to provide appropriate intellectual support.”

Most researchers have a pet hypothesis and an individual approach to their particular area of science. Sometimes that dogma and limitations in breadth may be exposed and challenged by students or colleagues. As a result, you need to be open to ideas and solutions from all other disciplines. You need to be ready to accept that you might be wrong, to acknowledge and study new directions you have never considered, and to congratulate your mentees for taking you down that pathway.

#### The initial project

“Ensure that all students have projects with at least some guaranteed biologically relevant results. Risky work (such as making a knockout mouse) should be balanced with other work that will ensure some results.”

This is related to getting the balance right, but a number of comments highlighted the fact that, in the beginning, students do not have the experience to make a decision on the first project. One mentee drew attention to the fact that, at the start of a PhD, it is the supervisor who has the knowledge, but as the PhD draws to a close, it is the student who has the



knowledge and who becomes the teacher. Those readers who are on graduate-student committees will probably have seen instances in which the initial project was a key question to be asked in the supervisor’s research programme, but was simply too hard to be the basis of a starting-out project. Many mentees identified being given the right kind of project as a key factor in their ultimate success.

#### Life after science

“M has always encouraged me not to forget to smell the roses.”

*I will always remember him telling me as a first-year PhD student that I needed to take up other activities besides science. My life has been a lot more fun because of his advice.”*

This was not a widespread observation but was clearly a positive feature to those who received this advice.

#### Celebration

“The first time a person comes up with a novel idea or experiment of their own. This should be an occasion for public recognition within the lab as it is a milestone of great significance for most young scientists.”

The importance of celebration and rewarding successes, large and small, is often neglected. Yet it can be highly encouraging to individuals and can contribute to the building of communities. It is a strategy that all mentors can introduce, although the extent of the celebration will vary depending on personalities and level of extroversion.

The guiding principle is that celebration, however large or small, is a powerful motivator. The range of celebrations mentioned in the awards nominations is worth listing here as a challenge to your imagination: off-campus lunches, the weighing of the PhD thesis on submission, cakes at morning or afternoon tea, barbecues at the mentor’s home or cocktail parties on graduation.

#### Building communities

A constant theme from the groups supporting their mentor was the sense of community. The successful mentors realized the need to build communities to create an environment where all under their care could flourish. They all had deliberate and varied strategies to build these communities. How often have

you experienced the negative impact of silo-building within departments? Positive and sustaining communities do not just happen, they have to be nurtured.

#### Of scientists

“M takes an inordinate amount of trouble to involve all the people around her in all aspects of the life of the lab, such as seminars, research-planning meetings and informal meetings with outside visitors. All these make you feel a valued member of the research team from the outset.”

Regular meetings have been commented on before. They include: whole-group planning meetings; meetings with external visitors; subgroup meetings with a specific task to report to the whole group; group-writing tasks; assigning a new junior staff member or student to a senior staff member or student mentor.

Especially important meetings were ‘journal clubs’, which many team leaders set up but often do not sustain.

“The journal club helps to make sure all of us read something other than immediately relevant research, at least once a week. The menu wanders around, sometimes classic papers, sometimes high-impact pieces in *Nature* or *Science*, sometimes chapters from a popular-science book, sometimes philosophy or psychology of science. Over time we have evolved the practice of going round the table first with each participant speaking for 3 minutes. There are always some people who have intelligent comments, but would never put them forward if it were left to them to find the right time to speak. The 3 minutes also restrains the talkative.”

#### Of people

“The most useful single thing I’ve learned is that chocolate biscuits do more for everyone’s good humour and enthusiasm than any amount of feel-good talk. The role of blood sugar should probably have been obvious to a biologist from the outset, but I only learned this by experience. Mind you, cheerful and encouraging conversations are good too, as are gin and tonic.”

Again some mentors’ disposition might not always lead to easy support and nurturing of a social group. But there is no doubt about how much such social activities were valued. Activities can be as simple as the chocolate biscuit or more adventurous, for example ‘Shakespeare under the stars’, wine tastings, ethnic dinners, dinner parties with visiting scientists, bird-watching days, video nights or celebration of every birthday at morning or afternoon tea. One group formed a jazz band, but commented that their gigs were not as favourably reviewed as their articles. One successful mentor noted that, having initially

created the social events, he/she now left it to the group, with a resulting range of events that reflected their interests from canoeing to cake-baking to karaoke.

#### Skill development

“M has focused on equipping people with the skills to be fully functioning members of the scientific community, able to prepare grant applications, review manuscripts, speak at conferences and engage with scientific administrators in a constructive manner. Such a holistic approach to running a scientific group will ultimately bring enormous benefit to the group’s alumni, giving them all the skills necessary to carve out their own niches in the academic world.”

It is clear that successful mentors work hard at developing the scientific skills of their charges. Again this depends on deliberate strategies and activities rather than leaving the outcome to chance. Not surprisingly, the following three skills were the ones that were most often commented on.

#### Criticism

“Our regular meetings would often entail the discussion and evaluation of recent published works. This process provided a great insight into the method of critiquing and assisted in driving our work into new methodological areas to answer questions in a greater depth.”

“The critical analysis of scientific publications is encouraged. No conclusions are taken at face value and fearless discussion of the analysis and interpretation of results takes place during our weekly laboratory meetings and, of course, in the preparation of papers.”

Again this is where a journal club has been used to good effect — students regularly take turns dissecting one or two relevant current papers and their background, with input from other students and faculty members. The successful strategies highlighted involve requiring students or young colleagues to write reviews of journal articles, referees’ reports and grant applications and then critiquing their efforts.

Instinctively you probably know the value of such activities, but do you always ask for individuals or groups of staff/students to have a go

first? Or do you simply involve them in critiquing your writing or your grant application? The last approach is not the way that works.

“M does not only guide his students in their research, but ensures that they learn how to critically review the literature. He often challenges his students with an exercise of reviewing a paper. He then patiently remarks on their review.”

As this quote illustrates, another way these activities benefit science is by preparing the mentees for their role as peer reviewers in the future. This is an activity often taken for granted. We believe that it shouldn’t be. Peer review is all too easily done badly, and is also all too easily put aside under the pressure of other commitments.

It is essential that the motivation to review papers and grant applications is instilled in young scientists. It is equally essential that they be required to practise such activities, under the scrutiny of their mentor. Only then are they likely to learn how to provide a combination of specific and constructive advice about significance, technical strengths and weaknesses, and (for papers) presentation (see Editorial, page 754.)

#### Writing

“Writing my first paper was a true experience. M asked me to write it, but the paper that was submitted had no resemblance to my initial written draft. Nevertheless, M went through my mistakes patiently and thoroughly, a writing experience from which I learned a great deal. This paper was accepted by *Cell* without any corrections, which is a very rare event.”



Writing is such a critical part of being a scientist that its development must not be taken for granted. Among

outstanding mentors, rapid turnaround over one to two days with clear feedback seemed the norm, as did resisting the temptation to do the rewrite for the student but, rather, assisting the mentees to rewrite several times. Also, it seems essential that this attention is paid to writing from the very beginning of a studentship. This requires deliberate action and task-setting by the mentor.

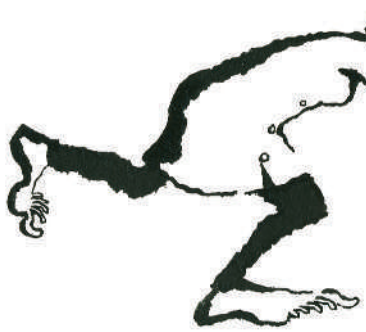
#### Oral presentation

“Although few students have a natural gift for giving a scientific talk, all can learn if given sufficient practice and advice. I always suggest that the student provides me with a run-through a week or two before

a presentation, to allow sufficient time for revisions.”

“I recall that one day M suggested that she and I should have a wager on who could ask the best question of the speakers at the chemistry seminars held weekly in the department. This meant you had to listen closely to the work being presented and to think about it, in order to come up with an insightful question. I recognized that what she really wanted to do was show the students how to get involved in a seminar and she used us as examples of how to engage with the topic presented. Her questions were always informal but probing. The audience, largely made up of postgraduate students in chemistry, of course loved this and soon got into the act.”

The quotes speak for themselves, but all mentors saw it as their role to ensure that their charges had ample opportunity to speak at international forums, and all highlighted the need for practice and critique beforehand. An often-neglected skill is the art of questioning as described in the second quote about the practice of an experienced mentor.



### Networking

All successful scientists have extensive networks spread across the globe. But do they all link their students into those networks as actively as they could? This was another of the standout attributes of the *Nature* finalists and, as commented on above, is one of the distinguishing features of a mentor over someone who is simply a good supervisor. Good mentors saw it as their responsibility to share their network.

### Use their contacts and promote their students/young staff

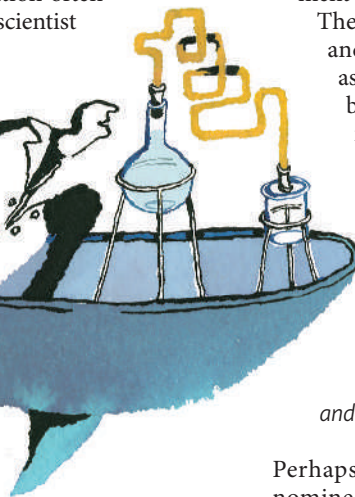
“M always made a large effort to develop the scientific careers of his students. He would actively encourage his students to attend national and international conferences and at these conferences would make a significant effort to introduce his students to other researchers in their field. He would also make a great effort to make sure others were aware of his students' achievements and work.

When it came time to leave his laboratory and develop links with others, M was a great source of contacts and ideas.”

All the mentors made special efforts to ensure that their charges were exposed and introduced to visitors who came into a laboratory. And they encouraged collaboration by introducing their mentees to potential collaborators. This was never left to chance but was planned.

“Similarly another practice was to try to secure a few hours of time from visiting international scientists during which students would present their work. This practice has a number of benefits. First it provided good-quality feedback and a range of helpful suggestions on the direction of particular pieces of research. Second, and perhaps of particular importance to Australian trainees, this practice gave an insight into the way some of the world's outstanding researchers think and helped demystify the work of such researchers.”

Departmental tradition often expects the visiting scientist



to present his or her findings to the department. Good mentors ensure that the visitor also gets to hear of the work of their students and staff.

As support for those who have left the laboratory continues, the advice of one mentor rings very true:

“Write only honest references. One slanted recommendation will damage the prospects of all that follow, because the writer's credibility goes out of the window.”

### Send overseas

“With the wisdom of hindsight, I think the single most important thing I did as supervisor of PhD students was to send each one of them overseas at least once in their candidature.”

Another recurring theme was gratitude from the mentees at the special efforts their mentors made to allow them to travel overseas to

conferences and/or visit the laboratories of colleagues in their networks. Some unselfishly suggested that their protégés should go instead of themselves. Others, when overseas, ensured that they arranged exposure of the work of their charges to world experts. Hence:

“She would attend conferences with her students and at such events would always make a point both of introducing her students to the leaders in the field, and of actively encouraging anyone to whom she was talking to go and see the students' work. She was renowned for arriving at her students' or postdocs' posters with a bemused world-expert in tow and then encouraging the student to explain the poster, letting the student do the talking but with M adding encouraging and supportive comments from the sideline. This is another practice I have adopted from M.”

Once aspiring young mentors appreciate just how important it is for all their students/staff to have opportunity to travel, it is important to negotiate financial support from the department or professional society or elsewhere.

There are sources of funding available, and good mentors seek these out, just as they actively look around to find the best match of conference and/or laboratories for their mentees.

### Advice on career decisions

“But perhaps the most important thing is his tireless attention to the needs and in particular the career development of the younger people around him. M always finds top placements for his students and postdocs.”

Perhaps a defining feature of the *Nature* nominees was that the goal of networking was not simply linked to their own research progress, or to ensure that the PhD was successful, or that the work of the postdoc or research assistant moved their projects forward. Rather, there was evidence of extensive communication, discussion and negotiation behind the scenes to ensure that when the student or colleague left the group they could travel along a pathway that was most likely to set them on a successful career. All the supporting mentees had successful careers and in all cases their mentor had helped them with their career.

### Conclusion

“Having a good mentor early in one's career can mean the difference between success and failure in any career.”

“Those who are good mentors get incalculably more out of it than they put into it.”

**Self-assessment: how good a mentor are you?**

Activity/Strategy	Question/Task	Example	What could be done better?
Appreciating individual differences	Give an example of an incident that illustrates your acknowledgement of individual difference		
Availability	Give an example of the strategy you use to be available to your students/staff		
Self-direction	What was your rating on the scale on page 793?		
Questioning	Describe how you last used active questioning to lead a mentee towards a solution		
Celebration	When did you last celebrate a student/staff member's achievement? How did you celebrate?		
Building a scientific community	Describe a deliberate strategy you use to build a scientific community in your group		
Building a social community	Describe a deliberate strategy you use to build your group as a social community		
Skill development	Describe steps you take to develop the critical, writing and presentation skills of your students/staff		
Networking	Describe one example of how you have introduced each of your students/staff into the scientific network of your research area		
Mentor for life	How many of your past students/staff are you in contact with?		
What one thing will you do differently after reading the description of the mentoring behaviour of the <i>Nature</i> mentors?			

This article concludes as it starts, with reference to just how important mentoring is to those under your care. The second quote highlights the positive satisfaction of being a good mentor.

From the entries we have read, it is clear that there are second generations of mentors now out there who learnt from their own mentors how to provide superb support for the scientists under their charge. Many reading these pages will themselves have been privileged to have been mentored by those applying many of the strategies described. Indeed, in the pages of nominations that was the inspiration for this article, it was also clear that the proposing mentees had taken on board the behaviours of their mentor and were themselves well on the way to being the next generation of successful mentors.

Our purpose, based on the rich resource provided by both mentees and mentors, is to

challenge you to reflect on how you are currently mentoring those under your charge. Is there anything you can learn? More importantly, can you improve what you do? What examples of exemplary mentoring activities do you use?

Equally important, for those young scientists newly embarked on a career in science or about to start building a research team: can you plan your approach to mentoring that team by including strategies, processes and behaviours described here that clearly work? If so, you will not only influence the next generation of scientists but also increase your own satisfaction by being in charge of a productive, enthusiastic, challenging and fun team.

As a stimulus to these reflections, we have drawn up a simple table (above) designed to aid your reflections. Whether you are setting out on a mentoring pathway or simply want to

see how your mentoring strategies stand up, we encourage you to fill out the table. It asks for the provision of specific examples: we consider this to be the best way to stimulate reflection on your approach to scientific mentoring.

Just as the values and strategies of the great mentors, nominated for the *Nature* awards, have benefited the careers of hundreds of now successful scientists, we hope that this distillation of approaches will have a beneficial effect on your mentoring of our future successful scientists.

**Adrian Lee** was pro-vice-chancellor (education and quality improvement) at the University of New South Wales, Australia, from 2000 to 2006.

**Carina Dennis** is Australasian correspondent of *Nature*.

**Philip Campbell** is editor-in-chief of *Nature*, and founded the *Nature* mentoring awards.

## ARTICLES

# Identification and analysis of functional elements in 1% of the human genome by the ENCODE pilot project

The ENCODE Project Consortium\*

We report the generation and analysis of functional data from multiple, diverse experiments performed on a targeted 1% of the human genome as part of the pilot phase of the ENCODE Project. These data have been further integrated and augmented by a number of evolutionary and computational analyses. Together, our results advance the collective knowledge about human genome function in several major areas. First, our studies provide convincing evidence that the genome is pervasively transcribed, such that the majority of its bases can be found in primary transcripts, including non-protein-coding transcripts, and those that extensively overlap one another. Second, systematic examination of transcriptional regulation has yielded new understanding about transcription start sites, including their relationship to specific regulatory sequences and features of chromatin accessibility and histone modification. Third, a more sophisticated view of chromatin structure has emerged, including its inter-relationship with DNA replication and transcriptional regulation. Finally, integration of these new sources of information, in particular with respect to mammalian evolution based on inter- and intra-species sequence comparisons, has yielded new mechanistic and evolutionary insights concerning the functional landscape of the human genome. Together, these studies are defining a path for pursuit of a more comprehensive characterization of human genome function.

The human genome is an elegant but cryptic store of information. The roughly three billion bases encode, either directly or indirectly, the instructions for synthesizing nearly all the molecules that form each human cell, tissue and organ. Sequencing the human genome<sup>1–3</sup> provided highly accurate DNA sequences for each of the 24 chromosomes. However, at present, we have an incomplete understanding of the protein-coding portions of the genome, and markedly less understanding of both non-protein-coding transcripts and genomic elements that temporally and spatially regulate gene expression. To understand the human genome, and by extension the biological processes it orchestrates and the ways in which its defects can give rise to disease, we need a more transparent view of the information it encodes.

The molecular mechanisms by which genomic information directs the synthesis of different biomolecules has been the focus of much of molecular biology research over the last three decades. Previous studies have typically concentrated on individual genes, with the resulting general principles then providing insights into transcription, chromatin remodelling, messenger RNA splicing, DNA replication and numerous other genomic processes. Although many such principles seem valid as additional genes are investigated, they generally have not provided genome-wide insights about biological function.

The first genome-wide analyses that shed light on human genome function made use of observing the actions of evolution. The ever-growing set of vertebrate genome sequences<sup>4–8</sup> is providing increasing power to reveal the genomic regions that have been most and least acted on by the forces of evolution. However, although these studies convincingly indicate the presence of numerous genomic regions under strong evolutionary constraint, they have less power in identifying the precise bases that are constrained and provide little, if any, insight into why those bases are biologically important. Furthermore, although we have good models for how protein-coding regions

evolve, our present understanding about the evolution of other functional genomic regions is poorly developed. Experimental studies that augment what we learn from evolutionary analyses are key for solidifying our insights regarding genome function.

The Encyclopedia of DNA Elements (ENCODE) Project<sup>9</sup> aims to provide a more biologically informative representation of the human genome by using high-throughput methods to identify and catalogue the functional elements encoded. In its pilot phase, 35 groups provided more than 200 experimental and computational data sets that examined in unprecedented detail a targeted 29,998 kilobases (kb) of the human genome. These roughly 30 Mb—equivalent to ~1% of the human genome—are sufficiently large and diverse to allow for rigorous pilot testing of multiple experimental and computational methods. These 30 Mb are divided among 44 genomic regions; approximately 15 Mb reside in 14 regions for which there is already substantial biological knowledge, whereas the other 15 Mb reside in 30 regions chosen by a stratified random-sampling method (see <http://www.genome.gov/10506161>). The highlights of our findings to date include:

- The human genome is pervasively transcribed, such that the majority of its bases are associated with at least one primary transcript and many transcripts link distal regions to established protein-coding loci.
- Many novel non-protein-coding transcripts have been identified, with many of these overlapping protein-coding loci and others located in regions of the genome previously thought to be transcriptionally silent.
- Numerous previously unrecognized transcription start sites have been identified, many of which show chromatin structure and sequence-specific protein-binding properties similar to well-understood promoters.

\*A list of authors and their affiliations appears at the end of the paper.

- Regulatory sequences that surround transcription start sites are symmetrically distributed, with no bias towards upstream regions.
- Chromatin accessibility and histone modification patterns are highly predictive of both the presence and activity of transcription start sites.
- Distal DNaseI hypersensitive sites have characteristic histone modification patterns that reliably distinguish them from promoters; some of these distal sites show marks consistent with insulator function.
- DNA replication timing is correlated with chromatin structure.
- A total of 5% of the bases in the genome can be confidently identified as being under evolutionary constraint in mammals; for approximately 60% of these constrained bases, there is evidence of function on the basis of the results of the experimental assays performed to date.
- Although there is general overlap between genomic regions identified as functional by experimental assays and those under evolutionary constraint, not all bases within these experimentally defined regions show evidence of constraint.
- Different functional elements vary greatly in their sequence variability across the human population and in their likelihood of residing within a structurally variable region of the genome.
- Surprisingly, many functional elements are seemingly unconstrained across mammalian evolution. This suggests the possibility of a large pool of neutral elements that are biochemically active but provide no specific benefit to the organism. This pool may serve as a 'warehouse' for natural selection, potentially acting as the source of lineage-specific elements and functionally conserved but non-orthologous elements between species.

Below, we first provide an overview of the experimental techniques used for our studies, after which we describe the insights gained from analysing and integrating the generated data sets. We conclude with a perspective of what we have learned to date about this 1% of the

human genome and what we believe the prospects are for a broader and deeper investigation of the functional elements in the human genome. To aid the reader, Box 1 provides a glossary for many of the abbreviations used throughout this paper.

### Experimental techniques

Table 1 (expanded in Supplementary Information section 1.1) lists the major experimental techniques used for the studies reported here, relevant acronyms, and references reporting the generated data sets. These data sets reflect over 400 million experimental data points (603 million data points if one includes comparative sequencing bases). In describing the major results and initial conclusions, we seek to distinguish 'biochemical function' from 'biological role'. Biochemical function reflects the direct behaviour of a molecule(s), whereas biological role is used to describe the consequence(s) of this function for the organism. Genome-analysis techniques nearly always focus on biochemical function but not necessarily on biological role. This is because the former is more amenable to large-scale data-generation methods, whereas the latter is more difficult to assay on a large scale.

The ENCODE pilot project aimed to establish redundancy with respect to the findings represented by different data sets. In some instances, this involved the intentional use of different assays that were based on a similar technique, whereas in other situations, different techniques assayed the same biochemical function. Such redundancy has allowed methods to be compared and consensus data sets to be generated, much of which is discussed in companion papers, such as the ChIP-chip platform comparison<sup>10,11</sup>. All ENCODE data have been released after verification but before this publication, as befits a 'community resource' project (see [http://www.wellcome.ac.uk/doc\\_wtd003208.html](http://www.wellcome.ac.uk/doc_wtd003208.html)). Verification is defined as when the experiment is reproducibly confirmed (see Supplementary Information section 1.2). The main portal for ENCODE data is provided by the UCSC Genome Browser (<http://genome.ucsc.edu/ENCODE/>); this is

### Box 1 | Frequently used abbreviations in this paper

AR	Ancient repeat: a repeat that was inserted into the early mammalian lineage and has since become dormant; the majority of ancient repeats are thought to be neutrally evolving.	Indel	An insertion or deletion; two sequences often show a length difference within alignments, but it is not always clear whether this reflects a previous insertion or a deletion
CAGE tag	A short sequence from the 5' end of a transcript	PET	A short sequence that contains both the 5' and 3' ends of a transcript
CDS	Coding sequence: a region of a cDNA or genome that encodes proteins	RACE	Rapid amplification of cDNA ends: a technique for amplifying cDNA sequences between a known internal position in a transcript and its 5' end
ChIP-chip	Chromatin immunoprecipitation followed by detection of the products using a genomic tiling array	RFBR	Regulatory factor binding region: a genomic region found by a ChIP-chip assay to be bound by a protein factor
CNV	Copy number variants: regions of the genome that have large duplications in some individuals in the human population	RFBR-Seqsp	Regulatory factor binding regions that are from sequence-specific binding factors
CS	Constrained sequence: a genomic region associated with evidence of negative selection (that is, rejection of mutations relative to neutral regions)	RT-PCR	Reverse transcriptase polymerase chain reaction: a technique for amplifying a specific region of a transcript
DHS	DNaseI hypersensitive site: a region of the genome showing a sharply different sensitivity to DNaseI compared with its immediate locale	RxFrag	Fragment of a RACE reaction: a genomic region found to be present in a RACE product by an unbiased tiling-array assay
EST	Expressed sequence tag: a short sequence of a cDNA indicative of expression at this point	SNP	Single nucleotide polymorphism: a single base pair change between two individuals in the human population
FAIRE	Formaldehyde-assisted isolation of regulatory elements: a method to assay open chromatin using formaldehyde crosslinking followed by detection of the products using a genomic tiling array	STAGE	Sequence tag analysis of genomic enrichment: a method similar to ChIP-chip for detecting protein factor binding regions but using extensive short sequence determination rather than genomic tiling arrays
FDR	False discovery rate: a statistical method for setting thresholds on statistical tests to correct for multiple testing	SVM	Support vector machine: a machine-learning technique that can establish an optimal classifier on the basis of labelled training data
GENCODE	Integrated annotation of existing cDNA and protein resources to define transcripts with both manual review and experimental testing procedures	TR50	A measure of replication timing corresponding to the time in the cell cycle when 50% of the cells have replicated their DNA at a specific genomic position
GSC	Genome structure correction: a method to adapt statistical tests to make fewer assumptions about the distribution of features on the genome sequence. This provides a conservative correction to standard tests	TSS	Transcription start site
HMM	Hidden Markov model: a machine-learning technique that can establish optimal parameters for a given model to explain the observed data	TxFrag	Fragment of a transcript: a genomic region found to be present in a transcript by an unbiased tiling-array assay
		Un.TxFrag	A TxFrag that is not associated with any other functional annotation
		UTR	Untranslated region: part of a cDNA either at the 5' or 3' end that does not encode a protein sequence

augmented by multiple other websites (see Supplementary Information section 1.1).

A common feature of genomic analyses is the need to assess the significance of the co-occurrence of features or of other statistical tests. One confounding factor is the heterogeneity of the genome, which can produce uninteresting correlations of variables distributed across the genome. We have developed and used a statistical framework that mitigates many of these hidden correlations by adjusting the appropriate null distribution of the test statistics. We term this correction procedure genome structure correction (GSC) (see Supplementary Information section 1.3).

In the next five sections, we detail the various biological insights of the pilot phase of the ENCODE Project.

### Transcription

**Overview.** RNA transcripts are involved in many cellular functions, either directly as biologically active molecules or indirectly by encoding other active molecules. In the conventional view of genome organization, sets of RNA transcripts (for example, messenger RNAs) are encoded by distinct loci, with each usually dedicated to a single biological role (for example, encoding a specific protein). However, this picture has substantially grown in complexity in recent years<sup>12</sup>. Other forms of RNA molecules (such as small nucleolar RNAs and micro (mi)RNAs) are known to exist, and often these are encoded by regions that intercalate with protein-coding genes. These observations are consistent with the well-known discrepancy between the levels of observable mRNAs and large structural RNAs

compared with the total RNA in a cell, suggesting that there are numerous RNA species yet to be classified<sup>13–15</sup>. In addition, studies of specific loci have indicated the presence of RNA transcripts that have a role in chromatin maintenance and other regulatory control. We sought to assay and analyse transcription comprehensively across the 44 ENCODE regions in an effort to understand the repertoire of encoded RNA molecules.

**Transcript maps.** We used three methods to identify transcripts emanating from the ENCODE regions: hybridization of RNA (either total or polyA-selected) to unbiased tiling arrays (see Supplementary Information section 2.1), tag sequencing of cap-selected RNA at the 5' or joint 5'/3' ends (see Supplementary Information sections 2.2 and S2.3), and integrated annotation of available complementary DNA and EST sequences involving computational, manual, and experimental approaches<sup>16</sup> (see Supplementary Information section 2.4). We abbreviate the regions identified by unbiased tiling arrays as TxFrag, the cap-selected RNAs as CAGE or PET tags (see Box 1), and the integrated annotation as GENCODE transcripts. When a TxFrag does not overlap a GENCODE annotation, we call it an Un.TxFrag. Validation of these various studies is described in papers reporting these data sets<sup>17</sup> (see Supplementary Information sections 2.1.4 and 2.1.5).

These methods recapitulate previous findings, but provide enhanced resolution owing to the larger number of tissues sampled and the integration of results across the three approaches (see Table 2). To begin with, our studies show that 14.7% of the bases represented in the unbiased tiling arrays are transcribed in at least one tissue sample. Consistent with previous work<sup>14,15</sup>, many (63%) TxFrag reside outside of GENCODE annotations, both in intronic (40.9%) and intergenic (22.6%) regions. GENCODE annotations are richer than the more-conservative RefSeq or Ensembl annotations, with 2,608 transcripts clustered into 487 loci, leading to an average of 5.4 transcripts per locus. Finally, extensive testing of predicted protein-coding sequences outside of GENCODE annotations was positive in only 2% of cases<sup>16</sup>, suggesting that GENCODE annotations cover nearly all protein-coding sequences. The GENCODE annotations are categorized both by likely function (mainly, the presence of an open reading frame) and by classification evidence (for example, transcripts based solely on ESTs are distinguished from other scenarios); this classification is not strongly correlated with expression levels (see Supplementary Information sections 2.4.2 and 2.4.3).

Analyses of more biological samples have allowed a richer description of the transcription specificity (see Fig. 1 and Supplementary Information section 2.5). We found that 40% of TxFrag are present in only one sample, whereas only 2% are present in all samples. Although exon-containing TxFrag are more likely (74%) to be expressed in more than one sample, 45% of unannotated TxFrag are also expressed in multiple samples. GENCODE annotations of separate loci often (42%) overlap with respect to their genomic coordinates, in particular on opposite strands (33% of loci). Further analysis of GENCODE-annotated sequences with respect to the positions of open reading frames revealed that some component exons do not have the expected synonymous versus non-synonymous substitution patterns of protein-coding sequence (see Supplementary Information section 2.6) and some have deletions incompatible with

**Table 1 | Summary of types of experimental techniques used in ENCODE**

Feature class	Experimental technique(s)	Abbreviations	References	Number of experimental data points
Transcription	Tiling array, integrated annotation	TxFrag, RxFrag, GENCODE	117, 118, 19, 119	63,348,656
5' ends of transcripts*	Tag sequencing	PET, CAGE	121, 13	864,964
Histone modifications	Tiling array	Histone nomenclature†, RFBR	46	4,401,291
Chromatin‡ structure	QT-PCR, tiling array	DHS, FAIRE	42, 43, 44, 122	15,318,324
Sequence-specific factors	Tiling array, tag sequencing, promoter assays	STAGE, ChIP-Chip, ChIP-PET, RFBR	41,52, 11,120, 123, 81, 34,51, 124, 49, 33, 40	324,846,018
Replication	Tiling array	TR50	59, 75	14,735,740
Computational analysis	Computational methods	CCI, RFBR cluster	80, 125, 10, 16, 126, 127	NA
Comparative sequence analysis*	Genomic sequencing, multi-sequence alignments, computational analyses	CS	87, 86, 26	NA
Polymorphisms*	Resequencing, copy number variation	CNV	103, 128	NA

\* Not all data generated by the ENCODE Project.

† Histone code nomenclature follows the Brno nomenclature as described in ref. 129.

‡ Also contains histone modification.

**Table 2 | Bases detected in processed transcripts either as a GENCODE exon, a TxFrag, or as either a GENCODE exon or a TxFrag**

	GENCODE exon	TxFrag	Either GENCODE exon or TxFrag
Total detectable transcripts (bases)	1,776,157 (5.9%)	1,369,611 (4.6%)	2,519,280 (8.4%)
Transcripts detected in tiled regions of arrays (bases)	1,447,192 (9.8%)	1,369,611 (9.3%)	2,163,303 (14.7%)

Percentages are of total bases in ENCODE in the first row and bases tiled in arrays in the second row.

protein structure<sup>18</sup>. Such exons are on average less expressed (25% versus 87% by RT-PCR; see Supplementary Information section 2.7) than exons involved in more than one transcript (see Supplementary Information section 2.4.3), but when expressed have a tissue distribution comparable to well-established genes.

Critical questions are raised by the presence of a large amount of unannotated transcription with respect to how the corresponding sequences are organized in the genome—do these reflect longer transcripts that include known loci, do they link known loci, or are they completely separate from known loci? We further investigated these issues using both computational and new experimental techniques. **Unannotated transcription.** Consistent with previous findings, the Un.TxFrags did not show evidence of encoding proteins (see Supplementary Information section 2.8). One might expect Un.TxFrags to be linked within transcripts that exhibit coordinated expression and have similar conservation profiles across species. To test this, we clustered Un.TxFrags using two methods. The first method<sup>19</sup> used expression levels in 11 cell lines or conditions, dinucleotide composition, location relative to annotated genes, and evolutionary conservation profiles to cluster TxFrags (both unannotated and annotated). By this method, 14% of Un.TxFrags could be assigned to annotated loci, and 21% could be clustered into 200 novel loci (with an average of  $\sim 7$  TxFrags per locus). We experimentally examined these novel loci to study the connectivity of transcripts amongst Un.TxFrags and between Un.TxFrags and known exons. Overall, about 40% of the connections (18 out of 46) were validated by RT-PCR. The second clustering method involved analysing a time course (0, 2, 8 and 32 h) of expression changes in human HL60 cells following retinoic-acid stimulation. There is a coordinated program of expression changes from annotated loci, which can be shown by plotting Pearson correlation values of the expression levels of exons inside annotated loci versus unrelated exons (see Supplementary Information section 2.8.2). Similarly, there is coordinated expression of nearby Un.TxFrags, albeit lower, though still significantly different from randomized sets. Both clustering methods indicate that there is coordinated behaviour of many Un.TxFrags, consistent with them residing in connected transcripts.

**Transcript connectivity.** We used a combination of RACE and tiling arrays<sup>20</sup> to investigate the diversity of transcripts emanating from protein-coding loci. Analogous to TxFrags, we refer to transcripts

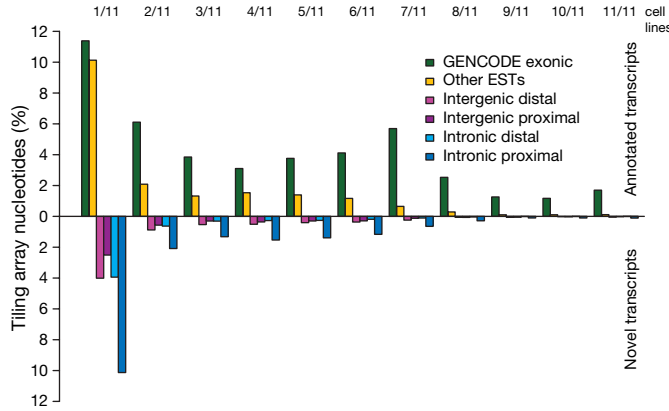


**Figure 1 | Annotated and unannotated TxFrags detected in different cell lines.** The proportion of different types of transcripts detected in the indicated number of cell lines (from 1/11 at the far left to 11/11 at the far right) is shown. The data for annotated and unannotated TxFrags are indicated separately, and also split into different categories based on GENCODE classification: exonic, intergenic (proximal being within 5 kb of a gene and distal being otherwise), intronic (proximal being within 5 kb of an intron and distal being otherwise), and matching other ESTs not used in the GENCODE annotation (principally because they were unspliced). The y axis indicates the per cent of tiling array nucleotides present in that class for that number of samples (combination of cell lines and tissues).

detected using RACE followed by hybridization to tiling arrays as RxFrags. We performed RACE to examine 399 protein-coding loci (those loci found entirely in ENCODE regions) using RNA derived from 12 tissues, and were able to unambiguously detect 4,573 RxFrags for 359 loci (see Supplementary Information section 2.9). Almost half of these RxFrags (2,324) do not overlap a GENCODE exon, and most (90%) loci have at least one novel RxFrag, which often extends a considerable distance beyond the 5' end of the locus. Figure 2 shows the distribution of distances between these new RACE-detected ends and the previously annotated TSS of each locus. The average distance of the extensions is between 50 kb and 100 kb, with many extensions (>20%) being more than 200 kb. Consistent with the known presence of overlapping genes in the human genome, our findings reveal evidence for an overlapping gene at 224 loci, with transcripts from 180 of these loci (~50% of the RACE-positive loci) appearing to have incorporated at least one exon from an upstream gene.

To characterize further the 5' RxFrag extensions, we performed RT-PCR followed by cloning and sequencing for 550 of the 5' RxFrags (including the 261 longest extensions identified for each locus). The approach of mapping RACE products using microarrays is a combination method previously described and validated in several studies<sup>14,17,20</sup>. Hybridization of the RT-PCR products to tiling arrays confirmed connectivity in almost 60% of the cases. Sequenced clones confirmed transcript extensions. Longer extensions were harder to clone and sequence, but 5 out of 18 RT-PCR-positive extensions over 100 kb were verified by sequencing (see Supplementary Information section 2.9.7 and ref. 17). The detection of numerous RxFrag extensions coupled with evidence of considerable intronic transcription indicates that protein-coding loci are more transcriptionally complex than previously thought. Instead of the traditional view that many genes have one or more alternative transcripts that code for alternative proteins, our data suggest that a given gene may both encode multiple protein products and produce other transcripts that include sequences from both strands and from neighbouring loci (often without encoding a different protein). Figure 3 illustrates such a case, in which a new fusion transcript is expressed in the small intestine, and consists of at least three coding exons from the *ATP5O* gene and at least two coding exons from the *DONSON*

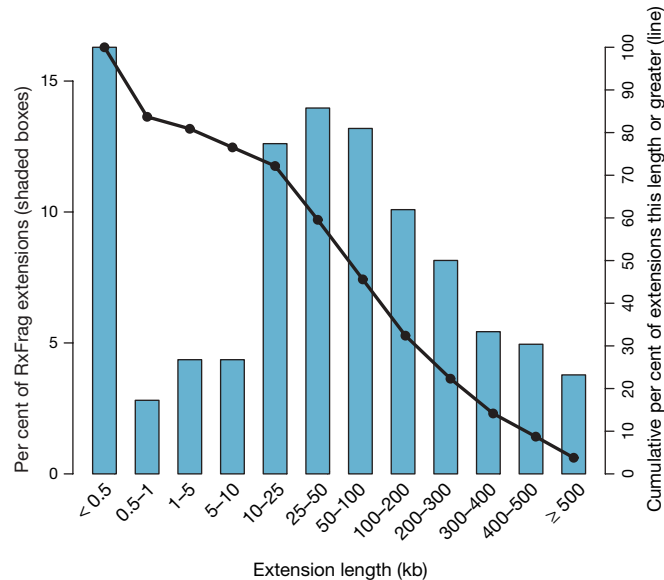


**Figure 2 | Length of genomic extensions to GENCODE-annotated genes on the basis of RACE experiments followed by array hybridizations (RxFrags).** The indicated bars reflect the frequency of extension lengths among different length classes. The solid line shows the cumulative frequency of extensions of that length or greater. Most of the extensions are greater than 50 kb from the annotated gene (see text for details).

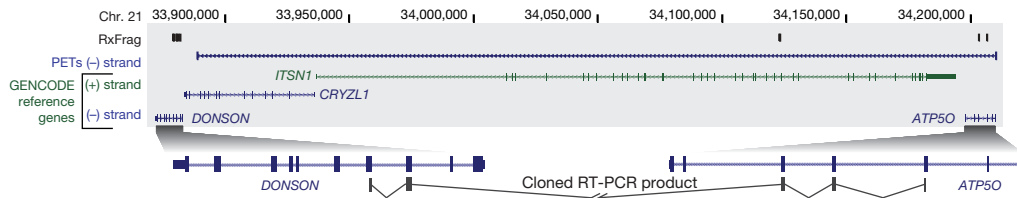


**Figure 3 | Overview of RACE experiments showing a gene fusion.**

Transcripts emanating from the region between the *DONSON* and *ATP5O* genes. A 330-kb interval of human chromosome 21 (within ENM005) is shown, which contains four annotated genes: *DONSON*, *CRYZL1*, *ITSN1* and *ATP5O*. The 5' RACE products generated from small intestine RNA and detected by

gene, with no evidence of sequences from two intervening protein-coding genes (*ITSN1* and *CRYZL1*).

**Pseudogenes.** Pseudogenes, reviewed in refs 21 and 22, are generally considered non-functional copies of genes, are sometimes transcribed and often complicate analysis of transcription owing to close sequence similarity to functional genes. We used various computational methods to identify 201 pseudogenes (124 processed and 77 non-processed) in the ENCODE regions (see Supplementary Information section 2.10 and ref. 23). Tiling-array analysis of 189 of these revealed that 56% overlapped at least one TxFrag. However, possible cross-hybridization between the pseudogenes and their corresponding parent genes may have confounded such analyses. To assess better the extent of pseudogene transcription, 160 pseudogenes (111 processed and 49 non-processed) were examined for expression using RACE/tiling-array analysis (see Supplementary Information section 2.9.2). Transcripts were detected for 14 pseudogenes (8 processed and 6 non-processed) in at least one of the 12 tested RNA sources, the majority (9) being in testis (see ref. 23). Additionally, there was evidence for the transcription of 25 pseudogenes on the basis of their proximity (within 100 bp of a pseudogene end) to CAGE tags (8), PETs (2), or cDNAs/ESTs (21). Overall, we estimate that at least 19% of the pseudogenes in the ENCODE regions are transcribed, which is consistent with previous estimates<sup>24,25</sup>.

**Non-protein-coding RNA.** Non-protein-coding RNAs (ncRNAs) include structural RNAs (for example, transfer RNAs, ribosomal RNAs, and small nuclear RNAs) and more recently discovered regulatory RNAs (for example, miRNAs). There are only 8 well-characterized ncRNA genes within the ENCODE regions (*U70*, *ACA36*, *ACA56*, *mir-192*, *mir-194-2*, *mir-196*, *mir-483* and *H19*), whereas representatives of other classes, (for example, box C/D snoRNAs, tRNAs, and functional snRNAs) seem to be completely absent in the ENCODE regions. Tiling-array data provided evidence for transcription in at least one of the assayed RNA samples for all of these ncRNAs, with the exception of *mir-483* (expression of *mir-483* might be specific to fetal liver, which was not tested). There is also evidence for the transcription of 6 out of 8 pseudogenes of ncRNAs (mainly snoRNA-derived). Similar to the analysis of protein-pseudogenes, the hybridization results could also originate from the known snoRNA gene elsewhere in the genome.

Many known ncRNAs are characterized by a well-defined RNA secondary structure. We applied two *de novo* ncRNA prediction algorithms—EvoFold and RNAz—to predict structured ncRNAs (as well as functional structures in mRNAs) using the multi-species sequence alignments (see below, Supplementary Information section 2.11 and ref. 26). Using a sensitivity threshold capable of detecting all known miRNAs and snoRNAs, we identified 4,986 and 3,707 candidate ncRNA loci with EvoFold and RNAz, respectively. Only 268 loci (5% and 7%, respectively) were found with both programs, representing a 1.6-fold enrichment over that expected by chance; the lack of more extensive overlap is due to the two programs having optimal sensitivity at different levels of GC content and conservation. We experimentally examined 50 of these targets using RACE/tiling-array analysis for brain and testis tissues (see Supplementary

tiling-array analyses (RxFags) are shown along the top. Along the bottom is shown the placement of a cloned and sequenced RT-PCR product that has two exons from the *DONSON* gene followed by three exons from the *ATP5O* gene; these sequences are separated by a 300 kb intron in the genome. A PET tag shows the termini of a transcript consistent with this RT-PCR product.

Information sections 2.11 and 2.9.3); the predictions were validated at a 56%, 65%, and 63% rate for EvoFold, RNAz and dual predictions, respectively.

**Primary transcripts.** The detection of numerous unannotated transcripts coupled with increasing knowledge of the general complexity of transcription prompted us to examine the extent of primary (that is, unspliced) transcripts across the ENCODE regions. Three data sources provide insight about these primary transcripts: the GENCODE annotation, PETs, and RxFags. Figure 4 summarizes the fraction of bases in the ENCODE regions that overlap transcripts identified by these technologies. Remarkably, 93% of bases are represented in a primary transcript identified by at least two independent observations (but potentially using the same technology); this figure is reduced to 74% in the case of primary transcripts detected by at least two different technologies. These increased spans are not mainly due to cell line rearrangements because they were present in multiple tissue experiments that confirmed the spans (see Supplementary Information section 2.12). These estimates assume that the presence of PETs or RxFags defining the terminal ends of a transcript imply that the entire intervening DNA is transcribed and then processed. Other mechanisms, thought to be unlikely in the human genome, such as *trans*-splicing or polymerase jumping would also produce these long termini and potentially should be reconsidered in more detail.

Previous studies have suggested a similar broad amount of transcription across the human<sup>14,15</sup> and mouse<sup>27</sup> genomes. Our studies confirm these results, and have investigated the genesis of these transcripts in greater detail, confirming the presence of substantial intragenic and intergenic transcription. At the same time, many of the resulting transcripts are neither traditional protein-coding

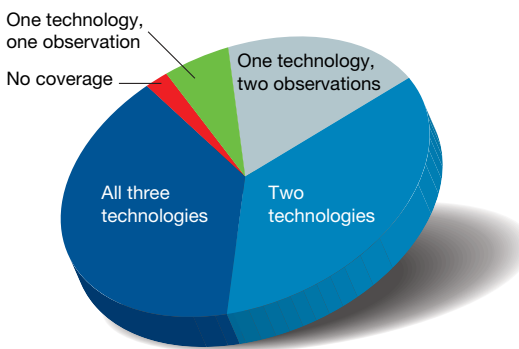


**Figure 4 | Coverage of primary transcripts across ENCODE regions.** Three different technologies (integrated annotation from GENCODE, RACE-array experiments (RxFags) and PET tags) were used to assess the presence of a nucleotide in a primary transcript. Use of these technologies provided the opportunity to have multiple observations of each finding. The proportion of genomic bases detected in the ENCODE regions associated with each of the following scenarios is depicted: detected by all three technologies, by two of the three technologies, by one technology but with multiple observations, and by one technology with only one observation. Also indicated are genomic bases without any detectable coverage of primary transcripts.

transcripts nor easily explained as structural non-coding RNAs. Other studies have noted complex transcription around specific loci or chimaeric-gene structures (for example refs 28–30), but these have often been considered exceptions; our data show that complex intercalated transcription is common at many loci. The results presented in the next section show extensive amounts of regulatory factors around novel TSSs, which is consistent with this extensive transcription. The biological relevance of these unannotated transcripts remains unanswered by these studies. Evolutionary information (detailed below) is mixed in this regard; for example, it indicates that unannotated transcripts show weaker evolutionary conservation than many other annotated features. As with other ENCODE-detected elements, it is difficult to identify clear biological roles for the majority of these transcripts; such experiments are challenging to perform on a large scale and, furthermore, it seems likely that many of the corresponding biochemical events may be evolutionarily neutral (see below).

### Regulation of transcription

**Overview.** A significant challenge in biology is to identify the transcriptional regulatory elements that control the expression of each transcript and to understand how the function of these elements is coordinated to execute complex cellular processes. A simple, commonplace view of transcriptional regulation involves five types of *cis*-acting regulatory sequences—promoters, enhancers, silencers, insulators and locus control regions<sup>31</sup>. Overall, transcriptional regulation involves the interplay of multiple components, whereby the availability of specific transcription factors and the accessibility of specific genomic regions determine whether a transcript is generated<sup>31</sup>. However, the current view of transcriptional regulation is known to be overly simplified, with many details remaining to be established. For example, the consensus sequences of transcription factor binding sites (typically 6 to 10 bases) have relatively little information content and are present numerous times in the genome, with the great majority of these not participating in transcriptional regulation. Does chromatin structure then determine whether such a sequence has a regulatory role? Are there complex inter-factor interactions that integrate the signals from multiple sites? How are signals from different distal regulatory elements coupled without affecting all neighbouring genes? Meanwhile, our understanding of the repertoire of transcriptional events is becoming more complex, with an increasing appreciation of alternative TSSs<sup>32,33</sup> and the presence of non-coding<sup>27,34</sup> and anti-sense transcripts<sup>35,36</sup>.

To better understand transcriptional regulation, we sought to begin cataloguing the regulatory elements residing within the 44 ENCODE regions. For this pilot project, we mainly focused on the binding of regulatory proteins and chromatin structure involved in transcriptional regulation. We analysed over 150 data sets, mainly from ChIP-chip<sup>37–39</sup>, ChIP-PET and STAGE<sup>40,41</sup> studies (see Supplementary Information section 3.1 and 3.2). These methods use chromatin immunoprecipitation with specific antibodies to enrich for DNA in physical contact with the targeted epitope. This enriched DNA can then be analysed using either microarrays (ChIP-chip) or high-throughput sequencing (ChIP-PET and STAGE). The assays included 18 sequence-specific transcription factors and components of the general transcription machinery (for example, RNA polymerase II (Pol II), TAF1 and TFIIB/GTF2B). In addition, we tested more than 600 potential promoter fragments for transcriptional activity by transient-transfection reporter assays that used 16 human cell lines<sup>33</sup>. We also examined chromatin structure by studying the ENCODE regions for DNaseI sensitivity (by quantitative PCR<sup>42</sup> and tiling arrays<sup>43,44</sup>, see Supplementary Information section 3.3), histone composition<sup>45</sup>, histone modifications (using ChIP-chip assays)<sup>37,46</sup>, and histone displacement (using FAIRE, see Supplementary Information section 3.4). Below, we detail these analyses, starting with the efforts to define and classify the 5' ends of transcripts with respect to their associated regulatory signals. Following that are summaries of

generated data about sequence-specific transcription factor binding and clusters of regulatory elements. Finally, we describe how this information can be integrated to make predictions about transcriptional regulation.

**Transcription start site catalogue.** We analysed two data sets to catalogue TSSs in the ENCODE regions: the 5' ends of GENCODE-annotated transcripts and the combined results of two 5'-end-capture technologies—CAGE and PET-tagging. The initial results suggested the potential presence of 16,051 unique TSSs. However, in many cases, multiple TSSs resided within a single small segment (up to ~200 bases); this was due to some promoters containing TSSs with many very close precise initiation sites<sup>47</sup>. To normalize for this effect, we grouped TSSs that were 60 or fewer bases apart into a single cluster, and in each case considered the most frequent CAGE or PET tag (or the 5'-most TSS in the case of TSSs identified only from GENCODE data) as representative of that cluster for downstream analyses.

The above effort yielded 7,157 TSS clusters in the ENCODE regions. We classified these TSSs into three categories: known (present at the end of GENCODE-defined transcripts), novel (supported by other evidence) and unsupported. The novel TSSs were further subdivided on the basis of the nature of the supporting evidence (see Table 3 and Supplementary Information section 3.5), with all four of the resulting subtypes showing significant overlap with experimental evidence using the GSC statistic. Although there is a larger relative proportion of singleton tags in the novel category, when analysis is restricted to only singleton tags, the novel TSSs continue to have highly significant overlap with supporting evidence (see Supplementary Information section 3.5.1).

**Correlating genomic features with chromatin structure and transcription factor binding.** By measuring relative sensitivity to DNaseI digestion (see Supplementary Information section 3.3), we identified DNaseI hypersensitive sites throughout the ENCODE regions. DHSs and TSSs both reflect genomic regions thought to be enriched for regulatory information and many DHSs reside at or near TSSs. We partitioned DHSs into those within 2.5 kb of a TSS (958; 46.5%) and the remaining ones, which were classified as distal (1,102; 53.5%). We then cross-analysed the TSSs and DHSs with data sets relating to histone modifications, chromatin accessibility and sequence-specific transcription factor binding by summarizing these signals in aggregate relative to the distance from TSSs or DHSs. Figure 5 shows representative profiles of specific histone modifications, Pol II and selected transcription factor binding for the different categories of TSSs. Further profiles and statistical analysis of these studies can be found in Supplementary Information 3.6.

In the case of the three TSS categories (known, novel and unsupported), known and novel TSSs are both associated with similar signals for multiple factors (ranging from histone modifications through DNaseI accessibility), whereas unsupported TSSs are not.

**Table 3 | Different categories of TSSs defined on the basis of support from different transcript-survey methods**

Category	Transcript survey method	Number of TSS clusters (non-redundant)*	P value†	Singleton clusters‡ (%)
Known	GENCODE 5' ends	1,730	$2 \times 10^{-70}$	25 (74 overall)
Novel	GENCODE sense exons	1,437	$6 \times 10^{-39}$	64
	GENCODE antisense exons	521	$3 \times 10^{-8}$	65
	Unbiased transcription survey	639	$7 \times 10^{-63}$	71
	CpG island	164	$4 \times 10^{-90}$	60
Unsupported	None	2,666	-	83.4

\* Number of TSS clusters with this support, excluding TSSs from higher categories.

† Probability of overlap between the transcript support and the PET/CAGE tags, as calculated by the Genome Structure Correction statistic (see Supplementary Information section 1.3).

‡ Per cent of clusters with only one tag. For the 'known' category this was calculated as the per cent of GENCODE 5' ends with tag support (25%) or overall (74%).

The enrichments seen with chromatin modifications and sequence-specific factors, along with the significant clustering of this evidence, indicate that the novel TSSs do not reflect false positives and probably use the same biological machinery as other promoters. Sequence-specific transcription factors show a marked increase in binding across the broad region that encompasses each TSS. This increase is notably symmetric, with binding equally likely upstream or downstream of a TSS (see Supplementary Information section 3.7 for an explanation of why this symmetrical signal is not an artefact of the analysis of the signals). Furthermore, there is enrichment of SMARCC1 binding (a member of the SWI/SNF chromatin-modifying complex), which persists across a broader extent than other factors. The broad signals with this factor indicate that the ChIP-chip results reflect both specific enrichment at the TSS and broader enrichments across  $\sim$ 5-kb regions (this is not due to technical issues, see Supplementary Information section 3.8).

We selected 577 GENCODE-defined TSSs at the 5' ends of a protein-coding transcript with over 3 exons, to assess expression status. Each transcript was classified as: (1) 'active' (gene on) or 'inactive' (gene off) on the basis of the unbiased transcript surveys, and (2) residing near a 'CpG island' or not ('non-CpG island') (see Supplementary Information section 3.17). As expected, the aggregate

signal of histone modifications is mainly attributable to active TSSs (Fig. 5), in particular those near CpG islands. Pronounced doublet peaks at the TSS can be seen with these large signals (similar to previous work in yeast<sup>48</sup>) owing to the chromatin accessibility at the TSS. Many of the histone marks and Pol II signals are now clearly asymmetrical, with a persistent level of Pol II into the genic region, as expected. However, the sequence-specific factors remain largely symmetrically distributed. TSSs near CpG islands show a broader distribution of histone marks than those not near CpG islands (see Supplementary Information section 3.6). The binding of some transcription factors (E2F1, E2F4 and MYC) is extensive in the case of active genes, and is lower (or absent) in the case of inactive genes.

**Chromatin signature of distal elements.** Distal DHSs show characteristic patterns of histone modification that are the inverse of TSSs, with high H3K4me1 accompanied by lower levels of H3K4Me3 and H3Ac (Fig. 5). Many factors with high occupancy at TSSs (for example, E2F4) show little enrichment at distal DHSs, whereas other factors (for example, MYC) are enriched at both TSSs and distal DHSs<sup>49</sup>. A particularly interesting observation is the relative enrichment of the insulator-associated factor CTCF<sup>50</sup> at both distal DHSs and TSSs; this contrasts with SWI/SNF components SMARCC2 and SMARCC1, which are TSS-centric. Such differential

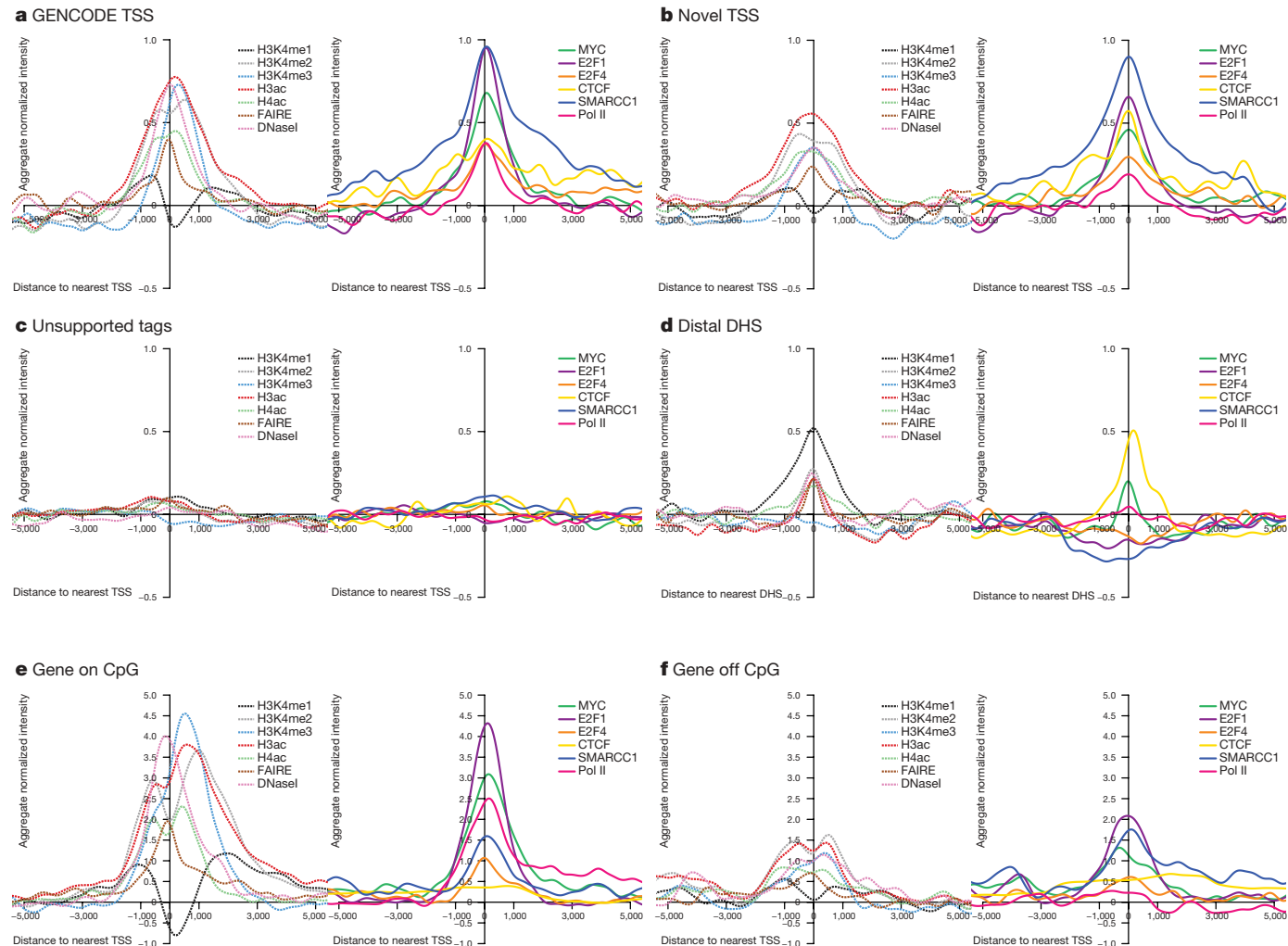


**Figure 5 | Aggregate signals of tiling-array experiments from either ChIP-chip or chromatin structure assays, represented for different classes of TSSs and DHSs.** For each plot, the signal was first normalized with a mean of 0 and standard deviation of 1, and then the normalized scores were summed at each position for that class of TSS or DHS and smoothed using a kernel density method (see Supplementary Information section 3.6). For each class of sites there are two adjacent plots. The left plot depicts the data for general

factors: FAIRE and DNaseI sensitivity as assays of chromatin accessibility and H3K4me1, H3K4me2, H3K4me3, H3ac and H4ac histone modifications (as indicated); the right plot shows the data for additional factors, namely MYC, E2F1, E2F4, CTCF, SMARCC1 and Pol II. The columns provide data for the different classes of TSS or DHS (unsmoothed data and statistical analysis shown in Supplementary Information section 3.6).

behaviour of sequence-specific factors points to distinct biological differences, mediated by transcription factors, between distal regulatory sites and TSSs.

**Unbiased maps of sequence-specific regulatory factor binding.** The previous section focused on specific positions defined by TSSs or DHSs. We then analysed sequence-specific transcription factor binding data in an unbiased fashion. We refer to regions with enriched binding of regulatory factors as RFBRs. RFBRs were identified on the basis of ChIP-chip data in two ways: first, each investigator developed and used their own analysis method(s) to define high-enrichment regions, and second (and independently), a stringent false discovery rate (FDR) method was applied to analyse all data using three cut-offs (1%, 5% and 10%). The laboratory-specific and FDR-based methods were highly correlated, particularly for regions with strong signals<sup>10,11</sup>. For consistency, we used the results obtained with the FDR-based method (see Supplementary Information section 3.10). These RFBRs can be used to find sequence motifs (see Supplementary Information section S3.11).

**RFBRs are associated with the 5' ends of transcripts.** The distribution of RFBRs is non-random (see ref. 10) and correlates with the positions of TSSs. We examined the distribution of specific RFBRs relative to the known TSSs. Different transcription factors and histone modifications vary with respect to their association with TSSs (Fig. 6; see Supplementary Information section 3.12 for modelling of random expectation). Factors for which binding sites are most enriched at the 5' ends of genes include histone modifications, TAF1 and RNA Pol II with a hypo-phosphorylated carboxy-terminal domain<sup>51</sup>—confirming previous expectations. Surprisingly, we found that E2F1, a sequence-specific factor that regulates the expression of many genes at the G1 to S transition<sup>52</sup>, is also tightly associated with TSSs<sup>52</sup>; this association is as strong as that of TAF1, the well-known TATA box-binding protein associated factor 1 (ref. 53). These results suggest that E2F1 has a more general role in transcription than previously suspected, similar to that for MYC<sup>54–56</sup>. In contrast, the large-scale assays did not support the promoter binding that was found in smaller-scale studies (for example, on SIRT1 and SPI1 (PU1)).

**Integration of data on sequence-specific factors.** We expect that regulatory information is not dispersed independently across the genome, but rather is clustered into distinct regions<sup>57</sup>. We refer to regions that contain multiple regulatory elements as ‘regulatory clusters’. We sought to predict the location of regulatory clusters by

cross-integrating data generated using all transcription factor and histone modification assays, including results falling below an arbitrary threshold in individual experiments. Specifically, we used four complementary methods to integrate the data from 129 ChIP-chip data sets (see Supplementary Information section 3.13 and ref. 58). These four methods detect different classes of regulatory clusters and as a whole identified 1,393 clusters. Of these, 344 were identified by all four methods, with another 500 found by three methods (see Supplementary Information section 3.13.5). 67% of the 344 regulatory clusters identified by all four methods (or 65% of the full set of 1,393) reside within 2.5 kb of a known or novel TSS (as defined above; see Table 3 and Supplementary Information section 3.14 for a breakdown by category). Restricting this analysis to previously annotated TSSs (for example, RefSeq or Ensembl) reveals that roughly 25% of the regulatory clusters are close to a previously identified TSS. These results suggest that many of the regulatory clusters identified by integrating the ChIP-chip data sets are undiscovered promoters or are somehow associated with transcription in another fashion. To test these possibilities, sets of 126 and 28 non-GENCODE-based regulatory clusters were tested for promoter activity (see Supplementary Information section 3.15) and by RACE, respectively. These studies revealed that 24.6% of the 126 tested regulatory clusters had promoter activity and that 78.6% of the 28 regulatory clusters analysed by RACE yielded products consistent with a TSS<sup>58</sup>. The ChIP-chip data sets were generated on a mixture of cell lines, predominantly HeLa and GM06990, and were different from the CAGE/PET data, meaning that tissue specificity contributes to the presence of unique TSSs and regulatory clusters. The large increase in promoter proximal regulatory clusters identified by including the additional novel TSSs coupled with the positive promoter and RACE assays suggests that most of the regulatory regions identifiable by these clustering methods represent bona fide promoters (see Supplementary Information 3.16). Although the regulatory factor assays were more biased towards regions associated with promoters, many of the sites from these experiments would have previously been described as distal to promoters. This suggests that commonplace use of RefSeq- or Ensembl-based gene definition to define promoter proximity will dramatically overestimate the number of distal sites.

**Predicting TSSs and transcriptional activity on the basis of chromatin structure.** The strong association between TSSs and both histone modifications and DHSs prompted us to investigate whether the location and activity of TSSs could be predicted solely on the basis of chromatin structure information. We trained a support vector machine (SVM) by using histone modification data anchored around DHSs to discriminate between DHSs near TSSs and those distant from TSSs. We used a selected 2,573 DHSs, split roughly between TSS-proximal DHSs and TSS-distal DHSs, as a training set. The SVM performed well, with an accuracy of 83% (see Supplementary Information section 3.17). Using this SVM, we then predicted new TSSs using information about DHSs and histone modifications—of 110 high-scoring predicted TSSs, 81 resided within 2.5 kb of a novel TSS. As expected, these show a significant overlap to the novel TSS groups (defined above) but without a strong bias towards any particular category (see Supplementary Information section 3.17.1.5).

To investigate the relationship between chromatin structure and gene expression, we examined transcript levels in two cell lines using a transcript-tiling array. We compared this transcript data with the results of ChIP-chip experiments that measured histone modifications across the ENCODE regions. From this, we developed a variety of predictors of expression status using chromatin modifications as variables; these were derived using both decision trees and SVMs (see Supplementary Information section 3.17). The best of these correctly predicts expression status (transcribed versus non-transcribed) in 91% of cases. This success rate did not decrease dramatically when the predicting algorithm incorporated the results from one cell line to predict the expression status of another cell line. Interestingly, despite

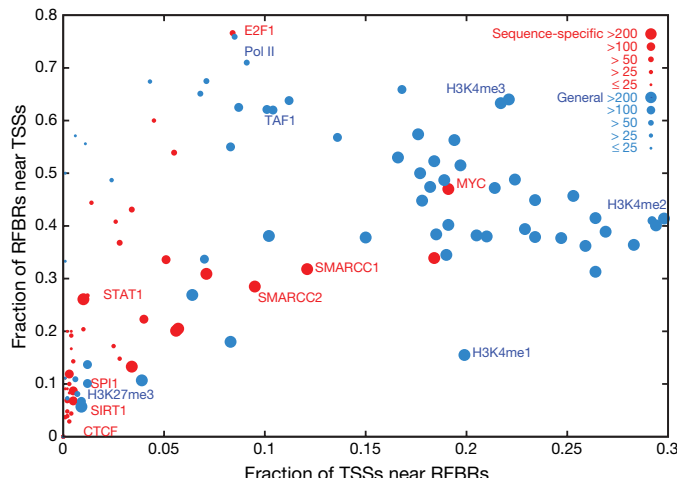


**Figure 6 | Distribution of RFBRs relative to GENCODE TSSs.** Different RFBRs from sequence-specific factors (red) or general factors (blue) are plotted showing their relative distribution near TSSs. The x axis indicates the proportion of TSSs close (within 2.5 kb) to the specified factor. The y axis indicates the proportion of RFBRs close to TSSs. The size of the circle provides an indication of the number of RFBRs for each factor. A handful of representative factors are labelled.

the striking difference in histone modification enrichments in TSSs residing near versus those more distal to CpG islands (see Fig. 5 and Supplementary Information section 3.6), including information about the proximity to CpG islands did not improve the predictors. This suggests that despite the marked differences in histone modifications among these TSS classes, a single predictor can be made, using the interactions between the different histone modification levels.

In summary, we have integrated many data sets to provide a more complete view of regulatory information, both around specific sites (TSSs and DHSs) and in an unbiased manner. From analysing multiple data sets, we find 4,491 known and novel TSSs in the ENCODE regions, almost tenfold more than the number of established genes. This large number of TSSs might explain the extensive transcription described above; it also begins to change our perspective about regulatory information—without such a large TSS catalogue, many of the regulatory clusters would have been classified as residing distal to promoters. In addition to this revelation about the abundance of promoter-proximal regulatory elements, we also identified a considerable number of putative distal regulatory elements, particularly on the basis of the presence of DHSs. Our study of distal regulatory elements was probably most hindered by the paucity of data generated using distal-element-associated transcription factors; nevertheless, we clearly detected a set of distal-DHS-associated segments bound by CTCF or MYC. Finally, we showed that information about chromatin structure alone could be used to make effective predictions about both the location and activity of TSSs.

## Replication

**Overview.** DNA replication must be carefully coordinated, both across the genome and with respect to development. On a larger scale, early replication in S phase is broadly correlated with gene density and transcriptional activity<sup>59–66</sup>; however, this relationship is not universal, as some actively transcribed genes replicate late and vice versa<sup>61,64–68</sup>. Importantly, the relationship between transcription and DNA replication emerges only when the signal of transcription is averaged over a large window (>100 kb)<sup>63</sup>, suggesting that larger-scale chromosomal architecture may be more important than the activity of specific genes<sup>69</sup>.

The ENCODE Project provided a unique opportunity to examine whether individual histone modifications on human chromatin can be correlated with the time of replication and whether such correlations support the general relationship of active, open chromatin with early replication. Our studies also tested whether segments showing interallelic variation in the time of replication have two different types of histone modifications consistent with an interallelic variation in chromatin state.

**DNA replication data set.** We mapped replication timing across the ENCODE regions by analysing Brd-U-labelled fractions from synchronized HeLa cells (collected at 2 h intervals throughout S phase) on tiling arrays (see Supplementary Information section 4.1). Although the HeLa cell line has a considerably altered karyotype, correlation of these data with other cell line data (see below) suggests the results are relevant to other cell types. The results are expressed as the time at which 50% of any given genomic position is replicated (TR50), with higher values signifying later replication times. In addition to the five ‘activating’ histone marks, we also correlated the TR50 with H3K27me3, a modification associated with polycomb-mediated transcriptional repression<sup>70–74</sup>. To provide a consistent comparison framework, the histone data were smoothed to 100-kb resolution, and then correlated with the TR50 data by a sliding window correlation analysis (see Supplementary Information section 4.2). The continuous profiles of the activating marks, histone H3K4 mono-, di-, and tri-methylation and histone H3 and H4 acetylation, are generally anti-correlated with the TR50 signal (Fig. 7a and Supplementary Information section 4.3). In contrast, H3K27me3 marks show a predominantly positive correlation with late-replicating segments (Fig. 7a; see Supplementary Information section 4.3 for additional analysis).

Although most genomic regions replicate in a temporally specific window in S phase, other regions demonstrate an atypical pattern of replication (Pan-S) where replication signals are seen in multiple parts of S phase. We have suggested that such a pattern of replication stems from interallelic variation in the chromatin structure<sup>59,75</sup>. If one allele is in active chromatin and the other in repressed chromatin, both types of modified histones are expected to be enriched in the Pan-S segments. An ENCODE region was classified as non-specific (or Pan-S) regions when >60% of the probes in a 10-kb window

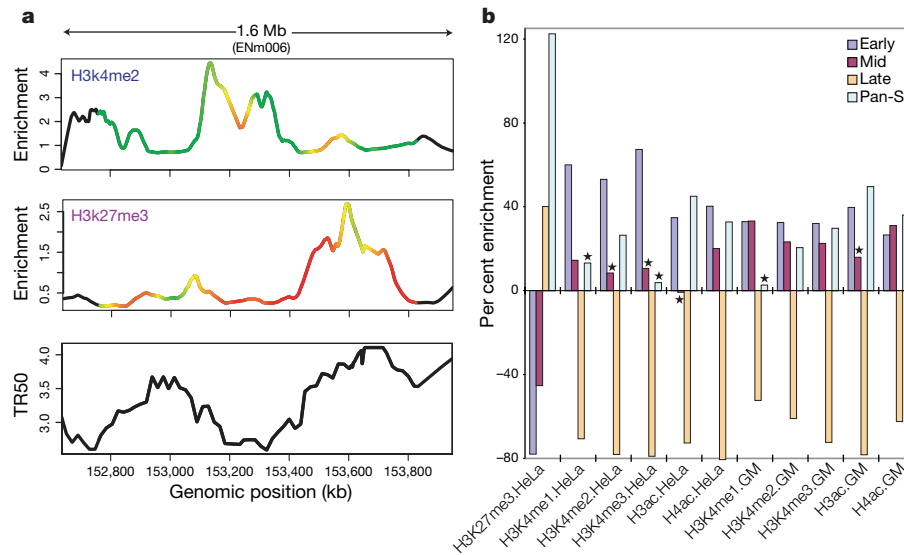


**Figure 7 | Correlation between replication timing and histone modifications.** **a**, Comparison of two histone modifications (H3K4me2 and H3K27me3), plotted as enrichment ratio from the Chip-chip experiments and the time for 50% of the DNA to replicate (TR50), indicated for ENCODE region ENm006. The colours on the curves reflect the correlation strength in a sliding 250-kb window. **b**, Differing levels of histone modification for

different TR50 partitions. The amounts of enrichment or depletion of different histone modifications in various cell lines are depicted (indicated along the bottom as ‘histone mark.cell line’; GM = GM06990). Asterisks indicate enrichments/depletions that are not significant on the basis of multiple tests. Each set has four partitions on the basis of replication timing: early, mid, late and Pan-S.

replicated in multiple intervals in S phase. The remaining regions were sub-classified into early-, mid- or late-replicating based on the average TR50 of the temporally specific probes within a 10-kb window<sup>75</sup>. For regions of each class of replication timing, we determined the relative enrichment of various histone modification peaks in HeLa cells (Fig. 7b; Supplementary Information section 4.4). The correlations of activating and repressing histone modification peaks with TR50 are confirmed by this analysis (Fig. 7b). Intriguingly, the Pan-S segments are unique in being enriched for both activating (H3K4me2, H3ac and H4ac) and repressing (H3K27me3) histones, consistent with the suggestion that the Pan-S replication pattern arises from interallelic variation in chromatin structure and time of replication<sup>75</sup>. This observation is also consistent with the Pan-S replication pattern seen for the H19/IGF2 locus, a known imprinted region with differential epigenetic modifications across the two alleles<sup>76</sup>.

The extensive rearrangements in the genome of HeLa cells led us to ask whether the detected correlations between TR50 and chromatin state are seen with other cell lines. The histone modification data with GM06990 cells allowed us to test whether the time of replication of genomic segments in HeLa cells correlated with the chromatin state in GM06990 cells. Early- and late-replicating segments in HeLa cells are enriched and depleted, respectively, for activating marks in GM06990 cells (Fig. 7b). Thus, despite the presence of genomic rearrangements (see Supplementary Information section 2.12), the TR50 and chromatin state in HeLa cells are not far from a constitutive baseline also seen with a cell line from a different lineage. The enrichment of multiple activating histone modifications and the depletion of a repressive modification from segments that replicate early in S phase extends previous work in the field at a level of detail and scale not attempted before in mammalian cells. The duality of histone modification patterns in Pan-S areas of the HeLa genome, and the concordance of chromatin marks and replication time across two disparate cell lines (HeLa and GM06990) confirm the coordination of histone modifications with replication in the human genome.

### Chromatin architecture and genomic domains

**Overview.** The packaging of genomic DNA into chromatin is intimately connected with the control of gene expression and other chromosomal processes. We next examined chromatin structure over a larger scale to ascertain its relation to transcription and other processes. Large domains (50 to >200 kb) of generalized DNaseI sensitivity have been detected around developmentally regulated gene clusters<sup>77</sup>, prompting speculation that the genome is organized

into ‘open’ and ‘closed’ chromatin territories that represent higher-order functional domains. We explored how different chromatin features, particularly histone modifications, correlate with chromatin structure, both over short and long distances.

**Chromatin accessibility and histone modifications.** We used histone modification studies and DNaseI sensitivity data sets (introduced above) to examine general chromatin accessibility without focusing on the specific DHS sites (see Supplementary Information sections 3.1, 3.3 and 3.4). A fundamental difficulty in analysing continuous data across large genomic regions is determining the appropriate scale for analysis (for example, 2 kb, 5 kb, 20 kb, and so on). To address this problem, we developed an approach based on wavelet analysis, a mathematical tool pioneered in the field of signal processing that has recently been applied to continuous-value genomic analyses. Wavelet analysis provides a means for consistently transforming continuous signals into different scales, enabling the correlation of different phenomena independently at differing scales in a consistent manner.

**Global correlations of chromatin accessibility and histone modifications.** We computed the regional correlation between DNaseI sensitivity and each histone modification at multiple scales using a wavelet approach (Fig. 8 and Supplementary Information section 4.2). To make quantitative comparisons between different histone modifications, we computed histograms of correlation values between DNaseI sensitivity and each histone modification at several scales and then tested these for significance at specific scales. Figure 8c shows the distribution of correlation values at a 16-kb scale, which is considerably larger than individual *cis*-acting regulatory elements. At this scale, H3K4me2, H3K4me3 and H3ac show similarly high correlation. However, they are significantly distinguished from H3K4me1 and H4ac modifications ( $P < 1.5 \times 10^{-33}$ ; see Supplementary Information section 4.5), which show lower correlation with DNaseI sensitivity. These results suggest that larger-scale relationships between chromatin accessibility and histone modifications are dominated by sub-regions in which higher average DNaseI sensitivity is accompanied by high levels of H3K4me2, H3K4me3 and H3ac modifications.

**Local correlations of chromatin accessibility and histone modifications.** Narrowing to a scale of ~2 kb revealed a more complex situation, in which H3K4me2 is the histone modification that is best correlated with DNaseI sensitivity. However, there is no clear combination of marks that correlate with DNaseI sensitivity in a way that is analogous to that seen at a larger scale (see Supplementary Information section 4.3). One explanation for the increased

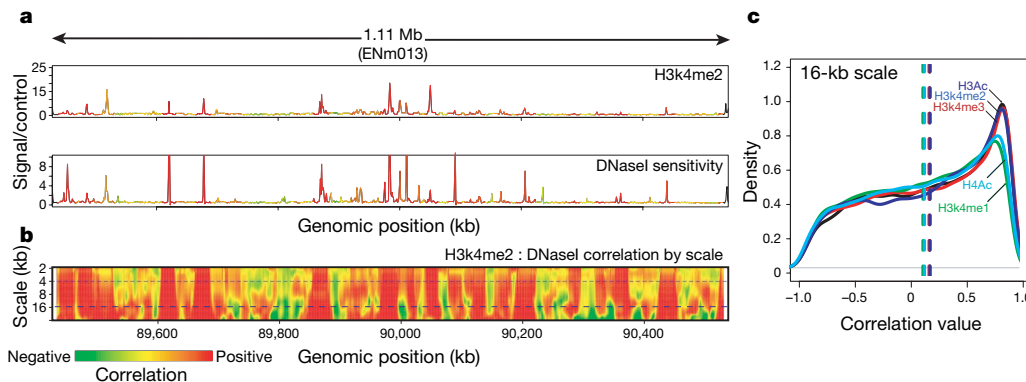


**Figure 8 | Wavelet correlations of histone marks and DNaseI sensitivity.**

As an example, correlations between DNaseI sensitivity and H3K4me2 (both in the GM06990 cell line) over a 1.1-Mb region on chromosome 7 (ENCODE region ENM013) are shown. **a**, The relationship between histone modification H3K4me2 (upper plot) and DNaseI sensitivity (lower plot) is shown for ENCODE region ENM013. The curves are coloured with the strength of the local correlation at the 4-kb scale (top dashed line in panel **b**). **b**, The same data as in **a** are represented as a wavelet correlation. The

y axis shows the differing scales decomposed by the wavelet analysis from large to small scale (in kb); the colour at each point in the heatmap represents the level of correlation at the given scale, measured in a 20 kb window centred at the given position. **c**, Distribution of correlation values at the 16 kb scale between the indicated histone marks. The y axis is the density of these correlation values across ENCODE; all modifications show a peak at a positive-correlation value.

complexity at smaller scales is that there is a mixture of different classes of accessible chromatin regions, each having a different pattern of histone modifications. To examine this, we computed the degree to which local peaks in histone methylation or acetylation occur at DHSs (see Supplementary Information section 4.5.1). We found that 84%, 91% and 93% of significant peaks in H3K4 mono-, di- and tri-methylation, respectively, and 93% and 81% of significant peaks in H3ac and H4ac acetylation, respectively, coincided with DHSs (see Supplementary Information section 4.5). Conversely, a proportion of DHSs seemed not to be associated with significant peaks in H3K4 mono-, di- or tri-methylation (37%, 29% and 47%, respectively), nor with peaks in H3 or H4 acetylation (both 57%). Because only a limited number of histone modification marks were assayed, the possibility remains that some DHSs harbour other histone modifications. The absence of a more complete concordance between DHSs and peaks in histone acetylation is surprising given the widely accepted notion that histone acetylation has a central role in mediating chromatin accessibility by disrupting higher-order chromatin folding.

**DNA structure at DHSs.** The observation that distinctive hydroxyl radical cleavage patterns are associated with specific DNA structures<sup>78</sup> prompted us to investigate whether DHS subclasses differed with respect to their local DNA structure. Conversely, because different DNA sequences can give rise to similar hydroxyl radical cleavage patterns<sup>79</sup>, genomic regions that adopt a particular local structure do not necessarily have the same nucleotide sequence. Using a Gibbs sampling algorithm on hydroxyl radical cleavage patterns of 3,150 DHSs<sup>80</sup>, we discovered an 8-base segment with a conserved cleavage signature (CORCS; see Supplementary Information section 4.6). The underlying DNA sequences that give rise to this pattern have little primary sequence similarity despite this similar structural pattern. Furthermore, this structural element is strongly enriched in promoter-proximal DHSs (11.3-fold enrichment compared to the rest of the ENCODE regions) relative to promoter-distal DHSs (1.5-fold enrichment); this element is enriched 10.9-fold in CpG islands, but is higher still (26.4-fold) in CpG islands that overlap a DHS.

**Large-scale domains in the ENCODE regions.** The presence of extensive correlations seen between histone modifications, DNaseI

sensitivity, replication, transcript density and protein factor binding led us to investigate whether all these features are organized systematically across the genome. To test this, we performed an unsupervised training of a two-state HMM with inputs from these different features (see Supplementary Information section 4.7 and ref. 81). No other information except for the experimental variables was used for the HMM training routines. We consistently found that one state ('active') generally corresponded to domains with high levels of H3ac and RNA transcription, low levels of H3K27me3 marks, and early replication timing, whereas the other state ('repressed') reflected domains with low H3ac and RNA, high H3K27me3, and late replication (see Fig. 9). In total, we identified 70 active regions spanning 11.4 Mb and 82 inactive regions spanning 17.8 Mb (median size 136 kb versus 104 kb respectively). The active domains are markedly enriched for GENCODE TSSs, CpG islands and Alu repetitive elements ( $P < 0.0001$  for each), whereas repressed regions are significantly enriched for LINE1 and LTR transposons ( $P < 0.001$ ). Taken together, these results demonstrate remarkable concordance between ENCODE functional data types and provide a view of higher-order functional domains defined by a broader range of factors at a markedly higher resolution than was previously available<sup>82</sup>.

### Evolutionary constraint and population variability

**Overview.** Functional genomic sequences can also be identified by examining evolutionary changes across multiple extant species and within the human population. Indeed, such studies complement experimental assays that identify specific functional elements<sup>83–85</sup>. Evolutionary constraint (that is, the rejection of mutations at a particular location) can be measured by either (i) comparing observed substitutions to neutral rates calculated from multi-sequence alignments<sup>86–88</sup>, or (ii) determining the presence and frequency of intra-species polymorphisms. Importantly, both approaches are indifferent to any specific function that the constrained sequence might confer.

Previous studies comparing the human, mouse, rat and dog genomes examined bulk evolutionary properties of all nucleotides in the genome, and provided little insight about the precise positions of constrained bases. Interestingly, these studies indicated that the

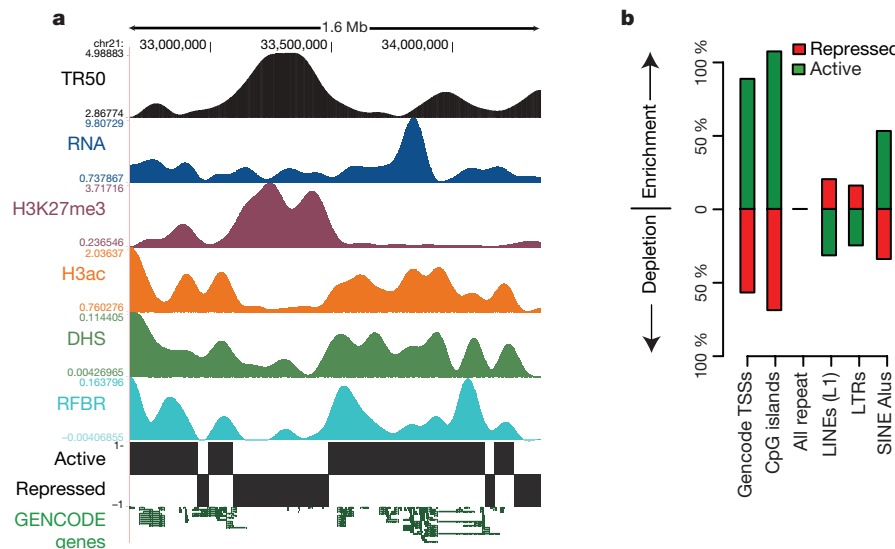


**Figure 9 | Higher-order functional domains in the genome.** The general concordance of multiple data types is shown for an illustrative ENCODE region (ENm005). **a**, Domains were determined by simultaneous HMM segmentation of replication time (TR50; black), bulk RNA transcription (blue), H3K27me3 (purple), H3ac (orange), DHS density (green), and RFBR density (light blue) measured continuously across the 1.6-Mb ENm005. All data were generated using HeLa cells. The histone, RNA, DHS and RFBR signals are wavelet-smoothed to an approximately 60-kb scale (see

Supplementary Information section 4.7). The HMM segmentation is shown as the blocks labelled 'active' and 'repressed' and the structure of GENCODE genes (not used in the training) is shown at the end. **b**, Enrichment or depletion of annotated sequence features (GENCODE TSSs, CpG islands, LINE1 repeats, Alu repeats, and non-exonic constrained sequences (CSs)) in active versus repressed domains. Note the marked enrichment of TSSs, CpG islands and Alus in active domains, and the enrichment of LINE and LTRs in repressed domains.

majority of constrained bases reside within the non-coding portion of the human genome. Meanwhile, increasingly rich data sets of polymorphisms across the human genome have been used extensively to establish connections between genetic variants and disease, but far fewer analyses have sought to use such data for assessing functional constraint<sup>85</sup>.

The ENCODE Project provides an excellent opportunity for more fully exploiting inter- and intra-species sequence comparisons to examine genome function in the context of extensive experimental studies on the same regions of the genome. We consolidated the experimentally derived information about the ENCODE regions and focused our analyses on 11 major classes of genomic elements. These classes are listed in Table 4 and include two non-experimentally derived data sets: ancient repeats (ARs; mobile elements that inserted early in the mammalian lineage, have subsequently become dormant, and are assumed to be neutrally evolving) and constrained sequences (CSs; regions that evolve detectably more slowly than neutral sequences).

**Comparative sequence data sets and analysis.** We generated 206 Mb of genomic sequence orthologous to the ENCODE regions from 14 mammalian species using a targeted strategy that involved isolating<sup>89</sup> and sequencing<sup>90</sup> individual bacterial artificial chromosome clones. For an additional 14 vertebrate species, we used 340 Mb of orthologous genomic sequence derived from genome-wide sequencing efforts<sup>3–8,91–93</sup>. The orthologous sequences were aligned using three alignment programs: TBA<sup>94</sup>, MAVID<sup>95</sup> and MLAGAN<sup>96</sup>. Four independent methods that generated highly concordant results<sup>97</sup> were then used to identify sequences under constraint (PhastCons<sup>88</sup>, GERP<sup>87</sup>, SCONE<sup>98</sup> and BinCons<sup>86</sup>). From these analyses, we developed a high-confidence set of ‘constrained sequences’ that correspond to 4.9% of the nucleotides in the ENCODE regions. The threshold for determining constraint was set using a FDR rate of 5% (see ref. 97); this level is similar to previous estimates of the fraction of the human genome under mammalian constraint<sup>4,86–88</sup> but the FDR rate was not chosen to fit this result. The median length of these constrained sequences is 19 bases, with the minimum being 8 bases—roughly the size of a typical transcription factor binding site. These analyses, therefore, provide a resolution of constrained sequences that is substantially better than that currently available using only whole-genome vertebrate sequences<sup>99–102</sup>.

Intra-species variation studies mainly used SNP data from Phases I and II, and the 10 re-sequenced regions in ENCODE regions with 48 individuals of the HapMap Project<sup>103</sup>; nucleotide insertion or deletion (indel) data were from the SNP Consortium and HapMap. We also examined the ENCODE regions for the presence of overlaps with known segmental duplications<sup>104</sup> and CNVs.

**Experimentally identified functional elements and constrained sequences.** We first compared the detected constrained sequences

with the positions of experimentally identified functional elements. A total of 40% of the constrained bases reside within protein-coding exons and their associated untranslated regions (Fig. 10) and, in agreement with previous genome-wide estimates, the remaining constrained bases do not overlap the mature transcripts of protein-coding genes<sup>4,5,88,105,106</sup>. When we included the other experimental annotations, we found that an additional 20% of the constrained bases overlap experimentally identified non-coding functional regions, although far fewer of these regions overlap constrained sequences compared to coding exons (see below). Most experimental annotations are significantly different from a random expectation for both base-pair or element-level overlaps (using the GSC statistic, see Supplementary Information section 1.3), with a more striking deviation when considering elements (Fig. 11). The exceptions to this are pseudogenes, Un.TxFrags and RxFrags. The increase in significance moving from base-pair measures to the element level suggests that discrete islands of constrained sequence exist within experimentally identified functional elements, with the surrounding bases apparently not showing evolutionary constraint. This notion is discussed in greater detail in ref. 97.

We also examined measures of human variation (heterozygosity, derived allele-frequency spectra and indel rates) within the sequences of the experimentally identified functional elements (Fig. 12). For these studies, ARs were used as a marker for neutrally evolving sequence. Most experimentally identified functional elements are associated with lower heterozygosity compared to ARs, and a few have lower indel rates compared with ARs. Striking outliers are 3' UTRs, which have dramatically increased indel rates without an obvious cause. This is discussed in more depth in ref. 107.

These findings indicate that the majority of the evolutionarily constrained, experimentally identified functional elements show evidence of negative selection both across mammalian species and within the human population. Furthermore, we have assigned at least one molecular function to the majority (60%) of all constrained bases in the ENCODE regions.

**Conservation of regulatory elements.** The relationship between individual classes of regulatory elements and constrained sequences varies considerably, ranging from cases where there is strong evolutionary constraint (for example, pan-vertebrate ultraconserved regions<sup>108,109</sup>) to examples of regulatory elements that are not conserved between orthologous human and mouse genes<sup>110</sup>. Within the ENCODE regions, 55% of RFBRs overlap the high-confidence

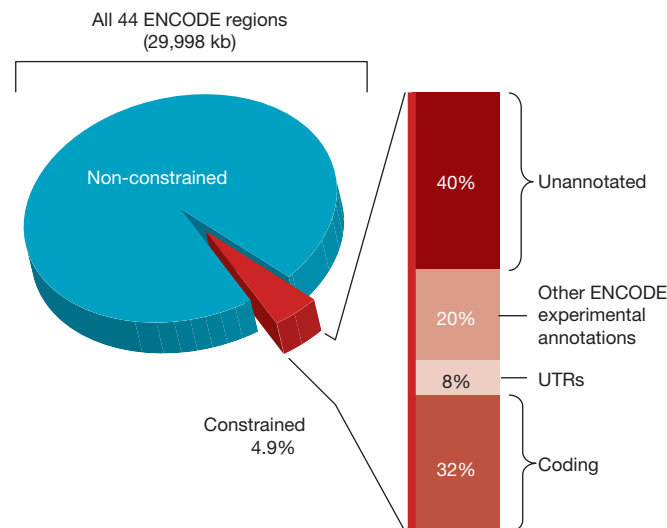


**Figure 10 | Relative proportion of different annotations among constrained sequences.** The 4.9% of bases in the ENCODE regions identified as constrained is subdivided into the portions that reflect known coding regions, UTRs, other experimentally annotated regions, and unannotated sequence.

constrained sequences. As expected, RFBRs have many unconstrained bases, presumably owing to the small size of the specific binding site. We investigated whether the binding sites in RFBRs could be further delimited using information about evolutionary constraint. For 7 out of 17 factors with either known TRANSFAC or Jaspar motifs, our ChIP-chip data revealed a marked enrichment of the appropriate motif within the constrained versus the unconstrained portions of the RFBRs (see Supplementary Information section 5.1). This enrichment was seen for levels of stringency used for defining ChIP-chip-positive sites (1% and 5% FDR level), indicating that combining sequence constraint and ChIP-chip data may provide a highly sensitive means for detecting factor binding sites in the human genome.

**Experimentally identified functional elements and genetic variation.** The above studies focus on purifying (negative) selection. We used nucleotide variation to detect potential signals of adaptive (positive) selection. We modified the standard McDonald–Kreitman test (MK-test<sup>111,112</sup>) and the Hudson–Kreitman–Aguade (HKA)<sup>113</sup> test (see Supplementary Information section 5.2.1), to examine whether an entire set of sequence elements shows an excess of polymorphisms or an excess of inter-species divergence. We found that constrained sequences and coding exons have an excess of polymorphisms (consistent with purifying selection), whereas 5' UTRs

show evidence of an excess of divergence (with a portion probably reflecting positive selection). In general, non-coding genomic regions show more variation, with both a large number of segments that undergo purifying selection and regions that are fast evolving.

We also examined structural variation (that is, CNVs, inversions and translocations<sup>114</sup>; see Supplementary Information section 5.2.2). Within these polymorphic regions, we encountered significant overrepresentation of CDSs, TxFrags, and intra-species constrained sequences ( $P < 10^{-3}$ , Fig. 13), and also detected a statistically significant under-representation of ARs ( $P = 10^{-3}$ ). A similar overrepresentation of CDSs and intra-species constrained sequences was found within non-polymorphic segmental duplications.

**Unexplained constrained sequences.** Despite the wealth of complementary data, 40% of the ENCODE-region sequences identified as constrained are not associated with any experimental evidence of function. There is no evidence indicating that mutational cold spots account for this constraint; they have similar measures of constraint to experimentally identified elements and harbour equal proportions of SNPs. To characterize further the unexplained constrained sequences, we examined their clustering and phylogenetic distribution. These sequences are not uniformly distributed across most ENCODE regions, and even in most ENCODE regions the distribution is different from constrained sequences within experimentally identified functional elements (see Supplementary Information section 5.3). The large fraction of constrained sequence that does not match any experimentally identified elements is not surprising considering that only a limited set of transcription factors, cell lines and biological conditions have thus far been examined.

**Unconstrained experimentally identified functional elements.** In contrast, an unexpectedly large fraction of experimentally identified functional elements show no evidence of evolutionary constraint ranging from 93% for Un.TxFrags to 12% for CDS. For most types of non-coding functional elements, roughly 50% of the individual elements seemed to be unconstrained across all mammals.

There are two methodological reasons that might explain the apparent excess of unconstrained experimentally identified functional elements: the underestimation of sequence constraint or overestimation of experimentally identified functional elements. We do not believe that either of these explanations fully accounts for the large and varied levels of unconstrained experimentally functional sequences. The set of constrained bases analysed here is highly accurate and complete due to the depth of the multiple alignment. Both by bulk fitting procedures and by comparison of SNP frequencies to constraint there is clearly a proportion of constrained bases not captured in the defined 4.9% of constrained sequences, but it is small (see

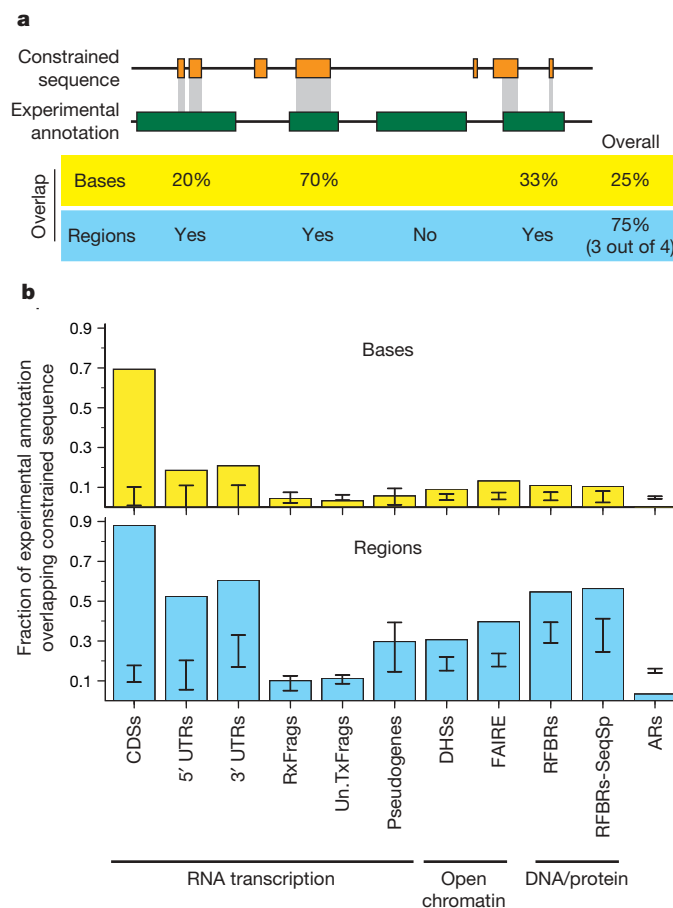


**Figure 11 | Overlap of constrained sequences and various experimental annotations.** **a**, A schematic depiction shows the different tests used for assessing overlap between experimental annotations and constrained sequences, both for individual bases and for entire regions. **b**, Observed fraction of overlap, depicted separately for bases and regions. The results are shown for selected experimental annotations. The internal bars indicate 95% confidence intervals of randomized placement of experimental elements using the GSC methodology to account for heterogeneity in the data sets. When the bar overlaps the observed value one cannot reject the hypothesis that these overlaps are consistent with random placements.

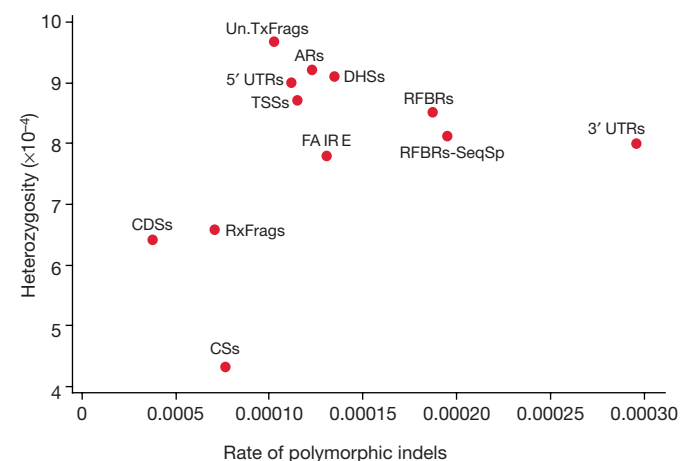


**Figure 12 | Relationship between heterozygosity and polymorphic indel rate for a variety of experimental annotations.** 3' UTRs are an expected outlier for the indel measures owing to the presence of low-complexity sequence (leading to a higher indel rate).

Supplementary Information section 5.4 and S5.5). More aggressive schemes to detect constraint only marginally increase the overlap with experimentally identified functional elements, and do so with considerably less specificity. Similarly, all experimental findings have been independently validated and, for the least constrained experimentally identified functional elements (Un.TxFrags and binding sites of sequence-specific factors), there is both internal validation and cross-validation from different experimental techniques. This suggests that there is probably not a significant overestimation of experimentally identified functional elements. Thus, these two explanations may contribute to the general observation about unconstrained functional elements, but cannot fully explain it.

Instead, we hypothesize five biological reasons to account for the presence of large amounts of unconstrained functional elements. The first two are particular to certain biological assays in which the elements being measured are connected to but do not coincide with the analysed region. An example of this is the parent transcript of an miRNA, where the current assays detect the exons (some of which are not under evolutionary selection), whereas the intronic miRNA actually harbours the constrained bases. Nevertheless, the transcript sequence provides the critical coupling between the regulated promoter and the miRNA. The sliding of transcription factors (which might bind a specific sequence but then migrate along the DNA) or the processivity of histone modifications across chromatin are more exotic examples of this. A related, second hypothesis is that delocalized behaviours of the genome, such as general chromatin accessibility, may be maintained by some biochemical processes (such as transcription of intergenic regions or specific factor binding) without the requirement for specific sequence elements. These two explanations of both connected components and diffuse components related to, but not coincident with, constrained sequences are particularly relevant for the considerable amount of unannotated and unconstrained transcripts.

The other three hypotheses may be more general—the presence of neutral (or near neutral) biochemical elements, of lineage-specific functional elements, and of functionally conserved but non-orthologous elements. We believe there is a considerable proportion of neutral biochemically active elements that do not confer a selective advantage or disadvantage to the organism. This neutral pool of sequence elements may turn over during evolutionary time,

emerging via certain mutations and disappearing by others. The size of the neutral pool would largely be determined by the rate of emergence and extinction through chance events; low information-content elements, such as transcription factor-binding sites<sup>110</sup> will have larger neutral pools. Second, from this neutral pool, some elements might occasionally acquire a biological role and so come under evolutionary selection. The acquisition of a new biological role would then create a lineage-specific element. Finally, a neutral element from the general pool could also become a peer of an existing selected functional element and either of the two elements could then be removed by chance. If the older element is removed, the newer element has, in essence, been conserved without using orthologous bases, providing a conserved function in the absence of constrained sequences. For example, a common HNF4A binding site in the human and mouse genomes may not reflect orthologous human and mouse bases, though the presence of an HNF4A site in that region was evolutionarily selected for in both lineages. Note that both the neutral turnover of elements and the ‘functional peering’ of elements has been suggested for *cis*-acting regulatory elements in *Drosophila*<sup>115,116</sup> and mammals<sup>110</sup>. Our data support these hypotheses, and we have generalized this idea over many different functional elements. The presence of conserved function encoded by conserved orthologous bases is a commonplace assumption in comparative genomics; our findings indicate that there could be a sizable set of functionally conserved but non-orthologous elements in the human genome, and that these seem unconstrained across mammals. Functional data akin to the ENCODE Project on other related species, such as mouse, would be critical to understanding the rate of such functionally conserved but non-orthologous elements.

## Conclusion

The generation and analyses of over 200 experimental data sets from studies examining the 44 ENCODE regions provide a rich source of functional information for 30 Mb of the human genome. The first conclusion of these efforts is that these data are remarkably informative. Although there will be ongoing work to enhance existing assays, invent new techniques and develop new data-analysis methods, the generation of genome-wide experimental data sets akin to the ENCODE pilot phase would provide an impressive platform for future genome exploration efforts. This now seems feasible in light of throughput improvements of many of the assays and the ever-declining costs of whole-genome tiling arrays and DNA sequencing. Such genome-wide functional data should be acquired and released openly, as has been done with other large-scale genome projects, to ensure its availability as a new foundation for all biologists studying the human genome. It is these biologists who will often provide the critical link from biochemical function to biological role for the identified elements.

The scale of the pilot phase of the ENCODE Project was also sufficiently large and unbiased to reveal important principles about the organization of functional elements in the human genome. In many cases, these principles agree with current mechanistic models. For example, we observe trimethylation of H3K4 enriched near active genes, and have improved the ability to accurately predict gene activity based on this and other histone modifications. However, we also uncovered some surprises that challenge the current dogma on biological mechanisms. The generation of numerous intercalated transcripts spanning the majority of the genome has been repeatedly suggested<sup>13,14</sup>, but this phenomenon has been met with mixed opinions about the biological importance of these transcripts. Our analyses of numerous orthogonal data sets firmly establish the presence of these transcripts, and thus the simple view of the genome as having a defined set of isolated loci transcribed independently does not seem to be accurate. Perhaps the genome encodes a network of transcripts, many of which are linked to protein-coding transcripts and to the majority of which we cannot (yet) assign a biological role. Our perspective of transcription and genes may have to evolve and also poses

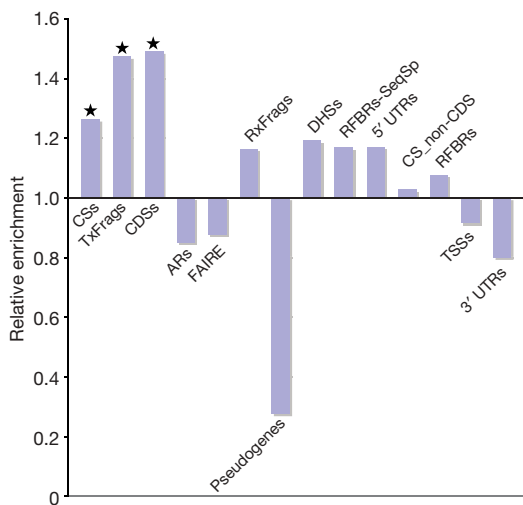


**Figure 13 | CNV enrichment.** The relative enrichment of different experimental annotations in the ENCODE regions associated with CNVs. CS\_non-CDS are constrained sequences outside of coding regions. A value of 1 or less indicates no enrichment, and values greater than 1 show enrichment. Starred columns are cases that are significant on the basis of this enrichment being found in less than 5% of randomizations that matched each element class for length and density of features.

some interesting mechanistic questions. For example, how are splicing signals coordinated and used when there are so many overlapping primary transcripts? Similarly, to what extent does this reflect neutral turnover of reproducible transcripts with no biological role?

We gained subtler but equally important mechanistic findings relating to transcription, replication and chromatin modification. Transcription factors previously thought to primarily bind promoters bind more generally, and those which do bind to promoters are equally likely to bind downstream of a TSS as upstream. Interestingly, many elements that previously were classified as distal enhancers are, in fact, close to one of the newly identified TSSs; only about 35% of sites showing evidence of binding by multiple transcription factors are actually distal to a TSS. This need not imply that most regulatory information is confined to classic promoters, but rather it does suggest that transcription and regulation are coordinated actions beyond just the traditional promoter sequences. Meanwhile, although distal regulatory elements could be identified in the ENCODE regions, they are currently difficult to classify, in part owing to the lack of a broad set of transcription factors to use in analysing such elements. Finally, we now have a much better appreciation of how DNA replication is coordinated with histone modifications.

At the outset of the ENCODE Project, many believed that the broad collection of experimental data would nicely dovetail with the detailed evolutionary information derived from comparing multiple mammalian sequences to provide a neat 'dictionary' of conserved genomic elements, each with a growing annotation about their biochemical function(s). In one sense, this was achieved; the majority of constrained bases in the ENCODE regions are now associated with at least some experimentally derived information about function. However, we have also encountered a remarkable excess of experimentally identified functional elements lacking evolutionary constraint, and these cannot be dismissed for technical reasons. This is perhaps the biggest surprise of the pilot phase of the ENCODE Project, and suggests that we take a more 'neutral' view of many of the functions conferred by the genome.

## METHODS

The methods are described in the Supplementary Information, with more technical details for each experiment often found in the references provided in Table 1. The Supplementary Information sections are arranged in the same order as the manuscript (with similar headings to facilitate cross-referencing). The first page of Supplementary Information also has an index to aid navigation. Raw data are available in ArrayExpress, GEO or EMBL/GenBank archives as appropriate, as detailed in Supplementary Information section 1.1. Processed data are also presented in a user-friendly manner at the UCSC Genome Browser's ENCODE portal (<http://genome.ucsc.edu/ENCODE/>).

Received 2 March; accepted 23 April 2007.

- International Human Genome Sequencing Consortium. Initial sequencing and analysis of the human genome. *Nature* **409**, 860–921 (2001).
- Venter, J. C. et al. The sequence of the human genome. *Science* **291**, 1304–1351 (2001).
- International Human Genome Sequencing Consortium. Finishing the euchromatic sequence of the human genome. *Nature* **431**, 931–945 (2004).
- Mouse Genome Sequencing Consortium. Initial sequencing and comparative analysis of the mouse genome. *Nature* **420**, 520–562 (2002).
- Rat Genome Sequencing Project Consortium. Genome sequence of the Brown Norway rat yields insights into mammalian evolution. *Nature* **428**, 493–521 (2004).
- Lindblad-Toh, K. et al. Genome sequence, comparative analysis and haplotype structure of the domestic dog. *Nature* **438**, 803–819 (2005).
- International Chicken Genome Sequencing Consortium. Sequence and comparative analysis of the chicken genome provide unique perspectives on vertebrate evolution. *Nature* **432**, 695–716 (2004).
- Chimpanzee Sequencing and Analysis Consortium. Initial sequence of the chimpanzee genome and comparison with the human genome. *Nature* **437**, 69–87 (2005).
- ENCODE Project Consortium. The ENCODE (ENCYclopedia Of DNA Elements) Project. *Science* **306**, 636–640 (2004).
- Zhang, Z. D. et al. Statistical analysis of the genomic distribution and correlation of regulatory elements in the ENCODE regions. *Genome Res.* **17**, 787–797 (2007).
- Euskirchen, G. M. et al. Mapping of transcription factor binding regions in mammalian cells by ChIP: comparison of array and sequencing based technologies. *Genome Res.* **17**, 898–909 (2007).
- Willingham, A. T. & Gingeras, T. R. TUF love for "junk" DNA. *Cell* **125**, 1215–1220 (2006).
- Carninci, P. et al. Genome-wide analysis of mammalian promoter architecture and evolution. *Nature Genet.* **38**, 626–635 (2006).
- Cheng, J. et al. Transcriptional maps of 10 human chromosomes at 5-nucleotide resolution. *Science* **308**, 1149–1154 (2005).
- Bertone, P. et al. Global identification of human transcribed sequences with genome tiling arrays. *Science* **306**, 2242–2246 (2004).
- Guigó, R. et al. EGASP: the human ENCODE Genome Annotation Assessment Project. *Genome Biol.* **7**, (Suppl. 1; S2) 1–31 (2006).
- Denoud, F. et al. Prominent use of distal 5' transcription start sites and discovery of a large number of additional exons in ENCODE regions. *Genome Res.* **17**, 746–759 (2007).
- Tress, M. L. et al. The implications of alternative splicing in the ENCODE protein complement. *Proc. Natl. Acad. Sci. USA* **104**, 5495–5500 (2007).
- Rozowsky, J. et al. The DART classification of unannotated transcription within ENCODE regions: Associating transcription with known and novel loci. *Genome Res.* **17**, 732–745 (2007).
- Kapranov, P. et al. Examples of the complex architecture of the human transcriptome revealed by RACE and high-density tiling arrays. *Genome Res.* **15**, 987–997 (2005).
- Balakirev, E. S. & Ayala, F. J. Pseudogenes: are they "junk" or functional DNA? *Annu. Rev. Genet.* **37**, 123–151 (2003).
- Mighell, A. J., Smith, N. R., Robinson, P. A. & Markham, A. F. Vertebrate pseudogenes. *FEBS Lett.* **468**, 109–114 (2000).
- Zheng, D. et al. Pseudogenes in the ENCODE regions: Consensus annotation, analysis of transcription and evolution. *Genome Res.* **17**, 839–851 (2007).
- Zheng, D. et al. Integrated pseudogene annotation for human chromosome 22: evidence for transcription. *J. Mol. Biol.* **349**, 27–45 (2005).
- Harrison, P. M., Zheng, D., Zhang, Z., Carrero, N. & Gerstein, M. Transcribed processed pseudogenes in the human genome: an intermediate form of expressed retrosequence lacking protein-coding ability. *Nucleic Acids Res.* **33**, 2374–2383 (2005).
- Washietl, S. et al. Structured RNAs in the ENCODE selected regions of the human genome. *Genome Res.* **17**, 852–864 (2007).
- Carninci, P. et al. The transcriptional landscape of the mammalian genome. *Science* **309**, 1559–1563 (2005).
- Runte, M. et al. The IC-SNURF-SNRPN transcript serves as a host for multiple small nucleolar RNA species and as an antisense RNA for UBE3A. *Hum. Mol. Genet.* **10**, 2687–2700 (2001).
- Seidl, C. I., Stricker, S. H. & Barlow, D. P. The imprinted Air ncRNA is an atypical RNAPII transcript that evades splicing and escapes nuclear export. *EMBO J.* **25**, 3565–3575 (2006).
- Parra, G. et al. Tandem chimerism as a means to increase protein complexity in the human genome. *Genome Res.* **16**, 37–44 (2006).
- Maston, G. A., Evans, S. K. & Green, M. R. Transcriptional regulatory elements in the human genome. *Annu. Rev. Genomics Hum. Genet.* **7**, 29–59 (2006).
- Trinklein, N. D., Aldred, S. J., Saldanha, A. J. & Myers, R. M. Identification and functional analysis of human transcriptional promoters. *Genome Res.* **13**, 308–312 (2003).
- Cooper, S. J., Trinklein, N. D., Anton, E. D., Nguyen, L. & Myers, R. M. Comprehensive analysis of transcriptional promoter structure and function in 1% of the human genome. *Genome Res.* **16**, 1–10 (2006).
- Cawley, S. et al. Unbiased mapping of transcription factor binding sites along human chromosomes 21 and 22 points to widespread regulation of noncoding RNAs. *Cell* **116**, 499–509 (2004).
- Yelin, R. et al. Widespread occurrence of antisense transcription in the human genome. *Nature Biotechnol.* **21**, 379–386 (2003).
- Katayama, S. et al. Antisense transcription in the mammalian transcriptome. *Science* **309**, 1564–1566 (2005).
- Ren, B. et al. Genome-wide location and function of DNA binding proteins. *Science* **290**, 2306–2309 (2000).
- Iyer, V. R. et al. Genomic binding sites of the yeast cell-cycle transcription factors SBF and MBF. *Nature* **409**, 533–538 (2001).
- Horak, C. E. et al. GATA-1 binding sites mapped in the  $\beta$ -globin locus by using mammalian ChIP-chip analysis. *Proc. Natl. Acad. Sci. USA* **99**, 2924–2929 (2002).
- Wei, C. L. et al. A global map of p53 transcription-factor binding sites in the human genome. *Cell* **124**, 207–219 (2006).
- Kim, J., Bhinge, A. A., Morgan, X. C. & Iyer, V. R. Mapping DNA–protein interactions in large genomes by sequence tag analysis of genomic enrichment. *Nature Methods* **2**, 47–53 (2005).
- Dorschner, M. O. et al. High-throughput localization of functional elements by quantitative chromatin profiling. *Nature Methods* **1**, 219–225 (2004).
- Sabo, P. J. et al. Genome-scale mapping of DNase I sensitivity *in vivo* using tiling DNA microarrays. *Nature Methods* **3**, 511–518 (2006).
- Crawford, G. E. et al. DNase-chip: a high-resolution method to identify DNase I hypersensitive sites using tiled microarrays. *Nature Methods* **3**, 503–509 (2006).
- Hogan, G. J., Lee, C. K. & Lieb, J. D. Cell cycle-specified fluctuation of nucleosome occupancy at gene promoters. *PLoS Genet.* **2**, e158 (2006).

46. Koch, C. M. *et al.* The landscape of histone modifications across 1% of the human genome in five human cell lines. *Genome Res.* **17**, 691–707 (2007).
47. Smale, S. T. & Kadonaga, J. T. The RNA polymerase II core promoter. *Annu. Rev. Biochem.* **72**, 449–479 (2003).
48. Mito, Y., Henikoff, J. G. & Henikoff, S. Genome-scale profiling of histone H3.3 replacement patterns. *Nature Genet.* **37**, 1090–1097 (2005).
49. Heintzman, N. D. *et al.* Distinct and predictive chromatin signatures of transcriptional promoters and enhancers in the human genome. *Nature Genet.* **39**, 311–318 (2007).
50. Yusufzai, T. M., Tagami, H., Nakatani, Y. & Felsenfeld, G. CTCF tethers an insulator to subnuclear sites, suggesting shared insulator mechanisms across species. *Mol. Cell* **13**, 291–298 (2004).
51. Kim, T. H. *et al.* Direct isolation and identification of promoters in the human genome. *Genome Res.* **15**, 830–839 (2005).
52. Bieda, M., Xu, X., Singer, M. A., Green, R. & Farnham, P. J. Unbiased location analysis of E2F1-binding sites suggests a widespread role for E2F1 in the human genome. *Genome Res.* **16**, 595–605 (2006).
53. Ruppert, S., Wang, E. H. & Tjian, R. Cloning and expression of human TAF<sub>II</sub>250: a TBP-associated factor implicated in cell-cycle regulation. *Nature* **362**, 175–179 (1993).
54. Fernandez, P. C. *et al.* Genomic targets of the human c-Myc protein. *Genes Dev.* **17**, 1115–1129 (2003).
55. Li, Z. *et al.* A global transcriptional regulatory role for c-Myc in Burkitt's lymphoma cells. *Proc. Natl Acad. Sci. USA* **100**, 8164–8169 (2003).
56. Orian, A. *et al.* Genomic binding by the *Drosophila* Myc, Max, Mad/Mnt transcription factor network. *Genes Dev.* **17**, 1101–1114 (2003).
57. de Laat, W. & Grosveld, F. Spatial organization of gene expression: the active chromatin hub. *Chromosome Res.* **11**, 447–459 (2003).
58. Trinklein, N. D. *et al.* Integrated analysis of experimental datasets reveals many novel promoters in 1% of the human genome. *Genome Res.* **17**, 720–731 (2007).
59. Jeon, Y. *et al.* Temporal profile of replication of human chromosomes. *Proc. Natl Acad. Sci. USA* **102**, 6419–6424 (2005).
60. Woodfine, K. *et al.* Replication timing of the human genome. *Hum. Mol. Genet.* **13**, 191–202 (2004).
61. White, E. J. *et al.* DNA replication-timing analysis of human chromosome 22 at high resolution and different developmental states. *Proc. Natl Acad. Sci. USA* **101**, 17771–17776 (2004).
62. Schubeler, D. *et al.* Genome-wide DNA replication profile for *Drosophila melanogaster*: a link between transcription and replication timing. *Nature Genet.* **32**, 438–442 (2002).
63. MacAlpine, D. M., Rodriguez, H. K. & Bell, S. P. Coordination of replication and transcription along a *Drosophila* chromosome. *Genes Dev.* **18**, 3094–3105 (2004).
64. Gilbert, D. M. Replication timing and transcriptional control: beyond cause and effect. *Curr. Opin. Cell Biol.* **14**, 377–383 (2002).
65. Schwaiger, M. & Schubeler, D. A question of timing: emerging links between transcription and replication. *Curr. Opin. Genet. Dev.* **16**, 177–183 (2006).
66. Hatton, K. S. *et al.* Replication program of active and inactive multigene families in mammalian cells. *Mol. Cell. Biol.* **8**, 2149–2158 (1988).
67. Gartler, S. M., Goldstein, L., Tyler-Freer, S. E. & Hansen, R. S. The timing of *XIST* replication: dominance of the domain. *Hum. Mol. Genet.* **8**, 1085–1089 (1999).
68. Azuara, V. *et al.* Heritable gene silencing in lymphocytes delays chromatid resolution without affecting the timing of DNA replication. *Nature Cell Biol.* **5**, 668–674 (2003).
69. Cohen, S. M., Furey, T. S., Doggett, N. A. & Kaufman, D. G. Genome-wide sequence and functional analysis of early replicating DNA in normal human fibroblasts. *BMC Genomics* **7**, 301 (2006).
70. Cao, R. *et al.* Role of histone H3 lysine 27 methylation in Polycomb-group silencing. *Science* **298**, 1039–1043 (2002).
71. Muller, J. *et al.* Histone methyltransferase activity of a *Drosophila* Polycomb group repressor complex. *Cell* **111**, 197–208 (2002).
72. Bracken, A. P., Dietrich, N., Pasini, D., Hansen, K. H. & Helin, K. Genome-wide mapping of Polycomb target genes unravels their roles in cell fate transitions. *Genes Dev.* **20**, 1123–1136 (2006).
73. Kirmizis, A. *et al.* Silencing of human polycomb target genes is associated with methylation of histone H3 Lys 27. *Genes Dev.* **18**, 1592–1605 (2004).
74. Lee, T. I. *et al.* Control of developmental regulators by Polycomb in human embryonic stem cells. *Cell* **125**, 301–313 (2006).
75. Karnani, N., Taylor, C., Malhotra, A. & Dutta, A. Pan-S replication patterns and chromosomal domains defined by genome tiling arrays of human chromosomes. *Genome Res.* **17**, 865–876 (2007).
76. Delaval, K., Wagschal, A. & Feil, R. Epigenetic deregulation of imprinting in congenital diseases of aberrant growth. *Bioessays* **28**, 453–459 (2006).
77. Dillon, N. Gene regulation and large-scale chromatin organization in the nucleus. *Chromosome Res.* **14**, 117–126 (2006).
78. Burkhoff, A. M. & Tullius, T. D. Structural details of an adenine tract that does not cause DNA to bend. *Nature* **331**, 455–457 (1988).
79. Price, M. A. & Tullius, T. D. How the structure of an adenine tract depends on sequence context: a new model for the structure of T<sub>n</sub>A<sub>n</sub> DNA sequences. *Biochemistry* **32**, 127–136 (1993).
80. Greenbaum, J. A., Parker, S. C. J. & Tullius, T. D. Detection of DNA structural motifs in functional genomic elements. *Genome Res.* **17**, 940–946 (2007).
81. Thurman, R. E., Day, N., Noble, W. S. & Stamatoyannopoulos, J. A. Identification of higher-order functional domains in the human ENCODE regions. *Genome Res.* **17**, 917–927 (2007).
82. Gilbert, N. *et al.* Chromatin architecture of the human genome: gene-rich domains are enriched in open chromatin fibers. *Cell* **118**, 555–566 (2004).
83. Nobrega, M. A., Ovcharenko, I., Afzal, V. & Rubin, E. M. Scanning human gene deserts for long-range enhancers. *Science* **302**, 413 (2003).
84. Woolfe, A. *et al.* Highly conserved non-coding sequences are associated with vertebrate development. *PLoS Biol.* **3**, e7 (2005).
85. Drake, J. A. *et al.* Conserved noncoding sequences are selectively constrained and not mutation cold spots. *Nature Genet.* **38**, 223–227 (2006).
86. Margulies, E. H., Blanchette, M., NISC Comparative Sequencing Program, Haussler D. & Green, E. D. Identification and characterization of multi-species conserved sequences. *Genome Res.* **13**, 2507–2518 (2003).
87. Cooper, G. M. *et al.* Distribution and intensity of constraint in mammalian genomic sequence. *Genome Res.* **15**, 901–913 (2005).
88. Siepel, A. *et al.* Evolutionarily conserved elements in vertebrate, insect, worm, and yeast genomes. *Genome Res.* **15**, 1034–1050 (2005).
89. Thomas, J. W. *et al.* Parallel construction of orthologous sequence-ready clone contig maps in multiple species. *Genome Res.* **12**, 1277–1285 (2002).
90. Blakesley, R. W. *et al.* An intermediate grade of finished genomic sequence suitable for comparative analyses. *Genome Res.* **14**, 2235–2244 (2004).
91. Aparicio, S. *et al.* Whole-genome shotgun assembly and analysis of the genome of *Fugu rubripes*. *Science* **297**, 1301–1310 (2002).
92. Jaillon, O. *et al.* Genome duplication in the teleost fish *Tetraodon nigroviridis* reveals the early vertebrate proto-karyotype. *Nature* **431**, 946–957 (2004).
93. Margulies, E. H. *et al.* An initial strategy for the systematic identification of functional elements in the human genome by low-redundancy comparative sequencing. *Proc. Natl Acad. Sci. USA* **102**, 4795–4800 (2005).
94. Blanchette, M. *et al.* Aligning multiple genomic sequences with the threaded blockset aligner. *Genome Res.* **14**, 708–715 (2004).
95. Bray, N. & Pachter, L. MAVID: constrained ancestral alignment of multiple sequences. *Genome Res.* **14**, 693–699 (2004).
96. Brudno, M. *et al.* LAGAN and Multi-LAGAN: efficient tools for large-scale multiple alignment of genomic DNA. *Genome Res.* **13**, 721–731 (2003).
97. Margulies, E. H. *et al.* Relationship between evolutionary constraint and genome function for 1% of the human genome. *Genome Res.* **17**, 760–774 (2007).
98. Asthana, S., Roytberg, M., Stamatoyannopoulos, J. A. & Sunyaev, S. Analysis of sequence conservation at nucleotide resolution. *PLoS Comp. Biol.* (submitted).
99. Cooper, G. M., Brudno, M., Green, E. D., Batzoglou, S. & Sidow, A. Quantitative estimates of sequence divergence for comparative analyses of mammalian genomes. *Genome Res.* **13**, 813–820 (2003).
100. Eddy, S. R. A model of the statistical power of comparative genome sequence analysis. *PLoS Biol.* **3**, e10 (2005).
101. Stone, E. A., Cooper, G. M. & Sidow, A. Trade-offs in detecting evolutionarily constrained sequence by comparative genomics. *Annu. Rev. Genomics Hum. Genet.* **6**, 143–164 (2005).
102. McAuliffe, J. D., Jordan, M. I. & Pachter, L. Subtree power analysis and species selection for comparative genomics. *Proc. Natl Acad. Sci. USA* **102**, 7900–7905 (2005).
103. International HapMap Consortium. A haplotype map of the human genome. *Nature* **437**, 1299–1320 (2005).
104. Cheng, Z. *et al.* A genome-wide comparison of recent chimpanzee and human segmental duplications. *Nature* **437**, 88–93 (2005).
105. Cooper, G. M. *et al.* Characterization of evolutionary rates and constraints in three Mammalian genomes. *Genome Res.* **14**, 539–548 (2004).
106. Dermitzakis, E. T., Reymond, A. & Antonarakis, S. E. Conserved non-genic sequences - an unexpected feature of mammalian genomes. *Nature Rev. Genet.* **6**, 151–157 (2005).
107. Clark, T. G. *et al.* Small insertions/deletions and functional constraint in the ENCODE regions. *Genome Biol.* (submitted) (2007).
108. Bejerano, G. *et al.* Ultraconserved elements in the human genome. *Science* **304**, 1321–1325 (2004).
109. Woolfe, A. *et al.* Highly conserved non-coding sequences are associated with vertebrate development. *PLoS Biol.* **3**, e7 (2005).
110. Dermitzakis, E. T. & Clark, A. G. Evolution of transcription factor binding sites in Mammalian gene regulatory regions: conservation and turnover. *Mol. Biol. Evol.* **19**, 1114–1121 (2002).
111. McDonald, J. H. & Kreitman, M. Adaptive protein evolution at the *Adh* locus in *Drosophila*. *Nature* **351**, 652–654 (1991).
112. Andolfatto, P. Adaptive evolution of non-coding DNA in *Drosophila*. *Nature* **437**, 1149–1152 (2005).
113. Hudson, R. R., Kreitman, M. & Aguade, M. A test of neutral molecular evolution based on nucleotide data. *Genetics* **116**, 153–159 (1987).
114. Feuk, L., Carson, A. R. & Scherer, S. W. Structural variation in the human genome. *Nature Rev. Genet.* **7**, 85–97 (2006).
115. Ludwig, M. Z. *et al.* Functional evolution of a *cis*-regulatory module. *PLoS Biol.* **3**, e93 (2005).
116. Ludwig, M. Z. & Kreitman, M. Evolutionary dynamics of the enhancer region of even-skipped in *Drosophila*. *Mol. Biol. Evol.* **12**, 1002–1011 (1995).
117. Harrow, J. *et al.* GENCODE: producing a reference annotation for ENCODE. *Genome Biol.* **7**, (Suppl. 1; S4) 1–9 (2006).

118. Emanuelsson, O. *et al.* Assessing the performance of different high-density tiling microarray strategies for mapping transcribed regions of the human genome. *Genome Res.* advance online publication, doi: 10.1101/gr.5014606 (21 November 2006).

119. Kapranov, P. *et al.* Large-scale transcriptional activity in chromosomes 21 and 22. *Science* **296**, 916–919 (2002).

120. Bhinge, A. A., Kim, J., Euskirchen, G., Snyder, M. & Iyer, V. R. Mapping the chromosomal targets of STAT1 by Sequence Tag Analysis of Genomic Enrichment (STAGE). *Genome Res.* **17**, 910–916 (2007).

121. Ng, P. *et al.* Gene identification signature (GIS) analysis for transcriptome characterization and genome annotation. *Nature Methods* **2**, 105–111 (2005).

122. Giresi, P. G., Kim, J., McDaniell, R. M., Iyer, V. R. & Lieb, J. D. FAIRE (Formaldehyde-Assisted Isolation of Regulatory Elements) isolates active regulatory elements from human chromatin. *Genome Res.* **17**, 877–885 (2006).

123. Rada-Iglesias, A. *et al.* Binding sites for metabolic disease related transcription factors inferred at base pair resolution by chromatin immunoprecipitation and genomic microarrays. *Hum. Mol. Genet.* **14**, 3435–3447 (2005).

124. Kim, T. H. *et al.* A high-resolution map of active promoters in the human genome. *Nature* **436**, 876–880 (2005).

125. Halees, A. S. & Weng, Z. PromoSer: improvements to the algorithm, visualization and accessibility. *Nucleic Acids Res.* **32**, W191–W194 (2004).

126. Bajic, V. B. *et al.* Performance assessment of promoter predictions on ENCODE regions in the EGASP experiment. *Genome Biol.* **7**, (Suppl 1; S3) 1–13 (2006).

127. Zheng, D. & Gerstein, M. B. A computational approach for identifying pseudogenes in the ENCODE regions. *Genome Biol.* **7**, S13.1–S13.10 (2006).

128. Stranger, B. E. *et al.* Genome-wide associations of gene expression variation in humans. *PLoS Genet.* **1**, e78 (2005).

129. Turner, B. M. Reading signals on the nucleosome with a new nomenclature for modified histones. *Nature Struct. Mol. Biol.* **12**, 110–112 (2005).

**Supplementary Information** is linked to the online version of the paper at [www.nature.com/nature](http://www.nature.com/nature).

**Acknowledgements** We thank D. Leja for providing graphical expertise and support. Funding support is acknowledged from the following sources: National Institutes of Health, The European Union BioSapiens NoE, Affymetrix, Swiss National Science Foundation, the Spanish Ministerio de Educación y Ciencia, Spanish Ministry of Education and Science, CIBERESP, Genome Spain and Generalitat de Catalunya, Ministry of Education, Culture, Sports, Science and Technology of Japan, the NCCR Frontiers in Genetics, the Jérôme Lejeune Foundation, the Childcare Foundation, the Novartis Foundations, the Danish Research Council, the Swedish Research Council, the Knut and Alice Wallenberg Foundation, the Wellcome Trust, the Howard Hughes Medical Institute, the Bio-X Institute, the RIKEN Institute, the US Army, National Science Foundation, the Deutsche Forschungsgemeinschaft, the Austrian Gen-AU program, the BBSRC and The European Molecular Biology Laboratory. We thank the Barcelona SuperComputing Center and the NIH Biowulf cluster for computer facilities. The Consortium thanks the ENCODE Scientific Advisory Panel for their advice on the project: G. Weinstock, M. Cherry, G. Churchill, M. Eisen, S. Elgin, J. Lis, J. Rine, M. Vidal and P. Zamore.

**Author Information** Reprints and permissions information is available at [www.nature.com/reprints](http://www.nature.com/reprints). The authors declare no competing financial interests. The list of individual authors is divided among the six main analysis groups and five organizational groups. Correspondence and requests for materials should be addressed to the co-chairs of the ENCODE analysis groups (listed in the Analysis Coordination group) E. Birney (birney@ebi.ac.uk); J. A. Stamatoyannopoulos (jstam@u.washington.edu); A. Dutta (ad8q@virginia.edu); R. Guigo (rigo@imim.es); T. R. Gingeras (Tom\_Gingeras@affymetrix.com); E. H. Margulies (elliott@nhgri.nih.gov); Z. Weng (zhiping@bu.edu); M. Snyder (michael.snyder@yale.edu); E. T. Dermitzakis (md4@sanger.ac.uk) or collectively (encode\_chairs@ebi.ac.uk).

## The ENCODE Project Consortium

**Analysis Coordination** Ewan Birney<sup>1</sup>, John A. Stamatoyannopoulos<sup>2</sup>, Anindya Dutta<sup>3</sup>, Roderic Guigo<sup>4,5</sup>, Thomas R. Gingeras<sup>6</sup>, Elliott H. Margulies<sup>7</sup>, Zhiping Weng<sup>8,9</sup>, Michael Snyder<sup>10,11</sup> & Emmanouil T. Dermitzakis<sup>12</sup>

**Chromatin and Replication** John A. Stamatoyannopoulos<sup>2</sup>, Robert E. Thurman<sup>2,13</sup>, Michael S. Kuehn<sup>2,13</sup>, Christopher M. Taylor<sup>3</sup>, Shane Neph<sup>2</sup>, Christoph M. Koch<sup>12</sup>, Saurabh Asthana<sup>14</sup>, Ankit Malhotra<sup>3</sup>, Ivan Adzhubei<sup>14</sup>, Jason A. Greenbaum<sup>15</sup>, Robert M. Andrews<sup>12</sup>, Paul Flicek<sup>1</sup>, Patrick J. Boyle<sup>3</sup>, Hua Cao<sup>13</sup>, Nigel P. Carter<sup>12</sup>, Gayle K. Clelland<sup>12</sup>, Sean Davis<sup>16</sup>, Nathan Day<sup>2</sup>, Pawandeep Dhami<sup>12</sup>, Shane C. Dillon<sup>12</sup>, Michael O. Dorschner<sup>2</sup>, Heike Fiegler<sup>12</sup>, Paul G. Giresi<sup>17</sup>, Jeff Goldy<sup>2</sup>, Michael Hawrylycz<sup>18</sup>, Andrew Haydock<sup>2</sup>, Richard Humbert<sup>2</sup>, Keith D. James<sup>12</sup>, Brett E. Johnson<sup>13</sup>, Ericka M. Johnson<sup>13</sup>, Tristant T. Frum<sup>13</sup>, Elizabeth R. Rosenzweig<sup>13</sup>, Neerja Karnani<sup>3</sup>, Kirsten Lee<sup>2</sup>, Gregory C. Lefebvre<sup>12</sup>, Patrick A. Navas<sup>13</sup>, Fidencio Neri<sup>2</sup>, Stephen C. J. Parker<sup>15</sup>, Peter J. Sabo<sup>2</sup>, Richard Sandstrom<sup>2</sup>, Anthony Shafer<sup>2</sup>, David Vetrone<sup>12</sup>, Molly Weaver<sup>2</sup>, Sarah

Wilcox<sup>12</sup>, Man Yu<sup>13</sup>, Francis S. Collins<sup>7</sup>, Job Dekker<sup>19</sup>, Jason D. Lieb<sup>17</sup>, Thomas D. Tullius<sup>15</sup>, Gregory E. Crawford<sup>20</sup>, Shamil Sunyaev<sup>14</sup>, William S. Noble<sup>2</sup>, Ian Dunham<sup>12</sup> & Anindya Dutta<sup>3</sup>

**Genes and Transcripts** Roderic Guigo<sup>4,5</sup>, France Denoeud<sup>5</sup>, Alexandre Reymond<sup>21,22</sup>, Philipp Kapranov<sup>6</sup>, Joel Rozowsky<sup>11</sup>, Deyou Zheng<sup>11</sup>, Robert Castelo<sup>5</sup>, Adam Frankish<sup>12</sup>, Jennifer Harrow<sup>12</sup>, Srinika Ghosh<sup>6</sup>, Albin Sandelin<sup>23</sup>, Ivo L. Hofacker<sup>24</sup>, Robert Baertsch<sup>25,26</sup>, Damian Keefe<sup>1</sup>, Paul Flicek<sup>1</sup>, Sujit Dike<sup>6</sup>, Jill Cheng<sup>6</sup>, Heather A. Hirsch<sup>27</sup>, Edward A. Sekinger<sup>27</sup>, Julien Lagarde<sup>5</sup>, Joseph F. Abril<sup>5,28</sup>, Atif Shahab<sup>29</sup>, Christoph Flamm<sup>24,30</sup>, Claudia Fried<sup>30</sup>, Jörg Hackermüller<sup>32</sup>, Jana Hertel<sup>30</sup>, Manja Lindemeyer<sup>30</sup>, Kristin Misra<sup>30,31</sup>, Andrea Tanzer<sup>24,30</sup>, Stefan Washietl<sup>24</sup>, Jan Korbel<sup>11</sup>, Olof Emanuelsson<sup>11</sup>, Jakob S. Pedersen<sup>26</sup>, Nancy Holroyd<sup>12</sup>, Ruth Taylor<sup>12</sup>, David Swarbreck<sup>12</sup>, Nicholas Matthews<sup>12</sup>, Mark C. Dickson<sup>33</sup>, Daryl J. Thomas<sup>25,26</sup>, Matthew T. Weirauch<sup>25</sup>, James Gilbert<sup>12</sup>, Jörg Drenkow<sup>6</sup>, Ian Bell<sup>6</sup>, XiaoDong Zhao<sup>34</sup>, K.G. Srinivasan<sup>34</sup>, Wing-Kin Sung<sup>34</sup>, Hong Sain Ooi<sup>34</sup>, Kuo Ping Chiu<sup>34</sup>, Sylvain Foissac<sup>4</sup>, Tyler Alioto<sup>4</sup>, Michael Brent<sup>35</sup>, Lior Pachter<sup>36</sup>, Michael L. Tress<sup>37</sup>, Alfonso Valencia<sup>37</sup>, Siew Woh Choo<sup>34</sup>, Chiou Yu Choo<sup>34</sup>, Catherine Uclat<sup>22</sup>, Caroline Manzano<sup>22</sup>, Carine Wyss<sup>22</sup>, Evelyn Cheung<sup>6</sup>, Taane G. Clark<sup>38</sup>, James B. Brown<sup>39</sup>, Madhavan Ganesh<sup>6</sup>, Sandeep Patel<sup>6</sup>, Hari Tammana<sup>6</sup>, Jacqueline Chrast<sup>21</sup>, Charlotte N. Henrichsen<sup>1</sup>, Chikatoshi Kai<sup>23</sup>, Jun Kawai<sup>23,40</sup>, Ugrappa Nagalakshmi<sup>10</sup>, Jiaqian Wu<sup>10</sup>, Zheng Lian<sup>41</sup>, Jin Lian<sup>41</sup>, Peter Newburger<sup>42</sup>, Xueqing Zhang<sup>42</sup>, Peter Bickel<sup>43</sup>, John S. Mattick<sup>44</sup>, Piero Carninci<sup>40</sup>, Yoshihide Hayashizaki<sup>23,40</sup>, Sherman Weissman<sup>41</sup>, Emmanouil T. Dermitzakis<sup>12</sup>, Elliott H. Margulies<sup>7</sup>, Tim Hubbard<sup>12</sup>, Richard M. Myers<sup>33</sup>, Jane Rogers<sup>12</sup>, Peter F. Stadler<sup>24,30,45</sup>, Todd M. Lowe<sup>25</sup>, Chia-Lin Wei<sup>34</sup>, Yijun Ruan<sup>34</sup>, Michael Snyder<sup>10,11</sup>, Ewan Birney<sup>1</sup>, Kevin Struhl<sup>27</sup>, Mark Gerstein<sup>11,46,47</sup>, Stylianos E. Antonarakis<sup>22</sup> & Thomas R. Gingeras<sup>6</sup>

**Integrated Analysis and Manuscript Preparation** James B. Brown<sup>39</sup>, Paul Flicek<sup>1</sup>, Yutao Fu<sup>8</sup>, Damian Keefe<sup>1</sup>, Ewan Birney<sup>1</sup>, France Denoeud<sup>5</sup>, Mark Gerstein<sup>11,46,47</sup>, Eric D. Green<sup>7,48</sup>, Philipp Kapranov<sup>6</sup>, Ulaş Karaöz<sup>8</sup>, Richard M. Myers<sup>33</sup>, William S. Noble<sup>2</sup>, Alexandre Reymond<sup>21,22</sup>, Joel Rozowsky<sup>11</sup>, Kevin Struhl<sup>27</sup>, Adam Siepel<sup>25,26</sup>, John A. Stamatoyannopoulos<sup>2</sup>, Christopher M. Taylor<sup>3</sup>, James Taylor<sup>49,50</sup>, Robert E. Thurman<sup>2,13</sup>, Thomas D. Tullius<sup>15</sup>, Stefan Washietl<sup>24</sup> & Deyou Zheng<sup>11</sup>

**Management Group** Laura A. Liefer<sup>51</sup>, Kris A. Wetterstrand<sup>51</sup>, Peter J. Good<sup>51</sup>, Elise A. Feingold<sup>51</sup>, Mark S. Guyer<sup>51</sup> & Francis S. Collins<sup>52</sup>

**Multi-species Sequence Analysis** Elliott H. Margulies<sup>7</sup>, Gregory M. Cooper<sup>33</sup>, George Asimenos<sup>53</sup>, Daryl J. Thomas<sup>25,26</sup>, Colin N. Dewey<sup>54</sup>, Adam Siepel<sup>25,26</sup>, Ewan Birney<sup>1</sup>, Damian Keefe<sup>1</sup>, Minmei Hou<sup>49,50</sup>, James Taylor<sup>49,50</sup>, Sergey Nikolaev<sup>22</sup>, Juan I. Montoya-Burgos<sup>55</sup>, Ari Löttynoja<sup>1</sup>, Simon Whelan<sup>1</sup>, Fabio Pardi<sup>1</sup>, Tim Massingham<sup>1</sup>, James B. Brown<sup>39</sup>, Haiyan Huang<sup>43</sup>, Nancy R. Zhang<sup>43,56</sup>, Peter Bickel<sup>43</sup>, Ian Holmes<sup>57</sup>, James C. Mullikin<sup>7,48</sup>, Abel Ureta-Vidal<sup>1</sup>, Benedict Paten<sup>1</sup>, Michael Seringhaus<sup>11</sup>, Deanna Church<sup>58</sup>, Kate Rosenbloom<sup>26</sup>, W. James Kent<sup>25,26</sup>, Eric A. Stone<sup>33</sup>, NISC Comparative Sequencing Program\*, Baylor College of Medicine Human Genome Sequencing Center\*, Washington University Genome Sequencing Center\*, Broad Institute\*, Children's Hospital Oakland Research Institute\*, Mark Gerstein<sup>11,46,47</sup>, Stylianos E. Antonarakis<sup>22</sup>, Serafim Batzoglou<sup>53</sup>, Nick Goldman<sup>1</sup>, Ross C. Hardison<sup>50,59</sup>, David Haussler<sup>25,26,60</sup>, Webb Miller<sup>49,50,61</sup>, Lior Pachter<sup>36</sup>, Eric D. Green<sup>7,48</sup> & Arend Sidow<sup>33,62</sup>

**Transcriptional Regulatory Elements** Zhiping Weng<sup>8,9</sup>, Nathan D. Trinklein<sup>33</sup>, Yutao Fu<sup>8</sup>, Zhengdong D. Zhang<sup>11</sup>, Ulaş Karaöz<sup>8</sup>, Leah Barrera<sup>68</sup>, Rhona Stuart<sup>68</sup>, Deyou Zheng<sup>11</sup>, Srinika Ghosh<sup>6</sup>, Paul Flicek<sup>1</sup>, David C. King<sup>50,59</sup>, James Taylor<sup>49,50</sup>, Adam Ameur<sup>69</sup>, Stefan Enroth<sup>69</sup>, Mark C. Bieda<sup>70</sup>, Christoph M. Koch<sup>12</sup>, Heather A. Hirsch<sup>27</sup>, Chia-Lin Wei<sup>34</sup>, Jill Cheng<sup>6</sup>, Jonghwan Kim<sup>71</sup>, Akshay A. Bhinge<sup>71</sup>, Paul G. Giresi<sup>17</sup>, Nan Jiang<sup>72</sup>, Jun Liu<sup>34</sup>, Fei Yao<sup>34</sup>, Wing-Kin Sung<sup>34</sup>, Kuo Ping Chiu<sup>34</sup>, Vinsensius B. Vega<sup>34</sup>, Charlie W.H. Lee<sup>34</sup>, Patrick Ng<sup>34</sup>, Atif Shahab<sup>29</sup>, Edward A. Sekinger<sup>27</sup>, Annie Yang<sup>27</sup>, Zarmik Moqtaderi<sup>27</sup>, Zhou Zhu<sup>27</sup>, Xiaoqin Xu<sup>70</sup>, Sharon Squazzo<sup>70</sup>, Matthew J. Oberley<sup>73</sup>, David Inman<sup>73</sup>, Michael A. Singer<sup>72</sup>, Todd A. Richmond<sup>72</sup>, Kyle J. Munn<sup>72,74</sup>, Alvaro Rada-Iglesias<sup>74</sup>, Ola Wallerman<sup>74</sup>, Jan Komorowski<sup>69</sup>, Gayle K. Clelland<sup>12</sup>, Sarah Wilcox<sup>12</sup>, Shane C. Dillon<sup>12</sup>, Robert M. Andrews<sup>12</sup>, Joanna C. Fowler<sup>12</sup>, Phillippe Couttet<sup>12</sup>, Keith D. James<sup>12</sup>, Gregory C. Lefebvre<sup>12</sup>, Alexander W. Bruce<sup>12</sup>, Oliver M. Dovey<sup>12</sup>, Peter D. Ellis<sup>12</sup>, Pawandeep Dhami<sup>12</sup>, Cordelia F. Langford<sup>12</sup>, Nigel P. Carter<sup>12</sup>, David Vetrone<sup>12</sup>, Philipp Kapranov<sup>6</sup>, David A. Nix<sup>6</sup>, Ian Bell<sup>6</sup>, Sandeep Patel<sup>6</sup>, Joel Rozowsky<sup>11</sup>, Ghia Euskirchen<sup>10</sup>, Stephen Hartman<sup>10</sup>, Jin Lian<sup>41</sup>, Jiaqian Wu<sup>10</sup>, Alexander E. Urban<sup>10</sup>, Peter Kraus<sup>10</sup>, Sara Van Calcar<sup>68</sup>, Nate Heintzman<sup>68</sup>, Tae Hoon Kim<sup>68</sup>, Kun Wang<sup>68</sup>, Chunxu Qu<sup>68</sup>, Gary Hon<sup>68</sup>, Rosa Luna<sup>75</sup>, Christopher K. Glass<sup>75</sup>, M. Geoff Rosenfeld<sup>75</sup>, Shelley Force Aldred<sup>33</sup>, Sara J. Cooper<sup>33</sup>, Anason Halees<sup>8</sup>, Jane M. Lin<sup>9</sup>, Hennady P. Shulha<sup>9</sup>, Xiaoling Zhang<sup>8</sup>, Mousheng Xu<sup>8</sup>, Jaafar N. S. Haidar<sup>9</sup>, Yong Yu<sup>9</sup>, Ewan Birney<sup>1</sup>, Sherman Weissman<sup>41</sup>, Yijun Ruan<sup>34</sup>, Jason D. Lieb<sup>17</sup>, Vishwanath R. Iyer<sup>71</sup>, Roland D. Green<sup>72</sup>, Thomas R. Gingeras<sup>6</sup>, Claes Wadelius<sup>74</sup>, Ian Dunham<sup>12</sup>, Kevin Struhl<sup>27</sup>, Ross C. Hardison<sup>50,59</sup>, Mark Gerstein<sup>11,46,47</sup>, Peggy J. Farnham<sup>70</sup>, Richard M. Myers<sup>33</sup>, Bing Ren<sup>68</sup> & Michael Snyder<sup>10,11</sup>

**UCSC Genome Browser** Daryl J. Thomas<sup>25,26</sup>, Kate Rosenbloom<sup>26</sup>, Rachel A. Harte<sup>26</sup>, Angie S. Hinrichs<sup>26</sup>, Heather Trumbower<sup>26</sup>, Hiram Clawson<sup>26</sup>, Jennifer Hillman-Jackson<sup>26</sup>, Ann S. Zweig<sup>26</sup>, Kayla Smith<sup>26</sup>, Archana Thakkapallayil<sup>26</sup>, Galt Barber<sup>26</sup>, Robert M. Kuhn<sup>26</sup>, Donna Karolchik<sup>26</sup>, David Haussler<sup>25,26,60</sup> & W. James Kent<sup>25,26</sup>

**Variation** Emmanouil T. Dermitzakis<sup>12</sup>, Lluís Armengol<sup>76</sup>, Christine P. Bird<sup>12</sup>, Taane G. Clark<sup>38</sup>, Gregory M. Cooper<sup>33†</sup>, Paul I. W. de Bakker<sup>77</sup>, Andrew D. Kern<sup>26</sup>, Nuria Lopez-Bigas<sup>5</sup>, Joel D. Martin<sup>50,59</sup>, Barbara E. Stranger<sup>12</sup>, Daryl J. Thomas<sup>25,26</sup>, Abigail Woodroffe<sup>78</sup>, Serafim Batzoglou<sup>53</sup>, Eugene Davydov<sup>53</sup>, Antigone Dimas<sup>12</sup>, Eduardo Eyras<sup>5</sup>, Ingileif B. Halgrímsdóttir<sup>79</sup>, Ross C. Hardison<sup>50,59</sup>, Julian Huppert<sup>12</sup>, Arend Sidow<sup>33,62</sup>, James Taylor<sup>49,50</sup>, Heather Trumbower<sup>26</sup>, Michael C. Zody<sup>77</sup>, Roderic Guigó<sup>4,5</sup>, James C. Mullikin<sup>7</sup>, Gonçalo R. Abecasis<sup>78</sup>, Xavier Estivill<sup>76,80</sup> & Ewan Birney<sup>1</sup>.

**\*NISC Comparative Sequencing Program** Gerard G. Bouffard<sup>7,48</sup>, Xiaobin Guan<sup>48</sup>, Nancy F. Hansen<sup>48</sup>, Jacquelyn R. Idol<sup>7</sup>, Valerie V.B. Maduro<sup>7</sup>, Baishali Maskeri<sup>48</sup>, Jennifer C. McDowell<sup>48</sup>, Morgan Park<sup>48</sup>, Pamela J. Thomas<sup>48</sup>, Alice C. Young<sup>48</sup> & Robert W. Blakesley<sup>7,48</sup>  
**Baylor College of Medicine, Human Genome Sequencing Center** Donna M. Muzny<sup>63</sup>, Erica Sodergren<sup>63</sup>, David A. Wheeler<sup>63</sup>, Kim C. Worley<sup>63</sup>, Huaiyang Jiang<sup>63</sup>, George M. Weinstock<sup>63</sup> & Richard A. Gibbs<sup>63</sup>,  
**Washington University Genome Sequencing Center** Tina Graves<sup>64</sup>, Robert Fulton<sup>64</sup>, Elaine R. Mardis<sup>64</sup> & Richard K. Wilson<sup>64</sup>  
**Broad Institute** Michele Clamp<sup>65</sup>, James Cuff<sup>65</sup>, Sante Gnerre<sup>65</sup>, David B. Jaffe<sup>65</sup>, Jean L. Chang<sup>65</sup>, Kerstin Lindblad-Toh<sup>65</sup> & Eric S. Lander<sup>65,66</sup>  
**Children's Hospital Oakland Research Institute** Maxim Koriabine<sup>67</sup>, Mikhail Nefedov<sup>67</sup>, Kazutoyo Osoegawa<sup>67</sup>, Yuko Yoshinaga<sup>67</sup>, Baoli Zhu<sup>67</sup> & Pieter J. de Jong<sup>67</sup>

Affiliations for participants: <sup>1</sup>EMBL-European Bioinformatics Institute, Wellcome Trust Genome Campus, Hinxton, Cambridge, CB10 1SD, UK. <sup>2</sup>Department of Genome Sciences, 1705 NE Pacific Street, Box 357730, University of Washington, Seattle, Washington 98195, USA. <sup>3</sup>Department of Biochemistry and Molecular Genetics, Jordan 1240, Box 800733, 1300 Jefferson Park Ave, University of Virginia School of Medicine, Charlottesville, Virginia 22908, USA. <sup>4</sup>Genomic Bioinformatics Program, Center for Genomic Regulation, <sup>5</sup>Research Group in Biomedical Informatics, Institut Municipal d'Investigació Mèdica/Universitat Pompeu Fabra, c/o Dr. Aiguader 88, Barcelona Biomedical Research Park Building, 08003 Barcelona, Catalonia, Spain. <sup>6</sup>Affymetrix, Inc., Santa Clara, California 95051, USA. <sup>7</sup>Genome Technology Branch, National Human Genome Research Institute, National Institutes of Health, Bethesda, Maryland 20892, USA. <sup>8</sup>Bioinformatics Program, Boston University, 24 Cummingston St., Boston, Massachusetts 02215, USA. <sup>9</sup>Biomedical Engineering Department, Boston University, 44 Cummingston St., Boston, Massachusetts 02215, USA. <sup>10</sup>Department of Molecular, Cellular, and Developmental Biology, Yale University, New Haven, Connecticut 06520, USA. <sup>11</sup>Department of Molecular Biophysics and Biochemistry, Yale University, PO Box 208114, New Haven, Connecticut 06520, USA. <sup>12</sup>The Wellcome Trust Sanger Institute, Wellcome Trust Genome Campus, Hinxton, Cambridge, CB10 1SA, UK. <sup>13</sup>Division of Medical Genetics, 1705 NE Pacific Street, Box 357720, University of Washington, Seattle, Washington 98195, USA. <sup>14</sup>Division of Genetics, Brigham and Women's Hospital and Harvard Medical School, 77 Avenue Louis Pasteur, Boston, Massachusetts 02115, USA. <sup>15</sup>Department of Chemistry and Program in Bioinformatics, Boston University, 590 Commonwealth Avenue, Boston, Massachusetts 02215, USA. <sup>16</sup>Genetics Branch, Center for Cancer Research, National Cancer Institute, National Institutes of Health, Bethesda, Maryland 20892, USA. <sup>17</sup>Department of Biology and Carolina Center for Genome Sciences, CB# 3280, 202 Fordham Hall, The University of North Carolina at Chapel Hill, Chapel Hill, North Carolina 27599, USA. <sup>18</sup>Allen Institute for Brain Sciences, 551 North 34th Street, Seattle, Washington 98103, USA. <sup>19</sup>Program in Gene Function and Expression and Department of Biochemistry and Molecular Pharmacology, University of Massachusetts Medical School, 364 Plantation Street, Worcester, Massachusetts 01605, USA. <sup>20</sup>Institute for Genome Sciences & Policy and Department of Pediatrics, 101 Science Drive, Duke University, Durham, North Carolina 27708, USA. <sup>21</sup>Center for Integrative Genomics, University of Lausanne, Genopode building, 1015 Lausanne, Switzerland. <sup>22</sup>Department of Genetic Medicine and Development, University of Geneva Medical School, 1211 Geneva, Switzerland. <sup>23</sup>Genome Exploration Research Group, RIKEN Genomic Sciences Center (GSC), RIKEN Yokohama Institute, 1-7-22, Suehiro-cho, Tsurumi-ku, Yokohama, Kanagawa, 230-0045, Japan. <sup>24</sup>Institute for Theoretical Chemistry, University of Vienna, Währingerstraße 17, A-1090 Wien, Austria. <sup>25</sup>Department of Biomolecular Engineering, University of California, Santa Cruz, 1156 High Street, Santa Cruz, California 95064, USA. <sup>26</sup>Center for Biomolecular Science and Engineering, Engineering 2, Suite 501, Mail Stop CBSE/ITI, University of California, Santa Cruz, California 95064, USA. <sup>27</sup>Department of Biological Chemistry & Molecular Pharmacology, Harvard Medical School, 240 Longwood Avenue, Boston, Massachusetts 02115, USA. <sup>28</sup>Department of Genetics, Facultat de Biologia, Universitat de Barcelona, Av Diagonal, 645, 08028, Barcelona, Catalonia, Spain. <sup>29</sup>Bioinformatics Institute, 30 Biopolis Street, #07-01 Matrix, Singapore, 138671, Singapore. <sup>30</sup>Bioinformatics Group, Department of Computer Science, <sup>31</sup>Interdisciplinary Center of Bioinformatics, University of Leipzig, Härtelstraße 16-18, D-04107 Leipzig, Germany. <sup>32</sup>Fraunhofer Institut für Zelltherapie und Immunologie - IZI, Deutscher Platz 5e, D-04103 Leipzig, Germany. <sup>33</sup>Department of Genetics, Stanford University School of Medicine, Stanford,

California 94305, USA. <sup>34</sup>Genome Institute of Singapore, 60 Biopolis Street, Singapore 138672, Singapore. <sup>35</sup>Laboratory for Computational Genomics, Washington University, Campus Box 1045, Saint Louis, Missouri 63130, USA. <sup>36</sup>Department of Mathematics and Computer Science, University of California, Berkeley, California 94720, USA. <sup>37</sup>Spanish National Cancer Research Centre, CNIO, Madrid, E-28029, Spain. <sup>38</sup>Department of Epidemiology and Public Health, Imperial College, St Mary's Campus, Norfolk Place, London W2 1PG, UK. <sup>39</sup>Department of Applied Science & Technology, University of California, Berkeley, California 94720, USA. <sup>40</sup>Genome Science Laboratory, Discovery and Research Institute, RIKEN Wako Institute, 2-1 Hirosawa, Wako, Saitama, 351-0198, Japan. <sup>41</sup>Department of Genetics, Yale University School of Medicine, 333 Cedar Street, New Haven, Connecticut 06510, USA. <sup>42</sup>Department of Pediatrics, University of Massachusetts Medical School, 55 Lake Avenue, North Worcester, Massachusetts 01605, USA. <sup>43</sup>Department of Statistics, University of California, Berkeley, California 94720, USA. <sup>44</sup>Institute for Molecular Bioscience, University of Queensland, St. Lucia, QLD 4072, Australia. <sup>45</sup>The Santa Fe Institute, 1399 Hyde Park Road, Santa Fe, New Mexico 87501, USA. <sup>46</sup>Department of Computer Science, Yale University, PO Box 208114, New Haven, Connecticut 06520-8114, USA. <sup>47</sup>Program in Computational Biology & Bioinformatics, Yale University, PO Box 208114, New Haven, Connecticut 06520-8114, USA. <sup>48</sup>NIH Intramural Sequencing Center, National Human Genome Research Institute, National Institutes of Health, Bethesda, Maryland 20892, USA. <sup>49</sup>Department of Computer Science and Engineering, The Pennsylvania State University, University Park, Pennsylvania 16802, USA. <sup>50</sup>Center for Comparative Genomics and Bioinformatics, Huck Institutes for Life Sciences, The Pennsylvania State University, University Park, Pennsylvania 16802, USA. <sup>51</sup>Division of Extramural Research, National Human Genome Research Institute, National Institute of Health, 5635 Fishers Lane, Suite 4076, Bethesda, Maryland 20892-9305, USA. <sup>52</sup>Office of the Director, National Human Genome Research Institute, National Institute of Health, 31 Center Drive, Suite 4B09, Bethesda, Maryland 20892-2152, USA. <sup>53</sup>Department of Computer Science, Stanford University, Stanford, California 94305, USA. <sup>54</sup>Department of Biostatistics and Medical Informatics, University of Wisconsin-Madison, 6720 MSC, 1300 University Ave, Madison, Wisconsin 53706, USA. <sup>55</sup>Department of Zoology and Animal Biology, Faculty of Sciences, University of Geneva, 1205 Geneva, Switzerland. <sup>56</sup>Department of Statistics, Stanford University, Stanford, California 94305, USA. <sup>57</sup>Department of Bioengineering, University of California, Berkeley, California 94720-1762, USA. <sup>58</sup>National Center for Biotechnology Information, National Institutes of Health, Bethesda, Maryland 20894, USA. <sup>59</sup>Department of Biochemistry and Molecular Biology, Huck Institutes of Life Sciences, The Pennsylvania State University, University Park, Pennsylvania 16802, USA. <sup>60</sup>Howard Hughes Medical Institute, University of California, Santa Cruz, California 95064, USA. <sup>61</sup>Department of Biology, The Pennsylvania State University, University Park, Pennsylvania 16802, USA. <sup>62</sup>Department of Pathology, Stanford University School of Medicine, Stanford, California 94305, USA. <sup>63</sup>Human Genome Sequencing Center and Department of Molecular and Human Genetics, Baylor College of Medicine, Houston, Texas 77030, USA. <sup>64</sup>Genome Sequencing Center, Washington University School of Medicine, Campus Box 8501, 4444 Forest Park Avenue, Saint Louis, Missouri 63108, USA. <sup>65</sup>Broad Institute of Harvard University and Massachusetts Institute of Technology, 320 Charles Street, Cambridge, Massachusetts 02141, USA. <sup>66</sup>Whitehead Institute for Biomedical Research, 9 Cambridge Center, Cambridge, Massachusetts 02142, USA. <sup>67</sup>Children's Hospital Oakland Research Institute, BACPAC Resources, 747 52nd Street, Oakland, California 94609, USA. <sup>68</sup>Ludwig Institute for Cancer Research, 9500 Gilman Drive, La Jolla, California 92093-0653, USA. <sup>69</sup>The Linnaeus Centre for Bioinformatics, Uppsala University, BMC, Box 598, SE-75124 Uppsala, Sweden. <sup>70</sup>Department of Pharmacology and the Genome Center, University of California, Davis, California 95616, USA. <sup>71</sup>Institute for Cellular & Molecular Biology, The University of Texas at Austin, 1 University Station A4800, Austin, Texas 78712, USA. <sup>72</sup>NimbleGen Systems, Inc., 1 Science Court, Madison, Wisconsin 53711, USA. <sup>73</sup>University of Wisconsin Medical School, Madison, Wisconsin 53706, USA. <sup>74</sup>Department of Genetics and Pathology, Rudbeck Laboratory, Uppsala University, SE-75185 Uppsala, Sweden. <sup>75</sup>University of California, San Diego School of Medicine, 9500 Gilman Drive, La Jolla, California 92093, USA. <sup>76</sup>Genes and Disease Program, Center for Genomic Regulation, c/o Dr. Aiguader 88, Barcelona Biomedical Research Park Building, 08003 Barcelona, Catalonia, Spain. <sup>77</sup>Broad Institute of MIT and Harvard, 7 Cambridge Center, Cambridge, Massachusetts 02142, USA. <sup>78</sup>Center for Statistical Genetics, Department of Biostatistics, SPH II, 1420 Washington Heights, Ann Arbor, Michigan 48109-2029, USA. <sup>79</sup>Department of Statistics, University of Oxford, Oxford OX1 3TG, UK. <sup>80</sup>Universitat Pompeu Fabra, c/o Dr. Aiguader 88, Barcelona Biomedical Research Park Building, 08003 Barcelona, Catalonia, Spain. <sup>†</sup>Present addresses: Department of Genome Sciences, University of Washington School of Medicine, Seattle, Washington 98195, USA (G.M.C.); Department of Biological Statistics & Computational Biology, Cornell University, Ithaca, New York 14853, USA (A.S.); Faculty of Life Sciences, University of Manchester, Michael Smith Building, Oxford Road, Manchester, M13 9PT, UK (S.W.); SwitchGear Genomics, 1455 Adams Drive, Suite 2015, Menlo Park, California 94025, USA (N.D.T.; S.F.A.).

## ARTICLES

# Exploitation of structural and regulatory diversity in glutamate racemases

Tomas Lundqvist<sup>1\*</sup>, Stewart L. Fisher<sup>2\*</sup>, Gunther Kern<sup>2</sup>, Rutger H. A. Folmer<sup>1</sup>, Yafeng Xue<sup>1</sup>, D. Trevor Newton<sup>2</sup>, Thomas A. Keating<sup>2</sup>, Richard A. Alm<sup>2</sup> & Boudewijn L. M. de Jonge<sup>2</sup>

Glutamate racemase is an enzyme essential to the bacterial cell wall biosynthesis pathway, and has therefore been considered as a target for antibacterial drug discovery. We characterized the glutamate racemases of several pathogenic bacteria using structural and biochemical approaches. Here we describe three distinct mechanisms of regulation for the family of glutamate racemases: allosteric activation by metabolic precursors, kinetic regulation through substrate inhibition, and D-glutamate recycling using a D-amino acid transaminase. In a search for selective inhibitors, we identified a series of uncompetitive inhibitors specifically targeting *Helicobacter pylori* glutamate racemase that bind to a cryptic allosteric site, and used these inhibitors to probe the mechanistic and dynamic features of the enzyme. These structural, kinetic and mutational studies provide insight into the physiological regulation of these essential enzymes and provide a basis for designing narrow-spectrum antimicrobial agents.

Peptidoglycan is an essential component of the bacterial cell wall that determines the cell morphology and protects the bacteria from osmotic rupture<sup>1</sup>. A key building block for peptidoglycan in pathogenic bacteria is D-glutamate, which is produced from L-glutamate by glutamate racemase (MurI)<sup>2–5</sup>. Both L- and D-glutamate are vital for the survival of bacteria, and regulation of their relative levels is critical because of the central role of L-glutamate in protein synthesis and metabolism<sup>6</sup>. A regulation mechanism for *Escherichia coli* MurI has been reported<sup>7,8</sup>. We set out to determine whether these observations extend to other species, and assess this enzyme as a target for broad-spectrum or species-specific antibacterial therapy. Remarkably, we found differences in enzyme kinetics, structure, and inhibition characteristics among glutamate racemases isolated from key pathogens. The discovery of potent specific inhibitors of *Helicobacter pylori* that act through inhibition of MurI by a novel allosteric mechanism demonstrates the potential to exploit these differences to identify selective agents.

## Biochemical and structural characterization

MurI enzymes, selected on primary sequence divergence (see Supplementary Fig. S1), revealed significant differences in biophysical properties and steady-state kinetics (Table 1). *E. coli* MurI is monomeric in solution and shows extremely low intrinsic activity in either direction (symmetrical kinetic profile), but catalytic turnover was upregulated over 1,000-fold by UDP-MurNAc-Ala, the product of the preceding enzyme in the peptidoglycan biosynthetic pathway (Table 1)<sup>7,8</sup>. This activation has been proposed as a feedback regulation mechanism for generating sufficient levels of D-glutamate to support cell growth, while maintaining high levels of L-glutamate, a key metabolic intermediate<sup>7–9</sup>. In contrast, *H. pylori* MurI forms a dimer, is unaffected by UDP-MurNAc-Ala and demonstrates a high degree of asymmetry in substrate processing with the Michaelis constant ( $K_M$ ) for D-glutamate approximately tenfold lower than for L-glutamate, and severe substrate inhibition by D-glutamate alone (Table 1). This profile can be attributed to a slow isomerization

step in the catalytic cycle, where substrate inhibition arises through oversaturation<sup>10</sup>, resulting in the lowest catalytic turnover of the MurI proteins studied, while retaining a similar overall catalytic efficiency ( $k_{cat}/K_M \approx 8.5 \times 10^5 \text{ M}^{-1} \text{ min}^{-1}$ ). Physiologically, the asymmetric profile and severe substrate inhibition by D-glutamate provide a different regulatory mechanism to control the D-glutamate levels in *H. pylori*, which are significantly lower than L-glutamate levels (this is true in *E. coli* as well<sup>11</sup>; see Supplementary Methods).

MurI enzymes from the Gram-positive species *Staphylococcus aureus*, *Enterococcus faecalis* and *Enterococcus faecium* share similar biophysical and biochemical characteristics that are distinct from *E. coli* and *H. pylori* MurI. All form homodimers in solution, are unaffected by UDP-MurNAc-Ala, and exhibit high intrinsic catalytic turnover (Table 1). These enzymes display asymmetry in substrate preference with elevated L-glutamate  $K_M$  values, but did not exhibit the severe substrate inhibition by D-glutamate seen for *H. pylori* MurI. As a result, the catalytic activity of these enzymes is not strictly governed; this may be because Gram-positive organisms require more D-glutamate than Gram-negative species because they have a thicker peptidoglycan layer. In addition, some of these organisms contain a D-amino acid transaminase<sup>12,13</sup> and because MurI was shown to be essential in Gram-positive pathogens<sup>14,15</sup>, it is likely that the transaminase is used to salvage excess D-glutamate.

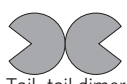
The different kinetic profiles exhibited across the species suggested fundamental structural differences and therefore the MurI enzymes were characterized using X-ray crystallography. Crystal structures were generated for each enzyme under similar, physiologically relevant conditions and almost all of these contained substrates in the active site at full occupancy (Table 1).

The crystal structures of the MurI monomers all shared a conserved topology and fold (see Supplementary Fig. S2) that is comprised of two domains that exhibit a pseudo-symmetry axis (shown for *H. pylori* MurI in Fig. 1a), consistent with the structure recently reported for *Bacillus subtilis* RacE (ref. 16). Catalysis takes place at the interface of the two domains, with each domain contributing

<sup>1</sup>AstraZeneca Global Structural Chemistry, AstraZeneca R&D Mölndal, SE-431 83, Mölndal, Sweden. <sup>2</sup>Infection Discovery, AstraZeneca R&D Boston, Waltham, 02451 Massachusetts, USA.

\*These authors contributed equally to this work.

**Table 1 | Biochemical and structural data of Murl proteins**

Murl protein	Biochemical data				Structural data	
	$K_{M,L/D}$ (μM), $k_{cat,L/D}$ (min <sup>-1</sup> ) and $K_{I_{S,L/D}}$ (μM)	UDP-MurNAc-Ala activation	Oligomerization state	Complex (resolution)	Schematic representation	
<i>H. pylori</i>	$K_{M,L} = 740 \pm 50$ $k_{cat,L} = 63 \pm 1$ $K_{M,D} = 63 \pm 0.4$ $k_{cat,D} = 12 \pm 0.2$ $K_{I_{S,D}} = 5.8 \pm 0.03$		No	Dimer	D-glutamate (1.9 Å); see Fig. 1a D-glutamate + compound A (1.86 Å); see Fig. 3a	 Head-head dimer
<i>H. pylori</i> A75T	$K_{M,L} = 7,430 \pm 840$ $k_{cat,L} = 107 \pm 4$ $K_{M,D} = 275 \pm 38$ $k_{cat,D} = 3.9 \pm 0.3$ $K_{I_{S,D}} = 661 \pm 66$		No	Dimer		
<i>H. pylori</i> E151K	$K_{M,L} = 7,360 \pm 240$ $k_{cat,L} = 136 \pm 2$ $K_{M,D} = 282 \pm 6$ $k_{cat,D} = 5.0 \pm 0.03$ $K_{I_{S,D}} > 100,000$		No	Dimer		
<i>E. coli</i>	$K_{M,L} = 1,200 \pm 140^*$ $k_{cat,L} = 730 \pm 20$	$K_{M,D} = 2,100 \pm 140$ $k_{cat,D} = 2,600 \pm 44$	Yes	Monomer	L-glutamate + UDP-MurNAc-Ala (1.9 Å); see Fig. 1c	 Activator-modulated monomer
<i>E. faecalis</i>	$K_{M,L} = 1,200 \pm 12$ $k_{cat,L} = 1,500 \pm 40$	$K_{M,D} = 250 \pm 20$ $k_{cat,D} = 704 \pm 14$	No	Dimer	D-glutamate (1.95 Å)	 Tail-tail dimer
					D-glutamate + L-glutamate (2.5 Å); see Fig. 1d	 Mixed forms dimer
<i>E. faecium</i>	$K_{M,L} = 1,100 \pm 100$ $k_{cat,L} = 2,200 \pm 50$	$K_{M,D} = 240 \pm 23$ $k_{cat,D} = 900 \pm 32$	No	Dimer	Phosphate (1.8 Å)	Tail-tail dimer
<i>S. aureus</i>	$K_{M,L} = 4,600 \pm 270$ $k_{cat,L} = 510 \pm 90$	$K_{M,D} = 140 \pm 10$ $k_{cat,D} = 34 \pm 3$	No	Dimer	D-glutamate (2.15 Å)	Tail-tail dimer

The solution oligomerization state was determined using equilibrium analytical ultracentrifugation methods at concentrations ranging from 5 to 50 μM protein. Additional structural information is available in the Supplementary Methods and Tables. Data represent the mean ± s.d. from nonlinear regressions fitting to the data ( $n \geq 10$  velocity data points) using the Michaelis–Menten equation or the substrate-inhibition model equation.  $K_{I_{S,D}}$  is the substrate inhibition constant (see Supplementary Methods).

\* The data for *E. coli* Murl were obtained in the presence of 400 μM UDP-MurNAc-Ala (fully activated).

the residues attributed to the enantiomeric deprotonations<sup>17</sup>. The domain that begins with the amino terminus (domain A) contains the conserved amino acids involved in deprotonation of D-glutamate (D7, S8, C70, T72), whereas the carboxy-terminal domain (domain B) contains the catalytic residues involved in L-glutamate deprotonation (E150, C181, T182, H183) (see Supplementary Fig. S3). Using domain A as an anchor, it is possible to overlay the monomers from the Murl structures. From this alignment, it is apparent that the two domains move with respect to each other and this movement is largely restricted to a rotation around a single axis, as illustrated for the *E. faecalis* structures (Fig. 1b). This hinge movement occurs at the two crossovers between the domains (rotation at a conserved glycine—G 91 for the *H. pylori* structure—and kinking of a helix mainly mapping into domain A) and a coordinated hinge movement is required to form the active site and permit catalysis.

The observed hinge movement of Murl is not only critical for catalytic function, but also adapts activity to meet physiological demands. The three distinct regulatory mechanisms that were differentiated by biochemical studies can be rationalized through detailed analyses of the Murl structures. *E. coli* Murl co-crystallized as a monomer with both L-glutamate and its activator UDP-MurNAc-Ala. The activator binds in the hinge region on the side opposite to the catalytically active site (Fig. 1c) through contacts between the uracil ring system and domain B and through specific salt bridge interactions with R104 in domain A and the alanyl moiety of the activator (see Supplementary Fig. S4), consistent with the strict requirement of the alanine and uracil moieties for activation<sup>7</sup>. These interactions are predicted to focus the hinge movement and to favour productive substrate binding, leading to higher catalytic efficiency in response to cellwall biosynthesis demand.

In contrast, *S. aureus*, *E. faecalis* and *E. faecium* all form homodimeric structures (exemplified by *E. faecalis* in Fig. 1d), similar to that observed for *B. subtilis* RacE (ref. 16) and consistent with solution studies on these enzymes (Table 1). In all these structures, the

monomers oligomerize in a tail-to-tail orientation with active sites opposed and fully exposed to solvent. Oligomerization occurs through interactions across a C2 symmetry axis, mainly involving helices from the A and B domains of each monomer, to create an interface that is conserved in all of the Gram-positive Murl proteins structurally characterized so far. The flexibility of this interaction is nicely illustrated in the *E. faecalis* structure containing L- and D-glutamate, providing some insight into the conformational changes required for catalysis (Fig. 1b). An even wider range of hinge movements could be observed in *E. faecium* enzyme while it interacts with various salts, indicating that the hinge movement adapts to molecules binding in the active site (see Supplementary Methods). In contrast to the Gram-positive Murl structures, the *H. pylori* Murl enzyme also forms a homodimer but with the active sites in close proximity in a face-to-face orientation, shielded from the solvent (Fig. 1a) in a manner that is distinct from, but similar to, the structure of *Aquifex pyrophilus* Murl (ref. 18).

A similar interaction is observed in the asymmetric unit of the structure reported for *B. subtilis*; however, significant differences exist between the *H. pylori* and the *B. subtilis* structures in this dimer interface (see Supplementary Table S9 and Figs S11–S14), which indicates that whereas the *H. pylori* dimer interface is biologically relevant, the *B. subtilis* AB interface probably results from crystal packing interactions, as noted in ref. 16. To ensure that this dimer interface was not just a crystal packing interaction, two independent structure determinations of the native *H. pylori* enzyme were carried out using crystals grown under different crystallization conditions and crystallographic space groups (see Supplementary Table S4). Comparative analysis of these two crystals forms demonstrated that the dimer interface was fully conserved, but each crystal form had its own unique set of packing interactions. No other dimer interactions were observed in any of the investigated crystal forms.

The *H. pylori* Murl structure contained only D-glutamate in the active site, despite growing the crystals in the presence of saturating

concentrations of racemic glutamate. This finding is consistent with the asymmetric, D-glutamate-inhibited kinetic profile of the enzyme and the structure most probably represents the substrate-inhibited, resting state of the enzyme. This arrangement suggests that the enzyme has evolved to stabilize the closed, glutamate-bound state to reduce overall catalytic turnover. Although dimerization occurs through inter-monomer interactions between both A and B domains, the B-domain interactions possess the majority of dimerization contacts. Logically, during hinge-movement transition between closed and open states, it is the A-domain interface that is predicted to separate to allow glutamate to enter and leave, whereas the B-domain interface is maintained. This hypothesis is supported by analysis of the nuclear magnetic resonance (NMR) titrations with glutamate, which indicate that domain A is more dynamic (see Supplementary Figs S6–S8).

### Selective inhibition mechanism

The structural and biochemical data clearly demonstrate distinguishing features among the MurI isozymes, and we envisioned that these differences could be exploited to identify selective inhibitors of *H. pylori* MurI. A high-throughput screen against the AstraZeneca compound collection (385,861 compounds) identified a pyrazolo-pyrimidinedione analogue (compound A; see structure in Fig. 2a) among the hit clusters. We chose compound A for further study because it had excellent potential for structural diversification. This compound demonstrated inhibition of the isolated enzyme and the enzyme in intact *H. pylori* cells (see Supplementary Methods), along

with excellent selectivity for *H. pylori* MurI. Inhibition by compound A had the hallmarks of stoichiometric, specific inhibition<sup>19,20</sup>: it was time-independent, fully reversible and insensitive to changes in enzyme or detergent concentration. The lack of structural similarity to glutamate prompted a detailed biochemical analysis of the mode of inhibition. Remarkably, kinetic inhibition studies indicated that compound A does not compete with glutamate and that glutamate binding was required for inhibition (Fig. 2b).

This uncompetitive inhibition mechanism is exceedingly rare for single-substrate enzymes<sup>21</sup>. Despite this precedent, all of the biochemically confirmed hits from the screen had this mode of inhibition (about ten series); no inhibitors were identified that were competitive with the substrate. Protein NMR using <sup>2</sup>H and <sup>15</sup>N isotopically labelled *H. pylori* MurI was carried out, and in the absence of glutamate, two-dimensional transverse relaxation-optimized spectroscopy (TROSY) indicated that the protein was quite flexible, assuming multiple conformations. However, addition of glutamate generated a highly resolved NMR spectrum and allowed full backbone resonance assignments (Fig. 2c, see Supplementary Methods and Figs S6–S8). Subsequent addition of compound A to the substrate-saturated enzyme caused significant peak shifts, indicating compound binding (Fig. 2c). In contrast, adding compound A to the substrate-free enzyme had no marked effect on its poorly resolved spectrum, indicating that compound A binds preferably to the substrate-bound form of the enzyme. These results were further supported by direct binding measurements using isothermal titration

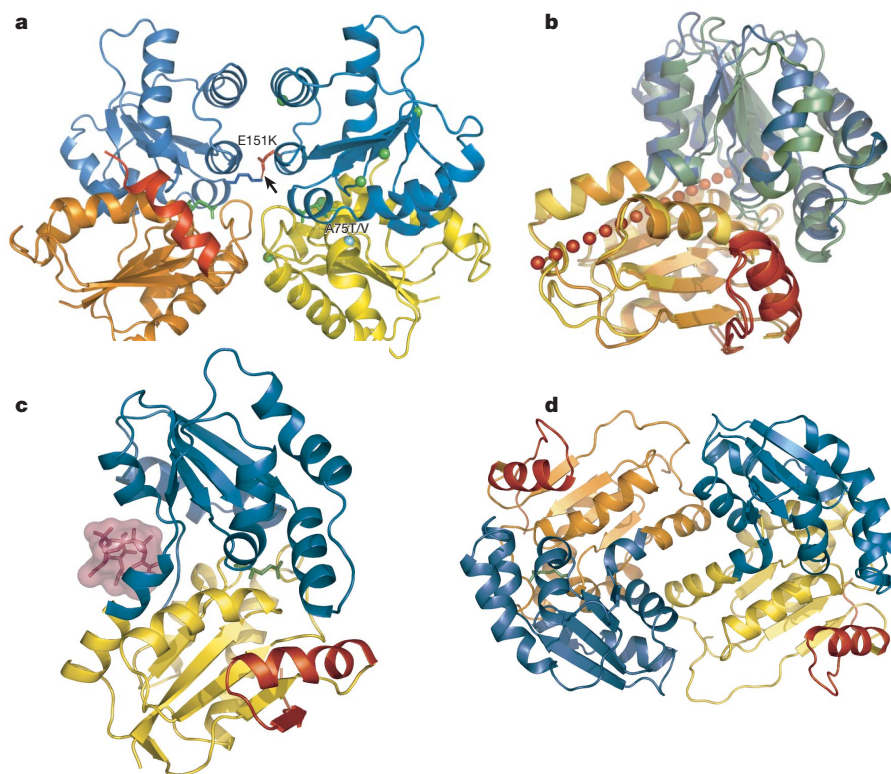


**Figure 1 | Crystal structures of MurI proteins.** **a**, Crystal structure of *H. pylori* MurI dimer containing D-glutamate (green) with monomer domains A (N-terminal domain; yellow/orange) and B (C-terminal domain; blue) and the C-terminal helix (red) in the left monomer highlighted. Resistance mutation sites A75T/V (cyan), E151K (red), A35T, C162Y, I178T, G180S, L186F, L206P, Q248R (all in green) and a putative intermonomer salt bridge contact between E151 & K117<sup>2</sup> (arrow) are shown. **b**, Overlay of MurI monomers (based on domain A) from *E. faecalis*/L-glutamate (blue) and *E. faecalis*/D-glutamate (green). Domain A is indicated in light colours. Glutamate substrates are shown. The hinge axis is shown as a line of red spheres. **c**, Crystal structure of *E. coli* MurI containing L-glutamate (green)

and the activator UDP-MurNAc-Ala (pink,  $2F_O - F_C$  electron density map contoured at  $1\sigma$ ) with monomer domains A (yellow) and B (blue). The C-terminal helix and the 12-amino-acid C-terminal extension (relative to *H. pylori* sequence) are in red. The orientation is equivalent to the left monomer of *H. pylori* MurI in **a**. **d**, Crystal structure of *E. faecalis* MurI containing L- (right monomer) and D-glutamate (left monomer), showing monomer domains A (yellow/orange) and B (blue); the C-terminal helix and extension (relative to *H. pylori* sequence) are highlighted in red. The orientation of the right monomer is equivalent to the left monomer in *H. pylori* MurI in **a**.

calorimetry and by protein fluorescence quenching on compound titration, for which in each case saturating levels of glutamate were required for compound binding (see Supplementary Methods and Fig. S5).

Crystals of *H. pylori* MurI containing D-glutamate and compound A were produced and a high-resolution structure was solved for this enzyme–substrate–inhibitor complex. The inhibitor bound in a cryptic pocket formed by a dislocation of the C-terminal helix (Fig. 3a). To our knowledge, this is the only example of an uncompetitive inhibitor of a single-substrate enzyme in which the inhibitor binds at a cryptic allosteric site<sup>22</sup>, and it highlights the power of

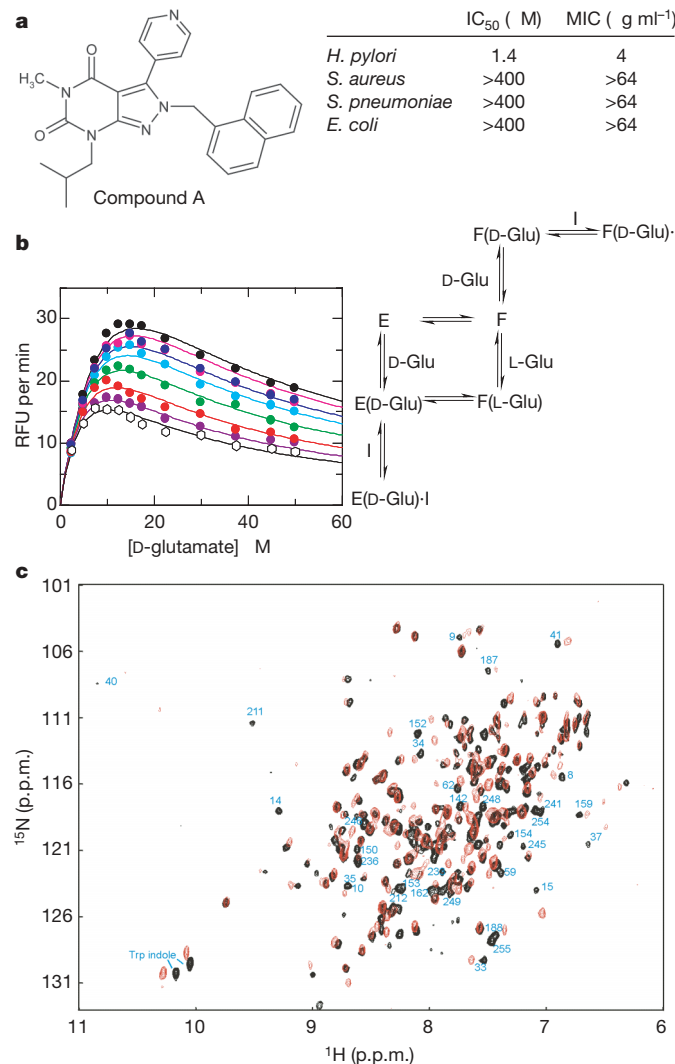


**Figure 2 | Inhibitor characterization.** **a**, Structure of the pyrazolopyrimidinedione inhibitor with *in vitro* activities. IC<sub>50</sub>, half-maximal inhibitory concentration. MIC, minimal inhibitory concentration to prevent bacterial growth. **b**, Kinetic mechanism of inhibition data and scheme for *H. pylori* MurI. Kinetic data of enzymatic turnover inhibition were collected, simultaneously varying D-glutamate (2.5–50  $\mu$ M) and compound A (0  $\mu$ M (black symbols) to 3.5  $\mu$ M (white open symbols), serial dilutions), and globally fitted to several models incorporating substrate inhibition. The best fit was found for the scheme shown, with inhibitor (I) binding to both the productive enzymes:substrate complex (E(D-Glu)) and the substrate-inhibited form of the enzyme (F(D-Glu)). RFU, relative fluorescence units. **c**, Two-dimensional TROSY <sup>1</sup>H, <sup>15</sup>N NMR spectrum of 0.3 mM *H. pylori* MurI with 1.8 mM D-glutamate (black) and with 1.8 mM D-glutamate and 0.4 mM compound A (red). Spectral differences indicate compound binding. Backbone peak assignments to selected amino acids are indicated by residue primary sequence number. Tryptophan indole ring resonances are denoted for clarity.

high-throughput screening to find enzyme inhibitors serendipitously. As in other examples of allosteric inhibitor binding<sup>23–26</sup>, the enzyme–substrate–inhibitor structure is highly similar to the native structure, with minimal differences from the native structure for regions outside the compound-binding site (root-mean-square deviation 0.718 Å for 488 C $\alpha$  atoms in the dimer). However, in contrast to the precedents of allosteric inhibition, in which inhibitor binding initiates a cascade of residue movements that alters the active site, no changes were observed in the *H. pylori* MurI active site on inhibitor binding.

Comparison of the enzyme–substrate–inhibitor and native *H. pylori* MurI structures demonstrated that the inhibitor-binding site does not exist in the native structure because it is fully occupied by residues of the C-terminal helix (Fig. 3b), and formation of this site could not be predicted from the native structure by computational

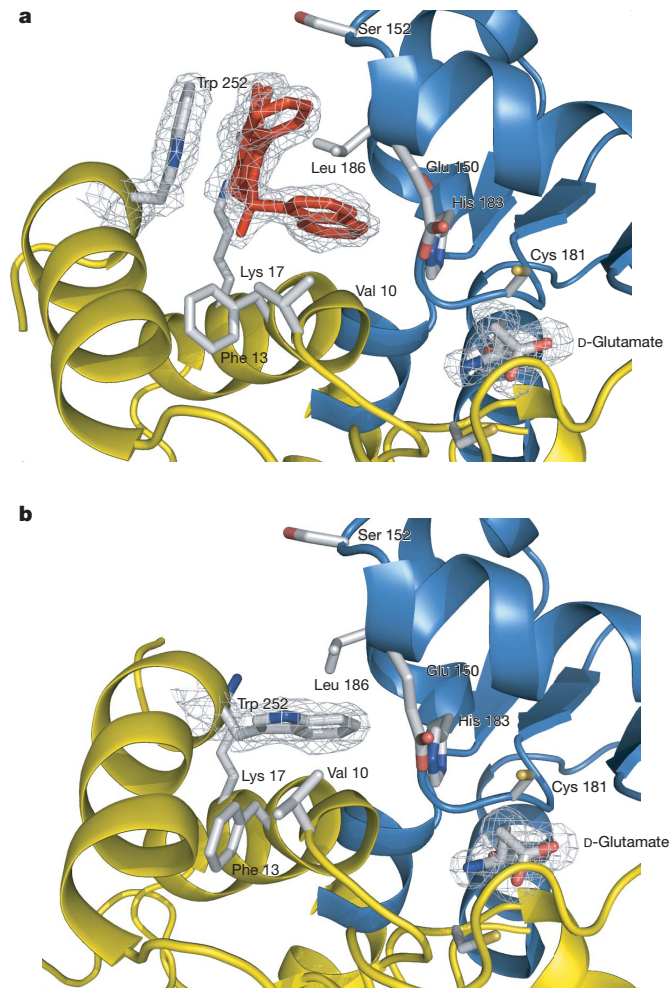


**Figure 3 | Inhibitor-binding site in *H. pylori* MurI.** **a**, Detailed view of compound binding site of the enzyme–substrate–inhibitor complex of *H. pylori* MurI and compound A. On compound binding, the C-terminal helix movement induces W252 side-chain displacement and rotation to form a surface for  $\pi$ -stacking with the pyrazolopyrimidinedione core of the inhibitor. The pocket vacated by the indole ring movement is filled with the naphthyl moiety of compound A and further stabilized by interactions with V10, G11 (not shown), H183, L186, and W244 (not shown). Additional interactions are formed between the isobutyl substituent of compound A and the F13, S14 (not shown), K17, L253 (not shown) residues, while the pyridyl ring substituent makes contacts with the main-chain atoms of residues E150 and S152. The N-methyl substituent resides in a large cleft that is accessible to solvent. Electron density map for compound A, the substrate and W244 are shown (2F<sub>O</sub>–F<sub>C</sub> electron density map contoured at 1 $\sigma$ ). **b**, Detailed view of compound binding site in the native *H. pylori* MurI structure. Colour scheme and key residues annotated as described for Fig. 1a.

methods. For example, none of the residues affected by compound binding adopted unfavourable dihedral angles (considered markers of allosteric sites) in the native enzyme structure<sup>22</sup>. On compound binding, the C-terminal helix movement induces W252 side-chain displacement and rotation to form a surface for  $\pi$ -stacking with the pyrazolopyrimidinedione core of the inhibitor. The pocket vacated by the movement of the indole ring is filled with the naphthyl moiety of compound A and further stabilized by additional interactions (Fig. 3a). The crystal structure is consistent with the solution NMR analyses as the inhibitor-binding site residues exhibited strong spectral shifts on compound titration (see Supplementary Methods). Taken together, these data suggest that the compound binds to a conformation that is dependent on the substrate-bound state and results in further stabilization of a closed form of the enzyme, which precludes movement of the A domains to expose the active site and allow release of product.

A comparison of the *H. pylori* structure bound with compound A and other MurI structures revealed the basis for selectivity. In *E. coli* many of the key residues in the corresponding pyrazolopyrimidinedione-binding region of the *H. pylori* enzyme, which is distinct from the UDP-MurNAc-Ala-binding and active sites, are not conserved, including the critical W252 (see Supplementary Fig. S9). Further, the *E. coli* C-terminal helix has a 12-residue extension that folds back and forms part of the  $\beta$ -sheet core of domain A (Fig. 1c). This extension presumably restricts movement of the C-terminal helix and prevents pocket formation. Inspection of the corresponding inhibitor-binding regions of the Gram-positive MurI structures revealed significant variation in geometries, even though many of the binding site residues were conserved (see Supplementary Fig. S9). In addition, like the *E. coli* structure, all of these structures contain a C-terminal extension that forms additional interactions with the core of domain A; these interactions are likely to restrict movement of the C-terminal helix that is required for inhibitor binding site formation (Fig. 1d).

### Potential resistance mechanism

Sequence analyses of diverse, clinically relevant *H. pylori* isolates showed that almost all of the interacting residues in this binding pocket were conserved in this species (see Supplementary Fig. S10), demonstrating the suitability of the site for inhibition of *H. pylori* MurI and indicating the importance of maintaining these residues. To assess the mutability of the binding pocket, an inhibitor with optimized potency was used to obtain resistant mutants (see Supplementary Methods). Mutants were not easily obtained because resistance rates using single-step selection methods were low.

The sequence analyses of those mutants that were obtained demonstrated that single amino acid changes distributed throughout the primary sequence of MurI generated the resistant phenotype. Only one of the mutations (L186F) was found in the inhibitor-binding pocket, indicating that mutations in this binding site are not well tolerated. The immutability of the allosteric compound-binding pocket is probably due to the critical role this site has in the hinge movement of the enzyme. All other mutations were located either at the dimer or domain interfaces, or within the core of domain B (Fig. 1a). In an effort to deconvolute the mechanism of resistance, two resistant mutant proteins, A75T and E151K, were purified and biochemically characterized.

Despite the fact that these mutations are not located within the active site of the enzyme, dramatic effects were observed in the kinetic profiles (Table 1). In both cases, increased substrate  $K_M$  values were observed along with compensatory changes in  $k_{cat}$  and the severe D-glutamate substrate inhibition observed with wild-type MurI was significantly reduced or absent. Further, the resistant mutant proteins had lower melting temperatures relative to the wild-type protein in the absence of substrate, but equivalent thermal stability in the presence of saturating substrate (see Supplementary Methods). These changes in kinetic and biophysical profile are expected to reduce the overall population of substrate-bound form of the enzyme under

physiological conditions, and thus the population of MurI to which these uncompetitive inhibitors bind (Fig. 2b). Although it is difficult to provide an easily validated structural rationalization for the A75T mutant, E151 does form an inter-monomer salt-bridge interaction with K117 in the native enzyme structure (Fig. 1a). This salt-bridge interaction helps stabilize the closed, substrate-bound form of the enzyme and the E151K mutation results in a repulsive interaction that disfavours substrate binding. Despite these changes, saturation of the enzyme *in vitro* with substrate overcomes this resistance mechanism, and the wild-type inhibitor affinity that was observed under saturating substrate conditions is consistent with this (see Supplementary Methods). The reduction of substrate-bound enzyme populations by decreasing substrate affinity while maintaining activity is a logical and ingenious solution to overcoming an uncompetitive inhibitor.

### Prospects for inhibitor development

These structural, biophysical and enzyme kinetic studies have identified at least three distinguishable types of MurI: (1) monomeric enzymes modulated by allosteric activation by metabolic precursors; (2) head-to-head dimers regulated through substrate inhibition; and (3) tail-to-tail dimers with high intrinsic turnover that rely on D-glutamate recycling using a D-amino-acid transaminase for cellular glutamate pool-level regulation. The pyrazolopyrimidinedione series faces several further hurdles in the progression to clinical treatment of *H. pylori* infections, particularly in the areas of serum protein binding and metabolism, but nevertheless this series demonstrates the potential to exploit the differences across MurI proteins to discover selective inhibitors with potent cellular activity.

### METHODS

See Supplementary Information for experimental details.

**Enzyme preparation and biochemical characterization.** Full-length MurI proteins were prepared by expression either as native (*H. pylori*, *E. coli*) or N-terminal 6His-tagged (*S. aureus*, *E. faecalis*, *E. faecium*) recombinant proteins in *E. coli* strains co-expressing the chaperone proteins GroEL/GroES<sup>27</sup> and purified using standard chromatographic methods. Enzyme activity was assayed by measuring the conversion of glutamate from D- to L-enantiomer using a coupled assay system monitoring the reduction of NAD<sup>+</sup> to NADH by L-glutamate dehydrogenase. MurI activity in the L-to-D direction was coupled to MurD (UDP-MurNAc-Ala:D-glutamate ligase) and measured as a function of phosphate production using 2-amino-6-mercaptopurine ribonucleoside and purine nucleoside phosphorylase (see Supplementary Methods). The protein oligomeric state was assessed using size exclusion chromatography with multi-angle light scattering detection and equilibrium or velocity sedimentation on a Beckman Optima XL-I Analytical ultracentrifuge over a range of enzyme concentrations.

**Structural and conformational studies.** Details on the crystallization conditions and refinement statistics for all protein structures can be found in Supplementary Tables S3–S8. NMR experiments were performed on *H. pylori* MurI (0.3 mM, pH 7.5) at 303 K on a Bruker Avance 800 MHz system, equipped with a triple-resonance (<sup>1</sup>H/<sup>13</sup>C/<sup>15</sup>N) single-gradient 5 mm probe. Details of the procedures used for backbone assignments can be found in the Supplementary Methods. <sup>[15</sup>N, <sup>1</sup>H] correlation experiments were recorded to assess protein stability with increasing D-glutamate concentration and to map the binding site of compound A. Residues with sufficient resolution for mapping exhibiting backbone trace resonance shifts of two or more linewidths were considered significant.

Received 4 April 2006; accepted 14 February 2007.

1. van Heijenoort, J. Recent advances in the formation of the bacterial peptidoglycan monomer unit. *Nat. Prod. Rep.* 18, 503–519 (2001).
2. Tanner, M. E. & Miao, S. The synthesis and stability of aziridino-glutamate, an irreversible inhibitor of glutamate racemase. *Tetrahedr. Lett.* 35, 4073–4076 (1994).
3. Ashiuchi, M., Yoshimura, T., Esaki, N., Ueno, H. & Soda, K. Inactivation of glutamate racemase of *Pediococcus pentosaceus* with L-serine O-sulfate. *Biosci. Biotechnol. Biochem.* 57, 1978–1979 (1993).
4. de Dios, A. *et al.* 4-Substituted D-glutamic acid analogues: The first potent inhibitors of glutamate racemase (MurI) enzyme with antibacterial activity. *J. Med. Chem.* 45, 4559–4570 (2002).

5. Glavas, S. & Tanner, M. E. The inhibition of glutamate racemase by D-N-hydroxyglutamate. *Bioorg. Med. Chem. Lett.* **7**, 2265–2270 (1997).
6. Newsholme, P., Procopio, J., Lima, M. M. R., Pithon-Curi, T. C. & Curi, R. Glutamine and glutamate—their central role in cell metabolism and function. *Cell Biochem. Funct.* **21**, 1–9 (2003).
7. Doublet, P., van Heijenoort, J. & Mengin-Lecreulx, D. The glutamate racemase activity from *Escherichia coli* is regulated by peptidoglycan precursor UDP-N-acetylglucosamyl-L-alanine. *Biochemistry* **33**, 5285–5290 (1994).
8. Ho, H.-T. et al. UDP-N-acetylglucosamyl-L-alanine functions as an activator in the regulation of the *Escherichia coli* glutamate racemase activity. *Biochemistry* **34**, 2464–2470 (1995).
9. Doublet, P., van Heijenoort, J. & Mengin-Lecreulx, D. Regulation of the glutamate racemase of *Escherichia coli* investigated by site-directed mutagenesis. *Microb. Drug Resist. Mechanisms Epidemiol. Dis.* **2**, 43–49 (1996).
10. Fisher, L. M., Albery, W. J. & Knowles, J. R. Energetics of proline racemase: racemization of unlabeled proline in the unsaturated, saturated, and oversaturated regimes. *Biochemistry* **25**, 2529–2537 (1986).
11. Mengin-Lecreulx, D., Flouret, B. & van Heijenoort, J. Cytoplasmic steps of peptidoglycan synthesis in *Escherichia coli*. *J. Bacteriol.* **151**, 1109–1117 (1982).
12. Fotheringham, I. G., Bledig, S. A. & Taylor, P. P. Characterization of the genes encoding D-amino acid transaminase and glutamate racemase, two D-glutamate biosynthetic enzymes of *Bacillus sphaericus* ATCC 10208. *J. Bacteriol.* **180**, 4319–4323 (1998).
13. Pucci, M. J., Thanassi, J. A., Ho, H. T., Falk, P. J. & Dougherty, T. J. *Staphylococcus haemolyticus* contains two D-glutamic acid biosynthetic activities, a glutamate racemase and a D-amino acid transaminase. *J. Bacteriol.* **177**, 336–342 (1995).
14. Song, J. H. et al. Identification of essential genes in *Streptococcus pneumoniae* by allelic replacement mutagenesis. *Mol. Cells* **19**, 365–374 (2005).
15. Wang, L. & Zamudio, C. A method for predicting operons in prokaryotes. US patent number US2005/0026189A1 (2005).
16. Ruzheinikov, S. N. et al. Substrate-induced conformational changes in *Bacillus subtilis* glutamate racemase and their implications for drug discovery. *Structure* **13**, 1707–1713 (2005).
17. Glavas, S. & Tanner, M. E. Active site residues of glutamate racemase. *Biochemistry* **40**, 6199–6204 (2001).
18. Hwang, K. Y. et al. Structure and mechanism of glutamate racemase from *Aquifex pyrophilus*. *Nature Struct. Biol.* **6**, 422–426 (1999).
19. McGovern, S. L., Helfand, B. T., Feng, B. & Shoichet, B. K. A specific mechanism of nonspecific inhibition. *J. Med. Chem.* **46**, 4265–4272 (2003).
20. Seidler, J., McGovern, S. L., Doman, T. N. & Shoichet, B. K. Identification and prediction of promiscuous aggregating inhibitors among known drugs. *J. Med. Chem.* **46**, 4477–4486 (2003).
21. Ghosh, N. K. & Fishman, W. H. On the mechanism of inhibition of intestinal alkaline phosphatase by L-phenylalanine. *J. Biol. Chem.* **241**, 2516–2522 (1966).
22. Hardy, J. A. & Wells, J. A. Searching for new allosteric sites in enzymes. *Curr. Opin. Struct. Biol.* **14**, 706–715 (2004).
23. Wiesmann, C. et al. Allosteric inhibition of protein tyrosine phosphatase 1B. *Nature Struct. Mol. Biol.* **11**, 730–737 (2004).
24. Pargellis, C. et al. Inhibition of p38 MAP kinase by utilizing a novel allosteric binding site. *Nature Struct. Biol.* **9**, 268–272 (2002).
25. Oikonomakos, N. G., Skamnaki, V. T., Tsitsanou, K. E., Gavalas, N. G. & Johnson, L. N. A new allosteric site in glycogen phosphorylase b as a target for drug interactions. *Struct. Fold. Des.* **8**, 575–584 (2000).
26. Hardy, J. A., Lam, J., Nguyen, J. T., O'Brien, T. & Wells, J. A. Discovery of an allosteric site in the caspases. *Proc. Natl. Acad. Sci. USA* **101**, 12461–12466 (2004).
27. Anderson, M. et al. Crystals of Murl from Gram negative, Gram positive, and atypical bacterium; computer-assisted method for screening, identifying, and designing inhibitors of Murl; inhibitors of Murl; and uses thereof. US patent number US2005/0037478 A1 (2005).

**Supplementary Information** is linked to the online version of the paper at [www.nature.com/nature](http://www.nature.com/nature).

**Acknowledgements** We thank M. Gowravaram for compound synthesis and characterization, and all members of the Murl Team and collaborators across AstraZeneca for support of this work.

**Author Contributions** S.L.F. and T.L. contributed equally to this work. S.L.F., G.K., D.T.N. and T.A.K. performed the protein biochemical and kinetic characterizations, Y.X. solved the *H. pylori* Murl Native I structure and T.L. solved all other protein structures. R.H.A.F. performed the NMR studies, R.A.A. performed the phylogenetic, genomic and sequence analyses and B.L.M.D.J. performed the microbial physiology analyses. All authors discussed the results, contributed and commented on the manuscript.

**Author Information** The atomic coordinates of the protein structures have been deposited in the European Bioinformatics Institute Macromolecular Structure Database: *H. pylori* Murl complexed with D-glutamate (Native I, accession code 2jfx; Native II, accession code 2jfy); *H. pylori* complex with D-glutamate and compound A, accession code 2jfz; *E. coli* Murl complexed with L-glutamate and UDP-MurNAc-Ala, accession code 2jfn; *S. aureus* Murl complexed with D-glutamate, accession code 2jqf; *E. faecalis* Murl complexed with D- or L-glutamate, accession code 2jfo; *E. faecalis* Murl complexed with D-glutamate, accession code 2jfp; *E. faecium* Murl complexed with phosphate, accession code 2jfu; *E. faecium* Murl complexed with citrate, accession code 2jfv; *E. faecium* Murl complexed with tartrate, accession code 2jfw. Reprints and permissions information is available at [www.nature.com/reprints](http://www.nature.com/reprints). The authors declare no competing financial interests. Correspondence and requests for materials should be addressed to S.L.F. (stewart.fisher@astrazeneca.com).

## ARTICLES

# MicroRNA silencing through RISC recruitment of eIF6

Thimmaiah P. Chendrimada<sup>1</sup>, Kenneth J. Finn<sup>3</sup>, Xinjun Ji<sup>2</sup>, David Baillat<sup>1†</sup>, Richard I. Gregory<sup>1</sup>, Stephen A. Liebhaber<sup>2</sup>, Amy E. Pasquinelli<sup>3</sup> & Ramin Shiekhattar<sup>1†</sup>

**MicroRNAs (miRNAs) are a class of small RNAs that act post-transcriptionally to regulate messenger RNA stability and translation. To elucidate how miRNAs mediate their repressive effects, we performed biochemical and functional assays to identify new factors in the miRNA pathway. Here we show that human RISC (RNA-induced silencing complex) associates with a multiprotein complex containing MOV10—which is the homologue of *Drosophila* translational repressor Armitage—and proteins of the 60S ribosome subunit. Notably, this complex contains the anti-association factor eIF6 (also called ITGB4BP or p27BBP), a ribosome inhibitory protein known to prevent productive assembly of the 80S ribosome. Depletion of eIF6 in human cells specifically abrogates miRNA-mediated regulation of target protein and mRNA levels. Similarly, depletion of eIF6 in *Caenorhabditis elegans* diminishes lin-4 miRNA-mediated repression of the endogenous LIN-14 and LIN-28 target protein and mRNA levels. These results uncover an evolutionarily conserved function of the ribosome anti-association factor eIF6 in miRNA-mediated post-transcriptional silencing.**

MicroRNAs function as ~22-nucleotide RNAs that negatively regulate target gene expression at the post-transcriptional level<sup>1</sup>. Although we recently described a minimal human RISC as a complex of Dicer, TRBP (also called TARBP2) and argonaute 2 (AGO2; also called EIF2C2) proteins that mediates miRNA-targeted RNA cleavage<sup>2</sup>, the repressive mechanism exerted by miRNAs that partially base pair to target sequences remains to be elucidated. In some cases, miRNAs appear primarily to inhibit translation but in others they seem to promote significant degradation of their mRNA targets<sup>3</sup>. The identification of specific factors required for miRNA function may help to resolve the many divergent mechanistic models in this new field.

In animals, miRNAs are usually not fully complementary to their targets, and therefore, they repress target gene expression by a mechanism that is independent of argonaute-mediated mRNA cleavage<sup>4</sup>. To uncover factors that function with miRNAs to regulate target mRNA expression, we isolated a large TRBP-containing complex that includes the human homologue of *Drosophila* Armitage<sup>5,6</sup> and the 60S subunit of the ribosome. Notably, this complex also contains the anti-association factor eIF6 (RefSeq NM\_002212), which is known to bind the 60S subunit and prevent the productive assembly of 80S ribosomes<sup>7–10</sup>.

## eIF6 is a component of a large TRBP-containing complex

Previously we identified an ~500-kDa complex comprised of Dicer–TRBP–AGO2 that could mediate RNA cleavage triggered by a miRNA that is fully complementary to its mRNA target<sup>2,11</sup>. During isolation of the minimal Dicer–TRBP–AGO2 complex using Flag-tagged TRBP-containing stable cell lines, we noticed a larger TRBP-containing complex with an apparent mass of ~2 MDa (Fig. 1a). The fraction eluting at 2 MDa was concentrated and subjected to SDS–polyacrylamide gel electrophoresis (SDS-PAGE) followed by colloidal blue staining (Supplementary Fig. 1a). Individual polypeptides were excised from the gel, and 39 specific TRBP-associated polypeptides were identified

in two independent mass spectrometric sequencing analyses (Supplementary Table 1). In addition to RISC subunits, we obtained protein sequences corresponding to nearly all subunits of the large (60S) ribosomal particle. In contrast, subunits from the small (40S) ribosomal particle and pre-ribosomal factors were not detected. Notably, we identified eIF6 as a TRBP-associated polypeptide<sup>12</sup>. eIF6 is a 60S ribosome-associated factor that prevents the assembly of a translationally competent (80S) ribosome<sup>7–10</sup>. We also obtained sequences for the RNA helicase MOV10 (NM\_020963), the human orthologue of the *Drosophila* protein Armitage<sup>5,6,13</sup>.

We next fractionated the Flag-affinity eluate by gel filtration (Fig. 1a, b). This analysis revealed the presence of two distinct complexes: a high-molecular-mass complex composed of most TRBP-associated polypeptides (fractions 16–18), and a smaller ~500-kDa complex, previously identified as RISC (fractions 26–28). Western blotting demonstrated that MOV10, the 60S ribosomal subunit (RPL7A, NM\_000972) and eIF6 associated with a fraction of Dicer, TRBP and AGO2 proteins in a large complex peaking in fraction 16 (Fig. 1b and Supplementary Fig. 1b).

To confirm the association of 60S ribosomal proteins and eIF6 with RISC, we purified RISC using stable cell lines expressing Flag–Dicer. The affinity matrix was washed with increasing salt concentrations (Supplementary Fig. 2a). Consistent with previous reports<sup>2,11</sup>, whereas the association of TRBP with Dicer persists after 500 mM a KCl wash, MOV10, RPL7A and eIF6 display decreased affinities for RISC as the salt concentration is increased (Supplementary Fig. 2a). To extend these results, we generated H1299-derived stable cell lines expressing Flag–eIF6. Western blot analysis of Flag–eIF6 affinity eluate demonstrated the association of RISC and 60S ribosome subunits with eIF6 (Supplementary Fig. 2b). We next analysed the eIF6 affinity eluate by northern blot analysis for the presence of miRNA using probes to miR-23b, an abundant miRNA in H1299 cells. This analysis revealed the specific association of miR-23b with eIF6 affinity eluate as well as affinity eluates corresponding to Flag–Dicer, Flag–TRBP and

<sup>1</sup>The Wistar Institute, 3601 Spruce Street, and <sup>2</sup>Department of Genetics and Medicine, University of Pennsylvania School of Medicine, Philadelphia, Pennsylvania 19104, USA.

<sup>3</sup>Department of Biology, University of California, San Diego, La Jolla, California 92093-0349, USA. <sup>†</sup>Present address: Center de Regulacio Genomica Dr. Aiguader, 88 08003 Barcelona, Spain.

Flag–Ago2 (Supplementary Fig. 2c, d). These results indicate that minimal RISC (Dicer–TRBP–AGO2) can form a larger complex with MOV10 and core proteins of the 60S ribosome as well as the regulatory factor eIF6.

### eIF6 mediates miRNA silencing in human cells

Our identification of eIF6 as a RISC-associated polypeptide suggests a role for this factor in miRNA-mediated target repression. Reporter constructs expressing *Renilla* luciferase mRNAs containing either one or two binding sites for let-7b (also called MIRNALET7B, RefSeq NT\_011523; ref. 14) (Fig. 1c) displayed decreased luciferase activity compared with that of a mutant construct after transfection into HeLa cells (Fig. 1d). Treatment of cells with 2'-O-methyl single-stranded RNA (let-7b as) complementary to let-7b miRNA completely abrogated let-7b-mediated translational repression (Fig. 1e). To assess the role of eIF6 in mediating post-transcriptional silencing, we depleted eIF6 levels by nearly 80% using small interfering (si)RNAs (Supplementary Figs 2e and 3a). Notably, knockdown of *eIF6* by siRNAs specifically and markedly relieved let-7b-mediated repression of the *Renilla* luciferase reporter, whereas the mutant construct was unaffected (Fig. 1e, f, and Supplementary Fig. 3b). Depletion of *MOV10* similarly diminished let-7b-mediated repression of the regulated reporter gene (Supplementary Fig. 3c).

We next assessed the effect of eIF6 depletion on miRNA-mediated regulation of a firefly luciferase reporter fused to the 2.7-kilobase (kb) 3' untranslated region (UTR) of human *LIN28* (NM\_024674; homologue of *C. elegans lin-28*) (Supplementary Fig. 4a, b)<sup>15</sup>. Depletion of eIF6 specifically abrogated miR-125b-mediated post-transcriptional

silencing of a reporter construct containing miR-125b-responsive sites (Supplementary Fig. 4a, b). Because in *Saccharomyces cerevisiae* eIF6 has been shown to function in 60S ribosome biogenesis<sup>16</sup>, we examined the possibility that disruption of this pathway might contribute to a loss of miRNA-mediated regulation by analysing the effect of depletion of human *BOP1*, another factor involved in 60S biogenesis<sup>17</sup>. In contrast to *eIF6* knockdown, RNA interference (RNAi) of *BOP1* resulted in a nonspecific reduction in the expression of both miR-125b-responsive and control constructs (Supplementary Fig. 4c).

To examine the global consequence of eIF6 depletion on the cellular translational machinery, we analysed polysomal profiles by sucrose gradient fractionation of cells depleted of eIF6 (Fig. 2a). Although there was no change in general polysomal profiles or the levels of free 40S ribosomal subunit, depletion of eIF6 led to a loss of the peak corresponding to free 60S ribosomal subunits (Fig. 2a). These results are consistent with previous reports that showed a specific loss of free 60S ribosomal subunits on inhibition of eIF6 anti-association activity in human cells<sup>7</sup> or depletion of this factor in yeast<sup>18,19</sup>. The loss of free 60S ribosomal subunits was accompanied by the appearance of an additional 'shoulder' on the 80S subunit, suggesting the association of the 60S with higher molecular mass complexes (Fig. 2a). The appearance of a large peak of 80S ribosome on our polysomal profiles may be due to cellular stress after multiple transfections of siRNAs.

Consistent with the absence of nonspecific effects on control reporter gene translation (Fig. 1f), RNAi knockdown of *eIF6* did not change the mRNA polysome profile of housekeeping genes such

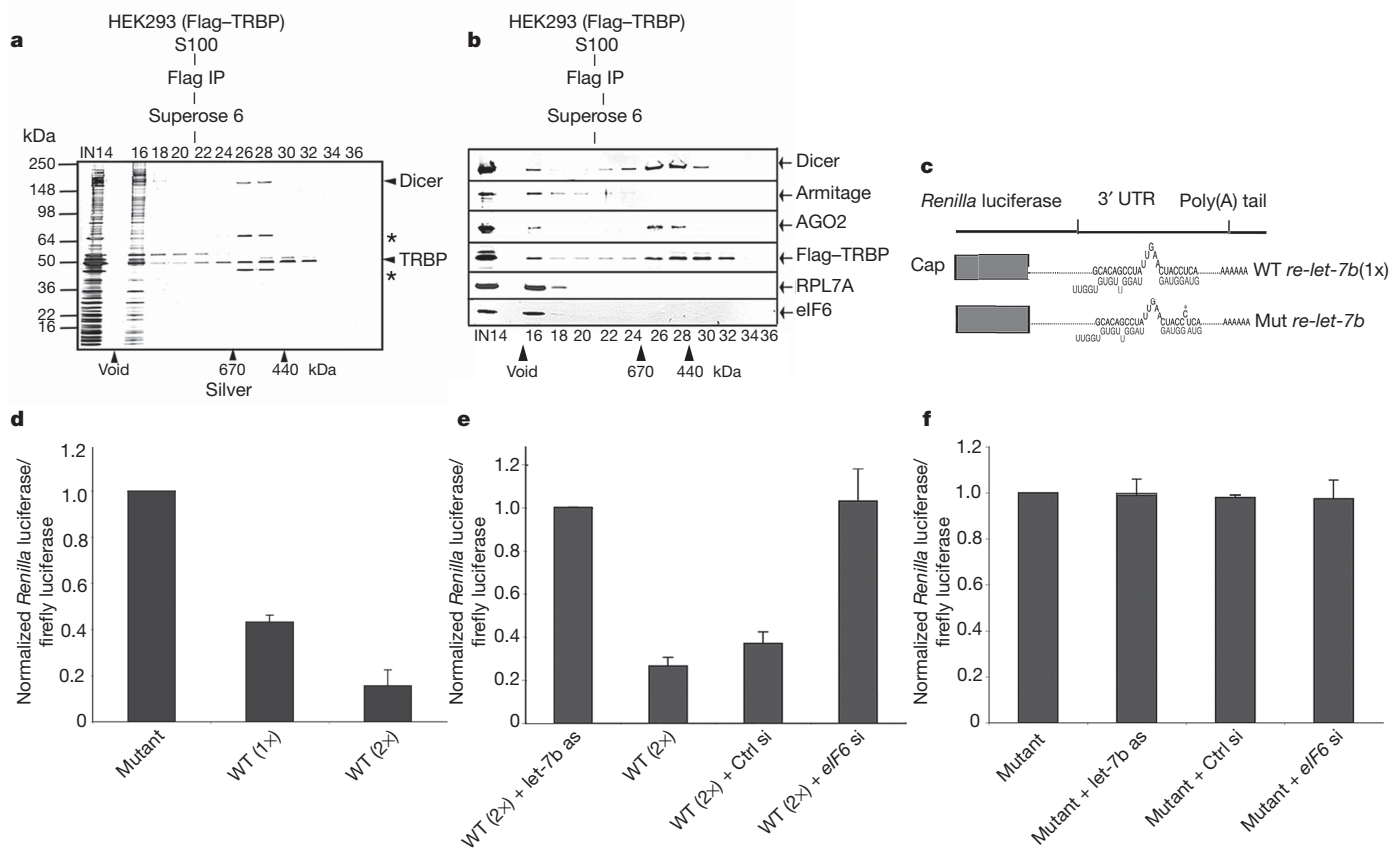


**Figure 1 | Biochemical and functional analysis of eIF6 in the miRNA pathway.** **a, b**, Flag affinity eluate was fractionated on a Superose 6 gel filtration medium after which the column fractions were subjected to SDS-PAGE and either silver staining or western blot analysis. Fractions of the column are denoted on the top and molecular mass markers are indicated at the bottom. Asterisks denote contaminating polypeptides. **c**, Illustration of *Renilla* luciferase containing the wild-type or mutant let-7b

sites. **d**, Reporter constructs containing one or two let-7b-responsive sites are repressed in HeLa cells. **e, f**, Treatment with 2'-O-methyl single-stranded RNA (let-7b as) or eIF6 knockdown abolishes let-7b-mediated translational repression without any effect on reporters with a mutant let-7b binding site. Each point represents at least three independent experiments. Error bars in **d–f** indicate s.e.m.

as GAPDH (Fig. 2b). Taken together, these data implicate the eIF6-containing complex in miRNA-mediated translational repression and are consistent with a mechanism whereby miRNA complexes recruit eIF6 to regulate ribosome assembly and translation of target mRNAs.

### eIF6 regulates let-7b-responsive mRNA in human cells

Recent experiments have pointed to an unexpected role of animal miRNAs in destabilization of their target mRNAs<sup>3</sup>. To examine the effect of eIF6 depletion on target mRNA, we assessed the fate of *Renilla* luciferase mRNA containing two let-7b sites in the 3' UTR (Fig. 2c). Consistent with recent reports<sup>15,20</sup> and experiments in *C. elegans* that will be described below, the let-7b-responsive reporter mRNA was reduced below the detection levels of RNase protection, whereas the mRNA levels corresponding to vector control and the reporter with a mutant let-7b site could be readily measured (Fig. 2c).

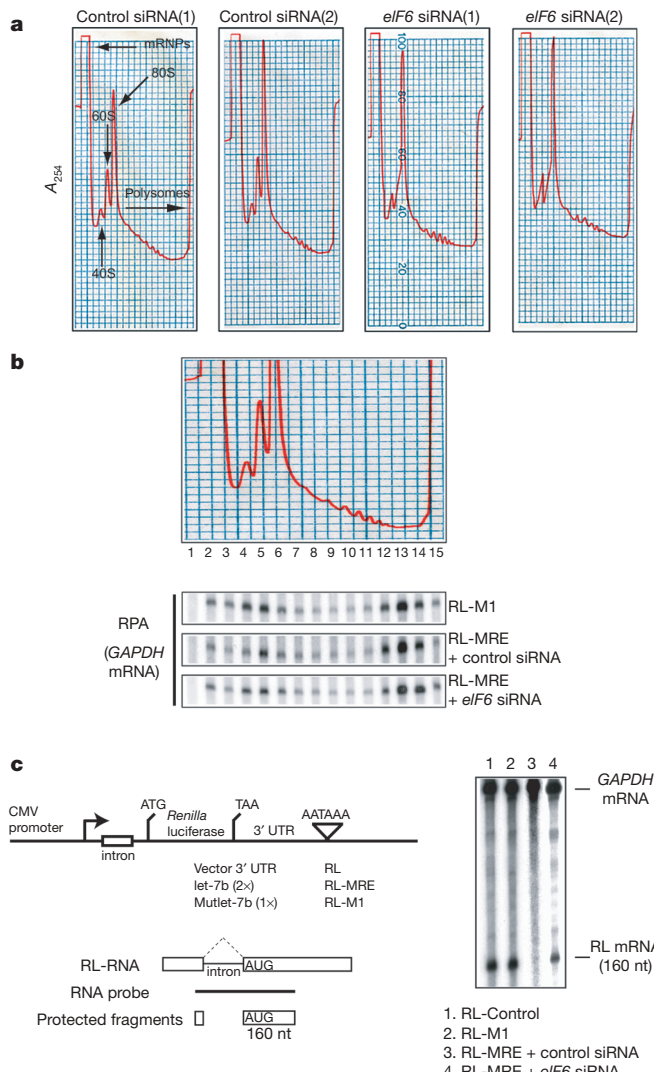


**Figure 2 | Impact of eIF6 depletion on let-7b-responsive reporter mRNA levels and on cellular polysome profiles.** **a**, Polysome profiles of transfected HeLa cells with or without eIF6 siRNA treatment. Results of two independent experiments are depicted as (1) and (2). The  $y$  axis shows absorbance at 254 nm. **b**, Detection of human GAPDH mRNAs across a HeLa polysome gradient. A typical polysome profile is shown (top). **c**, The expression construct used in this study and the probes used for the RNase protection assay (RPA) are depicted on the left of the figure. RPA quantification of let-7b-responsive *Renilla* mRNA reporter and GAPDH mRNA in cells treated with a control siRNA or an siRNA targeting eIF6 mRNA is shown to the right.

Depletion of eIF6 partially restored the mRNA levels of the let-7b-responsive reporter (Fig. 2c). These data show that efficient downregulation of target mRNA levels by miRNAs requires eIF6 protein.

### eIF6 regulates lin-4 miRNA targets in *C. elegans*

To test whether eIF6 has a conserved function in the miRNA pathway, we examined the role of this factor in the regulation of two endogenous genes in *C. elegans*. The *lin-14* and *lin-28* genes are negatively regulated by lin-4 miRNA through complementary base pairing in their 3' UTRs (Fig. 3a)<sup>21–23</sup>. We analysed miRNA-mediated silencing in nematodes undergoing RNAi against *eif-6*. The *eif-6(RNAi)* conditions yield an approximately twofold decrease in protein levels (Fig. 3b), which does not significantly affect development and viability of the nematodes over the course of the experiments (see

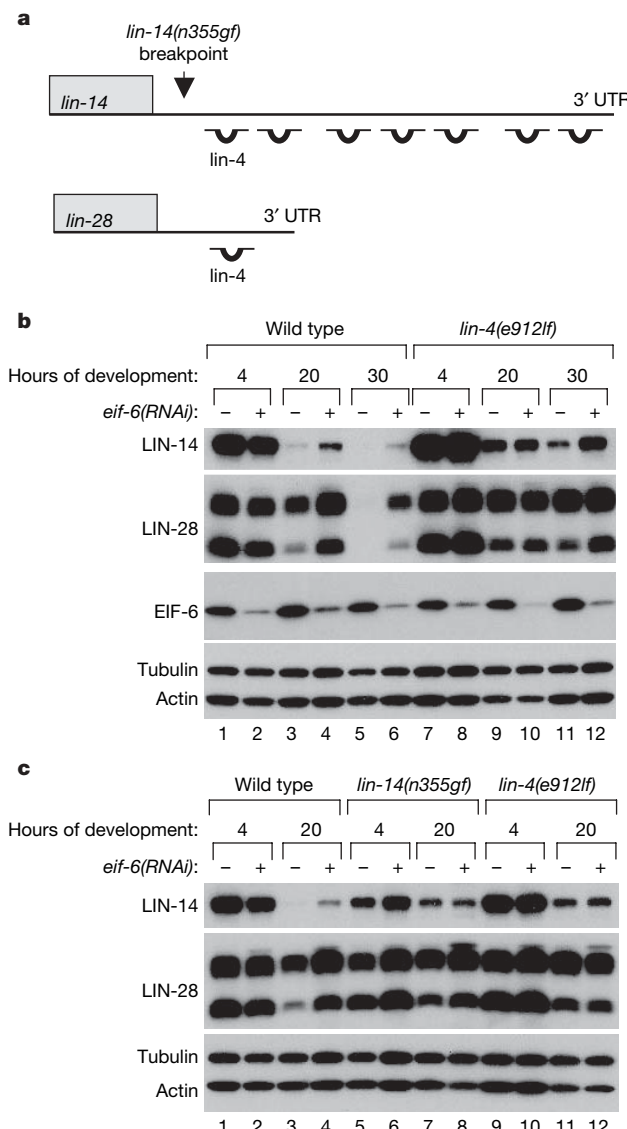


**Figure 3 | Depletion of eif-6 disrupts regulation of protein levels of lin-4 miRNA endogenous targets.** **a**, Schematic representation of lin-4 base-pairing in the 3' UTRs of *lin-14* and *lin-28* mRNAs<sup>22,23</sup>. The breakpoint in *lin-14(n355gf)* that removes the downstream predicted lin-4 complementary sites is indicated. **b**, Protein was isolated from wild-type or *lin-4(e912lf)* nematodes fed vector control (–) or *eif-6* (+) dsRNA-expressing bacteria at time points before (4 h) and after lin-4 miRNA (20 h, 30 h) expression, as indicated. Samples were analysed by western blotting to determine the LIN-14, LIN-28, EIF-6 and control actin and tubulin levels. **c**, Protein was isolated from *lin-14(n355gf)* nematodes as described in **b** and compared to *lin-4(e912lf)* samples at the 4- and 20-h time points.

below). Consistent with previous studies in wild-type nematodes<sup>22,24</sup>, LIN-14 and LIN-28 proteins are downregulated on expression of lin-4 miRNA in nematodes subjected to control RNAi conditions (Fig. 3b and Supplementary Fig. 5a–c). However, *eif-6(RNAi)* results in an approximately twofold accumulation of LIN-14 at the 20 h time point, relative to the vector (RNAi) control, and this misregulation continues to be apparent up to 30 h of development (Fig. 3b and Supplementary Fig. 5a–c). Furthermore, almost fivefold more LIN-28 protein remains in the samples from *eif-6(RNAi)* nematodes compared with control RNAi samples at 30 h of development (Fig. 3b and Supplementary Fig. 5a–c).

The effect of *eif-6(RNAi)* on LIN-28 and LIN-14 protein levels is primarily lin-4-dependent, as *lin-4(e912lf)* nematodes—which express no lin-4 miRNA<sup>21</sup>—subjected to *eif-6(RNAi)* show no significant accumulation of LIN-14 or LIN-28 relative to the vector (RNAi) control at 20 h of development (Fig. 3b and Supplementary Fig. 5a–c). Similarly, the level of LIN-14 protein in the nematode strain *lin-14(n355gf)*, which removes the lin-4-complementary sites from the *lin-14* 3' UTR, is unaffected by *eif-6(RNAi)* (Fig. 3c). The partial downregulation of LIN-14 protein from 4 to 20 h of development in *lin-4(e912lf)* and *lin-14(n355gf)* nematodes (Fig. 3b, c) has been previously documented<sup>22</sup> and supports the proposal that

additional factors regulate this gene<sup>25</sup>. The modest increase in LIN-14 levels in *eif-6(RNAi)* compared to control samples from *lin-4(e912lf)* nematodes at 30 h of development may indicate that other miRNAs contribute to LIN-14 regulation later in development, as previously suggested<sup>26</sup> (Fig. 3b and Supplementary Fig. 5a–c).

### EIF-6 regulates *lin-4*-responsive mRNA in *C. elegans*

During larval development, a substantial decrease in the steady-state levels of *lin-14* and *lin-28* mRNAs is dependent on accumulation of lin-4 miRNA in nematodes under standard culture<sup>20</sup> or vector control RNAi conditions (Figs 4a and 5). In contrast, wild-type nematodes subjected to *eif-6* RNAi are impaired in their ability to downregulate *lin-14* and *lin-28* mRNAs, despite the presence of equivalent levels of lin-4 miRNA (Figs 4a and 5). The greater than sixfold reduction during larval development in *lin-14* and *lin-28* mRNA levels observed in nematodes cultured under control RNAi conditions is diminished to approximately twofold in nematodes undergoing *eif-6(RNAi)* treatment (Fig. 4a). The misregulation of *lin-14* and *lin-28* mRNA levels is miRNA dependent, as *lin-4(e912lf)* nematodes show only a modest accumulation of these mRNAs at 20 h of larval development in *eif-6* compared to control RNAi conditions (Fig. 4b). Similarly, the *lin-14(n355gf)* nematodes exhibit a slight accumulation of *lin-14* mRNA in *eif-6(RNAi)* versus control samples

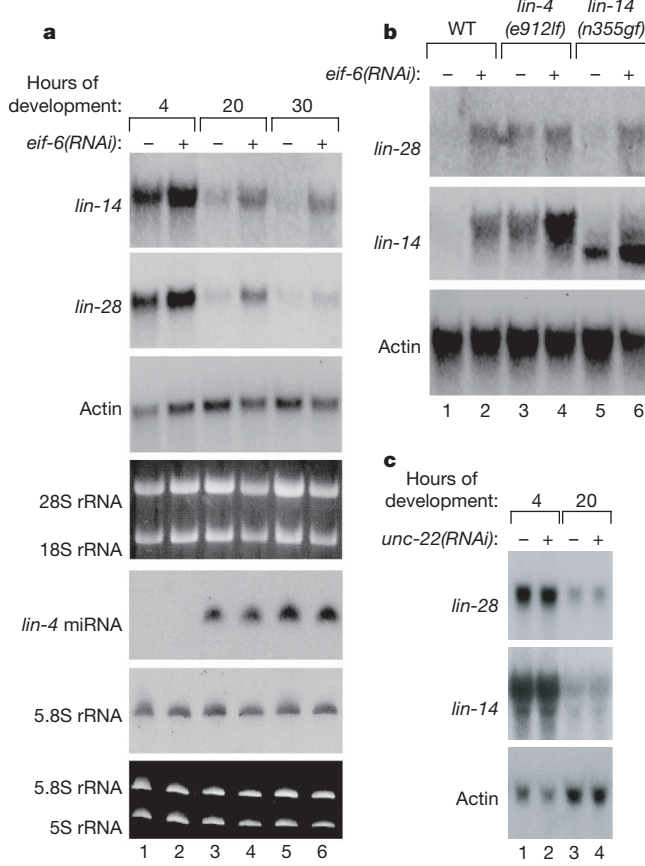


**Figure 4 | RNAi of *eif-6* results in misregulation of *lin-14* and *lin-28* target mRNA levels.** **a**, *lin-14* and *lin-28* mRNA levels were determined by northern blotting. Reprobing of the blot for actin mRNA and detection of the large ribosomal RNAs by ethidium bromide staining serve as controls. PAGE northern analysis of the same RNA samples was performed to detect lin-4 miRNA expression. Ethidium bromide staining of the small rRNAs and probing for 5.8S rRNA demonstrate similar levels of total RNA in all lanes. **b**, RNA samples were analysed by northern blot experiments to determine the *lin-28*, *lin-14* and control actin mRNA levels. The *lin-14(n355gf)* allele contains a deletion in the 3' UTR that removes the predicted lin-4 complementary sites and encodes ~1.3-kb shorter transcripts. **c**, RNA was isolated from wild-type nematodes fed vector control (–) or *unc-22* (+) dsRNA-expressing bacteria and analysed by northern blotting.

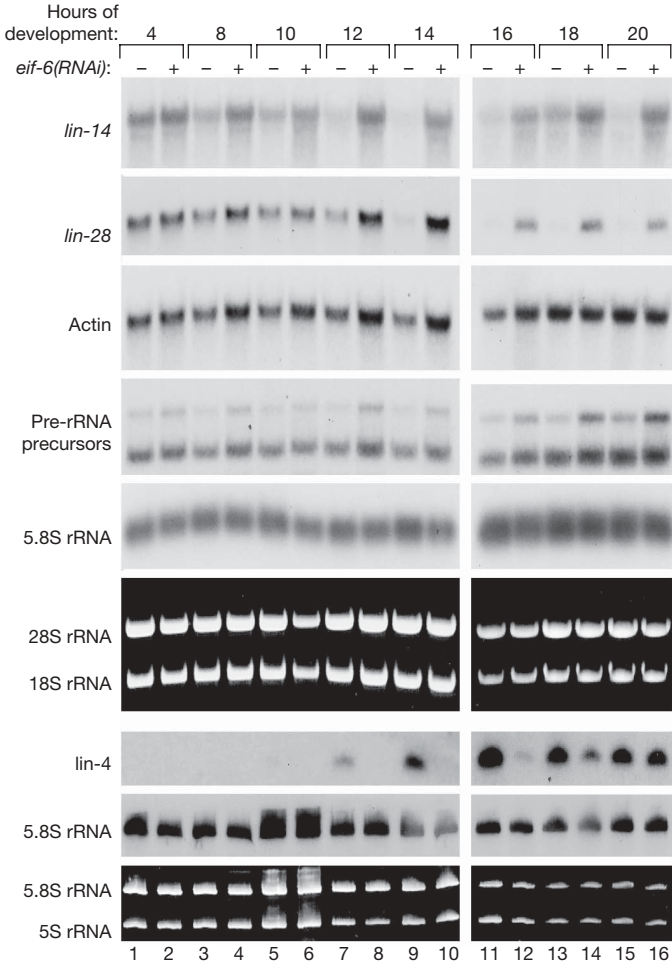


**Figure 5 | Depletion of EIF-6 during *C. elegans* larval development.** RNA was analysed by agarose northern blotting to determine the levels of *lin-14*, *lin-28* and actin mRNAs. A probe for 5.8S rRNA was used to detect both precursor and mature rRNAs containing this sequence. Mature large rRNAs stained with ethidium bromide are also shown. Denaturing PAGE northern blot analysis of the same RNA samples was performed to detect lin-4 miRNA expression. Total RNA control: ethidium bromide staining of the mature small rRNAs and radioactive probe for 5.8S rRNA.

(Fig. 4b). Moreover, control RNAi against *unc-22*, a control gene irrelevant to the miRNA pathway, has no effect on *lin-14* or *lin-14* mRNA levels (Fig. 4c).

To examine further the role of EIF-6 in regulating miRNA silencing, we attempted to identify a time point where the lin-4 miRNA directs translational repression before affecting *lin-14* or *lin-28* mRNA levels. lin-4 miRNA is first detected at 12 h of development and reaches maximal levels by 16 h<sup>27</sup> (Fig. 5). By 14 h of development the steady-state levels of *lin-14* and *lin-28* mRNAs show greater than fourfold reduction compared with the 4-h time point. Unexpectedly, we found a modest delay, about 4 h, in the temporal accumulation of lin-4 miRNA in nematodes undergoing *eif-6(RNAi)* (Fig. 5). Indistinguishable levels of lin-4 miRNA are present in control and *eif-6(RNAi)* samples by 20 and 30 h of development (Figs 4a and 5), indicating that misregulation of *lin-14* and *lin-28* target genes at these time points cannot be attributed to insufficient miRNA expression. Consistent with studies of EIF6 in yeast<sup>16</sup>, partial depletion of this factor in nematodes results in a slight accumulation of pre-ribosomal RNA precursors, but subsequent decrease in mature rRNAs was not apparent (Fig. 5 and Supplementary Fig. 6). Although presently it is unclear if the modest developmental delay in *eif-6(RNAi)* nematodes results from disruption of rRNA biogenesis or the miRNA pathway, depletion of the nematode miRNA argonaute-like gene *alg-1* also results in slow growth<sup>28</sup>. Taken together, these results support a new role for EIF-6 as a key factor required by lin-4 miRNA to regulate its endogenous targets in *C. elegans*.

## Discussion

We have isolated a multiprotein RISC-containing complex that includes MOV10, the translation inhibitory protein EIF6 and the 60S ribosome. These results are in accordance with an earlier report describing the association of *Drosophila* RISC and ribosomal subunits<sup>29</sup>. Additionally, we provide biochemical and functional evidence supporting a role of EIF6 in mediating miRNA-dependent gene silencing. This contention is not only based on evidence using reporter systems to analyse miRNA-mediated silencing in human cells, but also analysis of developmentally regulated endogenous miRNA targets in *C. elegans*. Thus, we propose a new role for EIF6 in mediating miRNA-directed gene silencing that has been conserved through evolution.

Animal miRNAs typically bind to partially complementary sites in the 3' UTRs of their target mRNAs and regulate mRNA stability and translation. Although recent experiments have suggested a role for processing bodies (P bodies) in miRNA-mediated gene silencing<sup>3,4</sup>, it is not clear whether the components associated with P bodies execute the silencing step or that the target RNA is directed to P bodies for degradation after miRNA-induced translational repression. Because P bodies are devoid of core translation components, our data suggest a mechanism by which EIF6-mediated repression of translation by miRNAs sets the stage for recruitment of the target RNA to P bodies. The ability of EIF6 to inhibit joining of the 60S and 40S subunits of the ribosome and, thus, to prevent formation of a translationally competent complex<sup>7–10</sup>, raises the possibility that EIF6 may repress translation by blocking initiation or ribosome recycling<sup>30,31</sup>. Although EIF6 is much more effective at inhibiting association compared with promoting disassociation of the ribosomal subunits<sup>8,9</sup>, it is presently unclear whether RISC could modulate this activity to disrupt translation elongation of a miRNA-targeted transcript<sup>32</sup>. In both human cells and *C. elegans*, translation inhibition can be accompanied by potent mRNA downregulation, and both aspects of miRNA regulation are perturbed by depletion of EIF6. We favour a model whereby miRNA-directed complexes use EIF6 to help disrupt productive polysome formation and expose the target mRNA for degradation.

## METHODS

**Biochemical identification of components of large TRBP-containing complex.** Flag-TRBP and specific interacting factors were isolated using anti-Flag

M2 affinity gel. Protein identification using liquid chromatography-mass spectrometry/mass spectrometry (LC-MS/MS) and analysis of TRBP by Superose 6 gel filtration was performed as detailed<sup>2</sup>.

**Transfections and dual luciferase activity analysis.** Cells were co-transfected with 500 ng per well of the reporter and 100 ng of either firefly or *Renilla* control plasmid DNAs. Where indicated, control siRNA, *eIF6* siRNA, *armitage* siRNA, 2'-O-Me antisense oligonucleotide complementary to *let-7b* RNA, or mir-125b duplexes were co-transfected at a final concentration of 100 nM. Dual luciferase activity assays were performed 48 h after transfection according to the manufacturer's directions (Promega). The results are represented as means of three independent experiments.

**Polysome analyses.** HeLa cells were incubated with 100 µg ml<sup>-1</sup> cycloheximide for 5 min and then lysed on ice. After clearing the nuclei, supernatants were loaded on top of sucrose gradients, which were then ultracentrifuged at 40,000 r.p.m. for 85 min at 4 °C (Beckman SW41 rotor). Fifteen fractions were collected and the gradient profile was monitored via ultraviolet absorbance at 254 nm with a UA-5 detector (ISCO). RNA was isolated and analysed by RNase protection assays.

**Nematode methods.** For two-generation RNAi experiments, synchronized wild-type L4-stage nematodes were cultured on RNAi plates seeded with bacteria containing vector control, *eif-6*, or *unc-22* double-stranded-RNA-expressing plasmids<sup>33</sup>. Nematodes were grown until the gravid adult stage, progeny were collected by standard bleaching methods, synchronized, and cultured on fresh RNAi plates. Nematodes were collected and processed for RNA or protein at the indicated time points. Polyacrylamide and agarose gel electrophoresis were used to separate RNAs for northern blot analyses as described<sup>20</sup>. Nematodes collected for protein were processed and analysed by western blotting as described<sup>34</sup>.

**Full Methods** and any associated references are available in the online version of the paper at [www.nature.com/nature](http://www.nature.com/nature).

Received 26 September 2006; accepted 13 April 2007.

Published online 16 May 2007.

1. Kim, V. N. MicroRNA biogenesis: coordinated cropping and dicing. *Nature Rev. Mol. Cell Biol.* 6, 376–385 (2005).
2. Gregory, R. I., Chendrimada, T. P., Cooch, N. & Shiekhattar, R. Human RISC couples microRNA biogenesis and posttranscriptional gene silencing. *Cell* 123, 631–640 (2005).
3. Jackson, R. J. & Standart, N. How do microRNAs regulate gene expression? *Sci. STKE* 2007, r61 (2007).
4. Valencia-Sanchez, M. A., Liu, J., Hannon, G. J. & Parker, R. Control of translation and mRNA degradation by miRNAs and siRNAs. *Genes Dev.* 20, 515–524 (2006).
5. Cook, H. A., Koppetsch, B. S., Wu, J. & Theurkauf, W. E. The *Drosophila* SDE3 homolog *armitage* is required for *oskar* mRNA silencing and embryonic axis specification. *Cell* 116, 817–829 (2004).
6. Tomari, Y. *et al.* RISC assembly defects in the *Drosophila* RNAi mutant *armitage*. *Cell* 116, 831–841 (2004).
7. Ceci, M. *et al.* Release of EIF6 (p27BBP) from the 60S subunit allows 80S ribosome assembly. *Nature* 426, 579–584 (2003).
8. Russell, D. W. & Spremulli, L. L. Purification and characterization of a ribosome dissociation factor (eukaryotic initiation factor 6) from wheat germ. *J. Biol. Chem.* 254, 8796–8800 (1979).
9. Valenzuela, D. M., Chaudhuri, A. & Maitra, U. Eukaryotic ribosomal subunit anti-association activity of calf liver is contained in a single polypeptide chain protein of  $M_r = 25,500$  (eukaryotic initiation factor 6). *J. Biol. Chem.* 257, 7712–7719 (1982).
10. Raychaudhuri, P., Stringer, E. A., Valenzuela, D. M. & Maitra, U. Ribosomal subunit anti-association activity in rabbit reticulocyte lysates. Evidence for a low molecular weight ribosomal subunit anti-association protein factor ( $M_r = 25,000$ ). *J. Biol. Chem.* 259, 11930–11935 (1984).
11. Chendrimada, T. P. *et al.* TRBP recruits the Dicer complex to Ago2 for microRNA processing and gene silencing. *Nature* 436, 740–744 (2005).
12. Si, K., Chaudhuri, J., Chevesich, J. & Maitra, U. Molecular cloning and functional expression of a human cDNA encoding translation initiation factor 6. *Proc. Natl. Acad. Sci. USA* 94, 14285–14290 (1997).
13. Meister, G. *et al.* Identification of novel argonaute-associated proteins. *Curr. Biol.* 15, 2149–2155 (2005).
14. Nelson, P. T., Hatzigeorgiou, A. G. & Mourelatos, Z. miRNP:mRNA association in polyribosomes in a human neuronal cell line. *RNA* 10, 387–394 (2004).
15. Wu, L. & Belasco, J. G. Micro-RNA regulation of the mammalian *lin-28* gene during neuronal differentiation of embryonal carcinoma cells. *Mol. Cell. Biol.* 25, 9198–9208 (2005).
16. Basu, U., Si, K., Warner, J. R. & Maitra, U. The *Saccharomyces cerevisiae* TIF6 gene encoding translation initiation factor 6 is required for 60S ribosomal subunit biogenesis. *Mol. Cell. Biol.* 21, 1453–1462 (2001).
17. Strezoska, Z., Pestov, D. G. & Lau, L. F. Bop1 is a mouse WD40 repeat nucleolar protein involved in 28S and 5.8S rRNA processing and 60S ribosome biogenesis. *Mol. Cell. Biol.* 20, 5516–5528 (2000).

18. Si, K. & Maitra, U. The *Saccharomyces cerevisiae* homologue of mammalian translation initiation factor 6 does not function as a translation initiation factor. *Mol. Cell. Biol.* **19**, 1416–1426 (1999).
19. Sanvito, F. *et al.* The B4 integrin interactor p27<sup>BBP/eIF6</sup> is an essential nuclear matrix protein involved in 60S ribosomal subunit assembly. *J. Cell Biol.* **14**, 823–837 (1999).
20. Bagga, S. *et al.* Regulation by let-7 and lin-4 miRNAs results in target mRNA degradation. *Cell* **122**, 553–563 (2005).
21. Lee, R. C., Feinbaum, R. L. & Ambros, V. The *C. elegans* heterochronic gene *lin-4* encodes small RNAs with antisense complementarity to *lin-14*. *Cell* **75**, 843–854 (1993).
22. Wightman, B., Ha, I. & Ruvkun, G. Posttranscriptional regulation of the heterochronic gene *lin-14* by *lin-4* mediates temporal pattern formation in *C. elegans*. *Cell* **75**, 855–862 (1993).
23. Moss, E. G., Lee, R. C. & Ambros, V. The cold shock domain protein LIN-28 controls developmental timing in *C. elegans* and is regulated by the *lin-4* RNA. *Cell* **88**, 637–646 (1997).
24. Seggerson, K., Tang, L. & Moss, E. G. Two genetic circuits repress the *Caenorhabditis elegans* heterochronic gene *lin-28* after translation initiation. *Dev. Biol.* **243**, 215–225 (2002).
25. Arasu, P., Wightman, B. & Ruvkun, G. Temporal regulation of *lin-14* by the antagonistic action of two other heterochronic genes, *lin-4* and *lin-28*. *Genes Dev.* **5**, 1825–1833 (1991).
26. Reinhart, B. J. *et al.* The 21-nucleotide *let-7* RNA regulates developmental timing in *Caenorhabditis elegans*. *Nature* **403**, 901–906 (2000).
27. Feinbaum, R. & Ambros, V. The timing of *lin-4* RNA accumulation controls the timing of postembryonic developmental events in *Caenorhabditis elegans*. *Dev. Biol.* **210**, 87–95 (1999).
28. Grishok, A. *et al.* Genes and mechanisms related to RNA interference regulate expression of the small temporal RNAs that control *C. elegans* developmental timing. *Cell* **106**, 23–34 (2001).
29. Pham, J. W., Pellino, J. L., Lee, Y. S., Carthew, R. W. & Sontheimer, E. J. A. Dicer-2-dependent 80S complex cleaves targeted mRNAs during RNAi in *Drosophila*. *Cell* **117**, 83–94 (2004).
30. Pillai, R. S. *et al.* Inhibition of translational initiation by Let-7 microRNA in human cells. *Science* **309**, 1573–1576 (2005).
31. Humphreys, D. T., Westman, B. J., Martin, D. I. & Preiss, T. MicroRNAs control translation initiation by inhibiting eukaryotic initiation factor 4E/cap and poly(A) tail function. *Proc. Natl. Acad. Sci. USA* **102**, 16961–16966 (2005).
32. Petersen, C. P., Bordeleau, M. E., Pelletier, J. & Sharp, P. A. Short RNAs repress translation after initiation in mammalian cells. *Mol. Cell* **21**, 533–542 (2006).
33. Kamath, R. S. *et al.* Systematic functional analysis of the *Caenorhabditis elegans* genome using RNAi. *Nature* **421**, 231–237 (2003).
34. Reinhart, B. J. & Ruvkun, G. Isoform-specific mutations in the *Caenorhabditis elegans* heterochronic gene *lin-14* affect stage-specific patterning. *Genetics* **157**, 199–209 (2001).

**Supplementary Information** is linked to the online version of the paper at [www.nature.com/nature](http://www.nature.com/nature).

**Acknowledgements** We thank Z. Mourelatos for providing the firefly luciferase plasmids containing let-7b binding sites; J. Belasco for Luc-lin28 (firefly luciferase reporter fused to the 2.7-kb 3' UTR of human *LN28*) and its mutants; G. Ruvkun and E. Moss for *LN14* and *LN28* antibodies, respectively; and J. Bracht, M. G. Lee, S. Bagga and G. Harris for technical assistance. We also thank T. Beer of the Wistar Proteomics Facility for expertise in the microcapillary HPLC/mass spectrometry. This work was supported by NIH (A.E.P., R.S., S.A.L.), the Searle and V Foundations (AEP), the Mathers Foundation (RS) and a Cooley's Anemia Foundation Fellowship to X.J.

**Author Contributions** T.P.C., K.J.F. and X.J. contributed equally to the work. T.P.C. performed experiments in human cells with help from R.I.G. and D.B. X.J. performed Fig. 2 experiments. R.S., A.E.P. and S.A.L. wrote the manuscript.

**Author Information** Reprints and permissions information is available at [www.nature.com/reprints](http://www.nature.com/reprints). The authors declare no competing financial interests. Correspondence and requests for materials should be addressed to R.S. (ramin.shiekhattar@crg.es) or A.E.P. (apasquin@ucsd.edu).

## METHODS

**Affinity purification of Flag–TRBP.** Flag–TRBP and a selectable marker for puromycin resistance were co-transfected into HEK293 human embryonic kidney cells. Transfected cells were grown in the presence of  $2.5 \mu\text{g ml}^{-1}$  puromycin, and individual colonies were isolated and analysed for Flag–TRBP expression. To purify the TRBP complex,  $\sim 150 \text{ mg}$  S100 extract was incubated with anti-Flag M2 affinity gel (Sigma). After washing twice with buffer A (20 mM Tris-HCl (pH 7.9), 0.5 M KCl, 10% glycerol, 1 mM EDTA, 0.2% NP40, 0.5 mM dithiothreitol (DTT), 0.2 mM PMSF), the affinity column was eluted with buffer A containing Flag peptide ( $400 \mu\text{g ml}^{-1}$ ) according to the manufacturer's instructions (Sigma). Analysis of TRBP by Superose 6 gel filtration (20 mM Tris-HCl (pH 7.9), 0.3 M KCl, 10% glycerol, 1 mM EDTA, 0.2% NP40, 0.5 mM DTT, 0.2 mM PMSF) was similar to that previously described<sup>2</sup>. Protein identification using LC-MS/MS was performed as detailed<sup>2</sup>. Polyclonal anti-eIF6 antibody (catalogue number 10291-1-AP) was purchased from Proteintech Group. Polyclonal anti-MOV10 (Armitage) antibodies were generated to the last 20 amino acids in the amino- and carboxy terminus of the protein (Open Biosystems). Polyclonal anti-TRBP, anti-Dicer and anti-AGO2 were described previously<sup>11</sup>.

**Transfections and dual luciferase activity analysis.** HeLa and H1299 cells were grown in Dulbecco's modified Eagle's medium (Gibco-BRL) supplemented with L-glutamine (2 mM) and 10% fetal calf serum, and maintained using standard protocols. Cells were transfected using Lipofectamine 2000 as recommended by the manufacturer (Invitrogen). All plasmids used for transfection were prepared using the Maxiprep kit (Qiagen). Cells were grown as a monolayer in 6-well plates and 500 ng per well of the reporter plasmid was co-transfected with 100 ng of either firefly or *Renilla* control plasmid DNAs. Where indicated, control siRNA (siRNA against TFII-I<sup>11</sup>), *eIF6* siRNAs (UAGCUUCCUACUAGCACCUCU), (CAAUUGAAGACCAGGAUGAUU), *armitage* siRNAs (UGAGAGUCUGG-UAGCUUA), (UUAUCCGCCUGGAUUUGAA) or 2'-O-Me antisense oligonucleotide complementary to *let-7b* RNA (AACACACACAACCUACUACCUA) were co-transfected at a final concentration of 100 nM. Where appropriate, duplex miR-125b (guide, UCCCUGAGACCUACUUGUGA; passenger, ACAAGUCAGGCUCUUGGGACCU) was exogenously introduced into H1299 cells by co-transfection to a final concentration of 100 nM. Dual luciferase activity assays were performed 48 h after transfection according to the manufacturer's directions (Promega). The results are represented as means of three independent experiments, with one of the conditions (as indicated in the figure legends) set to 1.

**RNA isolation and RT-PCR analysis.** To examine the siRNA effect, 2  $\mu\text{g}$  total RNA was prepared using Trizol reagent (Invitrogen) according to the manufacturer's instructions. RNA was subjected to cDNA synthesis with oligo-dT using the SuperScript first-strand synthesis system, followed by real-time PCR analysis of *eIF6* and *GAPDH* levels.

**Cell transfection and polysome analysis.** HeLa cells at 70% confluence were transfected with either control siRNA or *eIF6* siRNA using Lipofectamine 2000 according to the manufacturer's instruction. The siRNA transfections were repeated 20 h after the initial transfections. Cells were split after 8 h and cultured in complete DMEM medium overnight. Two micrograms of pRL-CMV or its derivatives were then transfected into non-transfected or siRNA-transfected HeLa cells and cultured in complete medium for another 24 h.

Ten to fifty per-cent linear sucrose gradients containing 100 mM KCl, 5 mM MgCl<sub>2</sub>, 2 mM DTT and 20 mM HEPES (pH 7.4) were prepared in 12-ml Beckman ultracentrifuge tubes with a two-chamber gradient mixer. HeLa cells were incubated with cycloheximide ( $100 \mu\text{g ml}^{-1}$ , freshly prepared in ethanol) for 5 min before harvesting. Cells were washed and then lysed on ice by treatment with 500  $\mu\text{l}$  of ice-cold TMK100 lysis buffer (10 mM Tris-HCl (pH 7.4), 5 mM MgCl<sub>2</sub>, 100 mM KCl, 2 mM DTT, 1% Triton X-100 and 100 U of RNase inhibitor (Promega) per ml in diethyl pyrocarbonate-treated water) for 5 min. The nuclei were cleared at 10,000g for 10 min at 4 °C, and the supernatants were loaded over the top of sucrose gradients. These gradients were ultracentrifuged at 40,000 r.p.m. for 85 min at 4 °C (Beckman SW41 rotor). Fifteen fractions (700  $\mu\text{l}$  per fraction) were collected into 1.5-ml microcentrifuge tubes containing 70  $\mu\text{l}$  of 10% SDS, and the gradient profile was monitored via ultraviolet absorbance at 254 nm with a UA-5 detector (ISCO). Each sample was digested with 8  $\mu\text{l}$  of proteinase K ( $20 \text{ mg ml}^{-1}$ ) solution at 37 °C for 30 min and stored at  $-80^\circ\text{C}$  before RNA extraction.

**RNase protection assay.** Two copies of native *let-7b* (2 $\times$ ) were cloned in the 3' UTR of pRL-CMV vector (Promega), and one copy of mutant *let-7b* (1 $\times$ ) was cloned into the same vector according to the literature<sup>35</sup>. A fragment of *Renilla Luc* spanning the CMV promoter and transcribed gene used in the transfection experiment was cloned into pTRIamp18 vector. The rLuciferase and human *GAPDH* (Ambion) templates were used to generate internally labelled RPA probes. *In vitro* transcriptions were carried out in the presence of [<sup>32</sup>P]CTP

(3,000 Ci mmol<sup>-1</sup>, 10 mCi ml<sup>-1</sup>; Amersham) using the Maxiscript SP6 kit under conditions recommended by the manufacturer (Ambion). RPA was carried out as described previously<sup>36</sup>. Radioactivity in bands of interest was quantified by PhosphorImager analysis (Storm 840; Molecular Dynamics).

**Nematode methods.** For two-generation RNAi experiments, synchronized wild-type (N2) L4-stage nematodes were cultured on RNAi plates seeded with bacteria containing vector control, *eif-6*, or *unc-22* dsRNA-expressing plasmids<sup>33</sup>. Nematodes were grown until the gravid adult stage, progeny were collected by standard bleaching methods, synchronized and cultured on fresh RNAi plates. Nematodes were collected and processed for RNA by the Trizol (Gibco-BRL) method at the indicated time points. Polyacrylamide and agarose gel electrophoresis was used to separate RNAs for northern analyses as described<sup>20</sup>. Sequences of primers used to generate the templates for radiolabelled probes used in the northern analyses are as follows:

*lin-14*, AACAGTTGAAACAGCTCCACCACTC and  
GGATAAGATGGGTGAAGAGACTGATG;  
*lin-28*, GACGGTAGTATCGGAGGGAAGGAATGATG and  
GCGTCGCCCGCAATAGCGGAACCTACG;  
actin, GTGTTCCCATCCATTGTCGGAAGAC and  
GCACTTGCAGGTGAACGATGGATGGATGG;  
5.8S rRNA, CTAGCTTCAGCGATGGATCGGTG and  
GAACCCAGACGTACCAACTGGAGGCC.

Nematodes collected for protein assays were processed as described<sup>34</sup>. Total protein concentrations for each sample were quantified using the BioRad Quick Start Bradford Assay. Similar overall levels of protein were also verified by staining total protein with SimplyBlue Safestain (Invitrogen) after separation on denaturing gels. For western blot analyses, equivalent protein concentrations were run in denaturing 4–20% Novex Tris-glycine gels (Invitrogen) and electroblotted to Immun-Blot PVDF membranes (BioRad). Anti-LIN-14 and anti-LIN-28 antibodies were supplied by G. Ruvkun and E. Moss, respectively, and used as previously described<sup>24,34</sup>. EIF-6 was detected using monoclonal mouse anti-human EIF-6 antibodies (BD Biosystems) at 1:1,000 dilution. Actin was detected using mAbC4 (ICF) at 1:20,000 dilutions and tubulin was detected using monoclonal mouse anti-tubulin antibodies (Sigma) at 1:1,000 dilution. Quantification of northern blots was performed by PhosphorImager Imagequant analysis (Amersham); quantification of western blots was performed using Quantity One (Biorad).

35. Kiriakidou, M. et al. A combined computational-experimental approach predicts human microRNA targets. *Genes Dev.* 18, 1165–1178 (2004).
36. Ji, X., Kong, J. & Liebhaber, S. A. *In vivo* association of the stability control protein  $\alpha$ CP with actively translating mRNAs. *Mol. Cell. Biol.* 23, 899–907 (2003).

# A giant outburst two years before the core-collapse of a massive star

A. Pastorello<sup>1</sup>, S. J. Smartt<sup>1</sup>, S. Mattila<sup>1</sup>, J. J. Eldridge<sup>1</sup>, D. Young<sup>1</sup>, K. Itagaki<sup>2</sup>, H. Yamaoka<sup>3</sup>, H. Navasardyan<sup>4</sup>, S. Valenti<sup>5,6</sup>, F. Patat<sup>5</sup>, I. Agnoletto<sup>4,7</sup>, T. Augusteijn<sup>8</sup>, S. Benetti<sup>4</sup>, E. Cappellaro<sup>4</sup>, T. Boles<sup>9</sup>, J.-M. Bonnet-Bidaud<sup>10</sup>, M. T. Botticella<sup>11</sup>, F. Bufano<sup>4,7</sup>, C. Cao<sup>12</sup>, J. Deng<sup>12,13</sup>, M. Dennefeld<sup>14</sup>, N. Elias-Rosa<sup>4,15</sup>, A. Harutyunyan<sup>4,7</sup>, F. P. Keenan<sup>1</sup>, T. Iijima<sup>16</sup>, V. Lorenzi<sup>17</sup>, P. A. Mazzali<sup>18,19</sup>, X. Meng<sup>12</sup>, S. Nakano<sup>20</sup>, T. B. Nielsen<sup>8</sup>, J. V. Smoker<sup>1</sup>, V. Stanishev<sup>21</sup>, M. Turatto<sup>4</sup>, D. Xu<sup>12</sup> & L. Zampieri<sup>4</sup>

The death of massive stars produces a variety of supernovae, which are linked to the structure of the exploding stars<sup>1,2</sup>. The detection of several precursor stars of type II supernovae has been reported (see, for example, ref. 3), but we do not yet have direct information on the progenitors of the hydrogen-deficient type Ib and Ic supernovae. Here we report that the peculiar type Ib supernova SN 2006jc is spatially coincident with a bright optical transient<sup>4</sup> that occurred in 2004. Spectroscopic and photometric monitoring of the supernova leads us to suggest that the progenitor was a carbon-oxygen Wolf-Rayet star embedded within a helium-rich circumstellar medium. There are different possible explanations for this pre-explosion transient. It appears similar to the giant outbursts of luminous blue variable stars (LBVs) of 60–100 solar masses<sup>5</sup>, but the progenitor of SN 2006jc was helium- and hydrogen-deficient (unlike LBVs). An LBV-like outburst of a Wolf-Rayet star could be invoked, but this would be the first observational evidence of such a phenomenon. Alternatively, a massive binary system composed of an LBV that erupted in 2004, and a Wolf-Rayet star exploding as SN 2006jc, could explain the observations.

SN 2006jc was discovered in UGC 4904 on 2006 October 9.75 UT at magnitude 13.8 (ref. 4). The early spectrum was that of a hydrogen-poor event with strong, narrow He I emission lines<sup>6–9</sup> superimposed on a broad-line spectrum of a type Ic supernova. In 2004, an optical transient was reported to the Central Bureau for Astronomical Telegrams (CBAT) which, when retrospectively compared with the SN 2006jc discovery images, appeared to be spatially coincident with the new supernova<sup>4</sup>. The 2004 transient was much fainter than SN 2006jc (magnitude ~18) and remained visible for only a few days after discovery. This event was never independently confirmed, and CBAT did not issue an official object designation. Given the new, bright supernova discovery, the nature of this transient (which we name UGC 4904-V1, that is, variable 1 in UGC 4904) has become intriguing. We have aligned the images containing the two transients using differential astrometry of 21 nearby stars, and find that UGC 4904-V1 and SN 2006jc are indeed coincident to within the

uncertainties (Fig. 1). In Supplementary Information, we give a comprehensive description of the method, the error analysis and a demonstration that the probability that these two events are chance coincidences is negligible.

We monitored the light curve and spectral evolution of SN 2006jc during the first ~2 months after discovery (Figs 2 and 3). An independent data set was presented in ref. 10. The object was discovered a few days past maximum, but its brightness is still comparable with that of the most luminous type Ic supernovae (Fig. 2), namely  $M_R < -18.3$  mag, adopting a host galaxy distance of  $25.8 \pm 2.6$  Mpc and a total reddening  $E(B-V) = 0.05$  (see Supplementary Information). However, SN 2006jc declines faster than most type Ib/c supernovae and the optical spectra are unusual. The broad emission lines commonly observed in type Ic supernovae are detected, although with an atypical profile (see Supplementary Information). In addition, prominent and relatively narrow (full-width at half-maximum, FWHM,  $\sim 2,200 \text{ km s}^{-1}$ ) He I emission lines are observed, hence the classification of SN 2006jc as a peculiar type Ib event<sup>6–10</sup>. Although very rare, objects like SN 2006jc have been observed before: SN 1999cq<sup>11</sup> and SN 2002ao<sup>10,12</sup> (Fig. 2b). The detection of narrow He I lines suggests that SN 2006jc-like events should be more properly classified as type Ibn, in analogy to the similar nomenclature (type IIn) used for supernovae that show narrow hydrogen emission lines. Another property of the spectra of SN 2006jc (in common with SN 1999cq and SN 2002ao) is the blue colour, which remains almost constant over the entire observational period.

The blue spectral continuum, the presence of narrower lines superimposed on broad spectral features (Fig. 3) and the strong X-ray emission<sup>13</sup> are normally interpreted as a signature of interaction between supernova ejecta and the circumstellar medium (CSM). The presence of prominent He I lines and the simultaneous lack of conspicuous hydrogen features suggest a helium-rich composition of the CSM, while the abundance of hydrogen must be modest. There is no evidence of broad helium components, suggesting that the progenitor of SN 2006jc had entirely lost its helium envelope and was a

<sup>1</sup>Astrophysics Research Centre, School of Mathematics and Physics, Queen's University Belfast, Belfast BT7 1NN, UK. <sup>2</sup>Itagaki Astronomical Observatory, Teppo-cho, Yamagata 990-2492, Japan. <sup>3</sup>Department of Physics, Kyushu University, Fukuoka 810-8560, Japan. <sup>4</sup>INAF Osservatorio Astronomico di Padova, Vicolo dell'Osservatorio 5, I-35122 Padova, Italy. <sup>5</sup>European Southern Observatory (ESO), Karl-Schwarzschild-Str. 2, D-85748 Garching bei München, Germany. <sup>6</sup>Dipartimento di Fisica, Università di Ferrara, via del Paradiso 12, I-44100 Ferrara, Italy. <sup>7</sup>Dipartimento di Astronomia, Università di Padova, Vicolo dell'Osservatorio 2, I-35122 Padova, Italy. <sup>8</sup>Nordic Optical Telescope, Apartado 474, E-38700 Santa Cruz de la Palma, Tenerife, Spain. <sup>9</sup>Coddenham Astronomical Observatory, Peel House, Coddenham, Suffolk, IP6 9QY, UK. <sup>10</sup>Service d'Astrophysique, DSM/DAPNIA/SAp, CE Saclay, F-91191 Gif-sur-Yvette Cedex, France. <sup>11</sup>Dipartimento di Scienze della Comunicazione, Università degli Studi di Teramo, Viale Crucili 122, I-64100 Teramo, Italy. <sup>12</sup>National Astronomical Observatories, Chinese Academy of Sciences, 20A Datun Road, Chaoyang District, Beijing 100012, China. <sup>13</sup>Centre de Physique des Particules de Marseille, CNRS-IN2P3 and University Aix Marseille II, Case 907, 13288 Marseille Cedex 9, France. <sup>14</sup>Institut d'Astrophysique de Paris, CNRS, and Université P. et M. Curie, 98bis Bd Arago, F-75014 Paris, France. <sup>15</sup>Universidad de La Laguna, Av. Astrofísico Francisco Sánchez s/n, E-38206 La Laguna, Tenerife, Spain. <sup>16</sup>INAF Osservatorio Astronomico di Padova, Sezione di Asiago, Via dell'Osservatorio 8, I-36012 Asiago (Vicenza), Italy. <sup>17</sup>Fundación Galileo Galilei-INAF, Telescopio Nazionale Galileo, E-38700 Santa Cruz de la Palma, Tenerife, Spain. <sup>18</sup>Max-Planck-Institut für Astrophysik, Karl-Schwarzschild-Str. 1, D-85748 Garching bei München, Germany. <sup>19</sup>INAF Osservatorio Astronomico di Trieste, Via Tiepolo 11, I-34131 Trieste, Italy. <sup>20</sup>Computing & Minor Planet Section (Center for Astrodynamics) of the Oriental Astronomical Association, Sumoto, Hyogo-Ken, 656-0011, Japan. <sup>21</sup>Department of Physics, Stockholm University, AlbaNova University Center, SE-10691 Stockholm, Sweden.

carbon–oxygen Wolf–Rayet star (WC or WO)<sup>10</sup>. Fast-moving ejecta produce the broad lines of intermediate-mass elements, whose width increases with time (from about 4,000 to 9,000 km s<sup>-1</sup>), whereas the slow-moving CSM produces moderately narrow (about 2,200 km s<sup>-1</sup>) He I emissions. In addition to these prominent features, weak, very narrow ( $\sim$ 500 km s<sup>-1</sup>) P Cygni absorptions attributed to He I and O I (and, possibly, H $\alpha$ ) are visible in the highest resolution spectra, and are indicative of further undisturbed, slowly moving shells originating from previous mass loss episodes (Supplementary Information). Severe mass loss is necessary to remove the outer helium and hydrogen layers, and to produce a massive carbon–oxygen core.

The 2004 outburst of UGC 4904-V1 reached a peak magnitude of  $M_R \approx -14.1$ , and we offer a few possible explanations of the event. Giant outbursts of LBVs<sup>14,15</sup> are well documented transients with a similar peak magnitude and sharp decline (Fig. 4 and Supplementary Information). LBVs are massive blue stars that show significant optical variability, due to unstable atmospheres and episodic mass loss. The only Galactic star well observed during such an eruption is  $\eta$  Carinae (in 1837–57; ref. 14), which has a current mass of approximately 90 solar masses ( $90 M_\odot$ ) and an initial mass of around  $150 M_\odot$  (ref. 16). Other LBVs in the local Universe that have shown giant outbursts of similar magnitude to UGC 4904-V1 are likely to have had initial masses in the range  $60$ – $100 M_\odot$  (Supplementary Information). However, despite the fact that the magnitude of the 2004 outburst of UGC 4904-V1 was similar to that of a typical LBV, an LBV scenario raises two problems. It is at odds with current stellar evolutionary theory, which predicts that massive stars do not undergo core-collapse in the LBV stage, and also that the subsequent

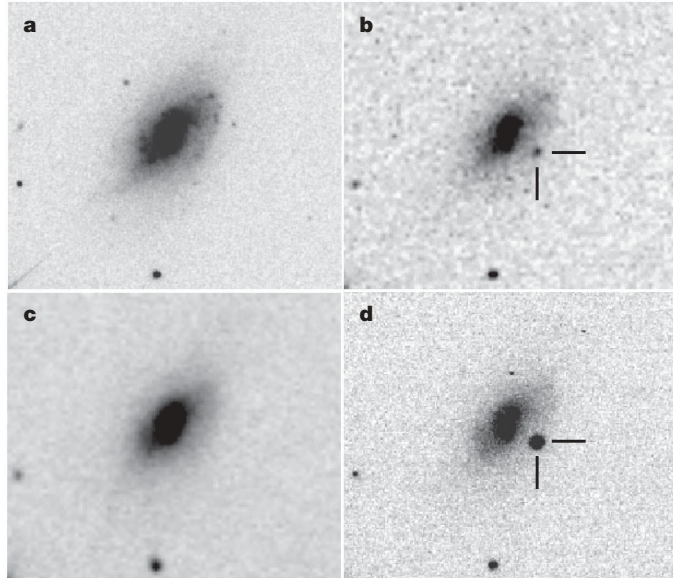


**Figure 1 | The transients UGC 4904-V1 and SN 2006jc.** Sequence of images of UGC 4904 rebinned to a pixel scale of 0.53 arcsec. **a, c**,  $r'$  band image of UGC 4904 from the Sloan Digital Sky Survey obtained on 2001 December 20. No transient is visible. **b**, Detection of UGC 4904-V1 on 2004 October 16 by K.I. (magnitude  $19.13 \pm 0.19$ ), using a 0.60-m f/5.7 reflector and Bitran-CCD (Kodak KAF 1001E). The transient was detected in five epochs between 2004 October 14 and 2004 October 23. The original image has a pixel size of 1.44 arcsec, and seeing of 2.2 arcsec. **c**, Another image obtained by K.I. (2006 September 21), showing no transient detection. **d**, R-band frame (original pixel scale of 0.473 arcsec, seeing of 2.0 arcsec) taken on 2006 October 29 with the Asiago 1.82-m Telescope equipped with AFOSC. We find that the two transients are coincident to within 0.1 arcsec, and the total error budget (including the uncertainty in the position measurements and the error of the geometric transformation) is 0.3 arcsec (see Supplementary Information). The transient UGC 4904-V1 was not detected before 2004 October 2001 or after 2004 November 2007, and it is not a moving object, as there is no apparent motion between the five epochs in which it was detected.

Wolf–Rayet star should have a lifetime of more than 200,000 years (refs 1, 2). Additionally, all the known LBVs that have undergone outbursts still have hydrogen- and helium-rich atmospheres<sup>14,16</sup> (Supplementary Information). The progenitor of SN 2006jc was different, because prominent hydrogen lines were not detected in early supernova spectra (Fig. 3). One could then propose that the progenitor star has been a Wolf–Rayet star for this timescale, and that the 2004 event was an LBV-like eruption of a Wolf–Rayet star<sup>10</sup>. In this case we need to invoke a novel explosion mechanism, as no carbon–oxygen star has ever been observed to produce such a bright outburst.

It is unquestionable that SN 2006jc is not a typical supernova, and hence this post-LBV channel is probably not the preferred one that produces type Ib or Ic supernovae, and the rarity of such events could be due to the high progenitor mass. If this scenario is true, then it has interesting implications. A star of  $60$ – $100 M_\odot$  has a carbon–oxygen core of mass  $15$ – $25 M_\odot$  as it enters the Wolf–Rayet phase<sup>1,2</sup> (Supplementary Information). The core-collapse of such an object is predicted to form a black hole by fall-back, producing a low yield of  $^{56}\text{Ni}$  and hence resulting in a very faint and under-energetic explosion<sup>17</sup>. However, although powered by the ejecta–CSM interaction, SN 2006jc is a high-luminosity event, and a plausible model for the production of a bright supernova from a black-hole-forming core is a jet-powered supernova<sup>2,17,18</sup>. Such events in helium- and hydrogen-free stars are the working models for long duration  $\gamma$ -ray bursts<sup>17</sup>.

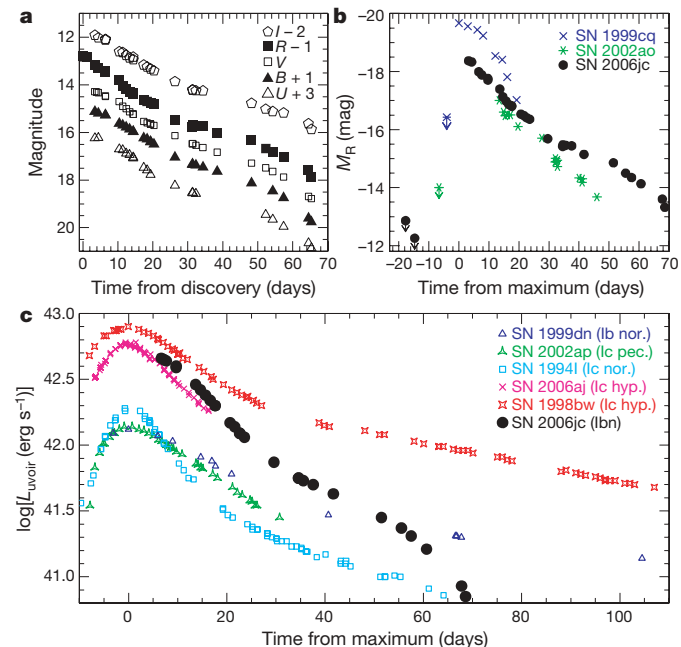


**Figure 2 | Light curve of SN 2006jc.** **a**,  $UBVRJ$  light curves of SN 2006jc. No significant colour evolution is visible from the available multiband photometry. **b**, The R-band absolute light curve of SN 2006jc is compared with unfiltered light curves of two similar interacting type Ib events: SN 1999cq and SN 2002ao (refs 10, 11, 24). The phases are estimated from the epochs of the approximated light curve maxima. The pre-explosion limit of SN 1999cq was very close ( $\sim$ 4 days) to the discovery epoch, which strongly constrains the epoch of this explosion and suggests (at least for this supernova) a very steep rise to maximum light, supporting the idea that the ejecta are strongly interacting with a CSM. **c**, Comparison between the quasi-bolometric (uvor) light curve of SN 2006jc and those of a sample of hydrogen-deficient core-collapse supernovae: SN 1999dn (normal type Ib, S.B. *et al.*, manuscript in preparation), SN 1994I (normal type Ic, ref. 25), SN 2002ap (high-velocity, moderate luminosity ('peculiar') type Ic, ref. 26), and the hypernova SN 2006aj and SN 1998bw (either associated with an X-ray flash or a  $\gamma$ -ray burst; refs 27–29 and references therein). The light curves of SN 2006jc and hypernova SN 2006aj peak in-between the luminous hypernova SN 1998bw and more normal type Ib/c supernovae, although the ejecta–CSM interaction might power significantly the observed light curve of SN 2006jc.

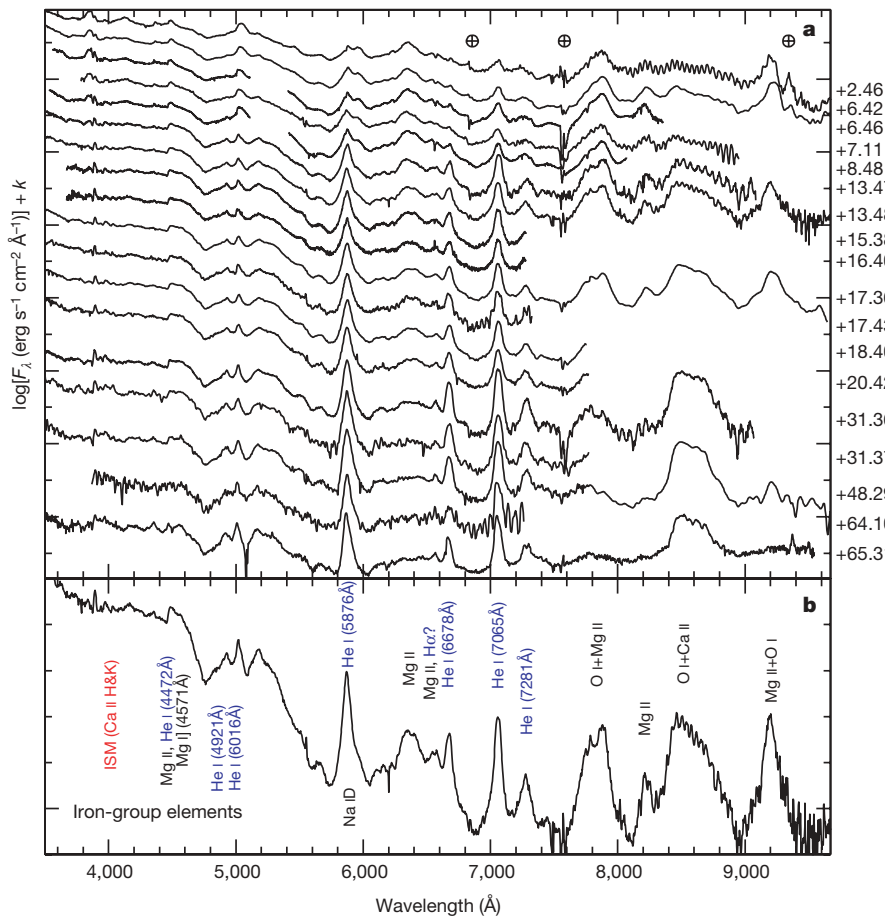


**Figure 3 | Spectra of SN 2006jc and line identification.** **a, b**, Spectral evolution of SN 2006jc (a) and identification of the main features in the spectrum at +14.38 days (b). All spectra have been shifted to the host galaxy rest wavelength. For clarity, the spectra have been shifted in the  $y$  axis (flux, in logarithmic scale) by an arbitrary constant  $k$ . The numbers on the right indicate the phase from the discovery (days). The spectra are dominated by a blue pseudo-continuum and broad lines (FWHM about 4,000–9,000  $\text{km s}^{-1}$ , depending on the phase; black labels) of intermediate-mass elements: Na I D, O I 7,774  $\text{\AA}$  and O I 9,264  $\text{\AA}$  (both blended with Mg II), Ca II IR triplet (blended with O I 8,446  $\text{\AA}$ ) and a number of Mg II lines (the most prominent being at wavelengths ( $\text{\AA}$ ) 4,481, 6,347 and 6,546; and 7,877–7,896, 8,214–8,235 and 9,218–9,244). In addition the spectra show narrower (FWHM  $\sim$ 2,200  $\text{km s}^{-1}$ ) He I emissions (blue labels), strengthening with time. Narrow, weak interstellar Ca II H&K lines are also visible (labelled in red). Moreover, the earliest spectra show some narrow unidentified emission lines in the blue region (for example, at 3,850  $\text{\AA}$ ), and a weak, narrow H $\alpha$  absorption is possibly detected, replaced by a weak component in pure emission in the latest spectra. This detection suggests that a small amount of hydrogen is present in the helium-dominated circumstellar environment of SN 2006jc. The nature of the flux excess in the blue region is unclear, possibly linked with the ejecta-CSM interaction (as observed in many type IIn supernovae, for example, SN 1997cy), but might also result from a strong contribution from Fe II lines<sup>10</sup>. Earth signs (crossed circles) mark telluric features.

As an alternative to the single star scenario, one could propose a massive binary system with two stars entering the final, violent, stages of their evolution. One of the components could have undergone a classical LBV outburst in 2004, while the companion was an evolved Wolf–Rayet star that collapsed to give SN 2006jc. The interaction of the ejecta within a complex, circumstellar environment shaped by the strong stellar winds of massive stars could explain the numerous gas

shells detected in the spectra (Supplementary Information). It has recently been suggested that  $\eta$  Carinae has a hot companion (around  $30M_{\odot}$ ), which is a nitrogen-rich late O-type or Wolf–Rayet star<sup>19</sup>. A similar scenario (a pair of  $30M_{\odot}$  and  $50M_{\odot}$  stars) was proposed for HD 5980, an LBV + Wolf–Rayet star binary in the Small Magellanic Cloud<sup>20</sup>. In neither of these cases is the Wolf–Rayet star a WC or WO, as it is still nitrogen- and helium-rich, but a more evolved system is a

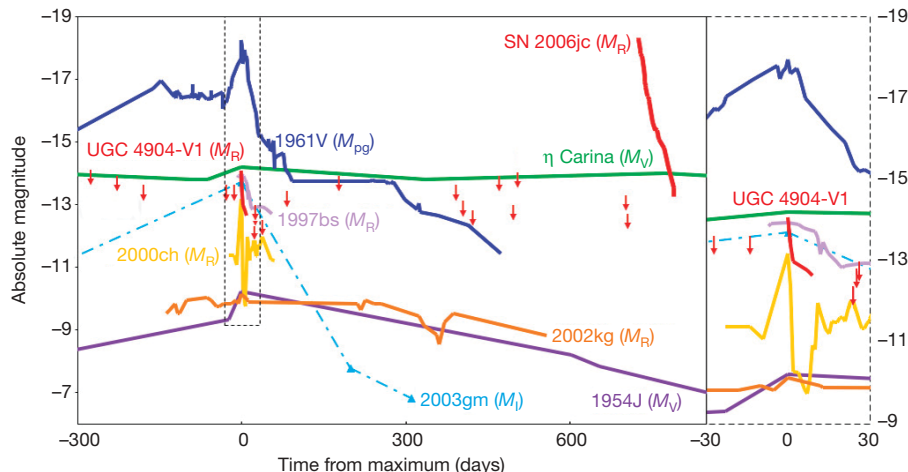


**Figure 4 | R-band light curves of UGC 4904-V1 and SN 2006jc compared with those of giant outbursts of LBVs.** The figure (without SN 2006jc) was first shown in ref. 15 (see references therein), and has since been supplemented with data from ref. 30. Although all of the extragalactic transients were originally given supernova labels, they are now commonly accepted as giant outbursts of LBVs and not core-collapse supernovae. SN 2002kg (which is the well known variable NGC 2403-V37) was not a giant outburst, but is part of fairly common S Doradus variability of LBVs. The

down-arrows are upper limits for UGC 4904-V1. Owing to many of the images of UGC 4904 having limiting magnitudes in the range 19–20, we have only detected the peak of the outburst. With a peak magnitude of about  $M_r = -14.1$  and such a sharp decline, a plausible explanation for UGC 4904-V1 is a giant LBV-like outburst (Supplementary Information), although alternatives are presented in the text. The magnitudes of each object shown in this figure are in different bands, depending on the available data.  $M_{pg}$ , photographic magnitude.

possible progenitor. Also, the system has only undergone moderate amplitude outbursts, reaching  $M_V = -10.6$ , significantly fainter than UGC 4904-V1. Theoretical models of pre-supernova evolution in massive binary systems show that type Ib/c supernovae can be produced, and a higher-mass system than that calculated in ref. 21 could be plausible, although a physically consistent scenario needs a detailed calculation.

Further observational and theoretical studies are required to determine which scenario is the more likely. The detection in very late spectra of SN 2006jc of more prominent, narrow hydrogen lines from the CSM (S.M. *et al.*, manuscript in preparation) might support a single, massive star scenario. Moreover, line profile measurements may determine the asphericity of the ejecta and explosion<sup>22</sup>, and radio modulations could eventually show that an LBV phase recently occurred<sup>23</sup>. Finally, deep high-resolution images from the Hubble Space Telescope could probe the presence of the possible binary companion, and a detailed comparison with the few similar supernovae<sup>10,11</sup> may help to provide additional clues to the progenitor scenario.

Received 24 November 2006; accepted 2 April 2007.

1. Eldridge, J. J. & Tout, C. A. The progenitors of core-collapse supernovae. *Mon. Not. R. Astron. Soc.* **353**, 87–97 (2004).
2. Heger, A. *et al.* How massive single stars end their life. *Astrophys. J.* **591**, 288–300 (2003).
3. Smartt, S. J. *et al.* Detection of a red supergiant star of a type II-plateau supernova. *Science* **303**, 499–503 (2004).
4. Nakano, S. *et al.* Possible supernova in UGC 4904. *CB Electron. Telegr.* **666** (2006).
5. Smith, N. & Owocki, S. P. On the role of continuum-driven eruptions in the evolution of very massive stars and population III stars. *Astrophys. J.* **645**, L45–L48 (2006).
6. Crotts, A. *et al.* Supernova 2006jc in UGC 4904. *CB Electron. Telegr.* **672**, 1 (2006).
7. Fesen, R., Milisavljevic, D. & Rudie, G. Supernova 2006jc in UGC 4904. *CB Electron. Telegr.* **672**, 2 (2006).
8. Benetti, S. *et al.* Supernova 2006jc in UGC 4904. *CB Electron. Telegr.* **674**, 2 (2006).
9. Modjaz, M. *et al.* Supernova 2006jc in UGC 4904. *CB Electron. Telegr.* **677**, 1 (2006).
10. Foley, R. J. *et al.* SN 2006jc: A Wolf-Rayet star exploding in a dense He-rich circumstellar medium. *Astrophys. J.* **657**, L105–L108 (2007).
11. Matheson, T. *et al.* Helium emission lines in the type Ic supernova 1999CQ. *Astron. J.* **119**, 2303–2310 (2000).
12. Filippenko, A. V. & Chornock, R. Supernovae 2002ao, 2002ap, 2002ar, 2002au, 2002av. *IAU Circ.* **7825** (2002).
13. Immler, S., Modjaz, M. & Brown, P. J. Detection of SN 2006jc in X-rays with Chandra. *Astron. Tel.* **934** (2006).
14. Davidson, K. & Humphreys, R. M. Eta Carinae and its environment. *Annu. Rev. Astron. Astrophys.* **35**, 1–32 (1997).
15. Van Dyk, S. V. *et al.* The type IIn supernova 2002kg: The outburst of a luminous blue variable star in NGC 2403. *Publ. Astron. Soc. Pacif.* (submitted); preprint at (<http://arXiv.org/astro-ph/0603025>) (2006).
16. Hillier, D. J. *et al.* On the nature of the central source in η Carinae. *Astrophys. J.* **553**, 837–860 (2001).
17. MacFadyen, A. I., Woosley, S. E. & Heger, A. Supernovae, jets, and collapsars. *Astrophys. J.* **550**, 410–425 (2001).
18. Nomoto, K. *et al.* in *A Massive Star Odyssey: From Main Sequence to Supernova* (eds van der Hucht, K., Herrero, A. & Esteban, C.) 395 (Proc. IAU Symp. 212, Astronomical Society of the Pacific, San Francisco, 2003).
19. Iping, R. C. *et al.* Detection of a hot binary companion of η Carinae. *Astrophys. J.* **633**, L37–L40 (2006).
20. Koenigsberger, G., Kurucz, R. L. & Georgiev, L. The photospheric absorption lines in the ultraviolet spectrum of the multiple system HD 5980. *Astrophys. J.* **581**, 598–609 (2002).
21. Podsiadlowski, Ph., Joss, P. C. & Hsu, J. J. L. Presupernova evolution in massive interacting binaries. *Astrophys. J.* **391**, 246–264 (1992).
22. Mazzali, P. A. *et al.* An asymmetric energetic type Ic supernova viewed off-axis, and a link to gamma ray bursts. *Science* **308**, 1284–1287 (2005).
23. Kotak, R. & Vink, J. S. Luminous blue variables as the progenitors of supernovae with quasi-periodic radio modulations. *Astron. Astrophys.* **460**, L5–L8 (2006).
24. Llapasset, J. M. SN 2002ao. (<http://www.astrosurf.com/snweb/2002/02ao/02aoMeas.htm>) (14 June 2002).
25. Richmond, M. W. *et al.* UVBRI photometry of the type Ic SN 1994I in M51. *Astron. J.* **111**, 327–339 (1996).
26. Mazzali, P. A. *et al.* The type Ic hypernova SN 2002ap. *Astrophys. J.* **572**, L61–L65 (2002).
27. Pian, E. *et al.* An optical supernova associated with the X-ray flash XRF 060218. *Nature* **442**, 1011–1013 (2006).
28. Mazzali, P. A. *et al.* A neutron-star-driven X-ray flash associated with supernova SN 2006aj. *Nature* **442**, 1018–1020 (2006).
29. Patat, F. *et al.* The metamorphosis of SN 1998bw. *Astrophys. J.* **555**, 900–917 (2001).
30. Maund, J. R. *et al.* Faint supernovae and supernova impostors: Case studies of SN 2002kg/NGC 2403–V37 and SN 2003gm. *Mon. Not. R. Astron. Soc.* **369**, 390–406 (2006).

**Supplementary Information** is linked to the online version of the paper at [www.nature.com/nature](http://www.nature.com/nature).

**Acknowledgements** This work, conducted as part of the award 'Understanding the lives of massive stars from birth to supernovae' made under the European Heads of Research Councils and European Science Foundation EURYI Awards scheme, was supported by the Participating Organisations of EURYI and the EC Sixth Framework Programme, and also the Leverhulme Trust. J.D. was supported by the NSFC. This Letter is based on observations collected at the Asiago Observatory (Italy), the 2.16-m Telescope of National Astronomical Observatories (China), the Observatoire de Haute-Provence (France), Telescopio Nazionale Galileo, the Nordst Optical Telescope, the Liverpool Telescope and the William Herschel Telescope (La Palma, Canary Islands, Spain). We thank the support astronomers working at the Liverpool Telescope and Telescopio Nazionale Galileo for performing the follow-up observations of SN 2006jc. We are grateful to M. Ganeshalingam, A. V. Filippenko, R. J. Foley and W. Li for providing the photometric data of SN 2002ao.

**Author Information** Reprints and permissions information is available at [www.nature.com/reprints](http://www.nature.com/reprints). The authors declare no competing financial interests. Correspondence and requests for materials should be addressed to A.P. (a.pastorello@qub.ac.uk).

# Tethys and Dione as sources of outward-flowing plasma in Saturn's magnetosphere

J. L. Burch<sup>1</sup>, J. Goldstein<sup>1</sup>, W. S. Lewis<sup>1</sup>, D. T. Young<sup>1</sup>, A. J. Coates<sup>2</sup>, M. K. Dougherty<sup>3</sup> & N. André<sup>4</sup>

Rotating at over twice the angular speed of Earth, Saturn imposes a rapid spin on its magnetosphere. As a result, cold, dense plasma is believed to be flung outward from the inner magnetosphere by centrifugal force and replaced by hotter, more tenuous plasma from the outer magnetosphere. The centrifugal interchange<sup>1</sup> of plasmas in rotating magnetospheres was predicted many years ago<sup>2–4</sup> and was conclusively demonstrated by observations in Jupiter's magnetosphere<sup>5–7</sup>, which—like that of Saturn (but unlike that of Earth)—is rotationally dominated. Recent observations in Saturn's magnetosphere<sup>8–10</sup> have revealed narrow injections of hot, tenuous plasma believed to be the inward-moving portion of the centrifugal interchange cycle. Here we report observations of the distribution of the angle between the electron velocity vector and the magnetic field vector ('pitch angle') obtained in the cold, dense plasma adjacent to these inward injection regions. The observed pitch-angle distributions are indicative of outward plasma flow and consistent with centrifugal interchange in Saturn's magnetosphere. Further, we conclude that the observed double-peaked ('butterfly') pitch-angle distributions result from the transport of plasma from regions near the orbits of Dione and Tethys, supporting the idea of distinct plasma tori associated with these moons<sup>11–13</sup>.

The inward plasma injections observed with the Cassini Plasma Spectrometer (CAPS) are very localized (several thousand to perhaps 20,000 km in width) events containing plasmas with higher temperatures and lower densities than their surroundings (Fig. 1). These injections are presumed to have source regions at larger distances, where plasmas are typically hotter and less dense. Within the injections the higher-energy (several keV) electrons have pitch-angle distributions characteristic of a trapped population (with fluxes peaked near 90°), while the low-energy electrons are often field-aligned, indicating the presence of magnetic-field-aligned currents.

In the colder, denser regions adjacent to the injections, the electrons have unique angular distributions, known as 'butterfly' distributions, with fluxes peaked at pitch angles falling between 0° and 90° and between 90° and 180°. The pitch angles at which the fluxes peak exhibit a striking correlation with electron energy (Fig. 2). A similar phenomenon occurs in Jupiter's magnetosphere, where butterfly distributions with flux peaks at the same pitch angle have been observed over a wide range of energies in the wake of Io. These distributions have been shown to be a unique identifier of an encounter with a localized reduced magnetic field<sup>14</sup>. The 'critical pitch angle' at which the peaks of the butterfly distributions occur corresponds to a mirror point within the weakened magnetic field at a latitude where the magnitude of the magnetic field is equal to the magnitude of the equatorial field in the upstream corotational flow at Jupiter<sup>14</sup>. For the critical-pitch-angle effect to apply, the source-region energy spectrum must be characterized by fluxes that decrease with increasing

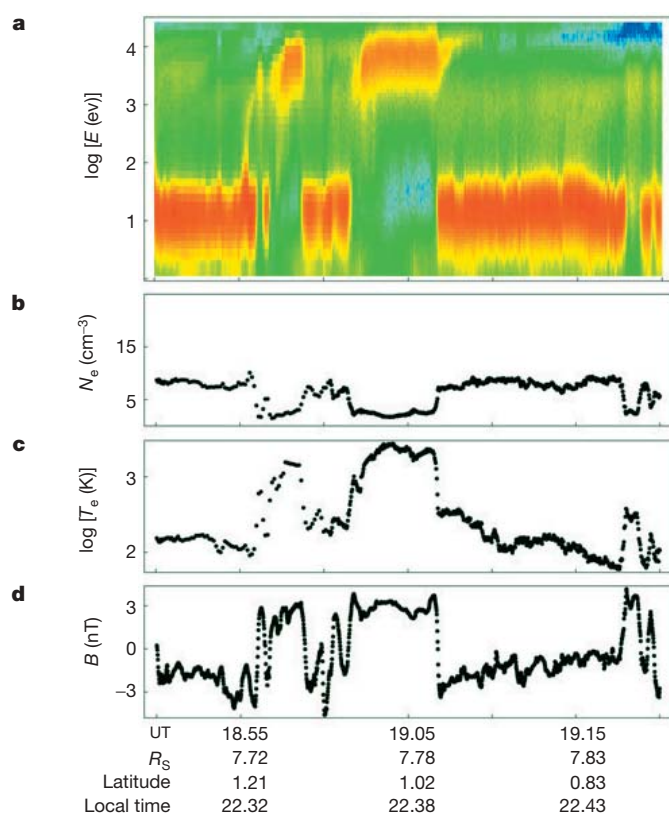


**Figure 1 | Electron and magnetic field data obtained by Cassini near the equatorial plane during the outbound leg of the orbit on 28 October 2004 (day 302).** **a**, Spectrogram of energy  $E$  versus time in UT of electron counts from the CAPS Electron Spectrometer instrument. The counts are colour-coded (high counts are red; low counts are blue) and are proportional to the electron energy flux. The pitch angle of the particles is near 90°, indicating locally trapped particles. **b**, Electron density  $N_e$  is integrated over the full CAPS Electron Spectrometer energy range from 1 eV up to 26 keV after subtraction of spacecraft photoelectrons. **c**, Electron temperature  $T_e$  calculated from the CAPS Electron Spectrometer energy-angle distributions. **d**, Deviation of the magnetic field magnitude  $B$  from the ambient values, which varied from 30.1 to 24.5 nT across the plot.  $x$  axis labels (at the bottom of the figure) show the universal time (UT), the radial distance of Cassini in units of  $R_S$ , the latitude and local time of Cassini. Two major plasma injections are evident, near 18:55 and 19:05 UT, along with other very narrow injections. In each case a clear density depression, a very large electron temperature increase, and a significant increase in magnetic field magnitude are observed. These variations are typically seen for injections close to the equatorial plane outside about  $6R_S$ , whereas the injections observed at higher latitude typically show a diamagnetic effect (a decrease in magnetic field strength) and less pronounced density depressions, while still showing the temperature increase.

<sup>1</sup>Southwest Research Institute, PO Drawer 28510, San Antonio, Texas, 78228-0510 USA. <sup>2</sup>Mullard Space Science Laboratory, Holmbury St Mary, Dorking Surrey, RH5 6NT, UK.

<sup>3</sup>Imperial College, Blackett Laboratory, London, SW7 2BZ, UK. <sup>4</sup>Research and Scientific Support Department, ESA, 2200 AG Noordwijk, The Netherlands.

energy, which is typically the case for keV-range electrons in planetary magnetospheres.

In contrast to those detected in the Io wake, the butterfly distributions observed by CAPS in Saturn's inner magnetosphere occur over a large range of radial distances, indicating that they are not associated with a radially localized weak magnetic field. The flux peaks observed at Saturn vary systematically with radial distance, suggesting that they can be traced inward to radially localized source regions of trapped electrons where the equatorial magnetic field strengths are equal to the mirror field strengths at the location of Cassini. If we assume a dipole magnetic field, the critical pitch angles for the higher-energy electrons shown in Fig. 2 are consistent with a source near the radial distance of Dione ( $6.26R_S$ , where  $R_S$  is the radius of Saturn), while those for the lower-energy electrons are consistent with a source near the radial distance of Tethys ( $4.88R_S$ ).

The difference in energy between electrons identified with Tethys and those identified with Dione may be explained in the following way. Plasma emitted from the satellites by sputtering or other processes will be immersed in a rapidly rotating magnetic field with the rotation velocity increasing with radius. The initial effect is pick-up of the ions, which will give them energies dependent on their mass, but the energies at Tethys ( $4.88R_S$ ) will be less than those at Dione by the ratio of their radii squared. Equipartition of energy between ions and electrons occurs in plasmas through various processes, including Coulomb collisions<sup>15</sup> and wave-particle interactions, with the electrons generally obtaining energies somewhat less than those of the ions.

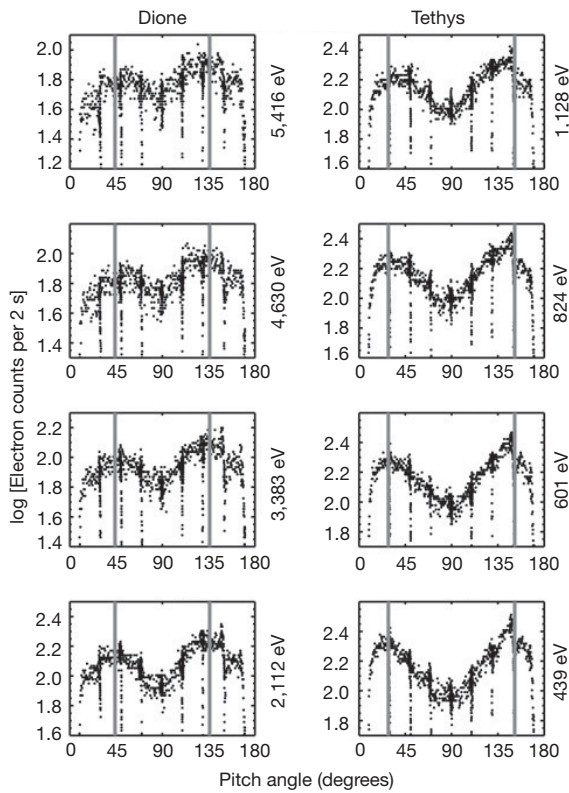


**Figure 2 | Scatter plots showing the correlation of the pitch angle of the peak electron flux with electron energy.** The logarithm of electron counts (per 2 s) is plotted against pitch angle for eight energies (noted to the right of each plot) for 19:10–19:15 UT on 28 October 2004. For the highest four energies shown, the peak fluxes all occur at similar pitch angles (near both  $45^\circ$  and  $135^\circ$ ), while at the lower four energies the peaks occur at pitch angles significantly closer to the magnetic field line (near  $30^\circ$  and  $150^\circ$ ). The vertical lines indicate these 'critical pitch angles', which correspond to source regions of trapped electrons at the orbits of Dione (left-hand column) and Tethys (right-hand column). The rapid falloffs in count rate that appear across each plot are an artefact resulting from partial shadowing of the field of view by other Cassini instruments.

To test the critical pitch-angle hypothesis, we analysed electron data obtained at the radial distance of Dione. As predicted, the data show trapped (peaked at  $90^\circ$ ) pitch-angle distributions for the higher-energy electrons and butterfly distributions for the lower-energy electrons, with peaks corresponding to a source at the orbit of Tethys (Fig. 3). An occasional dip in the  $90^\circ$  fluxes at the higher energies near Dione indicates the beginning of a weak butterfly distribution. Our modelling shows that this observation is consistent with the finite width of a possible Dione plasma torus.

As an additional test, we modelled the variation with radial distance of peak-flux pitch angles for sources at Dione and Tethys and found that the model compared favourably with the CAPS data (Fig. 4). This result, while further confirming the critical pitch-angle hypothesis, is surprising because our model does not conserve the first and second adiabatic invariants, which, for adiabatic transport in a dipole magnetic field, are expected to be conserved. Thus we also calculated the peak-flux pitch angles for outward transport from a Dione source that conserves the first and second adiabatic invariants and found that the calculated pitch angles deviate significantly from those observed (Fig. 4). (An example of a butterfly distribution that results from outward transport with both first and second adiabatic invariants conserved is described in the Supplementary Information.)

The explanation for this unexpected result may have to do with the fact that Saturn's magnetic field is not strictly dipolar even at radial distances between  $5R_S$  and  $10R_S$  (refs 16, 17). While the field approximates a dipole at middle to high latitudes, Cassini observations suggest that it could have a significant tail-like configuration at low latitudes. Examination of the magnetic signatures of numerous inward plasma injections observed by CAPS shows that only very near the equator is a dipolarization signature observed (Fig. 1), with a diamagnetic signature being seen at higher latitudes<sup>18</sup>. Because a precondition for dipolarization is the stretching of the field into a tail-like configuration that then relaxes into a more dipolar configuration, this observation of the dipolarization signatures only near the equator implies the prior presence of tail-like (and thus weaker) fields localized to the equatorial region.

As discussed above, the critical pitch angles for trapped electrons occur in regions where the magnitude of the magnetic field at the mirror points equals that of the equatorial field in the source region. At increasing radial distances these mirror points are located at higher latitudes, where the field assumes a more dipolar shape. As near-equatorial particles (those mirroring at latitudes below the critical pitch-angle mirror points) are transported outward into a weakening tail-like field, they must lose energy to conserve the first (or magnetic moment) adiabatic invariant<sup>14</sup>. On the other hand, particles mirroring at higher latitudes (above the critical pitch-angle mirror points) will lose less energy because the magnetic field strength falls off much more slowly with distance away from the

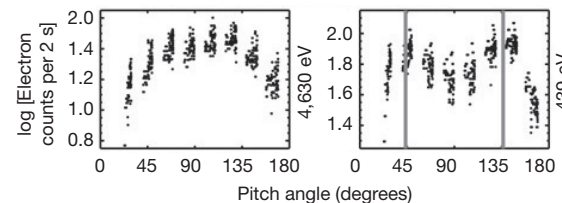


**Figure 3 | Scatter plots of electron counts versus pitch angle for two electron energies measured at the orbit of Dione.** The logarithm of counts (per 2 s) versus pitch angle plotted for two electron energies, 4,630 eV and 439 eV. The data were acquired during the interval 05:45–05:50 UT on 30 October 2005, when Cassini was at the orbital radius of Dione. Grey vertical lines in the right-hand plot denote the critical pitch angle for electrons transported from a source region of trapped electrons at the orbit of Tethys. At the higher energy (left-hand plot) the distribution is peaked near  $90^\circ$ , indicating that CAPS was measuring a trapped population at the orbital location of Dione.

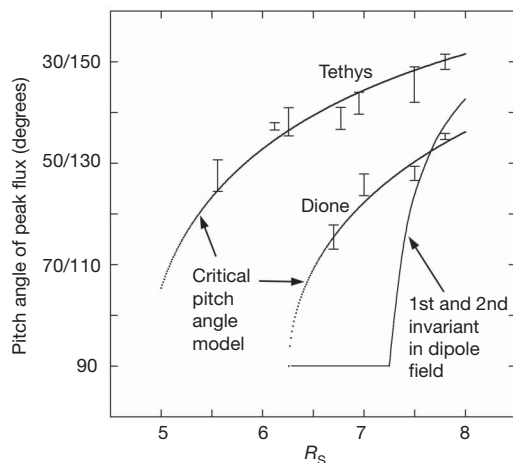


**Figure 4 | Comparison of observed and modelled peak-flux pitch angles for butterfly distributions versus radial distance from the centre of Saturn.**

For each data point, polynomial fits to five individual pitch-angle distributions observed over a five-minute period centred on the plotted radial distance were used to determine the mean and the standard deviation. Error bars indicate  $1\sigma$  standard deviation. Solid lines show the predictions of the critical pitch-angle hypothesis in an assumed dipole magnetic field for source regions at the orbits of Tethys and Dione. Energies of 2,112 eV and 439 eV were assumed for the particles originating at Dione and Tethys, respectively. The rightmost solid line shows the predictions of a model of conservation of the first and second adiabatic invariants in a dipole magnetic field for transport from a source at Dione.

presumed tail-like field that is localized near the equator. Because the electron flux in the source region is observed to decrease with increasing energy, for a given energy and location downstream from the source, the fluxes will be higher for electrons mirroring at higher latitudes than for those mirroring near the equator, thus producing the double-peaked 'butterfly' pitch-angle distribution. (A calculation of how such a scenario will lead to a butterfly distribution with peaks at the critical pitch angle is presented in the Supplementary Information.)

Another possible cause of butterfly distributions is absorption by dust particles. Because the dust in Saturn's E-ring is localized towards the equator, this absorption would be strongest for particles with low-latitude mirror points (equatorial pitch angles near  $90^\circ$ ), and moreover, the butterfly peaks would move closer to the field line with increasing distance, as observed. Even if dust absorption is the cause, the results shown in Fig. 4 would still point towards the Tethys and Dione orbits as the source regions. Certain effects of dust absorption were observed on Voyager<sup>19</sup>, but significant effects were only seen within  $5R_S$ . For this reason and because the critical pitch-angle hypothesis reproduces well the variation of the butterfly peaks with radial distance for two discrete sources, we strongly favour our simple hypothesis of adiabatic transport. Our suggestion that the observed pitch angle distributions are indicative of plasma sources at the orbits of Dione and Tethys is unique, but our observation of a general plasma outflow except for discrete injection events is supported

by other recently reported Cassini observations using different techniques<sup>20</sup>.

Received 25 August 2006; accepted 4 May 2007.

1. Kruskal, M. D. & Schwarzschild, M. Some instabilities of a completely ionized plasma. *Proc. R. Soc. Lond. A* **223**, 348–360 (1954).
2. Michel, F. C. & Sturrock, P. A. Centrifugal instability of the jovian magnetosphere and its interaction with the solar wind. *Planet. Space Sci.* **22**, 1501–1510 (1974).
3. Hill, T. W. Interchange stability of a rapidly rotating magnetosphere. *Planet. Space Sci.* **24**, 1151–1154 (1976).
4. Pontius, D. H. Jr, Hill, T. W. & Rassbach, M. E. Steady state plasma transport in a corotating-dominated magnetosphere. *Geophys. Res. Lett.* **13**, 1097–1100 (1986).
5. Bolton, S. J. *et al.* Enhanced whistler-mode emissions: signatures of interchange motion in the Io torus. *Geophys. Res. Lett.* **24**, 2123–2126 (1997).
6. Thorne, R. M. *et al.* Galileo evidence for rapid inward transport in the Io torus. *Geophys. Res. Lett.* **24**, 2131–2134 (1997).
7. Frank, L. A. & Paterson, W. R. Observations of plasmas in the Io torus with the Galileo spacecraft. *J. Geophys. Res.* **105**, 16,017–16,034 (2000).
8. Burch, J. L. *et al.* Properties of local plasma injections in Saturn's magnetosphere. *Geophys. Res. Lett.* **32**, L14S02, doi:10.1029/2005GL022611 (2005).
9. Hill, T. W. *et al.* Evidence for rotationally driven plasma transport in Saturn's magnetosphere. *Geophys. Res. Lett.* **32**, L14S10, doi:10.1029/2005GL022620 (2005).
10. Mauk, B. H. *et al.* Energetic particle injections in Saturn's magnetosphere. *Geophys. Res. Lett.* **32**, L14S05, doi:10.1029/2005GL022485 (2005).
11. Frank, L. A. *et al.* Plasma in Saturn's magnetosphere. *J. Geophys. Res.* **85**, 5695–5708 (1980).
12. Richardson, J. D., Eviatar, A. & Siscoe, G. L. Satellite tori at Saturn. *J. Geophys. Res.* **91**, 8749–8755 (1986).
13. Wahlund, J.-E. *et al.* The inner magnetosphere of Saturn: Cassini RPWS cold plasma results from the first encounter. *Geophys. Res. Lett.* **32**, L20S09, doi:10.1029/2005GL022699 (2005).
14. Thorne, R. M., Williams, D. J., Zhang, L. D. & Stone, S. Energetic electron butterfly distributions near Io. *J. Geophys. Res.* **104**, 14755–14766 (1999).
15. Rymer, A. M. *et al.* Electron sources in Saturn's magnetosphere. *J. Geophys. Res.* **112**, A02201, doi:10.1029/2006JA013017 (2007).
16. Connerney, J. E. P., Ness, N. F. & Acuna, M. H. Zonal harmonic model of Saturn's magnetic field from Voyager 1 and 2 observations. *Nature* **298**, 44–46 (1982).
17. Alexeev, I. I. *et al.* A global magnetic model of Saturn's magnetosphere and a comparison with Cassini SOL data. *Geophys. Res. Lett.* **33**, L08101, doi:10.1029/2006GL025896 (2006).
18. André, N. Magnetic signatures of plasma-depleted flux tubes in the Saturnian inner magnetosphere. *Geophys. Res. Lett.* (submitted).
19. Sittler, E. C. Jr, Ogilvie, K. W. & Scudder, J. D. Survey of low-energy plasma electrons in Saturn's magnetosphere: Voyagers 1 and 2. *J. Geophys. Res.* **88**, 8847–8870 (1983).
20. Sittler, E. C. Jr *et al.* Cassini observations of Saturn's inner plasmasphere: Saturn orbit insertion results. *Planet. Space Sci.* **54**, 1197–1210 (2006).

**Supplementary Information** is linked to the online version of the paper at [www.nature.com/nature](http://www.nature.com/nature).

**Acknowledgements** We gratefully acknowledge comments by F. Crary, B. Mauk, E. Sittler, M. Thomsen, T. Hill, and H. Waite.

**Author Contributions** J.L.B. developed the interpretation of the Cassini data and is lead author of this paper. J.G. and W.S.L. were responsible for data analysis and, respectively, for figure preparation and preparation of the text. D.T.Y., A.J.C. and M.K.D. are, respectively, the CAPS principal investigator, the CAPS Electron Spectrometer lead and the Cassini MAG principal investigator, and provided both data and analysis. N.A. contributed to the data analysis and modelling.

**Author Information** Reprints and permissions information is available at [www.nature.com/reprints](http://www.nature.com/reprints). The authors declare no competing financial interests. Correspondence and requests for materials should be addressed to W.S.L. (wlewis@swri.edu).

## LETTERS

# Demonstration of controlled-NOT quantum gates on a pair of superconducting quantum bits

J. H. Plantenberg<sup>1</sup>, P. C. de Groot<sup>1</sup>, C. J. P. M. Harmans<sup>1</sup> & J. E. Mooij<sup>1</sup>

Quantum computation requires quantum logic gates that use the interaction within pairs of quantum bits (qubits) to perform conditional operations<sup>1</sup>. Superconducting qubits may offer an attractive route towards scalable quantum computing. In previous experiments on coupled superconducting qubits, conditional gate behaviour<sup>2</sup> and entanglement<sup>3</sup> were demonstrated. Here we demonstrate selective execution of the complete set of four different controlled-NOT (CNOT) quantum logic gates, by applying microwave pulses of appropriate frequency to a single pair of coupled flux qubits. All two-qubit computational basis states and their superpositions are used as input, while two independent single-shot SQUID detectors measure the output state, including qubit–qubit correlations. We determined the gate’s truth table by directly measuring the state transfer amplitudes and by acquiring the relevant quantum phase shift using a Ramsey-like interference experiment. The four conditional gates result from the symmetry of the qubits in the pair: either qubit can assume the role of control or target, and the gate action can be conditioned on either the 0-state or the 1-state. These gates are now sufficiently characterized to be used in quantum algorithms, and together form an efficient set of versatile building blocks.

In order to use superconducting circuits in quantum computing implementations, it is necessary to find a way to implement efficient quantum logic gates on pairs of qubits. Single superconducting qubits can be designed to operate in the charge<sup>4</sup>, charge-phase<sup>5</sup>, flux<sup>6</sup> and phase<sup>7</sup> regimes. In our experiments, we use a flux qubit consisting of a superconducting loop interrupted by three Josephson junctions, which can behave as a quantum two-level system<sup>8</sup>. Varying the magnetic flux threading the loop controls the energy level separation. At exactly half a flux quantum, the two classical states carrying a clockwise and an anticlockwise persistent current are degenerate. Quantum mechanical level repulsion occurs, and the eigenstates are formed by a symmetric and an antisymmetric superposition of the classical current states. When moving away from the degeneracy point, the eigenstates approach the classical current states and produce a net magnetic field. The qubit state is manipulated using microwave pulses resonant with the level separation; the circulating currents are used to detect the state with a superconducting quantum interference device (SQUID) magnetometer.

Previously, in experiments on two interacting superconducting qubits, spectroscopy was demonstrated<sup>9–12</sup> as well as coherent qubit–qubit interaction controlled by non-adiabatic bias shifts<sup>2,3,13,14</sup>. In our experiments, we couple two flux qubits magnetically with a fixed strength, resulting in a four-level system that is tunable with the individual flux biases. Four different two-qubit operations are realized with simple microwave pulses. The sample is depicted in Fig. 1. The qubit pair is described by the hamiltonian

$$H = H_1 + H_2 + H_{12} = -\frac{1}{2}(\varepsilon_1 \sigma_z^1 + \Delta_1 \sigma_x^1 + \varepsilon_2 \sigma_z^2 + \Delta_2 \sigma_x^2) + J \sigma_z^1 \sigma_z^2 \quad (1)$$

where  $\varepsilon_i = 2I_{p,i}(\Phi_i - \frac{1}{2}\Phi_0)$  represent the magnetic energy biases with  $I_{p,i}$  the persistent currents,  $\Phi_i$  the fluxes threading the loop and  $\Phi_0$  the superconducting flux quantum,  $\Delta_i$  determine the coupling between the two classical current states of the single qubits,  $J$  is the qubit–qubit coupling energy and  $\sigma_{x,y,z}^i$  are the Pauli spin matrices. To use the flux

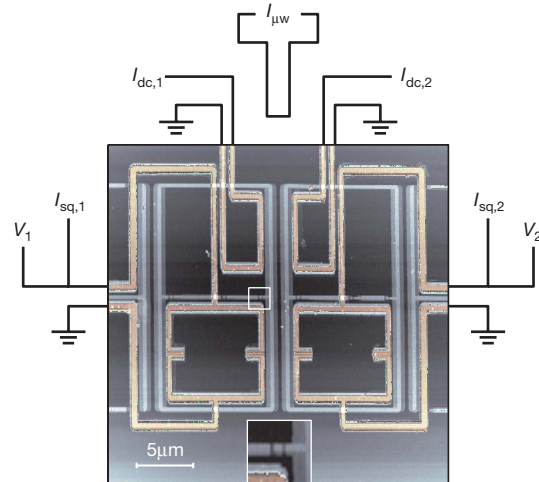


**Figure 1 | Coupled-qubits set-up.** Atomic force micrograph of the sample, showing the two ‘8’-shaped flux qubits in light grey. These are a gradiometric variety of the common three-junction flux qubit, using a trapped supercurrent in the outer uninterrupted loop to bias the qubit at its degeneracy point<sup>18</sup>. The three Josephson junctions defining the qubit are visible on the middle horizontal branches; a single junction (white box) is shown magnified in the inset. The qubits are fabricated with electron beam lithography and two-angle shadow evaporation of aluminium. Two junctions are characterized by the ratio of Josephson to charging energy,  $E_J/E_C = 36$ ; the relative area of the third is taken to be  $\alpha = 0.75$ . The persistent currents  $I_{p,i}$  and energy gaps  $\Delta_i$  are 450 nA and  $h \times 2.6$  GHz for the first qubit, and 480 nA and  $h \times 2.2$  GHz for the second. In the presented experiments, the first qubit is chosen to act as control (C) and the second as target (T). The coupling strength  $2J = h \times 400$  MHz. On top of the qubits, two SQUIDs (shown in orange), used as switching qubit-state detectors, are fabricated in a separate lithography step. They are electrically isolated from the qubits, and operated by carefully-timed sample-and-hold (5-ns and 250-ns) d.c. pulses from current sources  $I_{sq,1}$  and  $I_{sq,2}$  (ref. 6). The resulting voltages  $V_1$  and  $V_2$ , which depend on the qubit state, are detected using amplifiers and threshold detectors. Currents  $I_{dc,1}$  and  $I_{dc,2}$  bias the qubits through two small coils (shown in orange); in the experiments the energy level separations are  $\nu_C = 7$  GHz and  $\nu_T = 5$  GHz, applying currents  $I_{dc,i} \approx 10$  μA. Here the characteristic times are  $T_1 = 50$ –100 ns,  $T_{2,\text{free}} \approx 5$  ns and  $T_{2,\text{Rabi}} = 15$ –20 ns. Qubit transitions are induced magnetically using an on-chip wire connected to a 50 Ω microwave source,  $I_{\mu\text{w}}$ . The experiments are performed in a dilution refrigerator at  $T \approx 50$  mK, with all current and voltage connections carefully filtered and/or attenuated.

<sup>1</sup>Kavli Institute of NanoScience, Delft University of Technology, PO Box 5046, 2600 GA, Delft, The Netherlands.

coupling effectively, the qubits are operated far from their degeneracy points, that is  $\epsilon_i > \Delta_i$ , so the qubit energy separations are  $v_i = \sqrt{\epsilon_i^2 + \Delta_i^2} \approx \epsilon_i$ . As shown in Fig. 2a, this results in four resonance frequencies that change the state of either the first or second qubit. By way of the state-dependent circulating current, one qubit shifts the other's resonance frequency and vice versa. Consequently, all transitions are all either 0-controlled or 1-controlled operations, with 0 and 1 representing the state of the second qubit. Given the symmetry of the qubits in the pair, we are free to select either one to act as the control (C) qubit and the other as the target (T) qubit, thereby defining the computational basis  $0_C 0_T, 0_C 1_T, 1_C 0_T, 1_C 1_T$ . A resonant microwave pulse induces rotations in this basis, and its microwave phase determines the orientation of the rotation axis (see Supplementary Information). The pulse induces a quantum gate, which is characterized by a transfer matrix relating input to output states, both in amplitude and phase. For example, a microwave pulse inducing a rotation around the  $x$  axis of the  $1_C 0_T - 1_C 1_T$  transition (and thus off-resonant with respect to the  $0_C 0_T - 0_C 1_T$  transition) is expressed by the gate matrix:

$$\hat{R}_{1_C 0_T - 1_C 1_T}(\omega, \tau) = \begin{pmatrix} 1 & 0 & 0 & 0 \\ 0 & 1 & 0 & 0 \\ 0 & 0 & \cos \frac{\omega \tau}{2} & i \sin \frac{\omega \tau}{2} \\ 0 & 0 & i \sin \frac{\omega \tau}{2} & \cos \frac{\omega \tau}{2} \end{pmatrix} \quad (2)$$

where  $\tau$  is the pulse length and  $\omega$  is the Rabi frequency. This conditional rotation performs the ideal CNOT gate if  $\omega\tau = \pi$ , up to a single-qubit quantum phase shift. Here we only show measurements for this  $1_C$ -controlled excitation of the target qubit, corresponding to the usual CNOT gate. Similar results were obtained when the  $0_C$ -controlled transition was induced (see Supplementary Information) and when control and target qubits were interchanged, yielding the four transitions of different frequency. Note that with this scheme one can conveniently produce the four maximally entangled two-particle Bell states, by applying two consecutive microwave pulses. Comparable techniques have been used in nuclear magnetic resonance experiments<sup>15</sup>.

In Fig. 2d the microwave pulse scheme of the presented experiments is shown. The system is initialized by allowing it to relax to the

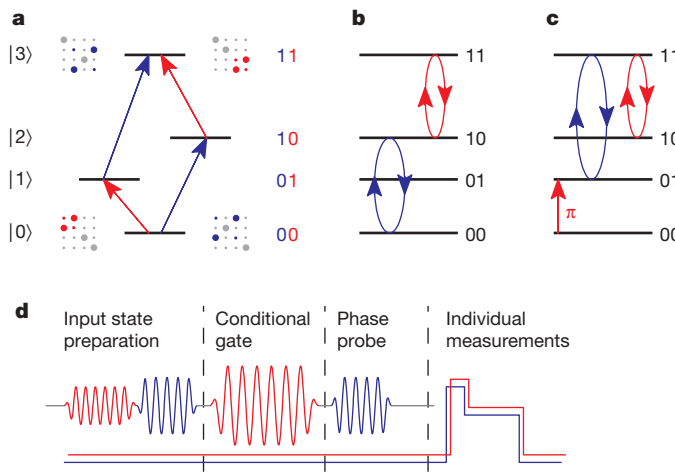


**Figure 2 | Operation of the coupled-qubits device.** **a**, Energy level diagram of the two-qubit system. The qubit transitions are indicated by blue and red arrows, and the corresponding rotation matrices are depicted schematically with the computational basis increasing from left to right and from top to bottom. **b**, Sequence of operations to determine the truth table amplitudes for superpositions of the  $0_C 0_T$  and  $1_C 0_T$  input states. **c**, As **b** but for superpositions of the  $0_C 1_T$  and  $1_C 1_T$  input states. The  $\pi$  pulse initializes the target qubit in the state  $1_T$ . **d**, General pulse sequence, displaying the applied microwave pulses and detector readout pulses.

ground state  $0_C 0_T$ , after which the desired input state is prepared. Now a two-qubit conditional gate is executed using a pulse selective to either a 0- or 1-controlled transition. Next, probe pulses can be applied to analyse the resulting density matrix. Finally, the states of the two qubits are determined simultaneously and independently using the two single-shot state detectors. Repeating this scheme  $N$  times, the result is represented by the state counts  $N_{00}, N_{01}, N_{10}$  and  $N_{11}$ , directly yielding the measured joint-probabilities  $P_{00}, P_{01}, P_{10}$  and  $P_{11}$ . In addition to the individual switching probabilities of the control and target qubit detectors,  $P_C = P_{10} + P_{11}$  and  $P_T = P_{01} + P_{11}$ , this method extracts correlation information,  $P_{C=T} = P_{00} + P_{11}$ .

To determine the output amplitudes of the CNOT gate for input superpositions of  $0_C 0_T$  and  $1_C 0_T$ , the pulse sequence depicted in Fig. 2b is used. After its creation, this state is subjected to the gate pulse resonant with the  $1_C 0_T - 1_C 1_T$  transition. In Fig. 3a, the switching probability of the control qubit detector shows the superposition created by the first pulse. Figure 3c shows that when the  $1_C$ -controlled gate pulse induces an odd number of  $\pi$  rotations it executes a CNOT gate, inverting the target qubit state only if the control qubit was in the state  $1_C$ ; for the  $0_C$  state the gate pulse is off-resonant, leaving the target qubit unaffected. Similarly, Fig. 2c illustrates the pulse sequence used to determine the matrix amplitudes for input superpositions of  $0_C 1_T$  and  $1_C 1_T$ . First, the target qubit is initialized in the  $1_T$  state by inducing a  $\pi$  rotation on the  $0_C 0_T - 0_C 1_T$  transition. The control qubit is then brought into a superposition by driving the  $0_C 1_T - 1_C 1_T$  transition, as depicted in Fig. 3b. Finally, the CNOT gate is executed with the identical microwave gate pulse as used previously for the  $0_C 0_T - 1_C 0_T$  superposition input states. Figure 3d shows that the gate only inverts the target qubit back to the state  $0_T$  if the control qubit was in the state  $1_C$ .

The truth table amplitudes follow directly from the joint-probabilities. In Fig. 4a the output state counts are depicted for the prepared computational basis input states. The measured data

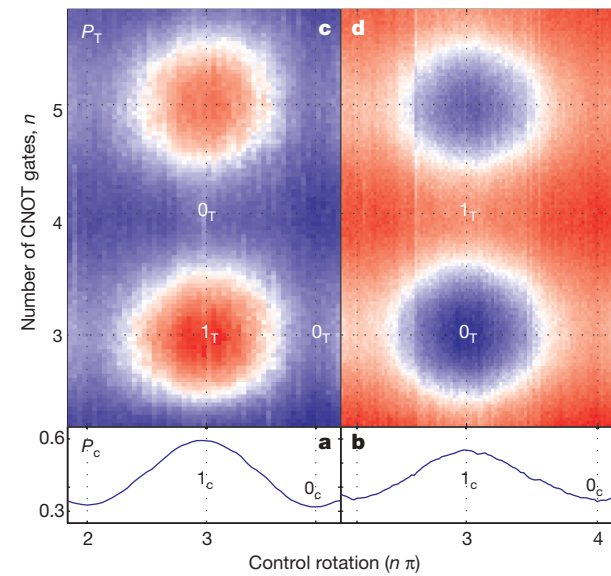


**Figure 3 |  $1_C$ -controlled gate operation.** The horizontal axis represents the control qubit rotation, and the ordinate of the colour figures sets the number of CNOT gates ( $n$ ) that was executed. The pulses needed for control and gate rotations significantly smaller than  $\pi$  were too short to generate reliably. **a, b**, Control qubit input state preparation, where  $P_C$  represents the measured switching probability of the control qubit detector. A  $2\pi$  rotation corresponds to a pulse length of 5 ns. **c, d**, Target qubit state after the CNOT pulse, where  $P_T$  represents the measured switching probability of the target qubit detector, ranging from 0.3 (blue) through 0.5 (white) to 0.7 (red). A single CNOT  $\pi$  rotation corresponds to a 3 ns pulse. **a, c**, Results for superpositions of the  $0_C 0_T$  and  $1_C 0_T$  input states, corresponding to the experimental scheme of Fig. 2b. **b, d**, Results for superpositions of the  $0_C 1_T$  and  $1_C 1_T$  input states, corresponding to the experimental scheme of Fig. 2c.

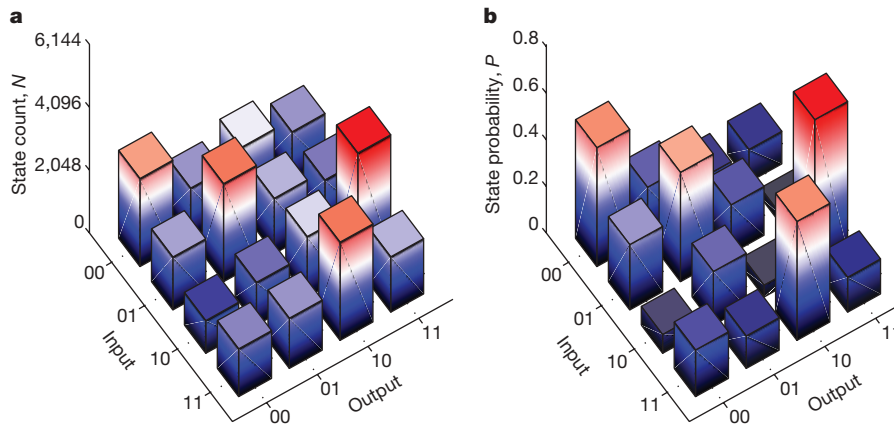


**Figure 4 | Truth table amplitudes of the CNOT quantum gate.** **a**, State counts ( $N_{00}$ ,  $N_{01}$ ,  $N_{10}$  and  $N_{11}$ ) of the detectors after  $n = 3$  CNOT rotations, for 8,192 single-shot measurements. **b**, Truth table amplitudes corrected for

qualitatively agree with the amplitude matrix of an ideal CNOT gate:

$$M_{\text{CNOT}} = \begin{pmatrix} 1 & 0 & 0 & 0 \\ 0 & 1 & 0 & 0 \\ 0 & 0 & 0 & 1 \\ 0 & 0 & 1 & 0 \end{pmatrix} \quad (3)$$

The input states  $0_{\text{C}0_{\text{T}}}$  and  $0_{\text{C}1_{\text{T}}}$  remain unaffected by the gate and translate directly to the same output state, hence the two high values on the diagonal of the matrix. For the states  $1_{\text{C}0_{\text{T}}}$  and  $1_{\text{C}1_{\text{T}}}$ , the gate inverts the target qubit, explaining the two high off-diagonal values. Figure 4a can be related to Fig. 3 by considering the points at the intersections of the dotted lines of the latter. Note that the states  $0_{\text{C}}$  and  $1_{\text{C}}$  correspond to the elements from Fig. 3 where a  $2\pi$  and  $3\pi$  rotation, respectively, were induced, which explains the comparable input state fidelities.

The major factors contributing to the deviations of Fig. 4a from the ideal transfer matrix  $M_{\text{CNOT}}$  are qubit decoherence, control errors and measurement visibility. The last is only 40% for this sample; note that more advanced SQUID detection methods have approached 90% visibility<sup>16</sup>. To compensate for this influence, we performed conditional spectroscopy measurements<sup>17</sup> that convert the normalized detector counts  $P_{ij}$  to qubit state occupation probabilities. For an ideal single-shot detector, these two sets are identical. As explained in Supplementary Information, conditional spectroscopy provides two detection mechanisms in parallel for the control qubit: one using the control qubit detector directly and a second using the excitation spectrum of the target qubit. The latter is now used as a means to calibrate the former, in this way compensating for the effect of the limited measurement visibility. Using this technique, the CNOT data of Fig. 4a are corrected, and the result is depicted in Fig. 4b. Note that the influences of decoherence and control errors are preserved. We quantify the resulting average of the logical basis amplitude fidelities by  $F = \text{Tr}(M_{\text{exp}} M_{\text{CNOT}}^T)/4$ , with  $F = 1$  for the ideal case. The experimental data from Fig. 4b can be represented by the matrix  $M_{\text{exp}}$ :

$$M_{\text{exp}} = \begin{pmatrix} 0.51 & 0.22 & 0.13 & 0.14 \\ 0.28 & 0.47 & 0.21 & 0.04 \\ 0.08 & 0.23 & 0.05 & 0.64 \\ 0.20 & 0.14 & 0.51 & 0.15 \end{pmatrix} \quad (4)$$

resulting in  $F = 0.4$ . The significant reduction of  $F$  is mostly due to the short coherence time of this particular sample. We expect to increase this number to gate performances similar to that of simple microwave-driven Rabi experiments<sup>6,16</sup>.

In order to use this gate in a quantum algorithm, the phase factors of the amplitudes of  $M_{\text{exp}}$  at the positions of non-zero elements of

measurement visibility using conditional spectroscopy measurements. The average gate fidelity equals  $F = 0.4$ .

$M_{\text{CNOT}}$  have to be determined. Using a Ramsey-like interference experiment on  $n$  consecutive CNOT gates, we show that these phase shifts agree with the driven Rabi evolution. Equation (2) predicts that for  $n = 2$  CNOT gates (that is,  $\omega\tau = 2\pi$ ) a PHASE gate is executed which inverts the phase of the states  $1_{\text{C}0_{\text{T}}}$  and  $1_{\text{C}1_{\text{T}}}$  relative to the states  $0_{\text{C}0_{\text{T}}}$  and  $0_{\text{C}1_{\text{T}}}$ . The scheme used to measure this shift is depicted in Fig. 5b. First a  $\frac{1}{2}\pi$  pulse with a fixed microwave phase is applied, bringing the control qubit into an equal weight superposition of states  $0_{\text{C}}$  and  $1_{\text{C}}$ . Next the CNOT gates are executed. The states before and after the gates are then interfered by means of a second  $\frac{1}{2}\pi$  probe pulse, of which the microwave phase  $\phi$ , corresponding to the rotation axis, is varied. In Fig. 5a the extra quantum phase between the states  $0_{\text{C}0_{\text{T}}}$  and  $1_{\text{C}0_{\text{T}}}$  is depicted. As expected, the Ramsey fringe is inverted by the quantum phase shift of  $180^\circ$  induced by a full Rabi cycle, thus executing a PHASE gate. Experimentally we find, in addition to the quantum phase, a second shift which is due to

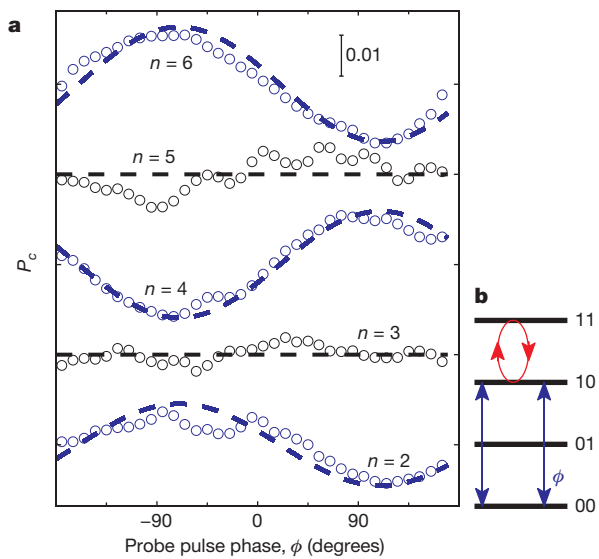


**Figure 5 | Quantum phase induced after  $n = 2$ –6 CNOT operations.** **a**, Phase probing of the control qubit with the relative microwave phase of the second Ramsey  $\frac{1}{2}\pi$  pulse along the horizontal axis. After an odd number  $n$  of CNOT gates, the system population is in an entangled superposition of the states  $0_{\text{C}0_{\text{T}}}$  and  $1_{\text{C}1_{\text{T}}}$  (Bell state), extinguishing the Ramsey interference pattern. An even number of gates executes  $n/2$  PHASE gates, and returns the system to a disentangled state, restoring the Ramsey signal. The  $180^\circ$  phase shift that occurs between even traces with  $\Delta n = 2$  agrees with the description of driven Rabi evolution. **b**, The sequence of operations used to acquire the quantum phase shift of the CNOT gates.

off-resonant effects of the CNOT microwave pulse on the control qubit transition. It is distinguished from the quantum phase by performing a second measurement with exactly the same pulse sequence with the target qubit detuned from any relevant frequency. In this case, the CNOT gate pulse only induces the off-resonant  $z$ -rotation of the control qubit. We find that this effect is nearly linear in driving power and it is compensated for in Fig. 5a, leaving only the genuine quantum phase shift.

In conclusion, we have implemented the complete set of four two-qubit CNOT gates in a symmetric pair of superconducting flux qubits. Complemented with longer coherence times<sup>6,16</sup> and optimized detector visibility<sup>16</sup>, the presented gates enable experiments on two-qubit quantum algorithms and solid-state qubit entanglement using the four Bell states. This scheme, combined with controllable coupling<sup>12</sup>, forms an attractive and generic approach to the implementation of solid-state quantum computing.

Received 21 February; accepted 26 April 2007.

1. Nielsen, M. A. & Chuang, I. L. *Quantum Computation and Quantum Information* (Cambridge Univ. Press, Cambridge, 2000).
2. Yamamoto, T., Pashkin, Yu. A., Astafiev, O., Nakamura, Y. & Tsai, J. S. Demonstration of conditional gate operation using superconducting charge qubits. *Nature* **425**, 941–944 (2003).
3. Steffen, M. et al. Measurement of the entanglement of two superconducting qubits via state tomography. *Science* **313**, 1423–1425 (2006).
4. Nakamura, Y., Pashkin, Yu. A. & Tsai, J. S. Coherent control of macroscopic quantum states in a single-Cooper-pair box. *Nature* **398**, 786–788 (1999).
5. Vion, D. et al. Manipulating the quantum state of an electrical circuit. *Science* **296**, 886–889 (2002).
6. Chiorescu, I., Nakamura, Y., Harmans, C. J. P. M. & Mooij, J. E. Coherent quantum dynamics of a superconducting flux qubit. *Science* **299**, 1869–1871 (2003).
7. Martinis, J. M., Nam, S., Aumentado, J. & Urbina, C. Rabi oscillations in a large Josephson-junction qubit. *Phys. Rev. Lett.* **89**, 117901 (2002).
8. Mooij, J. E. et al. Josephson persistent current qubit. *Science* **285**, 1036–1039 (1999).
9. Berkley, A. J. et al. Entangled macroscopic quantum states in two superconducting qubits. *Science* **300**, 1548–1550 (2003).
10. Majer, J. B., Paauw, F. G., Ter Haar, A. C. J., Harmans, C. J. P. M. & Mooij, J. E. Spectroscopy on two coupled superconducting flux qubits. *Phys. Rev. Lett.* **94**, 090501 (2005).
11. Grajcar, M. et al. Four-qubit device with mixed couplings. *Phys. Rev. Lett.* **96**, 047006 (2006).
12. Hime, T. et al. Solid-state qubits with current-controlled coupling. *Science* **314**, 1427–1429 (2006).
13. Pashkin, Yu. A. et al. Quantum oscillations in two coupled charge qubits. *Nature* **421**, 823–826 (2003).
14. McDermott, R. et al. Simultaneous state measurement of coupled Josephson phase qubits. *Science* **307**, 1299–1302 (2005).
15. Cory, D. G., Price, M. D. & Havel, T. F. Nuclear magnetic resonance spectroscopy: An experimentally accessible paradigm for quantum computing. *Physica D* **120**, 82–101 (1998).
16. Lupascu, A. et al. Quantum non-demolition measurement of a superconducting two-level system. *Nature Phys.* **3**, 119–125 (2007).
17. Ter Haar, A. C. J. *Single and Coupled Josephson Junction Quantum Bits*. PhD thesis, Delft Univ. Technology (2005).
18. Majer, J. B., Butcher, J. R. & Mooij, J. E. Simple phase bias for superconducting circuits. *Appl. Phys. Lett.* **80**, 3638–3640 (2002).

**Supplementary Information** is linked to the online version of the paper at [www.nature.com/nature](http://www.nature.com/nature).

**Acknowledgements** We thank L. M. K. Vandersypen and S. Lloyd for discussions, and R. N. Schouten and C. M. Huizinga for technical assistance. This work was supported by the Dutch organization for Fundamental Research on Matter (FOM), the EU projects SQUBIT2 and EuroSQIP, and the Dutch National Initiative on Nano Science and Technology, NanoNed.

**Author Information** Reprints and permissions information is available at [www.nature.com/reprints](http://www.nature.com/reprints). The authors declare no competing financial interests. Correspondence and requests for materials should be addressed to J.H.P. (j.h.plantenberg@tudelft.nl) and J.E.M. (j.e.mooij@tudelft.nl).

## LETTERS

# Evidence for an ancient martian ocean in the topography of deformed shorelines

J. Taylor Perron<sup>1</sup>†, Jerry X. Mitrovica<sup>2</sup>, Michael Manga<sup>1</sup>, Isamu Matsuyama<sup>3</sup> & Mark A. Richards<sup>1</sup>

A suite of observations suggests that the northern plains of Mars, which cover nearly one third of the planet's surface, may once have contained an ocean<sup>1–7</sup>. Perhaps the most provocative evidence for an ancient ocean is a set of surface features that ring the plains for thousands of kilometres and that have been interpreted as a series of palaeoshorelines of different age<sup>1,7</sup>. It has been shown, however, that topographic profiles along the putative shorelines contain long-wavelength trends with amplitudes of up to several kilometres<sup>4,5,8</sup>, and these trends have been taken as an argument against the martian shoreline (and ocean) hypothesis<sup>8</sup>. Here we show that the long-wavelength topography of the shorelines is consistent with deformation caused by true polar wander—a change in the orientation of a planet with respect to its rotation pole—and that the inferred pole path has the geometry expected for a true polar wander event that postdates the formation of the massive Tharsis volcanic rise.

Parker *et al.*<sup>1,3</sup> and Clifford and Parker<sup>7</sup> used an array of geologic and topographic features to identify several possible palaeoshorelines near the margins of the northern plains of Mars. Two of these can be traced without major interruptions for thousands of kilometres (Fig. 1): the Arabia shoreline (contact 1 of refs 1 and 3), which coincides roughly with the dichotomy in crustal thickness between the northern and southern hemisphere, and the Deuteronilus shoreline (contact 2 of refs 1 and 3), which is inferred to be younger because it is encircled by the Arabia shoreline and is less degraded. However, subsequent studies have challenged the notion that these features are shorelines<sup>9</sup>. The most basic objection stems from the observation that topographic profiles along the contacts do not follow surfaces of equal gravitational potential (that is, sea level)<sup>4,5,8</sup>, as the margins of a standing body of water should. In particular, the contacts contain significant long-wavelength trends, with amplitudes of  $\sim 2.5$  km for Arabia and  $\sim 0.7$  km for Deuteronilus (Fig. 1).

The antiquity of the putative shorelines (at least 2 billion years (Gyr), the age of most of the northern plains surface<sup>10</sup>) allows for the possibility that they have been subject to long-wavelength, large-amplitude deformation since their formation. On Earth, true polar wander—TPW, the reorientation of the planet relative to its rotation pole—has been implicated in very-long-wavelength sea-level variations with timescales exceeding  $10^6$ – $10^8$  years (refs 11, 12). In the following, we investigate whether TPW also provides a plausible explanation for the observed deformation of the Arabia and Deuteronilus contacts on Mars. That is, we seek a TPW path that is consistent with the displacements of these contacts away from an ancient equipotential surface, and that is compatible with the basic physical principles governing the rotational dynamics of a terrestrial planet.

The present-day figure of Mars provides an important constraint on the expected geometry of any TPW event that postdates the

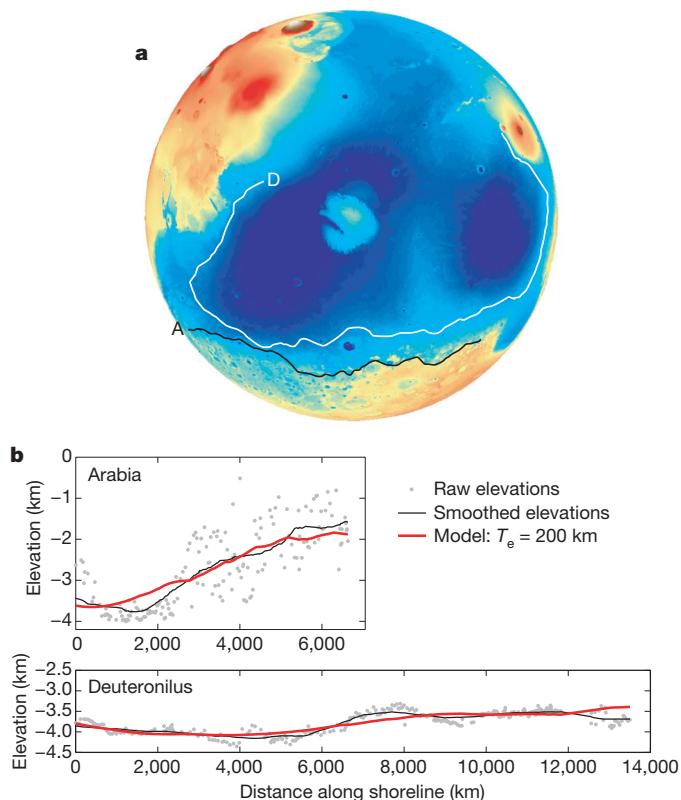


**Figure 1 | Possible palaeoshorelines on Mars.** **a**, Map of the northern hemisphere of Mars showing the portions of the hypothesized Arabia (black line A) and Deuteronilus (white line D) shorelines used in our analysis. Shoreline locations are from Carr and Head<sup>8</sup>. Orthographic spherical projection centred on the north pole. To avoid joining contacts that may have been formed at different times or by different processes, we used the longest section of each shoreline that can be traced continuously. This also avoids portions of the shorelines that may have been modified by more recent processes, such as erosion and sedimentation near the outflow channels in Chryse Planitia, crustal intrusion near Olympus Mons and west Tempe Terra, and sedimentary infilling in Isidis. **b**, Topographic profiles along the Arabia and Deuteronilus shorelines, beginning at locations A and D. The points are Mars Orbiter Laser Altimeter (MOLA) elevations reported by Carr and Head<sup>8</sup>, and the black lines are 2,000 km moving averages. The short-wavelength scatter arises at least in part from generalization of the mapped shorelines in areas of complex topography<sup>8</sup>, and detailed examination of these regions<sup>30</sup> suggests that the actual short-wavelength variations in elevation are small. Vertical and horizontal scales are the same for both profiles. Elevations are relative to the present-day 6 mbar geoid. Red lines are fits of equation (3) to the unsmoothed shoreline elevations for  $T_e = 200$  km (see Methods and Table 1).

<sup>1</sup>Department of Earth & Planetary Science, University of California, Berkeley, California 94720, USA. <sup>2</sup>Department of Physics, University of Toronto, Ontario M5S 1A7, Canada.

<sup>3</sup>Department of Terrestrial Magnetism, Carnegie Institution of Washington, Washington DC 20015, USA. <sup>†</sup>Present address: Department of Earth and Planetary Sciences, Harvard University, Cambridge, Massachusetts 02138, USA.

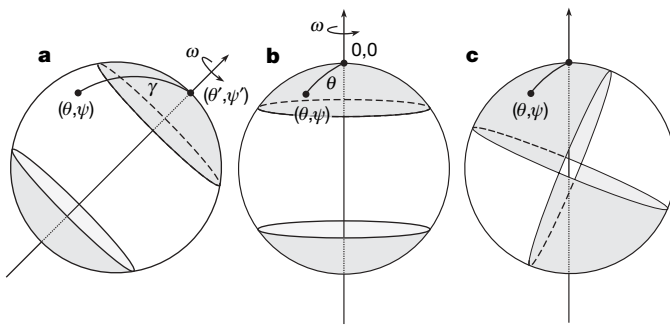


**Figure 2 | Changes in topography due to TPW.** **a** and **b** show the geographically variable component of the centrifugal potential for a TPW event that displaces the north pole of a planet with rotation rate  $\omega$  from some original position  $(\theta', \psi')$  (**a**) to the present orientation (**b**). In each state, the centrifugal potential is defined by a degree-two, order-zero spherical harmonic (that is, an oblateness term) plus a constant term, as illustrated by the shading. The change in the potential, and the associated change in topography, is characterized by a degree-two, order-one ‘quadrilateral’ geometry (**c**). These changes are zero along two great circles perpendicular to the pole path. The first great circle includes the point halfway along the (great circle) arc joining the initial and present pole position, and the second great circle is perpendicular to the first. The perturbation reaches a maximum value at four sites along the great circle that includes the pole path,  $45^\circ$  from the zeroes. The amplitude of the perturbation in the potential is a function of the displacement of the pole, while the topographic deflection associated with this perturbation is also a function of the thickness of the elastic lithosphere  $T_e$  (see Methods). The point  $(\theta, \psi)$  represents an observation site fixed to the surface geography. All geographic coordinates are relative to the final pole location.

formation of the Arabia and Deuteronilus contacts. The long-term motion of a planet’s rotation axis is controlled by the orientation of the non-hydrostatic geoid at spherical harmonic degree two<sup>13,14</sup>. On Mars, the degree-two, non-hydrostatic geoid is dominated by the Tharsis rise<sup>15</sup>, an immense volcanic construct centred slightly north of the equator<sup>16</sup>. The emplacement of an excess mass such as Tharsis will drive TPW that brings it to a position closer to the equator<sup>13</sup>, although this tendency may be inhibited by the presence of an elastic lithosphere<sup>14,17</sup> (see Supplementary Information). Equivalently, an excess mass near the equator will also resist a reorientation that would move it further from this position. Thus, any TPW of Mars occurring after the emplacement of Tharsis should, if driven by a load smaller than Tharsis, be constrained to follow a path that keeps Tharsis near the equator; such a path would be a great circle  $90^\circ$  from the centre of Tharsis<sup>17</sup>.

If a TPW event deformed the Arabia and Deuteronilus contacts, it would probably have been constrained to this geometry, because the contacts appear to be younger than Tharsis. The maps of Parker *et al.*<sup>1</sup> and Clifford and Parker<sup>7</sup> indicate that the Deuteronilus contact, and possibly a section of the Arabia contact, follows the outer margin of the Olympus Mons aureole, one of the youngest features on the Tharsis rise. The observation that the outflow channels in Chryse and Amazonis Planitia, carved by floods that are the most likely source of ocean water<sup>2,5,6</sup>, have eroded the outer margins of Tharsis further supports this ordering of ages.

With this physics in mind, we next turn to a direct estimate of palaeopole locations based on the assumption that the contacts are indeed shorelines and that their long-wavelength deformation

(Fig. 1) is due to TPW. Polar motion leads to a geographically variable change in a planet’s solid surface and geoid (sea surface). On a planet with an elastic lithosphere, these deflections will differ, even after all viscous stresses are relaxed, leading to a non-uniform change in sea level, and therefore also surface topography. The geometry of TPW-induced changes in topography<sup>11,12</sup> is illustrated schematically in Fig. 2. Our search for the palaeopoles followed the procedure described in the Methods. For each shoreline, we identified the palaeopole location that minimizes the misfit between the observed deformation along the contact and the predicted topographic response to the change in centrifugal potential. The topographic response was computed using fluid Love number theory. Table 1 lists the best-fit palaeopoles for various values of the lithospheric thickness  $T_e$  and Fig. 3 plots these locations for the specific case  $T_e = 200$  km. The fits we obtained (Table 1; thick model line in Fig. 1a for  $T_e = 200$  km) demonstrate that deformation associated with TPW can accurately reconcile the observed long-wavelength trends in both shorelines.

These palaeopoles are remarkable for three main reasons. First, the palaeopoles imply roughly  $30$ – $60^\circ$  of net TPW since the formation of the Arabia shoreline and  $5$ – $25^\circ$  since the formation of the Deuteronilus shoreline. These TPW angles are consistent with the relative ages of the shorelines, in the sense that the younger Deuteronilus shoreline corresponds to a pole location closer to the present-day pole. The location of the Arabia palaeopole implies that the oldest ocean was centred in the tropics rather than in the north polar region. Second, the best-fit palaeopoles for both shorelines lie within a few degrees of the same great circle (which passes through the present-day poles along the  $335^\circ$  E meridian), the expected path for TPW driven by an axisymmetric load<sup>13</sup>. This alignment is unlikely to occur by coincidence: the probability of randomly placed points falling this close to the same meridian, and in the appropriate age progression, is less than 0.0025. Nor is the alignment of the palaeopoles likely to be an artefact of background trends in Mars’ large-scale topography, given the large difference in amplitude (Fig. 1) between shoreline features that are in close proximity to one another. Finally, the great circle path through the palaeopoles is approximately  $90^\circ$  from the centre of the Tharsis rise ( $6.7^\circ$  N,  $248.3^\circ$  E; ref. 16, Fig. 3). As discussed above, this is the expected path of a post-Tharsis TPW event. The probability of randomly placed points falling this close to a great circle  $90^\circ$  from Tharsis is less than 0.0001.

What is the size and orientation of the post-Tharsis load necessary to drive our inferred TPW event? The answer to this question depends on the extent to which Tharsis itself perturbed the rotation pole (see Supplementary Information for a detailed discussion of this point, as summarized below). If the development of Tharsis moved the pole to a location near the great circle path inferred from the shorelines’ deformation (Fig. 3), then the equations governing rotational stability suggest that the displacement of the pole was either very small or nearly  $90^\circ$  (refs 14, 17); that is, Tharsis originally formed in either a nearly equatorial or nearly polar location. The former, small Tharsis-driven TPW solution precludes the possibility that surface mass loads were responsible for the post-Tharsis TPW that deformed the shorelines (Fig. 3, Table 1), and in this case internal loads associated with mantle convection were the probable driving mechanism for the TPW. In contrast, if Tharsis drove a large excursion of the pole<sup>18,19</sup>, a scenario less favoured in terms of the present-day figure of Mars (see Supplementary Information), then surface loads could have been sufficient to drive the subsequent TPW. In this

**Table 1 | Fluid Love numbers and best-fit palaeopole locations**

$T_e$ (km)	$h_f$	$(1 + k_f)$	Arabia			Deuteronilus		
			Latitude, longitude	$Z$ (km)	$\sigma_{r.m.s.}$ (km)	Latitude, longitude	$Z$ (km)	$\sigma_{r.m.s.}$ (km)
100	1.928	2.053	30, 332	-2.55	0.725	66, 340	-3.70	0.155
200	1.663	1.899	40, 334	-2.25	0.619	79, 337	-3.70	0.159
300	1.517	1.817	49, 332	-2.15	0.595	82, 327	-3.75	0.160
400	1.330	1.714	58, 327	-2.15	0.582	84, 326	-3.75	0.160

scenario, physical considerations suggest that the mass load(s) would lie near the great circle that includes our inferred TPW path (Fig. 3), that is, a path that keeps the pole  $\sim 90^\circ$  from Tharsis.

Given the challenge of identifying evidence of ancient internal loads that may no longer have an observable signature, we briefly review candidate surface loads for the large Tharsis-driven TPW scenario. The gravity signatures of most major impact basins—such as the Argyre basin (Fig. 3), which lies along the inferred great circle path—indicate that they are not significant mass anomalies<sup>15,20</sup>, and are therefore unlikely to have influenced the location of Mars' rotation pole. In contrast, the Elysium volcanic province and the Utopia impact basin (Fig. 3) are characterized by significant gravity highs<sup>15</sup>, the latter owing to infilling by a large volume of material<sup>21</sup>, and both lie on or near the great circle path. It is also interesting to note that the centroids of the Arabia and Deuteronilus palaeobasins (Fig. 3), which we calculated by subtracting the modelled deformation from the

present topography, lie very close to the great circle defined by our inferred TPW path. Thus, loading and unloading of these basins with water and sediment might also have influenced the pole's position along this path, although the magnitude of this effect would depend on the geometry of the load redistribution (see Supplementary Information).

Other processes may have contributed to the long-wavelength, large-amplitude topographic trends observed in the Arabia and Deuteronilus contacts. For example, the flexural response to the removal of the oceans would have altered the shoreline topography<sup>22</sup>, but numerical calculations indicate that the amplitude of this response would be far too small to explain the observed trends or to affect the best-fit palaeopole locations significantly (see Supplementary Information). We also used similar numerical procedures to predict the flexural response to the development of the Tharsis rise. In this case, the amplitude can be significant<sup>23</sup>, but the predicted trend, which diminishes with distance from Tharsis, does not match the elevation profile of either shoreline. Of course, this reasoning is also consistent with the conclusion that Tharsis was largely emplaced before the TPW episode we have invoked to explain the shoreline deformation.

The effect of internal loading on the observed shoreline deformation, either through the direct effect of dynamic topography<sup>24,25</sup> or via TPW-driven deformation, is difficult to assess. The greatest possible age difference between the Arabia shoreline, which may be as old as  $\sim 4$  Gyr (ref. 7), and the Deuteronilus shoreline, which encircles the Hesperian age<sup>10</sup> Vastitas Borealis Formation and is therefore at least  $\sim 2$  Gyr old, is  $\sim 2$  Gyr, and the diminution with time of the observed long-wavelength trends is roughly a factor of four (Fig. 1). Thus, dynamic topography would have had to diminish in amplitude by a factor of four over a period of at most 2 Gyr, and subsequently a much smaller amount over a period of at least 2 Gyr. However, a transient convective event, such as wholesale overturn of the mantle due to thermochemical instability<sup>26</sup>, might well attenuate in intensity on the timescale separating the Arabia and Deuteronilus shorelines, and thus contribute to the observed shoreline topography either directly through dynamic topography or indirectly by inducing TPW. As noted above, internal loading would be required to explain the inferred TPW path in Fig. 3 in the event that the growth of Tharsis drove relatively little TPW.

The long-wavelength deformation of the Arabia and Deuteronilus contacts has been used as a primary argument against their interpretation as shorelines, and has cast doubt on the idea that large standing bodies of water once existed on Mars. Our results support the hypothesis that the present topography of Mars, as sampled by the contacts, may not be representative of the topography at the time these features were formed. In particular, the difference is consistent with a TPW path that matches the expected rotational dynamics of Mars. The plausibility of an ancient northern ocean suggests several possible features that should serve as a focus for current and future Mars exploration, including the preservation of coastal and submarine sedimentary features such as transgressive-regressive sequences and turbidites, and the presence of relict ice in the sediments of the northern lowlands.

## METHODS

We use fluid Love number theory to calculate the topographic response to a TPW event. Consider the initial rotational state shown in Fig. 2a, where  $(\theta', \psi')$  are the colatitude and east longitude of the ancient north rotation pole. The centrifugal potential in this configuration at an arbitrary observation site  $(\theta, \psi)$  is given by<sup>27</sup>:

$$\phi(\theta, \psi) = \frac{1}{3} \omega^2 a^2 - \frac{1}{3} \omega^2 a^2 P_{2,0}(\cos \gamma) \quad (1)$$

where  $\omega$  and  $a$  are the rotation rate and mean radius, and  $\gamma$  is the angular distance between the observation site and the rotation pole (Fig. 2a). The function  $P_{2,0}$  is the unnormalized degree-two, order-zero Legendre polynomial:

$$P_{2,0}(\cos \eta) = \frac{1}{2} (3 \cos^2 \eta - 1).$$

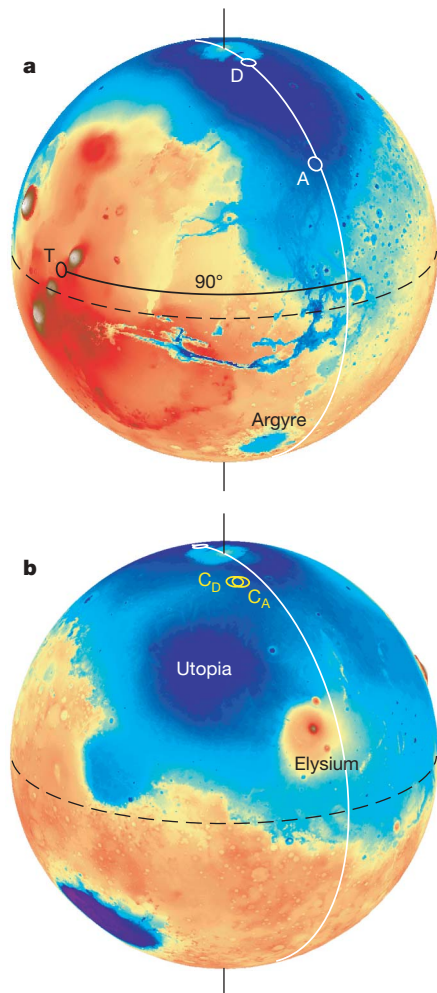


**Figure 3 | TPW path that reconciles shoreline deformation.** **a**, Best-fit palaeopoles inferred from the topography of the Arabia and Deuteronilus shorelines (small white circles labelled A and D) for  $T_e = 200$  km (see Methods and Table 1), a value close to most recently published estimates for Mars' lithospheric thickness<sup>25,28,29</sup>. The palaeopoles fall along a great circle (white line) that follows the  $335^\circ$  E meridian. This great circle is nearly perpendicular to the Tharsis rise, as shown by the black line extending  $90^\circ$  east from the centre of Tharsis (black circle T). Palaeopoles for other values of  $T_e$ , which fall along the same great circle, are listed in the Methods. Orthographic spherical projection centred at  $20^\circ$  N,  $30^\circ$  E. **b**, View from the opposite side of Mars, showing the depth-weighted centroids of the Arabia ( $C_A$ ) and Deuteronilus ( $C_D$ ) palaeo-ocean basins. Orthographic spherical projection centred at  $20^\circ$  N,  $210^\circ$  E. Locations of the Argyre and Utopia impact basins and the Elysium volcanic rise are labelled. The present-day equator (dashed line) and rotation poles are shown in both panels.

Assuming no change in  $\omega$ , the perturbation in the centrifugal potential at  $(\theta, \psi)$  as the rotation vector wanders from the initial orientation to the present one (Fig. 2b) is:

$$A(\theta, \psi) = \frac{1}{3} \omega^2 a^2 [P_{2,0}(\cos \gamma) - P_{2,0}(\cos \theta)] \quad (2)$$

Equation (2), represented graphically in Fig. 2c, describes the geometry of the topographic response to TPW. The amplitude of the response is<sup>12</sup>:

$$\Delta T(\theta, \psi) = \frac{A(\theta, \psi)}{g} [h_f - (1 + k_f)] + Z \quad (3)$$

where  $g$  is the surface gravitational acceleration, the parameters  $h_f$  and  $k_f$  are the degree-two fluid  $h$  and  $k$  tidal Love numbers, and  $Z$  is a constant included because the sea surface potential at the time of shoreline formation is not necessarily the same as the potential that defines the present geoid. The fluid Love numbers are functions of Mars' density structure<sup>28</sup> and lithospheric thickness. Table 1 lists calculated values of  $h_f$ , which governs the solid surface displacement, and  $(1 + k_f)$ , which governs the geoid or sea surface displacement, as a function of the elastic thickness of the lithosphere  $T_e$ .

For each shoreline, we identified the palaeopole location and the value of  $Z$  that minimize the root-mean-square deviation ( $\sigma_{r.m.s.}$ ) between equation (3) and the unsmoothed shoreline topography in Fig. 1. Best-fit palaeopoles and  $\sigma_{r.m.s.}$  values for  $100 \text{ km} \leq T_e \leq 400 \text{ km}$  (a range that encompasses most estimates for Mars<sup>25,28,29</sup>) are listed in Table 1.

Received 23 November 2006; accepted 18 April 2007.

1. Parker, T. J., Saunders, R. S. & Schneeberger, D. M. Transitional morphology in west Deuteronilus Mensae, Mars: Implications for modification of the lowland/upland boundary. *Icarus* **82**, 111–145 (1989).
2. Baker, V. R., Strom, R. G., Gulick, V. C., Kargel, J. S. & Komatsu, G. Ancient oceans, ice sheets and the hydrological cycle on Mars. *Nature* **352**, 589–594 (1991).
3. Parker, T. J., Goresline, D. S., Saunders, R. S., Pieri, D. C. & Schneeberger, D. M. Coastal geomorphology of the Martian northern plains. *J. Geophys. Res.* **98**, 11061–11078 (1993).
4. Head, J. W. *et al.* Oceans in the past history of Mars: Tests for their presence using Mars Orbiter Laser Altimeter (MOLA) data. *Geophys. Res. Lett.* **25**, 4401–4404 (1998).
5. Head, J. W. *et al.* Possible ancient oceans on Mars: evidence from Mars Orbiter Laser Altimeter data. *Science* **286**, 2134–2137 (1999).
6. Ivanov, M. A. & Head, J. W. Chryse Planitia, Mars: Topographic configuration, outflow channel continuity and sequence, and tests for hypothesized ancient bodies of water using Mars Orbiter Laser Altimeter (MOLA) data. *J. Geophys. Res.* **106**, 3275–3296 (2001).
7. Clifford, S. M. & Parker, T. J. The evolution of the martian hydrosphere: implications for the fate of a primordial ocean and the current state of the northern plains. *Icarus* **154**, 40–79 (2001).
8. Carr, M. H. & Head, J. W. Oceans on Mars: An assessment of the observational evidence and possible fate. *J. Geophys. Res.* **108**, 5042, doi:10.1029/2002JE001963 (2003).
9. Malin, M. C. & Edgett, K. S. Oceans or seas in the Martian northern lowlands: High resolution imaging tests of proposed coastlines. *Geophys. Res. Lett.* **26**, 3049–3052 (1999).
10. Tanaka, K. L. & Scott, D. H. Geologic map of the polar regions of Mars. *US Geol. Surv. Misc. Invest. Map I-1802C* (1987).
11. Sabadini, R., Doglioni, C. & Yuen, D. A. Eustatic sea level fluctuations induced by polar wander. *Nature* **345**, 708–710 (1990).
12. Mound, J. E. & Mitrovica, J. X. True polar wander as a mechanism for second-order sea-level variations. *Science* **279**, 534–537 (1998).
13. Gold, T. Instability of the Earth's axis of rotation. *Nature* **175**, 526–529 (1955).
14. Willemann, R. J. Reorientation of planets with elastic lithospheres. *Icarus* **60**, 701–709 (1984).
15. Smith, D. E. *et al.* The gravity field of Mars: results from Mars Global Surveyor. *Science* **286**, 94–97 (1999).
16. Zuber, M. T. & Smith, D. E. Mars without Tharsis. *J. Geophys. Res.* **102**, 28673–28686 (1997).
17. Matsuyama, I., Mitrovica, J. X., Manga, M., Perron, J. T. & Richards, M. A. Rotational stability of dynamic planets with elastic lithospheres. *J. Geophys. Res.* **111**, E02003, doi:10.1029/2005JE002447 (2006).
18. Arkani-Hamed, J. & Boutin, D. Paleomagnetic poles of Mars: revisited. *J. Geophys. Res.* **109**, E03011, doi:10.1029/2003JE002229 (2004).
19. Hood, L. L., Young, C. N., Richmond, N. C. & Harrison, K. P. Modeling of major martian magnetic anomalies: Further evidence for polar reorientations during the Noachian. *Icarus* **177**, 144–173 (2005).
20. Zuber, M. T. *et al.* Internal structure and early thermal evolution of Mars from Mars Global Surveyor topography and gravity. *Science* **287**, 1788–1793 (2000).
21. Searls, M. L., Banerdt, W. B. & Phillips, R. J. Utopia and Hellas basins, Mars: Twins separated at birth. *J. Geophys. Res.* **111**, E08005, doi:10.1029/2005JE002666 (2006).
22. Leverington, D. W. & Ghent, R. R. Differential subsidence and rebound in response to changes in water loading on Mars: Possible effects on the geometry of ancient shorelines. *J. Geophys. Res.* **109**, E01005, doi:10.1029/2003JE002141 (2004).
23. Willemann, R. J. & Turcotte, D. L. The role of lithospheric stress in the support of the Tharsis rise. *J. Geophys. Res.* **87**, 9793–9801 (1982).
24. Redmond, H. L. & King, S. D. A numerical study of a mantle plume beneath the Tharsis Rise: Reconciling dynamic uplift and lithospheric support models. *J. Geophys. Res.* **109**, E09008, doi:10.1029/2003JE002228 (2004).
25. Roberts, J. H. & Zhong, S. Plume-induced topography and geoid anomalies and their implications for the Tharsis rise on Mars. *J. Geophys. Res.* **109**, E03009, doi:10.1029/2003JE002226 (2004).
26. Elkins-Tanton, L. T., Zaranek, S. E., Parmentier, E. M. & Hess, P. C. Early magnetic field and magmatic activity on Mars from magma ocean cumulate overturn. *Earth Planet. Sci. Lett.* **236**, 1–12 (2005).
27. Lambeck, K. *The Earth's Variable Rotation* (Cambridge Univ. Press, Cambridge, UK, 2005).
28. Sohl, F. & Spohn, T. The interior structure of Mars: Implications from SNC meteorites. *J. Geophys. Res.* **102**, 1613–1636 (1997).
29. Banerdt, W. B., Golombek, M. P. & Tanaka, K. L. in *Mars* (eds Kieffer, H. H., Jakosky, B. M., Snyder, C. W. & Matthews, M. S.) 249–297 (Univ. Arizona Press, Tucson, Arizona, 1992).
30. Webb, V. E. Putative shorelines in northern Arabia Terra, Mars. *J. Geophys. Res.* **109**, E09010 (2004).

**Supplementary Information** is linked to the online version of the paper at [www.nature.com/nature](http://www.nature.com/nature).

**Acknowledgements** This work was supported by the NASA Astrobiology Institute (J.T.P. and M.M.), a Reginald A. Daly Postdoctoral Fellowship (J.T.P.), the Miller Institute for Basic Research in Science (J.X.M.), and NSERC (J.X.M.).

**Author Contributions** All authors contributed equally to this work.

**Author Information** Reprints and permissions information is available at [www.nature.com/reprints](http://www.nature.com/reprints). The authors declare no competing financial interests. Correspondence and requests for materials should be addressed to J.T.P. (perron@eps.harvard.edu).

## LETTERS

# A gigantic bird-like dinosaur from the Late Cretaceous of China

Xing Xu<sup>1</sup>, Qingwei Tan<sup>2</sup>, Jianmin Wang<sup>3</sup>, Xijin Zhao<sup>1</sup> & Lin Tan<sup>2</sup>

An evolutionary trend of decreasing size is present along the line to birds in coelurosaurian theropod evolution<sup>1,2</sup>, but size increases are seen in many coelurosaurian subgroups, in which large forms are less bird-like<sup>2,3</sup>. Here we report on a new non-avian dinosaur, *Gigantoraptor erlianensis*, gen. et sp. nov., from the Late Cretaceous Iren Dabasu Formation of Nei Mongol, China. Although it has a body mass of about 1,400 kg, a phylogenetic analysis positions this new taxon within the Oviraptorosauria, a group of small, feathered theropods rarely exceeding 40 kg in body mass<sup>2,4–7</sup>. A histological analysis suggests that *Gigantoraptor* gained this size by a growth rate considerably faster than large North American tyrannosaurs such as *Albertosaurus* and *Gorgosaurus*<sup>8</sup>. *Gigantoraptor* possesses several salient features previously unknown in any other dinosaur and its hind limb bone scaling and proportions are significantly different from those of other coelurosaurs<sup>9,10</sup>, thus increasing the morphological diversity among dinosaurs. Most significantly, the gigantic *Gigantoraptor* shows many bird-like features absent in its smaller oviraptorosaurian relatives, unlike the evolutionary trend seen in many other coelurosaurian subgroups<sup>2,3</sup>.

Theropoda Marsh, 1881

Oviraptorosauria Barsbold, 1976

*Gigantoraptor erlianensis* gen. et sp. nov.

**Etymology.** The generic name refers to the animal being a gigantic raptor dinosaur; the specific name is derived from the Erlian basin where the holotype was collected.

**Holotype.** LH V0011, an incomplete skeleton preserving a nearly complete mandible, several partial presacral vertebrae, most caudal vertebrae, nearly complete right scapula, much of the forelimbs, partial ilium, and nearly complete pubes and hind limbs.

**Type locality and horizon.** Saihangaozi, Sunitezuoqi, Nei Mongol Autonomous Region. Iren Dabasu Formation, Senonian, Late Cretaceous<sup>11</sup>.

**Diagnosis.** An oviraptorosaur distinguishable from other species in the following features: a short mandible less than 45% of femoral length, a fossa on the lateral surface of the dentary close to the anterior end and a second fossa bounded dorsally by a lateral flange anterodorsal to the external mandibular fenestra, a long posteroventral process of the dentary extending to the level of the glenoid, a small, posteriorly tapered retroarticular process much deeper than wide, a tail composed of opisthocoelous anterior caudal vertebrae, amphicoelous middle ones and procoelous posterior ones, pleurocoels present on most caudal vertebrae, a pair of vertically arranged pneumatic openings present on the lateral surface of anterior caudal centra, a large pneumatic opening present on the ventral surface of anterior and middle caudal centra, anterior caudal vertebrae with tall neural spines (about three times as tall as wide) and robust and rod-like transverse processes located posteriorly, posteroventral margin of anterior caudal centra

extending considerably ventrally, well-developed laminal system on the anterior caudal vertebrae (prespinal, postspinal, spinopostzygapophyseal, anterior centrodiapophyseal, posterior centrodiapophyseal, and prezygodiapophyseal laminae present on anterior caudal vertebrae), middle caudal vertebrae with vertical prezygapophyseal articular facets located proximal to the distal extremity of the process, a prominent convexity ventral to the acromion process on the lateral surface of the scapula, a laterally bowed humerus with a prominent, spherical humeral head and a strongly medially curved deltopectoral crest, a centrally constricted thick ridge running along the posterior margin of the proximal half of the humerus, a straight ulna with a sub-circular, concave proximal articular surface, a radius with a sub-spherical distal end, metacarpal I with a slightly convex medial margin of the proximal end and a medial condyle three times as high as and extending much more distally than the lateral one on the distal end, a metacarpal II with a prominent dorsolateral process on the proximal end and a longitudinal groove on the ventral margin of the proximal third of the shaft, manual unguals with a triangular set of lateral grooves, a laterally compressed pubis, a femur with a straight shaft, a constricted neck between the posteromedially oriented, spherical femoral head and the anteroposteriorly wide trochanteric crest which is much more robust and higher anteriorly than posteriorly, a distinct narrow groove medial to the trochanteric crest extending down the posterior margin of the femoral shaft, and a patellar groove present on the anterior surface of the distal end, a small calcaneum obscured from anterior view by the wide astragalar main body, a proximal projection on the lateral margin of distal tarsal IV, metatarsal III with ginglymoid distal end, and pedal unguals with two lateral grooves and a constricted proximal articular surface (Fig. 1b–g, i–t).

**Description and comparison.** The *Gigantoraptor* holotype is estimated to be 8 m in total length and 3.5 m high at the hip (Fig. 1a) and to be about 1,400 kg in body mass (see Supplementary Information). The mandible is intermediate in morphology between basal oviraptorosaurs and highly specialized oviraptorids<sup>12–15</sup>: the mandible is comparable to that of *Oviraptor philoceratops* in relative depth, the mandibular symphysis is U-shaped with an extended shelf, the large external mandibular fenestra is relatively shallow and is located more anteriorly than in basal oviraptorosaurs but less so than in oviraptorids, the dentary is edentulous, dorsoventrally deep, and posteriorly bifurcated, the coronoid region is high but lacks a dorsomedially extended surangular process, the surangular lacks an anterior projection to divide the external mandibular fenestra and is not as enlarged as in oviraptorids, and the glenoid articulation is convex in lateral view and expanded transversely (Fig. 1b, c). As in Caenagnathidae<sup>13,15</sup>, the mandibular symphysis is completely fused without any trace of suture (Fig. 1c).

Postcranially, *Gigantoraptor* also displays numerous derived similarities seen in the Oviraptorosauria or its more exclusive

<sup>1</sup>Institute of Vertebrate Paleontology and Paleoanthropology, Chinese Academy of Sciences, Beijing 100044, China. <sup>2</sup>Long Hao Institute of Geology and Paleontology, <sup>3</sup>Department of Land Resources, Hohhot, Nei Mongol 010010, China.

groups<sup>12,13,16</sup>: a deep groove present on the ventral surface of the caudal vertebral centra, short middle and posterior caudal vertebrae with dorsoventrally compressed centra, ventrally located transverse processes present on the posterior caudal vertebrae, caudal neural arches positioned on the anterior half of the respective centra, a radius as long as the ulna, and a pubis with a concave anterior margin. Like other oviraptorosaurs<sup>12,13</sup>, the caudal vertebrae are pneumatic, but in a previously unknown manner: the anterior caudal vertebrae bear a pair of vertically arranged pneumatic foramina on the central lateral surface (Fig. 1d) and a large pneumatic opening on the central ventral surface (Fig. 1g). Interestingly, despite a lack of pneumatic opening, the posterior caudal centra have spongy internal structures (Fig. 1h), superficially similar to those of the sauropod group Titanosauria, a feature probably related to weight saving<sup>17</sup>.

However, *Gigantoraptor* exhibits many features that are not seen in other oviraptorosaurians but do occur in more derived

maniraptorans<sup>2,3,18,19</sup>. The anterior caudal centra are wider transversely than deep dorsoventrally. The scapular blade is shallower distally without an expanded distal end. The forelimbs are proportionally long, with a humerus + radius + metacarpal II to femur + tibiotarsus + metatarsal III ratio of 0.60. The radius bears a sub-spherical distal end. Metacarpal I is less than one-third the length of metacarpal II and the latter is much more robust than the former (Fig. 1n). The pubis is laterally compressed and straplike for most of its length, though a long pubic symphysis is present. The femur is avian-like in having a spherical femoral head with a distinct neck, a high and prominent trochanteric crest much thicker and higher anteriorly than posteriorly (Fig. 1q), a shallow popliteal fossa distally bounded by a low shelf, and lacks a fourth trochanter. The tibia has a lateral margin subequal in depth to the medial margin on the distal end. The astragalar main body extends laterally to hide the small calcaneum from anterior view (Fig. 1s). A distinct proximal projection is present on

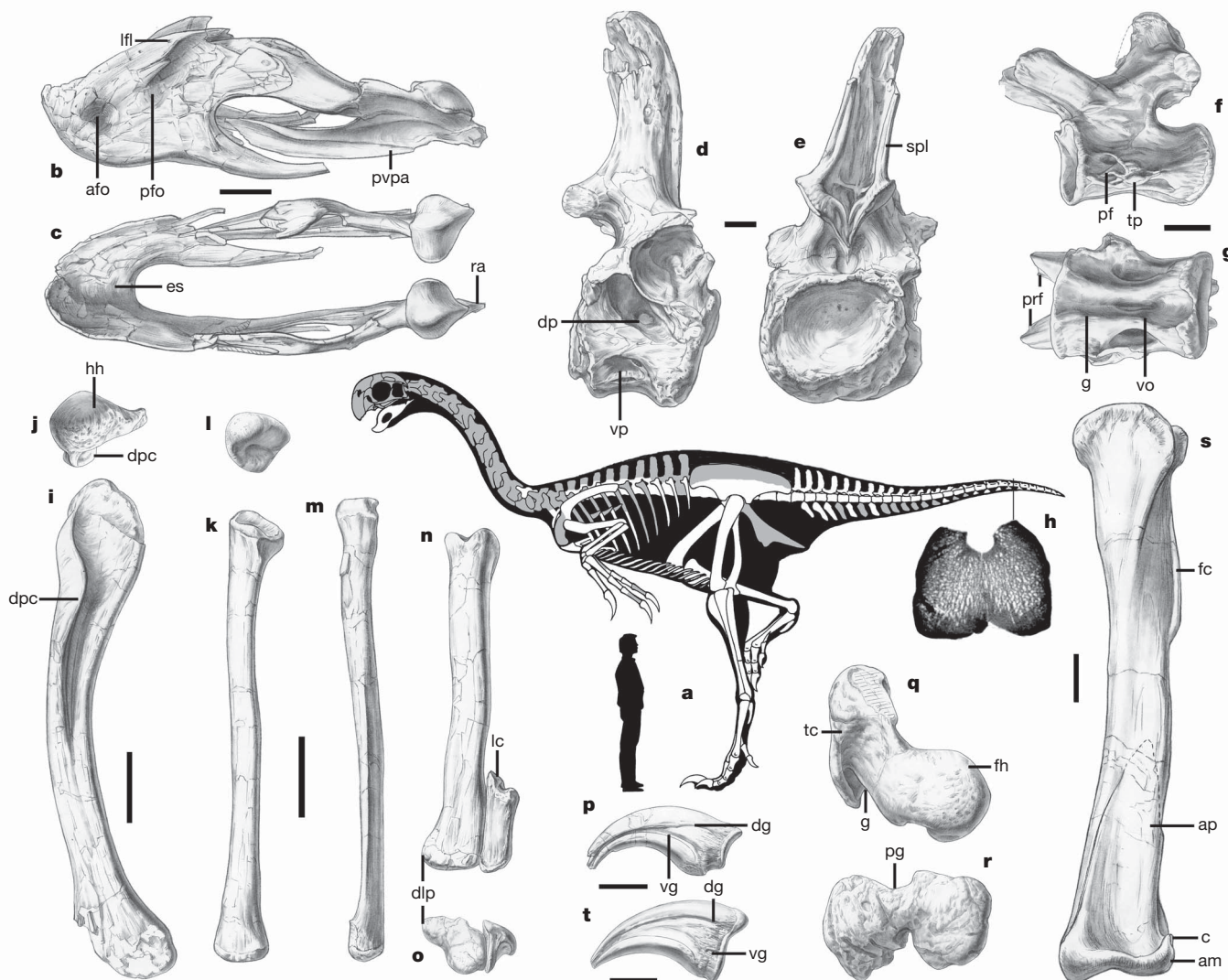


**Figure 1 | Skeletal anatomy of *Gigantoraptor* holotype (LH V0011).**

**a**, Skeletal reconstruction showing preserved elements, with a 175-cm-tall man for a scale. Bones are: mandible in lateral (**b**) and dorsal (**c**) views; anterior caudal vertebra in lateral (**d**) and posterior (**e**) views; middle caudal vertebra in lateral (**f**) and ventral (**g**) views; computed tomographic scan of a posterior caudal vertebral centrum showing the spongy internal structure (**h**); left humerus in anterior (**i**) and proximal (**j**) views; left ulna in anterior (**k**) and proximal (**l**) views; left radius in anterior view (**m**); left metacarpals I and II in anterior (**n**) and proximal (**o**) views; manual ungual in lateral view (**p**); right femur in proximal view (**q**) and left femur in distal view (**r**); left tibiotarsus in anterior view (**s**); pedal ungual in lateral view (**t**). Scale bars in

**b**, **c**, and **p**, 5 cm, in **d**–**f**, **g**, **n**, and **t**, 3 cm, and in **i**, **k**, **m**, and **s**, 10 cm. Abbreviations: afo, anterior fossa; am, astragalar main body; ap, ascending process; c, calcaneum; dg, dorsal groove; dlp, dorsolateral process; dp, dorsal pneumatic foramen; dpc, deltopectoral crest; es, extended shelf; fc, fibular crest; fh, femoral head; g, groove; hh, humeral head; lc, lateral condyle; lfl, lateral flange; pf, pneumatic foramen; pfo, posterior fossa; pp, patellar groove; prf, prezygapophyseal articular facet; pypa, articular facet for posteroverostral process of dentary; ra, retroarticular process; spl, spinopostzygapophyseal lamina; tc, trochanteric crest; tp, transverse process; vg, ventral groove; vo, ventral opening; vp, ventral pneumatic foramen.

the lateral margin of tarsal IV and metatarsal III is ginglymoid distally.

**Histological analysis.** We have conducted a histological analysis to determine the longevity, developmental stage, and growth strategy for the *Gigantoraptor* holotype (see Supplementary Information). A mid-diaphyseal petrographic thin section was made from the fibula. Although the medullary cavity is very small, the secondary osteons obliterate partial growth record in the inner cortex. A retrocalculation was thus made to assess the missing ages<sup>20,21</sup>. We calculated the number of the missing annual intervals by using the average width of the innermost three growth zones to divide the distance in question, which resulted in four years missing. The presence of seven sets of lines of arrested growth (LAGs) and the calculated four missing zones suggest that the *Gigantoraptor* holotype probably died during its eleventh year of life (Fig. 2).

The animal is inferred to be adult, as indicated by the extensive development of the secondary osteons, a moderate decrease in spacing between LAGs close to the periphery of the bone, and the presence of the outer circumferential layer comprising of a poorly vascularized layer of lamellar bone which indicates a slow rate of bone accretion<sup>20</sup>. Interestingly, the fourth to seventh sets of LAGs, which are within the outer circumferential layer, are not tightly packed as in a typical outer circumferential layer. We thus infer that the animal reached its young adult size within seven years and was still at relatively early young adult stage at the time of death and estimate that a full-sized *Gigantoraptor* is considerably heavier than 1,400 kg. This suggests that *Gigantoraptor* has an accelerated growth rate faster than most other theropods, including large North American tyrannosaurs such as *Albertosaurus* and *Gorgosaurus*<sup>8</sup>, a growth strategy seen in most gigantic dinosaurs<sup>21,22</sup>.

**Discussion.** As an oviraptorosaurian, *Gigantoraptor* is remarkable in its gigantic size (see Supplementary Information), about 300 times as heavy as basal oviraptorosaurians *Caudiperyx* and *Protarchaeopteryx*<sup>6,23,24</sup>, species known to bear pennaceous arm feathers and other types of feathers as well. A size disparity so dramatic might cause a change of integumentary coverings, such that large-sized forms lose filamentous integuments for insulation, as is the case in some mammals<sup>25</sup> and is inferred for the tyrannosaurs<sup>26</sup>. But *Gigantoraptor* might have at least retained arm feathers or their homologues from its ancestors, if not other types of feathers, given that the primary function of arm feathers is not to insulate the individual and their development is probably not related to size (see Supplementary Information).

Phylogenetic analysis posits *Gigantoraptor* at the base of the Oviraptoridae (see Supplementary Information), a hypothesis supported mainly by its mandibular morphology, intermediate between basal oviraptorosaurian and derived oviraptorid conditions<sup>13,16,27</sup>.



**Figure 2 | Photograph of transverse thin section of the fibular mid-shaft of *Gigantoraptor* holotype (LH V0011) under a polarized scope.** The section shows seven sets of single, paired, or grouped LAGs. Paired or grouped LAGs are seen in some non-avian and avian dinosaurs, some mammals and some ectothermic vertebrates<sup>20</sup>.

**Table 1 | Relative proportions of selected limb elements in oviraptorosaurs and some large theropods**

Taxa	Femur circumference/femur length	Tibiotarsus length/femur length	Metatarsus length/femur length
<i>Gigantoraptor</i> (femur length: 110 cm)	0.32	1.07	0.53
Oviraptorids (femur length: 15–30 cm)	0.34	1.23	0.55
Tyrannosauroids (femur length: 100–120 cm)	0.39	0.90	0.54
Carnosaurs and ceratosaurs (femur length: 100–120 cm)	0.40	0.86	0.39

Data were collected from original specimens or published literature<sup>9,10,30</sup>.

This intermediate systematic position is consistent with its geological age-Senonian, which is earlier than any other oviraptorids are known<sup>13,16,27</sup>.

*Gigantoraptor* possesses a large number of autapomorphies (see 'Diagnosis' section), indicating that it represents a highly specialized lineage in oviraptorosaurian evolution. In particular the presence of many features unknown in any other dinosaur, such as the highly specialized caudal vertebrae and the bizarre humerus, suggests that morphological diversity among the dinosaurs is higher than previously known. This is further indicated by *Gigantoraptor*'s unusual limb allometry. Among theropods, the tibiotarsus and metatarsus show negative allometry relative to the femur when size increases<sup>9,28</sup> and limb circumference scales to limb length<sup>10</sup>, though other factors, including phylogeny, contribute to the relative proportions and robustness of the limb elements as well<sup>9</sup>. A comparison of the femur circumference-to-length ratio, tibiotarsus-to-femur length ratio and metatarsus-to-femur length ratio values in *Gigantoraptor* and oviraptorids indicates that *Gigantoraptor* has values similar to those in its much smaller relatives (Table 1) and significantly different from theoretically predicted ones<sup>9,10,28</sup>. This is inconsistent with a general pattern that large-sized members of non-avian theropod sub-groups have proportionally stouter limbs and shorter lower legs than their small-sized relatives<sup>9</sup>. Compared with other similar-sized theropods including tyrannosauroids, *Gigantoraptor* has much more slender limbs and longer lower legs as indicated by the femur circumference-to-length ratio, tibiotarsus-to-femur length ratio and metatarsus-to-femur length ratio values (Table 1), suggesting that it might be the most cursorial theropod of comparable size.

*Gigantoraptor* is an exception to some general patterns seen during the gigantism of non-avian theropods. Contrary to the evolutionary trend of size decrease in coelurosaurian evolution<sup>1,2</sup>, which plays a key part in the origin of birds<sup>23,29</sup>, most non-avian coelurosaurian subgroups display a trend of size increase and their large-sized members tend to reverse to more primitive conditions in many bird-like characters<sup>2,3</sup>. The discovery of *Gigantoraptor* complicates this pattern, however. Although much larger than its close relatives, *Gigantoraptor* has proportionally the longest forelimb among oviraptorosaurs<sup>6,12,13</sup>, a manus resembling basal eumaniraptorans, bird-like hind limbs, and many other advanced features. These features are close to the conditions in birds but absent in other smaller oviraptorosaurs<sup>13</sup>, indicating an unusual pattern for the Oviraptorosauria among the non-avian coelurosaurian subgroups.

Received 9 February; accepted 18 April 2007.

1. Carrano, M. T. in *Amniote Paleobiology: Perspectives on the Evolution of Mammals, Birds, and Reptiles* (eds Carrano, M. T., Gaudin, T. J., Blob, R. W. & Wible, J. R.) 225–269 (Univ. Chicago Press, Chicago, 2006).
2. Sereno, P. C. The evolution of dinosaurs. *Science* **284**, 2137–2147 (1999).
3. Xu, X. & Norell, M. A. A new troodontid from China with avian-like sleeping posture. *Nature* **431**, 838–841 (2004).
4. Makovicky, P. J. & Norell, M. A. in *The Dinosauria* 2nd edn (eds Weishampel, D. B., Dodson, P. & Osmólska, H.) 184–195 (Univ. California Press, Berkeley, 2004).
5. Barsbold, R. On a new Late Cretaceous family of small theropods (Oviraptoridae fam. n.) of Mongolia. *Dokl. Akad. Nauk SSSR* **226**, 685–688 (1976).
6. Ji, Q., Currie, P. J., Norell, M. A. & Ji, S.-A. Two feathered dinosaur from China. *Nature* **393**, 753–761 (1998).

7. Zanno, L. E. & Sampson, S. D. A new oviraptorosaur (Theropoda, Maniraptora) from the Late Cretaceous (Campanian) of Utah. *J. Vert. Paleont.* **25**, 897–904 (2005).
8. Erickson, G. M. et al. Gigantism and comparative life-history parameters of tyrannosaurid dinosaurs. *Nature* **430**, 772–775 (2004).
9. Holtz, T. R. The arctometatarsalian pes, an unusual structure of the metatarsus of Cretaceous Theropoda (Dinosauria: Saurischia). *J. Vert. Paleont.* **14**, 480–519 (1994).
10. Christiansen, P. Long bone scaling and limb posture in non-avian theropods: evidence for differential allometry. *J. Vert. Paleont.* **19**, 666–680 (1999).
11. Currie, P. J. & Eberth, D. A. Palaeontology, sedimentology and palaeoecology of the Iren Dabasu formation (Upper Cretaceous), inner Mongolia, People's Republic of China. *Cretaceous Res.* **14**, 127–144 (1993).
12. Maryańska, T., Osmólska, H. & Wolsan, M. Avian status for Oviraptorosauria. *Acta Palaeontol. Pol.* **47**, 97–116 (2002).
13. Osmólska, H., Currie, P. J. & Barsbold, R. in *The Dinosauria* 2nd edn (eds Weishampel, D. B., Dodson, P. & Osmólska, H.) 165–183 (Univ. California Press, Berkeley, 2004).
14. Clark, J. A., Norell, M. A. & Rowe, T. Cranial anatomy of *Citipati osmolskiae* (Theropoda, Oviraptorosauria), and a reinterpretation of the holotype of *Oviraptor philoceratops*. *Am. Mus. Novit.* **3364**, 1–24 (2002).
15. Currie, P. J. & Godfrey, S. J. New caenagnathid (Dinosauria: Theropoda) specimens from the Upper Cretaceous of north America and Asia. *Can. J. Earth Sci.* **30**, 2255–2272 (1993).
16. Sues, H.-D. On *Chirostenotes*, a Late Cretaceous oviraptorosaur (Dinosauria: Theropoda) from western North America. *J. Vert. Paleont.* **17**, 698–716 (1997).
17. Upchurch, P. Evolutionary history of sauropod Dinosaurs. *Phil. Trans. R. Soc. Lond. B* **349**, 365–390 (1995).
18. Chiappe, L. M. Late Cretaceous birds of southern South America: anatomy and systematics of enantiornithes and *Patagopteryx deferrariisi*. *Munch. Geowiss. Abh.* **30**, 203–244 (1996).
19. Norell, M. A., Clark, J. M. & Makovicky, P. J. in *New Perspectives on the Origin and Evolution of Birds* (eds Gauthier, J. & Gall, L. F.) 49–67 (Yale Univ. Press, New Haven, 2001).
20. Chinsamy-Turan, A. *The Microstructure of Dinosaur Bone* (Johns Hopkins Univ. Press, Baltimore/London, 2005).
21. Horner, J. R. & Padian, K. Age and growth dynamics of *Tyrannosaurus rex*. *Proc. R. Soc. Lond. B* **271**, 1875–1880 (2004).
22. Sander, M. P. et al. Adaptive radiation in sauropod dinosaurs: bone histology indicates rapid evolution of giant body size through acceleration. *Org. Divers. Evol.* **4**, 165–173 (2004).
23. Xu, X. & Norell, M. A. Non-avian dinosaur fossils from the Lower Cretaceous Jehol Group of western Liaoning, China. *Geol. J.* **41**, 419–438 (2006).
24. Senter, P., Barsbold, R., Britt, B. B. & Burnham, D. A. Systematics and evolution of Dromaeosauridae (Dinosauria, theropoda). *Bull. Gunma Mus. Nat. Hist.* **8**, 1–20 (2004).
25. Spina, C. *Elephants* (T. & A. D. Poyser Ltd, London, 1994).
26. Xu, X. et al. Basal tyrannosauroids from China and evidence for protofeathers in tyrannosauroids. *Nature* **431**, 680–684 (2004).
27. Makovicky, P. J. & Sues, H.-D. Anatomy and phylogenetic relationships of the theropod dinosaur *Microvenator celer* from the Lower Cretaceous of Montana. *Am. Mus. Novit.* **3240**, 1–27 (1998).
28. Gatesy, S. M. Hind limb scaling in birds and other theropods: implications for terrestrial locomotion. *J. Morphol.* **209**, 83–96 (1991).
29. Hwang, S. H., Norell, M. A., Ji, Q. & Gao, K. New specimens of *Microraptor zhaoianus* (Theropoda: Dromaeosauridae) from northeastern China. *Am. Mus. Novit.* **3381**, 1–44 (2002).
30. Currie, P. J. Possible evidence of gregarious behavior in tyrannosaurids. *Gaia* **15**, 271–277 (1998).

**Supplementary Information** is linked to the online version of the paper at [www.nature.com/nature](http://www.nature.com/nature).

**Acknowledgements** We thank A. Chinsamy-Turan and G. M. Erickson for discussions on bone histology and critical comments on the histological section, J. A. Clark for comments on the manuscript, the technicians of the Long Hao Institute of Geology and Paleontology for contributions in the field and for preparation of fossil materials, R.-S. Li and W.-D. Zhang of the Institute of Vertebrate Paleontology and Paleoanthropology for drawings and photography. X.X.'s work is supported by grants from the Chinese Academy of Sciences, the National Natural Science Foundation of China, and the American Museum of Natural History. The fieldwork was supported by grants from the Ministry of Land and Resources PRC and the Department of Land and Resources of Nei Mongol.

**Author Information** Reprints and permissions information is available at [www.nature.com/reprints](http://www.nature.com/reprints). The authors declare no competing financial interests. Correspondence and requests for materials should be addressed to X.X. (xu.xing@ivpp.ac.cn).

## LETTERS

# The human footprint in the carbon cycle of temperate and boreal forests

Federico Magnani<sup>1</sup>, Maurizio Mencuccini<sup>2</sup>, Marco Borghetti<sup>3</sup>, Paul Berbigier<sup>4</sup>, Frank Berninger<sup>5</sup>, Sylvain Delzon<sup>4</sup>, Achim Grelle<sup>6</sup>, Pertti Hari<sup>7</sup>, Paul G. Jarvis<sup>2</sup>, Pasi Kolari<sup>7</sup>, Andrew S. Kowalski<sup>4</sup>, Harry Lankreijer<sup>8</sup>, Beverly E. Law<sup>9</sup>, Anders Lindroth<sup>8</sup>, Denis Loustau<sup>4</sup>, Giovanni Manca<sup>10†</sup>, John B. Moncrieff<sup>2</sup>, Mark Rayment<sup>2</sup>, Vanessa Tedeschi<sup>3</sup>, Riccardo Valentini<sup>10</sup> & John Grace<sup>2</sup>

Temperate and boreal forests in the Northern Hemisphere cover an area of about  $2 \times 10^7$  square kilometres and act as a substantial carbon sink (0.6–0.7 petagrams of carbon per year)<sup>1</sup>. Although forest expansion following agricultural abandonment is certainly responsible for an important fraction of this carbon sink activity, the additional effects on the carbon balance of established forests of increased atmospheric carbon dioxide, increasing temperatures, changes in management practices and nitrogen deposition are difficult to disentangle, despite an extensive network of measurement stations<sup>2,3</sup>. The relevance of this measurement effort has also been questioned<sup>4</sup>, because spot measurements fail to take into account the role of disturbances, either natural (fire, pests, windstorms) or anthropogenic (forest harvesting). Here we show that the temporal dynamics following stand-replacing disturbances do indeed account for a very large fraction of the overall variability in forest carbon sequestration. After the confounding effects of disturbance have been factored out, however, forest net carbon sequestration is found to be overwhelmingly driven by nitrogen deposition, largely the result of anthropogenic activities<sup>5</sup>. The effect is always positive over the range of nitrogen deposition covered by currently available data sets, casting doubts on the risk of widespread ecosystem nitrogen saturation<sup>6</sup> under natural conditions. The results demonstrate that mankind is ultimately controlling the carbon balance of temperate and boreal forests, either directly (through forest management) or indirectly (through nitrogen deposition).

The life of forest ecosystems is punctuated by stand-replacing disturbances, mainly associated with fire or forest management. After each event, the forest is typically a net source of carbon (C) over the first years, followed by a broad peak in C sequestration (NEP, net ecosystem production; Fig. 1a) and gross primary production (GPP; Fig. 1b) in maturing forests. In older stands, NEP usually declines as a result of the age-related reduction in growth<sup>7</sup>. Age effects account for 92% of the total variability in NEP in five chronosequences analysed as part of the CARBOEUROPE project (<http://www.bgc-jena.mpg.de/public/carboeur/>), spanning from boreal coniferous to temperate broadleaf forests. Forested landscapes, however, are a patchwork of stands of different age, and the mean C sequestration at this scale is more closely approximated by the average NEP over the entire rotation, that is, between two subsequent stand-replacing events (NEP<sub>av</sub>). When combining data from the five CARBOEUROPE chronosequences with several published literature data sets from boreal and

temperate established forests (Table 1), NEP<sub>av</sub> amounts to only 56% of peak NEP ( $38 \pm 15\%$  s.d. for individual forests; Fig. 2). Such a correction for disturbance effects could help reconcile flux- and inventory-based estimates of net C sequestration by terrestrial vegetation<sup>4</sup>.

Because of their magnitude, age-related dynamics make it difficult to assess what other factors control forest C sequestration at the regional and global level<sup>8</sup>. We therefore filtered out the effects of age by taking the average of C fluxes over the entire rotation. Both ecosystem respiration (RE<sub>av</sub>) and gross primary production (GPP<sub>av</sub>) were positively correlated with mean annual temperature at the site ( $R^2 = 0.83$  and 0.82, respectively); only one forest in the entire data set was known to be severely affected by water stress<sup>9</sup>, which appeared to reduce in parallel both photosynthesis and respiration. The correlation with temperature improved significantly when this dry site was excluded from the analysis (Fig. 3a and b), so highlighting the primary role of heat and

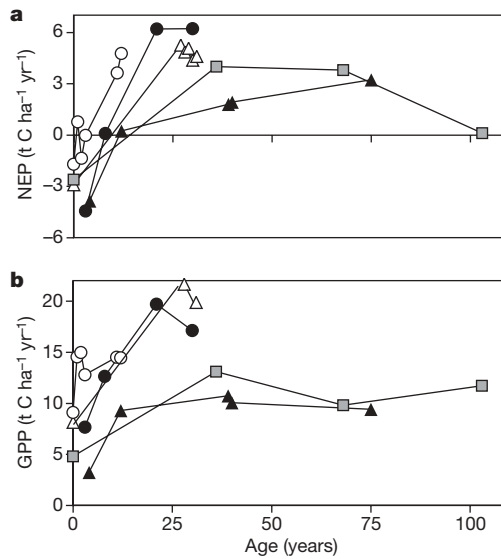


**Figure 1 | Age-related dynamics of C balance components in forest ecosystems following disturbance.** **a**, Dynamics of NEP; **b**, dynamics of GPP in five CARBOEUROPE chronosequences across Europe. Symbols refer to the following site codes (see Table 1): 7, black circles; 10, white triangles; 12, grey squares; 13, black triangles; 19, white circles.

<sup>1</sup>Department of Fruit Tree and Woody Plant Science, University of Bologna, Bologna I-40127, Italy. <sup>2</sup>School of GeoSciences, University of Edinburgh, Edinburgh EH93JU, UK.

<sup>3</sup>Department of Crop Systems, Forestry and Environmental Sciences, University of Basilicata, Potenza I-85100, Italy. <sup>4</sup>INRA, UR1263 EPHYSE, Villejuif F-33883, France.

<sup>5</sup>Department of Sciences Biologiques, University of Québec à Montréal, Montréal, Québec, H3C 3P8, Canada. <sup>6</sup>Department of Ecology and Environmental Research, Swedish University of Agricultural Sciences, SE-75007 Uppsala, Sweden. <sup>7</sup>Department of Forest Ecology, University of Helsinki, FIN-00014 Helsinki, Finland. <sup>8</sup>Department of Physical Geography and Ecosystems Analysis, Lund University, S-223 62 Lund, Sweden. <sup>9</sup>College of Forestry, Oregon State University, Corvallis, OR 97331, USA. <sup>10</sup>Department of Forest Resources and Environment, University of Tuscia, Viterbo I-01100 Italy. <sup>†</sup>Present address: Institute for Environment and Sustainability—Climate Change Unit, Joint Research Center, European Commission, I-21020 Ispra, Italy.

**Table 1 | Main site characteristics and C flux components of forest chronosequences used in the analysis**

Main species	Site code	Age (years)	Latitude (°N)	Longitude (°E)	Data type	Disturbance type	GPP <sub>av</sub> (t C ha <sup>-1</sup> yr <sup>-1</sup> )	RE <sub>av</sub> (t C ha <sup>-1</sup> yr <sup>-1</sup> )	NEP <sub>av</sub> (t C ha <sup>-1</sup> yr <sup>-1</sup> )	Maximum NEP (t C ha <sup>-1</sup> yr <sup>-1</sup> )	Reference
<i>Fagus sylvatica</i>	1	0–250*	51° 05'	10° 27'	EC	AB	15.6	10.7	4.9		23
	2	30–153	51° 20'	10° 22'	B	SW	16.1	11.5	4.6		24
<i>Nothofagus solandrii</i>	3	10–>160	43° 15'	171° 35'	B	WT			0.3		22
<i>Picea mariana</i>	4	3–151	55° 53'	–98° 20'	B	FF	6.6	6.2	0.4	1.1	25
	5	3–151	55° 53'	–98° 20'	B	FF	7.1	6.4	0.7	2.9	25
	6	11–130	55° 54'	–98° 28'	EC	FF	6.7	6.5	0.2	1.2	26
<i>Picea sitchensis</i>	7	3–30	55° 10'	2° 03'	EC, B	CC	15.4	12.7	2.7	5.5	†
<i>Pinus banksiana</i>	8	1–72	44° 35'	–84° 15'	B	FF			0.4	1.8	27
	9	0–79	53° 54'	–104° 39'	B	CC, FF	5.5	5.4	0.1	0.5	28
<i>Pinus pinaster</i>	10	0–50	44° 35'	0° 52'	EC, B	CC	18.3	14.8	3.6	6.5	†
<i>Pinus ponderosa</i>	11	9–316	44° 24'	–121° 36'	B	CC	7.8	7.2	0.6	1.6	9
<i>Pinus sylvestris</i>	12	0–103	60° 05'	17° 28'	EC, B	CC	10.1	8.5	1.6	3.7	†
	13	4–75	61° 51'	24° 17'	EC, B	CC	9.5	8.4	1.1	2.3	†
	14	12–266	60° 43'	89° 08'	B	FF	7.4	7.0	0.4	0.6	21
	15	14–215	60° 43'	89° 08'	B	FF	4.0	3.9	0.1	0.2	21
	16	2–383	60° 43'	89° 08'	B	FF	5.5	5.4	0.1	0.4	21
	17	2–95	60° 43'	89° 08'	B	FF	4.1	3.6	0.5	1.3	21
<i>Pseudotsuga menziesii</i>	18	0–500*	45° 49'	–121° 57'	B	AB	12.7	12.5	0.2		29
<i>Quercus cerris</i>	19	1–17	42° 24'	11° 55'	EC, B	CO	16.1	13.7	2.4	4.4	†
<i>Tsuga mertensiana</i>	20	14–262	43° 30'	–122° 00'	B	PE			0.1	0.6	30

EC, eddy covariance; B, biomass; CC, clear-cut; CO, coppice; SW, shelterwood; AB, abandoned; FF, forest fire; PE, pests; WT, windthrow. \*Uneven aged. †This study.

water stress in controlling the individual components of forest C balance. This confirms previous studies at the continental scale<sup>2,3</sup>, although with much lower scatter owing to the removal of age effects. In contrast with GPP<sub>av</sub> and RE<sub>av</sub>, mean NEP (NEP<sub>av</sub> = GPP<sub>av</sub> – RE<sub>av</sub>) is only weakly correlated with temperature (Fig. 3c). No correlation was found with either annual precipitation ( $R^2 = 0.01$ ) or site latitude ( $R^2 = 0.04$ ), leaving open the question of what could be driving C sequestration in boreal and temperate forests.

It was first recognized in the 1980s that human activities, by releasing into the atmosphere unprecedented amounts of active nitrogen (N), were not just altering the global N cycle<sup>5</sup>, but also resulting in the eutrophication of large parts of the biosphere<sup>10</sup>. Boreal and temperate forest ecosystems are generally N-limited and the addition of N through wet and dry deposition has been hypothesized to result in the stimulation of forest growth and C sequestration<sup>6</sup>. Earlier model simulations suggested that N deposition could account for an increased C sequestration of 0.44–0.74 Pg yr<sup>–1</sup>, mainly in temperate and boreal regions<sup>11</sup>. More recently, the relevance of N deposition for forest C sequestration has been questioned, on the basis of manipulation studies<sup>12</sup> and modelling extrapolation from N budgets<sup>13</sup>. In both studies, however, C sequestration was estimated from N fluxes themselves, assuming fixed C:N ratios. The relationship between N deposition and forest C sequestration has never been tested through direct observations across a range of forest conditions.

Using recently released gridded maps of N fluxes across Western Europe and North America<sup>14</sup>, we found a tight relationship between

average C sequestration and wet N deposition in the corresponding cell (Fig. 3d;  $R^2 = 0.97$ ), which is largely obscured by age effects when data from individual stands are considered. We used wet rather than total N deposition because dry deposition was not measured directly, but derived from transfer models based on a limited data set of atmospheric concentrations, resulting in very large uncertainties<sup>5</sup>. The substantial net C sequestration by many temperate forests appears to be overwhelmingly determined by the additional input of N induced by human activities. We therefore hypothesize that the observed response of GPP<sub>av</sub> and RE<sub>av</sub> to temperature is mainly controlled by soil organic matter decomposition, which releases the nutrients needed for photosynthesis and growth, and that human activities, by adding an additional source of N readily available to plants, have determined an imbalance between the two components of the feed-back loop, so resulting in the net sequestration of C by forest ecosystems. Although a comprehensive analysis should consider in detail the distribution of existing forests and their uneven age structure, as well as the loss of C

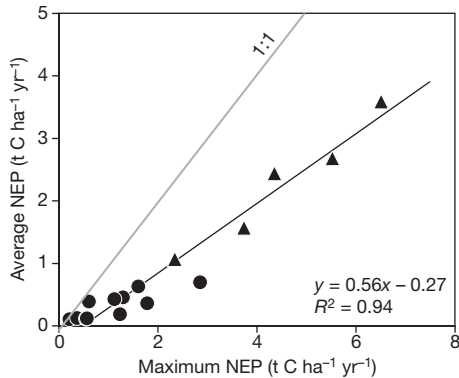


**Figure 2 | Relationship between average NEP over the entire rotation and peak NEP in mature stands.** Data from five CARBOEUROPE chronosequences (triangles) have been combined with eleven other literature data sets (see Table 1). Estimates of average and peak NEP are based on interpolated values of C fluxes; a linear function has been fitted by Type II regression ( $n = 16$ ).

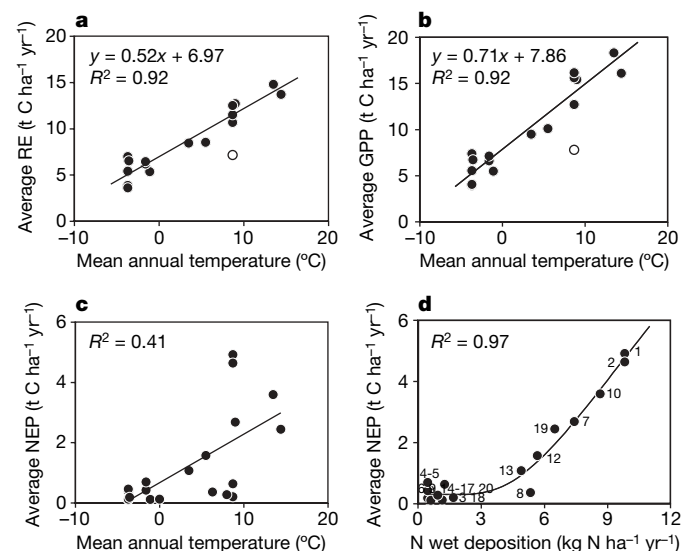


**Figure 3 | Environmental control of average C exchange over an entire rotation.** Linear relationships between average RE (a) and average ecosystem GPP (b) and mean annual temperature at the study sites. In both a and b, the only drought-prone site<sup>9</sup> (white circle) has been excluded from the analysis. c, Average NEP is only poorly correlated to temperature. d, Average NEP is strongly related to N deposition. Numbers refer to site codes in Table 1. An Arrhenius function has been empirically fitted onto the entire data set ( $n = 20$ ).

through wildfire and logging, this could amount to an important fraction of the estimated C sink in the Northern Hemisphere<sup>1</sup>.

The proposed mechanism of ecosystem response to N deposition implies that plants can readily access this additional nutrient source, in contrast with the results of several manipulative studies<sup>12</sup>. Under conditions of long-term, low-dose fertilization, however, plants are effective competitors for available N (ref. 15); moreover, their ability to compete for N would appear to increase with N availability, as the microbial demand for N becomes saturated by local organic sources with progressively lower C:N (ref. 15, 16). This could explain the increasing slope of the NEP<sub>av</sub> response at high levels of N deposition (Fig. 3d), as more and more nutrients would be absorbed by plants and used for the production of woody biomass, with a high C:N ratio.

Are temperate and boreal forest ecosystems bound to become themselves saturated with N, resulting in forest dieback and a reduction in C sequestration<sup>6</sup>? Long-term studies of N enrichment in forests have demonstrated that ecosystem function responds to addition rate, rather than cumulated N input, and that although intermediate deposition levels could have beneficial effects, these could disappear at super-optimal N levels<sup>17</sup>. No signs of N saturation were apparent in our data set (Fig. 3d), which explored a broad range of wet deposition up to 9.8 kg N ha<sup>-1</sup> yr<sup>-1</sup> ( $\sim$ 15 kg N ha<sup>-1</sup> yr<sup>-1</sup> of total N deposition), representative of more than 90% of the overall surface of Western Europe and the conterminous United States<sup>14</sup>. Long-term manipulation studies indicate that only at N addition levels of 50–60 kg N ha<sup>-1</sup> yr<sup>-1</sup> do clear signs of soil acidification, nutrient imbalances and tree damage become apparent<sup>17,18</sup>. Although these values are in excess of current maximum levels of atmospheric N deposition<sup>14</sup>, even higher rates are occasionally recorded and could occur in the future over entire regions<sup>5</sup>. Further chronosequence studies in selected areas with high N deposition could help us understand if the beneficial effects of N fertilization on the terrestrial C sink can be expected to persist over the next century.

## METHODS SUMMARY

Both C stocks and C fluxes<sup>2</sup> were measured in five representative forest chronosequences throughout Europe (Table 1), which comprised newly harvested, young and mature stands in the same locality. At each site, GPP and RE were also computed from NEP data. Data from 13 additional chronosequences and two uneven-aged stands were drawn from the literature (Table 1). When estimates based on the eddy-covariance technique were not available, GPP was derived from annual net primary production (NPP), assuming a constant relationship<sup>19</sup>, and RE estimated as the difference from NEP. All chronosequences were located either in natural forests or in plantations at least at second rotation and were not actively fertilized.

The chronosequence approach quantifies ecosystem C sink capacity at several stages in forest development; modelling tools were used to interpolate the resulting information over the entire rotation. A process-based approach was applied in the case of CARBOEUROPE chronosequences, for which direct flux and stock data were available, by linking two well-documented and tested ecosystem models<sup>19,20</sup>. In the case of literature chronosequences, flux integrals over the entire rotation were obtained by fitting suitable empirical equations<sup>9,21</sup> onto flux or ecosystem C data. In just one case<sup>22</sup>, because of the limited sample size, NEP<sub>av</sub> was estimated from the difference in ecosystem C between the newly regenerated stand and the old stand.

Estimates of N wet deposition in 1990 for sites in Western Europe and the conterminous United States were derived from recently published gridded maps<sup>14</sup>. Additional data for 1993 for the rest of the globe were derived from model simulations<sup>5</sup>; estimates of wet N deposition were then derived from modelled values of total N deposition, based on a correlation of values in the previous data set.

**Full Methods** and any associated references are available in the online version of the paper at [www.nature.com/nature](http://www.nature.com/nature).

Received 13 November 2006; accepted 11 April 2007.

1. Goodale, C. L. *et al.* Forest carbon sinks in the Northern Hemisphere. *Ecol. Appl.* 12, 891–899 (2002).
2. Valentini, R. *et al.* Respiration as the main determinant of carbon balance in European forests. *Nature* 404, 861–865 (2000).
3. Law, B. E. *et al.* Environmental controls over carbon dioxide and water vapor exchange of terrestrial vegetation. *Agric. For. Meteorol.* 113, 97–120 (2002).

4. Körner, C. Slow in, rapid out: carbon flux studies and Kyoto targets. *Science* 300, 1242–1243 (2003).
5. Galloway, J. N. *et al.* Nitrogen cycles: past, present, and future. *Biogeochemistry* 70, 153–226 (2004).
6. Aber, J. D. *et al.* Nitrogen saturation in temperate forest ecosystems. *Bioscience* 48, 921–934 (1998).
7. Pregitzer, K. S. & Euskirchen, E. S. Carbon cycling and storage in world forests: biome patterns related to forest age. *Glob. Change Biol.* 10, 2052–2077 (2004).
8. Thornton, P. E. *et al.* Modeling and measuring the effects of disturbance history and climate on carbon and water budgets in evergreen needleleaf forests. *Agric. For. Meteorol.* 113, 185–222 (2002).
9. Law, B. E., Sun, O. J., Campbell, J., vanTuyl, S. & Thornton, P. E. Changes in carbon storage and fluxes in a chronosequence of ponderosa pine. *Glob. Change Biol.* 9, 510–524 (2003).
10. Peterson, B. J. & Melillo, J. M. The potential storage of carbon caused by eutrophication of the biosphere. *Tellus B* 37, 117–127 (1985).
11. Townsend, A. R., Braswell, B. H., Holland, E. A. & Penner, J. E. Spatial and temporal patterns in terrestrial carbon storage due to deposition of fossil fuel nitrogen. *Ecol. Appl.* 6, 806–814 (1996).
12. Nadelhoffer, K. J. *et al.* Nitrogen deposition makes a minor contribution to carbon sequestration in temperate forests. *Nature* 398, 145–148 (1999).
13. De Vries, W., Reinds, G. J., Gundersen, P. & Sterba, H. The impact of nitrogen deposition on carbon sequestration in European forests and forest soils. *Glob. Change Biol.* 12, 1151–1173 (2006).
14. Holland, E. A., Braswell, B. H., Sulzman, J. & Lamarque, J. F. Nitrogen deposition onto the United States and Western Europe: synthesis of observations and models. *Ecol. Appl.* 15, 38–57 (2005).
15. Johnson, D. W. Nitrogen-retention in forest soils. *J. Environ. Qual.* 21, 1–12 (1992).
16. Schimel, J. P. & Bennett, J. Nitrogen mineralization: Challenges of a changing paradigm. *Ecology* 85, 591–602 (2004).
17. Höglberg, P., Fan, H., Quist, M., Binkley, D. & Tamm, C. O. Tree growth and soil acidification in response to 30 years of experimental nitrogen loading on boreal forest. *Glob. Change Biol.* 12, 489–499 (2006).
18. Magill, A. H. *et al.* Ecosystem response to 15 years of chronic nitrogen additions at the Harvard Forest LTER, Massachusetts, USA. *For. Ecol. Manage.* 196, 7–28 (2004).
19. Landsberg, J. J. & Waring, R. H. A generalized model of forest productivity using simplified concepts of radiation-use efficiency, carbon balance and partitioning. *For. Ecol. Manage.* 95, 209–228 (1997).
20. Andrén, O. & Kätterer, T. ICBM: the introductory carbon balance model for exploration of soil carbon balances. *Ecol. Appl.* 7, 1226–1236 (1997).
21. Wirth, C., Czimczik, C. I. & Schulze, E.-D. Beyond annual budgets: carbon flux at different temporal scales in fire-prone Siberian Scots pine forests. *Tellus B* 54, 611–630 (2002).
22. Davis, M. R., Allen, R. B. & Clinton, P. W. Carbon storage along a stand development sequence in a New Zealand *Nothofagus* forest. *For. Ecol. Manage.* 177, 313–321 (2003).
23. Knöhl, A., Schulze, E.-D., Kolle, O. & Buchmann, N. Large carbon uptake by an unmanaged 250-year-old deciduous forest in Central Germany. *Agric. For. Meteorol.* 118, 151–167 (2003).
24. Mund, M. *Carbon Pools of European Beech Forests (Fagus sylvatica) Under Different Silvicultural Management*. PhD thesis, Georg-August-Universität Göttingen (2004).
25. Bond-Lamberty, B., Wang, C. & Gower, S. T. Net primary production and net ecosystem production of a boreal black spruce wildfire chronosequence. *Glob. Change Biol.* 10, 473–487 (2004).
26. Litvak, M., Miller, S., Wofsy, S. C. & Goulden, M. Effect of stand age on whole ecosystem CO<sub>2</sub> exchange in the Canadian boreal forest. *J. Geophys. Res.* 108 (D3), 8225 (2003).
27. Rothstein, D. E., Yermakov, Z. & Buell, A. L. Loss and recovery of ecosystem carbon pools following stand-replacing wildfire in Michigan jack pine forests. *Can. J. For. Res.* 34, 1908–1918 (2004).
28. Howard, E. A., Gower, S. T., Foley, J. A. & Kucharik, C. J. Effects of logging on carbon dynamics of a jack pine forest in Saskatchewan, Canada. *Glob. Change Biol.* 10, 1267–1284 (2004).
29. Harmon, M. E. *et al.* Production, respiration, and overall carbon balance in an old-growth *Pseudotsuga-Tsuga* forest ecosystem. *Ecosystems* 7, 498–512 (2004).
30. Boone, R. D., Sollins, P. & Cromack, K. Stand and soil changes along a mountain hemlock death and regrowth sequence. *Ecology* 69, 714–722 (1988).

**Supplementary Information** is linked to the online version of the paper at [www.nature.com/nature](http://www.nature.com/nature).

**Acknowledgements** This work was supported by the European Commission (General Directorate XII, CARBO-AGE project in the CARBOEUROPE cluster) and further supported by several national programmes. F.M. was also supported by the MIUR Carbolitaly Project and by Società Produttori Sementi (Fondazione Cassa di Risparmio in Bologna) through the 'Selvicoltura' project.

**Author Information** Reprints and permissions information is available at [www.nature.com/reprints](http://www.nature.com/reprints). The authors declare no competing financial interests. Correspondence and requests for materials should be addressed to F.M. (federico.magnani@unibo.it).

## METHODS

The analysis was based on a combination of measurements from five European chronosequences, collected as part of the CARBOEUROPE project, and literature data from a total of 15 chronosequences or uneven aged stands. A chronosequence is defined as a collection of forest stands of different age but otherwise homogeneous for plant material and environmental conditions; the footprint area of a chronosequence is larger than those generally studied in manipulation experiments, partly compensating for the lack of experimental replicates. All chronosequences were located either in natural forests or in plantations at least at second rotation and were not actively fertilized.

**Description of CARBOEUROPE chronosequences.** We identified five representative managed forests throughout Europe (see Table 1), which comprised newly harvested, young and mature stands in the same locality. The UK series consists of stands of *Picea sitchensis* at Harwood in northwest England; soils are predominantly peaty gleys, formed over glacial tills. The forest is managed by clear-cutting; the usual rotation is 40 years, and the data reported here are from the second rotation. Measurements were taken in stands 0, 7, 21 and 30 years old. The Italian site is a coppice with standards of *Quercus cerris* at Roccarespampani in Central Italy. The soil is a Luvisol on a volcanic bedrock. The rotation length is 15–20 years. The ages of the available stands span the entire rotation: data are available for ages 1, 4, 10 and 17 years. The Finnish series consists of stands of *Pinus sylvestris* at Juupajoki in Southern Finland, on sandy glacial till of moderate fertility; the 40-year-old stand is 5 km away, in Hyttiälä, on coarse sandy glacial till. The rotation length is typically 80 years; the stands analysed are 3, 10, 40 and 75 years old. The Swedish sites are in Central Sweden, at Skyttorp (0, 30 and 60 years) and at Norunda (100 years); all the stands are dominated by *P. sylvestris*. The typical rotation length is about 100 years. The soil is a deep, boulder-rich sandy glacial till. The French site is part of Les Landes forest in southwestern France, and consists of mono-specific *Pinus pinaster* stands 0, 16, 26 and 50 years old on spodic sands. The typical rotation length is 50 years at the site.

Both C stocks (in soils, litter, woody debris and vegetation) and C fluxes were measured at each stand in the chronosequence; each stand in a chronosequence was large enough to satisfy conditions for measurement of CO<sub>2</sub> fluxes by the eddy covariance technique<sup>31</sup>. At each site, GPP and RE were also computed from NEP data, by assuming that respiration by day is the same as that at night after adjustment for the effect of the diurnal temperature cycle.

**Literature data sets.** Data from 13 additional chronosequences and 2 uneven-aged stands from boreal and temperate forests were drawn from the literature (see Table 1). The data set comprised only one chronosequence from the Southern Hemisphere. Direct measurements of NEP or ecosystem C were used for the estimation of average NEP over the entire rotation. C flux estimates in literature chronosequences were based either on the eddy-covariance technique or on biometric measurements (as detailed in Supplementary Table 1, see Supplementary Information). When data were provided only in graphical format, the relevant figure was captured from the electronic paper using commercial software (Paint Shop Pro 4.12, JASC) and individual datapoints digitized using the Un-Scan-It 5.0 dedicated software (Silk Scientific). When estimates based on the eddy-covariance technique were not available, GPP was derived from estimates of annual NPP, assuming a constant ratio<sup>32</sup>, and RE was estimated as the difference from NEP.

**Computation of average C fluxes in CARBOEUROPE chronosequences.** Although the chronosequence approach quantifies ecosystem C sink capacity at several stages in forest development, modelling tools are needed to interpolate the resulting information over the entire rotation. While such an integration procedure is needed to correct for any biases resulting from the limited sample size of each chronosequence, very similar results are obtained when raw means (and maxima) of field measurements are used instead (see Supplementary Information). A process-based approach was applied in the case of CARBOEUROPE chronosequences, for which direct flux and stock data were available, by linking two well-documented and tested ecosystem models. The 3PG-3 model stems from the combination of the 3PG (use of Physiological Principles in Predicting Growth) model<sup>19</sup>, to represent the NPP and growth of a forest stand, and the ICBM (Introductory Carbon Balance Model) model<sup>20</sup> for belowground C dynamics. The two models have been extensively documented and tested<sup>19,20,33–37</sup>. In addition, a third component has been added to represent the C exchange by the forest understorey (hence the suffix in 3PG-3), with a structure derived from the 3PG model with further simplifications.

**General model structure.** Because the aim of the model is to capture age-related differences among stands in a chronosequence, all experiencing the same conditions, the model overlooks the detailed response of primary production to individual environment factors, capturing it as a single reduction coefficient for the whole chronosequence irrespective of stand age. A single reduction

factor also captures the response of soil heterotrophic respiration to the soil environment (temperature, humidity, soil texture), irrespective of stand age. Age is assumed to have a direct effect (that is independent from the dynamics of C stocks) only on light-use efficiency, as described below. Because the seasonal dynamics of environmental factors are neglected, an annual time step is adopted throughout.

**NEP.** The representation of forest NPP is based on the light-use efficiency approach<sup>38</sup>. The amount of photosynthetically active radiation absorbed by the stand over the year  $\Phi_{\text{pa}}$  is a function of incoming radiation  $\Phi_p$  and stand foliage C ( $C_f$ ), following Beer's law:

$$\Phi_{\text{pa}} = \Phi_p (1 - a) [1 - \exp(-k \times \text{SLA} \times C_f)] \quad (1)$$

where  $a$  is canopy albedo,  $k$  is a light extinction coefficient (of value 0.5 for spherically distributed leaves) and SLA is foliage-specific leaf area (expressed in terms of leaf C content). Stand GPP is assumed to be linearly proportional to absorbed light:

$$\text{GPP} = \varepsilon \Phi_{\text{pa}} \quad (2)$$

Radiation light-use efficiency  $\varepsilon$  is reduced below its potential value  $\varepsilon_0$  as a result of environmental and age-related effects:

$$\varepsilon = \varepsilon_0 f_{\text{age}} f_{\text{tot}} \quad (3)$$

The empirical parameter  $f_{\text{tot}}$  captures the combined effects of all environmental factors over the entire season and is assumed to be independent of stand age. The direct effects of age  $A$  are captured by the parameter  $f_{\text{age}}$ , defined as<sup>19</sup>:

$$f_{\text{age}} = \frac{1}{1 + (A/A_{0.5})^4} \quad (4)$$

where the parameter  $A_{0.5}$  is the age corresponding to a 50% reduction in light-use efficiency. Stand NPP is finally assumed to be a constant fraction of GPP<sup>32</sup>. The same approach is applied to understorey primary production. The amount of light reaching the understorey  $\Phi_p^{\text{und}}$ , however, is first reduced by overstorey interception. Moreover, the light-use efficiency of the understorey is not reduced by age but only by the environment through the reduction factor  $f_{\text{tot}}^{\text{und}}$ .

**Growth and litter production.** Available C is assumed to be allocated between foliage ( $C_f$ ), fine root ( $C_r$ ) and woody biomass ( $C_w$ ; including coarse roots and stumps) in proportion to allocation coefficients  $\eta_f$ ,  $\eta_r$  and  $\eta_w$ , respectively. A constant value is assumed for allocation to foliage<sup>39</sup>. Allocation to roots, on the contrary, is assumed to increase in response to both environmental stress and age, in parallel with the reduction in light-use efficiency:

$$\eta_r = \frac{0.8}{1 + 2.5m \times f_{\text{tot}} f_{\text{age}}} \quad (5)$$

The empirical parameter  $m$  captures the effects of soil fertility on fine root growth, and increases with soil fertility. Allocation to wood production is represented as residual growth. Annual changes in the  $i$ -th tree compartment (foliage, fine root and woody tissues) are represented as the difference between new growth and litter losses:

$$\frac{\Delta C_i}{\Delta t} = \text{NPP} \eta_i - C_i \gamma_i \quad (6)$$

where the parameter  $\gamma_i$  represents the annual mortality of the  $i$ -th compartment and is equal to zero in the case of woody biomass. Steady-state conditions are assumed for the understorey; understorey litter production is therefore assumed to be equal to the corresponding NPP<sub>und</sub>.

**Soil respiration and net ecosystem exchange.** The representation of soil organic matter (SOM) dynamics is based on the two-compartment ICBM model<sup>20</sup>. A young (that is, readily decomposable) and an old (that is, refractory) SOM compartment, with widely different residence times, are distinguished in the model.

The annual change in the biomass  $Y$  of the young SOM compartment is the difference of litter input (from trees and the understorey) and young SOM decomposition, which is assumed to be proportional to  $Y$ :

$$\frac{\Delta Y}{\Delta t} = (C_f \gamma_f + C_r \gamma_r + \text{NPP}_{\text{und}}) - r k_1 Y \quad (7)$$

The empirical parameter  $r$  captures the combined effects of temperature, humidity and soil texture on the decomposition parameter  $k_1$ , which represents unit Y decomposition under standard conditions. Young SOM decomposition is partly lost as respiration, the remaining being transferred to the old SOM compartment

through humification. Young SOM respiration is expressed as:

$$R_{\text{SOM}}^Y = (1 - h) r k_1 Y \quad (8)$$

where  $h$  is a humification coefficient. The annual change in old SOM biomass  $O$  is therefore equal to:

$$\frac{\Delta O}{\Delta t} = r(k_1 Y h - k_2 O) \quad (9)$$

where  $k_2$  represents unit  $O$  decomposition under standard conditions, modulated by the same parameter  $r$  as a result of the environment. Old SOM respiration can be expressed as:

$$R_{\text{SOM}}^O = r k_2 O \quad (10)$$

NEP is the difference between tree and understorey NPP and the heterotrophic respiration from young and old SOM:

$$\text{NEP} = \text{NPP} + \text{NPP}_{\text{und}} - R_{\text{SOM}}^Y - R_{\text{SOM}}^O \quad (11)$$

**Model fitting procedure.** The combined model was implemented in Fortran 95, calibrated independently for each chronosequence on measurements available for a limited number of ages and used to estimate C fluxes at every age in the chronosequence. The procedure made it possible to compute average fluxes over the entire rotation without the risks coming from the limited sample size. In contrast with more empirical equations, such a process-based model can represent coherently and at the same time all of the main C-cycle variables that are amenable to direct measurement. The model was therefore calibrated so as best to represent the values of annual fluxes (NEP and GPP) and C stocks ( $C_p$ ,  $C_r$ ,  $C_w$ , total SOM) measured in individual stands of the chronosequence. The ability of the model to represent all these variables at the same time increased the confidence in model estimates.

To include these non-commensurate sources of information in the calibration process, the multi-objective global optimization approach described in ref. 40 was adopted. Before model calibration, each variable was normalized by its mean and variance, so as to achieve the conditions of zero mean and constant variance among variables, which is a pre-condition for the application of the overall Maximum Likelihood Estimator as an objective function.

A total of seven model parameters ( $f_{\text{tot}}$ ,  $f_{\text{tot}}^{\text{und}}$ ,  $A_{0.5}$ ,  $\gamma_r$ ,  $m$ ,  $h$ ,  $r$ ), plus three initial values of state variables ( $C_p$ ,  $Y$ ,  $O$ ), were estimated for each chronosequence, leaving a number of degrees of freedom ranging between 9 and 21, depending on the chronosequence considered. All other parameters and input variables were derived from direct field measurements. Overall, the model explained 91% of the variability in C stocks and fluxes within each chronosequence.

**Computation of average C fluxes in literature chronosequences.** If not already available, flux integrals over the entire rotation were obtained by fitting onto flux data the empirical equation proposed by ref. 9:

$$\text{NEP} = -a_1 + a_2 \exp\left\{-0.5[\ln(A/a_3)/a_4]^2\right\} \quad (12)$$

Alternatively, the empirical equation proposed by ref. 21 was fitted onto total ecosystem C data:

$$C_{\text{eco}} = b_1 + [b_2 \exp(-b_3 A)] + [b_4 A / (A + b_5)] \quad (13)$$

and annual NEP computed as the difference in ecosystem C between subsequent years. The two empirical models were fitted on experimental data with the NLIN procedure in the SAS 9.00 statistical package (SAS Institute). Average NEP over the rotation was computed as the mean of annual values between age zero and the maximum age in the chronosequence. In just one case<sup>22</sup>, because of the limited sample size, average NEP was estimated from the difference in ecosystem C between the newly regenerated and the old stand. Although its omission does

not have any appreciable effects on the results, this *Nothofagus* chronosequence has been included in the analysis because it is one of the few broadleaved forests and the only one from the Southern Hemisphere.

Annual GPP values were also integrated over the entire rotation, using the same function presented in equation (12).  $\text{RF}_{\text{av}}$  was computed as the difference between  $\text{GPP}_{\text{av}}$  and  $\text{NEP}_{\text{av}}$ . A detailed description of data type and integration procedures is presented in Supplementary Table 1 (see Supplementary Information).

**Computation of N wet deposition.** Estimates of N wet deposition in 1990 for sites in western Europe and the conterminous USA were derived from recently published gridded maps with  $0.5^\circ \times 0.5^\circ$  resolution derived from interpolated (krieged) ground data<sup>14</sup> (available at <http://www.daac.ornl.gov>), referring to the nearest node in the map (see Supplementary Fig. 1). Total wet deposition was computed as the sum of aqueous  $\text{NO}_3^-$  and  $\text{NH}_4^+$  fields, which were available for both regions. An estimate of total (modelled) N deposition was obtained as the sum of wet deposition and of the fields for deposition of  $\text{NO}_2$ ,  $\text{NH}_4$ ,  $\text{HNO}_3$  and  $\text{NO}_3^-$ . In the case of Europe, because only the sum of nitric acid and particulate nitrate was measured, the relative fields represent end-members assuming only one species<sup>14</sup> and we took the average value. In the case of the US data set,  $\text{NO}_2$  deposition rates were not available and their contribution to total N deposition was estimated from a regression of European values.

Additional data for 1993 for the rest of the globe were derived from model simulations<sup>5,41</sup>; estimates of wet N deposition were then derived from modelled values of total N deposition, based on a correlation of values from Western Europe in the previous data set (see Supplementary Fig. 2). The same correction factor was used in the comparison with N fertilization rates in manipulation experiments.

**Statistical analyses.** All statistical analyses were carried out using the SAS 9.00 statistical package (SAS Institute).

31. Aubinet, M. et al. Estimates of the annual net carbon and water exchange of forests: the Euroflux methodology. *Adv. Ecol. Res.* 30, 113–175 (2000).
32. Waring, R. H., Landsberg, J. J. & Williams, M. Net primary production of forests: a constant fraction of gross primary production? *Tree Physiol.* 18, 129–134 (1998).
33. Coops, N. C., Waring, R. H. & Landsberg, J. J. Assessing forest productivity in Australia and New Zealand using a physiologically-based model driven with averaged monthly weather data and satellite-derived estimates of canopy photosynthetic capacity. *For. Ecol. Manage.* 104, 113–127 (1998).
34. Paul, K. I., Polglase, P. J. & Richards, G. P. Predicted change in soil carbon following afforestation or reforestation, and analysis of controlling factors by linking a C accounting model (CAMFor) to models of forest growth (3PG), litter decomposition (GENDEC) and soil C turnover (RothC). *For. Ecol. Manage.* 177, 485–501 (2003).
35. Law, B. E., Waring, R. H., Anthoni, P. M. & Abers, J. D. Measurements of gross and net ecosystem productivity and water vapour exchange of a *Pinus ponderosa* ecosystem, and an evaluation of two generalized models. *Glob. Change Biol.* 6, 155–168 (2000).
36. Landsberg, J. J., Waring, R. H. & Coops, N. C. Performance of the forest productivity model 3-PG applied to a wide range of forest types. *For. Ecol. Manage.* 172, 199–214 (2003).
37. Kätterer, T. & André, O. The ICBM family of analytically solved models of soil carbon, nitrogen and microbial biomass dynamics. Descriptions and applications examples. *Ecol. Model.* 136, 191–207 (2001).
38. Landsberg, J. J. et al. in *The Use of Remote Sensing in the Modeling of Forest Productivity* (eds Ghosh, H. L., Nakane, K. & Shimoda, H.) 273–298 (Kluwer Academic, Dordrecht, 1996).
39. Santantonio, D. in *Biomass Production by Fast-Growing Trees* (eds Pereira, J. S. & Landsberg, J. J.) 57–72 (Kluwer Academic, Dordrecht, 1989).
40. Yapo, P. O., Gupta, H. V. & Sorooshian, S. Multi-objective global optimization for hydrologic models. *J. Hydrol.* 204, 83–97 (1998).
41. Dentener, F. J. *Global Maps of Atmospheric Nitrogen Deposition, 1860, 1993, and 2050. Data set.* (<http://daac.ornl.gov/>). (Oak Ridge National Laboratory Distributed Active Archive Center, Oak Ridge, Tennessee, 2006).

# Miniature eye movements enhance fine spatial detail

Michele Rucci<sup>1</sup>, Ramon Iovin<sup>1</sup>, Martina Poletti<sup>1</sup> & Fabrizio Santini<sup>1</sup>

Our eyes are constantly in motion. Even during visual fixation, small eye movements continually jitter the location of gaze<sup>1–4</sup>. It is known that visual percepts tend to fade when retinal image motion is eliminated in the laboratory<sup>5–9</sup>. However, it has long been debated whether, during natural viewing, fixational eye movements have functions in addition to preventing the visual scene from fading<sup>10–17</sup>. In this study, we analysed the influence in humans of fixational eye movements on the discrimination of gratings masked by noise that has a power spectrum similar to that of natural images. Using a new method of retinal image stabilization<sup>18</sup>, we selectively eliminated the motion of the retinal image that normally occurs during the intersaccadic intervals of visual fixation. Here we show that fixational eye movements improve discrimination of high spatial frequency stimuli, but not of low spatial frequency stimuli. This improvement originates from the temporal modulations introduced by fixational eye movements in the visual input to the retina, which emphasize the high spatial frequency harmonics of the stimulus. In a natural visual world dominated by low spatial frequencies, fixational eye movements appear to constitute an effective sampling strategy by which the visual system enhances the processing of spatial detail.

It was originally hypothesized<sup>10</sup> that fixational eye movements might contribute to the perception of fine spatial details, a proposal later refined into the dynamic theories of visual acuity<sup>11–13</sup>. Classical experiments that eliminated retinal image motion did not support these theories<sup>7,19–22</sup>. These pioneering experiments, however, suffered from significant technological limitations. Most notably, the devices used to stabilize images on the retina did not allow selective

stabilization during periods of visual fixation between saccades, as would have been necessary to study fixational eye movements in their natural context<sup>23–25</sup>. Instead, all trials with stabilized vision had to be run in uninterrupted blocks while the subject maintained fixation—a highly unnatural condition that unavoidably led to visual fatigue and fading.

In this study, we examined the influence of fixational eye movements on the discrimination of targets at different spatial frequencies (grating spacings). We compared discrimination performances measured in two conditions: with and without the retinal image motion produced by fixational eye movements. To overcome the limitations of previous experiments, we developed a new retinal stabilization technique based on real-time processing of eye-movement signals<sup>18</sup>. Like previous stabilization methods, this technique does not guarantee perfect elimination of retinal image motion; however, unlike previous methods, it combines a high quality of stabilization with experimental flexibility (see Supplementary Information). This flexibility enabled us to display and selectively stabilize the stimulus after a saccade, a method that isolates the normal fixational motion of the eye. It also allowed us to randomly alternate between trials with retinal stabilization and trials with normal retinal motion, a procedure that prevents visual fatigue and allows rigorous comparison of the two conditions, and to assess the accuracy of retinal stabilization independently from the subject's own judgement, a development that allows inexperienced and naive subjects to participate in experiments.

In a forced-choice task, subjects reported whether a grating was tilted by 45° clockwise or anticlockwise. Two separate experiments investigated the discrimination of the stimuli shown in Fig. 1a. In

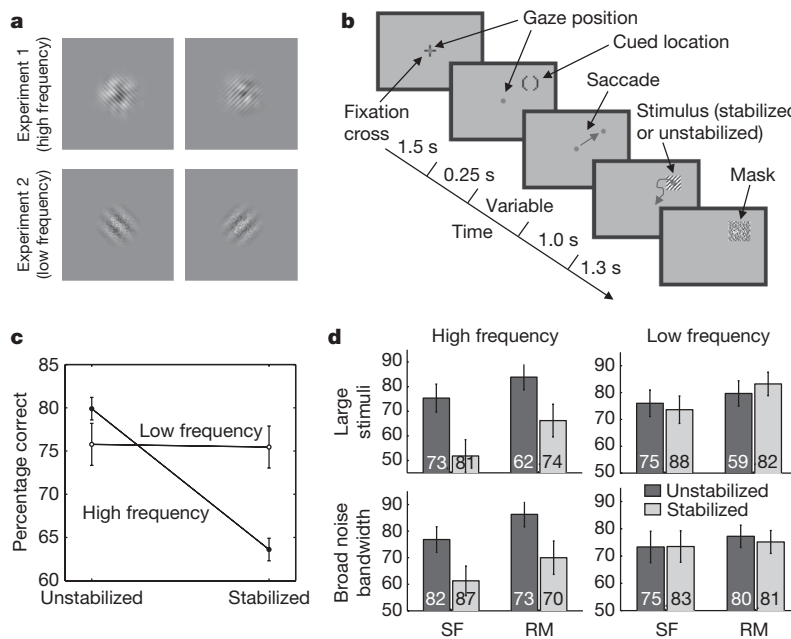


**Figure 1 | Impact of retinal stabilization.**

**a**, Examples of stimuli. **b**, Experimental procedure. The grey arrows and dots represent the subject's eye movements and the centre of gaze, respectively. **c**, Mean subject performance ( $N = 6$ ). For every subject, percentages were evaluated over a minimum of 80 trials. Individual performance differences between stabilized and unstabilized conditions were all significant in experiment one and were statistically indistinguishable in experiment two ( $P < 0.05$ ; one-tailed  $z$ -test). **d**, Results of control experiments. The large stimulus was 5.6°. For the broad bandwidth control, the frequency band of noise was 0–14 cycles per degree. For both subjects, performance dropped under stabilization using a grating with 11 cycles per degree (high frequency, experiment one) ( $P < 0.05$ ; one-tailed  $z$ -test), but not using a grating with 4 cycles per degree (low frequency, experiment two). The numbers of trials are indicated on each bar. In both **c** and **d**, error bars represent 95% confidence intervals. SF, RM, subjects.

<sup>1</sup>Department of Cognitive and Neural Systems, Boston University, Boston, Massachusetts 02215, USA.

experiment one, the stimulus was a high-frequency grating perturbed by noise at low spatial frequencies. In experiment two, the frequency bands of the grating and the noise were reversed: the grating was at low spatial frequencies and the noise was at high frequencies. In both cases, the power of the noise was inversely proportional to the square of the spatial frequency, similar to the power spectrum of natural images<sup>26</sup>.

As shown in Fig. 1c, when high-frequency gratings were used, mean percentages of orientation discrimination dropped by more than 16% in the presence of retinal stabilization, a change that was highly significant (experiment one:  $t = 19.1$ ,  $P < 0.01$ ; one-tailed paired  $t$ -test). By contrast, the retinal image motion produced by fixational eye movements did not improve performance with low-frequency gratings (experiment two:  $t = -0.2$ ,  $P > 0.05$ ). Thus, fixational eye movements improved discrimination of the orientation of a high-frequency grating masked by low-frequency noise but did not help with a low-frequency grating masked by high-frequency noise. This result is surprising because it contradicts traditional views of the influence of fixational eye movements on vision. Indeed, the pronounced reduction in contrast sensitivity at low spatial frequencies measured by previous experiments with prolonged retinal stabilization<sup>19–21</sup> predicts a more significant drop in performance with low-frequency than with high-frequency gratings.

Control experiments examined the robustness of this result. As shown by Fig. 1d, the same pattern of results was obtained in a first control experiment, which used a larger stimulus, and in a second experiment, in which the noise bandwidth was broadened to overlap the frequency of the grating. Furthermore, a beneficial effect of fixational eye movements was also found in the contrast thresholds—the lowest detectable contrast of a grating—measured at high spatial frequencies (Fig. 2). We concluded that the high-frequency discrimination impairment observed under retinal stabilization was not affected by the precise size of the stimulus or by the bandwidth of low-frequency noise.

To establish further evidence for the causal relationship between fixational modulations of luminance and performance, we eliminated retinal image motion on a selected axis while leaving motion on the orthogonal axis unaltered. As shown in Fig. 3, discrimination was impaired when retinal image motion was restricted to the axis parallel to the grating but was normal when motion occurred on the orthogonal axis. These results are consistent with the informational content of the modulations of luminance introduced by fixational eye movements. These modulations only convey information about the pattern of noise during motion parallel to the grating, but provide maximal information about the grating when motion occurs on the axis orthogonal to the grating. For one subject, we also artificially reconstructed the visual input signals resulting from fixational eye movements by moving an otherwise stabilized stimulus. Passive exposure to the fixational motion of the retinal image, obtained by motion of the stimulus instead of the eye, was sufficient for re-establishing a normal level of performance. These results confirm

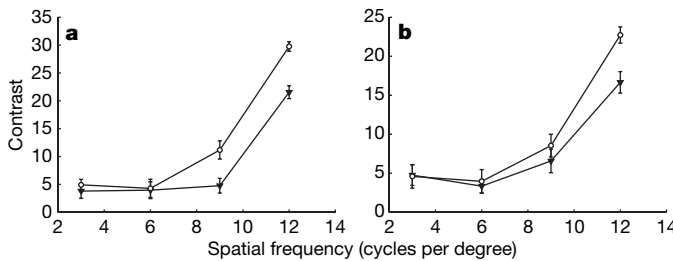


**Figure 2 | Contrast thresholds.** Mean levels of Michelson contrast  $\pm$  s.e.m. for two subjects: **a**, subject AR and **b**, subject GD. Consistent with the results of Fig. 1, the two conditions—normal retinal image motion (filled triangles) and retinal stabilization (open circles)—only produced different thresholds at high spatial frequencies.

that the discrimination impairment shown in Fig. 1 was caused by the absence of the retinal image motion produced by fixational eye movements.

To understand the mechanisms by which fixational eye movements improve the discrimination of high spatial frequency stimuli, we analysed the frequency contents of the spatiotemporal signals entering the eye in the unstabilized (stimuli fixed at a location on the screen) and stabilized (stimuli moved with the eye to cancel the retinal motion resulting from fixational eye movements) conditions of experiments 1 and 2 (the signals  $I_U(x, t)$  and  $I_S(x, t)$  received at time  $t$  by a receptor located at position  $x$  on the retina, see Fig. 4a). Under retinal stabilization,  $I_S(x, t)$  did not change with time, and its power was confined to the spatial frequency plane at zero temporal frequency. In contrast, in the unstabilized condition, the motion of the eye spread the spatial power of the stimulus across temporal frequencies away from zero frequency. As shown by Fig. 4b, the extent of this temporal spreading was not uniform throughout the spatial frequency plane; it increased with spatial frequency. This dependence on spatial frequency occurred because the average change in luminance produced by a small displacement of a grating increases with the grating frequency. This effect had a different impact on the visual input signals of the two experiments.

Figure 4c compares the power spectrum of the stimulus with the spatial frequency distribution of the power in  $I_U$ , which, as a consequence of oculomotor activity, left the temporal zero frequency plane and became available at non-zero temporal frequencies. This dynamic power is identical to the power of the change in luminance that occurs as a result of the motion of the eye—the signal  $\tilde{I}_U(x, t)$  in equation (2). With the stimuli of experiment one, these input modulations exhibited both attenuation of the low-frequency noise and

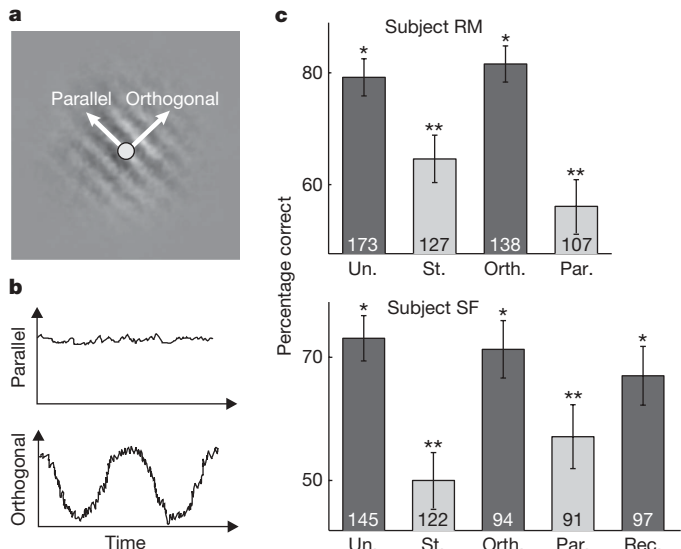


**Figure 3 | Controlled retinal image motion.** **a**, Selective stabilization of the stimulus on a single axis enables control of the signal-to-noise ratio of the visual input signals resulting from fixational eye movements. **b**, The fixational modulations of luminance experienced by a retinal receptor (the circle in **a**) convey no information about the grating when motion occurs on the axis parallel to the grating (Par.) and convey maximal information when motion occurs on the axis orthogonal to the grating (Orth.). **c**, Mean percentages of correct discrimination  $\pm$  s.e.m. for two subjects. Subject SF was also tested in an additional condition (Rec.), in which we reconstructed the fixational motion of the retinal image under retinal stabilization. In this condition, a recorded eye-movement trajectory was superimposed on the motion of an otherwise stabilized stimulus. In each trial, this trajectory was randomly selected from the pool of all previously recorded unstabilized trials that did not include fixational saccades. Significant differences from complete retinal stabilization (St.) and from normal retinal image motion (Un.) are indicated by \* and \*\*, respectively ( $P < 0.05$ ; one-tailed  $z$ -tests). The numbers of trials are indicated on each bar.

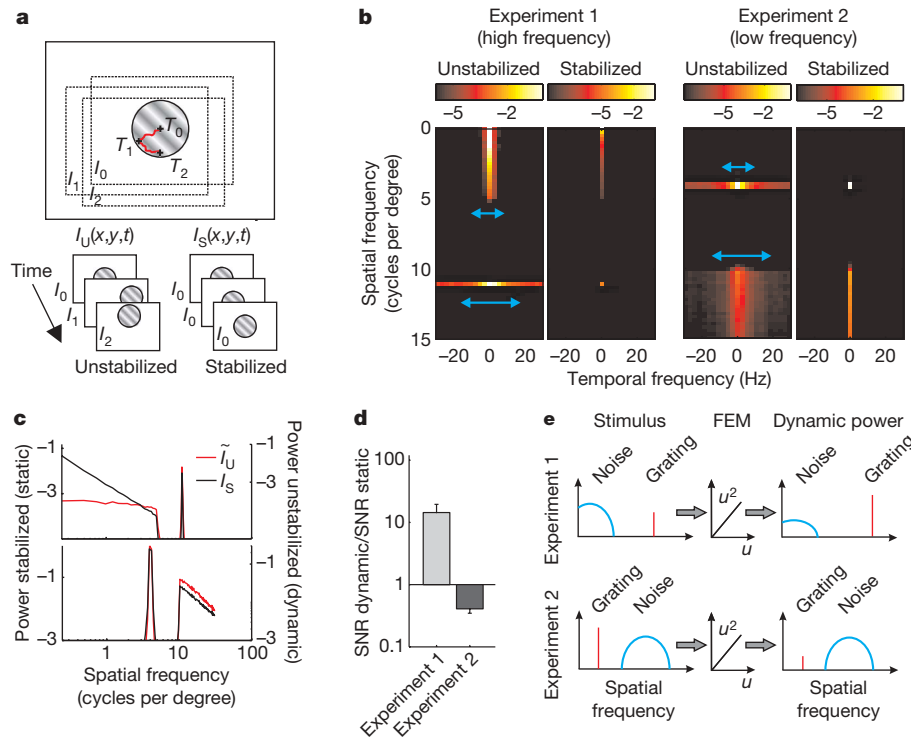


**Figure 4 | Influence of fixational eye movements on visual input.** **a**, For every trial in experiments one and two, a movie was generated to reconstruct the spatiotemporal input to the retina during the period of stimulus presentation. In the movie  $I_U(x,y,t)$  of an unstabilized trial, the frame at time  $T_i$  was an image  $I_i$  centred at the current location of gaze. In the movie  $I_S(x,y,t)$  of a stabilized trial, each frame was the same image  $I_0$ . Examples of these are included as Supplementary Movies. **b, c**, Power spectra of the signals entering the eye of subject MD. The full space–time spectra are shown in **b**. **c**, Spatial spectral densities, after integration over temporal frequency,

of  $I_S$  and of the changes in luminance caused by oculomotor activity ( $\tilde{I}_U$  in equation (2)). **d**, Ratio between the SNRs of  $\tilde{I}_U$  and  $I_S$  in the two experiments. Bars represent mean  $\pm$  s.d. across all subjects. **e**, Theoretical explanation of the impact of fixational eye movements. Fixational instability acts as a filter (FIM) that enhances high spatial frequencies in the temporal modulations of luminance present in the input to the retina. The total power at spatial frequency  $u$  of these input modulations (dynamic power) is approximately equal to the power of the stimulus multiplied by  $u^2$ .

enhancement of the power of the high-frequency grating. That is, the signal-to-noise-ratio (SNR, the ratio of the power of the grating to the power of the noise) of  $\tilde{I}_U$  was much higher than that of the stabilized input (SNR  $\tilde{I}_U$ /SNR  $I_S = 21$ ). In contrast, in the case of the low-frequency grating of experiment two, fixational modulations enhanced the noise relative to the grating. In this case, the SNR of  $\tilde{I}_U$  was lower than that of the stimulus (SNR  $\tilde{I}_U$ /SNR  $I_S = 0.33$ ). Therefore, fixational eye movements introduced temporal modulations that enhanced the grating with respect to the noise in experiment one but not in experiment two. On average, the SNR of the changes in luminance caused by oculomotor activity was more than 30 times larger with high-frequency gratings than it was with low-frequency gratings (Fig. 4d). This effect can be seen in the Supplementary Movies, which reconstruct the input to the retina.

The result of Fig. 4d can be explained on the basis of the spatial characteristics of fixational instability. Because of the small scale of fixational eye movements, it is possible to use a Taylor expansion to approximate the visual input:

$$I_U(\mathbf{x}, t) \approx S(\mathbf{x}) + \xi(t) \cdot \nabla S(\mathbf{x}) + \frac{1}{2} \xi(t) H_S \xi^T(t) \quad (1)$$

where  $S(\mathbf{x})$  is the stimulus luminance,  $H_S$  its Hessian, and the vector  $\xi(t)$  represents the eye trajectory during the presentation of the stimulus. Equation (1) enables an analytical approximation of the frequency content of the dynamic change in luminance that occurs as a result of the motion of the eye. It predicts that the total power of  $\tilde{I}_U$  at a given spatial frequency  $|\mathbf{u}|$  is proportional to  $R_{SS}(|\mathbf{u}|) |\mathbf{u}|^2$ , where  $R_{SS}$  is the power spectrum of the stimulus. That is, for small eye movements, the total power that becomes available at non-zero temporal frequency is given by the power spectrum of the stimulus multiplied by  $|\mathbf{u}|^2$ , a term that enhances high spatial frequencies and

attenuates low frequencies. As illustrated in Fig. 4e, this term amplifies the grating relative to the noise in experiment one and the noise relative to the grating in experiment two.

Our results show that vision is impaired at high spatial frequencies in the absence of fixational eye movements. This finding is consistent with the spatial frequency dependence of the temporal modulations resulting from fixational eye movements. Neurons in the early visual system are sensitive to these input modulations<sup>27–29</sup>. As with the stimuli of experiment one, natural visual environments possess substantial power at low spatial frequencies. Our results indicate that sampling visual information by means of a jittering fixation is an effective strategy for analysing natural scenes, facilitating the processing of spatial detail in the face of otherwise overwhelming low-frequency power.

## METHODS SUMMARY

Subjects reported the orientation ( $\pm 45^\circ$ ) of a grating masked by noise. In experiment one, a grating with 11 cycles per degree was perturbed by low spatial frequency noise (low-pass cutoff frequency  $f_c = 5$  cycles per degree). In experiment two, the stimulus was a grating with 4 cycles per degree overlapped by high spatial frequency noise (high-pass  $f_c = 10$  cycles per degree). Stimuli were displayed at the onset of fixation after a saccade towards a randomly cued location. Stimuli were either fixed at a location on the screen (unstabilized condition) or moved with the eye to cancel the retinal motion resulting from fixational eye movements (stabilized condition). In both experiments, the contrast of the gratings was individually adjusted for each subject so that performance levels in the unstabilized condition were approximately 75%.

Contrast thresholds were evaluated under conditions similar to those of experiments one and two using an adaptive tracking method<sup>30</sup>, both in the presence and in the absence of the retinal image motion originating from fixational eye movements.

In the experiment reported in Fig. 3, the task, stimuli and procedure were identical to those of experiment one, except that trials randomly alternated among all conditions. Random selections of the stabilization axis and the stimulus ensured lack of correlation between the direction of retinal image motion and the grating orientation.

Power spectra were evaluated using the Welch periodogram technique. In the unstabilized condition, the input signal  $I_U(\mathbf{x}, t)$  can be expressed as:

$$I_U(\mathbf{x}, t) = S(\mathbf{x} + \zeta(t)) = \bar{I}_U(\mathbf{x}) + \tilde{I}_U(\mathbf{x}, t) \quad (2)$$

where  $\bar{I}_U(\mathbf{x})$  is the mean luminance received by the receptor over the period of stimulus presentation. Figure 4 shows the spectra of  $I_S$ ,  $I_U$  and  $\tilde{I}_U$ .  $I_S$  and  $I_U$  possessed equal total power but differed in their spectral distributions.

**Full Methods** and any associated references are available in the online version of the paper at [www.nature.com/nature](http://www.nature.com/nature).

Received 5 March; accepted 18 April 2007.

1. Ratliff, F. & Riggs, L. A. Involuntary motions of the eye during monocular fixation. *J. Exp. Psychol.* **40**, 687–701 (1950).
2. Ditchburn, R. W. Eye movements in relation to retinal action. *Opt. Acta* **1**, 171–176 (1955).
3. Steinman, R. M., Haddad, G. M., Skavenski, A. A. & Wyman, D. Miniature eye movement. *Science* **181**, 810–819 (1973).
4. Murakami, I. & Cavanagh, P. A jitter after-effect reveals motion-based stabilization of vision. *Nature* **395**, 798–801 (1998).
5. Ditchburn, R. W. & Ginsborg, B. L. Vision with a stabilized retinal image. *Nature* **170**, 36–37 (1952).
6. Riggs, L. A. & Ratliff, F. The effects of counteracting the normal movements of the eye. *J. Opt. Soc. Am.* **42**, 872–873 (1952).
7. Riggs, L. A., Ratliff, F., Cornsweet, J. C. & Cornsweet, T. N. The disappearance of steadily fixated visual test objects. *J. Opt. Soc. Am.* **43**, 495–501 (1953).
8. Yarbus, A. L. *Eye Movements and Vision* (Plenum, New York, 1967).
9. Martinez-Conde, S., Macknik, S. L., Troncoso, X. G. & Dyar, T. A. Microsaccades counteract fading during fixation. *Neuron* **49**, 297–305 (2006).
10. Hering, E. Über die Grenzen der Sehschärfe. Berichte der Königlichen Sächsischen Gesellschaft der Wissenschaften. *Math. Phys. Klasse* **20**, 16–24 (1899).
11. Averill, H. I. & Weymouth, F. W. Visual perception and the retinal mosaic, II. The influence of eye movements on the displacement threshold. *J. Comp. Psychol.* **5**, 147–176 (1925).
12. Marshall, W. H. & Talbot, S. A. in *Biological Symposia—Visual Mechanisms*. Vol. 7 (ed. Kluver, H.) 117–164 (Cattell, Lancaster, Pennsylvania, 1942).
13. Arend, L. E. Spatial differential and integral operations in human vision: implications of stabilized retinal image fading. *Psychol. Rev.* **80**, 374–395 (1973).
14. Ahissar, E. & Arieli, A. Figuring space by time. *Neuron* **32**, 185–201 (2001).
15. Greschner, M., Bongard, M., Rujan, P. & Ammermüller, J. Retinal ganglion cell synchronization by fixational eye movements improves feature estimation. *Nature Neurosci.* **5**, 341–347 (2002).
16. Ölveczky, B. P., Baccus, S. A. & Meister, M. Segregation of object and background motion in the retina. *Nature* **423**, 401–408 (2003).
17. Rucci, M. & Casile, A. Fixational instability and natural image statistics: implications for early visual representations. *Network Comp. Neur. Syst.* **16**, 121–138 (2005).
18. Santini, F., Redner, G., Iovin, R. & Rucci, M. EyeRIS: A general-purpose system for eye movement contingent display control. *Behav. Res. Methods* (in the press).
19. Koenderink, J. J. Contrast enhancement and the negative afterimage. *J. Opt. Soc. Am. A* **62**, 685–689 (1972).
20. Kelly, D. H. Motion and vision. I. Stabilized images of stationary gratings. *J. Opt. Soc. Am.* **69**, 1266–1274 (1979).
21. Tulunay-Keesey, Ü. Fading of stabilized retinal images. *J. Opt. Soc. Am.* **72**, 440–447 (1982).
22. Tulunay-Keesey, Ü. & Jones, R. M. The effect of micromovements of the eye and exposure duration on contrast sensitivity. *Vision Res.* **16**, 481–488 (1976).
23. Steinman, R. M., Cunitz, R. J., Timberlake, G. T. & Herman, M. Voluntary control of microsaccades during maintained monocular fixation. *Science* **155**, 1577–1579 (1967).
24. Steinman, R. M. & Collewijn, H. Binocular retinal image motion during active head rotation. *Vision Res.* **20**, 415–429 (1980).
25. Kapoula, Z. A., Robinson, D. A. & Hain, T. C. Motion of the eye immediately after a saccade. *Exp. Brain Res.* **61**, 386–394 (1986).
26. Field, D. J. Relations between the statistics of natural images and the response properties of cortical cells. *J. Opt. Soc. Am. A* **4**, 2379–2394 (1987).
27. Leopold, D. A. & Logothetis, N. K. Microsaccades differentially modulate neural activity in the striate and extrastriate visual cortex. *Exp. Brain Res.* **123**, 341–345 (1998).
28. Martinez-Conde, S., Macknik, S. L. & Hubel, D. H. Microsaccadic eye movements and firing of single cells in the striate cortex of macaque monkeys. *Nature Neurosci.* **3**, 251–258 (2000).
29. Snodderly, D. M., Kagan, I. & Gur, M. Selective activation of visual cortex neurons by fixational eye movements: implications for neural coding. *Vis. Neurosci.* **18**, 259–277 (2001).
30. Macmillan, N. A. & Creelman, C. D. *Detection Theory—A User's Guide* 2nd edn (L.Erlbaum Associates, London, 2005).

**Supplementary Information** is linked to the online version of the paper at [www.nature.com/nature](http://www.nature.com/nature).

**Acknowledgements** We thank E. Ahissar, G. Desbordes, W. S. Geisler, K. J. Nielsen, E. L. Schwartz, D. M. Snodderly and J. D. Victor for help. This work was supported by grants from the National Institute of Health and the National Science Foundation to M.R.

**Author Information** Reprints and permissions information is available at [www.nature.com/reprints](http://www.nature.com/reprints). The authors declare no competing financial interests. Correspondence and requests for materials should be addressed to M.R. (rucci@cns.bu.edu).

## METHODS

**Subjects.** Five naive subjects and one experienced observer, all with normal vision, participated in the experiments. Informed consent was obtained from all subjects in accordance with the procedures approved by the Boston University Charles River Campus Institutional Review Board.

**Apparatus and stimuli.** To overcome the technical limitations of previous studies of retinal stabilization, the experiments of this study used EyeRIS (ref. 18), a custom-developed system based on a digital signal processor, which allows flexible gaze-contingent display control on a cathode-ray tube (CRT) monitor. This system processes eye movements in real time and guarantees refresh of the stimulus with a maximum delay equal to the time required to render two frames on the CRT display (10 ms at 200 Hz, typical delay 7.5 ms). Joint analysis of the performance of EyeRIS and eye-movement data shows that the error of retinal stabilization in the experiments was smaller than 1' (see Supplementary Methods). Such a high quality of retinal stabilization was possible because of the brief duration of stimulus presentation and the small amplitude of fixational eye movements.

Stimuli were designed on the basis of the predictions of equation (1) to enhance the impact of fixational eye movements on visual input signals. Gratings and noise fields were linearly superimposed, and the resulting patterns were weighted by a two-dimensional gaussian envelope so that the visible area covered approximately 30'. Such a small stimulus could be seen with a single fixation without the need for macroscopic eye movements. Stimuli were displayed on a grey background of uniform luminance equal to the mean luminance of the stimulus ( $21 \text{ cd m}^{-2}$ ). To compensate for individual differences in contrast sensitivity, contrast levels were adjusted for each subject in a preliminary experimental session, so that discrimination percentages were around 75% in the presence of the normally moving retinal image. Michelson contrast levels ranged from 4% to 9%.

Stimuli were displayed on a fast phosphor CRT monitor (Iiyama HM204DT) at a resolution of  $800 \times 600$  pixels and a vertical refresh rate of 200 Hz. Movements of the head were prevented by use of a bite bar with a customized dental imprint and a headrest. Eye position was measured with a Generation 6 DPI eyetracker (Fourward Technologies, Inc.).

**Procedure.** Stimuli were displayed for 1 s at the centre of the visual field. To study the normal motion of the retinal image that occurs when periods of fixation are separated by saccades, stimuli were presented after the subject performed a saccade from the centre of the screen to a randomly cued location at 1.5° of visual eccentricity. A real-time routine running on EyeRIS displayed the stimulus as soon as it detected the onset of a fixation within 30' of the cued location. Offline analysis of eye-movement traces showed that activation of the display occurred with an average delay of 12 ms after the onset of fixation, as evaluated by a human expert.

In each trial, the grating had equal probability of being tilted by  $\pm 45^\circ$  and was followed by a high-energy mask for 1.3 s. Subjects reported the orientation of the grating using a joypad after disappearance of the mask. Trials alternated randomly between the two conditions of normal retinal motion and stabilization. In the stabilized condition, the stimulus was actively translated on the screen under real-time computer control to compensate for the subject's eye movements and always appeared to be immobile at the centre of the fovea. Subjects did not report stimulus fading and were often unable to tell whether or not a trial was stabilized. Trials with saccades larger than 30', or in which the gaze exceeded a 30'-radius window centred on the stimulus, were discarded from data analysis.

Contrast thresholds were evaluated in the same conditions as experiments one and two. The grating contrast was changed at each trial following a 3-up-1-down rule, so that percentages of correct discrimination settled around 79%. To enable fine changes between trials, these experiments were conducted at a lower monitor contrast setting with a background luminance of  $6 \text{ cd m}^{-2}$ . Every few trials, an image randomly extracted from a database of natural scenes was presented for 2 s to ensure that fading did not affect the results. Each subject underwent a minimum of 60 trials until thresholds settled on steady values. The values shown in Fig. 2 are mean  $\pm$  s.d. evaluated over the last ten trials.

# Sensory neuron sodium channel $\text{Na}_v1.8$ is essential for pain at low temperatures

Katharina Zimmermann<sup>1\*</sup>, Andreas Leffler<sup>2\*</sup>, Alexandru Babes<sup>1,3</sup>, Cruz Miguel Cendan<sup>4</sup>, Richard W. Carr<sup>1</sup>, Jin-ichi Kobayashi<sup>5</sup>, Carla Nau<sup>2</sup>, John N. Wood<sup>4</sup> & Peter W. Reeh<sup>1</sup>

**Sensory acuity and motor dexterity deteriorate when human limbs cool down, but pain perception persists and cold-induced pain can become excruciating<sup>1</sup>. Evolutionary pressure to enforce protective behaviour requires that damage-sensing neurons (nociceptors) continue to function at low temperatures. Here we show that this goal is achieved by endowing superficial endings of slowly conducting nociceptive fibres with the tetrodotoxin-resistant voltage-gated sodium channel (VGSC)  $\text{Na}_v1.8$  (ref. 2). This channel is essential for sustained excitability of nociceptors when the skin is cooled. We show that cooling excitable membranes progressively enhances the voltage-dependent slow inactivation of tetrodotoxin-sensitive VGSCs. In contrast, the inactivation properties of  $\text{Na}_v1.8$  are entirely cold-resistant. Moreover, low temperatures decrease the activation threshold of the sodium currents and increase the membrane resistance, augmenting the voltage change caused by any membrane current. Thus, in the cold,  $\text{Na}_v1.8$  remains available as the sole electrical impulse generator in nociceptors that transmits nociceptive information to the central nervous system. Consistent with this concept is the observation that  $\text{Na}_v1.8$ -null mutant mice<sup>3</sup> show negligible responses to noxious cold and mechanical stimulation at low temperatures. Our data present strong evidence for a specialized role of  $\text{Na}_v1.8$  in nociceptors as the critical molecule for the perception of cold pain and pain in the cold.**

Nociceptors are peripheral sensory neurons that innervate the skin and 'deep' tissues and respond to stimuli that are capable of producing tissue damage and pain. Independent of the sensory transduction molecules required for cold sensing<sup>4–8</sup>, the generation of action potentials and their propagation to the central nervous system necessitate the activity of VGSCs. Sensory neurons express several VGSC  $\alpha$ -subunits, with fast (for example  $\text{Na}_v1.7$ ) or slow ( $\text{Na}_v1.8$  and  $\text{Na}_v1.9$ ) kinetics<sup>2,9–11</sup>. Whereas fast VGSCs are selectively blocked by the puffer-fish poison tetrodotoxin (TTX), both  $\text{Na}_v1.8$  and  $\text{Na}_v1.9$  are resistant to TTX (TTXr)<sup>2,11</sup>.  $\text{Na}_v1.8$  is expressed exclusively in sensory neurons, generates a slow-inactivating current with a high threshold for activation, and is the only VGSC in the nociceptor capable of generating action potentials in the presence of TTX<sup>9,12,13</sup>. Using TTX as a tool to detect action potentials generated by  $\text{Na}_v1.8$  in intact nociceptive terminals, we were able to define the conditions under which this channel becomes physiologically relevant as an impulse generator.

The isolated skin-nerve preparation<sup>14</sup> allows the focal application of physical stimuli and chemicals to the cutaneous receptive field of a single intact nociceptor and permits the measurement of the consequent electrical events, propagated action potentials. In rat preparations, we found that mechanocold-sensitive C-fibre (CMC) nociceptors were blocked at 30 °C after the application of 1  $\mu\text{M}$  TTX,

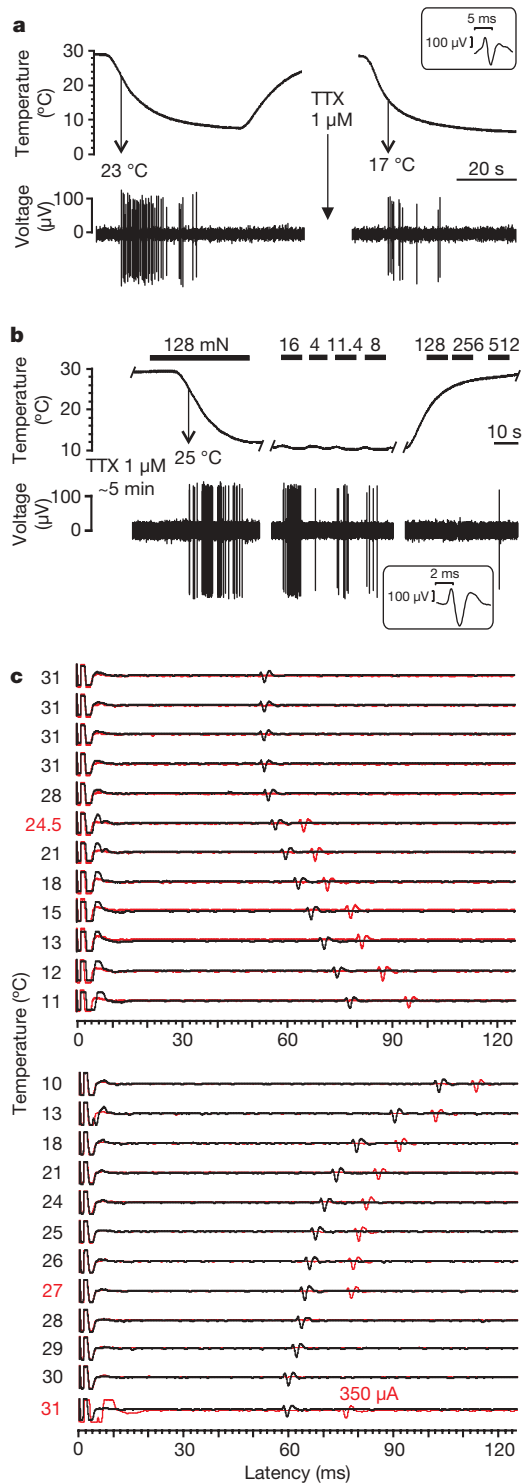
and as a result the nociceptors were rendered almost unexcitable when stimulated mechanically (using forces up to 1,000 mN) or electrically (to a maximum of 10 mA for 1 ms, applied with needle electrodes). However, TTX-treated nociceptors still responded to cold stimulation with action potential discharge, although with overall smaller cold responses and thresholds at lower temperatures (Fig. 1a). Almost all mechanosensitive C-fibres of all sensory categories in rat and mouse skin were blocked by TTX at 30 °C, but on cooling they regained excitability to mechanical (Fig. 1b) and electrical (Fig. 1c) stimulation with thresholds of activation that were similar to those without TTX. When the receptive field was warmed again, nociceptors returned to the almost unexcitable state of TTX block (Fig. 1b, c; see Supplementary Information and Supplementary Fig. S1).

These results indicate that the TTXr VGSC  $\text{Na}_v1.8$  becomes necessary for the generation of action potentials at low temperatures. To test this hypothesis we studied the influence of cooling on TTX-sensitive (TTXs) and TTXr (namely  $\text{Na}_v1.8$ ) sodium currents in dorsal root ganglion (DRG) neurons<sup>13,15,16</sup>. Cooling from 30 °C to 10 °C caused a slowing of activation and inactivation kinetics and reduced peak current amplitudes of both types of current (Fig. 2a, b). The decrease was significantly larger for TTXs than TTXr currents when cells were held at a membrane potential of  $-80$  mV, which is similar to the physiological membrane potential (Fig. 2c). This differential effect vanished when neurons were held at  $-120$  mV (Fig. 2c), a configuration that places sodium channels into a resting state devoid of inactivation. This implied a differential modulation by cooling of mechanisms of voltage-dependent inactivation. Cooling had little effect on fast inactivation (Fig. 2d) but markedly shifted the slow inactivation of TTXs currents towards more hyperpolarized potentials (Fig. 2e). In contrast, slow inactivation of TTXr currents was resistant to cooling (Fig. 2f). Cooling also caused a shift of the voltage-dependent activation towards more hyperpolarized potentials; however, this shift was small and similar for both TTXs and TTXr currents (Supplementary Fig. S3). These distinct properties of TTXs and TTXr currents were conserved in recombinant  $\text{Na}_v1.7$  (TTXs) and  $\text{Na}_v1.8$  (TTXr) channels; that is, cooling resulted in a leftward shift of slow inactivation of  $\text{Na}_v1.7$  (Fig. 2g) but not of  $\text{Na}_v1.8$  (Fig. 2h). Consequently, the decrease in current amplitudes on cooling was significantly stronger for  $\text{Na}_v1.7$  than for  $\text{Na}_v1.8$  (Fig. 2i). Thus, the differential sensitivity to cold of TTXs and TTXr currents in native neurons results from the inherent properties of specific VGSC subunits.

Whether these mechanisms are relevant for the generation of action potentials was first analysed by current-clamp recordings on DRG neurons (Fig. 2j, k). At 30 °C, electrically evoked action potentials in  $\text{Na}_v1.8$ -deficient neurons required stronger currents than in the wild type (WT; Fig. 2k, l). In addition, DRGs of both genotypes

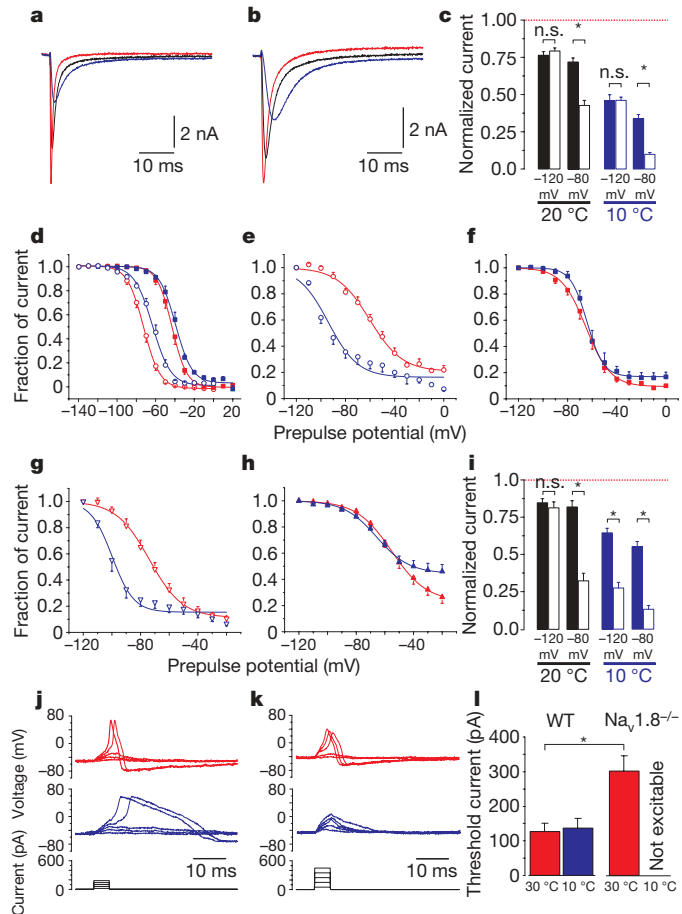
<sup>1</sup>Department of Physiology and Pathophysiology, <sup>2</sup>Department of Anesthesiology, Faculty of Medicine, Friedrich-Alexander University Erlangen-Nuremberg, 91054 Erlangen, Germany. <sup>3</sup>Department of Animal Physiology and Biophysics, Faculty of Biology, University of Bucharest, 050095 Bucharest, Romania. <sup>4</sup>Department of Biology, University College London, London WC1E 6BT, UK. <sup>5</sup>Department of Fixed Prosthodontics, Faculty of Dental Science, Kyushu University, Maidashi 3-1-1, Higashiku, Fukuoka 812-8582, Japan.

\*These authors contributed equally to this work.



were TTX-resistant at all temperatures (data not shown). Both findings are probably due to the low resting membrane potential of cultured neurons ( $-50 \text{ mV}$ ; Supplementary Fig. S4) at which most TTXs channels are inactivated (Fig. 2d). These findings imply that action potential generation at body temperature is largely resistant to TTX, involving  $\text{Na}_v1.8$  and voltage-gated calcium channels<sup>13,17</sup>. In contrast to the behaviour of WT neurons, even strong current injections failed to evoke action potentials in  $\text{Na}_v1.8^{-/-}$  neurons at  $10^\circ\text{C}$  (Fig. 2k, l). This suggests that action potential generation in DRG neurons depends entirely on  $\text{Na}_v1.8$  at low temperatures.

The importance of  $\text{Na}_v1.8$  as an action potential generator in nociceptive terminals was analysed with the skin-nerve preparation. In contrast to DRGs, WT and  $\text{Na}_v1.8^{-/-}$  fibres showed comparable thresholds for electrical (Fig. 3a) and mechanical (Fig. 3b) stimulation at both  $30^\circ\text{C}$  and  $10^\circ\text{C}$ . Cooling increased electrical thresholds in terminals of both genotypes by about 2.5-fold. Whereas  $\text{Na}_v1.8$ -deficient terminals lost excitability in the cold only in the presence of TTX, WT terminals regained their excitability at the same electrical threshold as in the absence of TTX (Fig. 3c, d). This implies that threshold responses



of WT afferents in the cold are due entirely to  $\text{Na}_v1.8$ , and that excitability of  $\text{Na}_v1.8$ -deficient afferents in the cold is retained only by virtue of TTXs channels<sup>3,16</sup>. We assessed nociceptor function in the cold by applying suprathreshold mechanical stimuli. In WT fibres, cooling decreased mechanically induced discharges (Fig. 3e). This decrease was even more pronounced in  $\text{Na}_v1.8^{-/-}$  fibres that displayed a severe impairment of mechanonociception in the cold (Fig. 3f, and Supplementary Fig. S5). Whereas noxious cold responsiveness in rat skin was found to be partly resistant to TTX (Fig. 1a), the comparatively poor cold responses in CMC fibres of mouse skin were retained in  $\text{Na}_v1.8^{-/-}$  (Supplementary Fig. S6). To induce more sustained responses to noxious cold, we applied the TRPM8 (transient receptor potential cation channel, subfamily M, member 8) agonist menthol<sup>4</sup> to the receptive field (500  $\mu\text{M}$ ; Fig. 3g, h). Whereas the excitatory effect of menthol at 30 °C was similar in both genotypes (Fig. 3g, and Supplementary Fig. S6), the menthol-sensitized cold responses observed in the WT were almost abolished in  $\text{Na}_v1.8^{-/-}$  mice (Fig. 3g, h) and blocked by TTX (not shown). Although transduction by cold (and menthol) is apparently intact in cutaneous terminals of  $\text{Na}_v1.8^{-/-}$  neurons, action potential generation in response to noxious cold is strongly impaired. The fact that C-fibre terminals but not DRG neurons of  $\text{Na}_v1.8$ -deficient mice were able to generate TTXs action potentials at 10 °C seems

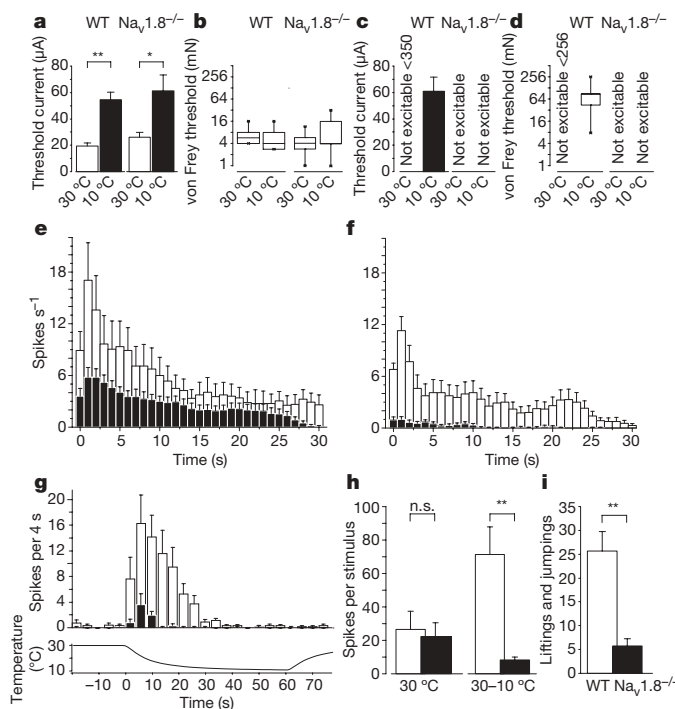


**Figure 3 | Loss of  $\text{Na}_v1.8$  impairs responsiveness to noxious stimulation in the cold.** **a–d**, Electrical (**a**, **c**) and von Frey (**b**, **d**) thresholds of C-fibre terminals in WT and  $\text{Na}_v1.8^{-/-}$  mice at 30 °C (open columns) and 10 °C (filled columns). With 1  $\mu\text{M}$  TTX (**c**, **d**), WT terminals regained excitability in the cold, whereas  $\text{Na}_v1.8^{-/-}$  terminals remained unexcitable ( $n = 10$ ). **e**, **f**, C-fibre responses to noxious mechanical stimulation (constant pressure of three times the von Frey threshold) of the terminals at 30 °C (open columns) and 10 °C (filled columns) in WT (**e**) and  $\text{Na}_v1.8^{-/-}$  (**f**) (52% decrease at 10 °C in WT; 92% decrease in  $\text{Na}_v1.8^{-/-}$ ;  $n = 10$ ; see Supplementary Fig. S5). **g**, Menthol (500  $\mu\text{M}$ )-sensitized cold responses of C-fibres in WT (open columns) and  $\text{Na}_v1.8^{-/-}$  (filled columns) (4-s bins, two-point adjacent averaging). **h**, At 30 °C menthol excited C-fibres from WT (open columns) and  $\text{Na}_v1.8^{-/-}$  (filled columns) similarly (action potentials per 2 min; see Supplementary Fig. S6b); sensitization to cold occurred only in WT (action potentials per 60 s;  $n = 7$ –12). **i**, Cold-plate test (0 °C).  $\text{Na}_v1.8^{-/-}$  mice showed negligible response to noxious cold ( $n = 9$ –10). Error bars indicate s.e.m. The boxes in **b** and **d** represent the 25th and 75th centiles; the horizontal lines inside the boxes show the median (if not identical with the 25th centile), and the ‘whiskers’ (enhanced by asterisks) indicate minima and maxima. Asterisk,  $P < 0.01$ ; two asterisks,  $P < 0.001$ ; Student’s *t*-test.

contradictory. However, the depolarized membrane potential of cultured DRG neurons is not representative for nerve terminals. Considering the strong voltage dependence of cold-induced slow inactivation of TTXs currents, a more hyperpolarized resting membrane potential would render TTXs sodium channels in terminals less susceptible to cold. Moreover, overexpression of TTXs channels<sup>3</sup> and altered inactivation properties of TTXs sodium currents in  $\text{Na}_v1.8$ -deficient neurons<sup>16</sup> have been proposed to compensate for the loss of  $\text{Na}_v1.8$ .

Consistent with the data obtained *in vitro* was the observation that the loss of  $\text{Na}_v1.8$  resulted in a very distinct phenotype in the cold-plate test as an *in vivo* assay for cold nociception<sup>6,18</sup>. The characteristic foot-lifting and jumping behaviour observed in WT mice was completely absent in  $\text{Na}_v1.8^{-/-}$  mice when placed on a plate held at 0 °C (Fig. 3i).

It remained puzzling why much lower currents were required in the cold than at 30 °C to trigger  $\text{Na}_v1.8$ -generated action potentials in TTX-treated WT terminals (Fig. 3c). It seems unlikely that the small shift of the activation curve of TTXr currents in the cold accounts fully for this marked decrease in activation threshold. We therefore studied the electrical excitability of rat skin-nerve terminals by analysing the electrical strength–duration relationship<sup>19</sup> to assess cold-induced changes in passive and active membrane properties (see Methods). Cooling caused an increase in the current threshold at shorter stimulus durations and a prolongation of the chronaxy, the most efficient stimulus duration in terms of charge transfer (Fig. 4a); both effects reflect the slowing of voltage-gated sodium channels in the cold (Supplementary Fig. S7)<sup>20</sup>. In addition, the chronaxy represents the passive membrane time constant,  $\tau_M = R_M \times C_M$ , and its prolongation indicates an increase in membrane input resistance<sup>19</sup>, which is a cogent consequence of cooling<sup>20–22</sup>. TTX increased both the current threshold at all stimulus durations and the chronaxy, which is consistent with the high threshold and slow kinetics of  $\text{Na}_v1.8$ . However, cooling under TTX clearly decreased current thresholds irrespective of stimulus duration (Fig. 4b, and Supplementary Fig. S7). This cold-induced increase in TTXr excitability is consistent with both a leftward shift of the TTXr activation curve and an increase in input membrane resistance. The latter effect may be of major importance in nerve endings (with their high ratio of

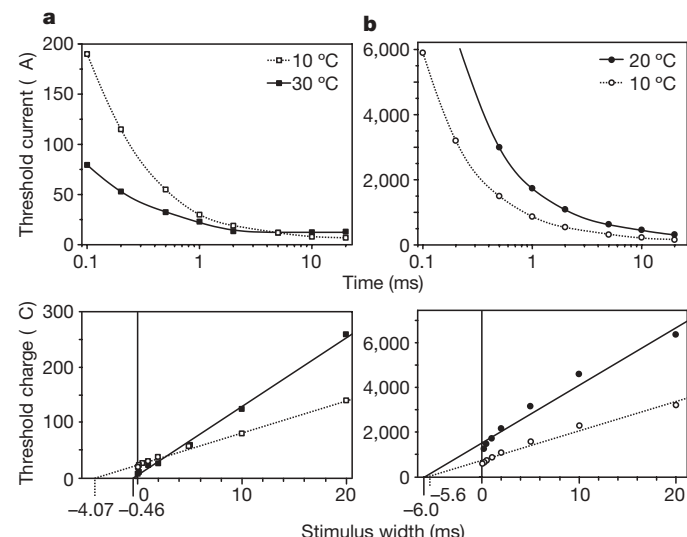


**Figure 4 | Cooling increases TTXr excitability in nociceptive terminals.** Electrical stimulus strength–duration measurements (upper panels) from a rat CMC-fibre terminal (0.47  $\text{m s}^{-1}$ ; 5.2 mN) at different temperatures<sup>19</sup>, without TTX (**a**) and in the presence of 1  $\mu\text{M}$  TTX (**b**). Lower panels: rheobase current and chronaxy were determined by the gradient and zero-charge intercept, respectively, of the regression of charge ( $Q$ ) on stimulus duration. In the absence of TTX (**a**), cooling increased current thresholds at shorter stimulus durations (less than chronaxy) but decreased the rheobase and prolonged the chronaxy. In **b**, TTX increased current thresholds and chronaxy, but cooling under TTX primarily decreased the rheobase and decreased rather than increased the chronaxy (see Supplementary Fig. S7).

surface area to volume), because it will decrease the current required to activate  $\text{Na}_v1.8$  by augmenting the voltage change across the membrane evoked by any depolarizing current<sup>21,22</sup>. The increase in input membrane resistance is consistent with physical laws and with cold-induced closure of certain potassium channels that have an established role in cold nociception<sup>23,24</sup>. Finally, a cold-induced block of the sodium–potassium (ATP-ase) pump<sup>25</sup> may also contribute to the increase in TTX<sub>r</sub> excitability.

Mammalian sodium channels are evolutionarily the most recent of the voltage-gated channels; however, they represent the best-characterized family. VGSCs are encoded by a family of genes that have been highly conserved throughout evolution, which reflects their function in the regulation of excitability<sup>10,26</sup>. The fact that  $\text{Na}_v1.8$  inactivation does not increase with cooling is likely to represent a conserved feature, vitally important for cold-blooded animals (poikilotherms), that has enabled homeotherms to detect and avoid tissue-damaging levels of cold. It may also explain the exquisite tissue specificity of  $\text{Na}_v1.8$  expression in mammals, in which it is expressed only in nociceptive neurons. Several findings imply a role for  $\text{Na}_v1.8$  in inflammatory and neuropathic pain<sup>15,27,28</sup>. One role for  $\text{Na}_v1.8$  in these conditions is to maintain the excitability of nociceptive neurons during repetitive firing and sustained depolarization that leads to progressive inactivation of TTX<sub>r</sub> sodium channels<sup>17</sup>. The high threshold for voltage-dependent fast inactivation of  $\text{Na}_v1.8$  is the distinguishing feature that renders it tolerant of tonic depolarization<sup>28</sup>. At dangerously low temperatures, however, the cold resistance of slow inactivation of  $\text{Na}_v1.8$  seems to be a decisive property making  $\text{Na}_v1.8$  an essential molecule for nociception in the cold and for cold pain.

## METHODS SUMMARY

**Animals.** Adult Wistar rats and littermates of WT and  $\text{Na}_v1.8$ -deficient mice<sup>3</sup> (continuously backcrossed to C57BL/6J since 1999) were used.

**Behavioural assays.** A cold-plate analgesia meter was used to assess noxious cold sensitivity on the plantar surface of the paw as described<sup>6</sup>.

**DRG cell culture.** Adult mice were killed by  $\text{CO}_2$  inhalation. DRGs from all spinal levels were removed and cultured as described<sup>29</sup>. Recordings were made within 24 h in culture.

**Transfection procedures.** Rat  $\text{Na}_v1.8$  was transiently transfected in the DRG neuroblastoma hybridoma cell line ND7/23, and human  $\text{Na}_v1.7$  was transiently transfected in HEK 293T cells as described<sup>29</sup>. Recordings were made within 3–4 days.

**Electrophysiology: single-fibre recordings.** The isolated skin–saphenous–nerve preparation and single-fibre recording technique were used as described<sup>14</sup>. Protocols for electrical stimulus strength–duration measurements were adapted<sup>19</sup>.

**Electrophysiology: patch-clamp recordings.** Whole-cell recordings were performed with an Axopatch 200B amplifier and pClamp 8.2 software (Axon Instruments) at defined temperatures<sup>30</sup>. Current-clamp recordings were made by using DRG neurons with a resting membrane potential more negative than  $-40\text{ mV}$ . Voltage-clamp recordings were performed on DRG neurons from WT mice ( $18.0 \pm 1.0\text{ pF}$ ,  $n = 39$ ) and  $\text{Na}_v1.8^{-/-}$  mice ( $16.9 \pm 1.0\text{ pF}$ ,  $n = 50$ ;  $P = 0.46$ , Student's *t*-test). TTX<sub>r</sub> currents were studied in the presence of  $250\text{ nM TTX}$ . Cells with an increase in passive leak current during cooling were discarded. Sodium channels of DRG neurons or heterologously expressed  $\text{Na}_v1.8$  and  $\text{Na}_v1.7$  were studied as described<sup>29</sup>. Values of all experiments are presented as means  $\pm$  s.e.m.; statistical comparisons were calculated with Student's *t*-test, significance symbols are defined in figure legends.

**Full Methods** and any associated references are available in the online version of the paper at [www.nature.com/nature](http://www.nature.com/nature).

Received 19 March; accepted 25 April 2007.

1. Solomon, S. & Stearns, C. R. On the role of the weather in the deaths of R. F. Scott and his companions. *Proc. Natl Acad. Sci. USA* **96**, 13012–13016 (1999).
2. Akopian, A. N., Sivilotti, L. & Wood, J. N. A tetrodotoxin-resistant voltage-gated sodium channel expressed by sensory neurons. *Nature* **379**, 257–262 (1996).
3. Akopian, A. N. *et al.* The tetrodotoxin-resistant sodium channel SNS has a specialized function in pain pathways. *Nature Neurosci.* **2**, 541–548 (1999).
4. Peier, A. M. *et al.* A TRP channel that senses cold stimuli and menthol. *Cell* **108**, 705–715 (2002).
5. McKemy, D. D., Neuhauser, W. M. & Julius, D. Identification of a cold receptor reveals a general role for TRP channels in thermosensation. *Nature* **416**, 52–58 (2002).

6. Kwan, K. Y. *et al.* TRPA1 contributes to cold, mechanical, and chemical nociception but is not essential for hair-cell transduction. *Neuron* **50**, 277–289 (2006).
7. Story, G. M. *et al.* ANKTM1, a TRP-like channel expressed in nociceptive neurons, is activated by cold temperatures. *Cell* **112**, 819–829 (2003).
8. Babes, A., Zorzon, D. & Reid, G. Two populations of cold-sensitive neurons in rat dorsal root ganglia and their modulation by nerve growth factor. *Eur. J. Neurosci.* **20**, 2276–2282 (2004).
9. Brock, J. A., McLachlan, E. M. & Belmonte, C. Tetrodotoxin-resistant impulses in single nociceptor nerve terminals in guinea-pig cornea. *J. Physiol. (Lond.)* **512**, 211–217 (1998).
10. Catterall, W. A., Goldin, A. L. & Waxman, S. G. International Union of Pharmacology. XLVII. Nomenclature and structure–function relationships of voltage-gated sodium channels. *Pharmacol. Rev.* **57**, 397–409 (2005).
11. Dib-Hajj, S., Black, J. A., Cummins, T. R. & Waxman, S. G.  $\text{NaN}/\text{Nav}1.9$ : a sodium channel with unique properties. *Trends Neurosci.* **25**, 253–259 (2002).
12. Strassman, A. M. & Raymond, S. A. Electrophysiological evidence for tetrodotoxin-resistant sodium channels in slowly conducting dural sensory fibers. *J. Neurophysiol.* **81**, 413–424 (1999).
13. Blair, N. T. & Bean, B. P. Roles of tetrodotoxin (TTX)-sensitive  $\text{Na}^+$  current, TTX-resistant  $\text{Na}^+$  current, and  $\text{Ca}^{2+}$  current in the action potentials of nociceptive sensory neurons. *J. Neurosci.* **22**, 10277–10290 (2002).
14. Reeh, P. W. Sensory receptors in mammalian skin in an *in vitro* preparation. *Neurosci. Lett.* **66**, 141–146 (1986).
15. Wood, J. N., Boorman, J. P., Okuse, K. & Baker, M. D. Voltage-gated sodium channels and pain pathways. *J. Neurobiol.* **61**, 55–71 (2004).
16. Matsutomi, T., Nakamoto, C., Zheng, T., Kakimura, J. & Ogata, N. Multiple types of  $\text{Na}^+$  currents mediate action potential electrogenesis in small neurons of mouse dorsal root ganglia. *Pflügers Arch.* **453**, 83–96 (2006).
17. Renganathan, M., Cummins, T. R. & Waxman, S. G. Contribution of  $\text{Na}_v1.8$  sodium channels to action potential electrogenesis in DRG neurons. *J. Neurophysiol.* **86**, 629–640 (2001).
18. Bautista, D. M. *et al.* TRPA1 mediates the inflammatory actions of environmental irritants and proalgesic agents. *Cell* **124**, 1269–1282 (2006).
19. Bostock, H. The strength–duration relationship for excitation of myelinated nerve: computed dependence on membrane parameters. *J. Physiol. (Lond.)* **341**, 59–74 (1983).
20. Hodgkin, A. L. & Katz, B. The effect of temperature on the electrical activity of the giant axon of the squid. *J. Physiol. (Lond.)* **109**, 240–249 (1949).
21. Thompson, S. M., Masukawa, L. M. & Prince, D. A. Temperature dependence of intrinsic membrane properties and synaptic potentials in hippocampal CA1 neurons *in vitro*. *J. Neurosci.* **5**, 817–824 (1985).
22. Volgushev, M., Vidyasagar, T. R., Chistiakova, M., Yousef, T. & Eysel, U. T. Membrane properties and spike generation in rat visual cortical cells during reversible cooling. *J. Physiol. (Lond.)* **522**, 59–76 (2000).
23. Reid, G. & Flonta, M. Cold transduction by inhibition of a background potassium conductance in rat primary sensory neurones. *Neurosci. Lett.* **297**, 171–174 (2001).
24. Viana, F., de la Pena, E. & Belmonte, C. Specificity of cold thermotransduction is determined by differential ionic channel expression. *Nature Neurosci.* **5**, 254–260 (2002).
25. Pierau, F. K., Torrey, P. & Carpenter, D. O. Mammalian cold receptor afferents: role of an electrogenic sodium pump in sensory transduction. *Brain Res.* **73**, 156–160 (1974).
26. Goldin, A. L. Evolution of voltage-gated  $\text{Na}^+$  channels. *J. Exp. Biol.* **205**, 575–584 (2002).
27. Matthews, E. A., Wood, J. N. & Dickenson, A. H. Nav 1.8-null mice show stimulus-dependent deficits in spinal neuronal activity. *Mol. Pain* **2**, 5 (2006).
28. Rush, A. M. *et al.* A single sodium channel mutation produces hyper- or hypoexcitability in different types of neurons. *Proc. Natl Acad. Sci. USA* **103**, 8245–8250 (2006).
29. Leffler, A., Reiprich, A., Mohapatra, D. P. & Nau, C. Use-dependent block by lidocaine but not amitriptyline is more pronounced in tetrodotoxin (TTX)-resistant  $\text{Na}_v1.8$  than in TTX-sensitive  $\text{Na}^+$  channels. *J. Pharmacol. Exp. Ther.* **320**, 354–364 (2007).
30. Dittert, I. *et al.* Improved superfusion technique for rapid cooling or heating of cultured cells under patch-clamp conditions. *J. Neurosci. Methods* **151**, 178–185 (2006).

**Supplementary Information** is linked to the online version of the paper at [www.nature.com/nature](http://www.nature.com/nature).

**Acknowledgements** We thank H. Bostock and O. Krishtal for discussions. This work was supported by the Wellcome Trust, the MRC, SEUI/MEC, the German Research Foundation and the Humboldt Foundation.

**Author Contributions** J.K. made the decisive discovery that TTX-blocked rat CMC fibres fired in response to noxious cold stimulation. A.L. performed the voltage-clamp recordings, A.B. the current-clamp recordings, and K.Z. and P.W.R. the skin–nerve recordings. J.N.W. and C.M.C. provided the mice and conducted behavioural experiments. C.N. provided heterologously expressed  $\text{Na}_v1.7$  and  $\text{Na}_v1.8$ . R.W.C. wrote a script for Spike2 enabling the modified excitability testing.

**Author Information** Reprints and permissions information is available at [www.nature.com/reprints](http://www.nature.com/reprints). The authors declare no competing financial interests. Correspondence and requests for materials should be addressed to K.Z. (zimmermann@physiologie1.uni-erlangen.de).

## METHODS

**Animals.** Wistar rats (150–200 g) and littermates of WT and  $\text{Na}_v1.8$ -deficient mice (either sex)<sup>3</sup> continuously backcrossed to C57BL/6J since 1999 (25–32 g), were used.

**Behavioural assays.** A cold-plate analgesia meter (IITC Life Science), maintained at  $0 \pm 0.5^\circ\text{C}$ , was used to assess noxious cold sensitivity of the plantar surface of the hind paws of the mice<sup>6</sup>. Nociceptive responses are given as means from two separate countings of the number of paw lifts during 5 min (60-min interval).

**Single-fibre electrophysiology.** We used the technique based on isolated skin-saphenous-nerve preparation and single-fibre recording<sup>14</sup>. To apply solutions of defined temperature, we designed a flow-through heater connected to a roller pump. A stainless steel cannula was coiled with an insulated resistive wire ( $10\ \Omega\text{ m}^{-1}$ ) over a length of 10 cm; the wire was connected to a computer-controlled power supply. The cold stimulus (60 s) consisted of a dynamic phase ( $30\text{--}12^\circ\text{C}$ ) and a subsequent static phase ( $12\text{--}10^\circ\text{C}$ ). The criterion for assigning cold responsiveness to a fibre (CMC) was a discharge of at least three spikes and/or sensitization to cooling after the application of 500  $\mu\text{M}$  menthol. Menthol was considered effective when the cold response at least doubled, when the unit discharged on menthol application at  $30^\circ\text{C}$ , or when a cold-insensitive unit developed responsiveness to cold. For temperature control, TTX superfusion and menthol superfusion, the receptive field was isolated with a metal ring (volume 500  $\mu\text{l}$ ) and continuously perfused at a rate of  $10\ \text{ml min}^{-1}$ . Noxious mechanical stimulation was performed with a gravity-driven von Frey type stimulus of threefold the threshold strength. DAPSYS (<http://www.dapsys.net>) was used to record and analyse the data.

**Electrical stimulus strength-duration measurements.** A high-impedance (9–12-M $\Omega$ ) needle electrode and a constant-current stimulus isolator (WPI) were used to perform excitability testing at the most sensitive spot of the receptive field (threshold current less than 50  $\mu\text{A}$  at 1 ms), applying electrical current pulses of variable strength and duration to the nerve ending. For each duration of current pulse the threshold current to evoke an action potential was determined by using the method of limits. The strength–duration relationship obtained for C-fibre excitation was converted to threshold-stimulus charge transfer ( $Q = It$ ) to use the linear function of charge ( $Q$ ) versus stimulus duration ( $t$ ) for the determination of two key parameters of excitability: rheobase current and chronaxy<sup>19</sup>. Rheobase is the minimal electric current of infinite duration that triggers an action potential; chronaxy is the stimulus duration for which a current of double the rheobase strength needs to be applied to evoke an action potential. The regression of threshold charge on stimulus duration was used to estimate rheobase (gradient) and the  $x$ -axis intercept at zero charge was used to estimate chronaxy. The effects of cold and TTX on C-fibre excitability are described in terms of changes in chronaxy and rheobase. Spike2 (CED) was used to record and analyse the data.

**Cell culture.** Adult mice were killed by  $\text{CO}_2$  inhalation. DRGs from all spinal levels were removed and cultured as described<sup>30</sup>. Recordings were made within 24 h in culture.

**Complementary DNA and transient transfection.** Rat  $\text{Na}_v1.8$  cDNA was transiently transfected in the DRG neuroblastoma hybridoma cell line ND7/23. Human  $\text{Na}_v1.7$  cDNA was transiently transfected in HEK 293T cells. ND7/23 and HEK 293T cells were maintained in DMEM (Gibco), supplemented with 10,000 U  $\text{ml}^{-1}$  penicillin/streptomycin (Gibco), 1 M HEPES (Gibco), 10% heat-inactivated FBS (HyClone) and 0.3 M taurine (Sigma) at  $37^\circ\text{C}$  and 5%  $\text{CO}_2$ . All cells were transfected by using the calcium phosphate precipitation method and included a reporter plasmid (1  $\mu\text{g}$  of CD8-*pih3m*). Transfected cells were used for experiments within 3–4 days.

**Whole-cell patch-clamp recordings.** Recordings were performed at defined temperatures<sup>30</sup> with an Axopatch 200B amplifier and pClamp 8.2 (Axon Instruments). Patch-clamp pipettes from borosilicate capillary glass (TW150F-3; WPI) were heat-polished to a resistance of 1–3 M $\Omega$ . Current-clamp recordings were made from small and medium-sized DRG neurons with a resting membrane potential of at least  $-40\text{ mV}$ . The extracellular solution contained (in mM):  $\text{NaCl}$  140,  $\text{KCl}$  4,  $\text{CaCl}_2$  2,  $\text{MgCl}_2$  1, glucose 5, HEPES 10 (adjusted to  $\text{pH } 7.4$  with  $\text{NaOH}$ ). The pipette (intracellular) solution contained (in mM):  $\text{KCl}$  140, EGTA 0.5, HEPES 5,  $\text{MgATP}$  3 (adjusted to  $\text{pH } 7.3$  with  $\text{NaOH}$ ). TTX was applied to the extracellular solution at a concentration of 250 nM. Voltage-clamp recordings were made on DRG neurons of WT mice ( $18.0 \pm 1.0\ \text{pF}$ ,  $n = 39$ ) and  $\text{Na}_v1.8^{-/-}$  mice ( $16.9 \pm 1.0\ \text{pF}$ ,  $n = 50$ ;  $P = 0.46$ , Student's *t*-test). TTX currents were studied in WT DRG neurons in the presence of 250 nM TTX; TTXs currents were studied in  $\text{Na}_v1.8^{-/-}$  DRGs.

The extracellular solution for DRG recordings contained (in mM):  $\text{NaCl}$  40, choline chloride 100,  $\text{KCl}$  3,  $\text{MgCl}_2$  1,  $\text{CaCl}_2$  1, HEPES 10 ( $\text{pH } 7.4$ ). The intracellular solution contained (in mM)  $\text{CsF}$  140, EGTA 1,  $\text{NaCl}$  10, HEPES 10 ( $\text{pH } 7.4$ ). Cells with increase in passive leak current during cooling were

discarded. The extracellular solution for recordings from ND7/23 and HEK 293T cells contained (in mM):  $\text{NaCl}$  65, choline chloride 85,  $\text{CaCl}_2$  2, HEPES 10 ( $\text{pH } 7.4$ ). The intracellular solution contained (in mM):  $\text{NaF}$  100,  $\text{NaCl}$  30, EGTA 10, HEPES 10 ( $\text{pH } 7.4$ ). Transfection-positive cells were identified with immunobeads (anti-CD-8 Dynabeads; Dynal A.S.). Cells with an initial seal of more than 1 G $\Omega$  and a leak current of less than 500 pA throughout the recording were used for the analysis. Voltage errors were minimized by using 70–80% series resistance compensation. The capacitance artefact was cancelled by using the computer-controlled circuitry of the patch-clamp amplifier. Linear leak subtraction was applied to all voltage-clamp recordings (using resistance estimates from four hyperpolarizing pulses applied before the depolarizing test potential). Membrane currents were filtered at 5 kHz and sampled at 20 kHz. Data were analysed with Clampex 8.2 and Origin 6.0 (Microcal Software). To calculate the midpoint of activation, the peak conductance  $g_m$  was estimated from the equation  $g_m = I_{\text{Na}}/(E_m - E_{\text{rev}})$ , where  $I_{\text{Na}}$  is the peak current,  $E_m$  is the corresponding voltage and  $E_{\text{rev}}$  is the estimated reversal potential. The data were least-squares fitted by using the Boltzmann equation  $y = 1/[1 + \exp\{(E_{0.5} - E)/k_b\}]$ , where  $y$  is the maximum conductance,  $E_{0.5}$  is the voltage at which  $g/g_{\text{max}} = 0.5$ , and  $k_b$  is the slope factor. To obtain the midpoint of steady-state fast and slow inactivation, test-pulse-evoked peak currents were measured, normalized and plotted against the conditioning prepulse potential. The data were least-squares fitted by using the Boltzmann equation  $y = 1/[1 + \exp\{(E_{\text{pp}} - h_{0.5})/k_h\}]$ , where  $h_{0.5}$  is the voltage at which  $y = 0.5$ , and  $k_h$  is the slope factor.

**Voltage-clamp protocols for DRGs.** Cold-induced reduction was examined on sodium currents activated by test pulses to  $-10\text{ mV}$  (TTXs) or  $0\text{ mV}$  (TTXr) ( $V_h = -120\text{ mV}$  or  $80\text{ mV}$ ). For steady-state fast inactivation, 50-ms prepulses from  $-140\text{ mV}$  (TTXs) or  $-120\text{ mV}$  (TTXr) to  $+20\text{ mV}$  in steps of  $10\text{ mV}$  were used, followed by a 50-ms test pulse to  $-10\text{ mV}$  (TTXs) or  $0\text{ mV}$  (TTXr) ( $V_h = -120\text{ mV}$  or  $80\text{ mV}$ ). For steady-state slow inactivation, 30-s prepulses from  $-120\text{ mV}$  to  $0\text{ mV}$  in steps of  $10\text{ mV}$  were used, followed by a 100-ms pulse to  $-120\text{ mV}$  to remove fast inactivation, and then by a 50-ms test pulse to  $-10\text{ mV}$  (TTXs) or  $0\text{ mV}$  (TTXr) ( $V_h = -120\text{ mV}$ ).

**Voltage-clamp protocols for ND7/23 and HEK 293T cells.** Cold-induced reduction was examined on sodium currents activated by test pulses to  $+50\text{ mV}$  ( $V_h = -120\text{ mV}$  or  $80\text{ mV}$ ). For steady-state fast inactivation, 50-ms prepulses from  $-140\text{ mV}$  (TTXs) or  $-120\text{ mV}$  (TTXr) to  $+20\text{ mV}$  in steps of  $10\text{ mV}$  were used, followed by a 50-ms test pulse to  $+50\text{ mV}$  ( $V_h = -120\text{ mV}$ ). For steady-state slow inactivation, 30-s prepulses from  $-120\text{ mV}$  to  $-10\text{ mV}$  in steps of  $10\text{ mV}$  were used, followed by a 100-ms pulse to  $-120\text{ mV}$  to remove fast inactivation, and then by a 50-ms test pulse to  $+50\text{ mV}$  (TTXr) ( $V_h = -120\text{ mV}$ ).

## LETTERS

# HDAC6 rescues neurodegeneration and provides an essential link between autophagy and the UPS

Udai Bhan Pandey<sup>1</sup>, Zhiping Nie<sup>1</sup>, Yakup Batlevi<sup>2</sup>, Brett A. McCray<sup>1</sup>, Gillian P. Ritson<sup>1</sup>, Natalia B. Nedelsky<sup>1</sup>, Stephanie L. Schwartz<sup>1</sup>, Nicholas A. DiProspero<sup>3</sup>, Melanie A. Knight<sup>3</sup>, Oren Schuldiner<sup>4</sup>, Ranjani Padmanabhan<sup>5</sup>, Marc Hild<sup>5</sup>, Deborah L. Berry<sup>2</sup>, Dan Garza<sup>5</sup>, Charlotte C. Hubbert<sup>6</sup>, Tso-Pang Yao<sup>6</sup>, Eric H. Baehrecke<sup>2</sup> & J. Paul Taylor<sup>1</sup>

A prominent feature of late-onset neurodegenerative diseases is accumulation of misfolded protein in vulnerable neurons<sup>1</sup>. When levels of misfolded protein overwhelm degradative pathways, the result is cellular toxicity and neurodegeneration<sup>2</sup>. Cellular mechanisms for degrading misfolded protein include the ubiquitin-proteasome system (UPS), the main non-lysosomal degradative pathway for ubiquitinated proteins, and autophagy, a lysosome-mediated degradative pathway<sup>3</sup>. The UPS and autophagy have long been viewed as complementary degradation systems with no point of intersection<sup>4,5</sup>. This view has been challenged by two observations suggesting an apparent interaction: impairment of the UPS induces autophagy *in vitro*, and conditional knockout of autophagy in the mouse brain leads to neurodegeneration with ubiquitin-positive pathology<sup>6–9</sup>. It is not known whether autophagy is strictly a parallel degradation system, or whether it is a compensatory degradation system when the UPS is impaired; furthermore, if there is a compensatory interaction between these systems, the molecular link is not known. Here we show that autophagy acts as a compensatory degradation system when the UPS is impaired in *Drosophila melanogaster*, and that histone deacetylase 6 (HDAC6), a microtubule-associated deacetylase that interacts with polyubiquitinated proteins<sup>10</sup>, is an essential mechanistic link in this compensatory interaction. We found that compensatory autophagy was induced in response to mutations affecting the proteasome and in response to UPS impairment in a fly model of the neurodegenerative disease spinobulbar muscular atrophy. Autophagy compensated for impaired UPS function in an HDAC6-dependent manner. Furthermore, expression of HDAC6 was sufficient to rescue degeneration associated with UPS dysfunction *in vivo* in an autophagy-dependent manner. This study suggests that impairment of autophagy (for example, associated with ageing or genetic variation) might predispose to neurodegeneration. Moreover, these findings suggest that it may be possible to intervene in neurodegeneration by augmenting HDAC6 to enhance autophagy.

DTS7 is a temperature sensitive, dominant negative mutant of the  $\beta 2$  subunit of the proteasome<sup>11</sup>. Using the UAS/GAL4 system<sup>12</sup>, we targeted DTS7 expression to the *Drosophila* eye to cause tissue-restricted proteasome impairment. At 22 °C, proteasome function is intact and eye morphology was normal (Fig. 1a). However, at 28 °C substantial degeneration of the retina occurred owing to proteasome impairment (Fig. 1b). To investigate the role of HDAC6 in the setting of misfolded protein stress, we generated transgenic flies

expressing wild-type *Drosophila* HDAC6 as well as wild-type and mutant versions of human HDAC6. Expression of either *Drosophila* HDAC6 or human HDAC6 strongly suppressed the degenerative phenotype associated with proteasome impairment (Fig. 1c, d). However, expression of a catalytically dead mutant of human HDAC6 (H216A;H611A) failed to modify the degenerative phenotype, indicating that the deacetylase function of HDAC6 is required for suppression (Fig. 1e). To assess the role of endogenous HDAC6, we used RNAi knockdown (Supplementary Fig. S3). Targeted knockdown of *Drosophila* HDAC6 did not noticeably alter eye morphology on its own (Supplementary Fig. S4), but strongly enhanced degeneration when the proteasome was impaired (Supplementary Fig. S5). HDAC6 did not modify the rough eye phenotype caused by ectopic expression of the positive regulator of cell death *reaper*, indicating that HDAC6 is not a general suppressor of cell death pathways (Supplementary Fig. S6). Ectopic expression of *Drosophila* HDAC3 and *Drosophila* HDAC11 did not suppress degeneration caused by proteasome impairment, indicating that this is not a general response of HDACs (not shown).

Impaired UPS function has been implicated in a broad array of neurodegenerative disorders, but *in vivo* evidence is lacking<sup>13</sup>. Spinobulbar muscular atrophy (SBMA) is an inherited neurodegenerative disease that is caused by polyglutamine (polyQ) repeat expansion in the androgen receptor (AR)<sup>14</sup>. Like most adult-onset neurodegenerative diseases, SBMA pathology features accumulation of ubiquitin-positive protein aggregates in vulnerable neurons<sup>15</sup>. To develop a *Drosophila* model of SBMA, we generated transgenic flies expressing full-length human AR with 12–121 glutamine repeats using the UAS/GAL4 system. Flies expressing polyQ-expanded AR recapitulate key features of human SBMA, including ligand-dependent, polyQ length-dependent degeneration (Fig. 1f, g and Supplementary Fig. S7), as previously reported<sup>16</sup>.

To evaluate UPS function in this fly model of SBMA, we generated transgenic flies expressing a fluorescent reporter of UPS function. CL1-GFP is a fusion protein created by introducing a degradation signal to otherwise stable green fluorescent protein (GFP)<sup>17</sup>. This protein is rapidly degraded by the UPS, and its steady state levels reflect the functional status of this pathway<sup>18</sup>. When stable GFP was expressed in eye imaginal discs from third-instar larvae, a robust fluorescent signal was detected by confocal microscopy (Fig. 1k). In contrast, eye imaginal discs from control flies expressing the CL1-GFP reporter emitted a low fluorescent signal, reflecting an active UPS (Fig. 1l). To test the ability of the UPS reporter flies to

<sup>1</sup>Department of Neurology, University of Pennsylvania School of Medicine, Philadelphia, Pennsylvania 19104, USA. <sup>2</sup>Center for Biosystems Research, University of Maryland Biotechnology Institute, College Park, Maryland 20742, USA. <sup>3</sup>Neurogenetics Branch, NINDS, NIH, Bethesda, Maryland 20817, USA. <sup>4</sup>Department of Biological Sciences, Stanford University, Stanford, California 94305, USA. <sup>5</sup>Novartis Institutes for Biomedical Research, Cambridge, Massachusetts 02139, USA. <sup>6</sup>Department of Pharmacology and Cancer Biology, Duke University, Durham, North Carolina 27710, USA.

detect proteasome impairment *in vivo*, we co-expressed CL1-GFP in the eye with DTS7. At 22 °C, CL1-GFP reporter levels remained low in eye imaginal discs co-expressing DTS7, consistent with normal proteasome function (Fig. 1m). In contrast, at 28 °C, there was a significant increase in the CL1-GFP signal, demonstrating the ability of the reporter to detect proteasome impairment associated with a degenerative phenotype *in vivo* (Fig. 1n and Supplementary Fig. S8). UPS reporter RNA levels were not altered by the conditions used in our experiments (Supplementary Fig. S9).

We next expressed the CL1-GFP reporter in SBMA flies. In AR121 flies not exposed to ligand, fluorescent signal from the UPS reporter remained low, indicating that proteasome function was normal despite high expression of polyQ-expanded AR (Fig. 1o). However, flies reared on dihydrotestosterone (DHT), the natural ligand of AR, exhibited a significant increase in reporter signal, indicating proteasome impairment in association with induction of toxicity (Fig. 1p and Supplementary Fig. S8). The ligand-dependent nature of this finding indicates that UPS impairment is not merely a consequence of overexpressed AR121. Proteasome impairment by AR expression is a polyQ length-dependent phenomenon, because no impairment was observed in flies expressing AR12 (Supplementary Fig. S8). The finding of proteasome impairment in SBMA flies is consistent with a prior report that polyQ toxicity *in vivo* is enhanced by proteasome mutations<sup>19</sup>.

The determination that there is impairment of the UPS in SBMA flies led us to examine the ability of HDAC6 to modify the degenerative phenotype in this model of human neurodegenerative disease. Consistent with the results using proteasome mutant flies, ectopic expression of either *Drosophila* or human HDAC6 suppressed the ligand-dependent degenerative phenotype in flies expressing polyQ-expanded AR (Fig. 1h, i). Expression of the catalytically dead mutant

of human HDAC6 (H216A;H611A) failed to modify the degenerative phenotype, indicating that the deacetylase function of HDAC6 is also required for suppression of polyQ toxicity (Fig. 1j). Knockdown of endogenous HDAC6 with RNAi enhanced ligand-dependent degeneration in AR52 flies (Supplementary Fig. S5). Thus, endogenous HDAC6 also plays a role in protecting cells from polyQ toxicity.

We previously reported induction of autophagy and sequestration of polyQ-expanded AR in autophagic vacuoles *in vitro*<sup>20</sup>. Induction of autophagy *in vitro* in response to proteasome impairment has also been described<sup>6,7</sup>. To determine whether autophagy is induced *in vivo* when the UPS is impaired, we performed ultrastructural evaluation by transmission electron microscopy (TEM) in the DTS7 and SBMA flies. In both cases, we found a significant increase in morphological features of autophagy (Fig. 2f). These included autophagic vacuoles such as early autophagosomes in which membranes surrounded cytoplasmic components (Fig. 2a, b), more mature autophagic vacuoles (Fig. 2c), multilamellar bodies (MLBs, Fig. 2d) and multi-vesicular bodies (MVBs, Fig. 2e).

To assess the role of autophagy when the UPS is impaired, we inhibited autophagy by RNAi knockdown of the autophagy genes *atg6* and *atg12*. Knockdown of either *atg6* or *atg12* did not affect eye morphology (Supplementary Fig. S10), indicating that the *Drosophila* eye can tolerate reduced autophagy when UPS function is intact, at least in 1-day-old flies. In contrast, knocking down either *atg6* or *atg12* strongly enhanced the rough eye phenotype associated with UPS impairment in DTS7 flies reared at 28 °C (Fig. 2g–i) and in AR52 flies reared on DHT (Fig. 2j–l). From these data, we can infer that the autophagy induced by UPS impairment is compensatory.

We hypothesized that ectopic expression of HDAC6 suppressed degeneration by promoting autophagic degradation of aberrant

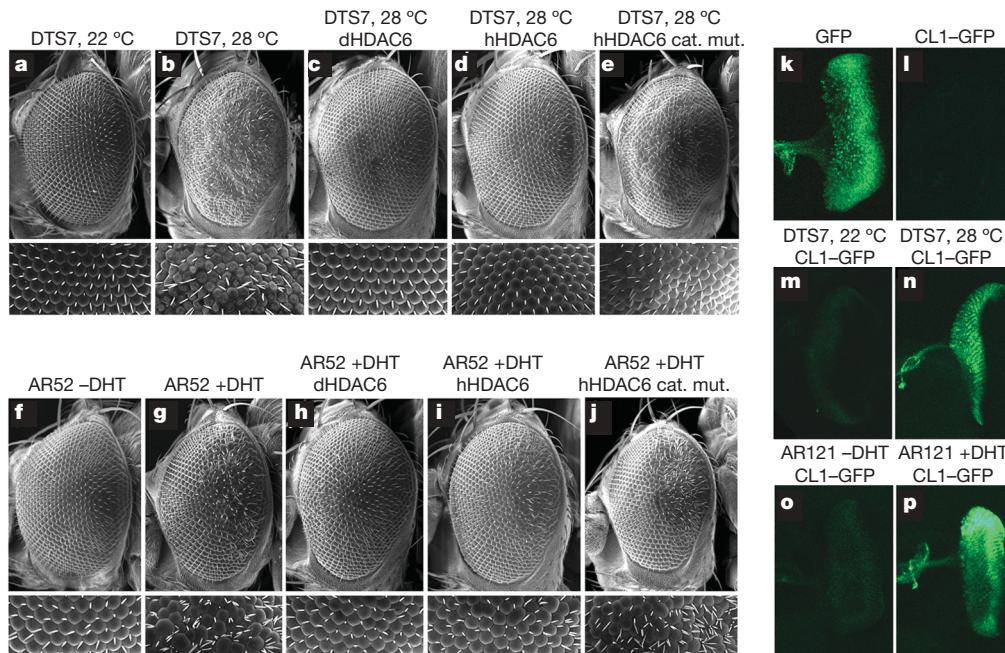


**Figure 1 | HDAC6 rescues degeneration in flies with proteasome impairment and in a fly model of SBMA that exhibits impaired UPS function.** **a–e**, Scanning electron microscopy (SEM) images of fly eyes expressing DTS7 with or without the indicated HDAC6 transgenes. Lower panels, magnification of ommatidia. **a**, Normal eyes in DTS7 flies reared at 22 °C. **b**, Rough eyes in DTS7 flies reared at 28 °C. **c, d**, Degeneration was suppressed by expression of *Drosophila* HDAC6 (dHDAC6; **c**) or human HDAC6 (hHDAC6; **d**), but not a catalytically dead mutant of hHDAC6 (cat. mut.; **e**). **f–j**, SEM images of fly eyes expressing AR52 with or without the indicated HDAC6 transgenes. Lower panels, magnification of ommatidia. **f**, Normal eyes in AR52 flies reared without (–) DHT. **g**, Rough eyes in AR52 flies reared with (+) DHT. Degeneration was suppressed by expression of

*Drosophila* HDAC6 (**h**) or human HDAC6 (**i**), but not a catalytically dead mutant of human HDAC6 (**j**). **k–p**, Detection of UPS reporter in imaginal eye discs from third-instar larvae by confocal microscopy. High level fluorescence was found in flies expressing GFP (**k**, positive control), but fluorescence was barely detectable in control flies expressing CL1-GFP (**l**, negative control). CL1-GFP accumulates in DTS7 flies with temperature-dependent proteasome impairment (compare **m** to **n**) and in AR52 flies with ligand-dependent degeneration (compare **o** to **p**). The retinal phenotypes of 200 to >1,000 flies of each genotype were examined. Quantitative analyses of eye phenotypes and proteasome impairment are presented in Supplementary Figs S2 and S3, respectively. (DHT, dihydrotestosterone.)

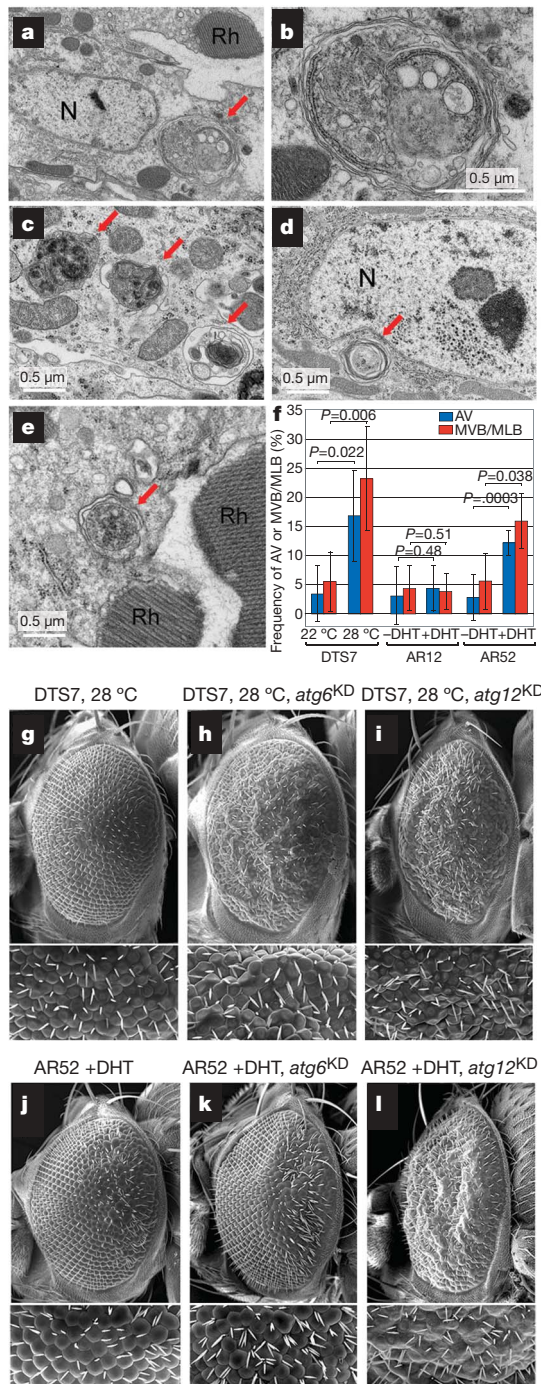


**Figure 2 | Induction of compensatory autophagy in flies with proteasome mutations and in SBMA flies.** **a–e**, Representative examples of autophagic vacuoles detected by TEM in retinal sections used to generate the quantitative data shown in **f**. **a**, An autophagosome (red arrow) containing cytoplasmic contents in a photoreceptor neuron from an AR52 fly reared on DHT. **b**, Higher magnification of the autophagosome in **a**. **c**, Multiple autophagolysosomes (red arrows) containing dense, amorphous material from an AR52 fly reared on DHT. **d**, A juxtanuclear multilamellar body (red arrow) from a DTS7 fly reared at 28 °C. **e**, A multivesicular body (red arrow) from a DTS7 fly reared at 28 °C. **f**, A significant increase in the frequency of neurons with autophagic figures in DTS7 flies reared at 28 °C compared to those reared at 22 °C, and in AR52 flies reared on DHT compared to those reared off DHT. Data show mean  $\pm$  s.d.,  $n = 59$ –82 neurons in 5 sections per condition. No accumulation of autophagic figures was found in AR12 flies. **g–l**, SEM images of fly eyes expressing the indicated transgenes. RNAi knockdown (KD) of *atg6* and *atg12* enhances degeneration in DTS7 flies reared at 28 °C (compare **h**, **i** to **g**) and AR52 flies reared on DHT (compare **k**, **l** to **j**). 200 to  $>1,000$  fly eyes of each genotype were examined. Quantitative analyses of eye phenotypes are presented in Supplementary Fig. S2. (N, nucleus; Rh, rhabdomere.)

protein. Thus, we examined AR levels *in vivo* and determined that expression of HDAC6 led to lower steady state levels of polyQ-expanded AR *in vivo*, whereas inhibition of autophagy by knockdown of *atg6* or *atg12* resulted in higher steady state levels (Fig. 3a). These altered steady state levels occurred despite no significant change in RNA levels (Supplementary Fig. S11), suggesting that HDAC6 accelerates the rate of AR degradation. To investigate this further, we adapted the inducible Geneswitch expression system<sup>21</sup> to monitor protein turnover. In *elav-GS;UAS-AR52* flies, no expression was detected before exposure to the inducing agent RU486 (data not shown). To induce expression, starved flies were fed sucrose media containing RU486 for one hour, which resulted in a pulse of expression that became detectable within 2 h, peaked after approximately 10 h, and then gradually decayed with a half-life of  $\sim 100$  min (Fig. 3b, c and Supplementary Fig. S12). In *elav-GS;UAS-AR52;UAS-dHDAC6* flies (dHDAC6 indicates *Drosophila* HDAC6), there was a parallel induction of AR52 expression, but an accelerated rate of decay, with a half-life of  $\sim 50$  min (Fig. 3c, d and Supplementary Fig. S12). Importantly, co-expression of *Drosophila* HDAC6 accelerated the turnover of not only AR52 monomers, but also high molecular weight aggregates that were trapped in the stacking gel (Fig. 3d).

We determined that treatment with rapamycin suppressed degeneration caused by either proteasome impairment or polyQ toxicity (Fig. 4a–d). This finding is consistent with a prior report, in which rapamycin suppressed degeneration in fly and mouse models of Huntington's disease<sup>22</sup>. Rescue by rapamycin has been attributed to inhibition of TOR and induction of autophagy, although a role for other TOR-regulated pathways could not be excluded<sup>22,23</sup>. We found that knockdown of *atg12* blocked the ability of rapamycin to suppress degeneration when the proteasome was impaired, verifying that rapamycin rescue is autophagy-dependent (Fig. 4e, f). Importantly,

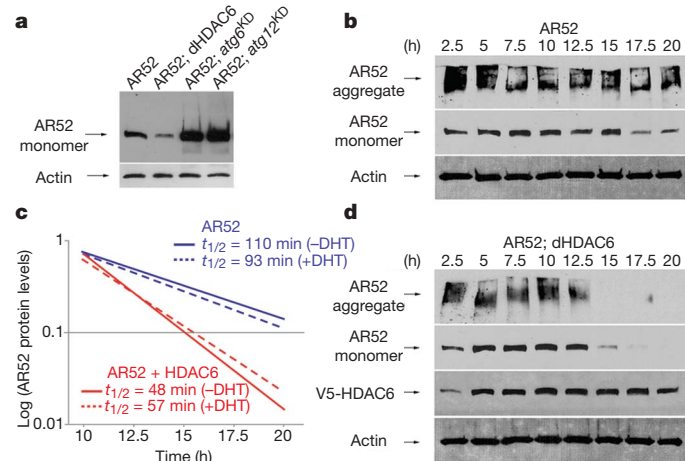


**Figure 3 | HDAC6 accelerates the turnover of polyQ-expanded AR.** **a**, Steady state levels of AR52 protein are reduced in flies overexpressing *Drosophila* HDAC6, but are elevated in flies in which *atg6* or *atg12* has been knocked down. **b**, Western blots showing the temporal profile of AR52 protein monomer and high molecular weight aggregate levels after a brief pulse of expression. AR52 protein became detectable by 2.5 h after treatment with RU486, reached a peak at 10 h, and then slowly decayed. **c**, A logarithmic plot of AR52/actin ratios was used to determine the line of best fit by regression analysis ( $y = Ae^{-Kx}$ ).  $R^2 = 0.9117$  (AR52 – DHT),  $R^2 = 0.7808$  (AR52 + DHT),  $R^2 = 0.9719$  (HDAC6 + (AR52 – DHT)),  $R^2 = 0.9644$  (HDAC6 + (AR52 + DHT)). Half-life was determined by the slope of the best fit line with the equation  $t_{1/2} = 0.693/K$ . Half-life of AR52 *in vivo* was reduced  $\sim 2$ -fold in flies co-expressing *Drosophila* HDAC6 and did not differ significantly in the presence (broken lines) or absence (solid lines) of DHT. Plots of the mean AR52/actin ratios are shown in Supplementary Fig. S12. **d**, Flies co-expressing *Drosophila* HDAC6 showed a nearly identical profile of induced expression as in **b**, but AR protein decayed at an accelerated rate. Exogenous *Drosophila* HDAC6 was detected by immunoblot against the V5 epitope.

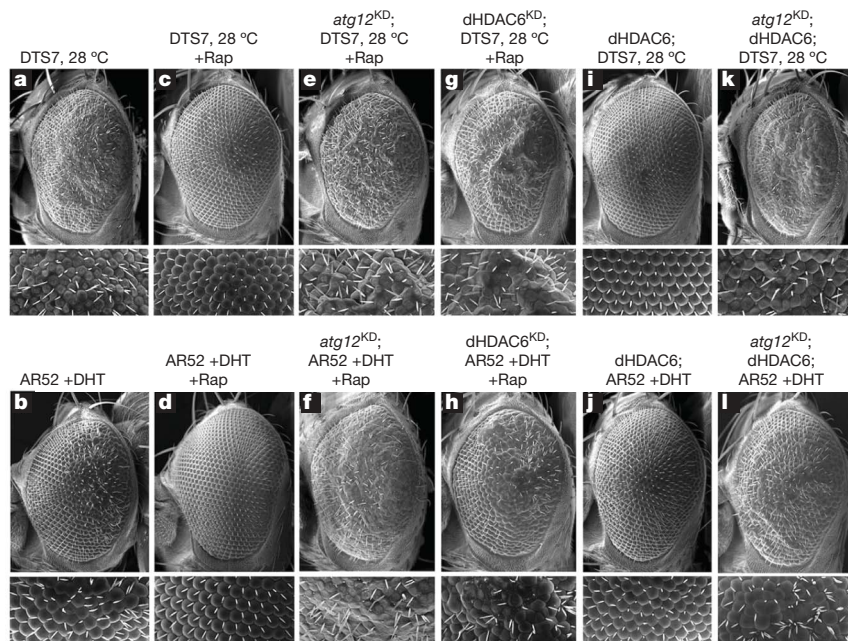


**Figure 4 | Rescue of degeneration by HDAC6 is autophagy-dependent.** a–l, SEM images of fly eyes expressing the indicated transgenes. The rough eye phenotypes caused by proteasome mutation (a) or by expression of polyQ-expanded AR (b) were both suppressed by rearing flies on the TOR inhibitor rapamycin (c, d). e, f, Rapamycin failed to suppress degeneration in an autophagy-deficient background created by knockdown of *atg12*, confirming that rescue by rapamycin is autophagy-dependent.

we also determined that knockdown of *Drosophila* HDAC6 blocked the ability of rapamycin to suppress degeneration, indicating that *Drosophila* HDAC6 is essential in order for induction of autophagy to compensate for proteasome impairment (Fig. 4g, h). Furthermore, we determined that the ability of *Drosophila* HDAC6 to suppress degeneration was autophagy-dependent, as rescue was blocked by knockdown of *atg12* (Fig. 4i–l). Thus, HDAC6 is integral to rescue of degeneration by autophagy and essential for autophagy to compensate for impaired UPS function.

Our findings extend previous studies in three important ways. First, we determined that induction of autophagy is sufficient to rescue degeneration associated with UPS impairment, dramatically illustrating the compensatory relationship between autophagy and the UPS. Second, we determined that HDAC6 activity is essential for autophagy to compensate for impaired UPS function. Finally, we determined that ectopic expression of HDAC6 alone is sufficient to rescue degeneration caused by proteasome mutations and polyQ toxicity, and does so in an autophagy-dependent manner. These observations are consistent with a mechanism in which HDAC6 facilitates turnover of aberrant proteins by autophagy, lowering their steady state levels and mitigating toxicity. We recently determined that overexpression of HDAC6 also suppressed degenerative phenotypes in additional models of neurodegenerative disease, including flies expressing pathologic A $\beta$  fragments and other polyQ-expanded proteins (U.B.P. and J.P.T., unpublished results). Thus, the HDAC6-mediated pathway of protein clearance may have broad relevance to degenerative proteopathies.

Although the current study indicates that the mechanism of HDAC6 rescue involves accelerated turnover of misfolded protein by autophagy, further study is required to determine the precise details of how this occurs. The mechanism could involve modulation of HSP90 activity, as this chaperone is a substrate of HDAC6 deacetylase activity<sup>24</sup>. Alternatively, HDAC6 may be involved in shuttling polyubiquitinated substrates to a location conducive to engulfment by autophagosomes, consistent with a known role for HDAC6 in the formation of aggresomes *in vitro*<sup>10</sup>. A third possibility is that HDAC6

g, h, Rapamycin also failed to suppress degeneration when HDAC6 levels were knocked down, demonstrating that suppression via the TOR pathway is HDAC6-dependent. k, l, HDAC6 failed to suppress degeneration in an autophagy-deficient background, confirming that rescue by HDAC6 is dependent on autophagy (compare k, l to i, j). 200 to >1,000 fly eyes of each genotype were examined. Quantitative analyses of eye phenotypes are presented in Supplementary Fig. S2.

may contribute to the transport of lysosomes to the site of autophagy, as suggested by the observation that HDAC6 knockdown results in dispersal of lysosomes away from the microtubule organizing centre<sup>6</sup>. Elucidating the precise role of HDAC6 in linking autophagy and the UPS promises substantial insights into cellular management of misfolded protein.

## METHODS

**Fly stocks and phenotypes.** *Drosophila* stocks were maintained on standard cornmeal agar media at 25 °C unless otherwise noted. Food was supplemented with DHT (Steraloids) and rapamycin (Sigma) once it had cooled to <50 °C to final concentrations of 1 mM and 1  $\mu$ M, respectively. Eye phenotypes of 200 to >1,000 flies of each genotype and condition were examined and scored as described in Supplementary Methods. Quantification of eye phenotypes is shown in Supplementary Fig. S2.

**Immunoblots and protein turnover.** Immunoblots were performed using antibodies against GFP (ab6556, Novus Biologicals), AR (N20, Santa Cruz Biotech), 119  $\beta$ -actin (119, Santa Cruz Biotech), tubulin (Sigma), V5 epitope (Invitrogen), and affinity-purified antibody against *Drosophila* HDAC6 as described<sup>25</sup>. To monitor protein turnover *in vivo*, 1-day-old adult flies of the appropriate genotype were starved for 12 h in a vial that contained only a Kimwipe soaked with 3 ml of water. After starvation, flies were placed in a vial that contained a Kimwipe soaked with 3 ml of 500  $\mu$ M RU486 (Steraloids) dissolved in a 2% sucrose solution (minus DHT condition) or 500  $\mu$ M RU486 and 1 mM DHT in a 2% sucrose solution (plus DHT condition) for 1 h, and then transferred to a vial containing standard food or food containing 1 mM DHT until collected for extract preparation.

**TEM.** To quantify morphologic features by TEM, we used longitudinal sections through the retina and identified photoreceptor neurons by the presence of rhabdomeres. 59–82 neurons from 5 flies per condition were scored for the presence of autophagic vacuoles, multivesicular bodies and multilamellar bodies, and comparisons between conditions were made with a paired *t*-test. A detailed description of all methods used in this study may be found in Supplementary Methods.

Received 19 December 2006; accepted 16 April 2007.

1. Taylor, J. P., Hardy, J. & Fischbeck, K. H. Toxic proteins in neurodegenerative disease. *Science* 296, 1991–1995 (2002).

2. Trojanowski, J. Q. & Lee, V. M. "Fatal attractions" of proteins. A comprehensive hypothetical mechanism underlying Alzheimer's disease and other neurodegenerative disorders. *Ann. NY Acad. Sci.* **924**, 62–67 (2000).
3. Rubinsztein, D. C. The roles of intracellular protein-degradation pathways in neurodegeneration. *Nature* **443**, 780–786 (2006).
4. Ciechanover, A., Finley, D. & Varshavsky, A. Ubiquitin dependence of selective protein degradation demonstrated in the mammalian cell cycle mutant ts85. *Cell* **37**, 57–66 (1984).
5. Pickart, C. M. Back to the future with ubiquitin. *Cell* **116**, 181–190 (2004).
6. Iwata, A., Riley, B. E., Johnston, J. A. & Kopito, R. R. HDAC6 and microtubules are required for autophagic degradation of aggregated huntingtin. *J. Biol. Chem.* **280**, 40282–40292 (2005).
7. Rideout, H. J., Lang-Rollin, I. & Stefanis, L. Involvement of macroautophagy in the dissolution of neuronal inclusions. *Int. J. Biochem. Cell Biol.* **36**, 2551–2562 (2004).
8. Komatsu, M. et al. Loss of autophagy in the central nervous system causes neurodegeneration in mice. *Nature* **441**, 880–884 (2006).
9. Hara, T. et al. Suppression of basal autophagy in neural cells causes neurodegenerative disease in mice. *Nature* **441**, 885–889 (2006).
10. Kawaguchi, Y. et al. The deacetylase HDAC6 regulates aggresome formation and cell viability in response to misfolded protein stress. *Cell* **115**, 727–738 (2003).
11. Smyth, K. A. & Belote, J. M. The dominant temperature-sensitive lethal DTS7 of *Drosophila melanogaster* encodes an altered 20S proteasome  $\beta$ -type subunit. *Genetics* **151**, 211–220 (1999).
12. Brand, A. H. & Perrimon, N. Targeted gene expression as a means of altering cell fates and generating dominant phenotypes. *Development* **118**, 401–415 (1993).
13. Ciechanover, A. & Brundin, P. The ubiquitin proteasome system in neurodegenerative diseases: Sometimes the chicken, sometimes the egg. *Neuron* **40**, 427–446 (2003).
14. La Spada, A. R., Wilson, E. M., Lubahn, D. B., Harding, A. E. & Fischbeck, K. H. Androgen receptor gene mutations in X-linked spinal and bulbar muscular atrophy. *Nature* **352**, 77–79 (1991).
15. Li, M. et al. Nuclear inclusions of the androgen receptor protein in spinal and bulbar muscular atrophy. *Ann. Neurol.* **44**, 249–254 (1998).
16. Takeyama, K. et al. Androgen-dependent neurodegeneration by polyglutamine-expanded human androgen receptor in *Drosophila*. *Neuron* **35**, 855–864 (2002).
17. Bence, N. F., Sampat, R. M. & Kopito, R. R. Impairment of the ubiquitin-proteasome system by protein aggregation. *Science* **292**, 1552–1555 (2001).
18. Neefjes, J. & Dantuma, N. P. Fluorescent probes for proteolysis: Tools for drug discovery. *Nature Rev. Drug Discov.* **3**, 58–69 (2004).
19. Chan, H. Y., Warrick, J. M., Andriola, I., Merry, D. & Bonini, N. M. Genetic modulation of polyglutamine toxicity by protein conjugation pathways in *Drosophila*. *Hum. Mol. Genet.* **11**, 2895–2904 (2002).
20. Taylor, J. P. et al. Aggresomes protect cells by enhancing the degradation of toxic polyglutamine-containing protein. *Hum. Mol. Genet.* **12**, 749–757 (2003).
21. McGuire, S. E., Mao, Z. & Davis, R. L. Spatiotemporal gene expression targeting with the TARGET and gene-switch systems in *Drosophila*. *Sci. STKE* **2004**, pl6 (2004).
22. Ravikumar, B. et al. Inhibition of mTOR induces autophagy and reduces toxicity of polyglutamine expansions in fly and mouse models of Huntington disease. *Nature Genet.* **36**, 585–595 (2004).
23. Harris, T. E. & Lawrence, J. C. Jr. TOR signaling. *Sci. STKE* **2003**, re15 (2003).
24. Kovacs, J. J. et al. HDAC6 regulates Hsp90 acetylation and chaperone-dependent activation of glucocorticoid receptor. *Mol. Cell* **18**, 601–607 (2005).
25. Taylor, J. P. et al. Aberrant histone acetylation, altered transcription, and retinal degeneration in a *Drosophila* model of polyglutamine disease are rescued by CREB-binding protein. *Genes Dev.* **17**, 1463–1468 (2003).

**Supplementary Information** is linked to the online version of the paper at [www.nature.com/nature](http://www.nature.com/nature).

**Acknowledgements** We thank the Laboratory for Biological Ultrastructure at the University of Maryland for assistance with SEM, the Biomedical Imaging Core at the University of Pennsylvania for assistance with TEM, J. Belote and K. Takeyama for flies, and R. Kopito for the CL1-GFP construct. Financial support was provided by NIH grants to T.-P.Y., E.H.B. and J.P.T., as well as support from the Morton Reich Research Fund, Kennedy's Disease Association, and Muscular Dystrophy Association to J.P.T.

**Author Contributions** Experimental work was performed by U.B.P., Z.N., Y.B., B.A.M., G.P.R., S.L.S., D.L.B. and J.P.T. Vital reagents were provided by N.A.D., M.A.K., O.S., R.P., M.H., D.G. and T.-P.Y. The manuscript was written by N.B.N., E.H.B. and J.P.T. All authors discussed results and commented on the manuscript.

**Author Information** Reprints and permissions information is available at [www.nature.com/reprints](http://www.nature.com/reprints). The authors declare no competing financial interests. Correspondence and requests for materials should be addressed to J.P.T. (jpt@mail.med.upenn.edu).

## LETTERS

# RAS-RAF-MEK-dependent oxidative cell death involving voltage-dependent anion channels

Nicholas Yagoda<sup>1\*</sup>, Moritz von Rechenberg<sup>3\*</sup>, Elma Zaganjor<sup>1\*</sup>, Andras J. Bauer<sup>1</sup>, Wan Seok Yang<sup>1</sup>, Daniel J. Fridman<sup>1</sup>, Adam J. Wolpaw<sup>1</sup>, Inese Smukste<sup>1</sup>, John M. Peltier<sup>3</sup>, J. Jay Boniface<sup>3</sup>, Richard Smith<sup>4</sup>, Stephen L. Lessnick<sup>4,5</sup>, Sudhir Sahasrabudhe<sup>3</sup> & Brent R. Stockwell<sup>1,2</sup>

Therapeutics that discriminate between the genetic makeup of normal cells and tumour cells are valuable for treating and understanding cancer. Small molecules with oncogene-selective lethality may reveal novel functions of oncoproteins and enable the creation of more selective drugs<sup>1</sup>. Here we describe the mechanism of action of the selective anti-tumour agent erastin, involving the RAS-RAF-MEK signalling pathway functioning in cell proliferation, differentiation and survival. Erastin exhibits greater lethality in human tumour cells harbouring mutations in the oncogenes *HRAS*, *KRAS* or *BRAF*. Using affinity purification and mass spectrometry, we discovered that erastin acts through mitochondrial voltage-dependent anion channels (VDACs)—a novel target for anti-cancer drugs. We show that erastin treatment of cells harbouring oncogenic RAS causes the appearance of oxidative species and subsequent death through an oxidative, non-apoptotic mechanism. RNA-interference-mediated knockdown of VDAC2 or VDAC3 caused resistance to erastin, implicating these two VDAC isoforms in the mechanism of action of erastin. Moreover, using purified mitochondria expressing a single VDAC isoform, we found that erastin alters the permeability of the outer mitochondrial membrane. Finally, using a radiolabelled analogue and a filter-binding assay, we show that erastin binds directly to VDAC2. These results demonstrate that ligands to VDAC proteins can induce non-apoptotic cell death selectively in some tumour cells harbouring activating mutations in the RAS-RAF-MEK pathway.

In a screen of about 24,000 compounds, we discovered erastin, which induces rapid death in engineered human tumour cells (BJ-TERT/LT/ST/RAS<sup>V12</sup> cells, ref. 2) with oncogenic v-Ha-ras Harvey rat sarcoma viral oncogene homologue (*HRAS*)<sup>V12</sup>, but not in isogenic, non-tumorigenic cells lacking oncogenic RAS (BJ-TERT/LT/ST cells) (Fig. 1a, Supplementary Fig. 1 and ref. 3). This cell death was not dependent on the rate of cell division, nor was it idiosyncratic to these cells (Fig. 1a and Supplementary Fig. 2), because cell lines engineered in a similar way responded similarly.

We found that erastin-treated cells did not display changes in nuclear morphology characteristic of apoptosis (Fig. 1c, ref. 3). However, imaging by electron microscopy did reveal changes in mitochondrial morphology, such as loss of structural integrity (Fig. 1b). These mitochondrial morphological changes were not observed in response to staurosporine, hydrogen peroxide or rapamycin—compounds that induce apoptosis, necrosis and autophagy, respectively (Fig. 1b and data not shown).

Given that erastin is a new compound found in a cell-based screen, we had no insight into its mechanism of action. We used a

two-pronged approach to define the mechanism, involving, first, a suppressor screen to identify annotated compounds that prevent erastin-induced cell death and, second, an affinity purification approach to identify proteins that mediate the activity of erastin. First, we performed a suppressor screen using a library of about 2,000 biologically active compounds<sup>4</sup> and found that antioxidants ( $\alpha$ -tocopherol, butylated hydroxytoluene and  $\beta$ -carotene) prevent erastin-induced death (Fig. 1d, Supplementary Fig. 3). Moreover, we detected generation of an oxidizing species in response to erastin treatment in BJ-TERT/LT/ST/RAS<sup>V12</sup> cells, but not in isogenic BJ-TERT cells (Fig. 1e, Supplementary Fig. 4). Finally, we found that erastin-induced death in the HT-1080 fibrosarcoma cell line was also suppressed by antioxidants (Supplementary Fig. 5).

To characterize the mode of erastin-induced cell death, we looked for features of well characterized death pathways. We determined that the oxidizing species generated in BJ-TERT/LT/ST/RAS<sup>V12</sup> cells in the presence of erastin emanate from mitochondria (see Supplementary Discussion), consistent with the perturbation in mitochondrial morphology. We discovered that the oxidizing species do not cause poly(ADP ribose) polymerase 1 (PARP1) cleavage (Fig. 1f, Supplementary Fig. 6), cytochrome c release from mitochondria (Fig. 1g), or pro-caspase-3 cleavage (Fig. 1h)<sup>3,5,6</sup>—all of which are hallmarks of apoptosis, a stereotypical form of cell death activated by many anti-tumour agents<sup>3,7–10</sup> as well as by staurosporine (Fig. 1f–h). Moreover, we looked for these hallmarks in four different cell lines sensitive to erastin; none showed activation of these markers (Fig. 1f, h). Other canonical hallmarks of apoptosis were similarly absent (see Supplementary Information). In summary, these initial studies revealed that erastin induces rapid, oxidative, non-apoptotic death in tumour cells with oncogenic *HRAS*.

To define the genetic basis of the selective lethality of erastin, we used a lentiviral-based RNA interference system<sup>11</sup>. We originally discovered erastin in a screen for oncogenic-*HRAS*-selective lethal compounds. However, v-Ki-ras2 Kirsten rat sarcoma viral oncogene homologue (*KRAS*) is more frequently mutated in human cancers than *HRAS*<sup>12</sup>. Selective toxicity in mutant-*KRAS*-expressing cell lines would broaden the applicability of erastin as a therapeutic. Thus, we tested whether erastin was selectively lethal to tumour cells harbouring oncogenic *KRAS*, and whether this lethality could be arrested by knockdown of *KRAS*. We found that a lung carcinoma cell line (Calu-1) with an activating mutation in *KRAS* was sensitive to erastin (half-maximal inhibitory concentration,  $IC_{50} = 4 \mu M$ ; Fig. 2a); when infected with lentiviral constructs expressing two different short hairpin RNAs (shRNAs) targeting

<sup>1</sup>Department of Biological Sciences, Fairchild Center, 1212 Amsterdam Avenue, MC 2406, <sup>2</sup>Department of Chemistry, Columbia University, New York, New York 10027, USA.

<sup>3</sup>Prolexys Pharmaceuticals, 2150 West Dauntless Avenue, Salt Lake City, Utah 84116, USA. <sup>4</sup>Center for Children, Huntsman Cancer Institute, 2000 Circle of Hope Salt Lake City, Utah 84112, USA. <sup>5</sup>Division of Pediatric Hematology/Oncology, the Department of Oncological Sciences.

\*These authors contributed equally to this work.

KRAS (Supplementary Table 4), these cells exhibited resistance to erasin (Fig. 2a, b).

RAS proteins are known to modulate many downstream pathways, and genetic lesions in these pathways are associated with many cancer types<sup>12</sup>. To clarify the connection between erasin and oncogenic RAS signalling, we sought evidence that erasin acts in a manner that is specific to cells with activated RAS-RAF-MEK signalling (Supplementary Table 1 and Supplementary Discussion). One cell line with moderate sensitivity to erasin was A-673 (Supplementary Table 1), containing an activating V600E mutation in *v-raf* murine sarcoma viral oncogene homologue B1 (BRAF)—a direct target of RAS<sup>13</sup>. To determine whether the activating mutation in BRAF influences erasin sensitivity, we created two different shRNAs targeting *BRAF* messenger RNA (Supplementary Table 4). We found that A-673 cells containing either of these constructs were resistant to erasin (Fig. 2c–e). Moreover, co-expression of a non-targetable V600E mutant BRAF partially restored sensitivity of these cells to erasin (Supplementary Fig. 7).

To confirm that activated RAS-RAF-MEK signalling renders other tumour cells sensitive to erasin, we examined the effect of mitogen-activated protein kinase (MAPK)/extracellular signal-regulated kinase (ERK) kinase 1/2 (MEK1/2) inhibitors on erasin sensitivity. All three inhibitors caused erasin resistance in both BJ-TERT/LT/ST/RAS<sup>V12</sup> and HT-1080 cells, with activating mutations in *HRAS* and *NRAS*, respectively (Fig. 2f and Supplementary Fig. 8; Supplementary Table 2 shows the effect of these MEK inhibitors alone on cell viability). Finally, we found a modest correlation between ERK1/2 phosphorylation status and erasin sensitivity in 12 sarcoma cell lines (Table 1). In summary, KRAS and BRAF knockdown, MEK inhibition, and

analysis of ERK1/2 phosphorylation status together suggest that erasin contains a degree of selectivity for cells in which the RAS-RAF-MEK pathway is constitutively activated.

For the second prong of our approach to defining the mechanism of action of erasin (affinity-based target identification), we synthesized erasin analogues that could be linked to a solid-phase resin for biochemical purification of potential targets. We found that replacement of the *p*-chloro substituent in erasin with the aminomethyl group necessary for linkage to a resin resulted in an analogue (erasin A6, Fig. 2g) that, though less potent, retained the ability to kill BJ-TERT/LT/ST/RAS<sup>V12</sup> cells, but not BJ-TERT cells (Supplementary Fig. 9). We also identified a suitable analogue (erasin B2, Supplementary Information) that lacked activity (Fig. 2g and Supplementary Fig. 9), and thus could serve as a negative control for target purification.

We immobilized erasin A6 and erasin B2 on solid-phase resin and sought proteins that interact with A6, but not B2. Using BJ-TERT/LT/ST/RAS<sup>V12</sup> cell lysates, we identified all three isoforms of the human mitochondrial voltage-dependent anion channels (VDAC1, VDAC2 and VDAC3) on the A6 resin, but only VDAC1 on the B2 resin (Supplementary Table 3, 7–14). Using BJ-TERT cell lysates, we identified a small amount of VDAC1 on the A6 resin, but none of the VDACs on the B2 resin. Thus, it appears that erasin A6 isolates VDAC2 and VDAC3 more efficiently than does erasin B2. Furthermore, the finding that erasin pulls down a mitochondrial protein (VDAC) is consistent with observations that erasin induces mitochondria-driven oxidative death.

VDACs (also known as eukaryotic porins) are membrane-spanning channels that facilitate transmembrane transport of ions

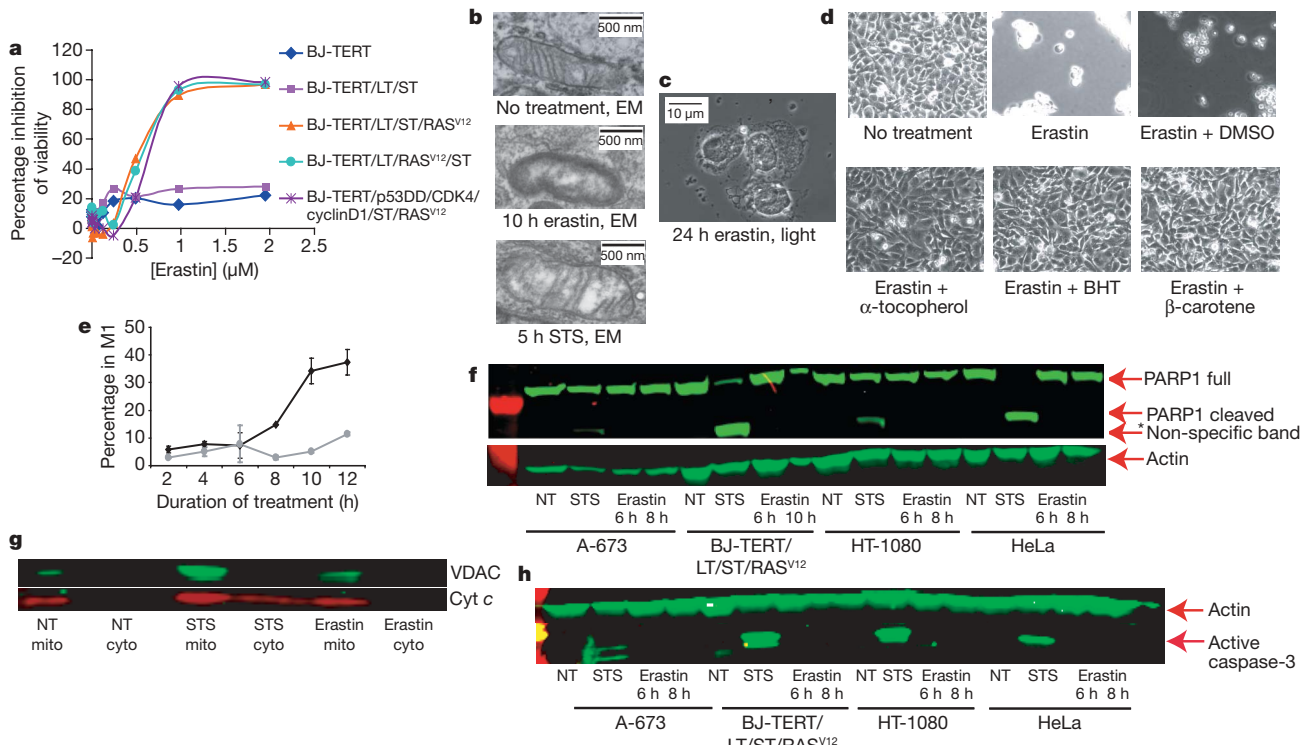
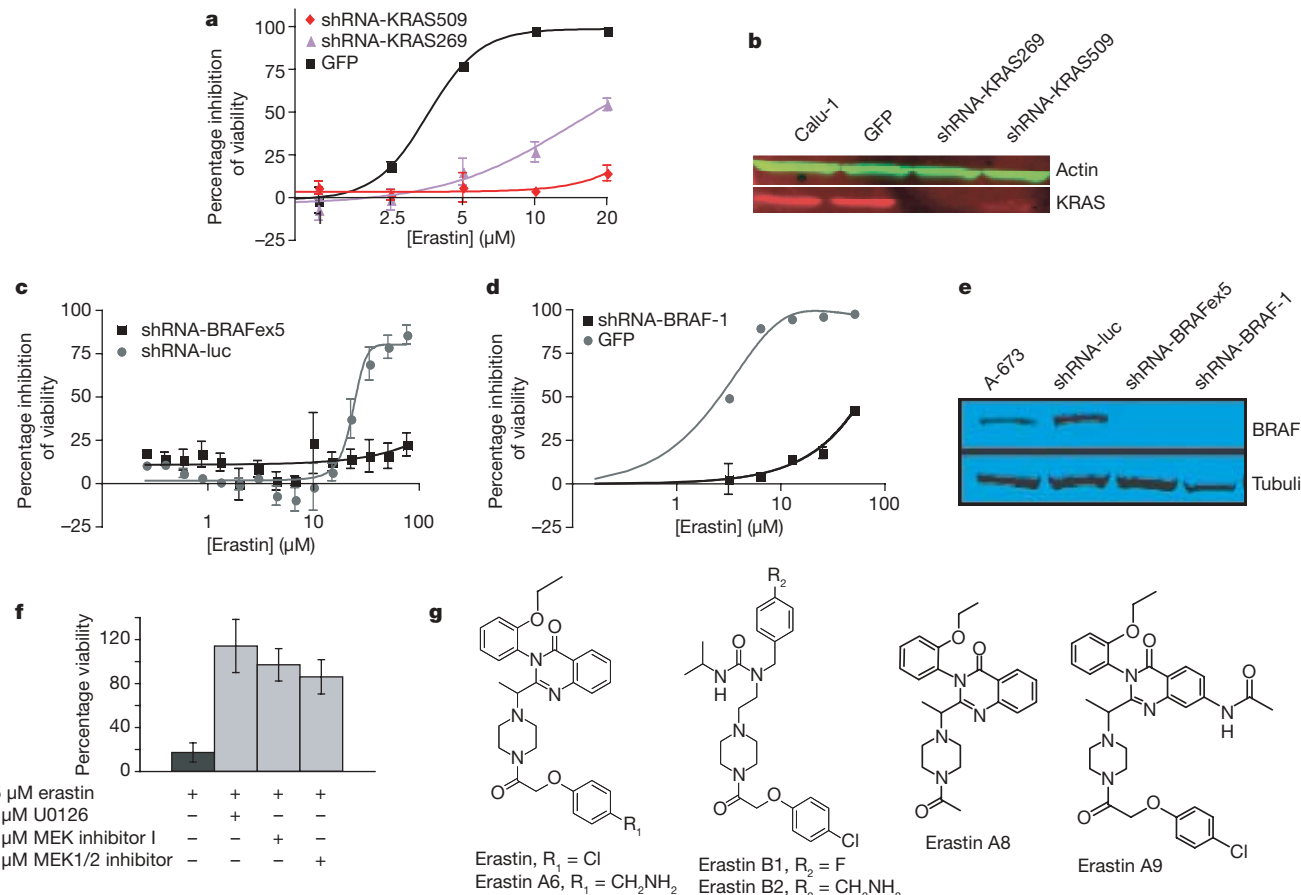


**Figure 1 | Erasin activates a rapid, oxidative, non-apoptotic cell death process.** **a**, HRAS<sup>V12</sup>-expressing cell lines are sensitive to erasin, whereas isogenic lines lacking HRAS<sup>V12</sup> are resistant, as determined by Trypan blue exclusion; the graph is a representative outcome of multiple independent experiments. **b**, Transmission electron microscopy images ( $\times 20,000$ ) of BJ-TERT/LT/ST/RAS<sup>V12</sup> mitochondria after cells were treated with nothing, erasin (37  $\mu$ M for 10 h) or staurosporine (STS, 1  $\mu$ M for 5 h). **c**, Phase-contrast photograph of BJ-TERT/LT/ST/RAS<sup>V12</sup> cells 24 h after 9  $\mu$ M erasin treatment indicates that nuclei are intact after cell death. **d**, Anti-oxidants suppress erasin-induced death in BJ-TERT/LT/ST/RAS<sup>V12</sup> cells. BHT, butylated hydroxytoluene; DMSO, dimethylsulphoxide. **e**, Level of intracellular oxidative species in BJ-TERT/LT/ST/RAS<sup>V12</sup> (black line) or BJ-TERT (grey line) cells treated with 4.6  $\mu$ M erasin. *y* axis, percentage of cells exhibiting dichlorofluorescein (DCF) fluorescence within region of interest, M1, as measured by flow cytometry; error bars, one standard deviation, *n* = 2. **f**, PARP1 cleavage is not seen during erasin-induced cell death in A-673, HT-1080 and HeLa cells. NT, no treatment. **g**, STS, but not erasin, induces cytochrome *c* (cyt *c*) release from BJ-TERT/LT/ST/RAS<sup>V12</sup> mitochondria; mitochondrial fraction, mito; cytosolic fraction, cyto. **h**, Pro-caspase-3 is not cleaved in response to erasin.

butylated hydroxytoluene; DMSO, dimethylsulphoxide. **e**, Level of intracellular oxidative species in BJ-TERT/LT/ST/RAS<sup>V12</sup> (black line) or BJ-TERT (grey line) cells treated with 4.6  $\mu$ M erasin. *y* axis, percentage of cells exhibiting dichlorofluorescein (DCF) fluorescence within region of interest, M1, as measured by flow cytometry; error bars, one standard deviation, *n* = 2. **f**, PARP1 cleavage is not seen during erasin-induced cell death in A-673, HT-1080 and HeLa cells. NT, no treatment. **g**, STS, but not erasin, induces cytochrome *c* (cyt *c*) release from BJ-TERT/LT/ST/RAS<sup>V12</sup> mitochondria; mitochondrial fraction, mito; cytosolic fraction, cyto. **h**, Pro-caspase-3 is not cleaved in response to erasin.



and metabolites<sup>14,15</sup>, most notably across the outer mitochondrial membrane<sup>16</sup>. It has been demonstrated that VDACs are gated by membrane voltage, at least *in vitro* (Supplementary Discussion): in the closed state, ions, but not small molecule metabolites, can penetrate VDAC pores<sup>17</sup>; in the open state, both ions and metabolites pass through VDAC channels. In addition, the closed state is cation-selective, whereas the open state is anion-selective.

Having identified VDACs as a potential target of erastin, we sought evidence that altered expression of VDACs contributes to altered erastin sensitivity. To determine whether VDACs are upregulated in response to oncogenic HRAS, we measured VDAC abundance in the BJ cell series (see ref. 2 and Supplementary Discussion for engineering and genetics of BJ cell series). In BJ-TERT/LT/ST/RAS<sup>V12</sup> cells, the total amount of VDAC protein is increased (Fig. 3a and Supplementary Fig. 10). These results suggest that erastin acts by a gain-of-function mechanism, and that cells with more VDAC protein are more sensitive to erastin, although other aspects of cellular physiology may also be relevant.

Next, using two-dimensional gel electrophoresis to evaluate protein expression in BJ-TERT/LT/ST/RAS<sup>V12</sup> cells (Supplementary Fig. 11), we found that, after 8 h of erastin treatment, VDAC3 was no longer detectable, and, after 10 h, VDAC2 became undetectable (Fig. 3b). Doxorubicin and camptothecin are examples of agents that act by a gain-of-function mechanism on their molecular targets, topoisomerase II $\alpha$  and topoisomerase I, respectively<sup>18</sup>. It may be that a cellular response to erastin is downregulation of VDAC2/3 after

percentage inhibition of viability (y axis) was measured using **c**, Alamar blue and **d**, Trypan blue. **Luc**, luciferase; **BRAFex5**, exon 5 of *BRAF* transcript. **e**, BRAF knockdown was confirmed by western blot analysis. **f**, 48 h treatment with MEK inhibitors (U0126, Sigma; MEK inhibitor 1, Calbiochem; MEK1/2 inhibitor, Calbiochem) prevents erastin-induced lethality in BJ-TERT/LT/ST/RAS<sup>V12</sup> cells; percentage viability (y axis) was determined using Trypan blue. **g**, Structures of erastin and related analogues. All error bars in Fig. 2 represent one standard deviation;  $n = 2$  or 3.

lethal oxidative species have been generated, as occurs with camptothecin and topoisomerase I following DNA damage. The fact that VDAC1 is still present at later time points suggests that the loss of VDAC2/3 is not simply caused by loss of mitochondria.

To test the gain-of-function hypothesis, we reduced VDAC protein levels using lentiviral shRNA expression<sup>11</sup>. We created multiple shRNA constructs targeting each VDAC isoform (Supplementary Table 4 and Supplementary Fig. 12) and tested their effects on cell sensitivity to erastin (Supplementary Figs 13–15). We found that knockdown of VDAC3 caused significant resistance to erastin (Fig. 3c, d and Supplementary Fig. 15). We also observed some degree of

**Table 1 | Correlation between erastin sensitivity and phospho-ERK level**

Human cell line	Erastin sensitivity (%)	Phospho-ERK1/2
A-673	54	0.66
BJ-TERT	22	0.09
BJ-TERT/LT/ST/RAS <sup>V12</sup>	100	0.92
EWS 502	42	0.12
HL-60	0	0.10
HT-1080	98	0.53
SK-ES-1	96	0.25
SK-N-MC	95	0.05
SW 872	0	0.12
TC 32	88	0.12
TC 71	92	0.23
U-937	73	0.27

The maximum percentage cell death induced by erastin in each cell line is shown, along with the level of phospho-ERK1/2 as quantified by western blot (arbitrary units). The correlation is 0.41.

erastin resistance when VDAC2 was knocked down (Fig. 3c, e and Supplementary Fig. 14). In contrast, overexpression of VDAC3 alone in BJ-TERT cells yielded no increase in sensitivity to erastin (Supplementary Fig. 16), suggesting that VDAC3, and to some degree VDAC2, is necessary but not sufficient for sensitivity to erastin and that other downstream features of RAS-RAF-MEK signalling are also needed. Overall, these results are consistent with a gain-of-function mechanism involving erastin and VDAC2/3. Furthermore, this effect is specific to erastin, and not to other lethal compounds: VDAC2-deficient embryonic stem cells have been shown to be more sensitive, not less sensitive, to staurosporine and etoposide<sup>19</sup>.

To test the hypothesis that erastin alters mitochondrial outer membrane permeability, we monitored the function of VDACs using purified mitochondria from yeast engineered to express a single mouse VDAC isoform in place of yeast VDAC<sup>20</sup>. A previous report demonstrated that the rate of NADH uptake through the outer

membrane of such mitochondria is dependent on the specific VDAC expressed in yeast. We found that erastin treatment yielded a decrease in the rate of NADH oxidation, suggesting a reduced permeability of these mitochondria to NADH when mouse VDAC1 or VDAC2 were expressed (Fig. 3f and Supplementary Fig. 17). We found little NADH oxidation in mitochondria expressing VDAC3, suggesting minimal intrinsic membrane permeability (Supplementary Fig. 17); this is consistent with previous reports that VDAC3 does not gate well *in vitro*<sup>20</sup>. Finally, we found that an inactive analogue of erastin (erastin A8, Fig. 2g and Supplementary Fig. 9) had no such effect (Fig. 3f and Supplementary Fig. 17). These results suggest that erastin affects VDAC gating, possibly switching its ion selectivity and allowing cationic species into mitochondria.

Having demonstrated interactions between erastin and VDAC using affinity-based target identification and VDAC functional assays, we explored the direct binding of erastin to VDACs. Using modified versions of previously reported protocols, we isolated VDAC2 from *Escherichia coli* for use in a competition binding experiment<sup>21,22</sup> using a radiolabelled analogue (erastin A9). The results demonstrate that the cold RAS-selective lethal erastin A9 ( $IC_{50} = 1.9 \mu M$ , Supplementary Fig. 9), unlike inactive erastin A8, directly binds to VDAC2 (dissociation constant,  $K_d = 112 nM$ ; Fig. 3g), in the process competing off radiolabelled erastin A9.

The data presented herein are consistent with a model in which erastin interacts with VDAC proteins to induce mitochondrial dysfunction, release of oxidative species and, ultimately, non-apoptotic, oxidative cell death. This process has a degree of selectivity for cells with activated RAS-RAF-MEK signalling. These results demonstrate that it is feasible to discover oncogene-selective compounds and to use them to clarify oncogene-related cell death mechanisms.

## METHODS SUMMARY

**VDAC identification using pull-down assay.** Erastin A6 and B2 were linked to a solid-phase resin, which was then incubated with BJ-TERT/LT/ST/RAS<sup>V12</sup> or BJ-TERT cell lysate and washed before protein was eluted and then digested as described<sup>23</sup>. Reverse-phase high-performance liquid chromatography was performed before samples were analysed using both a 4700 Proteomics Analyser matrix-assisted laser desorption/ionization-time of flight (TOF)/TOF (TOF/TOF; Applied Biosystems) and a Q Trap (AB/MDS Sciex). Tandem mass spectrometry (MS/MS) data was then compared against either the corrected NCBI nr protein sequence database or the Human NR database (<http://www.ncbi.nlm.nih.gov/>). GPS Explorer (Applied Biosystems) was used for submitting data acquired from the TOF/TOF for database searching.

**Knockdown using lentiviral shRNAs.** HT-1080 and Calu-1 cells were infected with lentiviruses expressing shRNAs targeting VDAC and KRAS, respectively (Supplementary Table 4). A-673 cells were infected with retroviruses<sup>24</sup> expressing shRNAs against either BRAF or luciferase (Supplementary Table 4).

**NADH oxidation assay.** NADH oxidation in the mitochondria was measured by resuspending mitochondria isolated from yeast in 25  $\mu M$  NADH, with or without erastin, and monitoring absorbance at  $\lambda = 340$  nm (ref. 20). As a control for mitochondrial intactness, parallel assays were run using hypotonically shocked mitochondria.

**VDAC2 binding assay.** VDAC2 protein was isolated from *E. coli* using a modified version of a previously described protocol<sup>22</sup>. To assay direct binding of erastin analogues, 40  $\mu g$  of purified VDAC2 was incubated in the presence of 20  $\mu M$  radiolabelled erastin A9 and serial dilutions of unlabelled erastin A9 or erastin A8. The mixture was then deposited onto a binding filter using vacuum filtration. After rinsing, radioactivity was detected on a liquid scintillation counter (LKB Wallac 1,211 RACKBETA).

**Full protocols.** For detailed methods, which additionally include cell culture, western blotting, cell viability assays, PARP cleavage, cytochrome *c* release, oxidative species detection, transmission electron microscopy, VDAC3 overexpression, PCR with reverse transcription and quantitative PCR, see Methods.

**Full Methods** and any associated references are available in the online version of the paper at [www.nature.com/nature](http://www.nature.com/nature).

Received 17 November 2006; accepted 17 April 2007.

1. Kaelin, W. G. The concept of synthetic lethality in the context of anticancer therapy. *Nature Rev. Cancer* 5, 689–698 (2005).

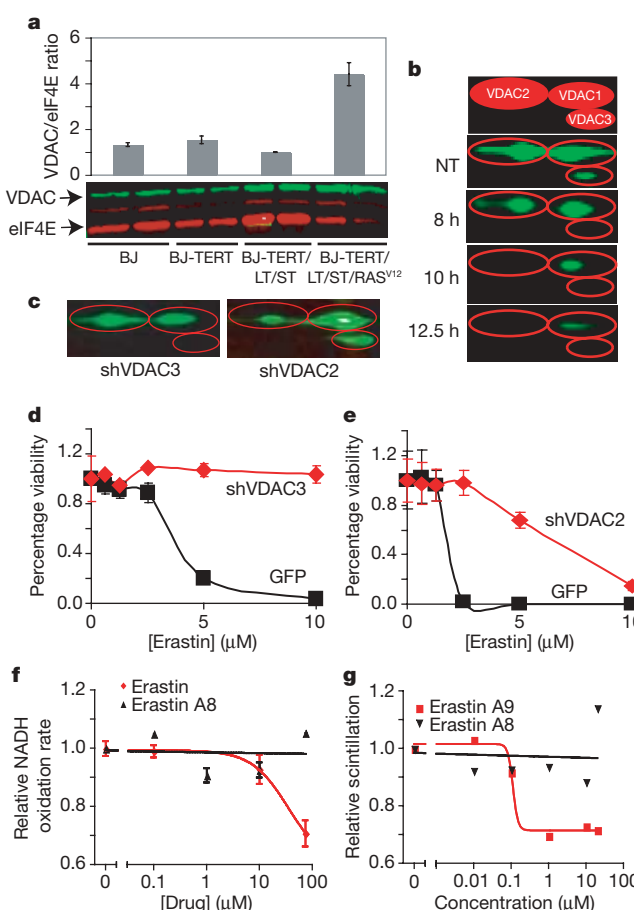


**Figure 3 | Erastin compounds act through VDACs.** **a**, VDAC/eukaryotic initiation factor 4E (eIF4E) protein ratio in engineered BJ-derived cells as quantified using western blot. **b**, BJ-TERT/LT/ST/RAS<sup>V12</sup> cells were treated with erastin and harvested at indicated time points for quantitative two-dimensional western blot. The top panel is an illustration of VDAC isoforms separated by two-dimensional gel electrophoresis. **c**, Isoform-specific knockdown of VDAC in HT-1080 cells infected with virus expressing either VDAC3- or VDAC2-targeted shRNA plasmid (shVDAC3 or shVDAC2) was confirmed using two-dimensional protein gels. **d, e**, These cells were then treated with erastin dilutions, and viability relative to no treatment (y axis) was determined using Trypan blue exclusion and compared to an identical process using a GFP control plasmid. **f**, Rate of NADH oxidation, normalized to no treatment, in mitochondria purified from VDAC-knockout yeast expressing murine VDAC2 was determined in the presence of erastin (red) or an inactive analogue, erastin A8 (black). **g**, Direct binding to VDAC2 was assayed using tritium-labelled erastin A9 in competition with unlabelled erastin A9 (red) or erastin A8 (black). All error bars in Fig. 3 represent one standard deviation,  $n = 2$  or 3.

2. Hahn, W. C. *et al.* Creation of human tumour cells with defined genetic elements. *Nature* **400**, 464–468 (1999).
3. Dolma, S., Lessnick, S. L., Hahn, W. C. & Stockwell, B. R. Identification of genotype-selective antitumor agents using synthetic lethal chemical screening in engineered human tumor cells. *Cancer Cell* **3**, 285–296 (2003).
4. Root, D. E., Flaherty, S. P., Kelley, B. P. & Stockwell, B. R. Biological mechanism profiling using an annotated compound library. *Chem. Biol.* **10**, 881–892 (2003).
5. Song, Z. & Steller, H. Death by design: mechanism and control of apoptosis. *Trends Cell Biol.* **9**, M49–M52 (1999).
6. Majno, G. & Joris, I. Apoptosis, oncosis, and necrosis. An overview of cell death. *Am. J. Pathol.* **146**, 3–15 (1995).
7. Wyllie, A. H. Glucocorticoid-induced thymocyte apoptosis is associated with endogenous endonuclease activation. *Nature* **284**, 555–556 (1980).
8. Kerr, J. F., Wyllie, A. H. & Currie, A. R. Apoptosis: a basic biological phenomenon with wide-ranging implications in tissue kinetics. *Br. J. Cancer* **26**, 239–257 (1972).
9. Martin, S. J. *et al.* Early redistribution of plasma membrane phosphatidylserine is a general feature of apoptosis regardless of the initiating stimulus: inhibition by overexpression of Bcl-2 and Abl. *J. Exp. Med.* **182**, 1545–1556 (1995).
10. Yuan, J., Shaham, S., Ledoux, S., Ellis, H. M. & Horvitz, H. R. The *C. elegans* cell death gene *ced-3* encodes protein similar to mammalian interleukin-1 beta-converting enzyme. *Cell* **75**, 641–652 (1993).
11. Moffat, J. *et al.* A lentiviral RNAi library for human and mouse genes applied to an arrayed viral high-content screen. *Cell* **124**, 1283–1298 (2006).
12. Downward, J. Targeting RAS signalling pathways in cancer therapy. *Nature Rev. Cancer* **3**, 11–22 (2003).
13. Davies, H. *et al.* Mutations of the *BRAF* gene in human cancer. *Nature* **417**, 949–954 (2002).
14. Graham, B. H. & Craigen, W. J. Genetic approaches to analyzing mitochondrial outer membrane permeability. *Curr. Top. Dev. Biol.* **59**, 87–118 (2004).
15. Baker, M. A., Lane, D. J., Ly, J. D., De Pinto, V. & Lawen, A. VDAC1 is a transplasma membrane NADH-ferricyanide reductase. *J. Biol. Chem.* **279**, 4811–4819 (2004).
16. Rostovtseva, T. & Colombini, M. ATP flux is controlled by a voltage-gated channel from the mitochondrial outer membrane. *J. Biol. Chem.* **271**, 28006–28008 (1996).
17. Mannella, C. A. Minireview: on the structure and gating mechanism of the mitochondrial channel, VDAC. *J. Bioenerg. Biomembr.* **29**, 525–531 (1997).
18. Beck, W. T. & Danks, M. K. Mechanisms of resistance to drugs that inhibit DNA topoisomerases. *Semin. Cancer Biol.* **2**, 235–244 (1991).
19. Cheng, E. H., Sheiko, T. V., Fisher, J. K., Craigen, W. J. & Korsmeyer, S. J. VDAC2 inhibits BAK activation and mitochondrial apoptosis. *Science* **301**, 513–517 (2003).
20. Xu, X., Decker, W., Sampson, M. J., Craigen, W. J. & Colombini, M. Mouse VDAC isoforms expressed in yeast: channel properties and their roles in mitochondrial outer membrane permeability. *J. Membr. Biol.* **170**, 89–102 (1999).
21. Poyurovsky, M. V. *et al.* Nucleotide binding by the Mdm2 RING domain facilitates Arf-independent Mdm2 nucleolar localization. *Mol. Cell* **12**, 875–887 (2003).
22. Koppel, D. A. *et al.* Bacterial expression and characterization of the mitochondrial outer membrane channel. Effects of n-terminal modifications. *J. Biol. Chem.* **273**, 13794–13800 (1998).
23. Zhen, Y. *et al.* Development of an LC-MALDI method for the analysis of protein complexes. *J. Am. Soc. Mass Spectrom.* **15**, 803–822 (2004).
24. Sage, J., Miller, A. L., Perez-Mancera, P. A., Wysocki, J. M. & Jacks, T. Acute mutation of retinoblastoma gene function is sufficient for cell cycle re-entry. *Nature* **424**, 223–228 (2003).

**Supplementary Information** is linked to the online version of the paper at [www.nature.com/nature](http://www.nature.com/nature).

**Acknowledgements** We thank S. Flaherty and S. Dolma for supporting experiments, H. Widlund for supplying the *BRAF* shRNA construct, R. Becklin and J. Savage for help with the analysis of the pull-down data, P. Robbins for help with the pull-down experiments, K. Brown for assistance with transmission electron microscopy, and M. Colombini for supplying engineered yeast and for discussions. B.R.S. is supported by a Career Award at the Scientific Interface from the Burroughs Wellcome Fund and by the National Cancer Institute. S.L.L. is supported by an NCI grant, an American Cancer Society Research Scholars Grant, the Terri Anna Perine Sarcoma Fund, a Primary Children's Medical Center Foundation Innovative Research Grant, a Hope Street Kids grant and a Catalyst Grant from the University of Utah School of Medicine.

**Author Contributions** N.Y. designed and performed the RNAi and VDAC overexpression, quantitative PCR, erastin analogue viability and chemical characterization experiments. E.Z. performed two-dimensional western analysis, PARP-1 and pro-caspase-3 cleavage, and cytochrome c release experiments. E.Z. and N.Y. performed transmission electron microscopy experiments. A.J.B., D.J.F. and N.Y. performed the NADH oxidation and direct binding experiments. W.S.Y. characterized sensitivity to erastin in the BJ-derived cell series. A.J.W. performed the MEK1/2 inhibitor experiment. I.S. and A.J.B. synthesized erastin analogues. R.S. and S.L.L. provided *BRAF* shRNAs, analysis of *BRAF* knockdown and the phospho-ERK western analysis. J.M.P., J.J.B. and S.S. were responsible for setting up the technology platform to pull down proteins binding to small molecule compounds. M.v.R. and J.M.P. performed the pull-down experiments. J.J.B., J.M.P. and S.S. designed, reviewed and supervised the pull-down experiments, and contributed to the analysis of the data. B.R.S. conceived of and supervised the project, designed and analysed experiments, and performed the anti-oxidant studies. B.R.S. and N.Y. prepared the manuscript.

**Author Information** Reprints and permissions information is available at [www.nature.com/reprints](http://www.nature.com/reprints). The authors declare no competing financial interests. Correspondence and requests for materials should be addressed to B.R.S. (stockwell@biology.columbia.edu).

## METHODS

**Cell culture and western blotting.** BJ-TERT/LT/ST/RAS<sup>V12</sup> cells were cultured as described in ref. 3. Other cell lines were grown according to specifications of the American Type Culture Collection. For western blots, medium was aspirated and each dish was washed twice with 10 ml ice-cold PBS. Cells were lysed with 200  $\mu$ l buffer (50 mM HEPES, 40 mM NaCl, 2 mM EDTA, 0.5% Triton-X, 1.5 mM sodium orthovanadate, 50 mM NaF, 10 mM sodium pyrophosphate, 10 mM sodium  $\beta$ -glycerophosphate and protease inhibitor tablet (Roche), (pH 7.4)). For one-dimensional western blots, samples were separated using SDS-polyacrylamide gel electrophoresis; for two-dimensional western blots, samples were prepared using the ZOOM IPGRunner System (Invitrogen). Following separation, samples were then transferred to a polyvinylidene difluoride membrane, blocked for 1 h at room temperature in Licor Odyssey Blocking Buffer and incubated with the necessary primary and secondary antibodies: anti-VDAC1 (Abcam, ab3434), anti-VDAC1 (Calbiochem, 529534), anti-VDAC2 (Abcam, ab22170), anti-eIF4E (Santa Cruz Biotechnology, sc-9976), anti- $\alpha$ -tubulin (Sigma, T6199), anti-actin (Santa Cruz Biotechnology, 1616R), IRDye 800 goat anti-rabbit antibody (Rockland Immunochemicals, 611-132-122), Alexa Fluor 680 goat anti-mouse (Molecular Probes, A21058), PathScan Multiplex Western Cocktail I Kit (Cell Signalling Technology) and anti-PARP (Abcam, ab105). Membranes were scanned using the Licor Odyssey Imaging System.

**PARP cleavage and cytochrome *c* release.** BJ-TERT/LT/ST/RAS<sup>V12</sup> cells were seeded in polystyrene 100  $\times$  20 mm dishes (Falcon, 353003) in 10 ml medium.  $3 \times 10^6$  cells were seeded in each dish. After overnight incubation at 37 °C with 5% CO<sub>2</sub>, BJ-TERT/LT/ST/RAS<sup>V12</sup> cells were treated with nothing, staurosporine (1  $\mu$ M) for 6 h, camptothecin (1  $\mu$ M) for 18 h, or erastin (20  $\mu$ g ml<sup>-1</sup>) for 6, 10, 12, 12.5, 13, 14, 18 or 26 h, and prepared for western blotting. For the cytochrome *c* release assay, cells were washed with 10 ml ice-cold PBS, suspended in 120  $\mu$ l buffer (300 mM sucrose, 0.1% BSA, 10 mM HEPES (pH 7.5), 10 mM KCl, 1.5 mM MgCl<sub>2</sub>, 1 mM EGTA, 1 mM EDTA, 1 mM dithiothreitol (DTT), 2 mM phenylmethanesulphonyl fluoride and one protease inhibitor tablet (Roche)) and incubated on ice for 15 min. Cells were lysed by passing them through a 25-gauge needle (5 strokes). Cell lysates were centrifuged at 400g for 5 min at 4 °C to remove the nuclear fraction. Mitochondria were removed from the soluble cytosolic fraction by pelletting at 10,500g. Supernatant and mitochondrial pellets were solubilized in SDS-polyacrylamide gel electrophoresis loading buffer and analysed by western blotting.

**Oxidative species detection.** 2'7'-dichlorodihydrofluorescein diacetate (H<sub>2</sub>DCF-DA, Molecular Probes) was used to measure oxidative species by flow cytometry. Non-fluorescent H<sub>2</sub>DCF-DA was cleaved by endogenous esterases and then was oxidized to generate fluorescent DCF. BJ-TERT/LT/ST/RAS<sup>V12</sup> and BJ-TERT cells were seeded at  $3 \times 10^5$  cells per dish in 60 mm dishes and allowed to grow overnight. Cells were treated with 4.6  $\mu$ M erastin for 2, 4, 6, 8, 10 and 12 h. For each time point, controls were maintained for untreated cells and also for positive control (treated directly with 500  $\mu$ M hydrogen peroxide for 5 min). Cells were incubated with 10  $\mu$ M H<sub>2</sub>DCF-DA for 10 min, harvested by trypsinization, washed twice with cold PBS, resuspended in 100  $\mu$ l PBS and incubated with 5  $\mu$ l of 50  $\mu$ g ml<sup>-1</sup> propidium iodide for 10 min. 400  $\mu$ l PBS was added and the solution was analysed by flow cytometry (FACSCalibur, Becton-Dickinson). FL1-H indicates arbitrary units of DCF fluorescence detected.

**VDAC pull-downs.** Cultures of BJ-TERT and BJ-TERT/LT/ST/RAS<sup>V12</sup> cells (ten 150-mm plates) were washed with PBS, lysed in 25 mM HEPES (pH 7.5), 150 mM NaCl, 1% NP-40, 10 mM MgCl<sub>2</sub>, 1 mM EDTA, 10% glycerol, 1 mM DTT and protease inhibitor cocktail. Total protein concentration was determined using a Bradford colorimetric assay.

Erastin A6 and B2 were dissolved in DMSO at 10 mg ml<sup>-1</sup>. 100  $\mu$ l AffiGel-10 (BioRad) was washed and resuspended in 400  $\mu$ l DMSO. 10  $\mu$ l compound and 3  $\mu$ l 1:100 dilution of triethylamine in DMSO were added. The suspension was incubated at room temperature for 14 h, washed (1 ml per wash) five times in DMSO, three times in PBS, resuspended in 3 M ethanolamine in PBS, incubated 1 h at room temperature, washed five times in PBS and resuspended in 200  $\mu$ l PBS. For the pull-down experiments, 50  $\mu$ l of the A6 or B2 gel slurry were washed with binding buffer (0.1 M KCl, 20 mM HEPES (pH 7.6), 0.1 mM EDTA, 10% glycerol, 0.1% NP-40, 1 mM DTT, 0.25 mM phenylmethanesulphonyl fluoride) and incubated with 1 ml cell lysate (2 mg ml<sup>-1</sup> for 1.5 h at 4 °C), washed with binding buffer, washed three times with high salt buffer (0.35 M KCl, 20 mM HEPES (pH 7.6), 0.1 mM EDTA, 10% glycerol, 0.1% NP-40, 1 mM DTT, 0.25 mM phenylmethanesulphonyl fluoride), washed with binding buffer, and eluted twice with 50  $\mu$ l elution buffer (binding buffer with 0.8% N-lauroyl sarcosine). Proteins from the supernatant were precipitated with 400  $\mu$ l ethanol, sedimented by centrifugation (16,800g) and digested as described<sup>23</sup>. Reverse-phase high-performance liquid chromatography was performed using a nano LC system (Dionex): a 75  $\mu$ m  $\times$  150 mm column, a Famos autosampler, a Switchos II

system and an UltiMate binary pumping module. Samples were analysed using both a 4700 Proteomics Analyser MALDI-TOF/TOF (TOF/TOF; Applied Biosystems) and a Q Trap (AB/MDS Sciex), and the peptide level data were combined. To construct the databases used for protein identification, the following steps were performed: the NCBI protein sequence FASTA file was downloaded, the GI numbers (sequence version identification) were updated, and the missing or incorrectly annotated taxonomies were fixed by referencing them to the NCBI taxonomy index (index of GI number versus species). The human subset of proteins in the database was extracted into a separate database (HumanNR). All protein sequences in HumanNR were matched to the corresponding protein in RefSeq using BLAST<sup>25</sup>. MS/MS data obtained from the TOF/TOF and Q Trap were searched using Mascot (Matrix Sciences, London, UK). All searches were performed against either the corrected NCBI protein sequence database or the HumanNR database. GPS Explorer (Applied Biosystems) was used for submitting data acquired from the TOF/TOF for database searching. The Mascot-based search was performed using the default settings for the specific instrument type as supplied by Matrix Science, except that ions with scores below ten were excluded from the results.

The spectra of the peptides identified in the automatic data analysis were manually inspected for the quality of the corresponding spectra and for consistency with the obtained results. Only high quality spectra and results with a peptide score of 20 or higher were accepted and used for the identification of proteins.

**Transmission electron microscopy of BJ-TERT/LT/ST/RAS<sup>V12</sup> cells treated with erastin.** Cells were incubated for 10 h in the presence of erastin (20  $\mu$ g ml<sup>-1</sup>) or nothing, fixed with 2.5% glutaraldehyde in 0.1 M Sorenson's buffer (0.1 M H<sub>2</sub>PO<sub>4</sub>, 0.1 M HPO<sub>4</sub> (pH 7.2)) for at least 1 h, and then treated with 1% OsO<sub>4</sub> in 0.1 M Sorenson's buffer for 1 h. Enblock staining used 1% tannic acid. After dehydration through an ethanol series, cells were embedded in Lx-112 (Ladd Research Industries) and Embed-812 (EMS). Thin sections were cut on an MT-7000 ultramicrotome, stained with 1% uranyl acetate and 0.4% lead citrate, and examined under a Jeol JEM-1200 EXII electron microscope. Pictures were taken on an ORCA-HR digital camera (Hamamatsu) at  $\sim$ 20,000-fold magnification, and measurements were made using the AMT Image Capture Engine.

**Knockdown using lentiviral shRNAs.** VDACs, KRAS and BRAF were knocked down in HT-1080, Calu-1 and A-673 cells, respectively, using shRNA lentiviral vectors (Supplementary Table 4). On day 1, 293T cells were seeded in 10 cm tissue culture dishes ( $2 \times 10^6$  cells per dish); on day 2, shRNA-plasmid construct (pLKO.1 vector for VDAC- and KRAS-targeting constructs; pSIRIP<sup>24</sup> for BRAF- or luciferase-targeting constructs; Supplementary Table 4) and the p $\Delta$ 8.9 and pVSV-G helper plasmids were co-transfected into the 293T cells using FuGENE 6 Transfection Reagent (Roche); on day 3, the medium was changed; on day 4, the supernatant, containing virus, was transferred to target cells in 10 cm tissue culture dishes ( $1 \times 10^6$  cells per dish); on day 5, cells were transferred to 175 cm<sup>2</sup> flasks and medium was supplemented with puromycin (1.5  $\mu$ g ml<sup>-1</sup>); on days 6 and 7, medium was changed and again supplemented with puromycin; on day 8, samples were harvested for western blot and quantitative PCR with reverse transcription, or reseeded in 6-well format ( $5 \times 10^5$  cells per well), in duplicate, and treated with erastin dilutions. All cells were cultured at 37 °C, 5% CO<sub>2</sub>, in growth media as recommended by ATCC (American Type Culture Collection).

**Overexpression of VDAC3 using lentiviral constructs.** VDAC3 was over-expressed in BJ-TERT cells using a human ORF clone (Invitrogen) recombined into the pLENTi6/V5-DEST lentiviral vector (Invitrogen). On day 1, 293T cells were seeded in 10 cm tissue culture dishes ( $2 \times 10^6$  cells per dish); on day 2, the VDAC3 construct and the p $\Delta$ 8.9 and pVSV-G helper plasmids were co-transfected into the 293T cells using FuGENE 6 Transfection Reagent (Roche); on day 3, the medium was changed; on day 4, the supernatant, containing virus, was transferred to BJ-TERT cells in 10 cm tissue-culture dishes ( $1 \times 10^6$  cells per dish); on day 5, cells were transferred to 175 cm<sup>2</sup> flasks and medium was supplemented with blasticidin (5  $\mu$ g ml<sup>-1</sup>); on days 6 and 7, medium was changed and again supplemented with blasticidin. These cells were maintained in selection medium for 12 days before samples were harvested for future assay.

**Reverse transcription and quantitative PCR.** Total RNA was isolated from cells using RNeasy Mini Kit (Qiagen). Reverse transcription was performed on 2  $\mu$ g isolated RNA using Taqman Reverse Transcription Reagents (Applied Biosystems). The ABI Prism 7,300 was then used for quantitative PCR. 20 ng complementary DNA product was mixed with Power SYBR Green PCR Master Mix (Applied Biosystems) and each of the appropriate forward/reverse primer set (Supplementary Table 5). Relative mRNA expression levels were quantified with Sequence Detection Software v1.3.1 (Applied Biosystems).

**NADH oxidation assay.** NADH oxidation in the mitochondria was measured by resuspending mitochondria isolated from yeast in R-buffer (0.65 M sucrose, 10 mM HEPES (pH 7.5), 10 mM KH<sub>2</sub>PO<sub>4</sub>, 5 mM KCl, 5 mM MgCl<sub>2</sub>) to a final

concentration of  $100 \mu\text{g ml}^{-1}$ . Mitochondrial concentration was measured by dissolving mitochondria in 0.6% SDS and reading absorbance at  $\lambda = 280 \text{ nm}$ . The mitochondrial suspension was then incubated with  $25 \mu\text{M}$  NADH, and the absorbance at  $\lambda = 340 \text{ nm}$  monitored over a 15 min period. The assay was repeated in the presence of erastin. To assess mitochondrial intactness, a parallel assay was run in which mitochondria were hypotonically shocked before addition of NADH. The mitochondrial pellet was resuspended in distilled  $\text{H}_2\text{O}$  and incubated on ice for 3 min to disrupt the outer mitochondrial membrane;  $2 \times \text{R-buffer}$  was then added to restore normal osmotic conditions.

**Cell viability assays.** Trypan blue exclusion: cells were trypsinized, pelleted and resuspended in 1 ml growth media. Trypan blue exclusion analysis was performed using the Vi-CELL Series Cell Viability Analyser 1.01 (Beckman Coulter). Alamar blue metabolism: 10% Alamar blue was added to assay plates, which were then incubated for an additional 16 h. Red fluorescence, resulting from reduction of Alamar blue, was detected on a Victor3 platereader (excitation/emission: 530/590).

**VDAC2 binding assay.** VDAC2 protein was isolated from *E. coli* using a modified version of the protocol originally described in ref. 22. Bacterial cultures were grown in Luria-Bertani broth containing  $50 \text{ mg l}^{-1}$  ampicillin to an absorbance of 0.6 ( $\lambda = 600 \text{ nm}$ ), and induced using  $0.4 \mu\text{M}$  isopropylthiogalactoside overnight. Cultures were harvested by centrifugation at  $6,000\text{g}$  for 10 min. The pellet was then washed with distilled  $\text{H}_2\text{O}$  and resuspended in buffer (20% sucrose, 20 mM Tris buffer (pH 8.0),  $50 \mu\text{M ml}^{-1}$  lysozyme) and incubated at  $25^\circ\text{C}$  for 10 min. The lysate was then sonicated for  $2 \times 30 \text{ s}$  and centrifuged at  $15,000\text{g}$  for 20 min. The pellet was resuspended in resuspension buffer (4.5 M guanidine-HCl, 0.1 M NaCl, 20 mM Tris (pH 8.0)) and incubated for 1 h at  $25^\circ\text{C}$ . The suspension was then centrifuged (20 min,  $15,000\text{g}$ ), and the supernatant was loaded on a Ni-NTA Superflow column (Qiagen) pre-equilibrated with five volumes of resuspension buffer. The column was washed with five column volumes of resuspension buffer containing 10 mM imidazole. The protein was eluted using resuspension buffer containing 225 mM imidazole. The eluate was then dialysed against 0.1 M NaCl, 20 mM Tris (pH 8.0) and 2% LDAO (Fluka) overnight, and then concentrated by means of centrifugation to  $4 \text{ mg ml}^{-1}$ . To assay direct binding of erastin analogues,  $40 \mu\text{g}$  of purified VDAC2 was resuspended in  $100 \mu\text{l}$  of binding buffer (25 mM HEPES (pH 8.0), 0.1% BSA, 7 mM  $\text{MgCl}_2$ , 15 mM NaCl), and then incubated in the presence of  $20 \mu\text{M}$  radiolabelled erastin A9 and serial dilutions of erastin A9 or erastin A8 for 15 min. The mixture was then deposited onto Protran BA85 0.45  $\mu\text{m}$  binding filters (Whatman) using vacuum filtration. The filter was rinsed 5 times with 1 ml wash buffer (25 mM HEPES, 0.1% BSA), and incubated in 5 ml scintillation liquid (Cytoscint, MP biomedicals). Radioactivity was detected on a LKB Wallac 1211 RACKBETA liquid scintillation counter.

25. Altschul, S. F., Gish, W., Miller, W., Myers, E. W. & Lipman, D. J. Basic local alignment search tool. *J. Mol. Biol.* **215**, 403–410 (1990).

## LETTERS

# Resolvin E1 and protectin D1 activate inflammation-resolution programmes

Jan M. Schwab<sup>1†\*</sup>, Nan Chiang<sup>1\*</sup>, Makoto Arita<sup>1†</sup> & Charles N. Serhan<sup>1</sup>

Resolution of acute inflammation is an active process essential for appropriate host responses, tissue protection and the return to homeostasis<sup>1–3</sup>. During resolution, specific omega-3 polyunsaturated fatty-acid-derived mediators are generated within resolving exudates, including resolvin E1 (RvE1)<sup>4</sup> and protectin D1 (PD1)<sup>5</sup>. It is thus important to pinpoint specific actions of RvE1 and PD1 in regulating tissue resolution. Here we report that RvE1 and PD1 in nanogram quantities promote phagocyte removal during acute inflammation by regulating leukocyte infiltration, increasing macrophage ingestion of apoptotic polymorphonuclear neutrophils *in vivo* and *in vitro*, and enhancing the appearance of phagocytes carrying engulfed zymosan in lymph nodes and spleen. In this tissue terrain, inhibition of either cyclooxygenase or lipoxygenases—pivotal enzymes in the temporal generation of both pro-inflammatory and pro-resolving mediators—caused a ‘resolution deficit’ that was rescued by RvE1, PD1 or aspirin-triggered lipoxin A<sub>4</sub> analogue. Also, new resolution routes were identified that involve phagocytes traversing perinodal adipose tissues and non-apoptotic polymorphonuclear neutrophils carrying engulfed zymosan to lymph nodes. Together, these results identify new active components for postexudate resolution traffic, and demonstrate that RvE1 and PD1 are potent agonists for resolution of inflamed tissues.

Acute local inflammation in healthy individuals is self-limited and resolves by means of an active termination programme<sup>1,2</sup>. Specialized chemical mediators are generated in this biochemically active process<sup>4–7</sup>. Their complete stereochemical assignments were recently established and organic syntheses achieved<sup>8–10</sup>. These include arachidonic acid (AA)-derived lipoxin A<sub>4</sub> (LXA<sub>4</sub>) and its epimer aspirin-triggered LXA<sub>4</sub><sup>8</sup>, eicosapentaenoic acid (EPA)-derived RvE1<sup>4,9</sup>, and docosahexaenoic acid (DHA)-derived PD1 (also known as neuro-protectin D1 when generated in neural tissues)<sup>5,10,11</sup> (Fig. 1). Recently, we assembled a ‘resolution map’ using lipidomics and proteomics to identify major cellular/molecular components, and introduced quantitative resolution indices<sup>12</sup> (Supplementary Fig. 1). Each of these endogenous mediators elicits specific actions within resolution circuitry, giving precise quantitative changes in resolution indices<sup>12</sup>.

The key histological event in tissue resolution is the loss of inflammatory polymorphonuclear neutrophils (PMNs)<sup>13</sup>. In a spontaneous resolving zymosan-initiated peritonitis, total leukocyte infiltration reached a maximum at ~12 h, and by 24 h had reduced by ~50% (ref. 12). Hence, 24 h post-zymosan is well within the classic resolution phase, and was selected to study the actions of RvE1 and PD1. When given together with zymosan, PD1 (300 ng, intraperitoneal) dramatically reduced PMN infiltration by >40% compared with mice challenged with zymosan alone ((6.7 ± 0.1) × 10<sup>6</sup> PMNs versus

(11.6 ± 1.0) × 10<sup>6</sup> PMNs), illustrating potent anti-inflammation (Fig. 1a, left). For comparison, equi-doses of aspirin-triggered lipoxin A<sub>4</sub> analogue (ATLa) gave ~26% PMN reduction, and RvE1 increased mononuclear infiltrates ~24%. These results indicate that each family of resolving mediators differentially affects the cellular composition of exudate. When ATLa, RvE1 and PD1 were given at the peak of inflammation (12 h after zymosan injection), each retained the ability to reduce PMN numbers at 24 h (Fig. 1a, right) and gave similar resolution intervals (Fig. 1b), demonstrating their potent proresolving actions.

Inflammation resolution is a dynamic process, with cells being recruited to (influx) and cleared from (efflux) local inflamed sites. Reduction in exudate cells by these mediators could reflect their actions on anti-inflammation (reducing cell recruitment), proresolution (enhancing cell exit), or on both. Hence, it was important to determine whether these mediators directly activate specific resolution programmes. We evaluated whether RvE1 and PD1 affect macrophage ingestion of apoptotic PMNs *in vivo*—an essential part of the resolution orchestra in tissues<sup>14</sup> (Fig. 2a). Exudate cells collected at 24 h were labelled with FITC-conjugated anti-F4/80 Ab (a specific surface marker for mouse macrophages). Subsequently, cells were permeabilized to enable the labelling of ingested PMNs with phycoerythrin (PE)-conjugated anti-Gr-1 antibody (a specific surface marker for mouse PMNs). Mice treated with either ATLa or PD1 showed increased numbers of macrophages with ingested PMNs (cells with positive staining of both F4/80 and Gr-1 (F4/80<sup>+</sup>Gr-1<sup>+</sup>)), and thus demonstrated enhanced phagocytosis at 24 h (Fig. 2a). ATLa, RvE1 or PD1 did not directly stimulate PMN apoptosis *in vivo* when given either at the initiation or at the peak of inflammation (Supplementary Fig. 2). In contrast, when given at the peak of inflammation, cyclin-dependent kinase and specific ERK1/2 inhibitors enhance resolution by promoting PMN apoptosis<sup>15,16</sup>; this is accomplished by means of a different mechanism to that used by polyunsaturated fatty acid (PUFA)-derived endogenous mediators.

We also examined phagocytosis *in vitro*. Coincubation of elicited macrophages with apoptotic PMNs induced generation of endogenous LXA<sub>4</sub> (Fig. 2b, inset), but not of pro-inflammatory leukotriene B<sub>4</sub>. LXA<sub>4</sub> peaked at 15 min during coincubations (20.7 ± 2.6 pg per 0.2 ml, ~280 pM), identified by diagnostic ions in its tandem mass spectrometry (MS/MS) spectrum (Fig. 2b). Macrophage phagocytosis was also apparent at 15 min, and gradually increased until 2 h. These findings indicated that, when ingested by macrophages, apoptotic PMNs rapidly initiated LXA<sub>4</sub> formation, which probably contributes to enhanced macrophage phagocytosis<sup>17</sup> at later intervals (30–120 min). Apoptotic Jurkat cells also stimulate LXA<sub>4</sub>

<sup>1</sup>Center for Experimental Therapeutics and Reperfusion Injury, Department of Anesthesiology, Perioperative and Pain Medicine, Brigham and Women's Hospital and Harvard Medical School, Boston, Massachusetts 02115, USA. <sup>†</sup>Present addresses: Klinik und Poliklinik für Neurologie & Experimentelle Neurologie, Campus-Mitte, Charité Universitätsmedizin Berlin, Charitéplatz 1, 10117 Berlin, Germany (J.M.S.); Department of Health Chemistry, Graduate School of Pharmaceutical Sciences, University of Tokyo, 7-3-1 Hongo, Bunkyo-ku, Tokyo 113-0033, Japan (M.A.).

\*These authors contributed equally to this work.

formation during macrophage phagocytosis<sup>18</sup>. Of interest, during phagocytosis, PD1 was generated ( $23.2 \pm 2.1 \text{ pg ml}^{-1}$ ,  $\sim 70 \text{ pM}$ ); this was monitored by liquid chromatography (LC)-MS/MS (Supplementary Fig. 3). RvE1 was also formed by isolated cells in the presence of aspirin ( $\sim 6 \text{ pg ml}^{-1}$ ,  $\sim 16 \text{ pM}$ ), and this level increased ( $\sim 11 \text{ pg ml}^{-1}$ ,  $\sim 30 \text{ pM}$ ) with substrate EPA (Fig. 2b, MS/MS spectrum in Supplementary Fig. 3). Thus, LXA<sub>4</sub>, RvE1 and PD1 are produced when macrophages phagocytose apoptotic PMNs.

To investigate whether this set of proresolving mediators has a direct effect on isolated macrophages, macrophages were exposed to LXA<sub>4</sub>, RvE1 or PD1 (100 nM) before apoptotic PMNs. Approximately 40% of macrophages ingested PMNs (F4/80<sup>+</sup>Gr-1<sup>+</sup>) at 60 min with vehicle alone. RvE1 and PD1 each enhanced F4/80<sup>+</sup>Gr-1<sup>+</sup> macrophages by 36 ± 5% and 44 ± 10%, respectively, compared with vehicle (Fig. 2c). LXA<sub>4</sub> increased F4/80<sup>+</sup>Gr-1<sup>+</sup> macrophages by ~20%, in line with earlier findings<sup>17</sup>. LXA<sub>4</sub>, RvE1 and PD1 each regulated release of chemokines/cytokines during phagocytosis, reducing interferon- $\gamma$  and interleukin-6 (Fig. 2c). In addition, LXA<sub>4</sub> increased anti-inflammatory interleukin-10. There were no apparent changes in levels of tumour necrosis factor- $\alpha$ , KC, JE and MIP-2 (Supplementary Fig. 4). These results indicated that RvE1 and PD1 each promoted nonphlogistic macrophage engulfment of apoptotic PMNs. Taken together, it is now evident that LXA<sub>4</sub>, RvE1 and PD1 were generated *in vitro* (within 60 min) during macrophage–apoptotic PMN interactions (Fig. 2b). In turn, when macrophages were exposed to these mediators (20 min), they stimulated ingestion

of apoptotic PMNs (Fig. 2c). Glucocorticoid-stimulated phagocytosis of apoptotic PMNs requires much longer intervals (3–24 h) by comparison, and involves annexin I generation<sup>19,20</sup>. The process of macrophage ingestion of apoptotic PMNs was recently termed ‘efferocytosis’<sup>21</sup>.

Recognition of zymosan models recognition of microbes by the innate immune system<sup>22</sup>. LXA<sub>4</sub>, RvE1 or PD1 (100 nM), incubated with macrophages, stimulated uptake of zymosan 93 ± 7%, 95 ± 27% and 119 ± 20%, respectively, compared with vehicle (Fig. 2d). These mediators also enhanced macrophage uptake of non-opsonized latex beads, albeit to a much lesser extent (Fig. 2d). Thus, in addition to apoptotic PMNs, LXA<sub>4</sub>, RvE1 and PD1 are potent stimulators of macrophage uptake of microbial particles—that is, opsonized zymosan.

We questioned whether these resolution agonists affect leukocyte traffic from zymosan-inflamed peritoneum by way of lymph nodes and spleen. In the resolution phase (24 h), the most pronounced locations of phagocytes carrying ingested zymosan (that is, leukocytes with engulfed zymosan, zymosan<sup>e</sup> leukocytes) were in the outer cortex of lymph nodes and in the spleen within the marginal zone surrounding white pulp (Fig. 3a). ATLa (300 ng) increased zymosan<sup>e</sup> leukocytes in lymph nodes at 24 h (Fig. 3a), giving >2-fold increase of total zymosan (0.23 ± 0.03 versus 0.09 ± 0.04  $\mu\text{g}$  zymosan per  $\mu\text{g}$  protein in mice given zymosan alone) (Fig. 3b). Significant increases in levels of zymosan in spleens were also observed. Passive efflux of nonengulfed zymosan was excluded, as significant

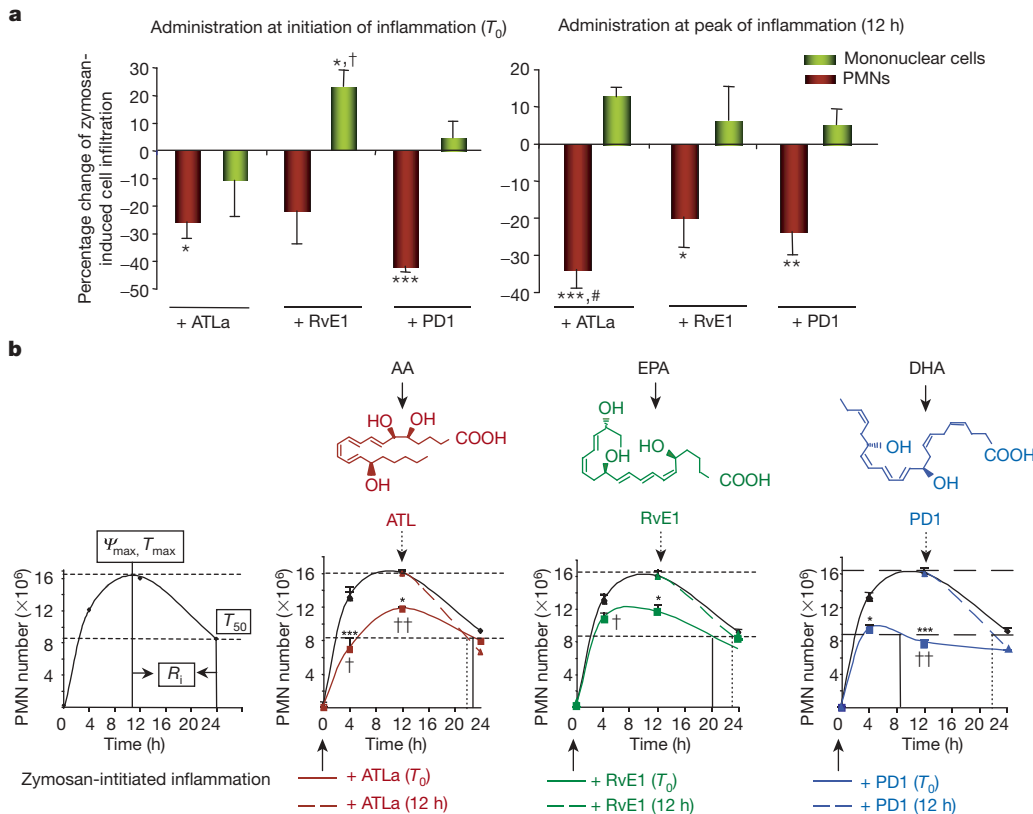


**Figure 1 | Pro-resolving lipid mediators RvE1, PD1 and ATLa direct local phagocyte tissue flux.** **a**, Peritonitis. ATLa, RvE1 or PD1 (300 ng, intraperitoneal) was given either with zymosan ( $T_0$ , left) or 12 h after zymosan (right), and peritoneal exudates collected (24 h). Results are the mean ± s.e.m. ( $n = 4–8$ ). \* $P < 0.05$ , \*\* $P < 0.01$ , \*\*\* $P < 0.001$ , compared with zymosan alone; † $P < 0.05$ , ATLa versus RvE1; # $P < 0.05$ ,  $T_0$  versus 12 h. **b**, Resolution indices were defined in ref. 12 (Supplementary Fig. 1), including  $\psi_{\max}$  (maximal PMN level),  $T_{\max}$  (time point when PMNs reach  $\psi_{\max}$ ),  $T_{50}$  (time point corresponding to ~50% PMN reduction) and  $R_i$  (resolution interval, the interval between  $T_{\max}$  and  $T_{50}$ ). These indices were calculated when compounds were given at the initiation ( $T_0$ , solid lines and

arrows) or peak (12 h, dashed lines and arrows) of inflammation. Results are the mean ± s.e.m. ( $n = 4–8$ ). \* $P < 0.05$ , \*\* $P < 0.01$ , \*\*\* $P < 0.001$ , compared with zymosan alone; † $P < 0.05$ , ATLa versus RvE1; †† $P < 0.01$ , ATLa versus PD1. For zymosan-initiated inflammation:  $\psi_{\max}$ ,  $16.5 \times 10^6$ ;  $T_{\max}$ , ~12 h;  $T_{50}$ , ~24 h;  $R_i$ , ~12 h. For plus ATLa ( $T_0$ , red solid line):  $\psi_{\max}$ ,  $13.2 \times 10^6$ ;  $T_{\max}$ , ~12 h;  $T_{50}$ , ~23 h;  $R_i$ , ~11 h. For plus ATLa (12 h, red broken line):  $T_{\max}$ , ~12 h;  $T_{50}$ , ~22 h;  $R_i$ , ~10 h. For plus RvE1 ( $T_0$ , green solid line):  $\psi_{\max}$ ,  $12.0 \times 10^6$ ;  $T_{\max}$ , ~8 h;  $T_{50}$ , ~20 h;  $R_i$ , ~12 h. For plus RvE1 (12 h, green broken line):  $T_{\max}$ , ~12 h;  $T_{50}$ , ~23 h;  $R_i$ , ~11 h. For plus PD1 ( $T_0$ , blue solid line):  $\psi_{\max}$ ,  $10.0 \times 10^6$ ;  $T_{\max}$ , ~5 h;  $T_{50}$ , ~11 h;  $R_i$ , ~6 h. For plus PD1 (12 h, blue broken line):  $T_{\max}$ , ~12 h;  $T_{50}$ , ~22 h;  $R_i$ , ~10 h.

extracellular association of zymosan was not apparent. Thus, total zymosan levels represent phagocytic leukocytes within lymph nodes and spleen. RvE1 also enhanced zymosan<sup>e</sup> leukocytes in both lymph nodes and spleen, with modest increases in lymph nodes compared with significant increases in the spleen. PD1-treated mice gave dramatic increases in zymosan levels of more than six-fold in lymph nodes and more than four-fold in the spleen. When ATLa, RvE1 or PD1 were each given at the peak of inflammation, they also enhanced, to a lesser extent, zymosan<sup>e</sup> leukocytes in lymph nodes and spleen (Fig. 3b). Thus, LXA<sub>4</sub>, RvE1 and PD1 are biosynthesized in inflammatory exudates<sup>12</sup> (Supplementary Fig. 5), and, when these mediators were added back, they promoted phagocyte removal of microbial challenge by way of lymphatics. It is noteworthy that their precursors (AA, EPA and DHA) were also elevated during peritonitis<sup>12</sup> (Supplementary Fig. 5).

Next we investigated whether disruption of biosynthetic pathways of these mediators altered resolution. In the biosynthesis of aspirin-triggered LXA<sub>4</sub> and RvE1, acetylated cyclooxygenase (COX)-2 is pivotal<sup>14,8</sup> (Supplementary Fig. 6). Pharmacologic inhibition of COX-2 delays resolution<sup>23</sup>. In peritoneal leukocytes, COX-2 was induced within 4 h after zymosan challenge and remained elevated until 72 h (not shown). COX-2 inhibition by NS-398 (10  $\mu$ M) decreased

macrophage phagocytosis of apoptotic PMNs *in vitro*, and reduced prostaglandin E<sub>2</sub> and LXA<sub>4</sub> (Supplementary Fig. 7). Lipoxygenases (LOX) are also essential in biosynthesis of PUFA-derived mediators<sup>4,5,8,24</sup>. LOX inhibition by baicalein<sup>25</sup> (10  $\mu$ M) impaired macrophage phagocytosis and reduced LXA<sub>4</sub>, 15-hydroxyeicosatetraenoic acid (15-HETE) and 12-HETE, as well as 17-hydroxy-docos-4Z,7Z,10Z,13Z,15E,19Z-hexaenoic acid (17-HDHA)—a marker of PD1 biosynthesis (Supplementary Fig. 7). Thus, reduction in protective mediators (for example, LXA<sub>4</sub>) could reflect hampered phagocytosis when COX and LOX inhibitors were present.

During peritonitis, COX inhibition by NS-398 (ref. 23; 100  $\mu$ g) increased exudate leukocytes by ~22% and PMNs by ~41% at 24 h (Fig. 3c and Supplementary Table 1). In addition, zymosan amounts in both lymph nodes and spleen were significantly reduced by >50%, indicating impaired resolution. When ATLa, RvE1 or PD1 (300 ng) was administered along with a COX-2 inhibitor, each markedly reduced exudate leukocytes and increased zymosan amounts in lymphatics to levels comparable to those in zymosan-challenged mice (Fig. 3c). The LOX inhibitor (100  $\mu$ g) gave similar results (Fig. 3d and Supplementary Table 1). Hence, disrupting biosynthesis of these protective mediators with either COX-2 or LOX inhibitors caused a ‘resolution deficit’ phenotype, blocking phagocytic removal

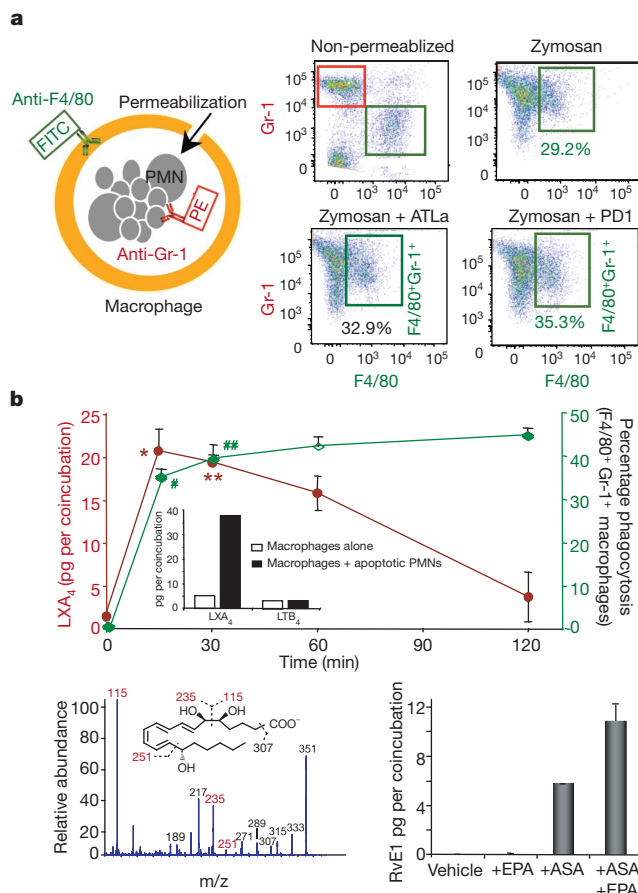
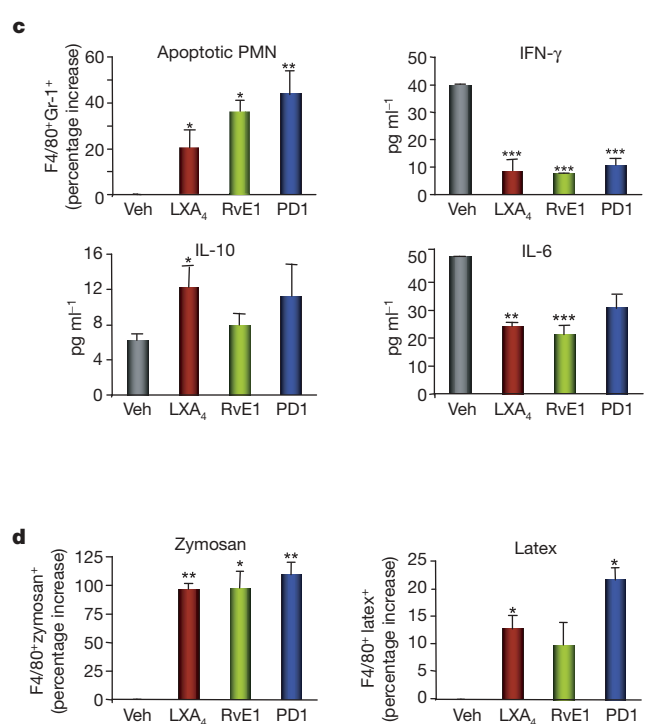


**Figure 2 | RvE1 and PD1 increase macrophage phagocytic activity *in vivo* and *in vitro*.** **a**, *In vivo* phagocytosis with representative dot plots of FACS analysis. **b**, Top, time course of eicosanoid generation and phagocytosis activity *in vitro*. Results are mean  $\pm$  s.e.m. ( $n = 3$ ). LXA<sub>4</sub> amounts are expressed as pg per coincubation ( $0.4 \times 10^6$  PMNs +  $0.2 \times 10^6$  macrophages in 0.2 ml). \* $P = 0.01$ , \*\* $P = 0.02$  (versus time 0 or 120 min). Phagocytosis activities are expressed as [ $F4/80^+Gr-1^-/F4/80^+$ ]  $\times 100\%$ . # $P = 0.03$ , ## $P = 0.01$  (versus time 120 min). Inset, LXA<sub>4</sub> and LTB<sub>4</sub> generation at 60 min. Bottom left, MS/MS spectrum of LXA<sub>4</sub> ( $m/z$  351: [M-H]<sup>-</sup>). Bottom right, RvE1 generation. Macrophages were incubated with acetylsalicylic acid (ASA) (500  $\mu$ M, 30 min) followed by EPA (20  $\mu$ M, 45 min), before incubation with apoptotic PMNs. RvE1 was determined by LC-MS/MS and



expressed as pg per coincubation ( $2 \times 10^6$  PMNs +  $1 \times 10^6$  macrophages in 1 ml). **c**, Phagocytosis of apoptotic PMNs *in vitro*. Results are the mean  $\pm$  s.e.m. ( $n = 3$ ) and are expressed as percentage increase of F4/80<sup>+</sup>Gr-1<sup>+</sup> macrophages compared with vehicle (Veh) alone. Cytokine and chemokine levels are expressed as mean  $\pm$  s.e.m. ( $n = 3$ ). \* $P < 0.05$ , \*\* $P < 0.01$ , \*\*\* $P < 0.001$ , compared with vehicle alone. **d**, Phagocytosis of zymosan and latex particles *in vitro*. Results are the mean  $\pm$  s.e.m. ( $n = 3$ ) and are expressed as percentage increase of F4/80<sup>+</sup>zymosan<sup>+</sup> or F4/80<sup>+</sup>latex<sup>+</sup> macrophages (F4/80-positive macrophages with ingested fluorescent zymosan or latex beads, respectively) compared with vehicle alone. Results are the mean  $\pm$  s.e.m. ( $n = 3$ ). \* $P < 0.05$ , \*\* $P < 0.01$  compared with vehicle alone.

of microbial challenge, thereby delaying resolution. These results emphasize a pivotal homeostatic role for COX-2 (ref. 23) and LOX (ref. 24) in resolution of acute inflammation. Importantly, pro-resolving mediators at much lower doses (by at least two log orders) rescued defective resolution caused by these pharmacological interventions.

To further study phagocytes leaving the inflamed peritoneum, mice were injected with fluorescein isothiocyanate (FITC)-labelled zymosan. As early as 4 h, we found leukocytes carrying FITC-zymosan (FITC-zymosan<sup>e</sup> leukocytes) beginning to appear in the perinodal adipose tissue ( $12 \pm 5$  FITC-zymosan<sup>e</sup> leukocytes per high power field (HPF), Fig. 4A and 4Bc–f), indicating that exiting leukocyte traffic from the inflamed site started early, namely during the acute inflammatory phase. In contrast, few FITC-zymosan<sup>e</sup> leukocytes were noted in lymph nodes, and none were apparent in spleen. With progression of resolution at 24 h, FITC-zymosan<sup>e</sup> leukocytes increased  $>2$ -fold in perinodal adipose tissue, with the highest numbers in lymph nodes ( $\sim 50$  FITC-zymosan<sup>e</sup> leukocytes/HPF); they also appeared within the spleen. In lymph nodes, a small population of FITC-zymosan<sup>e</sup> leukocytes observed within cortex areas were

PMNs ( $\sim 10\%$ ) (Fig. 4Bg–i), indicating that these PMNs were phagocytically active, directly transporting zymosan to lymph nodes before their apoptosis and later engulfment by macrophages. Some of the FITC-zymosan<sup>e</sup> leukocytes displayed dendritic cell-like morphology with characteristic fine cellular protrusions within afferent lymph vessels (Fig. 4Bj) and spleen (Fig. 4Bk,l).

The widely appreciated exit routes of leukocytes from inflamed peritoneum involve drainage by means of afferent lymph vessels into lymph nodes (lymphatic) and subsequently into the spleen (humoral)<sup>13</sup> (Supplementary Fig. 9). In addition to these, we identified high numbers of FITC-zymosan<sup>e</sup> leukocytes extravasating from the afferent lymph vessels into perinodal adipose tissue before reaching lymph nodes (subcapsular sinus; Fig. 4Bc–f). We termed this process 'lipopassage', because it is a new trafficking route for leukocytes to exit exudates. Macrophage efflux from the peritoneum into lymphatics is dependent on different adhesion molecules, such as  $\beta 1$ -integrin<sup>26</sup> and Mac-1 (also known as CD11b/CD18)<sup>27</sup>. CD18 is involved in LXA<sub>4</sub>-stimulated macrophage phagocytosis of apoptotic PMNs<sup>17</sup>. Hence, it is likely that adhesion molecules play a role in lipopassage. Adipocytes are anatomically associated with lymph

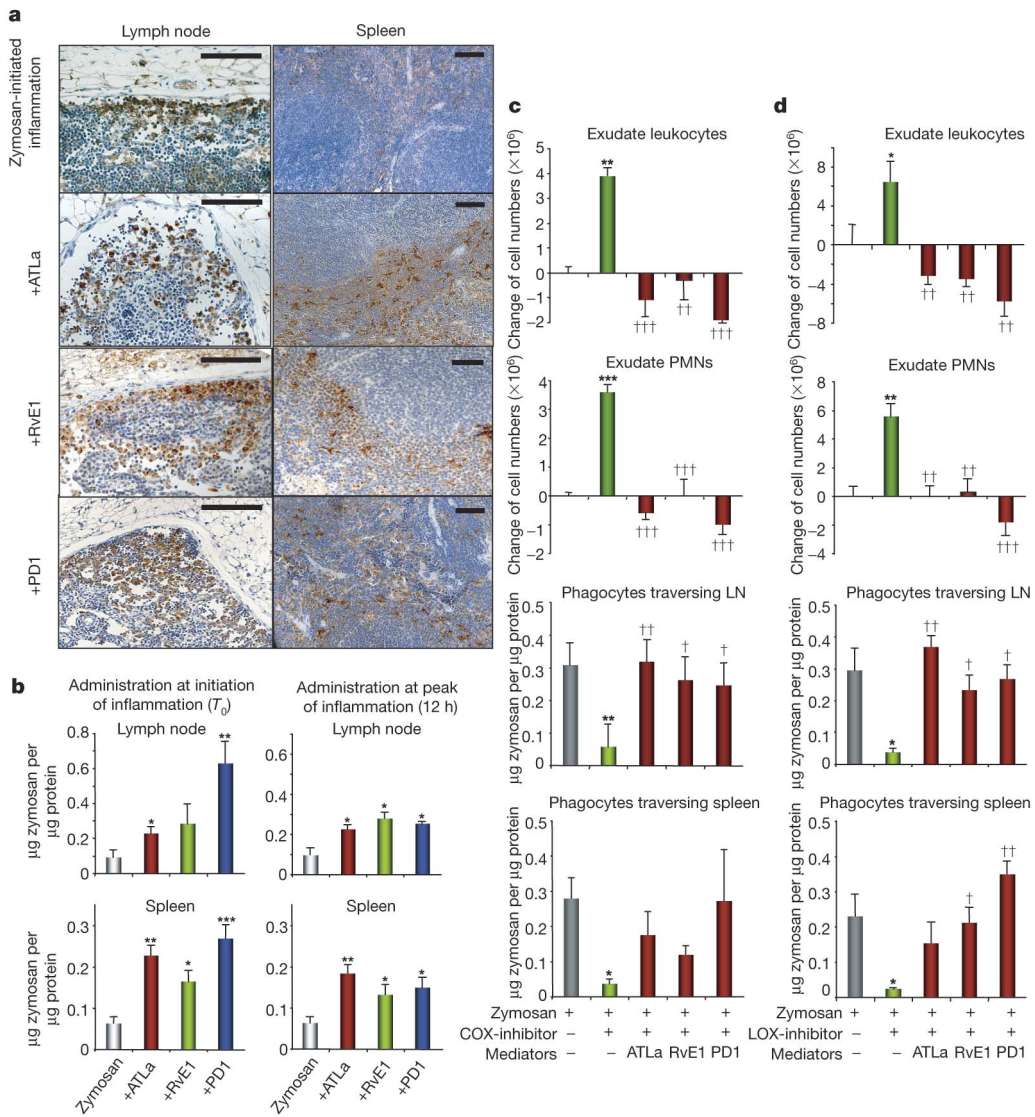


**Figure 3 | RvE1 and PD1 enhance leukocytes carrying phagocytosed zymosan in lymph nodes and spleen.** **a**, Leukocytes with engulfed-zymosan particles (zymosan<sup>e</sup>) in the cortex of the lymph nodes and marginal zone of the spleen. The brown particles are positive staining of zymosan. Scale bars, 50  $\mu$ m. **b**, Quantification of zymosan. ATLa, RvE1 or PD1 was given at initiation ( $T_0$ ) or at peak (12 h) of inflammation. Results are mean  $\pm$  s.e.m.

( $n = 4$ –8). \* $P = 0.05$ , \*\* $P < 0.01$ , \*\*\* $P < 0.001$ . **c**, **d**, COX or LOX inhibitor was given 30 min before zymosan challenge with or without mediators. Results are mean  $\pm$  s.e.m. ( $n = 3$ –4). \* $P = 0.05$ , \*\* $P < 0.01$ , \*\*\* $P < 0.001$ , compared with zymosan alone; † $P = 0.05$ , †† $P < 0.01$ , ††† $P < 0.001$ , compared with **c**, zymosan plus COX-inhibitor or **d**, zymosan plus LOX-inhibitor.

nodes and might be involved in modulating inflammation<sup>28</sup>. Our present findings provide a potential link between perinodal adipose tissue and phagocyte removal from exudates during resolution. In addition, nonapoptotic PMNs carrying zymosan exit exudates, providing evidence that PMNs themselves actively contribute to resolution of inflammation, along with macrophages. Thus, disease processes recently linked to inflammation (for example, diabetes and obesity)<sup>29</sup> might involve resolution deficits as part of their pathogenesis.

Here we demonstrate novel protective actions for RvE1 and PD1 in promoting resolution following microbial challenge, as evidenced

by their regulating leukocyte infiltration, stimulating macrophage phagocytosis of apoptotic PMNs, and increasing phagocytes carrying zymosan in lymph nodes and spleen (Supplementary Fig. 10). These potent 'resolution agonists' orchestrate the return of the tissue to homeostasis and are able to rescue resolution deficits emplaced by pharmacological inhibitors of COX and LOX. Together, these results emphasize that resolution agonists (for example, RvE1 and PD1) and resolution programmes might have therapeutic potential when sustained inflammation and/or impaired resolution are components of pathophysiology.

## METHODS SUMMARY

**Murine peritonitis.** FVB mice were given lipid mediators (300 ng) at the same time as or 12 h after zymosan A (1 mg ml<sup>-1</sup>; Sigma) by intraperitoneal injection. A COX-2 inhibitor (NS-398; Cayman Chemicals) or LOX inhibitor (baicalein; Sigma) was given (100 µg) 30 min before zymosan challenge.

**Phagocytosis and apoptosis.** For PMN apoptosis, exudate cells were labelled with FITC-conjugated anti-annexin-V antibody and PE-conjugated anti-mouse Gr-1 antibody (eBioscience). For phagocytosis *in vivo*, exudate cells were labelled with FITC-conjugated anti-mouse F4/80 antibody, permeabilized with 0.1% Triton X-100, and then labelled with PE-anti-Gr-1 antibody. For phagocytosis *in vitro*, aged PMNs were labelled with PE-anti-Gr-1 antibody. Elicited macrophages were incubated with lipid mediators. PE-anti-Gr-1 antibody-labelled PMNs were then coincubated with treated macrophages at a 2:1 ratio. In separate experiments, fluorescent-labelled zymosan or latex particles (Molecular Probes) were added to treated macrophages at a 10:1 ratio. Macrophages were then labelled with FITC-anti-F4/80 antibody and monitored by flow cytometry.

**Mediator lipidomics.** Mass spectral analyses were performed using a Qstar XL Hybrid LC/MS/MS system equipped with a Turbospray ion source (Applied Biosystems) and operated in negative electrospray mode.

**Zymosan quantitation.** Inguinal lymph nodes and spleens from zymosan-injected mice were harvested, zymosan was extracted by homogenization and sonication, and supernatants were collected. For zymosan quantitation, 96-well plates were pre-coated with anti-zymosan IgG (Molecular Probes), followed by addition of FITC-zymosan and supernatants containing zymosan. Fluorescence was monitored by fluorometry.

**Immunohistochemistry.** Immunohistochemistry slides prepared from paraffin-embedded sections were incubated with either rabbit anti-zymosan antibody (Molecular Probes) or rabbit anti-FITC antibody (Dako), followed by biotinylated swine anti-rabbit IgG and peroxidase-conjugated streptavidin-biotin complex (Dako). The bound peroxidase was visualized with diaminobenzidine (brown precipitate). Zymosan-containing cells were determined by counting in ten high-power fields (×200).

**Statistics.** Results are expressed as mean ± standard error of mean (s.e.m.). Group comparisons were carried out using one-way analysis of variance or Student's *t*-test, with *P* values ≤0.05 taken as statistically significant.

**Full Methods** and any associated references are available in the online version of the paper at [www.nature.com/nature](http://www.nature.com/nature).

Received 20 March; accepted 25 April 2007.

1. Serhan, C. N. & Savill, J. Resolution of inflammation: the beginning programs the end. *Nature Immunol.* 6, 1191–1197 (2005).
2. Gilroy, D. W., Lawrence, T., Perretti, M. & Rossi, A. G. Inflammatory resolution: new opportunities for drug discovery. *Nature Rev. Drug Discov.* 3, 401–416 (2004).
3. Nathan, C. Points of control in inflammation. *Nature* 420, 846–852 (2002).
4. Serhan, C. N. *et al.* Novel functional sets of lipid-derived mediators with antiinflammatory actions generated from omega-3 fatty acids via cyclooxygenase 2-nonsteroidal antiinflammatory drugs and transcellular processing. *J. Exp. Med.* 192, 1197–1204 (2000).
5. Hong, S., Gronert, K., Devchand, P., Moussignac, R.-L. & Serhan, C. N. Novel docosatrienes and 17S-resolvin generated from docosahexaenoic acid in murine brain, human blood and glial cells: autacoids in anti-inflammation. *J. Biol. Chem.* 278, 14677–14687 (2003).
6. Levy, B. D., Clish, C. B., Schmidt, B., Gronert, K. & Serhan, C. N. Lipid mediator class switching during acute inflammation: signals in resolution. *Nature Immunol.* 2, 612–619 (2001).
7. Maddox, J. F. & Serhan, C. N. Lipoxin A<sub>4</sub> and B<sub>4</sub> are potent stimuli for human monocyte migration and adhesion: selective inactivation by dehydrogenation and reduction. *J. Exp. Med.* 183, 137–146 (1996).
8. Serhan, C. N. Special issue on lipoxins and aspirin-triggered lipoxins. *Prostaglandins Leukot. Essent. Fatty Acids* 73, 139–321 (2005).

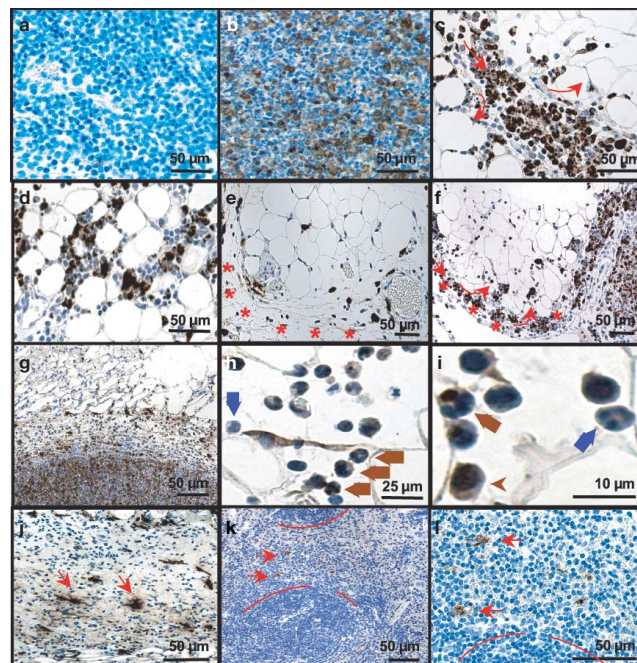
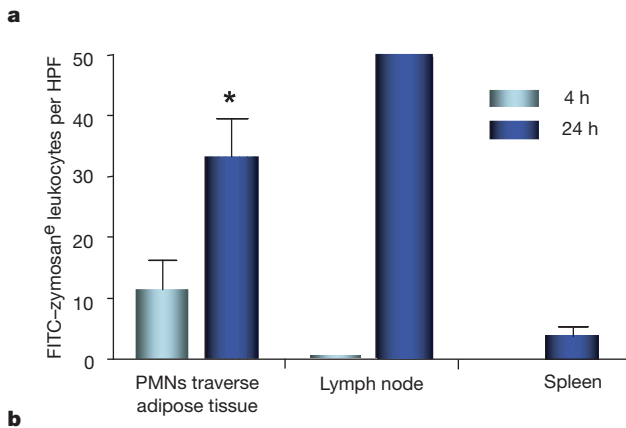


**Figure 4 | Active removal of leukocytes from the inflammatory exudate.** **A**, Quantification of FITC-zymosan<sup>+</sup> leukocytes. Results are mean ± s.e.m. (*n* = 3). \**P* = 0.05 (4 h versus 24 h). **B**, Tracking of FITC-zymosan<sup>+</sup> leukocytes 24 h after FITC-zymosan injection in **a**, the absence or **b**, the presence of the primary anti-FITC antibody. The brown particles are immunopositive FITC-zymosan ingested by leukocytes. **c**, Lipopassage (arrows). **d**, Zymosan<sup>+</sup> leukocytes in perinodal adipose tissue. **e**, In perinodal adipose tissue, lymph vessels (stars) conduct zymosan<sup>+</sup> leukocytes in proximity to blood vessels. **f**, Zymosan<sup>+</sup> leukocytes in the afferent lymph vessel (stars) and subcapsular sinus. **g**, In the lymph nodes, zymosan<sup>+</sup> leukocytes were detected markedly in cortex areas. **h, i**, Zymosan<sup>+</sup> leukocytes consisted of monocytes/macrophages (arrowheads), and non-apoptotic PMNs with engulfed-zymosan (brown arrows) or without (blue arrows). **j**, Dendritic-like (fine cell protrusions), zymosan<sup>+</sup> leukocytes in the afferent lymph vessels (arrows). **k, l**, In the spleen, some zymosan<sup>+</sup> leukocytes also displaced morphological characteristics of dendritic cells (arrows).

9. Arita, M. et al. Stereochemical assignment, anti-inflammatory properties, and receptor for the omega-3 lipid mediator resolvin E1. *J. Exp. Med.* **201**, 713–722 (2005).
10. Serhan, C. N. et al. Anti-inflammatory actions of neuroprotectin D1/protectin D1 and its natural stereoisomers: assignments of dihydroxy-containing docosatrienes. *J. Immunol.* **176**, 1848–1859 (2006).
11. Bazan, N. G. Cell survival matters: docosahexaenoic acid signaling, neuroprotection and photoreceptors. *Trends Neurosci.* **29**, 263–271 (2006).
12. Bannenberg, G. L. et al. Molecular circuits of resolution: formation and actions of resolvins and protectins. *J. Immunol.* **174**, 4345–4355 (2005).
13. Cotran, R. S., Kumar, V. & Collins, T. (eds) *Robbins Pathologic Basis of Disease* (W. B. Saunders, Philadelphia, 1999).
14. Savill, J., Dransfield, I., Gregory, C. & Haslett, C. A blast from the past: clearance of apoptotic cells regulates immune responses. *Nature Rev. Immunol.* **2**, 965–975 (2002).
15. Sawatzky, D. A., Willoughby, D. A., Colville-Nash, P. R. & Rossi, A. G. The involvement of the apoptosis-modulating proteins ERK 1/2, Bcl-xL and Bax in the resolution of acute inflammation *in vivo*. *Am. J. Pathol.* **168**, 33–41 (2006).
16. Rossi, A. G. et al. Cyclin-dependent kinase inhibitors enhance the resolution of inflammation by promoting inflammatory cell apoptosis. *Nature Med.* **12**, 1056–1064 (2006).
17. Reville, K., Crean, J. K., Vivers, S., Dransfield, I. & Godson, C. Lipoxin A4 redistributes myosin IIA and Cdc42 in macrophages: implications for phagocytosis of apoptotic leukocytes. *J. Immunol.* **176**, 1878–1888 (2006).
18. Freire-de-Lima, C. G. et al. Apoptotic cells, through transforming growth factor-beta, coordinately induce anti-inflammatory and suppress pro-inflammatory eicosanoid and NO synthesis in murine macrophages. *J. Biol. Chem.* **281**, 38376–38384 (2006).
19. Maderna, P., Yona, S., Perretti, M. & Godson, C. Modulation of phagocytosis of apoptotic neutrophils by supernatant from dexamethasone-treated macrophages and annexin-derived peptide Ac(2–26). *J. Immunol.* **174**, 3727–3733 (2005).
20. Liu, Y. et al. Glucocorticoids promote nonphlogistic phagocytosis of apoptotic leukocytes. *J. Immunol.* **162**, 3639–3646 (1999).
21. Vandivier, R. W., Henson, P. M. & Douglas, I. S. Burying the dead: the impact of failed apoptotic cell removal (efferocytosis) on chronic inflammatory lung disease. *Chest* **129**, 1673–1682 (2006).
22. Underhill, D. M. Macrophage recognition of zymosan particles. *J. Endotoxin Res.* **9**, 176–180 (2003).
23. Gilroy, D. W. et al. Inducible cyclooxygenase may have anti-inflammatory properties. *Nature Med.* **5**, 698–701 (1999).
24. Gronert, K. et al. A role for the mouse 12/15-lipoxygenase pathway in promoting epithelial wound healing and host defense. *J. Biol. Chem.* **280**, 15267–15278 (2005).
25. Sadik, C. D., Sies, H. & Schewe, T. Inhibition of 15-lipoxygenases by flavonoids: structure-activity relations and mode of action. *Biochem. Pharmacol.* **65**, 773–781 (2003).
26. Bellinger, G. J. et al. Adhesion molecule-dependent mechanisms regulate the rate of macrophage clearance during the resolution of peritoneal inflammation. *J. Exp. Med.* **196**, 1515–1521 (2002).
27. Cao, C., Lawrence, D. A., Strickland, D. K. & Zhang, L. A specific role of integrin Mac-1 in accelerated macrophage efflux to the lymphatics. *Blood* **106**, 3234–3241 (2005).
28. Pond, C. M. Adipose tissue and the immune system. *Prostaglandins Leukot. Essent. Fatty Acids* **73**, 17–30 (2005).
29. Wellen, K. E. & Hotamisligil, G. S. Inflammation, stress, and diabetes. *J. Clin. Invest.* **115**, 1111–1119 (2005).

**Supplementary Information** is linked to the online version of the paper at [www.nature.com/nature](http://www.nature.com/nature).

**Acknowledgements** These studies were supported in part by the NIH (C.N.S.) and a Research Fellowship from the Deutsche Forschungsgemeinschaft (J.M.S.). We thank J. Kutok for discussion regarding immunohistology, G. Fredman for assistance with fluorescence-activated cell sorting (FACS) and S. Elangovan for technical support. We also thank L. Xu and K. Gotlinger for mass spectral analyses and M. Halm Small for manuscript preparation. We also acknowledge NIH support for the Organic Synthesis Core (NAP) of the NIH-supported P50 Center grant (C.N.S.).

**Author Contributions** C.N.S. planned the project, designed experiments, analysed data and wrote the manuscript; N.C. and J.M.S. designed and carried out experiments, analysed data, and wrote the manuscript; M.A. analysed and discussed data.

**Author Information** Reprints and permissions information is available at [www.nature.com/reprints](http://www.nature.com/reprints). The authors declare competing financial interests: details accompany the full text HTML version of the paper at [www.nature.com/nature](http://www.nature.com/nature). Correspondence and requests for materials should be addressed to C.N.S. (cnserhan@zeus.bwh.harvard.edu).

## METHODS

**Murine peritonitis.** Male FVB mice (6–8 weeks; Charles River) were anaesthetized with isoflurane. Zymosan A (1 mg ml<sup>-1</sup>, Sigma) was administered intraperitoneally alone or with specific lipid mediators (ATLa, RvE1 or PD1, 300 ng per mouse or ~12 µg kg<sup>-1</sup>, intraperitoneal) for these experiments. In separate groups, ATLa, RvE1 or PD1 was given 12 h after zymosan injection. ATLa, RvE1 and PD1 were prepared by total organic synthesis in the Organic Synthesis Core of the Specialized Center for Research by N. Petasis<sup>8–10</sup> in accordance with recently published physical and biological criteria. In the case of COX-2 inhibitor (NS-398, Cayman Chemicals) and LOX inhibitor (baicalein, Sigma), each was given at 100 µg per mouse (or ~4 mg kg<sup>-1</sup>) 30 min before zymosan challenge. At indicated time intervals, mice were euthanized with an overdose of isoflurane, peritoneal exudate cells were collected, and differential leukocyte counts were determined. All animal procedures were conducted in accordance with the Harvard Medical Area Standing Committee on Animals (protocol number 02570).

**FACS analysis for phagocytosis and apoptosis.** To determine macrophage ingestion of PMNs *in vivo*, cells were first blocked with anti-mouse CD16/32 blocking antibody (0.5 µg per 0.5 × 10<sup>6</sup> cells, eBioscience) for 5 min, labelled with FITC-conjugated anti-mouse F4/80 antibody (0.5 µg per 0.5 × 10<sup>6</sup> cells, eBioscience) for 20 min, and permeabilized with 0.1% Triton X-100 (100 µl) for 10 min. Subsequently, permeabilized cells were labelled with phycoerythrin (PE)-conjugated anti-mouse Gr-1 (also known as Ly-6G) antibody (0.5 µg per 0.5 × 10<sup>6</sup> cells, eBioscience) for 20 min. The F4/80<sup>+</sup>Gr-1<sup>+</sup> macrophage population was determined by FACS analysis.

For determining PMN apoptosis *in vivo*, exudate cells were labelled with FITC-conjugated anti-annexin-V antibody (0.5 µg per 0.5 × 10<sup>6</sup> cells, eBioscience) and PE-conjugated Ly-6G (0.5 µg antibody per 0.5 × 10<sup>6</sup> cells, eBioscience) for 20 min. The annexin-V<sup>+</sup>Gr-1<sup>+</sup> PMN population was monitored by FACS.

For determining macrophage phagocytosis of apoptotic PMNs *in vitro*, murine peritoneal PMNs were collected after 4 h peritonitis, aged for 24 h in culture in complete RPMI (BioWhittaker), and then labelled with PE-conjugated anti-mouse Gr-1 antibody. Elicited macrophages were collected after 72 h peritonitis and incubated with lipid mediators (LXA<sub>4</sub>, RvE1 or PD1, 100 nM) or vehicle alone for 20 min. LXA<sub>4</sub> was from Calbiochem. PE-Gr-1 antibody-labelled apoptotic PMNs were then coincubated with previously treated macrophages at a 2:1 ratio for the time indicated. Finally, macrophages were labelled with FITC-conjugated anti-mouse F4/80 antibody, and F4/80<sup>+</sup>Gr-1<sup>+</sup> macrophages were evaluated using FACsort software gated for 10,000 events.

For determining macrophage phagocytosis of zymosan (Texas red-labelled, Molecular Probes) or latex (Fluo Spheres carboxylate-modified microspheres, 1.0 µm, orange fluorescent; Molecular Probes), elicited macrophages were collected after 72 h peritonitis and incubated with lipid mediators (LXA<sub>4</sub>, RvE1 or PD1, 100 nM) or vehicle alone for 20 min. Zymosan or latex particles were then incubated with previously treated macrophages at a 10:1 ratio for 60 min. Macrophages were collected and labelled with FITC-conjugated anti-mouse F4/80 antibody. F4/80<sup>+</sup>zymosan<sup>+</sup> or F4/80<sup>+</sup>latex<sup>+</sup> macrophages were evaluated using FACsort software gated for 10,000 events.

**Mediator lipidomics.** Samples were extracted with deuterium-labelled internal standards (1–2 ng deuterium-labelled PGE<sub>2</sub> and 0.4 ng deuterium-labelled PD1)

using C18 solid phase extraction (Alltech Associates). For LC-MS/MS analysis, an Applied Biosystems Qstar XL was used, equipped with a LUNA C18-2 (100 mm × 2 mm × 5 µm; Phenomenex) column. High-performance liquid chromatography conditions: 0–8 min, 50% A, 50% B; 8–30 min, 100% B (A, 0.01% acetic acid; B, acetonitrile:methanol:acetic acid 50:50:0.01%), flow rate 0.2 ml min<sup>-1</sup>, UV 190–400 nm. All mass spectral analyses were performed using a Qstar XL equipped with a Turbospray ion source (Applied Biosystems) and operated in negative electrospray mode. Parameters for TOF mass scan and product ion scans were: Cur, 30 p.s.i.; GS1, 40 p.s.i.; GS2, 50 p.s.i.; CAD 5; TEM, 400 °C; DP, -50 V; FP, -220; DP2, -10; ISV, -4,200. Q1 resolution unit. The voltage used for collisional activated dissociation varied according to molecular species and ranged from -20 V to -30 V for product ion scan. A mixture of synthetic 15-, 12-, 5-HETE, LXA<sub>4</sub>, RvE1, 17S-HDHA and PD1 was used to obtain standard curves for each compound. Linear regression gave R<sup>2</sup> values of >0.99 for each. In some experiments, LXA<sub>4</sub> and LTB<sub>4</sub> formation were also determined by ELISA (Neogen).

**Quantitation of zymosan A particles.** Inguinal lymph nodes and spleens were collected (24 h after zymosan injection), and dried in an oven (60 °C). Dried tissues were pulverized mechanically, resuspended in 50 mM PBS with 1% Triton-X, and homogenized, followed by sonication and three cycles of freeze-thaw. Samples were centrifuged, supernatants collected and total protein amounts determined using Bio-Rad protein assay (Bio-Rad). For zymosan quantitation, polystyrene 96-well plates were precoated with rabbit anti-zymosan IgG (1 µg per well, Molecular Probes). The competitive assay was initiated by adding FITC-zymosan (0.5 µg 50 µl<sup>-1</sup>), together with either zymosan standards (serial dilutions from 1 to 200 µg ml<sup>-1</sup>) or samples (50 µl) into each well. After incubation for 2 h at room temperature and three washings with wash buffer, fluorescence was then determined by a fluorometer. All samples were assayed in triplicate, and zymosan levels were normalized by either dry tissue weight or total protein amounts in each sample.

**Immunohistochemistry.** Inguinal lymph nodes, corresponding afferent lymph vessels, and perinodal adipose tissues were excised 4 and 24 h following zymosan or FITC-zymosan challenge. Slides for immunohistology were prepared for a service fee by the Specialized Histopathology Core Laboratory, Department of Pathology, Brigham and Women's Hospital, Boston, USA. After formaldehyde fixation and paraffin-embedding, sections were incubated with the primary rabbit anti-zymosan antibody (Molecular Probes, 1:500) or rabbit anti-FITC antibody (Dako) overnight at 4 °C. Specific binding of the antibody was detected with a secondary biotinylated swine anti-rabbit IgG F(ab)2 fragment (1:400, 30 min, Dako), followed by incubation with a peroxidase-conjugated streptavidin-biotin complex (Dako). The bound peroxidase was then visualized with diaminobenzidine as a chromogen (brown precipitate). Sections were counterstained with Mayer's Hemalum. Negative controls consisted of sections incubated in the absence of the primary antibody. The number of cells with engulfed FITC-zymosan in the perinodal adipose tissue, lymph nodes and spleen was determined by counting in 10 HPFs (×200 magnification).

**Statistics.** All results were calculated and expressed as mean ± s.e.m. Group comparisons were carried out using one-way analysis of variance or Student's *t*-test where appropriate, with *P* values ≤ 0.05 taken as statistically significant (sufficient to reject the null hypothesis).

## LETTERS

# Drosophila miR2 induces pseudo-polysomes and inhibits translation initiation

Rolf Thermann<sup>1</sup> & Matthias W. Hentze<sup>1</sup>

MicroRNAs (miRs) inhibit protein synthesis by mechanisms that are as yet unresolved<sup>1–11</sup>. We developed a cell-free system from *Drosophila melanogaster* embryos that faithfully recapitulates miR2-mediated translational control by means of the 3' untranslated region of the *D. melanogaster* reaper messenger RNA. Here we show that miR2 inhibits translation initiation without affecting mRNA stability. Surprisingly, miR2 induces the formation of dense (heavier than 80S) miRNPs ('pseudo-polysomes') even when polyribosome formation and 60S ribosomal subunit joining are blocked. An mRNA bearing an ApppG instead of an m<sup>7</sup>GpppG cap structure escapes the miR2-mediated translational block. These results directly show the inhibition of m<sup>7</sup>GpppG cap-mediated translation initiation as the mechanism of miR2 function, and uncover pseudo-polysomal messenger ribonucleoprotein assemblies that may help to explain earlier findings.

MicroRNAs (miRs) represent a large class of gene regulatory molecules that control fundamental cellular processes in animals and plants<sup>10–12</sup>. Computational predictions suggest that miRs regulate up to 30% of all vertebrate genes<sup>13,14</sup>. Regulation by miRs is typically mediated by the formation of imperfect hybrids with 3' untranslated region (UTR) sequences of target mRNAs, inducing translational repression and/or mRNA degradation<sup>6–9,15,16</sup>. miRs, their mRNA targets and RISC (RNA-induced silencing complex) proteins concentrate together with other marker proteins in 'P (processing) bodies', cytoplasmic foci for mRNA degradation and some forms of translational inhibition<sup>6,17,18</sup>.

The mechanism of translational regulation by miRs is a matter of controversy. The *Caenorhabditis elegans* miRs lin-4 and let-7 target mRNAs for translational repression during larval development without displaying differences in polysomal sedimentation profiles, suggesting an inhibitory mechanism that acts after the initiation of translation<sup>4,5</sup>. Similar conclusions were reached from analyses of human cells<sup>1–3</sup>. By contrast, mRNAs initiating translation from an internal ribosomal entry sequence (IRES) rather than the m<sup>7</sup>GpppN cap structure were found to be 'immune' to miR-mediated translational repression in transfected cells<sup>6,7</sup>, implicating translation initiation as the regulated step.

To reconstitute miR function, we developed a cell-free system based on endogenous miR/miRISC and a biologically relevant and validated miR–mRNA interaction. We chose the regulation of *D. melanogaster* reaper mRNA by the miR2/13 family not only for its biological importance and validation by two groups<sup>19,20</sup> but also because miR2 is relatively abundant in *D. melanogaster* embryos<sup>20</sup>. Because miR2a, miR2b and miR2c differ by only one nucleotide, we cannot distinguish between these family members and refer to them collectively as miR2.

Reporter mRNAs with six copies of the reaper mRNA miR2-binding site including 25 nucleotides of native reaper flanking sequences were introduced into the 3' UTR of a firefly luciferase

mRNA bearing a m<sup>7</sup>GpppG cap structure and an A<sub>62</sub> tail (Fig. 1a, FL-WT). An identical mRNA bearing the flanking sequences only and with the miR2-binding sites replaced by *Xba*I sites served as a negative control (Fig. 1a, FL-mut). We validated the FL-WT reporter mRNA by RNA co-transfection with a *Renilla* luciferase transfection efficiency control into *D. melanogaster* Schneider S2 cells expressing miR2 (ref. 21). This analysis showed that the FL-WT mRNA is translated about 3.5-fold less efficiently than the FL-mut reporter (Supplementary Fig. 1a), without differences in mRNA stability (Supplementary Fig. 1b). Using this result as a reference, we adapted a protocol that had previously been used to study the siRNA mechanism in *D. melanogaster* embryo extracts<sup>22</sup>. When we compared the

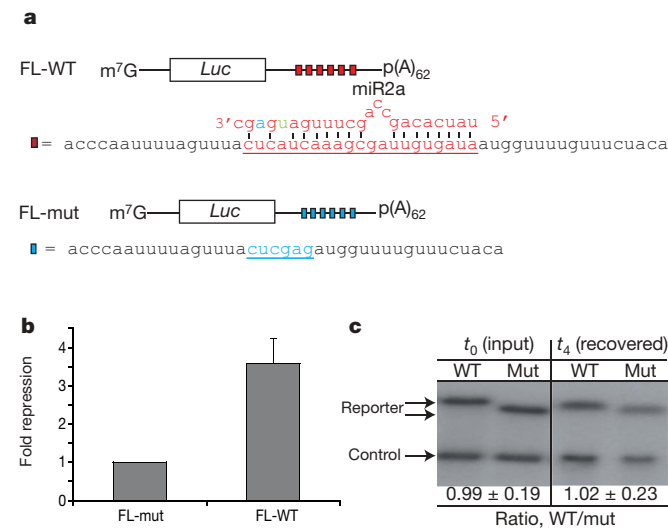


**Figure 1 | Translational repression of a miR2 reporter mRNA in vitro.** **a**, Schematic representation of the FL-WT (2,283 nucleotides) and FL-mut (2,181 nucleotides) mRNAs. The FL-WT miR2-binding site is depicted in red, and the FL-mut motif is in blue. Binding of miR2 to the target sequence is shown in red, and the single letters marked in blue and green are the nucleotides that differ between miR2a and miR2b (green, u to g) or miR2a and miR2c (blue, u to a). **b**, Reporter and control mRNAs were translated *in vitro*. Firefly luciferase values were normalized to the *Renilla* luciferase values. Translational repression by miR2 was calculated by dividing the normalized FL-mut value by the normalized FL-WT value (FL-mut = 1.0). The graph shows means and s.d. from three independent experiments. **c**, Stability of FL-WT and FL-mut mRNAs. Total RNA (including the labelled mRNAs) was isolated before (*t*<sub>0</sub>) and after (*t*<sub>4</sub>) translation and separated by gel electrophoresis. The signal from the firefly luciferase reporter mRNAs was normalized by using the respective intensity from the *Renilla* luciferase (control) mRNA. Below the gel, the normalized FL-WT/FL-mut band intensity ratios are given, and are shown as means ± s.d. Average values from three experiments are shown.

<sup>1</sup>European Molecular Biology Laboratory, Meyerhofstrasse 1, D-69117 Heidelberg, Germany.

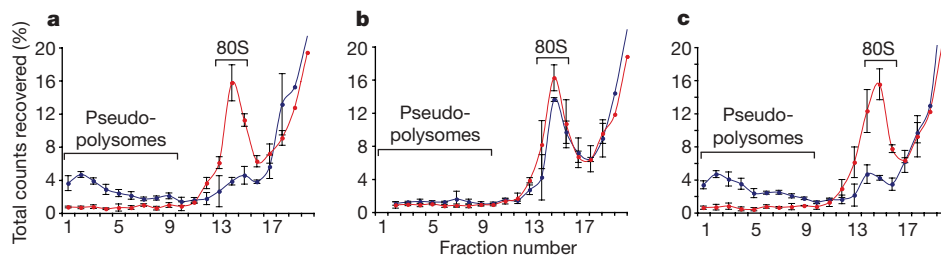


**Figure 2 | miR2 inhibits 80S complex formation and induces heavy mRNP assemblies.** *In vitro* translation reactions containing  $^{32}\text{P}$ -labelled S-ORF-WT (blue lines) and S-ORF mut (red lines) mRNAs were performed in the presence of cycloheximide to inhibit translation elongation and to prevent the formation of polysomes. **a**, Control reactions, no LNA competitor added. **b, c**, Reactions were supplemented with the specific (anti-miR2, **b**) or the

non-specific (anti-let7e, **c**) LNA competitor. The complexes were resolved by sucrose-density-gradient centrifugation (15–45%) and fractions were analysed by scintillation counting. Radioactivity is expressed as percentage of total counts recovered and plotted against the fraction number. Results are means  $\pm$  s.d., calculated from three independent experiments.

FL-WT and FL-mut mRNAs in this system during a 60-min incubation, no differences in translation were observed (data not shown). Because competition by the translation machinery might interfere with the establishment of miR-mediated repression, we explored a preincubation protocol. In *D. melanogaster* embryo extracts, translation is reduced to background levels in reactions lacking creatine phosphate (CrP) (data not shown). After 3 h of preincubation of reporter mRNAs in extracts without CrP (see Methods Summary), fresh extract containing CrP was added and the reporter mRNAs were translated for 1 h. This protocol fully recapitulates the approximately 3.5-fold difference in the translation of the FL-WT reporter compared with the FL-mut reporter mRNAs found in transfected cells (Fig. 1b). Re-extraction of the mRNAs and analysis by gel electrophoresis show that both FL-WT and the slightly shorter FL-mut mRNAs have identical stabilities (Fig. 1c). As seen for miR-mediated regulation *in vivo*, translational repression increases with the number of miR2-binding sites *in vitro* (Supplementary Fig. 2).

Next, the role of miR2 was addressed by competition assays (Supplementary Fig. 3), using small RNA transcripts (lacking an ORF) of the miR2-binding sites and the *Xba*I mutant sequences present in FL-WT (WT-comp) and FL-mut (mut-comp), respectively (Supplementary Fig. 3a). Specific competition with the WT-comp RNA completely relieves the translational inhibition of the FL-WT reporter, whereas the mut-comp RNA does not affect repression (Supplementary Fig. 3a). We also used antisense locked nucleic acid (LNA) oligonucleotides to inactivate miR2 by the formation of stable LNA-miR hybrids<sup>23</sup>. Whereas the LNA oligonucleotide targeting the FL-WT reporter, the reporter remains repressed after the addition of the anti-let7e control oligonucleotide (Supplementary Fig. 3b). The LNA anti-miRs do not affect the stability of the mRNAs (Supplementary Fig. 3c). Thus, the *D. melanogaster* embryo cell-free system specifically recapitulates miR2-mediated translational inhibition by means of the reaper 3' UTR-binding sites.

We next performed sucrose gradient analysis to test whether miR2 affects the formation of translation initiation complexes. Because

mRNA length critically affects the resolution of translation complexes in sucrose gradient analyses<sup>24</sup>, we created variants of FL-WT and FL-mut with a short ORF<sup>25</sup> (Supplementary Fig. 4a). Cycloheximide, an inhibitor of translation elongation that allows initiation and 80S ribosome assembly, was added to the extract before the reporter mRNAs and was present throughout the experiment, preventing the formation of polyribosomes (see Supplementary Figs 4b and 5a, for example). As expected, ribosomal 80S complexes assemble efficiently on S-ORF-mut mRNA. By contrast, 80S formation is strongly reduced on the S-ORF-WT mRNA (Supplementary Fig. 4a). The decrease in 80S formation on S-ORF-WT mRNA is dependent on miR2, because 80S complexes assemble when miR2 is sequestered by the anti-miR2 LNA (Supplementary Fig. 4). An unusually high fraction (about 50%) of the S-ORF-WT mRNA pellets when 80S formation is repressed by miR2, in contrast with less than 20% of the S-ORF-mut or the S-ORF-WT mRNA under non-repressive conditions (Supplementary Table 1). After the sucrose density gradient had been changed to a concentration range used to resolve polyribosomes, the 80S peak of the S-ORF-mut mRNA shifted to fractions 12–16 (Fig. 2). No additional peaks formed further towards the bottom of the gradient (fractions 1–11), showing that cycloheximide fully blocks polyribosome formation. The S-ORF-WT mRNA that is repressed by miR2 sediments as dense messenger ribonucleoprotein particles (mRNPs) (heavier than 80S) (Fig. 2a). When miR2 is blocked by the anti-miR2 LNA (Fig. 2b), 80S formation is restored and dense mRNP formation is suppressed, which is not seen with the anti-let7e LNA oligonucleotide (Fig. 2c). These data show that miR-induced repression causes the formation of non-polysomal mRNPs that sediment together with polysomes. We refer to these assemblies as 'pseudo-polysomes'.

The inhibition of 80S complex formation indicates that miR2-mediated repression targets translation initiation, although the data are also consistent with the completion of 80S assembly and subsequent sequestration into pseudo-polysomes. To distinguish between these possibilities, we performed sucrose-density-gradient

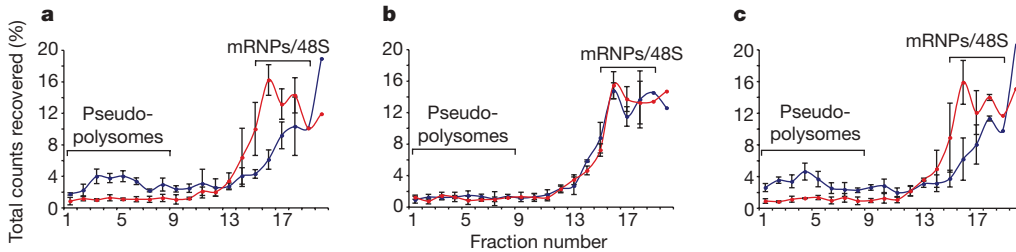


**Figure 3 | miR2 induces the formation of heavy mRNP assemblies even when 60S ribosomal subunit joining is blocked.** *In vitro* translation reactions containing  $^{32}\text{P}$ -labelled S-ORF-WT (blue lines) and S-ORF mut (red lines) mRNAs were performed in the presence of GMP-PNP and cycloheximide. **a**, Control reactions, no LNA competitor added.

**b, c**, Reactions were supplemented with the specific (anti-miR2, **b**) or the non-specific (anti-let7e, **c**) LNA competitor. Reactions were analysed by sucrose-density-gradient centrifugation (15–45%). Results are means  $\pm$  s.d., calculated from three independent experiments.

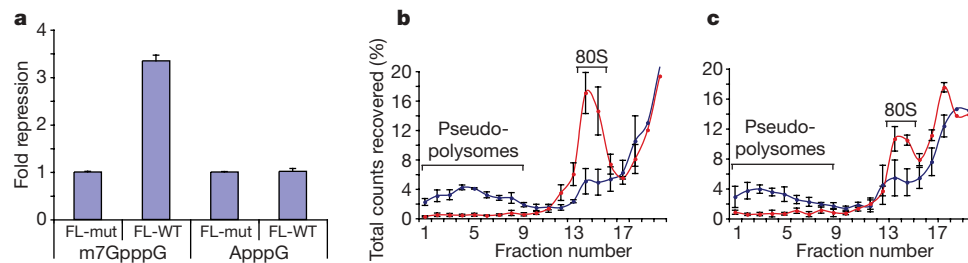


**Figure 4 | The m<sup>7</sup>GpppN cap structure is essential for miR2-mediated translational repression but not for the formation of 'pseudo-polysomes'.** **a**, Firefly luciferase reporter mRNAs bearing an m<sup>7</sup>GpppG cap (left) or an ApppG cap (right) were analysed as described in the legend to Fig. 1. The absolute translational activity of the ApppG-capped mRNAs was about

3.5-fold (about 70%) lower than the m<sup>7</sup>GpppG-capped mRNAs. **b, c**, m<sup>7</sup>G-capped (**b**) and A-capped (**c**) mRNAs were analysed by sucrose-density-gradient analysis (15–45%). Blue lines, S-ORF-WT; red lines, S-ORF mut. Results are means  $\pm$  s.d., calculated from three independent experiments.

analyses of translation initiation complexes forming in the presence of GMP-PNP, a non-hydrolysable GTP analogue that inhibits joining of the 60S ribosomal subunit<sup>26,27</sup>. In the presence of GMP-PNP, 48S complexes form with the S-ORF-mut mRNA, whereas it is strongly reduced on the S-ORF-WT reporter when miR2 represses translation (Supplementary Fig. 5a, c) unless miR2 is sequestered by the anti-miR LNA (Supplementary Fig. 5b). Again, a large fraction of the repressed mRNA pellets through 5–25% sucrose density gradients (Supplementary Table 2), indicating that pseudo-polysomes might form even when 60S joining is inhibited. This hypothesis was directly confirmed with 15–45% sucrose density gradients (Fig. 3). Thus, miR2 inhibits 48S complex formation, and the assembly of pseudo-polysomes is independent of the formation of an 80S ribosomal complex.

Consistent with their non-ribosomal nature is the fact that pseudo-polysomes form even in the presence of the polysome-disrupting agent puromycin (Supplementary Fig. 6b). By contrast, they are sensitive to EDTA (Supplementary Fig. 6c), showing that both pseudo-polysomes and polysomes are metal-stabilized, non-covalent complexes.

When our S-ORF-WT reporter mRNA was added to the extract, miR2 specifically shifted from the lighter fractions into pseudo-polysomes, indicating that miR2 is a component of the pseudo-polysomes (Supplementary Fig. 7).

Transfection experiments had indicated that the m<sup>7</sup>GpppN cap structure is a target for miR-mediated repression<sup>6,7</sup>. To assess the role of the cap structure directly in both translational inhibition and pseudo-polysome formation, we synthesized the reporter mRNAs with either an m<sup>7</sup>GpppG or an ApppG cap structure, which cannot mediate cap-dependent translation initiation. Translation from the A-capped mRNA was resistant to miR2-mediated repression (Fig. 4a), whereas the physiologically capped FL-WT mRNA was repressed by miR2, as seen previously.

To investigate the relationship between translational inhibition and pseudo-polysome formation, m<sup>7</sup>G- and A-capped versions of the mRNAs were incubated with cycloheximide and analysed on sucrose density gradients (Fig. 4b, c). Consistent with the reduced translational efficiency of A-capped mRNAs, the efficiency of 80S complex formation on the A-capped mRNA was reduced in comparison with the m<sup>7</sup>G-capped variant (Fig. 4b, c). High-density miRNPs also form on A-capped mRNAs bearing miR2-binding sites (Fig. 4c). Thus, the presence of 3' UTR miR2-binding sites suffices for pseudo-polysome formation but not for translational inhibition. Although these experiments directly identify the inhibition of m<sup>7</sup>GpppN cap-dependent translation initiation as the mechanism of miR2 function, they do not formally exclude the possibility that miR2 may act through additional mechanisms. Translational control has been recognized to employ fail-safe mechanisms in some cases, such as the regulation of *msl-2* mRNA by Sex-lethal<sup>28</sup> or of *oskar* mRNA by Bruno<sup>29</sup>. If additional mechanisms exist, they have to be consistent with the lack of inhibition of the ApppG-capped mRNA.

Previous studies reached contradictory conclusions about the mechanism of miR function<sup>1,4,6,7</sup>. We show that miR2 inhibits translation initiation without changes in mRNA stability. Our experiments uncover dense miR-mRNA assemblies (pseudo-polysomes) that have the sedimentation characteristics of polysomes but form under conditions of effectively blocked 60S ribosomal subunit joining and blocked translation elongation. With the use of the approach described here, it should be feasible to examine other *D. melanogaster* miRs with different mRNA targets. Application of our protocol may also help to establish *in vitro* systems for other species.

How does miR2 inhibit translation initiation, and how does this relate to pseudo-polysome formation? Our data show that pseudo-polysome formation is not sufficient for translational inhibition, because pseudo-polysomes form with ApppG-capped S-ORF-WT mRNA that is not repressed (Fig. 4c). We propose that miR2-induced pseudo-polysome formation causes inhibition only when translation initiates by means of the physiological cap structure (Supplementary Fig. 8). Pseudo-polysomes may represent a biochemical counterpart of P-bodies<sup>18</sup>, which have not yet been characterized biochemically. Their sensitivity to EDTA and their continued formation in the presence of puromycin (Supplementary Fig. 6) is fully consistent with this interesting possibility. Although pseudo-polysomes may represent precursors of the repressed mRNPs, their formation may not be necessary for inhibition. Alternatively, miR binding to the 3' UTR may repress translation before repressed mRNAs assemble into pseudo-polysomes. The association of miR-regulated mRNAs with 'polysomes' is a major argument supporting miR interference with translation after initiation. The discovery of pseudo-polysomes sheds new light on this issue and offers an alternative interpretation for at least some 'polysome-associated' mRNAs.

## METHODS SUMMARY

**Plasmids and general techniques.** Detailed information on the cloning of plasmids, synthesis of reporter mRNAs, *in vitro* translation reactions and sucrose-density-gradient analysis is provided in Methods.

**Investigation of miR function in *D. melanogaster* embryo extract.** *D. melanogaster* embryo cell-free translation extracts were prepared by modifying a published protocol for RNA interference<sup>22</sup>, which is described in detail in Methods. *In vitro* translations of the FL-reporter mRNAs were performed in a reaction volume of 10  $\mu$ l. Reactions were assembled on ice and contained 50% (v/v) embryo extract, 10% lysis buffer (v/v), 100  $\mu$ M amino acid mix (complete), 10  $\mu$ g ml<sup>-1</sup> creatine phosphokinase, 0.5 mM ATP, 0.1 mM GTP, 0.01 U  $\mu$ l<sup>-1</sup> RNasin (Promega) and 10 mM creatine phosphate (where indicated). The final concentration of potassium acetate was adjusted to 100 mM. Where indicated, 134 fmol of competitor RNAs or 134 fmol of anti-miR LNA oligonucleotides was added.

After a 10-min preincubation step at 25 °C, 6.7 fmol of either of the firefly luciferase mRNA reporters (FL-WT and FL-mut) was incubated together with 2 fmol of *Renilla* luciferase control mRNA in a reaction lacking creatine phosphate for 60 min at 25 °C. Subsequently, the reaction containing the reporter mRNAs was mixed with an equal volume of a fresh reaction lacking reporter mRNAs and creatine phosphate and half of the reaction was discarded. The remainder was again incubated for 60 min at 25 °C and this entire procedure

was repeated one more time. After a total preincubation time of 3 h, the reaction was added to a fresh reaction mixture containing creatine phosphate, half of the reaction was discarded, and the sample was incubated for 1 h at 25 °C. During this procedure, the mRNAs underwent an eightfold dilution. The reaction was quenched with Passive Lysis Buffer (Promega), and luciferase activity was determined with the Dual-Luciferase Assay System (Promega). Synthetic LNA oligonucleotides complementary to *D. melanogaster* miR2 and human let7e were purchased from Exiqon.

**Full Methods** and any associated references are available in the online version of the paper at [www.nature.com/nature](http://www.nature.com/nature).

Received 7 November 2006; accepted 26 April 2007.

Published online 16 May 2007.

1. Petersen, C. P., Bordeleau, M. E., Pelletier, J. & Sharp, P. A. Short RNAs repress translation after initiation in mammalian cells. *Mol. Cell* **21**, 533–542 (2006).
2. Nottrott, S., Simard, M. J. & Richter, J. D. Human let-7a miRNA blocks protein production on actively translating polyribosomes. *Nature Struct. Mol. Biol.* **13**, 1108–1114 (2006).
3. Maroney, P. A., Yu, Y., Fisher, J. & Nilsen, T. W. Evidence that microRNAs are associated with translating messenger RNAs in human cells. *Nature Struct. Mol. Biol.* **13**, 1102–1107 (2006).
4. Olsen, P. H. & Ambros, V. The lin-4 regulatory RNA controls developmental timing in *Caenorhabditis elegans* by blocking LIN-14 protein synthesis after the initiation of translation. *Dev. Biol.* **216**, 671–680 (1999).
5. Seggerson, K., Tang, L. & Moss, E. G. Two genetic circuits repress the *Caenorhabditis elegans* heterochronic gene *lin-28* after translation initiation. *Dev. Biol.* **243**, 215–225 (2002).
6. Pillai, R. S. *et al.* Inhibition of translational initiation by Let-7 MicroRNA in human cells. *Science* **309**, 1573–1576 (2005).
7. Humphreys, D. T., Westman, B. J., Martin, D. I. & Preiss, T. MicroRNAs control translation initiation by inhibiting eukaryotic initiation factor 4E/cap and poly(A) tail function. *Proc. Natl Acad. Sci. USA* **102**, 16961–16966 (2005).
8. Wu, L., Fan, J. & Belasco, J. G. MicroRNAs direct rapid deadenylation of mRNA. *Proc. Natl Acad. Sci. USA* **103**, 4034–4039 (2006).
9. Bagga, S. *et al.* Regulation by let-7 and lin-4 miRNAs results in target mRNA degradation. *Cell* **122**, 553–563 (2005).
10. Bartel, D. P. MicroRNAs: genomics, biogenesis, mechanism, and function. *Cell* **116**, 281–297 (2004).
11. Ambros, V. The functions of animal microRNAs. *Nature* **431**, 350–355 (2004).
12. Baulcombe, D. RNA silencing in plants. *Nature* **431**, 356–363 (2004).
13. Lewis, B. P., Burge, C. B. & Bartel, D. P. Conserved seed pairing, often flanked by adenines, indicates that thousands of human genes are microRNA targets. *Cell* **120**, 15–20 (2005).
14. Xie, X. *et al.* Systematic discovery of regulatory motifs in human promoters and 3' UTRs by comparison of several mammals. *Nature* **434**, 338–345 (2005).
15. Lim, L. P. *et al.* Microarray analysis shows that some microRNAs downregulate large numbers of target mRNAs. *Nature* **433**, 769–773 (2005).
16. Yekta, S., Shih, I. H. & Bartel, D. P. MicroRNA-directed cleavage of HOXB8 mRNA. *Science* **304**, 594–596 (2004).
17. Sen, G. L. & Blau, H. M. Argonaute 2/RISC resides in sites of mammalian mRNA decay known as cytoplasmic bodies. *Nature Cell Biol.* **7**, 633–636 (2005).
18. Liu, J., Valencia-Sanchez, M. A., Hannon, G. J. & Parker, R. MicroRNA-dependent localization of targeted mRNAs to mammalian P-bodies. *Nature Cell Biol.* **7**, 719–723 (2005).
19. Stark, A., Brennecke, J., Russell, R. B. & Cohen, S. M. Identification of *Drosophila* MicroRNA targets. *PLoS Biol.* **1**, 397–409 (2003).
20. Leaman, D. *et al.* Antisense-mediated depletion reveals essential and specific functions of microRNAs in *Drosophila* development. *Cell* **121**, 1097–1108 (2005).
21. Lagos-Quintana, M., Rauhut, R., Lendeckel, W. & Tuschl, T. Identification of novel genes coding for small expressed RNAs. *Science* **294**, 853–858 (2001).
22. Tuschl, T., Zamore, P. D., Lehmann, R., Bartel, D. P. & Sharp, P. A. Targeted mRNA degradation by double-stranded RNA *in vitro*. *Genes Dev.* **13**, 3191–3197 (1999).
23. Lecellier, C. H. *et al.* A cellular microRNA mediates antiviral defense in human cells. *Science* **308**, 557–560 (2005).
24. Gray, N. K. & Hentze, M. W. Iron regulatory protein prevents binding of the 43S translation pre-initiation complex to ferritin and eALAS mRNAs. *EMBO J.* **13**, 3882–3891 (1994).
25. Gebauer, F., Grskovic, M. & Hentze, M. W. *Drosophila* sex-lethal inhibits the stable association of the 40S ribosomal subunit with msl-2 mRNA. *Mol. Cell* **11**, 1397–1404 (2003).
26. Hershey, J. W. & Monro, R. E. A competitive inhibitor of the GTP reaction in protein synthesis. *J. Mol. Biol.* **18**, 68–76 (1966).
27. Anthony, D. D. & Merrick, W. C. Analysis of 40 S and 80 S complexes with mRNA as measured by sucrose density gradients and primer extension inhibition. *J. Biol. Chem.* **267**, 1554–1562 (1992).
28. Beckmann, K., Grskovic, M., Gebauer, F. & Hentze, M. W. A dual inhibitory mechanism restricts msl-2 mRNA translation for dosage compensation in *Drosophila*. *Cell* **122**, 529–540 (2005).
29. Chekulaeva, M., Hentze, M. W. & Ephrussi, A. Bruno acts as a dual repressor of oskar translation, promoting mRNA oligomerization and formation of silencing particles. *Cell* **124**, 521–533 (2006).

**Supplementary Information** is linked to the online version of the paper at [www.nature.com/nature](http://www.nature.com/nature).

**Acknowledgements** We thank S. Cohen and J. Brennecke for advice, and R. Jackson and the members of the Hentze laboratory for discussions. This work was supported by a grant from the Deutsche Forschungsgemeinschaft to M.W.H.

**Author Contributions** R.T. performed the experiments. R.T. and M.W.H. designed, analysed and interpreted the experiments and wrote the paper.

**Author Information** Reprints and permissions information is available at [www.nature.com/reprints](http://www.nature.com/reprints). The authors declare no competing financial interests. Correspondence and requests for materials should be addressed to M.W.H. (hentze@embl.de).

## METHODS

**Plasmids.** The plasmids FL-WT and FL-mut were obtained by insertion of a *Hind*III restriction site into the 3' UTR of the plasmid 'no IRES'<sup>30</sup>, at position 3900 by oligonucleotide-directed mutagenesis with primers t3A-mut-sense and t3A-mut-asense (see below), generating plasmid t3A-*Hind*III. The miR2-binding site of *Drosophila melanogaster* reaper mRNA including 25 nucleotides flanking the sequence on either site (Fig. 1a) was obtained by amplification with the polymerase chain reaction (PCR) from a plasmid containing the reaper 3' UTR<sup>19</sup>, using primers Reap-WT-sense and Reap-WT-asense. This PCR fragment was digested with *Spel*-*Hind*III and subsequently cloned into the *Spel*-*Hind*III sites of t3A-*Hind*III, generating FL-WT-1x. Repeated insertion of *Bam*HI-*Hind*III-digested PCR fragments into *Bgl*II-*Hind*III digested FL-WT-1x generated the plasmid FL-WT after five rounds of cloning, which had six miR2-binding sites in its 3' UTR. Plasmid FL-mut was generated by overlap-extension PCR with primers Reap-mut-sense and Reap-mut-asense, resulting in a PCR fragment containing a *Xhol* recognition sequence plus a 25-nucleotide reaper 3' UTR flanking sequence (Fig. 1a). This fragment was subcloned and multimerized into the *Spel*-*Hind*III sites of t3A-*Hind*III as described for FL-WT. To generate plasmids S-ORF-WT and S-ORF-mut, the firefly luciferase ORF was replaced by a short ORF of 180 nucleotides<sup>25</sup>. This was achieved by PCR amplification of the short ORF from the plasmid BmS(EF)m (ref. 28) using primers S-ORF-sense and S-ORF-asense. A *Kpn*I-*Spel* fragment of FL-WT and FL-mut, which contains the firefly luciferase ORF, was replaced by the S-ORF PCR fragment to yield plasmids S-ORF-WT and S-ORF-mut (Supplementary Fig. 2a). The plasmids WT-comp and mut-comp were obtained by removing the 5' UTR and firefly luciferase ORF of the plasmids FL-WT and FL-mut by digestion with *Kpn*I-*Spel*, followed by treatment with Klenow polymerase and religation. The *Renilla* luciferase control plasmid was made by the digestion of pRL-null (Promega) with *Xba*I-*Bam*HI, and the subsequent insertion of an 880-base-pair *Xba*I-*Bam*HI fragment containing a 98-nucleotide poly(A) tail from pIRE.CAT-A98 (ref. 31). All plasmids were verified by DNA sequencing. For *in vitro* transcription, the plasmids FL-WT, FL-mut, S-ORF-WT and S-ORF-mut were linearized with *Eco*I-*II*, the plasmids WT-comp and mut-comp were linearized with *Hind*III, and the *Renilla* luciferase control plasmid was linearized with *Bam*HI.

[ $\alpha$ -<sup>32</sup>P]UTP-labelled RNAs were synthesized as described<sup>30</sup> except that the 3'-O-Me-m<sup>7</sup>GpppG cap (New England Biolabs) was used instead of an m<sup>7</sup>GpppG cap. Where indicated, an ApppG cap was used instead of a 3'-O-Me-m<sup>7</sup>GpppG cap.

**Preparation of *D. melanogaster* embryo extract.** Cell-free translation extracts from *D. melanogaster* embryos were prepared by using a modified procedure based on a published protocol for RNA interference<sup>22</sup>. Embryos 0–16 h old from the Oregon R strain of *D. melanogaster* were collected, washed with tap water, transferred to a glass cylinder containing freshly prepared ice-cold EW buffer (0.7% NaCl, 0.04% Triton X-100) and sedimented by gravity. This procedure was repeated twice, using fresh ice-cold EW buffer each time. Embryos were dechorionated for 3 min in 260 ml of ice-cold EW buffer containing 3% sodium hypochlorite, with vigorous agitation. After transfer to sieves, embryos were washed with ice-cold water for 5–10 min, transferred to a glass cylinder containing freshly prepared ice-cold lysis buffer (100 mM potassium acetate, 30 mM HEPES-KOH pH 7.4, 2 mM magnesium acetate, 5 mM dithiothreitol (DTT)) and settled by gravity. Floating (dead) embryos were eliminated by suction, and the embryos were washed twice with ice-cold lysis buffer. The embryos were then resuspended in an equal volume (with respect to the settled embryos) of ice-cold lysis buffer plus 1  $\times$  complete protease inhibitor (Roche). The embryo-containing suspension was transferred to a chilled Potter-Elvehjem homogenizer and lysed at 4 °C by 15–20 strokes (1,200 r.p.m.). The lysate was centrifuged for 25 min at 14,500 g and 4 °C, and the clear aqueous interphase was adjusted to a final concentration of 10% glycerol. Aliquots were flash-frozen in liquid nitrogen and stored at –80 °C.

**Sucrose-density-gradient analysis.** Translation initiation intermediates were assembled on <sup>32</sup>P-labelled mRNAs in 50- $\mu$ l *in vitro* translation reactions containing either 1 mM cycloheximide (80S), 1 mM puromycin, 30 mM EDTA or 1 mM cycloheximide and 5 mM GMP-PNP (48S)<sup>32</sup>. Samples containing 33.5 fmol of mRNA were preincubated without creatine phosphate for 3 h as described above (Methods summary) and finally incubated for 30 min in the presence of creatine phosphate. Cycloheximide (80S), puromycin, EDTA or cycloheximide and GMP-PNP (48S) were present throughout the whole procedure. The samples were then diluted 1:1 with ice-cold sucrose gradient buffer (24 mM HEPES-KOH pH 7.4, 100 mM potassium acetate, 2 mM magnesium acetate, 1 mM DTT) and loaded on top of 5–25% or 15–45% linear sucrose gradients. The gradients were centrifuged in a SW 55Ti rotor (Beckman) for 83 min at 45,000 r.p.m. (5–25% sucrose gradients) or for 136 min at 28,500 r.p.m. (15–45% sucrose gradients), fractionated from the bottom of the gradient and analysed by scintillation

counting. Where indicated, 670 fmol of competitor RNAs or 670 fmol of anti-miR LNA oligonucleotides (Exiqon) were present from the beginning.

**miRNA Northern blots.** Translation initiation reactions in the presence of cycloheximide were performed as described above except that 100.5 fmol of mRNA was used per 50- $\mu$ l reaction. Translation initiation intermediates were analysed by sucrose gradient analysis as described above. Gradients were fractionated from the bottom and fractions were combined for subsequent mRNA isolation as follows: fractions 1–7 (pseudo-polysomes, P), fractions 8–14 (middle, M) and fractions 15–20 (top, T). Total RNA from the pooled gradient fractions was isolated by using Trizol reagent (Invitrogen). Northern blots were performed as described<sup>33</sup> with miRCURY LNA detection probes (Exiqon) against *D. melanogaster* miR2 and miR1.

**Cell culture and RNA transfections.** Schneider 2 cells were maintained at 25 °C in Schneider's Medium (Gibco) supplemented with L-glutamine and penicillin/streptomycin (both from Gibco) and 10% fetal bovine serum (FBS; Invitrogen). RNA transfections were performed with the TransMessenger Transfection Reagent (Qiagen) in accordance with the manufacturer's protocol. Exponentially growing Schneider S2 cells were seeded at a density of  $5 \times 10^5$  cells per well in 24-well plates 24 h before transfection. Cells were transfected with 134 fmol of each of the FL-reporter mRNAs and 100 fmol of the *Renilla* luciferase control mRNA. Cells were lysed after 48 h in 1  $\times$  Passive Lysis Buffer (Promega), and firefly and *Renilla* luciferase activity was determined with the Dual-Luciferase Assay System (Promega).

**Quantitative PCR.** Total RNA from transfected cells was prepared with Trizol in accordance with the manufacturer's protocol. For RT-PCR analysis, RNA was treated with RNase-free DNase RQ1 (Promega). DNase-treated RNA (4  $\mu$ g) was reverse-transcribed with (dT)<sub>20</sub> primers and Superscript III Reverse Transcriptase (Invitrogen) in accordance with the manufacturer's protocol. After 20-fold dilution in water, 5  $\mu$ l of each of these samples was used for quantitative PCR (qPCR) using primers Firefly-sense, Firefly-asense, Renilla-sense and Renilla-asense. qPCR was performed with the SYBR Green PCR Master Mix (Applied Biosystems) on an ABI PRISM 7500 instrument (Applied Biosystems). We performed an identical reaction without reverse transcriptase to confirm the RNA dependence of the synthesized cDNAs.

**Primers.** The following primers were used: t3A-mut-sense, 5'-CCACTAGTTC-TAGAGCGGAAGCTTCCGCCACCGCGGTGG-3'; t3A-mut-asense, 5'-CCACCGCGGTGGCGGAAGCTTCCGCTCTAGAACTAGTGG-3'; Reap-WT-sense, 5'-TTTACTAGTGCAGCCGCGATCCACAAACACCCACCCAATTAGTAC-TAC-3'; Reap-WT-asense, 5'-TTTAAGCTTGTGACAGATCTGCTTTTT-GTAGAAACAAACATTATC-3'; Reap-mut-sense, 5'-TTTACTAGTGTGCG-GCCGCGGATCCACAAACACCCACCCAATTAGTAC-TCTCGAGATGTT-TTGTTC-3'; Reap-mut-asense, 5'-TTTAAGCTTGTGACAGATCTGCT-TTTTTGAGAAACAAACACTCGAGTAAACAAATTGGG-3'; S-ORF-sense, 5'-TTTGTGACCGACATGGACTACAAAGACGATGACGAC-3'; S-ORF-asense, 5'-TTTACTAGTGGATTACATTTGGACTTCCGCCCTT-CTTGGCC-3'; Firefly-sense, 5'-CCTCTGGATCTACTGGGTTACCTAAG-3'; Firefly-asense, 5'-GAATTTCAGCATATCTGAACCAT-3'; Renilla-sense, 5'-GAATTTCAGCATATCTGAACCAT-3'; Renilla-asense, 5'-GGATTTCAC-GAGGCCATGATAA-3'.

30. Thoma, C. et al. Enhancement of IRES-mediated translation of the c-myc and BiP mRNAs by the poly(A) tail is independent of intact eIF4G and PABP. *Mol. Cell* 15, 925–935 (2004).
31. Preiss, T., Muckenthaler, M. & Hentze, M. W. Poly(A)-tail-promoted translation in yeast: implications for translational control. *RNA* 4, 1321–1331 (1998).
32. Ostareck, D. H. et al. Lipoxygenase mRNA silencing in erythroid differentiation: The 3'UTR regulatory complex controls 60S ribosomal subunit joining. *Cell* 104, 281–290 (2001).
33. Valoczi, A. et al. Sensitive and specific detection of microRNAs by northern blot analysis using LNA-modified oligonucleotide probes. *Nucleic Acids Res.* 32, e175 (2004).

## CORRIGENDUM

doi:10.1038/nature05812

## Pluripotency of mesenchymal stem cells derived from adult marrow

Yuehua Jiang, Balkrishna N. Jahagirdar, R. Lee Reinhardt, Robert E. Schwartz, C. Dirk Keene, Xilma R. Ortiz-Gonzalez, Morayma Reyes, Todd Lenvik, Troy Lund, Mark Blackstad, Jingbo Du, Sara Aldrich, Aaron Lisberg, Walter C. Low, David A. Largaespada & Catherine M. Verfaillie

*Nature* 418, 41–49 (2002); doi:10.1038/nature00870; published online 20 June 2002

In response to questions raised recently about flow cytometry data reported in Fig. 1 of this Article, we had the flow cytometry data for Fig. 1 and the experimental approach used to generate them reviewed by flow cytometry experts.

The flow cytometry data in the original Fig. 1b were found to be flawed in that corresponding IgG isotype control tracings for several of the plots differ by 1 log in fluorescence intensity, even though the same IgG subtype was used. The plots for these antigens (CD19, CD34, Sca-1, Thy-1 and MHC II) in the original Fig. 1b should therefore not be relied upon as an accurate representation of MAPC surface marker profiles. Details of the specific flaws are individually listed as Supplementary Information to this Corrigendum. A corrected version of Fig. 1b is now provided as Fig. 1 below.

The FACS plots in the original Fig. 1b were obtained from the ROSA26 cell line also used for the blastocyst injection studies and the postnatal transplantation in NOD-SCID mice. In Fig. 1 we now provide additional FACS analysis data for these specific antigens from the GFP transduced mouse MAPC line we described in the original Article at population doubling 120 (this line was also used to demonstrate the single-cell origin of endothelium-like, hepatocyte-like and neuroectoderm-like cell differentiation *in vitro*). These data appear not to be subject to the same technical problem. On the basis of this analysis, we have summarized the FACS phenotype of MAPC in Table 1 below. The phenotype of MAPC isolated subsequently and published by our group<sup>1,2</sup> are also not affected by the same flaws in the plots published in the original Article. It should also be noted that

**Table 1 | Cell surface characteristics of MAPC**

Phenotype	The original Article	This Corrigendum*	References 1 and 2
CD45	NEG	NEG	NEG
CD44	NEG	NEG	NEG
MHC I	NEG† (incorrect plot inserted)	NEG	NEG
MHC II	NEG†‡	NEG	NEG
Sca-1	NEG/DIM‡	NEG	NEG
Thy-1	DIM‡	DIM	NEG
c-Kit	NEG	NEG	POS
CD34	NEG‡	NEG	NEG
Flk-1	DIM	DIM	Not tested
SSEA-1	DIM/POS	DIM/POS	Not tested
CD3	NEG	NEG	NEG
Mac-1	NEG	NEG	NEG
CD19	NEG‡	NEG	NEG
CD13	POS	POS	Not tested

\* Corrections based on data provided in Fig. 1.

† The superscripts 'k' in MHC II (I-A<sup>k</sup>) and MHC I (H-2K<sup>k</sup>) should be 'b'.

‡ Erroneous IgG control stains.

NEG, negative; DIM, minimally positive; POS, positive.

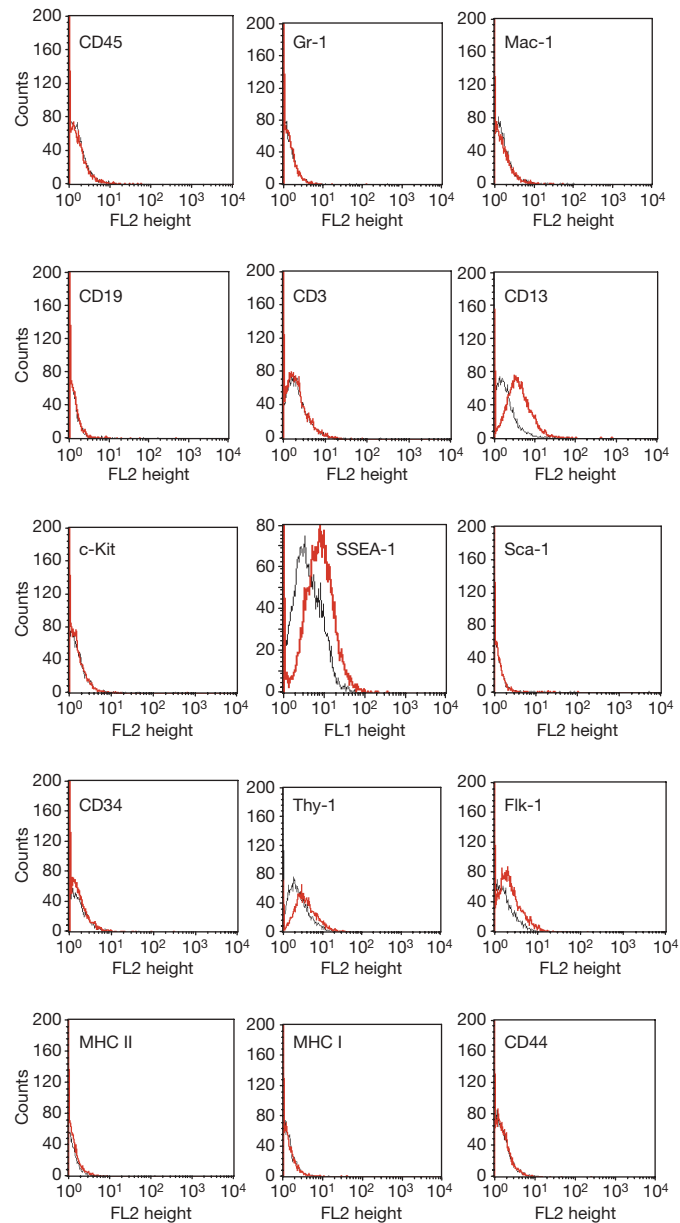


**Figure 1 | This is the corrected version of the original Fig. 1b.** Single cell derived GFP transduced MAPC were collected after 120 population doublings and stained with a PE-coupled antibody against MHC II (I-A<sup>b</sup>) and MHC I (H-2K<sup>b</sup>) (mIgG2a); CD19, and Sca-1 (rIgG2a); Gr-1, Mac-1, CD3, CD44, CD45, Thy-1 and c-Kit (rIgG2b); CD13 (rIgG1); or with an unconjugated IgG2a antibody directed at CD34 or Flk-1 followed by a secondary PE-coupled antibody. For each sample an individual tube of cells was stained with a control IgG antibody of the correct IgG subtype either directly coupled to PE, or followed by a secondary PE-coupled antibody. All antibodies were from Becton Dickinson. For SSEA-1, ROSA26 mouse-derived MAPC were collected after 120 population doublings and stained with an unconjugated anti-SSEA-1 antibody (mIgM, obtained from Iowa Hybridoma Bank) followed by a FITC-coupled secondary antibody. Cells were analysed using a FACSscan (Becton Dickinson). Black line, isotype control; red line, specific antibody stain.

in the original Fig. 1b, the plot for MHC I was a duplication of the FACS plot for Mac-1, although the correct FACS plot acquisition data for MHC I was presented in the original Supplementary Fig. 1 of the original Article.

Although problems with these specific FACS plots (as published in Fig. 1) undermine their utility as markers of the MAPC surface phenotype, the specific errors in these FACS plots do not alter the conclusions of the Article. Nevertheless, we wish to inform other scientists of the problems with these published FACS profiles, and provide an accurate representation of the phenotype of MAPC we described.

We submitted some minor corrections to *Nature* in 2002, but owing to administrative errors by the authors and *Nature* these were not seen through to publication. The three changes requested are as follows.

- (1) In the legend to Fig. 1b, the superscripts 'k' in MHC II ( $I-A^k$ ) and MHC I ( $H-2K^k$ ) should be 'b'.
- (2) In the Methods under 'Differentiation culture and analysis', the concentration of  $10^9$  M dexamethasone should be 0.05  $\mu$ M.
- (3) In the Supplementary Information, the sequence of the primers rex-1 and oct-4 should correctly read as follows. Mrex<sub>a</sub>: aag cgt ttc ctg gat ttc; Mrex<sub>b</sub>: ttt gcg tgg gtt agg atg tg; Moct4<sub>a</sub>: gaa gcc gac aac aat gag aac; Moct4<sub>b</sub>: aca gaa cca tac tcg aac cac a.

1. Serafini, M, et al. Long-term lymphohematopoietic reconstitution from nonhematopoietic cells. *J. Exp. Med.* **129–139**, 129–139 (2007).
2. Breyer, A, et al. Multipotent adult progenitor cell (MAPC) isolation and culture procedures. *Exp. Hematol.* **34**, 1596–1601 (2006).

**Supplementary Information** is linked to the online version of this Corrigendum at [www.nature.com/nature](http://www.nature.com/nature).

# naturejobs

## JOBS OF THE WEEK

**W**hat makes a good mentor? *Naturejobs* often revisits this complex query. On page 791 of this issue, *Nature* presents an in-depth guide for mentors and mentees based on testimonials from the mentees who nominated their mentors for a *Nature*-sponsored award last year. Although anecdotal, the observations and experiences provide ample lessons for fledgling scientists and the scholars who guide them.

The best mentors are lifelong, leaving their doors open, virtual or otherwise, throughout their careers. They're generous with their time and they don't just provide guidance for a project, they offer sage advice about potential career paths. They find fresh ways to present the same techniques and principles. They deftly find a project that suits the mentee, while also investigating why a student might lack passion for their work.

Great mentors have a sympathetic ear. They appreciate that problems can arise as students try to balance family life and research. They know how to inspire discouraged students. Mentors should be unselfish, surrendering their ideas, no strings attached, so that students feel like actual collaborators. Mentors should guide their students but allow them enough independence to devise their own theories. And they reward successes with celebrations — whether a lunch out, a barbecue or a graduation-day cocktail party. The best mentors teach how to evaluate published work, how to write and revise journal papers, and how to ask fellow scientists probing questions about their research. They embrace networking, introducing students to top scientists with an eye towards their career paths.

Taken together, these traits are quite a tall order. Is such a 'super-mentor' out there, a selfless soul who is an expert teacher, life coach and networker-extraordinaire all wrapped into one? It's an élite group, no doubt. But if scientific results are only as good as the scientists who produce them, then becoming a super-mentor is as worthy an aspiration as, say, curing cancer, understanding an ecosystem or identifying the stuff that makes up the Universe.

**Gene Russo, acting editor of *Naturejobs***

### CONTACTS

**Acting Editor:** Gene Russo

**European Head Office, London**  
The Macmillan Building,  
4 Crinan Street,  
London N1 9XW, UK  
Tel: +44 (0) 20 7843 4961  
Fax: +44 (0) 20 7843 4996  
e-mail: [naturejobs@nature.com](mailto:naturejobs@nature.com)

**European Sales Manager:**  
Andy Douglas (4975)  
e-mail: [a.douglas@nature.com](mailto:a.douglas@nature.com)

**Business Development Manager:**  
Amelia Pequignot (4974)  
e-mail: [a.pequignot@nature.com](mailto:a.pequignot@nature.com)

**Natureevents:**  
Claudia Paulsen Young  
(+44 (0) 20 7014 4015)  
e-mail: [c.paulsenyoung@nature.com](mailto:c.paulsenyoung@nature.com)

### France/Switzerland/Belgium:

Muriel Lestringuez (4994)

### Southwest UK/RoW:

Nils Moeller (4953)

### Scandinavia/Spain/Portugal/Italy:

Evelina Rubio-Hakansson (4973)

### Northeast UK/Ireland:

Matthew Ward (+44 (0) 20 7014 4059)

### North Germany/The Netherlands:

Reya Silao (4970)

### South Germany/Austria:

Hildi Rowland (+44 (0) 20 7014 4084)

### Advertising Production Manager:

Stephen Russell

To send materials use London  
address above.

Tel: +44 (0) 20 7843 4816

Fax: +44 (0) 20 7843 4996

e-mail: [naturejobs@nature.com](mailto:naturejobs@nature.com)

### Naturejobs web development:

Tom Hancock

### *Naturejobs* online production:

Jasmine Myer

### US Head Office, New York

75 Varick Street, 9th Floor,

New York, NY 10013-1917

Tel: +1 800 989 7718

Fax: +1 800 989 7103

e-mail: [naturejobs@natureny.com](mailto:naturejobs@natureny.com)

### US Sales Manager:

Peter Bless

### Japan Head Office, Tokyo

Chiyoda Building,

2-37 Ichigaya-tamachi,

Shinjuku-ku, Tokyo 162-0843

Tel: +81 3 3267 8751

Fax: +81 3 3267 8746

### Asia-Pacific Sales Manager:

Ayako Watanabe

Tel: +81-3-3267-8765

e-mail: [a.watanabe@natureasia.com](mailto:a.watanabe@natureasia.com)

# MOVERS

**John Mather, chief scientist, Science Mission Directorate, NASA, Washington DC**



**1995–present:** Study scientist and senior project scientist, James Webb Space Telescope

**1993–present:** Senior astrophysicist and Goddard fellow, NASA Goddard Space Flight Center, Greenbelt, Maryland

**1990–93:** Head, infrared astrophysics branch, NASA Goddard Space Flight Center, Greenbelt, Maryland

NASA, beset with morale problems and criticized by some in the research community for its focus on human spaceflight over scientific research, has made a significant gesture by appointing John Mather as its chief scientist. "Elevating John to this position makes clear that NASA highly values science," says Michael Hauser, deputy director at the Space Telescope Science Institute in Baltimore, Maryland. "His impact in astrophysics has been profound."

Mather came to astronomy by accident early in his career. It was elementary particle physics that excited him as a graduate student. But then he came across a dissertation project to experimentally validate the Big Bang theory. A 1974 NASA funding opportunity for explorer satellites provided the opportunity to test it in space. Still a postdoc, Mather assembled a team and wrote a winning proposal.

Mather hadn't expected to embark on a 33-year career at NASA — he had imagined becoming a professor — but that was before the space programme had a higher profile and funding boom. At NASA, he has had the same responsibility all his career: leading science projects.

At Goddard Space Flight Center he oversaw the Cosmic Background Explorer (COBE) satellite, designed to measure the diffuse infrared and microwave radiation from the early Universe. "We were in the technological Dark Ages," he says. There was no precedent for the project. "Pocket calculators were brand new."

At the January 1990 American Astronomical Society meeting Mather showed that the COBE observations agreed exquisitely with the Big Bang theory — which allowed physicists to better understand how galaxies formed in the Universe. His former NASA colleague, retired astronomer Nancy Boggess, remembers the standing ovation that followed. The work won Mather the Nobel Prize in Physics last year.

After the success of COBE, Mather went on to help design and implement the James Webb Space Telescope, which is set to launch in 2013. It will unfold in space and orbit more than a million kilometres from Earth.

Overcoming the immense technological hurdles involved in building the biggest-ever space telescope sparked his interest in other NASA projects — an asset in his new role as NASA's chief scientist.

"NASA hasn't had, in my estimation, a good chief scientist since the 1990s," says Boggess. "John will be the kind of anchor that NASA administrators will listen to." ■

**Virginia Gewin**

# BRICKS & MORTAR

## Southern light

Australian science will get a major boost with the opening of the country's first synchrotron in July. The Australian Synchrotron, a Aus\$207-million (US\$169-million) platform that accelerates electrons to nearly the speed of light, will be in Clayton, Victoria, home to Monash University.

It's a third-generation, 3-giga-electronvolt (medium energy) light source, the largest in the Southern Hemisphere. "A technologically healthy country without a synchrotron to train its young researchers and to provide state-of-the-art facilities for its forefront industries will unavoidably fall behind," says Daniel Häusermann, a Swiss physicist who was recruited to design one of the beamlines.

"Some of the animal models for lung-disease studies are genetically modified organisms, and it is extremely difficult if not impossible to carry out this work overseas," says Karen Siu, a lecturer at Monash University who studies lung diseases, including cystic fibrosis. She will use the synchrotron to develop phase-contrast X-ray imaging to diagnose disease and reveal the efficacy of gene therapy for cystic fibrosis.

The Australian Synchrotron has the capacity for more than 30 beamlines.

Nine have been proposed, and five have already been installed, including ones for high-throughput protein crystallography, powder diffraction, X-ray absorption spectroscopy, soft X-ray spectroscopy and infrared spectroscopy. Forensic sciences, drug design, radiation therapy and studies of oocyte maturation for *in vitro* fertilization are among scientists' applications for the light source.

A 150-metre-long medical imaging beamline will be used for imaging studies and therapy. It will deliver more precise and effective radiation therapies and detect cancers near the single-cell stage. "If you have a better understanding of how the tumour develops, you can understand the mechanisms and develop better drugs," says Häusermann. A new biomedical imaging development centre will be located nearby.

Scientists from around the world have been recruited, including Mark Tobin, from Britain's Synchrotron Radiation Source at Daresbury.

The platform has been funded by universities, research bodies, five Australian states and the government of New Zealand. The Australian government has promised Aus\$50 million over the facility's first five years of operation. ■

**Hannah Hoag**

## POSTDOC JOURNAL

# What kind of difference?

A few weeks ago, I was fortunate to attend a guest lecture given by the world-renowned physician and anthropologist Paul Farmer, someone who has improved the lives of multitudes in underdeveloped regions through clinical, academic, advocacy and charitable activities.

Hearing from someone who is changing the lives of those with whom they live and work is inspiring. Many of the questions and comments from the audience after the lecture made it abundantly clear that he has numerous admirers.

Having written of the allure of making a difference in my first journal entry, the lecture led me to ponder the nature of the difference I hope to make. Is the abstract awareness that I've contributed to the sum total of human knowledge going to be enough? Or is there something about improving the lot of a fellow human being directly — through medicine, counselling or other activities of the 'helping professions' — that promises an unmatched level of satisfaction?

Scientific knowledge and understanding help us to help others. Indeed, Farmer urged us to continue the research that has underscored so many of the improvements in public health seen around the world. However, the absence of a human face can disconnect us from the reality of those who endure the diseases we study. Awakening to this reality may well change our lives. ■

**Peter Jordan** is a visiting fellow at the National Institute of Diabetes and Digestive and Kidney Diseases in Bethesda, Maryland.

The inside track from academia and industry

# The time is ripe

With pharmaceutical companies outsourcing drug testing, jobs in clinical research are growing fast.



Mike Mortimer

If you are considering a career in clinical research, your timing could not be better. Pharmaceutical companies are increasingly opting to outsource clinical testing of potential new drugs. This shift is fuelling massive growth among the contract research organizations (CROs) engaged in doing the work — a trend that seems likely to continue for some time.

Pharmaceutical companies are under increasing pressure to develop blockbuster drugs quickly and at the lowest possible cost, while fending off challenges from manufacturers producing generic versions of drugs that have come off patent. Clinical studies typically account for nearly half of the billion-dollar cost of developing a drug, so companies are now tending to engage CROs to run the trials in order to maximize investment by reducing the time required to develop and bring a new drug to market.

A 2006 Goldman Sachs report concluded that the CRO industry is expected to grow at an annual rate of 13% through to 2010, while biotech and pharma spending on drug development is expected to grow at an annual rate of only 11.1% for the same period — suggesting that the role of CROs is expanding in size and importance.

This is leading to a growing backlog of trials among some CROs, which translates into a need for more staff. Here at Quintiles

Transnational, for example, we anticipate expanding our workforce by up to 5,000 people over the next five years.

CRO professionals not only need to have a good understanding of science and the pharmaceutical industry, but should also be intellectually inquisitive, individual self-

**"If you are considering a career in clinical research, your timing could not be better."**

starters. A clinical-trial monitor, who often visits investigator sites, may identify ways to improve patient enrolment or assure greater accuracy of data entry, for example. And project managers need to find ways to improve clinical-trial protocols through the use of new technologies.

With CROs proliferating, it is also worth assessing whether your potential employer matches your career aspirations. Seek out a company that will invest in you, support your growth and development, and offer a culture that meshes with your work habits and lifestyle.

Career-development courses at CROs are a good way to build a skill-set for the profession. At Quintiles, for example, our staff have access to more than 150 technical courses and over 2,000 professional-development classes covering various aspects of clinical-trial preparation, planning, conduct, monitoring and management. Courses range from an introduction to clinical research to those on specialist subjects such as human gene therapy.

Career-development courses may also focus on the causes, diagnoses and treatment of specific disorders — useful for clinical-trial monitors, or project managers who need to learn more about a particular disorder or want to specialize in a specific therapeutic area.

A wide range of practical courses is also offered, for would-be project managers, for clinical-trial monitors (in subjects such as drug accountability) and for drug salespersons (in business and accounts management), to name but a few.

Training courses take place through Webcasts, CD or DVD, teleconferences, online, and on site with clinical-research associates. Web-based teleconferences also offer distance learning so that staff can listen to others' voices and hear each other's questions.

The growth in CROs is offering opportunities at all levels. Many new hires start out as clinical-research associates, typically with a nursing or life-science background. Within three to five years they can advance to supervisory and then management positions. This dynamic environment means

**"For those with the right educational background, and a willingness to take on cutting-edge clinical science and to learn managerial skills, an engaging and stimulating career awaits."**

companies need to be progressive as employers, offering flexibility and mobility. For instance, employees should be able to work from home; they should be encouraged to move within the company; and, if possible, be given the opportunity to spend time working abroad.

The CRO industry is clearly growing, as are the associated careers opportunities. For those with the right educational background, and a willingness to take on cutting-edge clinical science and to learn managerial skills, an engaging and stimulating career awaits.

**Mike Mortimer** is executive vice-president of global human resources at Quintiles Transnational in Durham, North Carolina.

## Web links

Association of Clinical Research Organizations

► [www.acrohealth.org](http://www.acrohealth.org)

Drug Information Association

► [www.diahome.org](http://www.diahome.org)

Regulatory Affairs Professionals Society

► [www.raps.org](http://www.raps.org)

Project Management Institute

► [www.pmi.org](http://www.pmi.org)